UNIVERSITÉ SORBONNE PARIS CITÉ

Thèse préparée
À l'UNIVERSITÉ PARIS DIDEROT
École doctorale STEP'UP – ED N°560
Laboratoire AIM – UMR 7158
CEA-Saclay, Département d'Astrophysique
Laboratoire de Cosmologie et Évolution des Galaxies

Star and stellar cluster formation in gas-dominated galaxies

par
Jérémy Fensch

Présentée et soutenue publiquement le
28 septembre 2017

Thèse de doctorat de Physique de l'Univers dirigée par
Pierre-Alain Duc

devant un jury composé de :

Isabelle Grenier Professeur (Université Paris Diderot)	Présidente
Dominique Aubert Maître de conférence (Observatoire de Strasbourg)	Rapporteur
Andreas Burkert Professeur (Ludwig Maximilians University, Munich)	Rapporteur
Philippe Amram Professeur (Laboratoire d'astrophysique de Marseille)	Examinateur
Yohan Dubois Chargé de recherche (Institut d'astrophysique de Paris)	Examinateur
Frédéric Bournaud Chercheur (CEA-Saclay)	Invité
Pierre-Alain Duc Directeur de recherche (Observatoire de Strasbourg)	Directeur de thèse

Acknowledgements

Je souhaiterais tout d'abord remercier mon directeur de thèse, Pierre-Alain. Merci pour ta disponibilité et ton encadrement, malgré mon déplacement vers les simulations et ton déplacement à Strasbourg. Merci pour la confiance que tu m'as témoignée et pour tout ce que tu m'as transmis, de ta passion à ta rigueur. Et félicitations pour ton installation à mi-chemin entre Paris et Munich, qui se révelera certainement très pratique pour de futures fructueuses collaborations.

Merci Frédéric pour ton rôle dans cette thèse. Tu aurais pu être mon second superviseur, ce qui m'aurait d'ailleurs évité des questions sur la force de Coriolis en fin de soutenance ;) ... Merci pour ton encadrement, pour ta réactivité surnaturelle aux e-mails – de jour comme de nuit – et pour tout ces moments de physique générale, au tableau blanc, feutre à la main.

Merci Florent, tu fus comme un troisième superviseur. Merci pour le temps et l'énergie que tu m'as consacrés, ainsi qu'à ton intransigeance qui a su me remettre sur le droit chemin et me faire garder la tête froide.

Merci Bilal, pour ces trois années de dur labeur, entre les pauses café/thé/maté et les retours peu glorieux avec la navette du CEA, à refaire le monde dans les bouchons de l'A6. Je te souhaite tout le bonheur pour la suite.

Merci Mathilde G., ma co-bureau, pour toutes ces grandes discussions à bâtons rompus grace auxquelles on a pu transformer notre bureau 272 en trou noir pour la productivité des pauvres innocents passant dans le couloir. Ce fut un réel plaisir de partager ce bureau avec toi et je te souhaite bon courage pour cette dernière année.

Merci Laure pour tout ces précieux moments de détente, pour ton écoute et pour tes conseils avisés. Bon retour à Marseille !

Merci Orianne pour ton aide ces deux premières années et toutes nos discussions, de métaphysique comme de python.

Merci David, Emeric et Emanuele pour nos nombreuses discussions. Merci Mathias pour m'avoir aidé dans ces tracasseries administratives. Merci Anaelle et Sébastien pour tous vos conseils scientifiques. Merci Pierre, Marguerite et Modeste pour tous vos conseils musicaux. Merci Bruno et Damien pour ces magnifiques rendus 3D pour ma soutenance. Merci David pour tes chansons. Merci Max, Rose, Antonello, Shuowen, Emin, Anita, Francesco, Yueh-Ning, Tao, Kyle, Yu-Yen, Maryam, Olivier, Cécile, Linc, Maud et Valeska pour tout ce que nous avons partagé ces dernières années.

Merci Sarah, pour ton soutien durant cette ultime année et en particulier, merci pour ton exil en Laponie pendant la rédaction de ce manuscript.

Merci Mathilde R., Joe, Paupau, Caca, Yoyo et Nico de me supporter de ces glorieuses années lyonnaises jusqu'à ces nuits parisiennes. Déjà neuf années, vous avez du courage...

Merci Alia, Bey, H, Rémi, Amélie, DLDK, Quentin, Flo et Pau pour m'avoir toujours encouragé dans cette voie, de ces années plâtaliques jusqu'à la soutenance.

Merci Marine, Marion et Anais, les Pailloux altiers, de me supporter depuis le lycée. Et merci Simon, indéfectible soutien douteux, depuis ces années communes à la crèche de Lédignan.

Merci Amandine et Julie pour les cours de piano sur le centre du CEA, et un merci spécial à l'inconnu qui a eu la merveilleuse idée de déposer un piano à queue dans l'amphi Galilée.

Merci enfin à mes parents et à mon frère, qui m'ont toujours soutenu, depuis ma naissance à la clinique de l'Étoile...

Contents

Chapter 1

Introduction

1.1 Historical context

The birth of extragalactic astrophysics can be dated from Edwin Hubble's publication in 1929[1] which stated that the famous and long-known Andromeda *spiral nebula*, also known as Messier 31 or M 31 and shown in Fig. 1.1, was located outside of our Milky Way[2] and is a comparable stellar system to our Galaxy, the Milky Way.

This discovery drew to an end a major scientific debate[3], confirming the hypothesis, already raised by Immanuel Kant[4], that our Galaxy is only an *Island Universe* among a multitude of others.

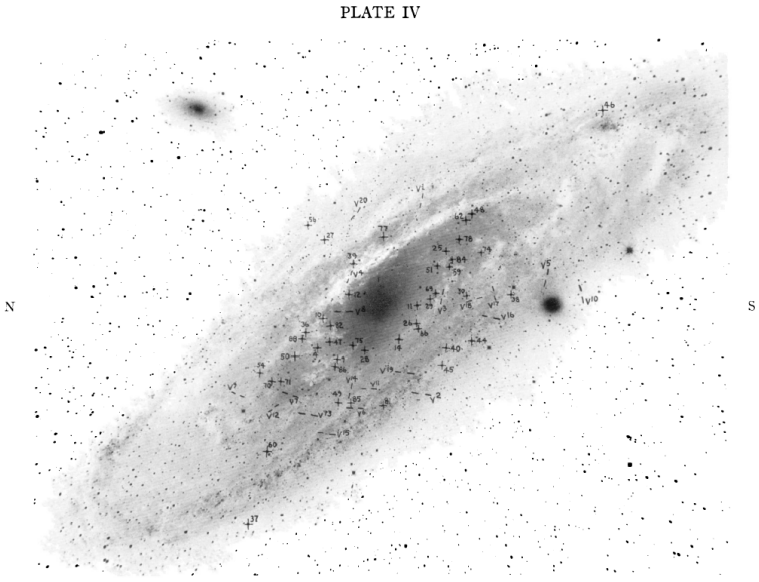

FIGURE 1.1: Plate IV of Hubble (1929). Abridged original caption: MESSIER 31 [...] 24-inch reflector at Yerkes Observatory, September 18, 1901. [...] Novae are indicated by crosses; variables, by lines and V preceding the number.

[1] *A spiral nebula as a stellar system, Messier 31*, Hubble (1929)

[2] Edwin Hubble used Cepheid stars, variable stars whose location are indicated on Fig. 1.1, and whose period of luminosity time variation is linked to their luminosity (Leavitt and Pickering, 1912). Hubble found a distance of 275 kpc which, if greatly underestimated (current estimate is $\simeq$ 783.7 kpc Holland (see e.g. 1998)) was enough to conclude the M31 was not part of our Galaxy.

[3] The *Great Debate* or Shapley-Curtis debate, took place in Smithsonian Museum of Natural History, Washington D.C., in 1920.

[4] *Allgemeine Naturgeschichte und Theorie des Himmels, Part I*, Kant (1755)

Since Hubble's pioneer works on galaxies, our vision of the Universe has been challenged several times. The discovery of the *cosmic microwave background* in 1961 by Penzias and Wilson (shared Nobel Prize in 1978) confirmed the Big Bang theory – still pretty much controversial in the fifties. The presence of a non-baryonic form of matter, which dominates over the classically known form of matter and is called *dark matter*, has been inferred from a number of different probes, from the rotation curves of galaxies (Rubin, Thonnard, and Ford, 1978) to the power spectrum of the cosmic microwave background (Planck Collaboration, 2016). Measurements of distance and recession velocities of distant galaxies by Riess et al. (1998) and Perlmutter et al. (1999) (Nobel Prize in 2011) confirmed the exponential expansion the Universe and the presence of an *dark energy* which remains of an unknown origin.

To quote Alexandre Koyré[5], we went from a static and eternal *closed world* in a lonely island Universe, to an *infinite universe*, with a finite history, undergoing exponential expansion, and from which we know $\simeq 5\%$ of the energy budget. And all this in less than a century.

1.2 This thesis

In this thesis we will be concerned with these mere $\simeq 5\%$, of which, let's admit it, much remains to be understood. The problem we will be interested in is star formation in gas-dominated galaxies.

This question arises from two major interrogations in the current understanding of star and stellar cluster formation across cosmic time, which can be simplified in these terms:

- The currently accepted cosmological model, studied through cosmological simulations, does not reproduce the observed cosmic rate of star formation: simulations form their stars too soon in the history of the Universe. It might be that our formalism for the conversion of gas to star is too efficient, at a time where galaxies were gas-dominated.
- The origin of very massive and old star clusters around galaxies, the so-called globular clusters, is not yet clearly understood. Gas-dominated galaxies might be their birth place.

The following chapter will introduce the terms in which these two problems can be accurately quantified. The third chapter will describe the numerical code that I used during the thesis. I will focus on the numerical limitation on the treatment of gas. In chapters 4 and 5, I will describe the different projects I led to investigate the dynamics, ionization processes and stellar cluster formation in gas-dominated galaxy. I will end this thesis with a conclusion on the role of the gas mass fraction and a presentation of the future prospects I plan to investigate in the coming years.

[5] *From the Closed World to the Infinite Universe*, Baltimore, The Johns Hopkins University Press, 1957. Koyré used these terms to describe the transition between Aristotle's and Newton's cosmological models. If not outshining the breakthrough in scientific history performed by Galileo, Kepler and Newton, I think that the scientific advances in cosmology of the XX*th* century have had a significant impact on the popular view of our Universe and, I am convinced, some influence on the advent of modern philosophical movements.

Chapter 2

Astrophysical gas in a cosmological context

In this chapter, I will present the cosmological context of our studies. I will present the typology of gas-dominated galaxies over cosmic time and describe the mechanisms of gas disk instabilities. In the fourth and fifth subsections, I will give details the star and stellar cluster formation in galaxies and I will finish this introduction with a short presentation of the impact of galaxy interactions and fusions.

2.1 Gas in the ΛCDM model

According to the ΛCDM cosmological model – which is our reference model in this thesis – our Universe is composed of:

- **Dark energy (Λ):** First introduced by Einstein in 1917 for an incorrect reason[1], dark energy is now used to explain the accelerated expansion of the Universe, probed by the redshifted spectrum of distant galaxies (Riess et al., 1998; Perlmutter et al., 1999). Dark energy acts like a negative pressure fluid with constant density. Therefore, its abundance in the expanding Universe grows with time and now reaches 69.4% of the energy budget of the Universe (Planck Collaboration, 2016).

- **Dark matter:** Form of matter which only interacts gravitationally. Its nature is yet unknown, although its contribution to the energy budget reaches 25.8% (Planck Collaboration, 2016) which makes dark matter five times more abundant than ordinary matter in the Universe. First introduced by Zwicky in 1933 to explain the velocity dispersion of galaxies in the Coma galaxy cluster(Zwicky, 1933), dark matter could also explain simultaneously the flatness of galaxy rotation curves (Rubin, Thonnard, and Ford, 1978) and the power spectrum of inhomogeneities in the cosmic microwave background.

- **Baryonic matter:** Ordinary matter, which makes up stars, planets and astrophysical gas. Most of it is composed of hydrogen ($\simeq 75\%$), and helium ($\simeq 25\%$), formed during the Big Bang nucleosynthesis. Heavier elements, that are called *metals* in the astrophysical community, compose about 0.03% of the baryonic mass budget and are formed during the stellar and explosive nucleosynthesis.

[1] Einstein added a constant Λ in its equation of General Relativity to stabilize the solution of a static Universe, in which he believed. He called it the *biggest blunder of [his] life*. See *Kosmologische Betrachtungen zur allgemeinen Relativitätstheorie*, Einstein (1917)

The currently accepted Big Bang scenario in the ΛCDM cosmological model states that density fluctuations in the initially homogeneous Universe led to the structuration of the Universe into the present cosmic web, traced by the light of galaxies in Fig. 2.1.

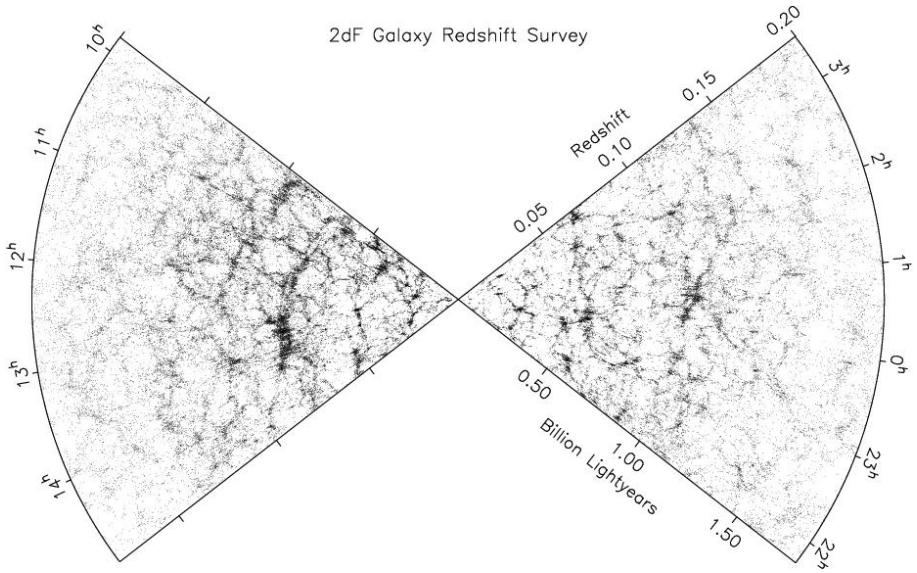

FIGURE 2.1: Position of galaxies around our Galaxy, from (Colless et al., 2001). We can see a structuration along a kind of web pattern, with bright knots and walls. The spatial scale is indicated by both the luminosity distance and the redshift from the expansion of the Universe. In the following we will only use the redshift $z = \lambda_{\text{observed}}/\lambda_{\text{emitted}} - 1$.

The ΛCDM model states that the structure of the Universe formed in a *hierarchical* way: as we can see in Fig. 2.2 small structures formed first and bigger structures formed from the merging of smaller ones. This *bottom-up* hierarchical structuration, observationally probed by the early formation of galaxies as compared to bigger scale structures such as galaxy clusters (Zeldovich, Einasto, and Shandarin, 1982; Blumenthal et al., 1984), advocates for the kinematically cold nature of dark matter, and thus the appellation CDM for cold dark matter. Indeed, if dark matter particle where too kinematically hot[2], they would wipe out small variations.

Before recombination, radiation pressure prevents baryonic matter fluctuation to grow. Therefore only dark matter fluctuation may lead to a gravitational collapse on scales larger than the Jeans' scale (see section 2.3.1). However, as dark matter interacting only gravitationally it cannot dissipate its kinetic energy. The collapsing matter will form a *halo* at hydrostatic equilibrium. This equilibrium verifies the virial condition:

$$2K + W = 0 \tag{2.1}$$

K is the kinetic energy of the halo, given by $K = \frac{1}{2}M\sigma^2$, with M and σ the mass and velocity dispersion of the halo. W is the gravitational energy, which depends on

[2]Precisely, relativistic at the time of matter-radiation equality, z $\simeq$ 3000.

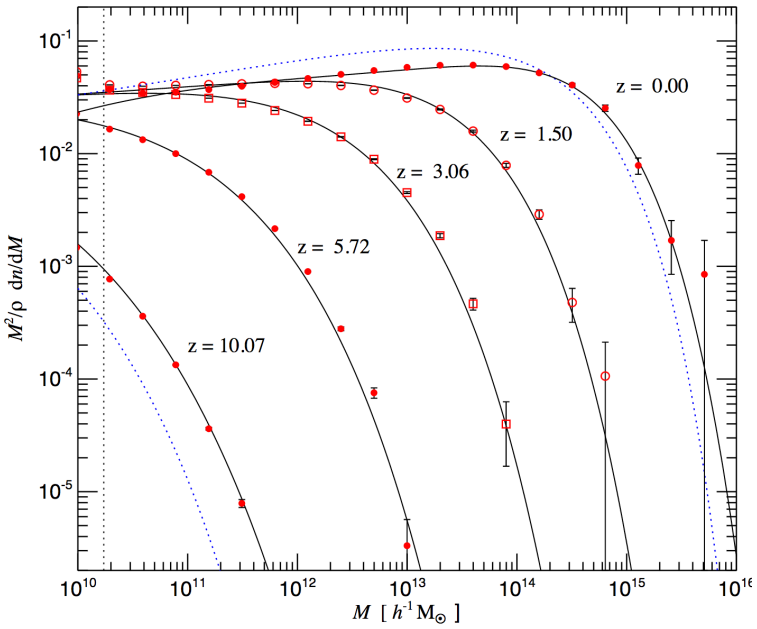

FIGURE 2.2: Differential dark matter halo number density as a function of mass and redshift from the Millennium simulation Springel et al. (2005). We see that less massive haloes are formed earlier.

the density radial profile $\rho(r)$: $W = -4\pi \mathrm{G} \int_0^\infty \rho(r) M r dr$.

After recombination, baryonic matter fluctuations grow to match the dark matter fluctuations.

2.1.1 Spherical gas accretion

Let's consider a spherical cloud of gas associated with a collapsing dark matter halo. This gas falls onto the dark matter halo at a supersonic speed and, gas being having a collisional nature, an accretion shock forms between infalling gas and the gas structure which has already collapsed, typically at the virial radius of the halo. This shock will heat the gas to the virial temperature of the halo, typically several 10^5 to 10^6 K. However, gas also radiates energy away along several channels, according to its temperature:

- **T > 10^7 K:** Gas is close to be completely ionized. Cooling is dominated by emission from electron-ion interaction. This is called *Bremsstrahlung*.
- **10^4<T<10^7 K:** Gas is mostly neutral. Atoms are collisionally excited and electrons radiate energy when decaying to lower energy states.
- **T < 10^4 K:** Gas is neutral. Cooling can occur through de-excitation of rotation or vibrational levels of molecules, and, if metals are present, through the decaying of fine and hyperfine structures.

The amount of energy radiated away per unit volume through these processes is given by:

$$\frac{d\epsilon}{dt} = n_{\mathrm{H}}^2 \Lambda(T, Z) \tag{2.2}$$

where $n_{\rm H}^2$ is the number density of hydrogen atoms and the cooling function, $\Lambda(T, Z)$ is shown in Fig. 2.3 for different metal abundances (given in [Fe/H] units, see BOX 1). We see that the cooling curve depends massively on the presence of metals between 10^4<T<10^7 K and that the cooling curve drops for T < 10^4 K.

BOX 1: Metallicity indicators:

In the literature, and in this thesis, the metallicity can be indicated by one of these definitions:

- **Z:** Z is the mass fraction of elements others than hydrogen, X, and helium, Y. The metallicity of the Sun is $Z_\odot = 0.02$.
- **[Fe/H]:** In stars, the iron abundance can easily be measured from the strength of the Fe absorption lines. One may define their metallicity by [Fe/H] = $\log_{10}(\frac{N_{\rm Fe}}{N_{\rm H}})_{\rm star} - \log_{10}(\frac{N_{\rm Fe}}{N_{\rm H}})_\odot$, with N the number density of the designated atoms. By definition, $[{\rm Fe/H}]_\odot$ = 0. This indicator is often used for stellar structures.
- **12 + $\log_{10}$(O/H):** For interstellar gas, it is easier to measure oxygen abundances through their emission lines. One may define its metallicity through 12 + $\log_{10}$(O/H) = 12 + $\log_{10}(\frac{N_{\rm O}}{N_{\rm H}})$, with $N_{\rm X}$ the abundance of the species X. The Sun has a value of 12+$\log_{10}(\rm O/H)_\odot$ = 8.69 (Asplund et al., 2009).

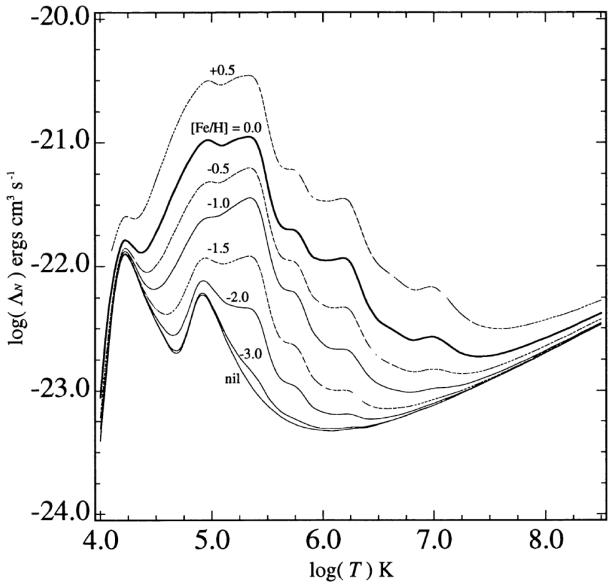

FIGURE 2.3: Cooling curve from Sutherland and Dopita (1993). [Fe/H] = 0 indicates solar metal abundance and [Fe/H] = -1 the tenth of a solar abundance.

If the cooling timescale is shorter than the free-fall time, cooling allows the gas to collapse to the center of the dark matter halo. The cooling time – due to bremsstrahlung, recombination and collisional-excited line emission – and the free-fall time can be written:

$$t_{\rm cool} = \frac{3k_B T}{\rho_{\rm gas}\Lambda(T, Z)} \tag{2.3}$$

$$t_{\rm ff} = \sqrt{\frac{3\pi}{32{\rm G}\rho_{\rm gas}}} \tag{2.4}$$

The locus where $t_{\rm cool} < t_{\rm ff}$ is shown as the area C on the density-temperature plane in Fig. 2.4. Any cloud of gas reaching this locus of the n-T diagram will cool down to 10^4 K and collapse on a free-fall time scale towards the center of the host dark matter halo.

The locus where $t_{\rm cool} > t_{\rm ff}$ is shown as the areas A and B. Clouds in these regions will remain pressure-supported at hydrostatic equilibrium as *hot haloes*: they will radiate and contract quasistaticaly following a line of constant Jeans' mass, shown with dashed lines. Such a trajectory will eventually bring the cloud to the C locus where it will be able to cool down efficiently. However, this process takes a long time: only clouds in the dashed region B, for which $t_{\rm cool} < 10^{10}$ Gyr had time to reach domain C by the current epoch.

The vertical dashed line corresponds to the current minimal over density (5.5 times the current critical density) to be able to collapse by the present time. Clouds to the left are not dense enough to be able to decouple from the Hubble flow. It is interesting to note that all clouds in the mass range 10^{10-12} $M_\odot$ have collapsed by the present time.

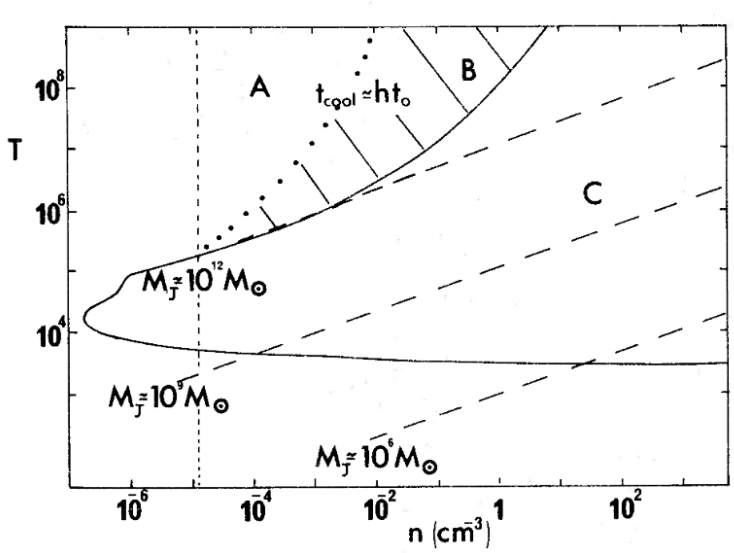

FIGURE 2.4: From Rees and Ostriker (1977). The different regions are described in the text.

Gas clouds allowed to cool will then fall on the center of the halo, and fragment and form stars, which lit the new-born galaxy at the center of the halo.

2.1.2 Two modes of accretion

Birnboim and Dekel (2003) and Kereš et al. (2005) showed that an accretion shock develops only for halo more massive than a threshold mass of $10^{12}{\rm M}_\odot$. We have therefore two types of accretion, summed up on Fig. 2.5:

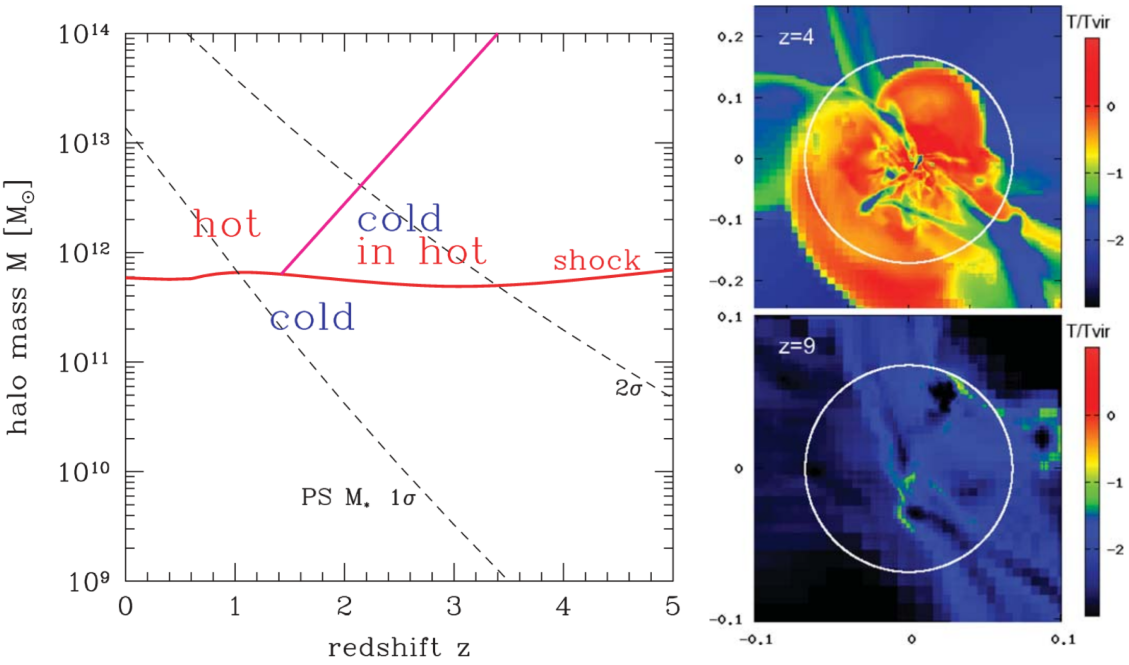

FIGURE 2.5: From Dekel and Birnboim (2006). Right: Locus of the two modes of accretion on the redshift-halo mass plane. The dashed lines show Press and Schechter (1974) estimates of the forming halo masses: the fraction of total mass above the 1σ (resp. $2\ \sigma$), is 22% (resp. 4.7 %). Top right: temperature map in units of the virial temperature from a numerical simulation showing a shock at the virial radius, represented by the white circle, around a galaxy. Some cold flows can still reach the host galaxy. Bottom right: same galaxy seen at higher redshift, and lower mass. Gas accretion occurs without any shock heating.

- **Cold mode accretion:** For halo masses below $10^{12}M_{\odot}$, gas can cool down to 10^4 K reach the center the halo and directly feed the galaxy on a free-fall timescale.
- **Hot mode accretion:** For halo masses above $10^{12}M_{\odot}$, gas is heated at the virial temperature and need to cool radiatively before it can rain down on the galaxy, as described in the previous section. However, for z > 2, filaments are more irregular and present over densities of gas and with a short enough $t_{\rm cool}$ to be able to cool down to the core of the host galaxy.

This process is predicted by several cosmological numerical simulations (Ocvirk, Pichon, and Teyssier, 2008; Dekel et al., 2009) and would explain how galaxies above $z > 2$ can sustain their very high star formation rate (Förster Schreiber et al., 2009). This gas accretion is thought to represent the two third of the galaxy mass growth, the last third coming from the merging from the hierarchical build-up (Kereš et al., 2005; Ocvirk, Pichon, and Teyssier, 2008; Brooks et al., 2009).

2.1.3 Hierarchical build-up

The ΛCDM model claims that big dark matter structures formed from the consecutive merging of smaller structures, as seen in Fig. 2.2 and Fig. 2.6. When two dark

matter haloes merge, their host galaxies interact and will eventually lose kinetic energy through dynamical friction with baryons and dark matter[3] from the other halo (Chandrasekhar, 1943) and eventually merge. Dynamical aspect of galaxy mergers and interactions will be discussed in Section 2.6. This way, small galaxies formed at high redshift merged to form the current massive galaxies.

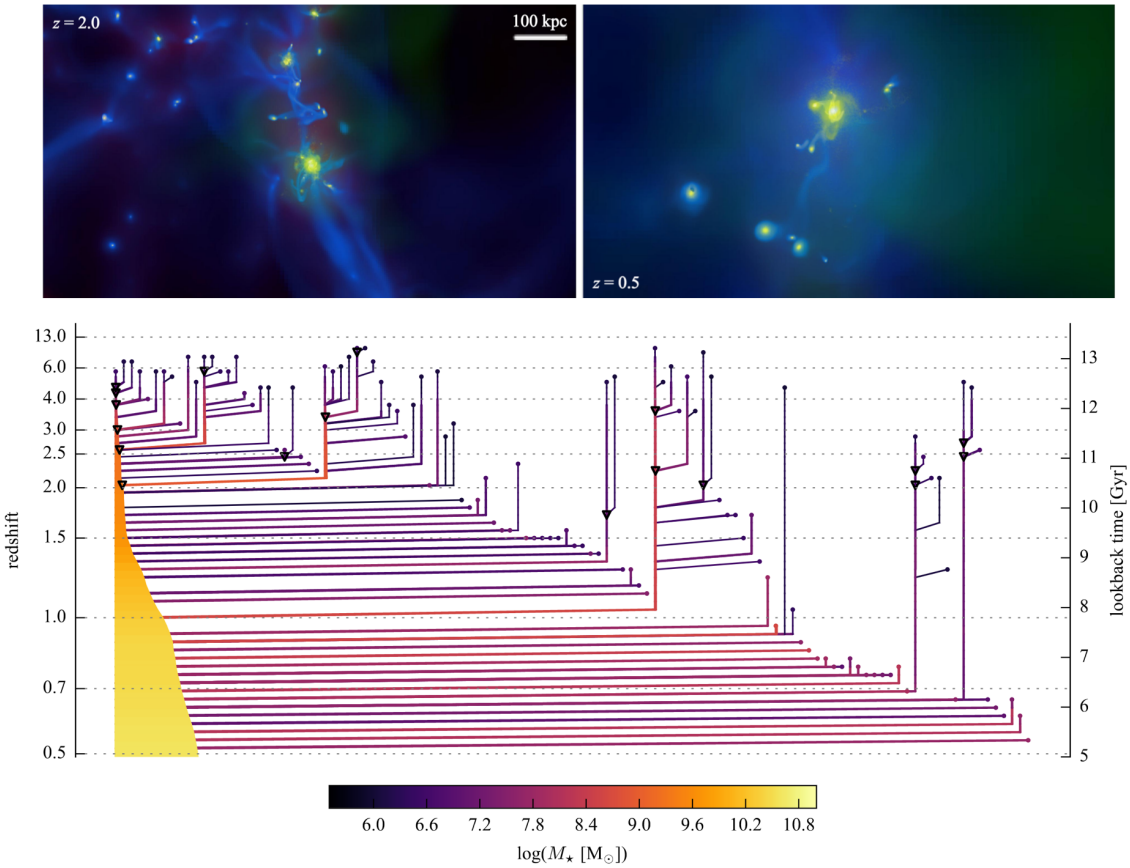

FIGURE 2.6: From Renaud, Agertz, and Gieles (2017). Up: Morphology of simulated neighbourhood of a Milky Way-type galaxy at two epochs, showing the gas density (blue), dark matter (red), stars (yellow) and iron density (green). Bottom: Merger-tree of a Milky Way-type halo. Merger with mass ratio higher than 1:10 are indicated by triangles.

Thereafter a galaxy merger will be called a *major merger* if the mass ratio is higher than 1:3. The merger rate can be obtained from numerical simulations (Hopkins et al., 2010; Rodriguez-Gomez et al., 2015) and by observation of galaxy pairs (Kartaltepe et al., 2007; Lotz et al., 2011). These studies all agree with a galaxy major merger rate increasing with redshift as $\propto (1+z)^{\alpha}$ with $\alpha \simeq 2.5 \pm 0.5$. One should note that the rate of minor merger is much higher: Stewart et al. (2008) showed that only 20% of current Milky-Way type dark matter halo (10^{12}M$_{\odot}$) have experienced a merger with a mass ratio > 0.3 during the last 10 Gyr, when $\simeq 80\%$ have experienced a merger with mass ratio > 0.1 during the same time-lapse.

[3] Alternative theories to dark matter, such as MOND (Milgrom, 1983) have no dynamical friction and therefore predicts a much smaller galaxy merging rate. For the impact of MOND on star formation in interacting galaxies, see Renaud, Famaey, and Kroupa (2016).

One important aspect of the hierarchical mass building through galaxy-galaxy mergers is the morphological transformation. The violent relaxation following a major merger may destroy the disks and form a massive spheroidal merger remnant. If the disks survive, or in the case of minor mergers (Bournaud, Jog, and Combes, 2005), the merger contribute to the formation of a massive stellar spheroidal component, called the bulge.

This process may be the cause of the decrease in cosmic time of the average disk to bulge ratio in galaxies (Bruce et al., 2014). An important consequence, in terms of gas dynamics, is that the presence of a massive central spheroidal component stabilizes the disk of gas against fragmentation and prevent star formation: this will be discussed in details in section 2.3.3.

2.2 Gas in galaxies

2.2.1 Physical Conditions

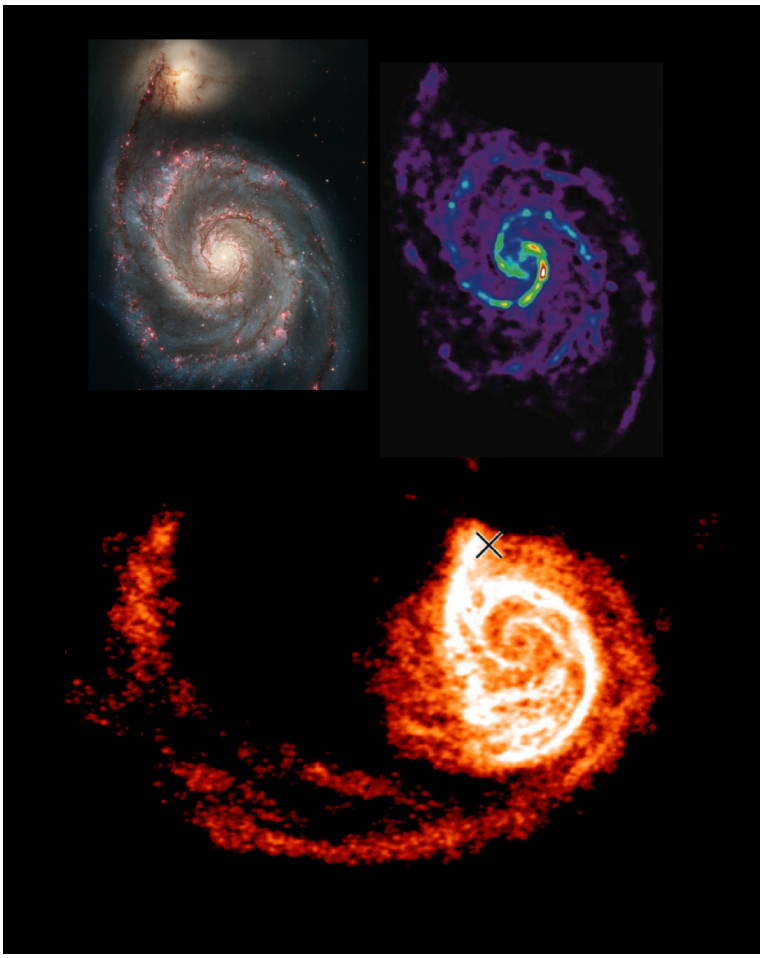

FIGURE 2.7: The local spiral M 51. Top left: optical color image with superimposed H_α emission. From NASA/Hubble. Top right: CO (1-0) map of M 51 (Koda et al., 2011). Bottom: HI emission from the 21 cm line. The scale is smaller than in the top panels in order to see the tidal feature. The companion galaxy is shown with a black cross. (Credits: THINGS collaboration, Sukanya Chakrabarti/UC Berkeley)

One may distinguish several phases of gas in galaxies (Ferrière, 2001):

- **Hot ionized phase:** with T $\simeq 10^6$ K and $n \simeq 10^{-3}$ cm^{-3}. This phase is almost totally ionized and found in the halo of the galaxies. However, we are not interested in this external gas in this thesis, as it is not directly related to star formation. It still remains a hot topic in astrophysics as hot haloes around galaxies may host ≃80% of the baryonic matter of the Universe (Sommer-Larsen, 2006).

- **Warm ionized phase:** with T $\simeq 10^4$ K and $n \simeq 5 \times 10^1$ cm^{-3}. This phase is typically found around massive stars whose UV emission is energetic enough to ionize hydrogen. One can see these regions through the recombinations lines of hydrogen, such as H_α (6563 Å). This H_α emission can be seen for the local spiral M 51 as the pinkish regions in the upper left panel of Fig. 2.7.

- **Neutral medium:** two thermal phases of atomic gas are stable, a warm phase (T$\simeq 10^4$ K and $n \simeq 5 \times 10^1$ cm^{-3}) and a cold phase (T$\simeq 10^2$ K and $n \simeq 20 - 50$ cm^{-3}). These two phases correspond to two cooling mechanisms: cooling through fine structure of metals for the cold phase, cooling through decaying energized electrons lines for the warm phase. Atomic hydrogen can be observed in the radio through the 21-cm line[4]. This phase typically extends well beyond times the stellar radius of spiral galaxies, as we can see for M 51 in the bottom panel of Fig. 2.7, where it shows an extended structure, sign of an interaction with a companion galaxy (see Section 2.6).

- **Molecular medium:** with T $\simeq 10 - 20$ K and $n > 10^2$ cm^{-3}. It is the gas phase in which stars form and is typically located in a thin disk in both ellipticals and spiral galaxies. Molecular hydrogen can only form in optically thick regions, opaque to energetic photons which may easily photo-dissociate the molecule.

  Astrophysicists often use CO emission, shown in the upper right panel of Fig. 2.7 for M 51, to probe this phase, which is translated to H_2 abundance through a conversion factor[5]. This conversion factor, usually called X_{CO}, depends on the environment, such as the metallicity (Genzel et al., 2012), turbulence (Bournaud et al., 2015) and flux of cosmic rays (Bisbas et al., 2017). CO also photo-dissociates more easily than H_2 which leads to some molecular regions being CO dark (Cormier et al., 2014). However, independent measurements of X_{CO} using dust temperature yield consistent results (see e.g. Magnelli et al., 2014).

Most of the the mass of the ISM resides in the cold neutral and molecular phases. The sound speed is typically $c_s \simeq 10$ km s^{-1}at $T = 10^4$ K and decreases with T as $\propto \sqrt{T}$, which brings the sound speed below the typical macroscopic velocity dispersion of the gas, $\sigma = 10$ km s^{-1}at z = 0[6]. This gas is then supersonically turbulent and its density distribution follows a log-normal PDF (see e.g. Nordlund and Padoan, 1999):

$$f_\omega(x) = \frac{1}{x\sqrt{2\omega^2\pi}} \exp\Big(- \frac{\big(\ln(x) - \omega^2/2\big)^2}{2\omega^2} \Big) \tag{2.5}$$

[4]Hyper-fine transition of hydrogen

[5]Direct measurements of H_2 abundance are difficult as it is a symmetric molecule with no permanent electric dipole. It can only by observed in extreme environments (shocks, UV heating) with very high temperatures and therefore do not trace the cold medium anymore. The CO molecule is the most used tracer of H_2.

[6]σ reaches larger values at higher z, see Section 2.2.2.

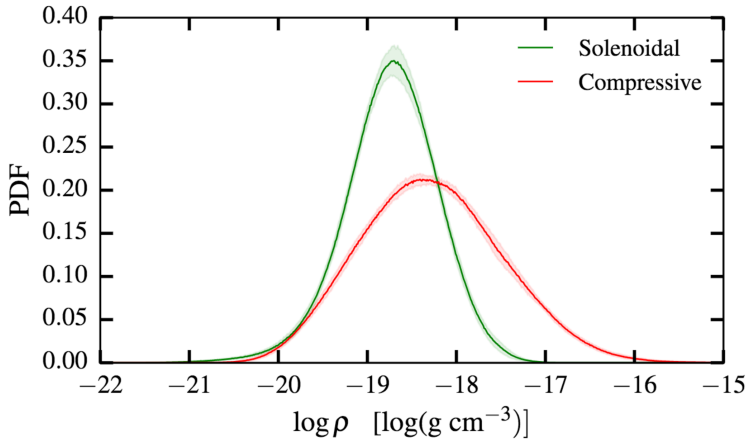

FIGURE 2.8: Gas density PDF of a supersonically turbulent medium in a numerical simulation. The turbulence field was imposed at the beginning to be fully in the compressive mode or solenoidal mode. The PDF are both drawn at the time of the Mach number equal 5.5. (Liptai et al., 2017)

where x is the gas density and ω is a dimensionless width: $\omega^2 \simeq \ln(1 + [1 - 2b/3]^2\mathcal{M}^2)$, with $\mathcal{M} = \sigma/c_s$ the Mach number and b a factor depending on the nature of the turbulence which can be split into a compressive and a solenoidal mode (see Box 2 and Fig. 2.8). $b = 0$ for a purely compressive mode and b = 1 for a purely solenoidal mode (Federrath, Klessen, and Schmidt, 2008; Molina et al., 2012).

BOX 2: Turbulence modes
Helmholtz's theorem states that vector fields in three dimensions can be decomposed by the sum of a curl-free and a divergence-free component.

The velocity dispersion vector field $\vec{\sigma}$ can be decomposed in this way:

$$\vec{\sigma} = \vec{\sigma}_{\rm comp} + \vec{\sigma}_{\rm sol} \tag{2.6}$$

with a curl-free *compressive* mode, $\nabla \times \vec{\sigma}_{\rm comp} = \vec{0}$, and a divergence-free *solenoidal* mode, $\nabla \cdot \vec{\sigma}_{\rm sol} = \vec{0}$.

Compression acts only along the radial dimension, when solenoidal motions are a two-dimensional process. Equipartition is therefore reached, for scales smaller than injection scale and larger than dissipation scale of turbulence, when 1/3 of the turbulent energy is carried by the compressive mode and 2/3 by the solenoidal mode (Federrath et al., 2010).

2.2.2 Gas-dominated galaxies at high-redshift

In the following, the gas mass fraction of a galaxy is defined as $f_{\rm gas} = M_{\rm gas}/(M_{\rm gas} + M_{\rm star})$, with $M_{\rm gas}$ and $M_{\rm star}$ the total gas and stellar mass of the galaxy.

Galaxies in the Local Universe, such as M 51 in Fig. 2.7, are typically stellar-dominated: they have f_{gas} between a few percent for elliptical galaxies to at most 10% for late spirals (Blanton and Moustakas, 2009). One may cite the exception of local dwarf galaxies, which have a higher f_{gas} they will be discussed in Section 2.2.3.

Observations of galaxies at $z > 0$ have shown that $f_{gas}$was a steeply increasing function of redshift: Combes et al. (2013) showed an increase by a factor 3 between $z = 0.2$ and $z < 1$. Above $z = 2$ we can find massive gas-dominated galaxies, whose gas fraction can reach 60% (Daddi et al., 2010b; Tacconi et al., 2010; Tacconi et al., 2013). One should note that we can only probe molecular gas at these redshifts.

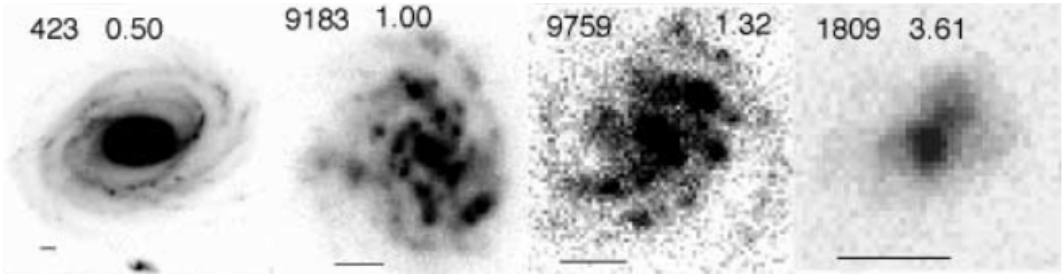

FIGURE 2.9: Typical disk galaxies at different redshifts from the Hubble Ultra-Deep Field (UDF), using the i_{775} filter. The UDF ID is shown on the upper left corner and the redshift is indicated on the upper right corner. The bottom bar shows 1 arcmin. (Elmegreen et al., 2007)

A first striking difference between local and higher redshift galaxies is the morphology. Fig. 2.9, shows the typical morphology of disk galaxies at different redshifts. We see that $z > 1$ galaxies tend to have a disturbed morphology whose light is dominated by bright *clumps* of sizes 100-1000 pc and stellar masses of $10^{7-9}M_{\odot}$(Elmegreen and Elmegreen, 2005). These clumps are quite faint in near-IR, suggesting an age of stellar population typically younger than 200 Myr (Wuyts et al., 2012). Clumpy galaxies are prevalent at redshift between 1 and 3: between 50 to 75% of galaxies at this cosmic time have a disturbed morphology (Elmegreen et al., 2007; Guo et al., 2012; Wuyts et al., 2012) and Huertas-Company et al. (2016) finds that 80% of the stellar mass at $z = 2$ is located in galaxies with disturbed morphology.

Several hypothesis for their origin are still being discussed: clumps might form as the result of internal instabilities (Elmegreen et al., 2007; Dekel, Sari, and Ceverino, 2009), accretion from a clumpy filament (Ceverino et al., 2016), and satellite dwarf galaxies (Conselice, Rajgor, and Myers, 2008). The average young ages (<100 Myr) of the stellar population (Wuyts et al., 2012), the presence of very young clumps (Zanella et al., 2015) and the disk -like velocity profile of clumpy galaxies (Förster Schreiber et al., 2011; Wuyts et al., 2012) suggest that a majority of these clumps are actually formed in-situ. Cosmological simulations showed that around 80% of the clumps are formed inside the host galaxies when 20% are accounted for by the merging of smaller galaxies (Mandelker et al., 2014). Some candidates for accreted dwarfs, characterized by an older age, lower metallicity and deviation from underlying disk velocities can be found (see e.g. Förster Schreiber et al., 2011).

The gas fraction and morphology are not the only difference between low- and high-redshift galaxies. I will here compare these galaxies with their low-redshift

counter-parts.

- **Size:** For the same baryonic mass, high-redshift galaxies are more compact, typically a factor 2 between $z = 2$ and $z = 0$ (van der Wel et al., 2014; Ribeiro et al., 2016). This is likely due to the mass growth at $z < 2$ being dominated by satellite accretion – and mass deposition on the galaxy outskirts – and no more by in-situ star formation (see e.g. van Dokkum et al., 2010).
- **Metallicity:** High-redshift galaxies being observed in their early evolution, their gas is less enriched with metals than local galaxies. Milky-Way type local galaxies have typically a solar metallicity when their $z = 2$ counterparts typically show less than half-solar metallicity (Erb et al., 2006).
- **Rotation curves:** Recent observations have shown that the H_α kinematics of seven $z = 2$ galaxies seem to have a rotation curve dominated by baryons close to their nucleus, which hints for a less important contribution of dark matter to their central kinematics than low-redshift galaxies (Genzel et al., 2017).
- **Gas turbulence:** Velocity dispersion in the gas of high-redshift star forming galaxies have been shown to have an important amplitude, typically 40 km s^{-1} (Förster Schreiber et al., 2009; Stott et al., 2016), which is much higher than typical local disks which show a velocity dispersions of around 10 km s^{-1} (Epinat et al., 2008).

2.2.3 Local analogues of high-z galaxies

If high-redshift galaxies allow us to probe the star formation condition in a very gas-rich environment, their distance prohibits detailed studies with the current observing facilities. One may therefore look for local analogues to these systems to get a more detailed insight into their star formation properties.

The first analogues that may come to one mind are the blue compact dwarf galaxies (BCDGs). These galaxies are typically very gas-rich and turbulent. Their blue color comes from a very recent burst of star formation. One should note that they host a major part of their mass in an old stellar component. However, their low mass prohibits them from keeping the processed material from old stellar activity. Their metallicity is therefore very low: it can go down to 1/40th $Z_\odot$ – a still Universe-wide record – for Zw18, shown in Fig. 2.10. Furthermore, their extended red stellar emission showed that these systems are actually old systems (Loose and Thuan, 1986; Papaderos et al., 1996).

In this thesis I will study another type of dwarf, which can be considered as a better analogue to high-z galaxies: *tidal dwarf galaxies*[7].

Tidal dwarf galaxies (hereafter called TDGs) are gravitationally bound objects of stars and gas formed in the material expelled from the outskirts of an host massive galaxy during an encounter with another massive galaxy. They are typically found in tidal tails, as we can see in Fig. 2.11. I will focus in this subsection on their physical properties, while their formation process will be described in more details in Section 2.6.

[7] For a complete review of these objects, I refer the reader to Duc and Mirabel (1999)

FIGURE 2.10: The most metal-poor galaxy of the Universe, Zwicky 18. Credits: NASA/ESA/Izotov and T. Thuan.

The outskirts of galaxies being dominated by HI gas, TDGs usually contain a relatively small old stellar population, if not at all (Boquien et al., 2007; Boquien et al., 2010). As they are formed from *recycled* matter, their gas is already pre-enriched to about half-solar metallicity (Duc and Mirabel, 1998; Weilbacher, Duc, and Fritze-v. Alvensleben, 2003). They are typically very gas-rich, $f_{gas} > 60\%$ (see e.g. Bournaud et al., 2007), and show a young, 10 to 100 Myr old, stellar population (Duc and Mirabel, 1998; Boquien et al., 2007). They are very turbulent young systems, with $\sigma \sim 40$ km s^{-1} (Lelli et al., 2015). As they are formed in tidally expelled features, they are located in the outskirts of the host galaxy dark matter halo and their kinematics are therefore baryon-dominated (Bournaud et al., 2007; Bournaud and Elmegreen, 2009).

All these characteristics make star formation conditions in TDGs analogous to the conditions in high-redshift clumpy star forming galaxies. Given their mass range of 10^{8-9} M$_\odot$, we will consider that TDGs are analogous to the giant clumps seen in $z = 2$ galaxies.

2.3 Disk Instabilities

Structures in galaxies, such as spiral arms, clumps and giant molecular clouds (GMCs) which will host star formation, arise from disk instabilities. In this section we will review the theory of disk instabilities and, in particular, the effect of the gas fraction.

2.3.1 Jeans instability

Let's first consider instabilities in a homogeneous medium of gas of gas density ρ_0. Instabilities can grow if the internal pressure cannot counter-balance self-gravity, which always happen for a large enough spatial scale. Jeans (1902) first computed the minimum radius for which gravity overcomes pressure and leads to collapse of the encircled region.

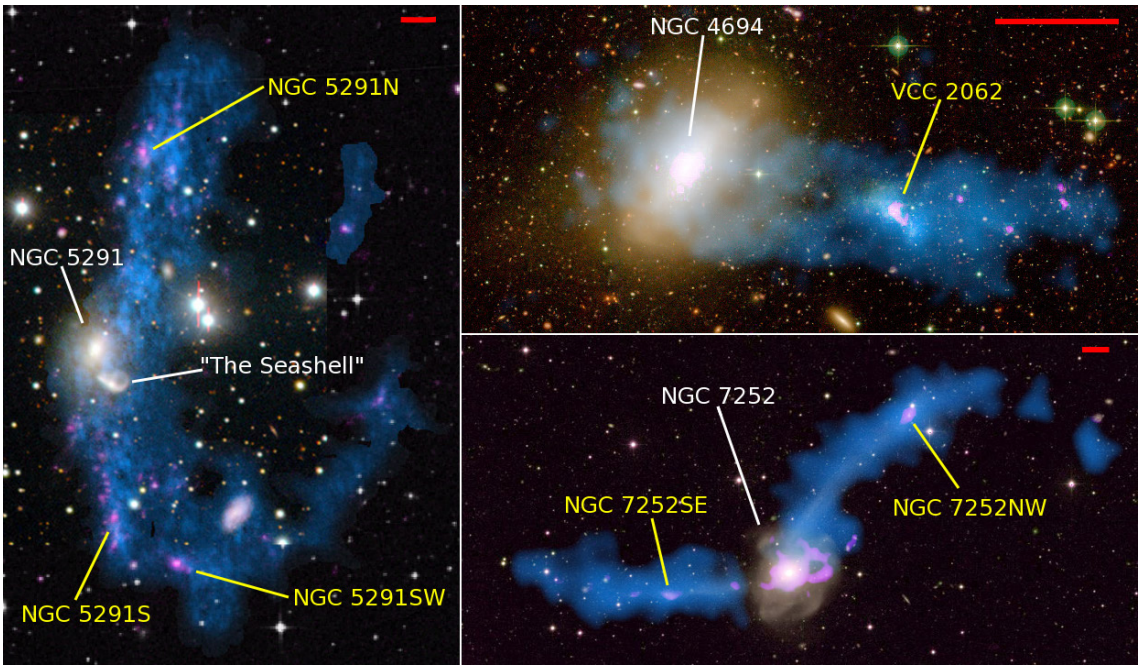

FIGURE 2.11: Interacting systems with TDGs. Far ultraviolet (FUV) emission from GALEX is shown in pink and HI emission is shown in blue. TDGs are indicated by yellow labels. The red bar corresponds to 10 kpc at the assumed distances of these systems. From Lelli et al. (2015).

One way to derive the Jeans instability criterion is to study the propagation of density waves in an homogeneous medium. Let's study a sound wave of the form $\exp[i(\vec{k} \cdot \vec{x} - \omega t)]$ propagating in this medium. If $\Re(-i\omega) > 0$ the perturbation grows exponentially with time, which set the disk instability criterion. One can show that this density wave verifies the following dispersion relation (see e.g. Binney and Tremaine, 2008):

$$\omega^2 = k^2 \, c_s^2 - 4\pi \mathrm{G}\rho_0 \tag{2.7}$$

with c_s the sound speed in the medium, ω the pulsation, and $k = ||\vec{k}||$ the norm of the wavenumber of the sound wave. As all quantities on the right-hand side are real, ω^2 is also real. Therefore, the instability criterion $\Re(-i\omega) > 0$, that is $\omega^2 < 0$, becomes $|k| < \sqrt{4\pi \mathrm{G}\rho_0 / c_s^2} = k_J$.

Thus, wavelengths longer than the *Jeans length* $\lambda_J = 2\pi/k_J$ are subject to gravitational instabilities, that is for:

$$\lambda > \lambda_J = \sqrt{\frac{\pi c_s^2}{\mathrm{G}\rho_0}} \tag{2.8}$$

2.3.2 Toomre instability

Let's now consider an uniformly rotating disk of gas, with constant angular velocity Ω, zero thickness and constant gas surface density Σ_{gas} and sound speed c_s. One can show that sound waves of the form $\exp[i(\vec{k} \cdot \vec{x} - \omega t)]$ propagating in this medium verify the following dispersion relation (see e.g. Binney and Tremaine, 2008):

$$\omega^2 = k^2\, c_s^2 - 2\pi \mathrm{G}\Sigma_{gas}\, |k| + 4\, \Omega^2 \tag{2.9}$$

This dispersion relation is similar to equation 2.7, with a new term referring to the rotation. One may look at equation 2.9 in two extreme cases:

- **No rotation ($\Omega = 0$):** In this case we go back to the Jeans instability case[8]: wavelengths longer than $\lambda = c_s^2/\mathrm{G}\Sigma_{gas}$ are subject to gravitational instabilities.
- **No pressure ($c_s = 0$):** In this case, instabilities arise for wavelengths smaller than $\lambda = \pi^2 \mathrm{G}\Sigma_{gas}/\Omega^2$.

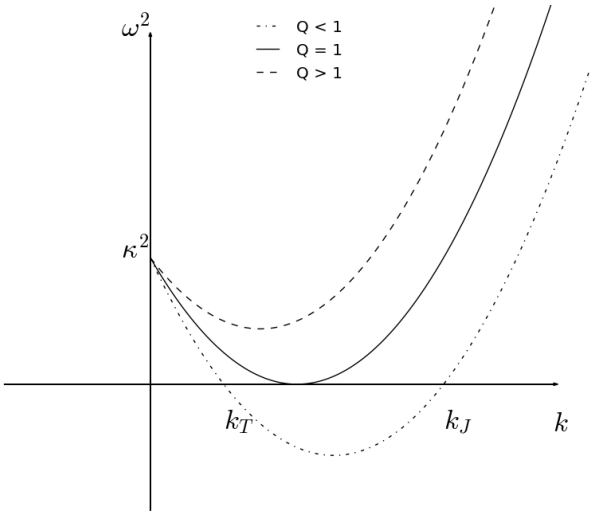

FIGURE 2.12: ω^2 against the wavenumber k for different values of Q. The stability was modified by increasing the gas surface density Σ_{gas}. The two characteristic values k_T and k_J are shown for the $Q < 1$ case. Instability arises for scales such that $k_T < k < k_J$.

Thus, rotation stabilizes the long wavelengths while thermal pressure stabilizes the small wavelengths. In the general case, instabilities arise for $k_T < k < k_J$ where $\omega(k_T) = \omega(k_J) = 0$. The disk is thus stable if no such k exist, that is if these two roots are non-real, or equivalently, if and only if:

$$\frac{2c_s\Omega}{\pi \mathrm{G}\Sigma_{gas}} > 1 \tag{2.10}$$

This criterion is called the *Toomre stability condition* (Toomre, 1964). In local disks, $c_s \sim 10$ km s^{-1}and the thermal pressure is comparable to the turbulent pressure. However, the turbulence in the gas-dominated objects of interest in this thesis, high-redshift disks and TDGs, present a supersonic turbulence, which dominates the pressure term. One may therefore replace c_s by σ_{gas} in Equation 2.11. Furthermore, Ω and Σ_{gas} are both a function of the distance r from the center of the disk. To study

[8]We come back to the previously found Jeans' length if we set $\rho_0 = \Sigma_{gas}/\lambda_J$.

the stability of local patches, one may replacing the angular velocity Ω by $\kappa(r)/2$, with κ the epicyclic frequency[9]. We therefore define the *Toomre parameter* Q as:

$$Q = \frac{\kappa\sigma_{gas}}{\pi \mathrm{G}\Sigma_{gas}} \tag{2.11}$$

where Q, κ, σ_{gas} and Σ_{gas} are function of the distance to the disk center.

The stability threshold of $Q = 1$ should be considered as a rule of thumb (, as one should keep in mind that this formulation is very idealistic, as it assumes a zero thickness, non-dissipative, homogeneous rotating disk,.

2.3.3 Further considerations on disk stability

Additions to the Toomre Analysis

For a more precise analysis of gas-rich disk instability analysis, one should take into account the following considerations:

- **Adding a stellar component:** Toomre (1964) achieved the same analysis than above but for a stellar disk. He found a very similar stability parameter:

$$Q_\star = \frac{\kappa\sigma_\star}{3.36\mathrm{G}\Sigma_\star} \tag{2.12}$$

  where $\sigma_\star$ and $\Sigma_\star$ are the velocity dispersion and the surface density of the stars. Adding the contribution of stars gives the following total stability parameter Q_{total} (Jog and Solomon, 1984; Elmegreen et al., 1995):

$$\frac{1}{Q_{\mathrm{total}}} = \frac{2}{Q_{\mathrm{gas}}}\frac{Rq}{1+q^2R^2} + \frac{2}{Q_\star}\frac{q}{1+q^2} \tag{2.13}$$

  with $R = \sigma_{\mathrm{gas}}/\sigma_\star$ and $q = k\sigma_\star/\kappa$.

  The effect of the gas fraction on the stability can be heuristically illustrated using this full formulation of the Toomre parameter. For simplicity, let's replace the 3.36 with π in the expression of the stellar Toomre parameter. A bit of algebra can lead us to this equivalent formulation for the total Toomre parameter:

$$Q_{\mathrm{total}} = 2\pi \mathrm{G}k\left[\frac{\Sigma_{\mathrm{gas}}}{\kappa^2 + k^2\sigma_{\mathrm{gas}}^2} + \frac{\Sigma_\star}{\kappa^2 + k^2\sigma_\star^2}\right] \tag{2.14}$$

  If one replaces stars from the disk by gas, $\Sigma_\star$ and Σ_{gas} respectively decreases and increases and their sum stays constant. However, the stellar component being kinematically hotter than the gas component, and being unable to cool, $\sigma_\star > \sigma_{\mathrm{gas}}$ and the denominator of the stellar component is higher than the gas component denominator in equation 2.14. Therefore, the decrease of $\Sigma_\star$ is overcompensated by the gaseous component, which results in a decrease of Q_{total} and a destabilization of the disk.

- **Gas dissipation:** Contrary to the stellar component, gas dissipates its kinetic energy. Elmegreen (2011) has shown that this dissipation makes zero thickness

[9] The epicyclic frequency is the frequency at which a radially displaced patch of gas oscillates. It is given by $\kappa(r)^2 = \frac{2\Omega}{r}\frac{d}{dr}(r^2\Omega)$ where r is the radial distance to the center of rotation.

disks unstable for all Q, and moves the stability threshold to $Q = 2-3$ for thick disks.

Self-regulation

The Toomre instability provides the mean for a self-regulation. If mass accumulates enough to drive $Q = \kappa\sigma_{gas}/\pi \mathrm{G}\Sigma_0 < Q_c$, fragmentation will increase σ_{gas} through interaction between fragments and star-formation feedback (see Section 2.4.2). Self-regulation is achieved if this increase in turbulence can increase Q back to the stability threshold.

In the scenario of Dekel, Sari, and Ceverino (2009), if massive bound clumps form in the disk, their interactions can increase the turbulence on timescales smaller than the turbulence decay. They have shown that if around at least 20% of the disk mass is contained in the massive clumps, interactions between clumps are enough to self-regulate the instability in gas-rich galaxies. This is consistent with observations which show that around 10% to 40% of the mass is contained in massive clumps (Elmegreen and Elmegreen, 2005; Elmegreen et al., 2007).

Encounters between the clumps, along with the dynamical friction, lead to a migration of the clumps towards the center, in about 500 Myr. This migration timescale is confirmed by observed radial gradients of age in clumpy galaxies (Förster Schreiber et al., 2011; Guo et al., 2012). This migration can contribute to the formation of a central spheroidal stellar over density, which might become the progenitor of the bulges of local galaxies, in addition to interactions.

Morphological stabilization

The presence of a central spheroidal over density, such as a bulge, impacts the stability criterion. The epicyclic frequency is higher than for a pure disk and stabilizes the disk. This central mass concentration also enhances the galactic tidal field, preventing not dense enough gas to collapse. Bournaud and Elmegreen (2009) have shown that the formation of massive clumps required that almost all stars are located in a disk.

These tow process can stop disk fragmentation and bring to an end the star formation in bulge-dominated galaxies: this process is called *morphological quenching* (Martig et al., 2009).

2.4 Star formation

Gas instabilities described in the last section drive the formation of dense molecular gas structures, which then collapse into smaller cores that eventually become stars.

Star formation at the scale of GMCs is a very active open field of research, much more complicated than the spherical collapse described in the previous section. In this subsection, I will briefly describe the life-cycle of stars, the feedback effect on the galaxy and galaxy-wide star formation scaling relations.

2.4.1 Life cycle of stars

Early stages

In the first collapsed structure, density grows and the Jeans' length decreases. The cloud then further fragments in several sub-fragments whose size equals the local Jeans' length. When the fragment density is high enough to be opaque to the fragment own radiation from gas cooling, the fragmentation stops. When the core temperature is high enough to allow the fusion of hydrogen to be launched, pressure from these thermonuclear reaction compensates the self-gravity of the gas structure. The collapsing cloud reaches hydrostatic equilibrium and can be therefore called a star. The collapse timescale is of the order of a few million years.

A consequence of this process is that young stars form in stellar clusters (Lada and Lada, 2003; Chandar, Fall, and Whitmore, 2015). These clusters do not need to be very massive and can be composed of only a few tens of stars as in Fig. 2.13.

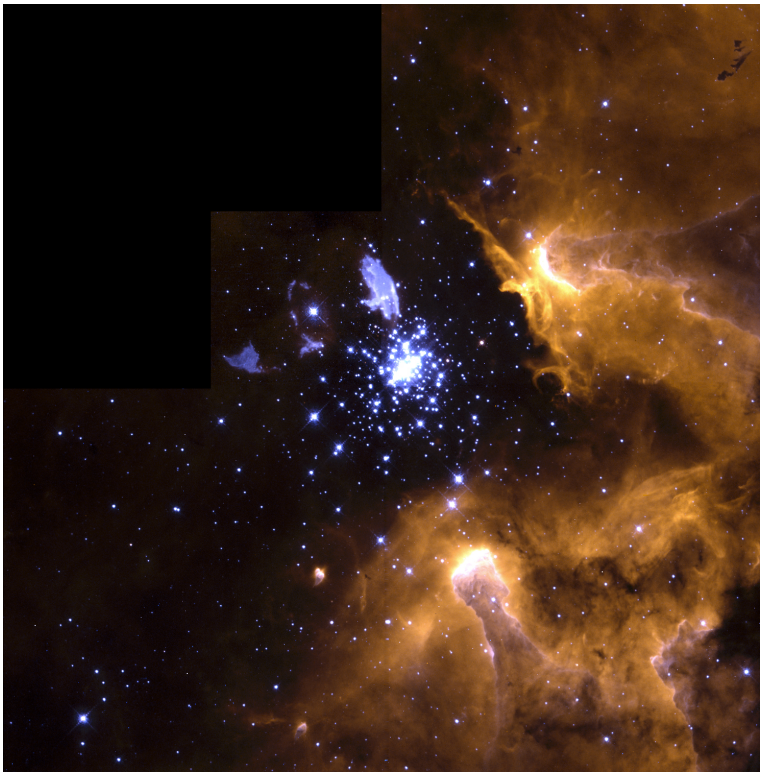

FIGURE 2.13: Young star cluster (NGC 3603) surrounded by a shell of dust and gas. Credits: NASA/ESA/Hubble Heritage Team/STScI.

We have seen that the gas collapse cascade follows a hierarchical way. This cascade is at the origin of the *initial mass function* (IMF), ξ, which gives the number of star of mass M just after a burst of star formation in a typical GMC:

$$\frac{dN}{dM} = N_0 \xi(M) \tag{2.15}$$

where N_0 is a normalizing constant[10]. While the IMF is well known for supra-solar masses from (Salpeter, 1955), its evolution is debated for sub-solar masses (Kroupa,

[10] If ξ is normalized such that $\int dM\ M\ \xi(M) = \mathrm{M}_\odot$, N_0 is the number of solar-mass stars in the star forming region.

2001; Chabrier, 2003), as illustrated on Fig. 2.14.

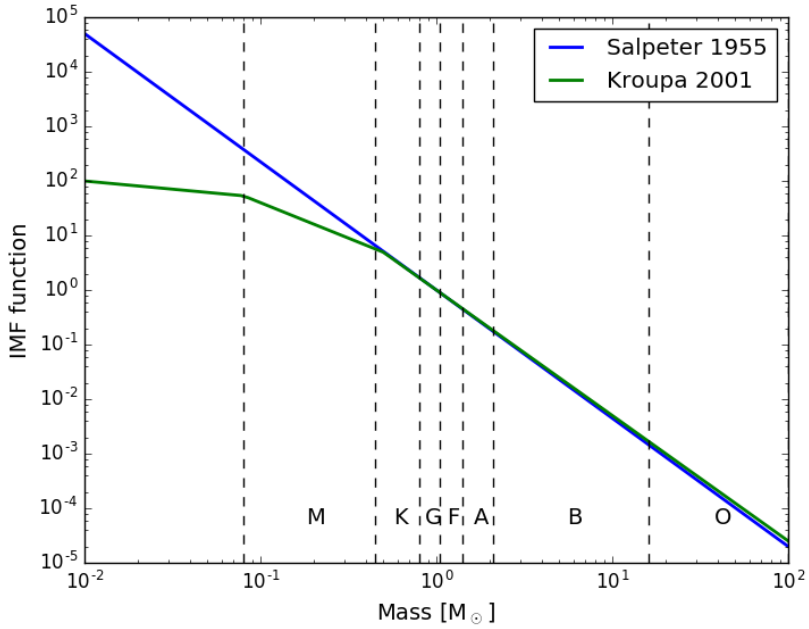

FIGURE 2.14: Salpeter (1955) and Kroupa (2001) IMF functions. The letters show the mass range of the stellar types described in the subsection 2.4.1 (Habets and Heintze, 1981).

Main sequence

The life of a star is then controlled, *at first order* by only one parameter, which is its birth mass, $\mathrm{M_{init}}$. This way, one may class stars in mass categories, following the Morgan–Keenan classification : OBAFGKM[11]. The mass range from Habets and Heintze (1981) for the different types are indicated in Fig. 2.14.

After ignition, the star follows a relation between its luminosity (or mass) and color (or temperature), called the main-sequence. It is where stars spend most of their lifetime, transforming the raw hydrogen from the Big Bang nucleosynthesis in heavier elements through the proton-proton and C-N-O cycles, creating metals.

One can show that the time of consumption of hydrogen through internal thermonuclear reactions decreases with the initial mass as $\propto M_{init}^{-2}$. It is ~ 10 Gyr for the Sun, and is lower than 40 Myr for O-type stars. When stars run out of fuel, there is not more pressure to support the star which collapses by its own gravity.

Late stages

Death of stars depends on their birth mass. Stars with $\mathrm{M_{init}} < 8\ \mathrm{M_\odot}$ expel their outer layers of processed materials in a *planetary nebula*.

Stars with $\mathrm{M_{init}} > 8\ \mathrm{M_\odot}$ end their life in a powerful explosion, called a type II Supernova (SNII). This process also expels their outer layers of processed materials,

[11]This sequence comes originaly from the strength of the hydrogen absorption lines in the stellar spectrum. This strange sequence is easily remembered with the sentence : *Oh Be A Fine Guy/Girl, Kiss Me*.

but the explosion allows numerous ejected ^{4}He atoms to fusion with the metals created during the star lifetime.

Therefore, star death allows the new elements formed in the stars to be released in the ISM, and enrich it in metals. This will increase the metallicity of future stars. However, stars do not only enrich the ISM. In the following subsection we will see how star formation feedback energy impact the host galaxy.

2.4.2 Star formation feedback

Radiative and ionizing feedback

Stars emit photons that will heat and even – for O-type and B-type stars – ionize the surrounding gas. The ionization is seen as pink bubbles in star-forming galaxies: the pink light is the H_α (λ = 656.28 nm) emission line which comes from ionized hydrogen recombination. This regions are called HII regions, or Strömgren spheres. Emitted photons are also scattered through the matter of the cloud and exerts a radiative pressure.

Supernovae

As we have seen in Section 2.4.1, stars more massive than 8 $M_\odot$ end their life in a SNII explosion[12]. This explosion releases typically 10^{51} erg in the ISM. This blast wave generates shocks in the ISM and releases thermal and kinetic energy. SNII typically occur 10 Myr after the onset of star formation in a cloud.

Qualitative effect of feedback

The quantitative effect of these feedback will be discussed in Section 3.2.3.

Qualitatively, these two types of feedback processes from star formation can clear the gas surrounding the star forming region, as it seen in Fig. 2.13. Stellar feedback can also sculpture the surrounding gas, through radiative pressure and blast waves, and create pillars where the density is enhanced, as on the right part of Fig. 2.13. The extremity of these pillars can host new star forming region.

Stellar feedback is also the likely cause of the observed galactic outflows, such as the ones seen around M 82 in Fig. 2.15. The typical velocity of these gas outflows is 100-500 $\mathrm{km\ s^{-1}}$ (Bournaud et al., 2014), which is comparable to the escape velocities of dwarf galaxies. Star formation feedback can then remove their gas and prohibits future star formation. In the case the Milky-Way type galaxies, gas ejected through such stellar outflows will fall back on the host galaxy. This process, called a *galactic fountain*, typically redistributes the gas from the center to the outskirts of the galaxy.

[12]There are other types of supernova explosion. One may cite type Ia supernovae (SNIa) which is caused by a white dwarf whose masse overcomes the so-called Chandrasekhar mass (1.44 $M_\odot$), through accretion of the outer envelope of a companion star. They typically happen 100 Myr after the onset of star formation.

FIGURE 2.15: Optical image of M 82 with the HST. The red light is the recombination emission of hydrogen through the H_α line. A SNIa discovered January 2014 is indicated.

2.4.3 Star formation scaling relations

Schmidt-Kennicutt Law

Schmidt (1959) and later (Kennicutt, 1998) have shown that the star formation rate on galactic scales tend to follow a relation with the gas surface density, of the form:

$$\Sigma_{\rm SFR} \propto \Sigma_{\rm gas}^{N} \tag{2.16}$$

with $N \simeq 1.4 \pm 0.15$. This relation is shown on Fig. 2.16.

The scatter of this relation is reduced if one take only CO gas abundance into accountwhich traces gas with densities between 10^{2-4} cm^{-3} (Bigiel et al., 2008), or even HCN, which traces gas with densities above 10^4 cm^{-3}(Gao and Solomon, 2004).

Fig. 2.16 shows two interesting features. First, we see that there is a surface gas density threshold at $\Sigma_{\rm gas} = 10 {\rm M}_\odot$ pc^{-2}. Below this threshold, star formation seems much less efficient. Indeed, diffuse gas cannot protect itself against hard UV photons, which heat the gas and prevent the formation of molecular gas, and therefore stars.

The second interesting feature is the fact that there two sequences, which are not differentiated by their redshift, but by their dynamical time. It shows that there is two modes of star formation for a given gas surface density, which does not depend on redshift, but on the dynamical timescale of the galaxy (Daddi et al., 2010a; Genzel et al., 2010). This separation disappears when using HCN measurements (Gao and Solomon, 2004). This suggests a replenishment of the denser part of the gas distribution by dynamical processes such as shocks and galaxy interactions (Renaud, Kraljic, and Bournaud, 2012).

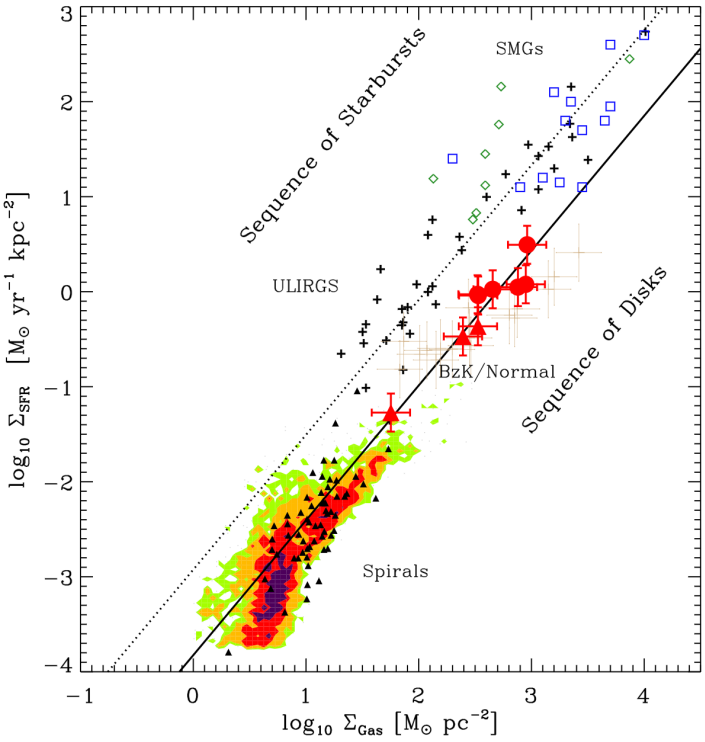

FIGURE 2.16: From Daddi et al. (2010a). SFR surface density against gas surface density (including both atomic and molecular gas) for local spirals and ULIRGs, and $z = 1.5$ BzK galaxies and SMGs.

Star forming main sequence

While the $\Sigma_{\rm gas}$-$\Sigma_{\rm SFR}$ probes the instantaneous gas consumption rate, positioning the galaxies on a $M_{\rm star}$-SFR plane probes the relation between the current and the cumulative star formation activity. Elbaz et al. (2007) and Noeske et al. (2007) have shown that galaxies follow a tight relation in this plane, SFR $\propto M_{\rm star}$, with an roughly constant scatter of 0.3 dex. This relation is called Main-Sequence (MS), in analogy to the stellar main-sequence. There are also outliers of this relation: the starburst galaxies which are located above, and represent about 2-4% of the star-forming galaxies. This proportion remains surprisingly constant with redshift (Rodighiero et al., 2011; Schreiber et al., 2015).

This tight relation can be interpreted as a consequence of the domination of a steady mode over a stochastic mode of star formation, the latter being for instance caused by galaxy interactions.

2.5 Stellar clusters

Because of the hierarchical collapse of gas, stars usually form in clusters. However, in most local galaxies, these clusters are not massive enough to remain bound and eventually evaporate (Lada and Lada, 2003).

In some extreme environment, such as starbursting or interacting galaxies, one may find very massive ($\simeq 10^6 M_\odot$) and young (< 50 Myr) stellar clusters, which are called *super star clusters* (SSCs), or *young massive clusters* (YMCs) (Whitmore and

Schweizer, 1995). The formation of super star clusters in interacting galaxies is also predicted by simulations (Bekki et al., 2002; Bournaud, Duc, and Emsellem, 2008; Renaud, Bournaud, and Duc, 2015).

It should be noted that if such clusters are not found in local isolated massive galaxies, such as the Milky Way, it is possible to find SSCs in less massive galaxies. For instance some BCDGs (presented in section 2.2.3) do present SSCs such as SBS 0335-052 which hosts 6 SSCs of mass $> 2 \times 10^5 M_\odot$(Adamo et al., 2010). The main driver of the formation of these SSC seems to be the high mean density of the gas: SBS 0335-052 have a mean gas density 20 times higher than the similar galaxy IZw18, shown in Fig. 2.10, which does not show any SSCs, but has a similar metallicity and even a higher gas fraction (Schneider, Hunt, and Valiante, 2016).

These SSCs bring a clue to the formation of globular clusters (GCs) which are found in the halo around galaxies. They are the oldest and densest stellar structures known in the Universe, and their formation scenario is still an open problem (Ashman and Zepf, 1992; Côté, Marzke, and West, 1998). Indeed, they share the same mass and size scales, as we see in Fig. 2.17. However, the survival of stellar clusters in these extreme environments is a still an open problem (Renaud et al., 2013; Gieles and Renaud, 2016).

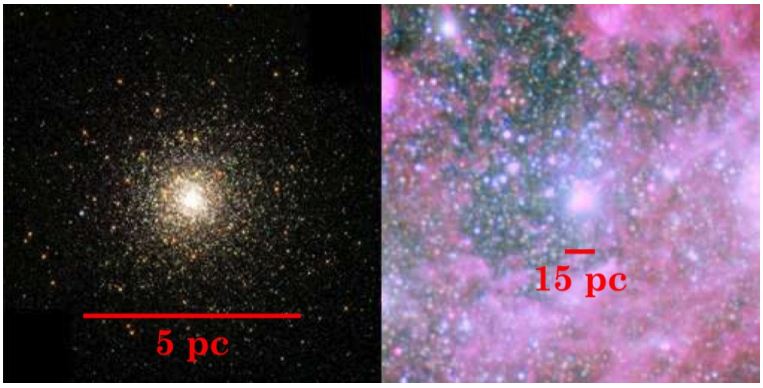

FIGURE 2.17: From Kruijssen (2016). Left: The Galactic GC M80, with a mass of $10^{5.6} M_\odot$. Image credit: NASA and The Hubble Heritage Team (STScI/AURA).Right: The most massive young massive cluster in the nearby starburst NGC 1569, with a mass of $10^6 M_\odot$. Image credit: NASA, ESA, the Hubble Heritage Team (STScI/AURA), and A. Aloisi (STScI/ESA).

The population of GCs around galaxies is not uniform but bimodal and can be split into two metallicity groups (Peng et al., 2006; Schuberth et al., 2010):

- **Metal-poor:** [Fe/H] around -1.5. They have an extended distribution around their host, resembling the dark matter halo mass profile and do not show a global rotation.
- **Metal-rich:** [Fe/H] around -0.5, which is still not very metal-rich in a local galactic standard. They have a narrower distribution around their host, resembling the visible halo light and sometimes show a rotation pattern around the host galaxy.

It has been noticed that the peaks of both distributions shift towards the metal-rich side for the most massive bins, M > 5×10^5 $M_\odot$ (see e.g. Strader et al., 2006; Mieske et al., 2010). This might be due to self-enrichment (Bailin and Harris, 2009; Fensch et al., 2014, in Annexe).

This dichotomy, both in internal and orbital properties, hints for two different formation scenarios. Their low metallicity ensures that they formed at around $z = 3 - 6$, probably in a very gas-rich environment (Shapiro, Genzel, and Förster Schreiber, 2010; Renaud, Agertz, and Gieles, 2017).

2.6 Interacting galaxies

Merging of galaxies is a consequence of the hierarchical build-up of large-scale structure. When two dark matter halo interact, their host galaxies will evacuate their orbital energy into random motions through dynamical friction and eventually merge[13].

As seen in Fig. 2.18, a close interactions between two galaxies can lead to the formation of extended (1-2 kpc) and diffuse structures. Using the advent of numerical simulations, it was shown that variations in the gravitational potential induced by the encounter were able to create these structures[14] (Toomre and Toomre, 1972).

2.6.1 Tidal field

During an interaction, the tidal field from the companion breaks the symmetry of the gravitational potential, which leads to a dynamical response of the disk. As we can see in Fig. 2.19, gas whose angular velocity is higher than the angular velocity of the interacting companion is subject to a negative torque, which result in a loss of angular momentum, and drive this gas towards the nucleus (Barnes and Hernquist, 1991). On the contrary, if some gas has a higher angular velocity than the interacting companion is subject to a positive torque, which drive it out of the disk to form tidal tails.

One should note that the impact of the interaction in terms of torques is dependent on the spin-orbit coupling of the interacting system. Fig. 2.19 presents the idealised case of an aligned spin-orbit coupling: the blue galaxy is rotating in the same direction than the orbital motion of the companion. This case is called *prograde* encounter.

If the galaxy spin is counter-aligned with the orbital motion, which is called a *retrograde* encounter, the interaction will have a very different effect. On the one hand, all the gas will have a smaller orbital velocity than the companion and will be subjected to a negative torque, therefore there will be no tidal tails. On the other hand these tides act on a shorter amount of time (see review by Duc and Renaud, 2013). The impact of the spin-orbit coupling on tidal structure formation can be seen

[13] For the impact of MOND on star formation in interacting galaxies, see Renaud, Famaey, and Kroupa (2016)

[14] Previous unsuccessful hypothesis included matter ejected from an increased rate of supernovae explosions (Zwicky, 1962), or jets (Sérsic, 1968; Arp, 1972). A detailed review of the discussion on the origin of these features can be found in Duc and Renaud (2013).

FIGURE 2.18: Sample of interacting systems illustrating different stages of major mergers, from the initial phases of the interaction to the formation of a relaxed system. As in Fig. 2.11, the atomic hydrogen, probed by 21-cm emission, is superimposed in blue. Image from (Duc and Renaud, 2013).

in Fig. 2.20.

Numerical simulations have also shown that the interactions can generate regions of *fully compressive tidal field* (see BOX 3 and Renaud et al., 2008). This regions appear in the nuclei and in the tidal arms of the galaxies, as we can see on Fig. 2.20. They have been shown to correlate with regions of formation of SSCs (Renaud et al., 2008).

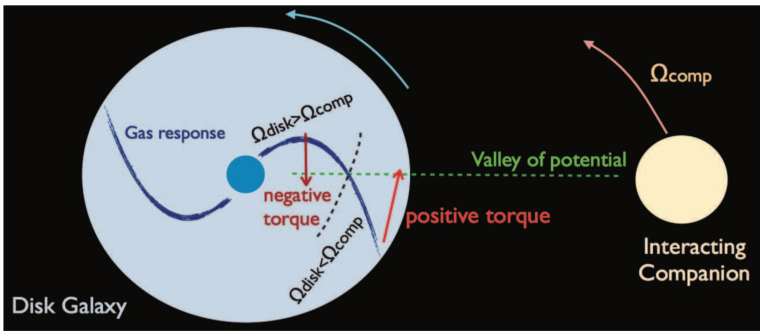

FIGURE 2.19: Simplified picture of the gravitational torques due to the passage of an interacting companion. From Bournaud (2010)

BOX 3: Fully compressive tides

The differential acceleration due to an external gravitational potential ϕ_{ext}, can be written in the form of the *tidal tensor* T_{ij}:

$$T_{ij} = -\partial_i \partial j \phi_{ext} \tag{2.17}$$

The tidal tensor is therefore symmetrical and can be diagonalized. Let's call $\lambda_{1,2,3}$ the three eigenvalues of T_{ij}. The sign of each eigenvalue indicates the nature of the tidal field along each engeinvectors: it is extensive if $\lambda > 0$ and compressive if $\lambda < 0$.

The sum of the eigenvalues reads, using the Poisson equation:

$$\sum_{i=1}^{3} \lambda_i = -\partial_i \partial i \phi_{ext} = -\Delta \phi_{ext} = -4\pi \mathrm{G} \rho \tag{2.18}$$

where ρ is the local density. The sum of the eigenvalues is always negative: at least one axis is compressive. In the following, we define as *compressive regions* the fully compressive regions, i.e regions where the three eigenvalues are negative.

To say it in another way, in compressive regions the Hessian matrix of ϕ_{ext} has three negative eigenvalues, which means that the gravitational potential is locally convex. This happens for instance in cored gravitational potentials.

2.6.2 Star and star cluster formation in interactions

In the local Universe, galaxy interactions are known to trigger intense episodes of star formation. They are typically classified as ULIRGs and found on the starburst sequence (see Fig. 2.16). At $z = 0$, all ULIRGs are undergoing an interaction (see review by Sanders and Mirabel, 1996, and references therein). One should note that the reciprocal is not true: some interacting systems do not show any significant enhancement of star formation (Bergvall, Laurikainen, and Aalto, 2003; Jogee et al., 2009). This raises questions on both the impact of the orbital parameters and the duration of the star formation enhancement due to an interaction. The dependance of the star formation burst with orbital parameters has been extensively studied in the GALMER simulation set[15] (Di Matteo et al., 2007; Di Matteo et al., 2008). It shows that only about 10% of major mergers and interactions have a strong starburst, which

[15]Simulation database accessible at http://galmer.obspm.fr

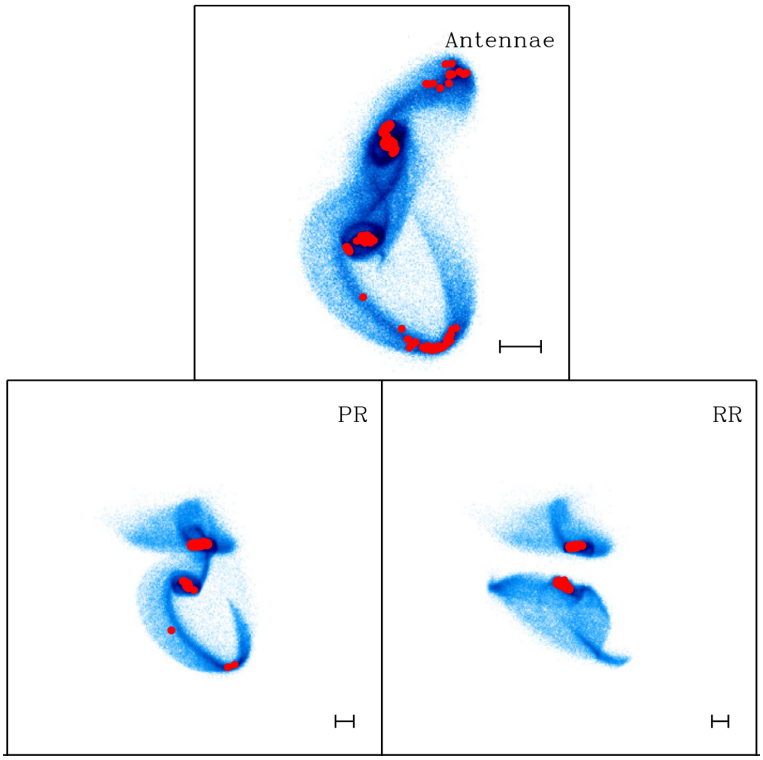

FIGURE 2.20: N-body simulation of interacting galaxies on different spin-orbit combinations. Blue dots show the location of baryonic matter and red dots indicate the location of fully compressive tidal field, in the N-body simulation of Renaud et al. (2009). The top model mimics the Antennae galaxies, first system shown in Fig. 2.18, where the two galaxies are prograde. In the bottom picture, P means prograde and R retrograde. The black line corresponds to 10 kpc.

is defined as a factor 10 increase of SFR between the peak and the pre-interaction phase. On average, the SFR peaks above a factor 3 to 4 above the pre-interaction one. One should note that the efficiency to produce a burst also increases when the mass ratio is closer to 1:1 (Cox et al., 2008).

The first observations of ULIRGs suggested that the star formation mainly occurs in the galactic nuclei (Sanders and Mirabel, 1996; Duc, Mirabel, and Maza, 1997). This is explained by the strong nuclear gas inflows that are triggered by the interaction (Barnes and Hernquist, 1991), which we discussed in the last section.

The emergence of a compressive tidal field also participate to the burst of star formation. First, the presence of a tidal field impacts the Jeans' length. Let's call T_0 the largest eigenvector of the tidal tensor (See BOX 3). The modified Jeans' length is given by:

$$\lambda'_J = \lambda_J / \sqrt{1 - T_0/(4\pi \mathrm{G}\rho_0)} \tag{2.19}$$

where ρ_0 is the local gas density (Jog, 2013). If the field is compressive, $T_0 < 0$ and the Jeans' length is decreased, when it is the opposite for a non-compressive field. It means that in the presence of a compressive field, in the center of the merging system and part of the tidal tails (see Fig. 2.20), gas will be more prone to gravitational instabilities.

Second, the compressive tidal field as been shown to force the compressive mode of turbulence (see BOX 2 and (Renaud et al., 2014)). This coupling, at which one may add the higher occurrence of shocks (Saitoh et al., 2009), can modify the gas density distribution, and bring more gas to the high-density end of the PDF (see Fig. 2.8 and Renaud et al., 2014; Elmegreen et al., 2016). The transformation of the shape of the PDF can explain the position on the starburst sequence of the Kennicutt-Schmidt diagram (Renaud, Kraljic, and Bournaud, 2012).

One should note that, to resolve this fragmentation process in numerical simulations, one should allow gas to cool. Indeed, changes in the macroscopic turbulence may be wiped out by the thermal turbulence if the gas is too hot (Teyssier, Chapon, and Bournaud, 2010; Bournaud et al., 2011). This numerical limitation will be discussed in the next chapter.

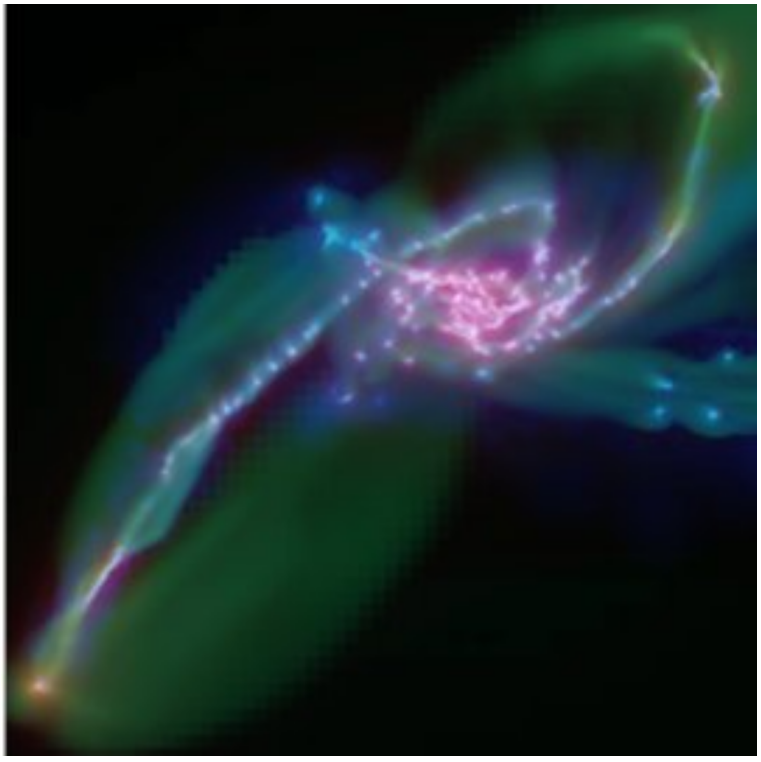

FIGURE 2.21: Map of the simulation of the collisions of the Antennae galaxies (Teyssier, Chapon, and Bournaud, 2010). Gas is in green, young stars in blue and and stars in red.

Last but not least, star formation can happen in the tidal features. In Fig. 2.21, we see that recent star formation, in blue, occurs on the tidal tail, forming clusters almost equally spaced, often described as *beads on a string*. This kind of structure is also seen in observations (Smith et al., 2008). The beads are typically separated by a Jeans length, which hints for a gravitational instability origin. The turbulence being relatively high in these regions, the typical mass of these clusters can be massive, up to $10^7 M_\odot$. These are SSCs which might, if they survive, be the progenitors of GCs.

Another kind of object can be seen at the tip of the tail. This stellar structure probbly formed by the pile-up of material (Duc, Bournaud, and Masset, 2004). These are the tidal dwarf galaxies, described previously. Interacting galaxies typically form

one to two such systems. One should note that there seem to be a competition between the formation of TDGs and SSCs (Knierman et al., 2003).

2.6.3 Relation to the high-redshift universe

As we have seen earlier, dynamical process at play in galaxy interactions increases both the gas surface density locally, because of stellar inflows and shocks, and increases the turbulence, because of the rapid evolution of the gravitational potential and the loss of orbital energy by dynamical friction. Therefore, the local gas condition in the midst of interacting galaxies may be compared to the normal conditions in high-redshift gas-dominated galaxies.

In particular, one may wonder if gas-dominated galaxies may form SSCs as their normal star formation activity, which may be analoguous the formation of SSCs in local interacting galaxies (Shapiro, Genzel, and Förster Schreiber, 2010; Kruijssen, 2016). This question will be addressed in Chapter 5.2.

Chapter 3

Numerical simulations

Internal processes in galaxies are very complex to model and predictions from theory are difficult to develop in a purely analytical form. To understand the predictions of the models that we develop, simulations can be used. The first example of galaxy simulation dates from Holmberg (1941): the author simulated a galaxy merger using light bulbs and photodetectors. The ingenious idea is that the light flux from a light bulb decreases with the distance d as $\propto d^{-2}$, as would the gravitational force do in the case of a point mass. The author used this analogy between light flux and gravitational force: light bulbs represent lumps of matter, whose effective mass is set by the candle power, and are distributed to simulate a galactic disk, as we can see on the left hand side of Fig. 3.1.

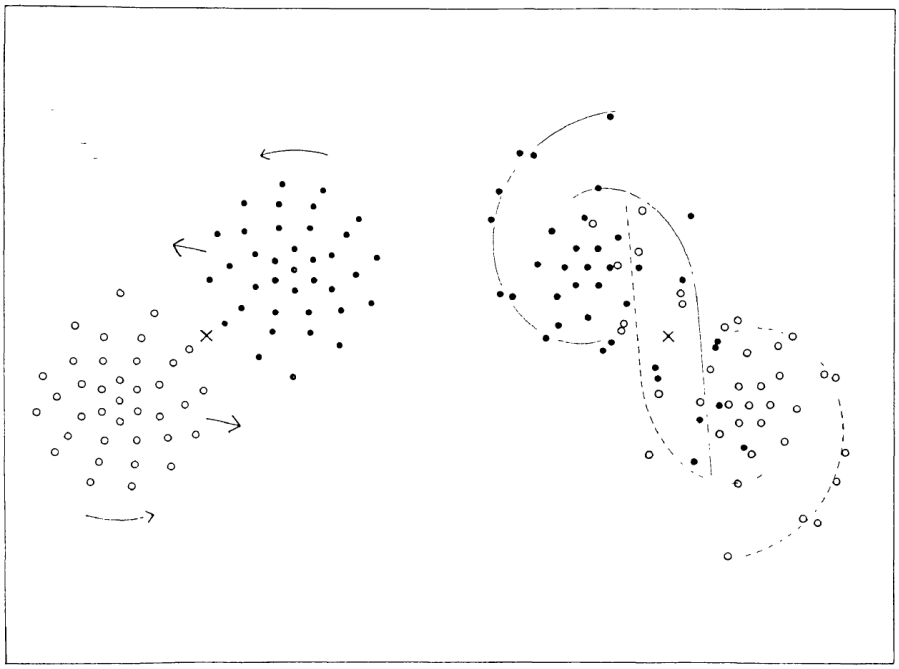

FIGURE 3.1: Prograde-prograde parabolic interaction between two disks simulated using 37 light bulbs per galaxy (Holmberg, 1941)

This very simple, but clever, set-up allowed the author to run the very first galaxy interaction simulations. The orbital parameters were chosen to be very simple as galaxies are aligned on the orbital plane for obvious technical reasons. The integration did not go far beyond the first pericenter passage for wall-clock time reasons, but the set-up already yielded nice results, for instance that tidal features form along a direction which depends on the spin-orbit coupling.

It should be noted that this pioneering work is often forgotten in discussions of the tidal origin of peculiar features around galaxies. In the early 70s, with the onset of super-computers which have replaced light bulbs, Toomre and Toomre (1972) have shown, through a series of numerical simulations, that the tidal forces induced by the interaction could trigger the formation of such structures.

However, this philosophy of simulations, for which gas is represented by a distribution of massive particles is still in use today for smooth-particle hydrodynamic (SPH) codes (such as GADGET-2 Springel, 2005). In this thesis, the numerical simulations were run using the code RAMSES[1] (Teyssier, 2002), which use a grid-based numerical method.

The choice of a good numerical code depends both on the scientific purpose and the available facilities. In this introduction I will present to which extent RAMSES, including its additional sub-grid models, is appropriate to run galaxy simulations. After discussing how its limitations may impact the dynamics of the gas.

3.1 Hydrodynamics on a grid

In RAMSES we have two types of objects:

- **Stars and dark matter particles:** they are considered as non-collisional point masses. They have a unique ID and the code stores the time of their creation in the simulation.
- **Gas.** Astrophysical gas is treated as a fluid. Each cell contains the local physical parameters of the gas, such as its velocity $\vec{u}$, its density ρ, its pressure P and its internal energy ϵ.

The hydrodynamical equations in the Eulerian form give:

$$\frac{\partial \rho}{\partial t} + \vec{\nabla} \cdot (\rho \vec{u}) = S_m \tag{3.1}$$

$$\frac{\partial \rho \vec{u}}{\partial t} + \vec{\nabla} \cdot (\rho \vec{u} \times \vec{u}) = \vec{S_p} \tag{3.2}$$

$$\frac{\partial E}{\partial t} + \vec{\nabla} \cdot (E \vec{u}) = S_e \tag{3.3}$$

with $E = \rho\epsilon + \frac{1}{2}\rho\vec{u} \cdot \vec{u}$. S_m, S_p, S_e are the source terms, which depends on conditions beyond the cell. For instance, in the case of a self-gravitating incompressible fluid we have these typical source terms:

- $S_m = -\frac{\partial \rho_\star}{\partial t}$, where $\rho_\star$ is the depletion due to star formation.
- $\vec{S_p} = -\vec{\nabla} P + \vec{F}_{\rm grav}$, where $\vec{F}_{\rm grav} = -\rho\vec{\nabla}\phi$ is the gravitational force.
- $S_e = -\vec{\nabla} \cdot (P\vec{u}) + n_H^2(\mathcal{H} - \Lambda) + \vec{F}_{\rm grav} \cdot \vec{u}$, where $\mathcal{H}$ and Λ are the heating and cooling functions and n_H the number density of hydrogen.

[1] Available at: http://www.ics.uzh.ch/ teyssier/ramses/RAMSES.html. Urban legend says it is an acronym for *Raffinement par adaptation de mailles sans effort surhumain* (adaptive mesh refinement without surhuman hassle).

This canonical form, $\frac{\partial}{\partial t}\vec{U}+\vec{\nabla}\cdot\vec{F}=\vec{S}$, shows that these equations are conservation laws. The evolution of the quantities $\vec{U}$ is obtained by summing up all the fluxes $\vec{F}$ through the cell boundaries, to which is added the contribution from the source terms $\vec{S}$.

The details of the hydro-dynamical solver used in RAMSES is a highly technical subject and is out of the scope of this thesis. In the following, I will focus on the numerical limitations of grid codes to treat gas dynamics.

3.1.1 Octree grid refinement

Cells in RAMSES can evolve between two refinement level limits, set at the beginning of the simulation : l_{min} and l_{max}. In a simulation box of size L, cells at refinement level l have a size $\Delta x = L/2^l$. RAMSES uses a cell-based refinement method: the physical conditions in a cell, or its neighbors, can trigger its refinement into 8 cells at the next refinement level, as is shown in Fig. 3.2 in a 2-D case. The refinement strategy will be discussed in subsection 3.1.6.

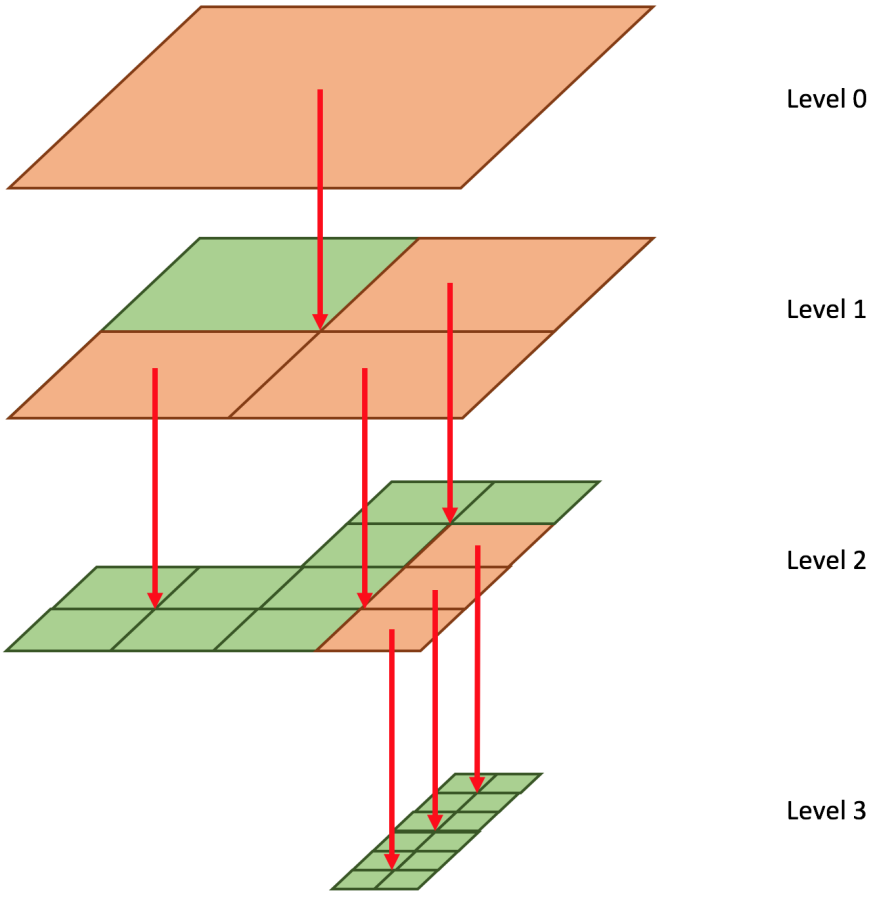

FIGURE 3.2: 2-D quadtree refinement levels (projected version of a 3-D octree). For each level, the green cells will be computed at this level, while the orange cells are refined to a finer level.

3.1.2 Time-steps and Courant-Friedrich-Lewy condition

To ensure the stability of the numerical scheme, one needs to prevent gas from traveling more than the length of a cell in one time-step. Heuristically, if we authorize (outward mass flux) $\times$ (time-step) > the cell mass, we may end up with negative mass cells ! If Δx and $v = ||\vec{v}||$ are the spatial size of a cell and the velocity of its gas, the time-step Δt should abide by the following relation, called the Courant-Friedrich-Lewy (CFL) condition:

$$\frac{c\Delta t}{\Delta x} < C \tag{3.4}$$

where C < 1 is called the Courant factor (Courant, Friedrichs, and Lewy, 1928). In RAMSES, C is set to 0.5: gas cannot cross more than half a cell.

The time-step for a refinement level is set as the minimum Δt which verifies the CFL condition for every cell of the refinement level. The *fine time-step* is chosen as the smallest time-step. It is often dictated by the high refined level, $l_{\max}$.

A cell at a refinement level $l-1$ is twice the size of a cell at refinement level l: $\Delta x^{l-1} = 2 \times \Delta x^l$. Therefore, choosing $\Delta t^{l-1} < 2 \times \Delta t^l$, iteratively back to the coarser level permits to verify the CFL condition on every refinement level. In RAMSES we typically chose $\Delta t^{l-1} = 2 \times \Delta t^l$.

This adaptive time refinement also allows us to compute the state of cells at refinement level l cells every $2^{l_{\max}-l}$ fine timesteps. This is called 2-sub-cycling and reduces the computational cost of the simulation. In practice, sub-cycling imposes to keep outdated cells in memory, which may slow down the simulation. Having a 2-sub-cycling for the five finest levels and synchronizing the time-steps of the coarser levels yields the smallest computational costs.

Relation 3.4 also shows that resolving gas with a high velocity costs a lot of computational time. Luckily, the densest phases we are interested in have typical temperatures below 10^4 K. One should note that only one cell at a high temperature in a small cell can slow down the whole simulation. This may happen because of stellar feedback. This is why some very high resolution simulations use an equation of state instead of heating and cooling functions (see e.g. Renaud et al., 2013). In this thesis we set a temperature upper limit of 10^8 K. This way, we limits thermal velocity to $\simeq 1000$ km s^{-1}, and still allow hot gas from outflows to remain in the halo and not cool down too fast on the galaxy.

3.1.3 Numerical diffusion

Solving hydrodynamical equations on a grid can induce an artificial diffusion of the physical quantities. For instance, let's consider the simplified case of a single patch of fluid moving along one axis, as depicted in Fig. 3.3. As the patch does not move by exactly one cell in one time-step, its mass is distributed on the neighboring cells, which result in a blurring of boundaries, which can be critical for instance in the case of shock fronts. In this thesis we are more concerned about resolving the gravitational instabilities: let's investigate how numerical diffusion may impact how we resolve the Jeans' length.

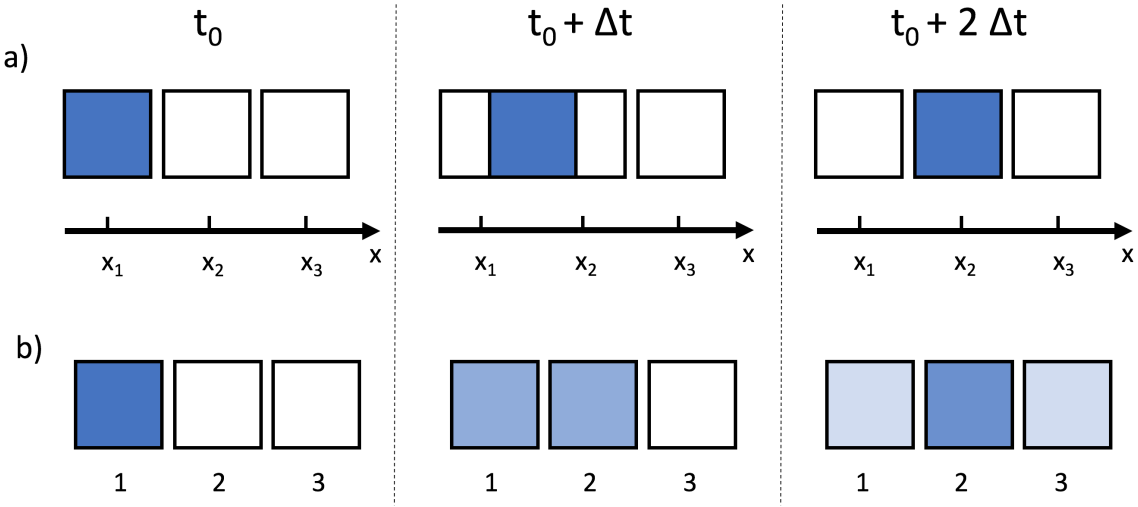

FIGURE 3.3: Illustration of the effect of numerical diffusion. The top row shows the displacement of a patch of fluid along the x axis. The bottom row shows how the mass is distributed in the different cells.

Numerically, numerical diffusion acts as a viscous term $\nu_{\rm num} = \frac{c\Delta x}{2}$, where c is the velocity of the wave – typically the sound speed – and Δx the cell size (see e.g. Teyssier, 2015). The hydrodynamical equations then become:

$$\frac{\partial \rho}{\partial t} + \vec{\nabla} \cdot (\rho \vec{u}) = \nu_{\rm num} \Delta \rho \tag{3.5}$$

$$\frac{\partial \rho \vec{u}}{\partial t} + \vec{\nabla} \cdot (\rho \vec{u} \times \vec{u}) = \nu_{\rm num} \Delta \vec{u} - \vec{\nabla} P - \rho \vec{\nabla} \phi \tag{3.6}$$

A perturbation analysis around an equilibrium state at density ρ_0 and velocity $\vec{u_0} = \vec{0}$ a gives a dispersion relation for the propagation of sound waves similar to equation 2.7, but for a new term in k^4:

$$\omega^2 = k^4 \, \nu_{\rm num}^2 + k^2 \, c_s^2 - 4\pi {\rm G} \rho_0 \tag{3.7}$$

The positive solution $\tilde{k}_J$ of the equation $\omega^2(k) = 0$ gives a new Jeans' length $\tilde{\lambda}_J = 2\pi/\tilde{k}_J$, given by:

$$\tilde{\lambda}^2 = \lambda_J^2 \frac{\sqrt{1 + (2\pi \Delta x / \lambda_J)^2} - 1}{0.5 (\Delta x / \lambda_J)^2} \tag{3.8}$$

where $\lambda_J = \sqrt{\pi c_s^2 / (\rho_0 {\rm G})}$ is the classical Jeans' length derived in section 2.3.1.

As we will see in the next subsection, we ensure that the Jeans' length is always resolved by at least four cells. Therefore the Jeans' length may be overestimated by 2% in the worst case scenario: the effect of numerical diffusion is negligible in our study of gravitational instabilities.

3.1.4 Numerical fragmentation

The limited resolution implies that we do not resolve the propagation of small scale perturbations. In nature, these missing small scales perturbation bring a pressure support to the ISM. Truelove et al. (1997) have shown that not resolving them might therefore trigger numerical fragmentation, and it can be avoided if we resolve the

Jeans' length by at least four resolution elements.

In RAMSES, one can trigger the refinement of cells when the local Jeans' length is not resolved by at least 4 cells. If theses cells are already at the finest allowed refinement level, the code artificially maintains an artificially higher pressure to prevent marginal fragmentation. This can be seen as a sub-grid model of the missing turbulent support due to the limited resolution.

Considering that the sound speed is given by $c_s \propto \sqrt{P/\rho}$, one may write the pressure floor P_J:

$$P_J \propto \rho\, c_s^2 = \frac{\mathrm{G}}{\pi}\rho^2\lambda_J^2 = \frac{16\ \mathrm{G}}{\pi}\rho^2(\Delta x)^2 \tag{3.9}$$

where we have introduced the Jeans' length λ, which is equal to four times the cell size. In RAMSES, this pressure floor is implemented as a heating function, called the *Jeans polytrope* in the following: $T \propto P_J/\rho \propto \rho$.

Our simulations reach typical maximum resolutions of 3 to 6 pc. We then resolve Jeans's lengths as small as 24 pc, which is an order of magnitude below the typical Jeans' length of high-redshift gas-dominated galaxies (300 to 1000 pc).

One may note that alternatives to the Jeans' polytrope exist. In regions where the Jeans' length is not resolved, Bate, Bonnell, and Price (1995) propose for instance to introduce a sink particle, which is a collisionless particle which accretes gas, with which one may treat sub-grid physics.

3.1.5 Particles on a grid

Star and dark matter particles are subjected to the gravitational force only. Their contribution to the gravitational field is projected on the grid using a *particle mesh* (PM) method. The one used in RAMSES is the cloud-in-cell (CIC) method (Hockney and Eastwood, 1981), pictured in Fig. 3.4. The mass m of the test particle is distributed onto the neighboring cells, with a factor equal to the overlap volume fraction between this cell and a fictuous cell of the same size centered on the test particle.

One can show that, in a cartesian grid, such a projection of the mass does not create a force on the test particle, which would be called a *self-force*. This is however the case in cylindrical grids, where a correction factor is added.

Once the mass of each particle has been added to the gas mass across all the grid, one may compute the total gravitational potential ϕ, which verifies the Poisson equation $\Delta\phi = 4\pi\mathrm{G}\rho$ in each cell. This potential is not solved directly, but with a relaxation method: a first gravitational potential ϕ_0 is assumed – typically the gravitational potential of the last time step – and its Lagrangian $\Delta\phi_0$ is compared to $4\pi\mathrm{G}\rho$ in each cell. The value of the gravitational potential is then iteratively modified until it converges to a potential which verifies the Poisson equation to a given precision. Several iteration methods exist and our version of RAMSES uses the multi-grid conjugate gradient method (Guillet and Teyssier, 2011).

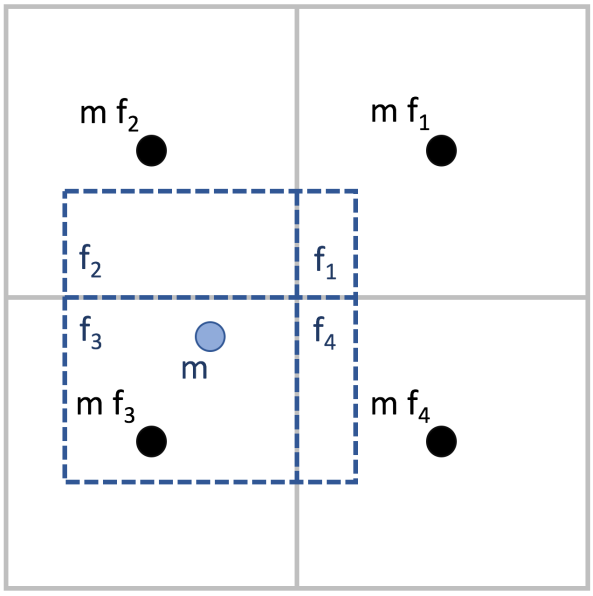

FIGURE 3.4: 2-D picture of the cloud-in-cell method. The mass m of the test particle is projected onto the grid. f_i is the surface fraction (volume fraction in 3D) of the overlap between cell i and a fictuous cell centered on the test particle. We have $\sum_i f_i = 1$.

Interactions between particles closer than a few cell size are thus not resolved. In particular, our simulation set-up does not allow us to resolve the relaxation, star evaporation, mass-segregation and core collapse of compact star clusters, which have a typical effective radius of a few parsecs, similar to the finest cell sizes. To study the mass and size evolution of a star cluster from an AMR simulation, a solution can be to post-process this simulation using a N-body code, using the galactic context as initial conditions (see e.g. Renaud, Gieles, and Boily, 2011).

3.1.6 Refinement strategies

In this thesis we will use several refinement criteria. Let's consider a cell at the refinement level $l < l_{\max}$.

- **Particle number threshold:** if the number of particle in this cell is higher than a certain threshold $n_{\max}(l)$ the cell is refined to the next level. A typical value for $n_{\max}(l)$ is 50.
- **Gas mass threshold:** if the gas mass in the cell is more massive than a certain value $n_{\max}(l) \times M_{\rm SPH}(l)$, the cell is refined to the next level.
- **Jeans length threshold:** if the local Jeans's length is smaller than four times the size of the cell, the cell is refined to the next level.
- **Refined neighbor:** The difference of refinement level between two neighboring cells cannot be greater than 1. If a neighboring cell is refined to a level larger than $l + 2$, the cell is refined to the next level.

The resulting refinement level map can be seen in Fig. 3.5. We see that the refinement follows the over densities of gas.

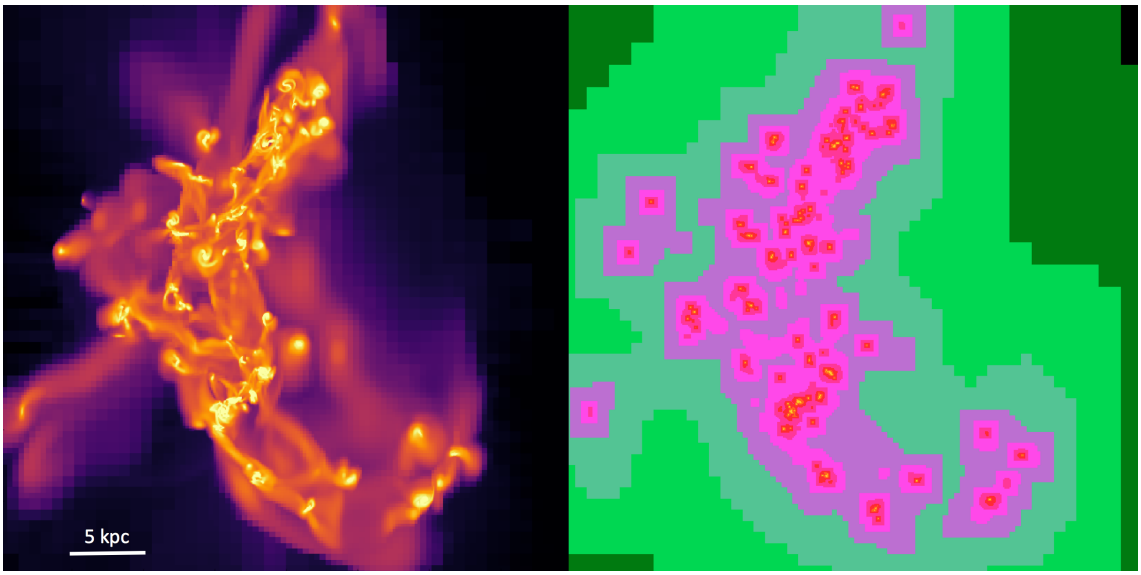

FIGURE 3.5: Left: gas density map of a collision between two galaxies (Fensch et al., 2017). Right: corresponding refinement level map (maximum in the line-of-sight), from $l_{\rm min} = 6$ in black to $l_{\rm max} = 15$ in yellow. The box size is 200 kpc.

The values of $n_{\rm max}(l)$ and $M_{\rm SPH}(l)$ depend on the refinement level l. Lowering $M_{\rm SPH}(l)$ induces a higher refinement of cells at level l to level $l+1$. This is important because, to study gas fragmentation, it is more interesting to better refine moderate density gas than better refine very dense gas.

3.1.7 Some differences with SPH codes.

The name $M_{\rm SPH}$ was chosen to ease the comparison with another type of code called smooth-particle hydrodynamic (SPH) codes (such as GADGET-2, Springel, 2005).

In SPH codes, gas is modeled as massive particles. Physical quantities are computed using a softening kernel, typically in number of particles. If the mass of gas particle is called $M_{\rm SPH}$ and the number of particles in the kernel called $n_{\rm SPH}$, the mass resolution is $M_{\rm SPH} \times n_{\rm SPH}$, which is analogous to the AMR mass resolution $M_{\rm SPH}(l) \times n_{\rm max}(l)$. To easily compare the spatial resolution between AMR and SPH codes, one may compute a spatial element size Δx of a SPH region of density ρ by: $\Delta x = \left[n_{\rm max}(l) \times M_{\rm SPH}(l)/\rho\right]^{1/3}$.

Using smoothing kernels have several impacts on how the gas is treated in the simulation. First, the spatial resolution is only set by the gas density. Low density regions, such as galaxy outflows, needs a very high number of particle to be well resolved, when AMR can enforce a minimal grid size with a lower computational cost. Furthermore, the smoothing kernel can smooth out fluid instabilities with a high density gradient, such as shocks and Kelvin-Helmholtz instabilities (Agertz et al., 2007)., which are crucial to understand how GMCs form in galaxies (see e.g. Renaud et al., 2013). This issue has been solved by adding an artificial thermal conductivity term (Price, 2008).

A last but not least difference is the parallelized scaling ability of the code. Thanks to its octree structure, RAMSES, and AMR in general, permits a much better scaling than SPH codes for the same resolution. In other words, for the same amount of wall-clock time, RAMSES allows a higher resolution than SPH codes.

3.2 Sub-grid models in RAMSES

The hydrodynamical equations do not contain all the physics we want to model. For instance, heating and cooling functions depends on the metallicity, temperature and density of the gas phase, and is implemented aside. Furthermore, the limited spatial resolution implies that we cannot resolve a number of processes, in particular star formation and its associated feedback on the interstellar medium. One has to implement numerical recipes, following theoretically-motived models, which allow one to study their effect on the host galaxy.

3.2.1 Cooling and heating functions

We have seen in Section 2.5 that gas can cool down through several radiative process. The cooling function Λ and its dependance on metallicity and temperature was shown in Fig. 2.3. In this thesis we do not account for the propagation of metals and their advection on stars. The presence of metals are important to allow the cooling, especially where they are scarce (Krumholz and Dekel, 2012). For computational time reasons, and their second order impact on gas fragmentation we assume a constant solar metallicity for all the considered gas.

To this cooling function is added a heating function, $\mathcal{H}$, from the UV radiation background (Courty and Alimi, 2004) and from the Jeans polytrope at high density, described in section 3.1.4. The resulting location of the gas in the snapshot of Fig. 3.2 is shown in Fig. 3.6. On this Figure one can see the Jeans polytrope at high density and an isothermal line at 5×10^4 K, which is the temperature of the gas in (Strömgren, 1939) spheres (see *photoionization* below).

3.2.2 Star formation

Single solar mass star formation would imply happens on scale several orders of magnitude below the higher spatial resolution that will be presented in this thesis.

Star formation is therefore modeled at the parsec scale. In the simulation, we want the local star formation rate (SFR) to follow the Schmidt (1959) law:

$$\rho_{\rm SFR} = \epsilon_{\rm SF}\,\frac{\rho}{t_{\rm ff}} \tag{3.10}$$

In this equation $t_{\rm ff} = \sqrt{3\pi/(32{\rm G}\rho)}$ is the free-fall time and $\epsilon_{\rm SF}$ is the star formation efficiency (SFE). The SFE represents the fraction of the gas that ends up in the stars and depends on the spatial scale we consider. Typical values of $\epsilon_{\rm SF}$ are 1-4% for parsec scale simulations, and would be higher for higher resolution.

At each time-step dt, cells denser than certain density threshold ρ_0 and colder than 2×10^4 K can form stars[2]. For each cell, a random integer number n is drawn

[2]In practice, the condition is that the gas is not more than 2×10^4 K above the Jeans' polytrope temperature.

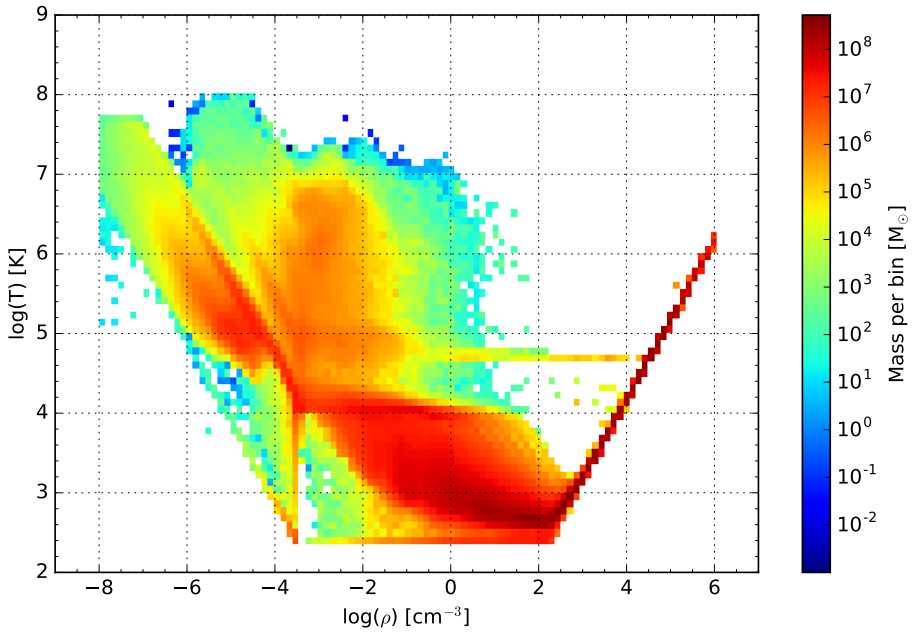

FIGURE 3.6: Resulting location of the gas on the $\rho - T$ diagram. The Jeans' polytrope, $T \propto \rho$, is seen for densities above 300 cm^{-3}.

from a Poisson distribution of mean value $\lambda = \rho_{\rm SFR}(\Delta x)^3 dt/M_\star$, where Δx is the size of the cell, dt the timestep at the corresponding refinement level, and $M_\star$ a mass chosen by the user (Katz, 1992):

$$P(n = N) = \frac{\lambda}{N!} e^{-\lambda} \tag{3.11}$$

If $n > 0$ a particle of mass $nM_\star$ is created in the cell. For computational reasons and because we do not resolve two-body interactions at sub-parsec scales (see subsection 3.1.5), we do not want to form individual stars. $M_\star$ is set to be at least several 100 M$_\odot$. Our new stellar particles are then star clusters, and all contain massive stars which will have a feedback effect on the surrounding gas.

The choice of the density threshold ρ_0 is relatively arbitrary. As $\rho_{\rm SFR} \propto \rho^{3/2}$, star formation is dominated by the highest density regions. Moreover, a high ρ_0 can help save some computational time as fewer cells will be concerned by the star formation routine. ρ is typically set to be higher than a hundred M$_\odot$ cm^{-3}.

3.2.3 Star formation feedback

As we have seen in Section 2.4.2, star formation has an effect on the surrounding gas, through hard UV emission from massive young stars and type II supernovae explosions. In practice we only consider feedback from OB-type stars, whose mass represent $\simeq 20\%$ of the new stellar particle for a Salpeter (1955) IMF, and happens in the first 10 Myr after its the formation. Their effects are computed every time step of the coarser refinement level. In the following I will describe how these feedback effects are implemented in the code.

Photoionization

OB stars emission contains photons more energetic than 13.6 eV, and are able to ionize the surrounding neutral hydrogen gas. This ionization results in a net heating of the surrounding gas to a chosen temperature, typically several 10^4 K. This isothermal branch can be seen on Fig. 3.6. The impacted region is a (Strömgren, 1939) sphere centered on the new stellar particle. The radius of this sphere is set to:

$$R_{\rm HII} = \left(\frac{3 L_\star}{4\pi n_e^2 \alpha_r} \right)^{1/3} \tag{3.12}$$

In this equation, $L_\star$ is the luminosity of the stellar particle in terms of ionizing photons, n_e the ambient number density and α_r is the recombination rate: $\alpha_r = 2.1 \times 10^{-10}$ cm^{3}s^{-1}(T$_{\rm HII}$ / 1 K)$^{-3/4}$. (Renaud et al., 2013). A new stellar particle of 10^4 M$_\odot$ formed in gas in mean density 10 cm^{-3}, will form a Strömgren sphere with radius 27 pc.

Radiative pressure

Scattering between energetic photons and charged particles creates radiative pressure. This is accounted for by an injection of kinetic energy inside the Strömgren sphere measured in the previous subsection: each enclosed cell receives an additional velocity component in the opposite direction to the new stellar particle, whose norm is set to :

$$\Delta v = s \frac{L_\star h \nu}{M_{\rm HII} c} \Delta t \tag{3.13}$$

In this equation, h is the Planck constant, c the speed of light, $M_{\rm HII}$ the total mass contained in the Strömgren sphere, ν a characteristic frequency of the scattering photons (the frequency of the Lyα line in Renaud et al., 2013), and Δt the timestep of the coarsest level. The multiplicative factor s represents the how many times a photon will deposit the momentum of the characteristic frequency, through multiple scattering. Normalized to the Lyα frequency, this factor is typically 2 to 5 (Krumholz and Dekel, 2010; Perret et al., 2014).

Supernova explosions

We consider that this 20% mass fraction of the stellar particle which creates this ionization and radiative pressure eventually explode as type II supernovae, after 10 Myr. We do not have the resolution to study individual explosions and blast waves and their impact on the surrounding medium. However, clustered supernovae explosions can create *superbubbles*, which are at the origin of galactic outflows, and have a typical size of 150 pc (see e.g. Dubois and Teyssier, 2008, and references therein).

Dubois and Teyssier (2008) implemented the physics of superbubbles in RAMSES: the stellar particle gives 20% of its mass to the surrounding gas, to which is also transferred the energy of the explosion, $E_{\rm SN} = 10^{51}$ erg per supernova in the stellar particle, in a mix of kinetic and thermal energy. The weight of each component is chosen by the user.

The combination of photoionization, radiative pressure and supernovae feedback effects on the gas do not scale linearly, as is shown in Fig. 3.7. Outflows rate from the combination of all feedback is much larger than the sum of the outflow rates from each feedback separately. Photoionization and radiative pressure can creates zones of lower densities around the star forming region, such as chimneys, which makes easier for the subsequent supernova feedback to launch galactic outflows.

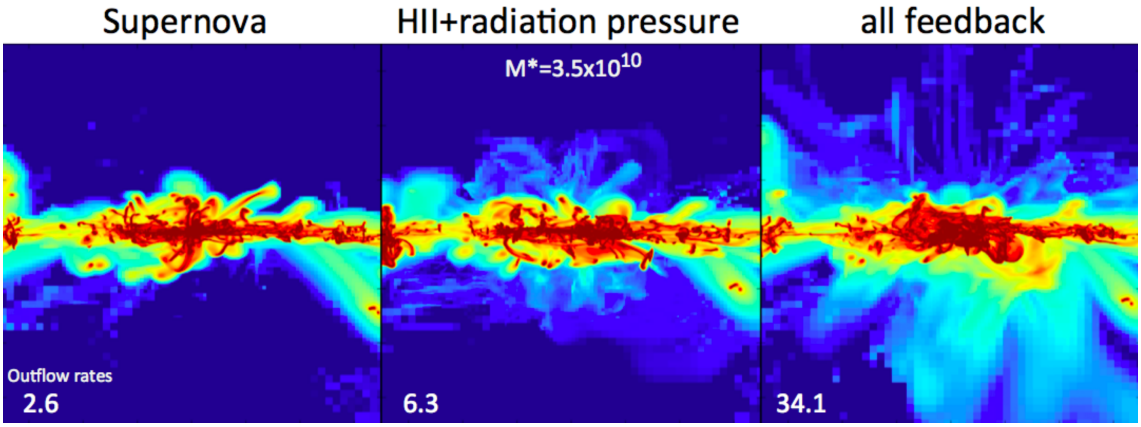

FIGURE 3.7: Outflow rates in $M_\odot$/yr for a gas-dominated galaxy with stellar mass 3.5×10^{10} $M_\odot$ and with different types of feedback allowed (Bournaud, 2016). We see that the combination of photoionization, radiative pressure and supernovae explosions do not add linearly.

3.3 What we left over

3.3.1 Metal advection

RAMSES allows the use to account for the ejection of metals through supernovae explosions, and its subsequent diffusion in the ISM. We have seen in section 2.5 that cooling at $T = 10^{5-7}$ K is more efficient in a more metallic medium. Indeed, metallicity may have an important effect on gas fragmentation for very metal-poor galaxies (Krumholz and Dekel, 2012). However, the massive galaxies we are interested in already have a moderate metallicity, up to $Z_\odot/2$ at $z = 2$ (Erb et al., 2006). Created metals in the simulation will therefore not drastically affect the fragmentation of our gas on parsec scales, and we chose, for simplicity and computer memory reasons, a constant gas metallicity in our simulations.

3.3.2 Radiative transfer

The radiative processes of stellar feedback in the described implementation have been averaged into simplified sub-grid models. A direct treatment of radiative transfer would allow for a better model of the ISM structure, because it would take into account gas inhomogeneity.

Complete treatment of radiative transfer has been implemented in RAMSES (RAMSES-RT, Rosdahl et al., 2013). However, it has an important computational cost. Using this direct radiative transfer method would thus force us to reduce the spatial resolution to run our simulations in a wall-clock time compatible with a PhD thesis

duration. Degrading the spatial resolution would lead us closer to a state where most of the radiation is absorbed in the cell where star formation happens and there would be no advantage in using a direct treatment of radiative transfer.

In this thesis we thus stick to an average effect of radiative feedback, physically motivated, which leads to outflow rates consistent with observations (Bournaud, 2016).

3.3.3 Magnetic fields

Measurements of the magnetic field in galaxies, using the Zeeman splitting of the atomic hydrogen 21-cm line, have shown that local star forming disks harbor magnetic fields amplitude of 5 to 10 μG, and shown a correlation between their magnetic field and star formation rate : $||\vec{B}|| \propto \mathrm{SFR}^{1/2}$ (Lisenfeld, Voelk, and Xu, 1996). If we extrapolate this relation to high-redshift galaxies, they should harbor magnetic field amplitudes of $\simeq 20 - 100$ μG (Beck, 2009).

Studies have shown that magnetic fields can hinder the fragmentation of the gas at the scale of a GMC (Shu, Adams, and Lizano, 1987), even though it is also claimed that turbulence is a more important driver of gas collapse regulation (see e.g. Padoan and Nordlund, 2011; Federrath and Klessen, 2013). At galactic disk scales, magnetic fields are shown to reduce the effect of the galactic shear and tend to destabilize the disk (Elmegreen, 1987; Kim, Ostriker, and Stone, 2002). However, studies of star formation isolated and merging galaxies, with and without magnetic field, have shown no significant changes in their star formation history (see e.g. Kotarba et al., 2010, for the Antennae system). For simplicity we chose to ignore the effect of magnetic fields in the simulations presented in this thesis.

BOX 4: Epistemological view point on numerical simulations in this thesis

Before detailing the numerical code I used, I would like to briefly describe the epistemological background on which we consider the outputs of the numerical simulations presented in this thesis. Two usages can be usually taken towards numerical simulations.

First, numerical simulations can be used to test an hypothesis on a given system. For instance, in Duc and Bournaud (2008) a numerical simulation showed that high-velocity collisions can reproduce *fake dark galaxies* by reproducing the physical parameters of a dark HI cloud in the Virgo cluster. This does not represent a proof[a] of the hypothesis, but rather shows that the hypothesis is not inconsistent with the laws of physics as we know them, under the limitation of biases due to their numerical implementation. One may call this use a *numerical consistency test*.

Second, numerical simulations can be used as a testbed to *observe the predictions* of a combination of models (e.g. gravity, hydrodynamics, star formation, feedback...), when an analytical analysis is not possible, for time or complexity reasons. Numerical simulations thus allow the user to *observe* where would lead an extrapolation of a set of models beyond what has been observed, that is in a range of parameters for which the theory or combination of models have not been tested and/or calibrated by observations/experiments. Numerical simulations also allow the user to resolve physical properties on scales – in space or time – which are not resolved with observations/experiments. One may call this use a *numerical observation of the theory*. The term observation is used to highlight the fact that this use may also be subject to biases, in particular numerical biases due to the numerical setup.
In this second usage of numerical simulation, the initial conditions constrain the applicability of the models to the real Universe. This is particularly crucial when the physical state of the studied system is barely resolved by observations/experiments.

In this thesis, we will not seek to reproduce a given system or to model existing low- and high- redshift galaxies, but only a canonical galactic environment. This gives us the freedom to test the impact of a single physical parameter on our combination of models for galaxy evolution, which in this thesis is the *gas mass fraction*. We will therefore locate ourselves in the second view point on numerical simulations described above.

However, the purpose of our work is to use our numerical results to improve our understanding of the real Universe. We will do so assuming that the gas mass fraction of a galaxy is a proxy for the look-back time. This is of course unrealistic, as we have described in section 2.2.2 a number of other differences between low- and high-redshift star forming galaxies. Before extrapolating our numerical results to the real Universe, the impact of these neglected parameters will therefore always be discussed.

[a] One may argue, following Karl Popper, that an hypothesis on a physical phenomenon may only be refuted or considered as acceptable until it is refuted.

Chapter 4

Star and stellar cluster in gas-rich environments

4.1 Formation and evolution of massive clumps

In Section 2.2.2, I presented the typical morphology of typical gas-dominated galaxies at $z = 2$, whose gas and young stellar component show a clumpy distribution. These clumps have a typical size of a few hundred parsecs and masses between 10^7 and 10^9 $M_\odot$(see e.g. Elmegreen and Elmegreen, 2005), and most of them are thought to have been formed inside the host galaxy (Mandelker et al., 2014).

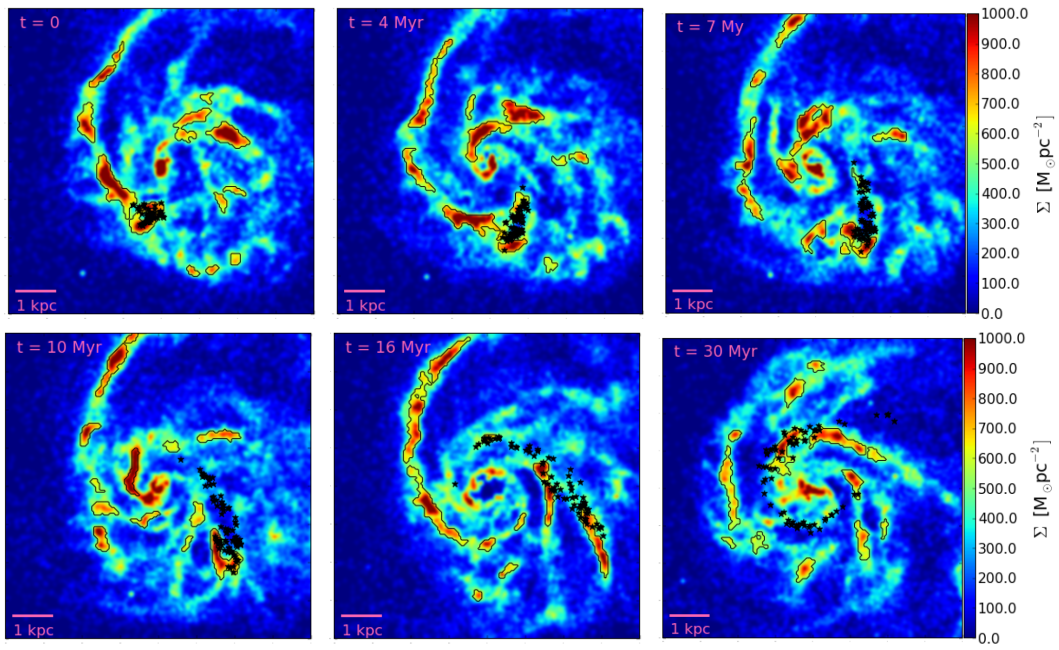

FIGURE 4.1: Time sequence of stellar surface density maps of the simulated galaxies from Oklopčić et al. (2017), spanning 30 Myr at z $\simeq$ 1.8. Time is indicated on the top right corner. The black stars show the position of stars formed in the same clump in the first snapshot.

The evolution of these clumps, and in particular the timescale of their survival in their host galaxy, is still an open field of research.

On the one hand, several numerical simulations suggest that the clumps are disrupted by stellar feedback in short timescales, that is several tens of Myr (Genel et al., 2012; Oklopčić et al., 2017). An example of such a disrupting clump from Oklopčić

et al. (2017) is shown in Fig. 4.1. Stars formed in the same clump are spread around in a spiral-like structure spanning several kpc, in around 30 Myr. These simulations do not seem to agree with observed stellar population in giant clumps with ages around 100-200 Myr (Wuyts et al., 2012), and age gradients consistent with clump migration (Förster Schreiber et al., 2011; Guo et al., 2012; Guo et al., 2015).

On the other hand, several simulations including a thorough model of stellar feedback (supernovae, radiation pressure, ionization by HII regions) do show the formation of relatively long-lived (> 100-500 Myr) clumps (Perret et al., 2014; Bournaud et al., 2014; Ceverino et al., 2014). For instance, (Perez et al., 2013) show that clumps can survive even when strong outflows – consistent with observations (Genzel et al., 2011; Newman et al., 2012) – are launched from their star formation activity.

We stress that, to allow the formation of clumps in galaxy simulations, one should have have spatial resolution elements smaller than a few times the Jeans length, that is smaller than 25-50 pc (see e.g. Teyssier, Chapon, and Bournaud, 2010), and have a cooling model which takes into account gas cooling below 10^4 K, to allow gas to dissipate its kinetic energy (see e.g. Bournaud et al., 2011).

The aim of this section if to understand if the short lifetime of clumps in the aforementioned numerical simulations comes from a bias towards the gas mass fraction of the galaxies.

In section 2.3 we have shown how a high gas mass fraction could destabilize the disk and lead to the formation of bound massive structures. The galaxy presented in Fig. 4.1 results from a zoom-in on a cosmological simulation, and a current open issue in cosmological simulations is the fact that they do not reproduce the typical gas mass fraction at a given redshift (see also Kereš et al., 2012, for the Illustris simulation). The reason is that simulated galaxies turn gas in stars too efficiently and cannot reproduce the cosmic star formation history (Dekel and Mandelker, 2014; Mac Low, 2013, for a review). In particular, the gas mass fraction[1] of the galaxy presented in (Oklopčić et al., 2017) has a gas mass fraction of 25% at redshift 2, which is around a factor 2 lower than expected for typical galaxies at this redshift (Combes et al., 2013; Tacconi et al., 2013). We would like to stress that such a relatively gas-poor galaxy may exist at this redshift, but it is not representative of the bulk of clumpy galaxies at this redshift.

In this section, I will present a numerical work to study the case of the galaxy presented in Fig. 4.1 and better understand the formation of giant gas clumps. I derived the approximate characteristics of the galaxy and used it as a testbed to test the impact of different physical parameters on the formation of gas and stellar structures. This work will be presented in a forthcoming paper, Bournaud & Fensch (in prep.).

4.1.1 Simulation set

In this work, I propose to test the impact of two physical properties, the strength of the feedback implementation and the gas mass fraction of the simulation. This work should be considered as an answer to Oklopčić et al. (2017). We wanted to test their claim that high redshift gas clumps are short-lived with gas mass fraction which are

[1] Their measurement of the gas mass also takes into account the diffuse hot gas around the galaxy. Thus we assume a slightly lower value, 25%, for the gas mass fraction in the disk only.

more realistic to what is observed at $z = 2$.

First, numericians have not yet agree on the most realistic way to implement stellar feedback in their simulation. This is a long-standing issue, and will remain so until computing facilities allow us to simulate galaxies with a resolution down to the formation of single stars and to include very numerically costly physics such as radiative transfer and magnetic fields. What we propose in this thesis is to use the prescription described in section 3.2.3, which is physically motivated and gives the right order of magnitude for gas distribution and outflows. To test the impact of a stronger or weaker feedback implementation, we modify several input parameters for the temperature in HII regions, scattering factor and the partition between kinetic and thermal energy release from type II supernovae. This results in three models of feedback, which are summed up in Table 4.1.

TABLE 4.1: Characteristics of the feedback used in the simulation set. These parameters are detailed in section 3.2.3

Type of feedback	HII region temperature [K]	Scattering factor	Energy fraction released thermally	Energy fraction released kinetically
Weak	5×10^4	2.5	100 %	0 %
Average	10^5	4	42%	8%
Strong	2×10^5	7	80%	20%

Second, we want to test the impact of the gas mass fraction on the formation and evolution of these structures. To do so, we initialize our disks with different gas mass fractions. To get insight on this sole parameter – which can be seen as a proxy for the look-back time – we do not change the other parameters of the simulation, such as the dark matter halo and galaxy size. The most important point is that we keep the same stellar bulge profile, in order to keep the same rotation curve, galactic shear and tidal field for each galaxy of our simulation set. To sum up, we only replace disk stars by gas. As described in the analysis if equation 2.14, we expect that disks will be more unstable with a higher gas mass fraction. One should note that, if we keep the same gas density threshold for star formation, 10 cm^{-3}, we do not use the same star formation efficiency: 0.04 for the 20 and 25% gas mass fraction cases, and 0.0025 for the 50 and 60% gas mass fraction cases. Tweaking the star formation efficiency allows us to ensure that the galaxy forms stars at a realistic rate, which corresponds to the disk sequence on the Schmidt-Kennicutt diagram for a given gas surface density.

We run simulations with four different gas mass fractions, from 20% to 60%. The respective characteristics of the galaxies are summed up in the Table 4.2. The gas mass fractions 20% and 25% are motivated by the values given by (Oklopčić et al., 2017). We use a refinement strategy similar to their simulation, which is density based, to mimic the SPH refinement behavior (see Section 3.1.7): a cell is refined if it contains more than 50 dark matter or old stellar particles, or if its mass is higher than $50 \times 3.7 \times 10^5$ $M_\odot$.

TABLE 4.2: Characteristics of the galaxies used in the simulations

Galaxy	20%	25%	50%	60%
Total baryonic mass [$\times 10^{10} M_{\odot}$]	5.14			
Gas Disc (exponential profile)				
mass [$\times 10^{10} M_{\odot}$]	1.0	1.2	2.6	3.1
characteristic radius [kpc]	2.5			
truncation radius [kpc]	5			
characteristic height [kpc]	0.25			
truncation height [kpc]	0.6			
Stellar Disk (exponential profile)				
mass [$\times 10^{10} M_{\odot}$]	3.56	3.22	1.96	1.16
characteristic radius [kpc]	2			
truncation radius [kpc]	4.5			
characteristic height [kpc]	0.25			
truncation height [kpc]	0.6			
Bulge (Hernquist profile)				
mass [$\times 10^{10} M_{\odot}$]	0.58			
characteristic height [kpc]	0.25			
truncation height [kpc]	0.6			

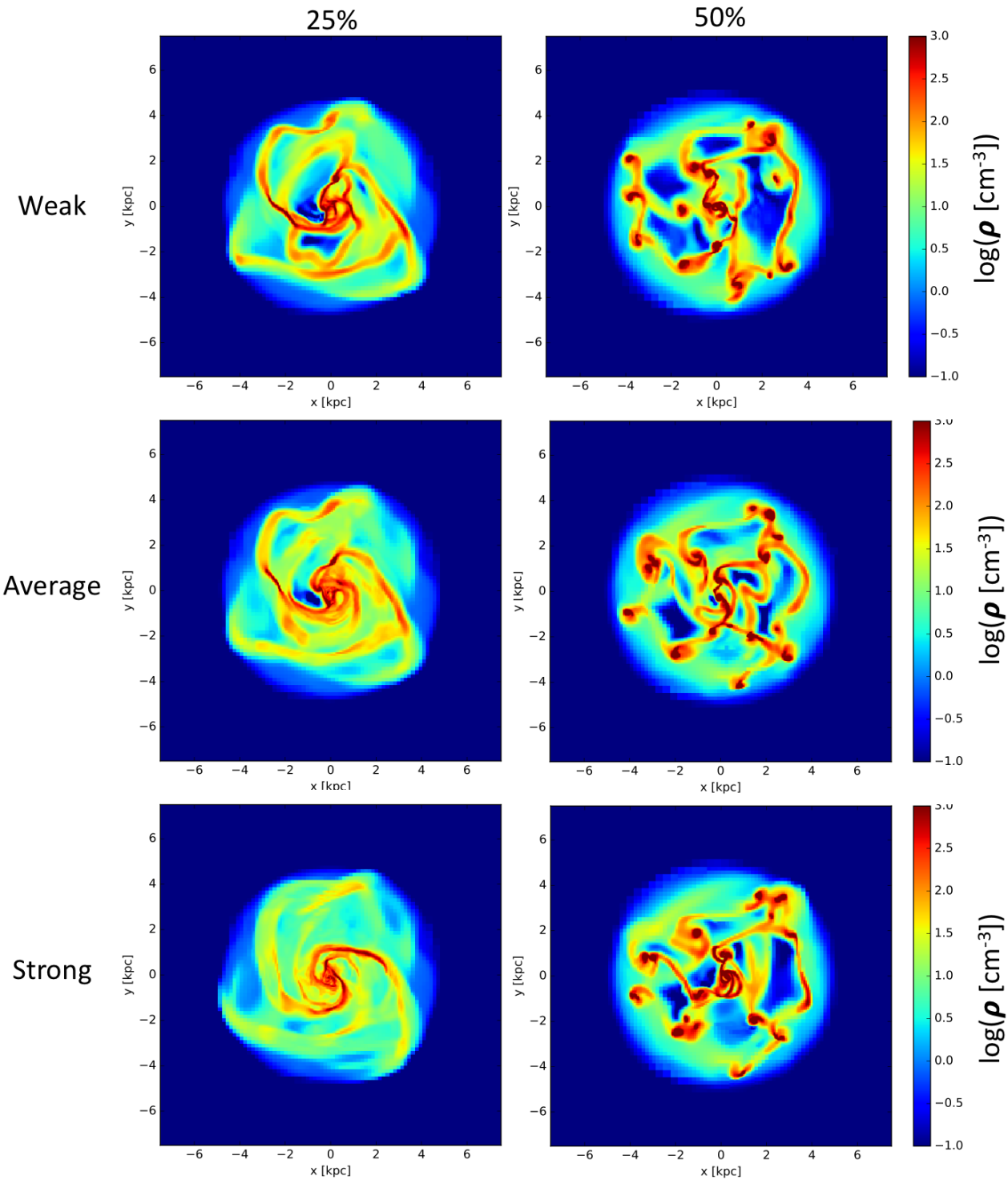

FIGURE 4.2: Gas density map of the simulations after 150 Myr of simulation time. The left and right panels show respectively the 25% and 50% gas mass fraction models. The rows correspond to different feedback models as described in table 4.1, from top to bottom: weak, average and strong.

4.1.2 Impact of stellar feedback and gas mass fraction on clump formation and evolution

In Fig. 4.2 one can see the gas density maps of six simulations, with $f_{\rm gas} = 25\%$ and 50% and the three models of feedback, after the same simulation time, 150 Myr. We can see that the gas-poor cases, on the left-hand side, show the formation of well-defined spiral structures while the gas-rich cases show the formation of dense ($\rho > 10^3$ cm^{-3}) clumps of gas. One can also see that the stronger models of feedback in the 25% gas mass fraction runs make the spiral pattern more diffuse, when they do not seem, at first sight, to affect much the formation of the giant gaseous clump of the 50% gas mass fraction runs. In Fig. 4.3 we track two gas clumps in the 20% gas mass fraction simulation with average feedback. We see that they are transient features which remain visible over three snapshots, that is for about $\simeq 25$ Myr. This is consistent with the results from Oklopčić et al. (2017).

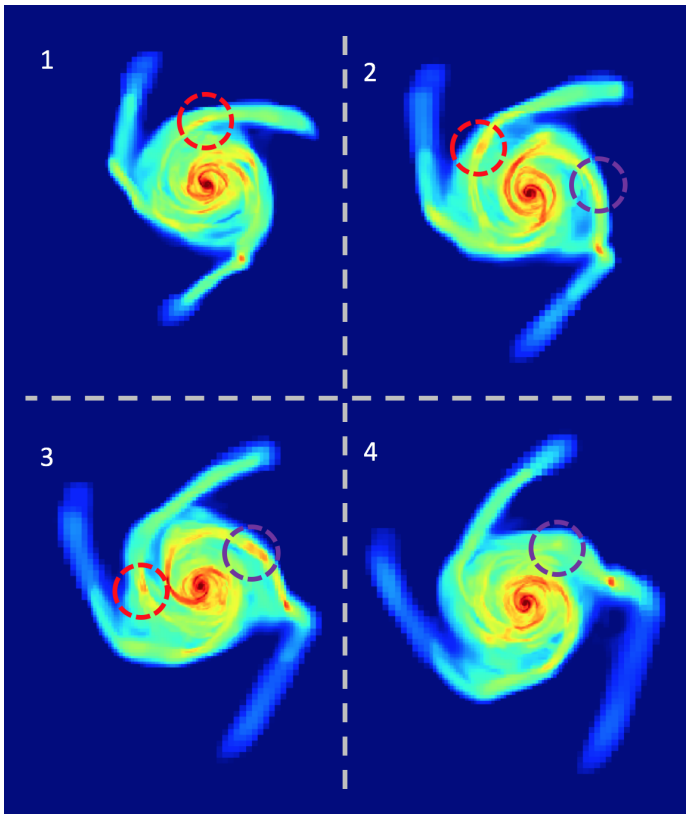

FIGURE 4.3: Time sequence of gas density maps from the 20% gas mass fraction simulation run with the average model of feedback. The color scale is the same as in Fig. 4.2. Snapshots are separated by $\simeq 8$ Myr. The red and purple dashed circles follow the evolution of two gas clumps.

We select the clumps by eye, then follow the peak of density on following outputs. Their size limits are obtained iterationaly using concentric circles on the star plus gas column density map, using an incremental value of 50 pc. We stop the iteration when the mass of the previous iteration is close enough to that of the background (less than a factor 1.33). The background column density is estimated from the mean column density at the galactic radius of the clump, excluding zones less than 0.5 kpc away of the clump. This technic is similar to observational measures of

clump masses (see e.g. Guo et al., 2012).

We get the clump mass functions (CMF thereafter) shown in Fig. 4.4. We see that, at first detection, clumps in the most gas rich cases are slightly more massive. The distribution peaks at $10^{7.9}$ $M_\odot$and $10^{8.1}$ $M_\odot$ for respectively the low and high gas mass fraction cases.

We then measured the mass distribution for each detection. Although the same clump is present several times in the same histogram, the difference between this stacked CMF and the initial CMF shows the mean mass evolution of the clump during their lifetime. For instance, we can see that, in the gas poor case, the bulk of clump moves from $10^{7.9}$ $M_\odot$ to below $10^{7.6}$ $M_\odot$. Moreover, the very massive clumps, with mass over $10^{8.2}$ $M_\odot$, represent around 10% of the clump abundance in the initial CMF drops to around 5% on the stacked CMF. This suggests that clumps mass tend to follow a global decreasing trend in the gas-poor case simulations.

The opposite trend is observed in the gas-rich case. Comparing the initial CMF and the stacked CMF we see that, if clumps with mass below 10^8 $M_\odot$ represent 52% of the initial CMF, their relative abundance drops to below 40% of the stacked CMF, while the high mass tail of the distribution show an increased abundance. This comparison suggests that on average the mass of clumps increase with time in the gas-rich runs.

To get a deeper insight on the evolution of these structures, we measure their *virial parameter* α, defined in Oklopčić et al. (2017) by $\alpha = \frac{5\sigma^2 R}{GM}$, with σ the 1D velocity dispersion along the vertical axis, R and M the radius and mass of the clump (see also Bertoldi and McKee, 1992). They use this parameter to distinguish between bound ($\alpha < 1$) and unbound ($\alpha > 1$) structures. We measure α in our simulations, on clumps of mass between $10^{7.8}$ and $10^{8.2}$ $M_\odot$, to prevent a bias due to the different CMF at the low- and high-mass ends between the gas-poor and gas-rich runs. We get the following results:

TABLE 4.3: Average virial parameter measured in the simulation set. See text for details.

	F20-F25	F50-F60
Weak	2.3	0.6
Average	2.5	0.9
Strong	2.9	1.1

First, we see that the clumps in the gas-poor cases (f_{gas} = 20-25%) are not bound on average. This value for α is consistent with the average value found in (Oklopčić et al., 2017) ($\alpha \simeq 3$, see their Fig. 9). This measure of α also shows the effect of the feedback on the gas-rich clumps, which are at the limit of being bound for the stronger feedback model.

To understand which processes make these clumps lose or gain mass we do a detailed analysis of the gas and star behavior around the clump. For each cell of gas, we compute the relative velocity with respect to the center of mass of the clump. If a linear extrapolation of this velocity on a small time-step – typically 1 Myr – makes the cell cross the border of the clump inwards it is counted as gas accretion, if it

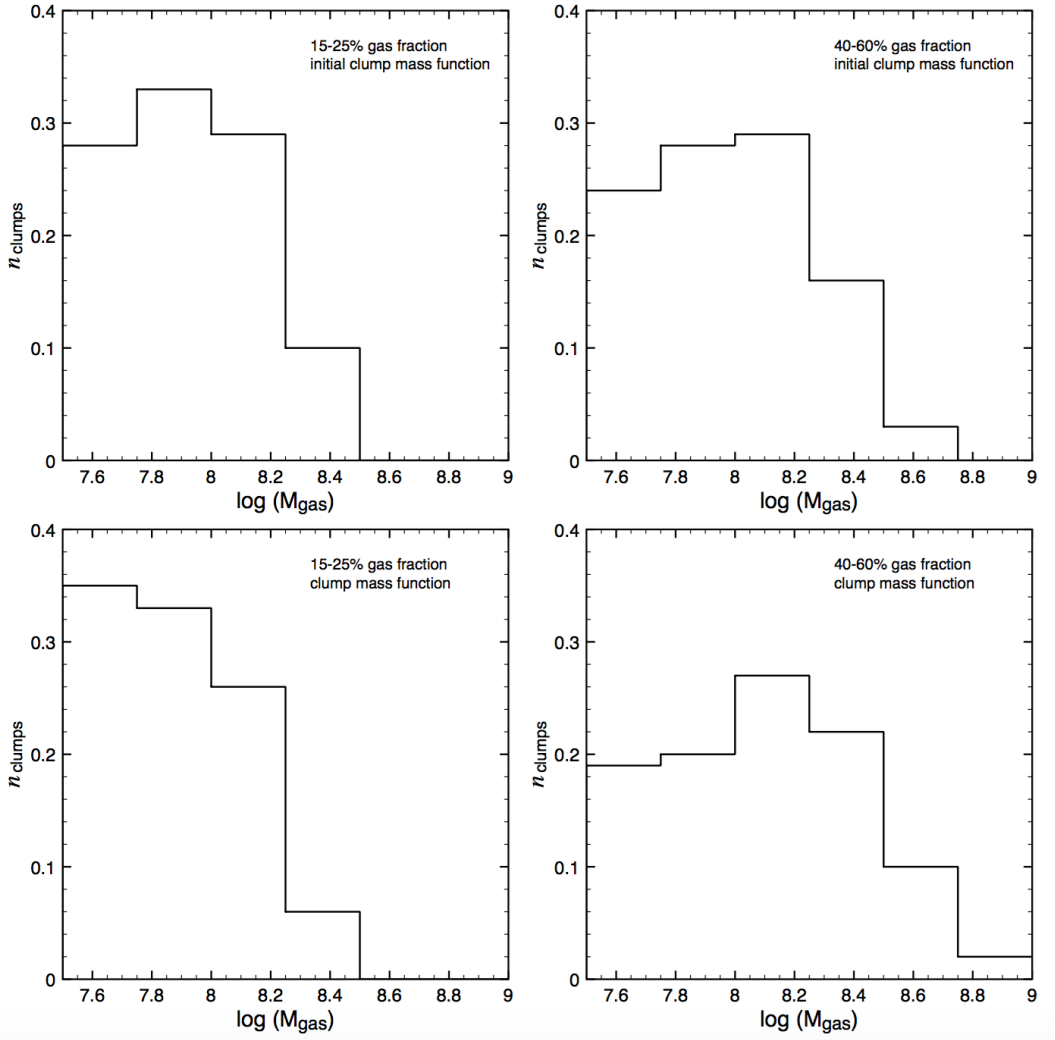

FIGURE 4.4: Clump mass function. The left panels represent the low gas mass fraction cases and the right panel represents the high gas mass fraction cases. The top panels show the clump mass function at the first detection and the bottom panels show the clump mass function for all detections.

crosses outwards it is counted as gas removal, by feedback if the temperature of the cell is above 10^4 K, by stripping otherwise. The same method is applied to stars inside the clump size. We also accounts for gas depletion by star formation by measuring the instantaneous star formation rate in the clump from the implementation formalism described in section 3.2.2. We then divide each of these values by the mass of the clump to get the timescale for gas and star loss and accretion. The results are summed up in table 4.4.

This table quantifies what is seen in the previous figures, namely that gas removal of gaseous clumps is very efficient in the low gas mass fraction case. It should be noted that this gas removal is mainly due to stripping – induced by shear and tidal effects – whiile in the gas-rich case, the gas removal is mainly due to feedback.

This higher sensitivity of shear of clumps in the low gas mass fraction runs seems to be in contradiction with other works, such as Reina-Campos and Kruijssen (2017),

TABLE 4.4: Timescale for gas and star mass loss or accretion for the different gas mass fraction and feedback models.

Timescale for... (in Myr)	15-25% gas fraction *Feedback model:* *weak*	*average*	*strong*	40-60% gas fraction *Feedback model:* *weak*	*average*	*strong*
Gas removal *(by feedback/stripping)*	75 *(355/95)*	70 *(265/95)*	55 *(195/75)*	520 *(890/1250)*	215 *(304/730)*	195 *(270/700)*
Stellar mass loss	215	200	185	660	370	315
Gas (re-)accretion	485	405	415	225	195	185
Gas depletion (internal SF)	225	340	360	260	275	325

which claim that gas clumps change from being shear-limited to being feedback-limited as galaxies become less gas-rich. One should note that in the low gas mass fraction cases, gas clumps form in spiral arms which are regions with high shear. Measures of the shear parameter for clumps in the low and high gas mass fraction runs are presented in Fig. 4.5. We can see that, on average, gas clumps in the low gas mass fraction case are located in regions of higher shear than in the high gas mass fraction case, which results in their higher sensitivity to shear disruption.

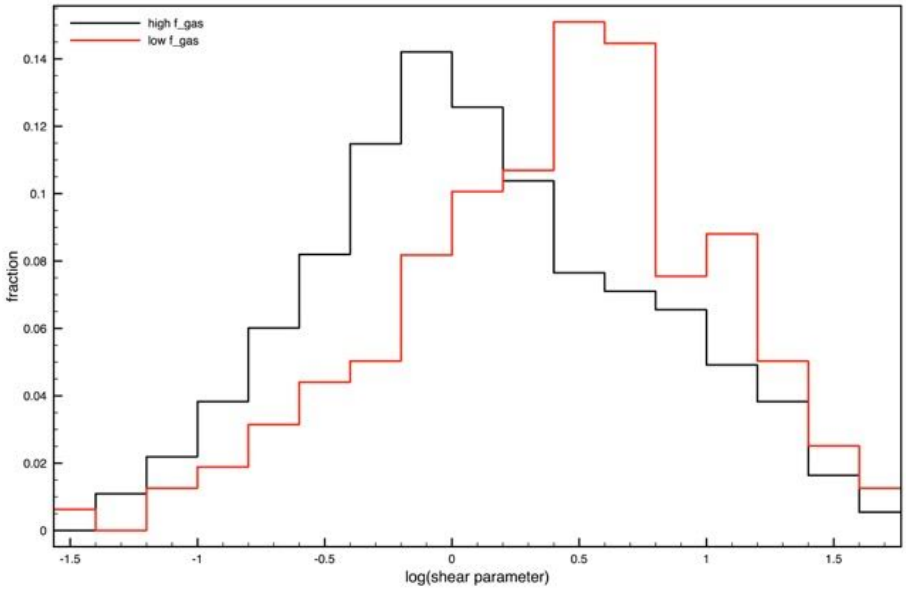

FIGURE 4.5: Histogram of the shear parameter measured for all clump detections, in red for the low gas mass fraction runs and black for the high gas mass fraction case.

4.1.3 Concluding remarks

We have seen that increasing the gas content of galactic disks triggers the formation of massive bound clumps of gas, which survive form stellar feedback and environment disruption (shear and tides) on timescales larger than 200 Myr. These simulations strengthen the scenario of the formation of massive long-lived gas clumps in

gas-rich galactic disks at high-redshift.

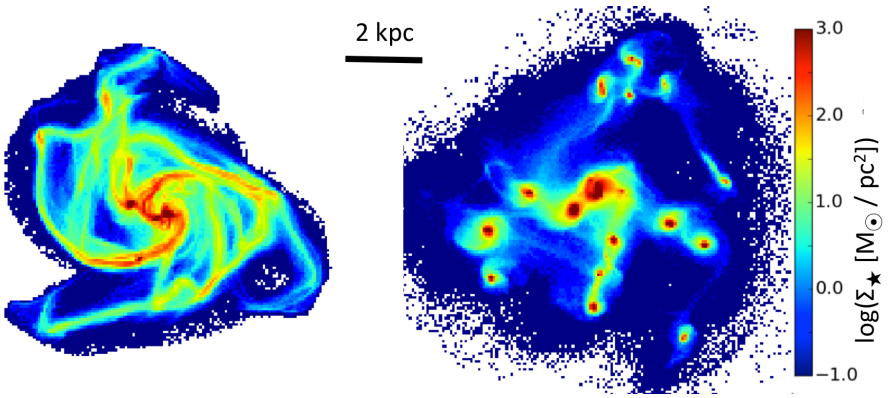

FIGURE 4.6: Stellar surface density of stars formed in the simulation for the simulations with 25% and 50% gas mass fraction and average feedback after 160 Myr of simulation time.

The long lifetime of these gas clumps induces clustered star formation. In Fig. 4.6, we can see the stellar surface density of stars formed during the simulation. We see that in the low gas mass fraction case stars are spread over the spiral structure while, in the gas-rich case, stars are distributed in stellar clumps. A thorough study of the formation and evolution of stellar clusters in gas-rich galaxies will be the purpose of Section 5.2.

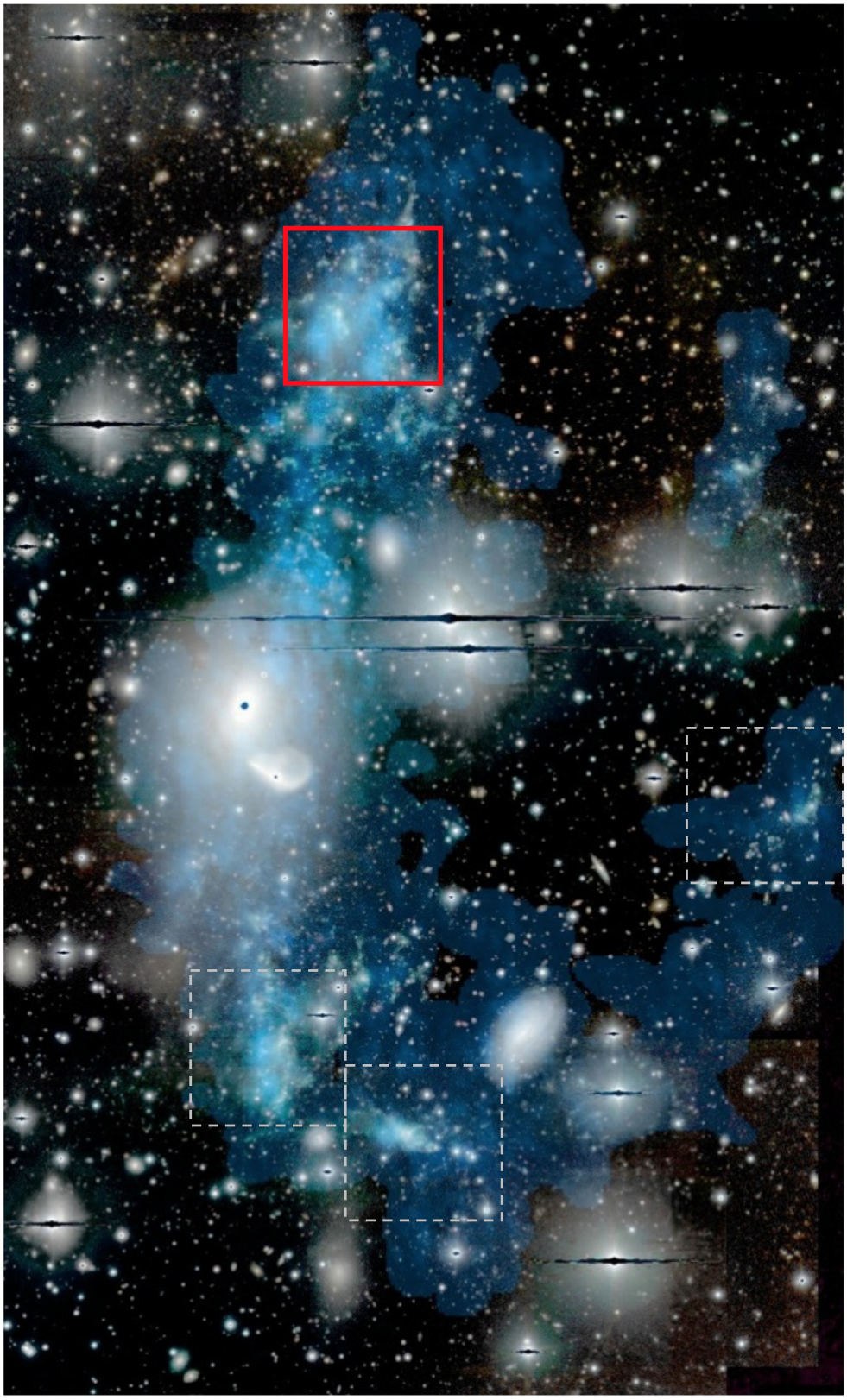

FIGURE 4.7: Composite color FORS@VLT image. HI emission from the VLA is superimposed in blue. The MUSE field of view is shown by the red square (1′ × 1′, 18 kpc×18 kpc). Three other TDGs are shown with dashed gray squares.

4.2 Ionization processes in a local analogue of a high-z giant clump

In the previous Section, we have seen how the gas mass fraction impacts the internal dynamics of a galaxy and induces a clumpy morphology. One may now wonder how this gas mass fraction impacts other physical processes, such as the ionization state of the gas. However, observational constraints of the ionization state of the gas are difficult to obtain for high-redshift clumpy galaxies, because of the distance to us: using the current instrumentation, only clump integrated measurements can be done (see e.g. Förster Schreiber et al., 2009; Wisnioski et al., 2015; Zanella et al., 2015).

To get a deeper insight into the structure of the gas clumps, I have studied a local analogue to these high-redshift clumps, NGC 5291N. This object is a tidal dwarf galaxy (TDG), located in a huge HI ring – 180 kpc diameter and $M_{HI} > 10^{10}$ $M_{\odot}$ (Duc and Mirabel, 1998) – depicted in Fig[2]. 4.7. This ring formed after a head-on encounter between the galaxy NGC 5291 and a massive interloper (Bournaud et al., 2007). Gas in this ring collapsed, forming stars and also several massive and gravitationally bound structures with mass as high as $2 \times 10^9 M_{\odot}$(Lelli et al., 2015). These structures are very gas rich, $f_{gas} \simeq 80\%$ (Bournaud et al., 2007), show CO emission (Braine et al., 2000) and have a clumpy morphology. The simulation predicts a young age for these structures (<500 Myr), which is supported by observations of Wolf-Rayet features in their optical spectra, and by their SED being consistent with the absence of stars older than 1 Gyr (Boquien et al., 2010). Despite their youth, they inherited the metal enriched gas from their parent galaxy and have a half-solar metallicity.

As argued in Section 2.2.3, these TDGs are indeed good analogues of clumps of gas rich galaxies at high-redshift. In the following we will be interested in the northern condensation NGC 5291N, indicated by the red square in Fig. 4.7, which was our target for a MUSE Science Verification proposal (PI: Duc). The following work has been published in Fensch et al. (2016) (F16 thereafter).

4.2.1 MUSE observations

MUSE is an integral field spectrograph mounted on the VLT, and had its first light in January 2014. It works in the optical range (4650-9350 Å), has a spatial resolution of $0.2'' \times 0.2''$ and a spectral sampling of 0.8 Å after data reduction which was carried out by our collaborator P. Weilbacher with a dedicated pipeline (Weilbacher et al., 2012).

Part of a spectrum from a single pixel, taken in the center of the dwarf, is shown in Fig. 4.8. It shows the presence of strong emission lines such as the recombination lines $H_{\alpha}$and H_{β}, but also forbidden lines[3] such as [OIII], [NII], [SII] and [OI]. On the bottom panel of Fig. 4.8, we can also see a continuum emission, with a blue slope.

[2]This picture has been the object of an image release by ESO: www.eso.org/public/news/eso1547/

[3]The term forbidden comes from the probability of de-excitation of these energy levels through photon emission which is very low compared to collisional mechanisms. These lines cannot be observed in the laboratory. However, at densities as low as in the ISM, de-excitation can occur mainly trough photon emission. The convention is to use brackets for forbidden emission lines.

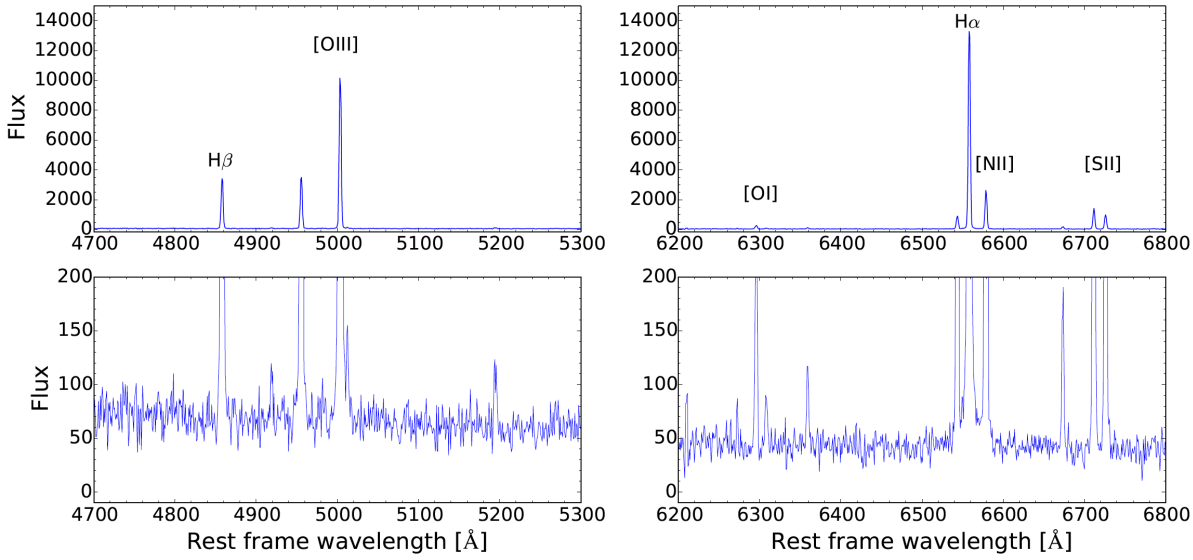

FIGURE 4.8: Example of a spectrum from a single extracted pixel. The bottom panel show a zoom-in on the continuum for the same spectral range. Several emission lines which will be used in the following are labelled.

I removed the continuum emission using the *continuum* task under PyRAF[4]. A composite color image of the continuum is shown on the left hand panel of Fig. 4.9. One can see the presence of a blue diffuse continuum emission around the dwarf galaxy in the middle. A study of the continuum emission, and a discussion of its origin is presented in F16. In the following I will mainly present my results on the emission lines.

I modeled the emission lines shown in Fig. 4.8 with gaussians. A composite color image using different emission lines ([OIII], $H_\alpha$and [NII]) is shown in Fig. 4.9. We can see that their emission is not homogeneous across the field of view. For instance, there are strong [OIII] emission in small isolated regions. In the following I will describe the spatial variations of the emission lines and how to interpret them.

4.2.2 Physical properties

Emission line ratios may be used to probe the following characteristics of the ISM, this list being non-exhaustive.

- **Electron density:** For all forbidden line doublets, the relative intensity of the two lines depends on the density in the medium (Osterbrock and Ferland, 2006). This is due to a transition between a low density medium where the transition is dominated by light emission, and a high density medium where the transition is dominated by collisions. This transition depends on the species, and the relative intensity of the two lines of the [SII] doublet (at 6717Å and 6731Å rest frame) can probe densities between 10 and 10^4 cm^{-3}. In our case, the density at the scale of 180 pc$\times$180 pc reaches a maximum value of 300 cm^{-3}

[4]http://www.stsci.edu/institute/software_hardware/pyraf

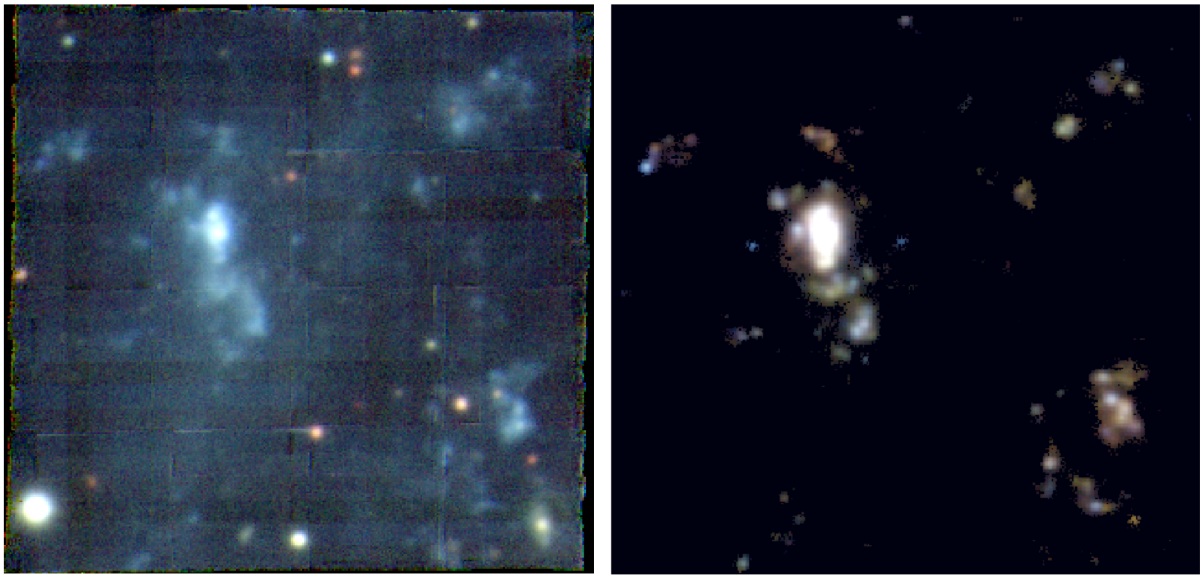

FIGURE 4.9: Composite color images. Left: Emission from the extracted continuum. Right: Emission from different emission lines: [OIII] (blue), H_α(green) and [NII] (red). The field of view spans 18 kpc $\times$ 18 kpc.

- **Extinction:** For the characteristics of the medium we are interested in[5], the theoretical ratio between H_α and H_β, called the Balmer decrement, is $\simeq 2.86$ (Osterbrock and Ferland, 2006). The difference between the observed and theoretical Balmer decrement probes the reddening due to the dust extinction, which affects more the bluer part of the optical spectrum. In F16 we show that the attenuation A_V is between 0 and 1 mag which is consistent with the SED analysis performed by Boquien et al. (2010).
- **Metallicity:** The metallicity is often obtained through a direct computation of the electron temperature using the [OIII] line at 4363Å (Osterbrock and Ferland, 2006), which is however out of our spectral range. Therefore we use an empirical calibration from Marino et al. (2013), which uses the O3N2 = $\log_{10}\left(\frac{[\mathrm{OIII}]/\mathrm{H}_\beta}{[\mathrm{NII}]/\mathrm{H}_\alpha}\right)$ parameter. We find a homogeneous value of 12 + log(O/H) $\simeq 8.35$ all across the TDG, consistent with no enrichment from recent star formation activity yet. This value is consistent with previous studies (Duc and Mirabel, 1998; Boquien et al., 2010), which have further shown, with a lower spatial resolution, that the metallicity is the same for all star forming regions across the HI ring.

In addition to these physical parameters, emission lines can also probe the ionization state of the gas. To do so, one may use BPT[6] diagrams (Baldwin, Phillips, and Terlevich, 1981). The diagnostic is done by locating a galaxy in an emission line ratio plane. These emission line ratio are [OIII]/H_β against X/H_α, where X is a forbidden emission line close to the H_α line to prevent any redenning effect due to the attenuation, typically [NII], [SII] or [OI]. The idea behind this diagram is that forbidden levels are specifically populated through collisional excitation and shocks, or

[5]The assumptions are: case B recombination, electron density of 100 cm^{-3} and electron temperature of 10^4 K.

[6]This is an acronym for Baldwin, Phillips and Terlevich, first authors of the first paper using these diagnostic diagrams.

through high-energy ionization, typically close to an active galactic nucleus (AGN) (see Osterbrock and Ferland, 2006). Baldwin, Phillips, and Terlevich (1981) have found lines for which the ratio of forbidden lines to recombination lines behavior changes significantly, allowing them to propose a classification.

These diagrams were first used on the integrated spectrum of galaxies and succeeded in discriminating whether the gas was primarily ionized through pure photo-ionization from stellar light, by an AGN or low-ionization nuclear emission-line regions (LINER). The discrimination lines have been updated from the original BPT paper, and have been set both by observations (Kauffmann et al., 2003, using Sloan Digital Sky Survey spectral data) and theoretical modeling (Kewley et al., 2001).

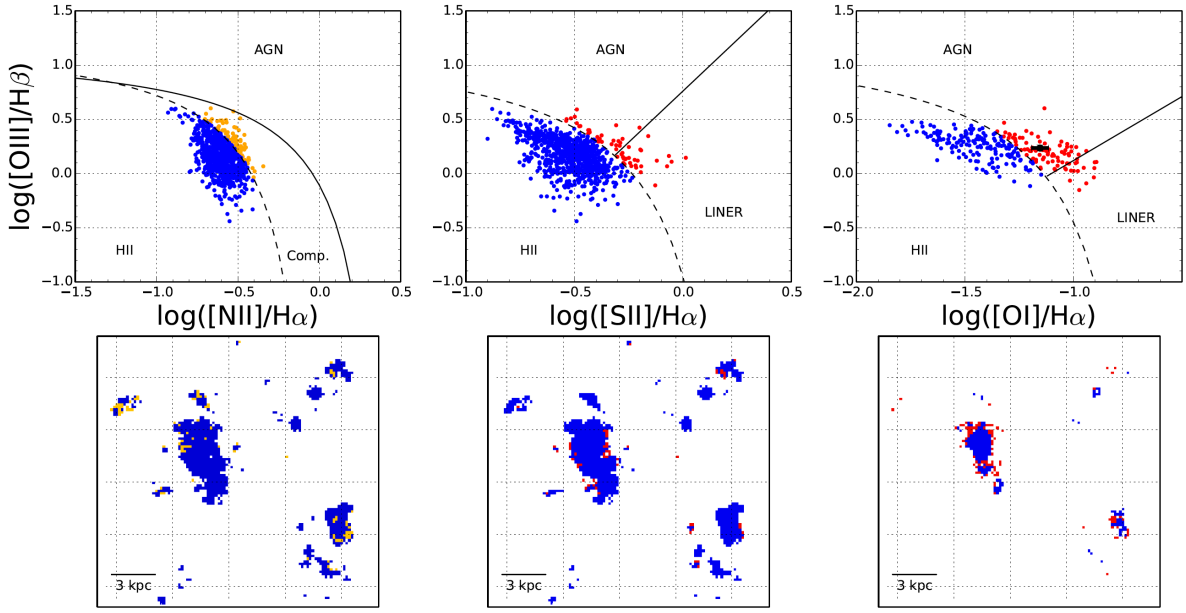

FIGURE 4.10: BPT diagnostics for different emission line ratios. On the [OIII]/H_β vs [NII]/H_α diagram, the dotted line delineates the pure starburst region, as defined by Kauffmann et al. (2003). The spaxels belonging to this region are shown in blue, those outside it in orange; their spatial location is shown in the figure below. The field of view is the same as in Fig. 4.9. The solid line traces the upper theoretical limit to pure HII regions computed by Kewley et al. (2001). For the other diagrams, the dashed lines defined by Kewley et al. (2006) separate the starburst (blue points) from the AGN/LINER (red points) regions. The solid lines further distinguish between AGN ionization (above the line) and LINER ionization (below). The corresponding spatial distribution of starburst/non-starburst binned spaxels are shown below. The highest fraction of spaxels inconsistent with a photoionization by a starburst show up on the [OIII]//H_β vs [OI]/$H_\alpha$diagram. Their spectra have been stacked and the resulting extracted line ratios are shown with the black point, together with the error bar.

I applied these diagnostic diagrams on NGC 5291N, this time on each resolution element. The resulting BPT diagrams are shown in the upper panel of Fig. 4.10. The blue points correspond to spatial regions were the emission lines are consistent with originating from pure photo-ionization: their spatial location is shown on the

lower panel, for each diagram. The red points are however not consistent with pure photo-ionization models. We see that extended regions of the dwarf galaxy, namely around the main star forming region, are not on the photo-ionization region of the [OI]/ H_α BPT diagram.

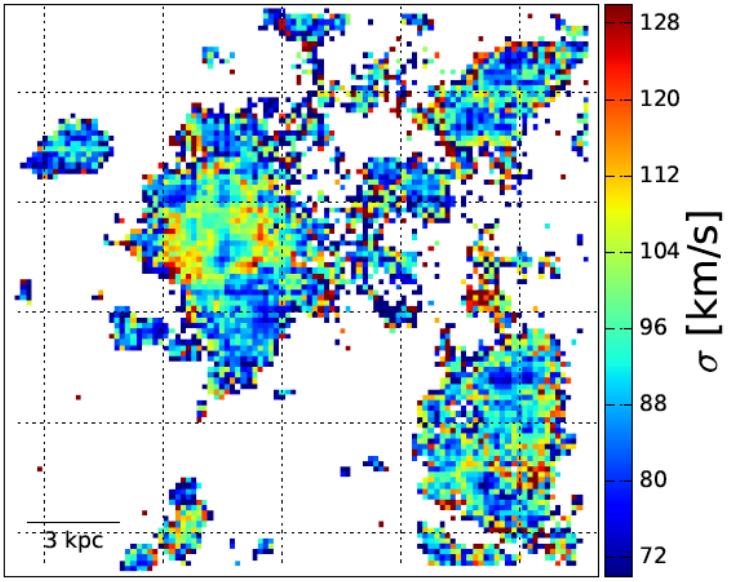

FIGURE 4.11: Velocity dispersion measured from the width of the H_α emission line. We subtracted a constant value of 2.34 Åto the width of the line, corresponding to the average Gaussian FWHM close to the H_α line.

To test the hypothesis of a shock-heating origin for this strong [OI]/H_α emission, I have measured the velocity dispersion through the width of the H_α line. The result is shown on Fig. 4.11. We see that the velocity dispersion is indeed higher on the outskirts of the galaxy. This suggests the possibility of shock-ionization in this region.

I tested the shock hypothesis with the fast radiative shock model from Allen et al. (2008), which is based on MAPPINGS III (Sutherland and Dopita, 1993). The resulting grids superimposed on the BPT diagrams are shown in Fig. 4.12. The purple dashed line is the ionization model prediction, using a metallicity Z = 0.5 $Z_\odot$. The ionization parameter goes from log U = -2 to log U = -3.5, as indicated on the third diagram. The shaded grey regions shows the area covered by the shock model: we see that shocks can bring emission line regions to the same locus as our observations on the [OI]/ H_α BPT diagram.

Several hypotheses could explain the presence of shocks around the dwarf. For instance, they might be due to strong outflows from the intense star formation in the dwarf. However, there is no sign of an underlying broad emission in $H_\alpha$across the TDG. Another hypothesis would be the accretion of gas onto the dwarf. Were it the case one may wonder why we see this emission not only around the most massive component but also around surrounding regions. A last hypothesis is that these high velocity dispersions are the remaining signature of the collision which created the HI ring. However, the numerical simulation of this system presented in

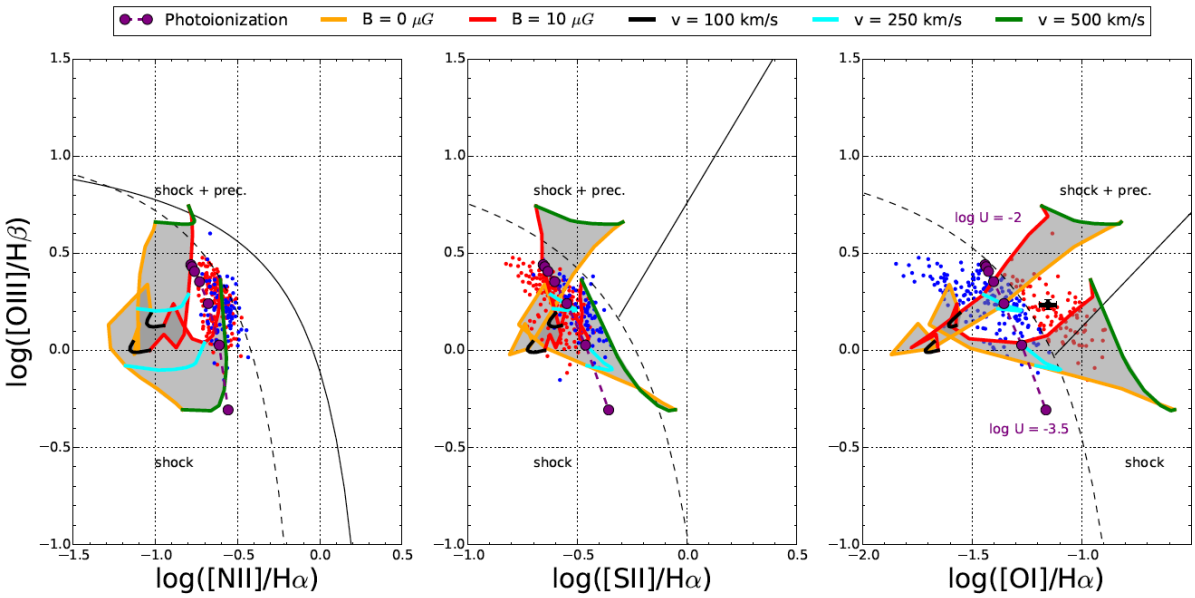

FIGURE 4.12: Shock models on the BPT diagrams. Only points with detected [OI] emission are indicated. The blue (resp. red) points lie in (resp. out of) the star formation locus on the [OI] / H_α BPT diagram. The locus of both grids are shaded. The parameters are described in the text.

Bournaud et al. (2007) predicts that the velocity dispersion is the ring should have decreased to $\simeq 40\ \mathrm{km\ s^{-1}}$, which is not enough to explain this emission if we refer to Fig. 4.12.

It is interesting to note that other nearby dwarfs show strong [OI]/H_α ratio on their outskirts (Cairós et al., 2010). The only other dwarf targeted by MUSE so far, a BCDG named ESO 338-IG04, shows strong outflows probed by H_α broad emission and highly ionized cones (Bik et al., 2015). It is interesting to note that these features is absent from our targeted galaxy.

To further study the origin of this strong [OI]/ H_α emission, we applied for MUSE observation of the other three dwarfs showed in Fig. 4.7. We obtained the time (PI:Boquien) but because of the bad weather only one dwarf could be observed during the two periods (the middle bottom TDG on Fig. 4.7). Reduction of this data is on-going.

Astronomy & Astrophysics manuscript no. Article_final
September 30, 2015

Ionization processes in a local analogue of distant clumpy galaxies: VLT MUSE IFU spectroscopy and FORS deep images⋆ of the TDG NGC 5291N

J. Fensch[1], P.-A. Duc[1], P. M. Weilbacher[2], M. Boquien[3,4], and E. Zackrisson[5]

[1] Laboratoire AIM Paris-Saclay, CEA/IRFU/SAp, Universite Paris Diderot, F-91191 Gif-sur-Yvette Cedex, France
[2] Leibniz-Institut für Astrophysik, An der Sternwarte 16, 14482 Potsdam, Germany
[3] Institute of Astronomy, University of Cambridge, Madingley Road, Cambridge, CB3 0HA, United Kingdom
[4] Unidad de Astronomía, Fac. de Ciencias Básicas, Universidad de Antofagasta, Avda. U. de Antofagasta 02800, Antofagasta, Chile
[5] Department of Physics and Astronomy, Uppsala University, 751 20 Uppsala, Sweden

ABSTRACT

Context. We present IFU observations with MUSE@VLT and deep imaging with FORS@VLT of a dwarf galaxy recently formed within the giant collisional HI ring surrounding NGC 5291. This TDG-like object has the characteristics of typical z=1-2 gas-rich spiral galaxies: a high gas fraction, a rather turbulent clumpy ISM, the absence of an old stellar population, a moderate metallicity and star formation efficiency.
Aims. The MUSE spectra allow us to determine the physical conditions within the various complex substructures revealed by the deep optical images, and to scrutinize at unprecedented spatial resolution the ionization processes at play in this specific medium.
Methods. Starburst age, extinction and metallicity maps of the TDG and surrounding regions were determined using the strong emission lines Hβ, [OIII], [OI], [NII], Hα and [SII] combined with empirical diagnostics. Discrimination between different ionization mechanisms was made using BPT–like diagrams and shock plus photoionization models.
Results. Globally, the physical conditions within the star–forming regions are homogeneous, with in particular an uniform half-solar oxygen abundance. At small scales, the derived extinction map shows narrow dust lanes. Regions with atypically strong [OI] emission line immediately surround the TDG. The [OI] / Hα ratio cannot be easily accounted for by photoionization by young stars or shock models. At larger distances from the main star–foming clumps, a faint diffuse blue continuum emission is observed, both with the deep FORS images and MUSE data. It does not have a clear counterpart in the UV regime probed by GALEX. A stacked spectrum towards this region does not exhibit any emission line, excluding faint levels of star formation, nor stellar absorption lines that might have revealed the presence of old stars. Several hypotheses are discussed for the origin of these intriguing features.

Key words. galaxies: dwarf – galaxies: individual: NGC 5291N – galaxies: interactions – galaxies: ISM – galaxies: starburst – galaxies: star formation – HII regions

1. Introduction

Under the current paradigm of a ΛCDM cosmology, dwarf galaxies are considered the building blocks of today's massive galaxies (Kauffmann et al. 1993), and as such numerous detailed studies are devoted to nearby dwarfs. Among them, the starbursting Blue Compact Dwarf Galaxies (BCDGs), which are less than 1 kpc large and show very low metallicities (1/40th $Z_\odot$ < Z < $Z_\odot$ / 3), have long been believed to be very young objects (Sargent & Searle 1970; Kunth et al. 1988), just like the newly formed galaxies at high redshift. However, the detection of extended red stellar emission (Loose & Thuan 1986; Papaderos et al. 1996) showed that most BCDGs are actually old systems.

The object investigated in this paper, NGC 5291N (NED[1] distance: 63.1 Mpc), was originally classified as a BCDG (Maza et al. 1991). It however stands out as it shows no hint for an old stellar component (Boquien et al. 2007, 2010) , is very gaseous – M_{gas} is around 85 % of the total mass (Bournaud et al. 2007) – and has a clumpy structure. Its metallicity, about half-solar (Duc & Mirabel 1998, thereafter DM98) is higher than in classical BCDGs, but not so different than that of a number of distant star–forming galaxies with metallicities greater than 0.4 $Z_\odot$ at z = 2 (Erb et al. 2006; Stark et al. 2008; Steidel et al. 2014; Zanella et al. 2015). Therefore, the dynamically young dwarf NGC 5291N (Bournaud et al. 2007) appears as one of the most promising (low–mass) analogue of the distant gas-dominated clumpy galaxies, that are found in number in deep cosmological fields. It was formed in a huge gaseous ring ($M_{HI} > 10^{10}$ $M_\odot$, DM98), surrounding the early-type galaxy NGC 5291 that expanded in the intergalactic medium after a violent collision with a bullet galaxy. According to numerical simulations, the encounter occurred 360 millions years ago (Bournaud et al. 2007). The HI rich ring formed a series of star–forming clumps. A kinematical analysis (Bournaud et al. 2007; Lelli submitted) revealed that three of the gas condensations are most likely gravitationally bound. Our target, NGC 5291N, is the most massive of them. Similar to Tidal Dwarf Galaxies (TDGs, see review by Duc & Mirabel 1999), NGC 5291N has a low dark matter (DM) content. As a matter of fact, NGC 5291N shares many properties with the 10^8 $M_\odot$ individual clumps, which formed within the gravi-

Send offprint requests to: J. Fensch (jeremy.fensch@cea.fr)
⋆ Based on observations collected at the European Organisation for Astronomical Research in the Southern Hemisphere, Chile: ESO MUSE program 60.A-9320(A) and FORS program 382.B-0213(A)
[1] NASA/IPAC Extragalactic Database.

tationally unstable gas-dominated disk of distant clumpy galaxies (Zanella et al. 2015), and are also presumably dark-matter poor. The stability of such objects against internal feedback is a matter of active debate (e.g. see Genel et al. 2012; Bournaud et al. 2014). It can be investigated in NGC 5291N, with great accuracy, keeping in mind however that the star–formation rate of this local analogue is much lower: around 0.14 $M_{\odot}yr^{-1}$ for NGSC 5291N (Boquien et al. 2010) compared to 32 ± 6 $M_{\odot}$ yr^{-1} for the z = 2 clump in Zanella et al. (2015).

The ring of NGC 5291 and its dwarf galaxies within it have been observed by a wide range of ground-based and spatial instruments, resulting to an extensive wavelength coverage: HI 21-cm line with the VLA (Bournaud et al. 2007), far–infrared with PACS and SPIRE on Herschel (Boquien et al., in prep.), mid–infrared with Spitzer (Boquien et al. 2007), near-infrared with ISAAC on the ESO VLT, optical slit with EMMI on the NTT and Hα integral field spectroscopy with a Fabry-Perot (FP) unit on the ESO 3.6m (Bournaud et al. 2004), and Far and Near Ultra-Violet with GALEX (Boquien et al. 2007). The slit optical spectroscopy of NGC 5291N disclosed a number of bright emission lines, presumably associated with H II regions; FP observations revealed complex kinematical features within the dwarf on top of the ordered rotation also seen in the HI component. A better understanding of the physical conditions in the interstellar medium requires 3D spectroscopic information, at good spatial and spectral resolution, and a relatively large field of view. This is the capability of the Multi Unit Spectroscopic Explorer (MUSE), which has been recently mounted on the VLT, at Paranal observatory (Bacon et al. 2010), and that is about to revolutionize this field of research. We present here MUSE observations of NGC 5291N. They provide us with several ten thousands of resolved spectra and allow us to probe the ionizing processes in the dwarf at physical spatial scales of only 200 pc. Their exploitation is backed by deep multi-band images obtained with the FORS instrument on the ESO VLT.

Former IFU observations of dwarf galaxies have already given us some insight on the ionization properties of these galaxies (Izotov et al. 2006; Lagos et al. 2009, 2012, 2014; James et al. 2009, 2010, 2013a,b) and led to the identification of regions with Wolf-Rayet stars (Cairós et al. 2010; Kehrig et al. 2013), the presence of non-thermal ionization processes such as shocks (Cairós et al. 2010) or the existence of a central AGN (Cairós et al. 2009). To our knowledge, this paper is only the second one presenting MUSE observations of a dwarf galaxy, and the first one focused on a colliding system. Previously, ionized cones associated with formerly observed Lyα photons leakage, and possibly correlated with outflows, have been identified around the starburst ESO 338-IG04 (Bik et al. 2015).

The paper is structured as follows: Sect. 2 describes the observation and data reduction procedures. Sect. 3 presents the detailed analysis of the emission lines and continuum emission, with a focus on their spatial variations. These results are discussed in Sect. 4. The final conclusions are drawn in Sect. 5.

2. Observation and Data Reduction

2.1. MUSE data

NGC 5291N was observed using the integral field spectrograph Multi-Unit Spectroscopic Explorer (MUSE) (Bacon et al. 2010) mounted on the Very Large Telescope (VLT). The observations were performed on June 2014 during the first science verification run (60.A-9320(A), PI: P.-A. Duc). We obtained spectra between 4750 Å and 9350 Å over a field of view of 1′×1′, which corresponds to 18 kpc×18 kpc at a distance of 63.1 Mpc.

The observations consisted of three on source exposures of 600 s each, obtained at three position angles (0, 90, and 180°). Two exposures of 100 s were done on an offset (blank) sky field. Twilight sky flats taken the following evening were used in the data reduction process; an exposure of the spectrophotometric standard star LTT 7987 taken in the following morning twilight was used for flux calibration. The reduction used the MUSE pipeline (Weilbacher et al. 2012) through the EsoRex program. We used a development version of the pipeline, but the code was very close to the 1.0 release[2]

We followed the usual steps, with bias subtraction, flat-fielding, and spectral tracing using the lamp-flat exposures, wavelength calibration, all using daytime calibrations made the morning after the observations. The standard geometry table and astrometric solution derived during Commissioning 2a were used to create the intermediate pixel tables. Since the observations were done at a low ambient temperature of $\sim 6°$C, slice 6 of channel was not illuminated and could not be traced. We followed the procedure outlined in the pipeline manual to delete the data of this slice from the science pixel tables.

Sky spectra were created using 75% of the field of view of the two offset sky fields, and the line-spread function derived from the same wavelength calibration exposures was then used to decompose the spectrum into sky emission lines and continuum.

The science reduction was then assigned the sky continuum that was taken closest in time to the science exposure, and we allowed the sky emission line fluxes to be re-adjusted for the science data. The data were corrected for atmospheric refraction, corrected to barycentric velocities (the corrections were about $-23.8\,km\,s^{-1}$), before being combined into the final cube. We chose a non-standard sampling in the spectral direction, so that the output cube has steps of $0''.2 \times 0''.2 \times 0.8$ Å. The spatial FWHM measured on the white-light image created from this final, combined cube, is about 0″.8.

An example of the extracted spectrum for a single spaxel is shown in Fig. 1. It exhibits the very strong emission lines of the Balmer lines Hβ and Hα, but also forbidden lines such as [OIII] $\lambda\lambda$4959, 5007, [NII] λ6583, [SII][3] $\lambda\lambda$6717, 6731 and [OI] λ6300 line. To create reliable spatial maps of line fluxes, the data cube was re-binned by 3x3. Given the depth of the data, using an adaptative smoothing routine was not necessary: for most regions, a signal to noise ratio (S/N) higher than 3 was reached with the adopted fixed 3x3 binning. The resulting spatial dimensions of the final 3x3 spaxels are $0''.6 \times 0''.6$, or 180 pc×180 pc.

The continuum emission was extracted from the spectra with the PYRAF *continuum* procedure. Emission line fluxes were computed with custom-made Python scripts based on Gaussian fits. We only studied regions where the emission was 3σ above the noise and we made sure that our Gaussian fitting error was less than 10% of the total line flux. Unfortunately, the redshift of the galaxy put the $[SII]_{\lambda6731}$ very close to airglow lines at 6827 Å, making it very hard to detect at low luminosity. However, the [SHII]λ6717/[SII]λ6731ratio is a tracer of the electron density. In the low-density limit, it reaches 1.45. In the brightest region in our field, the lowest value is 1.15, corresponding to an electron density of 300 cm^{-3}. Therefore, in the case of a non-detection

[2] Available from ESO via `http://www.eso.org/sci/software/pipelines/muse/muse-pipe-recipes.html`.

[3] Unless stated otherwise, [SII] refers to [SII]λ6717 + [SII]λ6731.

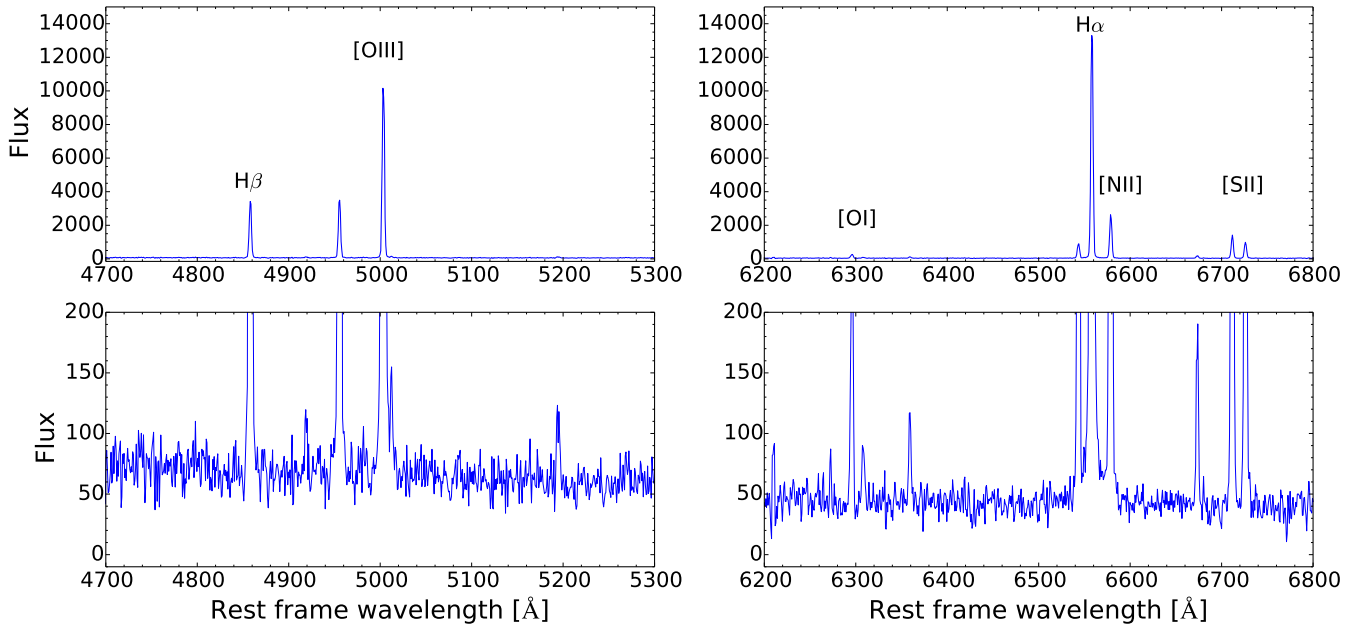

Fig. 1. Top: Spectrum of a single spaxel, before the re-binning, at the position of the brightest region with the position of the main emission lines. Bottom: Zoom on the same spectrum. The flux unit is 10^{-20}erg.cm^{-2}.s^{-1}.

of [SII]$_{\lambda 6731}$ but a good detection of every other lines, a value of [SII]$_{\lambda 6731}$ = [SII]$_{\lambda 6717}$/1.42 is chosen, which corresponds to a maximum error of 9% on the value of [SII] = [SII]$_{\lambda 6717}$ + [SII]$_{\lambda 6731}$ for the densest regions, which is lower than the uncertainty on the Gaussian fit, and less than 2% for regions with $n_e < 100$ cm^{-3} which are the hardest to resolve. The uncertainty for the value of [SII]$_{\lambda 6731}$ is not available for the spaxels which needs this method, as it is dominated by the noise from the sky line. When mean uncertainties involving the [SII] emission doublet are to be assessed, points where [SII]$_{\lambda 6731}$ is blended by the airglow line will not be taken into account.

2.2. FORS data

The deep optical V, R and I images have been acquired in March 2010 with the instrument FORS on the VLT (Program 382.B-0213(A), PI: E. Zackrisson). The final images, covering a total field of view of 11.2′× 15.5′were obtained by registering and combining 26 individual exposures of 300 sec, 300 sec and 240 sec in the V, R and I Bessel filters respectively. Photometric zero-points were provided by the ESO pipeline. The limiting surface brightness in the V band is estimated to 27 mag arcsec^{-2} (Vega), from the local fluctuations in the background. The average FWHM of point sources in the stacked image is 1.0″.

The FORS image of the whole system, including the collisional ring and its host galaxy, is shown on the left part of Fig. 2, with the HI emission from the VLA superimposed in blue. The radio data highlights the shape of the ring structure. The field of view of the MUSE observations towards the TDG NGC 5291N is delineated by the white square. Both the composite FORS broad-band image (Fig 2, top-right) and the MUSE narrow-band image (Fig. 2, bottom-right) reveal the clumpy structure of the ISM of NGC 5291N. The FORS image mostly exhibits continuum emission; the MUSE image is a combination of emission from three main lines: [OIII] (λ5007), Hα. and [NII] (λ6583). As shown by comparing the FORS and MUSE images (see also Fig. 2), the individual clumps are associated to strong emission lines and are embedded in regions with extended diffuse continuum emission.

3. Results

As illustrated in Fig. 2, the MUSE spectrophotometric data show a striking large heterogeneity towards a recently born object, NGC 5291N, which could a priori be considered simple. While the continuum emission has a rather uniform blue color, the emission line ratios strongly vary at small scales. We analyse in the following the spatial variations of the observed spectral lines and investigate various diagnostics to account for them.

3.1. Dust extinction

Before investigating the spatial variations of the emission line ratios, dust extinction maps were computed to allow for reddening correction of the emission line fluxes. These maps were derived from the Hα/Hβ Balmer line ratio. The LMC extinction law from Gordon et al. (2003), with R_V = 3.41, was used in combination with a theoretical value for the unobscured line ratio for case B recombination of Hα/Hβ = 2.86, for T_e = 10,000 K and n_e = 100 cm^{-3} (Osterbrock & Bochkarev 1989).

As shown in Fig. 3, the extinction is globally low with however local variations of Av by up to 1 mag. The dust reddening peaks at a value of $A_V \simeq 1.25$ mag towards regions where dust emission had been observed with Spitzer and Herschel. The FORS color image also show the presence of narrow dust lanes at this location (Fig. 4). The extinction derived from the MUSE data is consistent with the one derived by Boquien et al. (2010) from their fit of the Spectral Energy Distribution probed by the FUV, NUV, B, V, R, J, H, and K bands. It is higher than that originally estimated by DM98 from slit spectroscopy.

In the following all emission line fluxes are corrected for dust extinction.

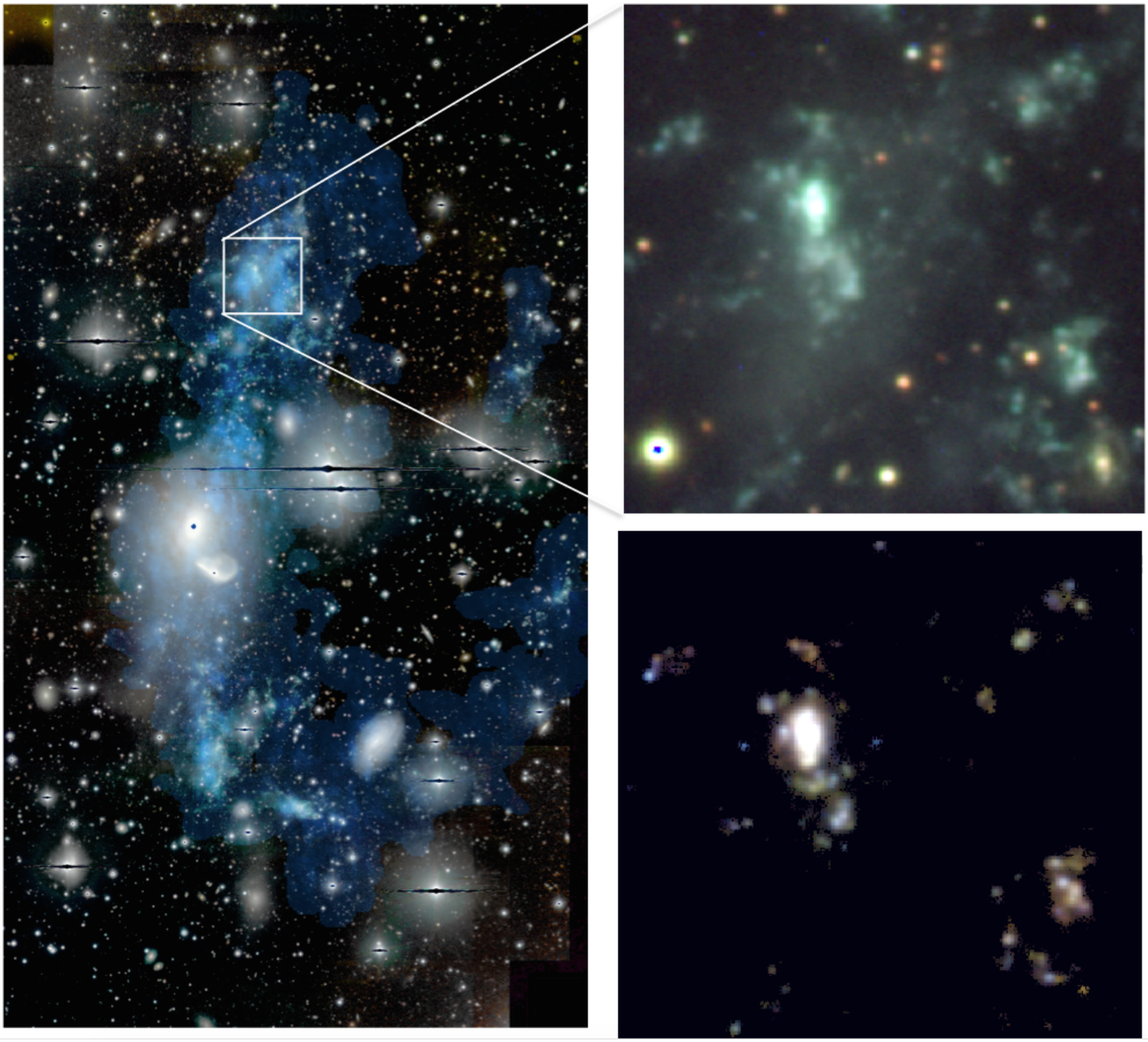

Fig. 2. Left: Composite image of the NGC 5291 collisional ring. Background is a FORS composite color image obtained with the V, R, and I bands. HI data from the VLA is superimposed in blue. North is up and East is left. The white square centred on NGC 5291N delineates the MUSE field of view. Upper right: FORS V, R, I composite color image of the MUSE target. Lower right: MUSE composite color image using three different emission lines: *Red:*[NII]λ6583, *Green:* Hα, *Blue:* [OIII]λ5007. Each pixel covers a 60 pc $\times$ 60 pc region and the full image corresponds to 1′×1′, or about 18 kpc x 18 kpc at the distance of NGC 5291N, 63.1 Mpc.

3.2. Spatial Variation of the Emission Line Ratios

The spatial variations of the main emission line ratios are plotted in Fig. 5. An inside-out positive gradient is seen in the [NII]λ6584 / Hα, [SII]$\lambda\lambda$6717,6731 / Hα and [OI]λ6300 / Hα maps whereas the gradient is negative for the [OIII]λ5007/Hβ line ratio. Besides these large scale variations, some clumps exhibit deviant emission line ratios (see also the lower right panel of Fig. 2). The one immediately North of the TDG has the strongest [NII]/Hα ratio in the field and the clump to the North-West the strongest [OIII]/Hβ ratio.

The flux ratios also depend on the flux intensity of the lines. In Fig. 6, the emission line ratios are plotted as a function of the Hα flux. [SII]/Hα and [OI]/Hα ratios increase significantly with lower Hα surface brightness, whereas [OIII] / Hβ decreases.

The scatter is large at low Hα surface brightness, partly due to the increase of the measurement errors.

The ISM can be ionized by several mechanisms: photoionization due to ultraviolet (UV) photons from young, hot stars, photoionization from an Active Galactic Nucleus (AGN), shock ionization due to stellar winds and supernovae, or shock ionization from dynamical processes such as collisions. In order to gain insight into the processes at play, line ratio diagnostics diagrams, known as BPT diagrams (Baldwin et al. 1981; Veilleux & Osterbrock 1987) are used: [OIII]λ5007 / Hβ versus [NII]λ6584 / Hα, [SII]$\lambda\lambda$6717,6731 / Hα and [OI]λ6300 / Hα. Although

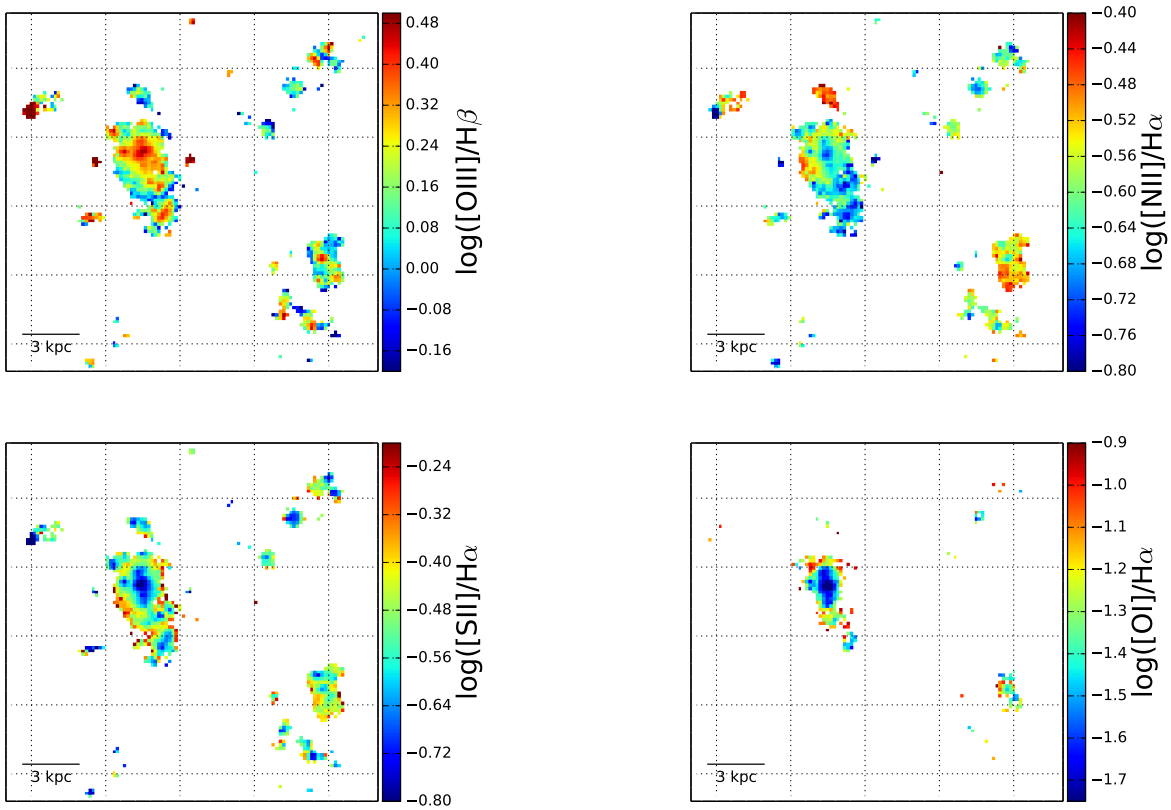

Fig. 5. Spatial distribution of the principle emission-line flux ratios. A logarithmic scale is used for coding the line ratios. The field of view is the same as in Fig. 3.

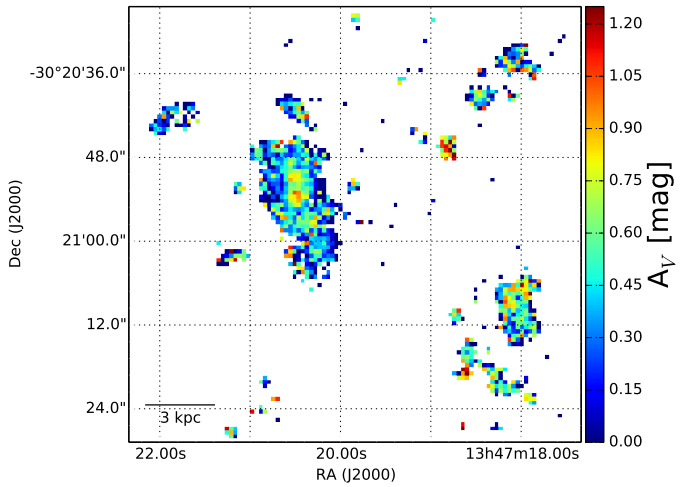

Fig. 3. Spatial distribution of the dust extinction, A_V. The dust is heterogeneously distributed in the system, but its distribution peaks where star formation is the most recent, see Fig. 8.

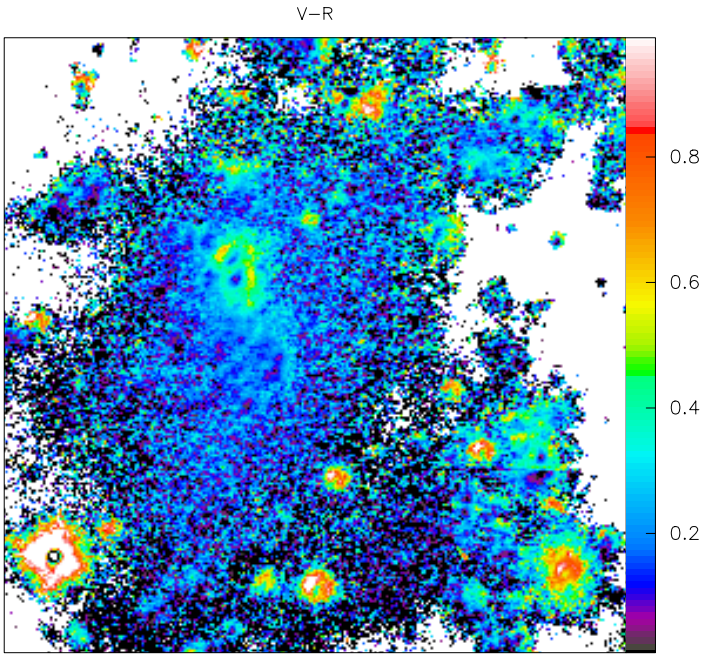

Fig. 4. V-R color map of NGC 5291N derived from the FORS deep image, scaled in mag. The field of view is the same as in Fig. 3.

BPT-like diagrams were originally applied to central galactic regions or even to entire galaxies to diagnose AGN or LINER emission, they are used here at the scale of a spaxel to identify the different ionizing processes.

Emission line ratios for individual rebinned spaxels are plotted on the BPT diagnostic diagrams shown in Fig. 7 . Most of our data points fall in the locus of star forming regions for two diagnostic diagrams. However, the distribution on the [OI]/Hα diagnostic does not look standard. It shows a high number of points located outside of the locus for classical H II regions. As shown in Fig. 7, bottom, the deviant points are located in the

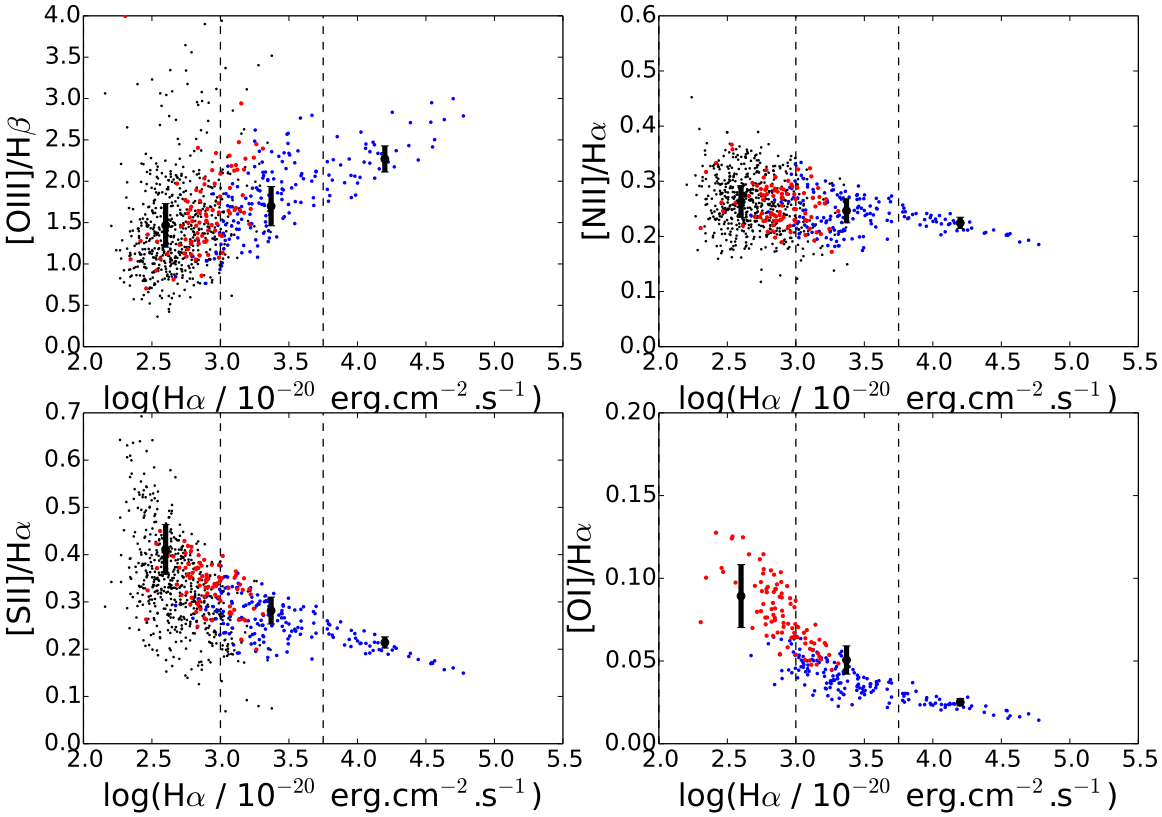

Fig. 6. Distribution of emission-line ratios as a function of the Hα flux, also tracing the local Hα flux surface brightness. The blue resp. red points correspond to those located inside resp. outside the starburst locus in the [OI]/Hα BPT diagnostic diagram (see Fig. 7). The small black points correspond to spaxels with undetected [OI] line. The error bars are 1σ typical dispersion and their y-axis position is the mean value of the ratio in the given Hα flux range.

outskirts of the star–forming regions. The mean uncertainty on the value of log([OI] /Hα) for the red points is 0.19, which is not enough to explain their location in the AGN part of the BPT diagram. One should also note that the stacked spectrum of these regions is clearly located in the AGN region of the diagram, with very little uncertainty on the measure.

We investigate in the following the possible causes of the spatial variations of the emission line ratios, starting from the innermost regions to the external ones.

3.3. Star–forming regions

The equivalent width of Hβ (EW(Hβ)) gives constraints on the age of a starburst episode (Stasińska & Leitherer 1996; Zackrisson et al. 2001; Terlevich et al. 2004). The spatial distribution shown in Fig. 8 peaks at 230 Å, in the centre of the brightest region. EW(Hβ) decreases further out to 30 Å in the outskirts of the dwarf. Following Boquien et al. (2007), PEGASE II models (Fioc & Rocca-Volmerange 1997, 1999) were used to estimate the ages of the star–formation episodes. Assuming an instantaneous starburst and a constant metallicity Z = 0.008 (see Sect. 3.4), we obtained starburst ages of 3 Myr for the central region and 7 Myr for the oldest regions. Under the assumption that the underlying continuum is only due to the newly formed stars (see Sect. 3.6 and 4.2), the EW(Hβ) map looks consistent with an outside-in star–formation episode.

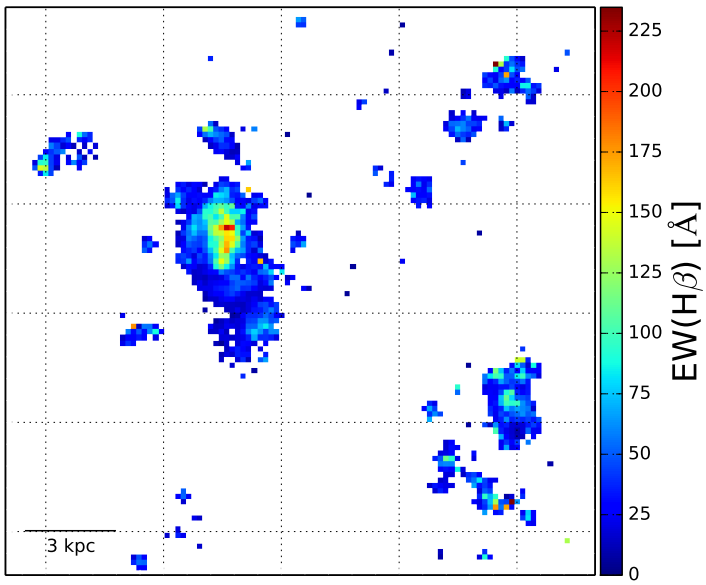

Fig. 8. Spatial distribution of the equivalent width of Hβ. The field of view is the same as in Fig. 3.

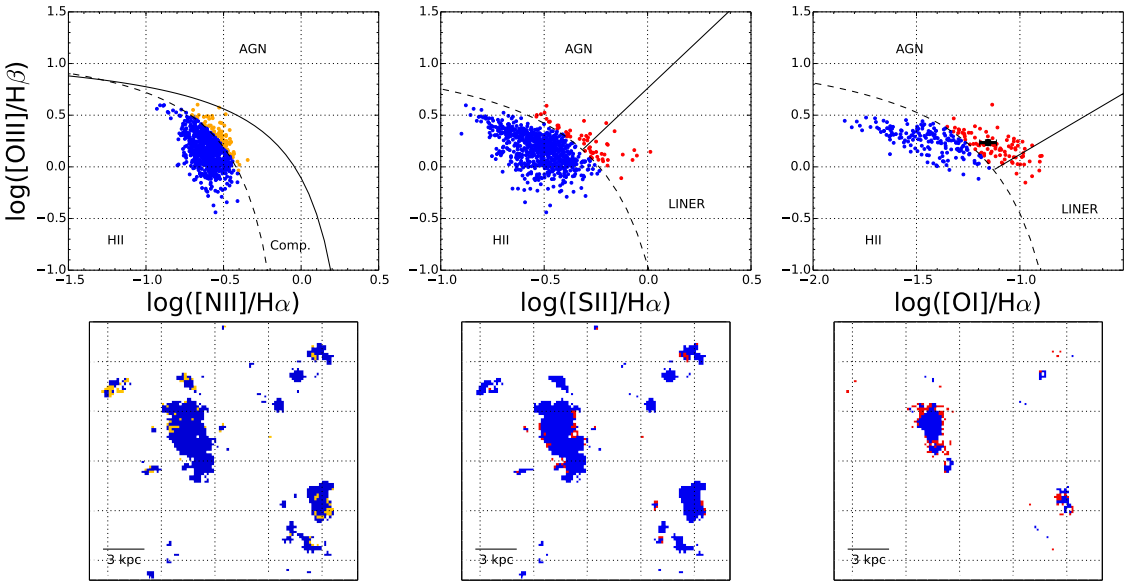

Fig. 7. BPT diagnostics for different emission line ratios. On the [OIII]/Hβ vs [NII]/Hα diagram, the dotted line delineates the pure starburst region, as defined by Kauffmann et al. (2003) using a set of Sloan Digital Sky Survey (SDSS) spectra. The spaxels belonging to this region are shown in blue, those outside it in orange; their spatial location is shown in the figure below. The field of view is the same as in Fig. 3. The solid line traces the upper theoretical limit to pure H II regions measured by Kewley et al. (2001). For the other diagrams, the dashed lines defined by Kewley et al. (2006) separate the starburst (blue points) from the AGN/Liner (red points) regions. The solid lines further distinguish between AGN ionization (above the line) and LINER ionization (below). The corresponding spatial distribution of starburst/non-starburst 3×3 binned spaxels are shown below. The highest fraction of spaxels inconsistent with a photoionization by a starburst show up on the [OIII]/Hβ vs [OI]/Hα diagram. Their spectra have been stacked and the resulting extracted line ratios are shown with the black point, together with the error bar.

Given the very young age of the central starburst, the presence of Wolf-Rayet (WR) stars is expected. Indeed, DM98 detected a WR bump in their long-slit spectra of NGC 5291N. However, our spectral window does not allow us to reach the location of the bump: the blue boundary of our spectral range is 4682 Å in rest-frame referential whereas the WR bump peaks at 4686 Å. A rising at the far blue end of the spectrum was glimpsed, consistent with the WR feature, but could not be discriminated from an observational bias. Furthermore the red WR bump around 5650 to 5800 Å is not observed in the MUSE data.

3.4. Metallicity

The chemo-dynamical simulations of Ploeckinger et al. (2014) predict some level of self-enrichment in Tidal Dwarf Galaxies which should translate into spatial variations of the metallicity and thus contributes to the scatter observed in each BPT diagram of Fig. 7.

We derived the metallicity from the strong emission lines ratios. Unfortunately, our spectral range does not include the [OIII]λ4363, so we could not compute the electron temperature, needed for a direct measurement of the metallicity.

Instead, we estimated the metallicity from the empirical calibrations based on the parameter O3N2 = $\log_{10}\left(\frac{[OIII]\lambda5007/H\beta}{[NII]\lambda6548/H\alpha}\right)$. Initial estimates by DM98 indicated rather high values – about half solar – for the oxygen abundance. The Marino et al. (2013) empirical calibration was then chosen. Indeed, compared to other calibrations using this parameter (e.g. Pettini & Pagel 2004), it includes high metallicity H II regions and should provide better estimates for high Z regions. Following their calibration:

$$12 + \log_{10}(O/H) = 8.55 - 0.221 \times O3N2 \quad (1)$$

for O3N2 < 1.7, we get <12 + log(O/H)> = 8.38 with a standard deviation σ = 0.05, which corresponds to an abundance of Z $\simeq$ 0.5 $Z_\odot$, using 12 + log(O/H)$_\odot$ = 8.69 (Asplund et al. 2009). This calibration has a typical uncertainty of ± 0.2 dex.

The spatial distribution of the metallicity is shown in Fig. 9. An apparent decrease of the metallicity seems to be observed towards the brightest and dustier regions. This is at odds with the simulations of Ploeckinger et al. (2014) that predict a higher metallicity where star–formation is the most active.

However, our positive metallicity gradient is of 0.2 dex, i.e. within the uncertainty of the method we used. So it may in fact corresponds to variations of other physical parameters such as the ionization parameter, and the data are consistent with a homogenous metal distribution within NGC 5291N. One should note that previous studies, such as DM98, detected no metallicity gradient over the whole HI ring surrounding NGC 5291, whose radius is around 200 kpc and which contains several other star–forming condensations.

3.5. Ionization Parameter

The ionization parameter q[4], defined as the ratio between the flux of ionizing photons and the number density of hydrogen atoms,

[4] The dimensionless ionizing parameter U = q/c, where c is the speed of light, is used in the following.

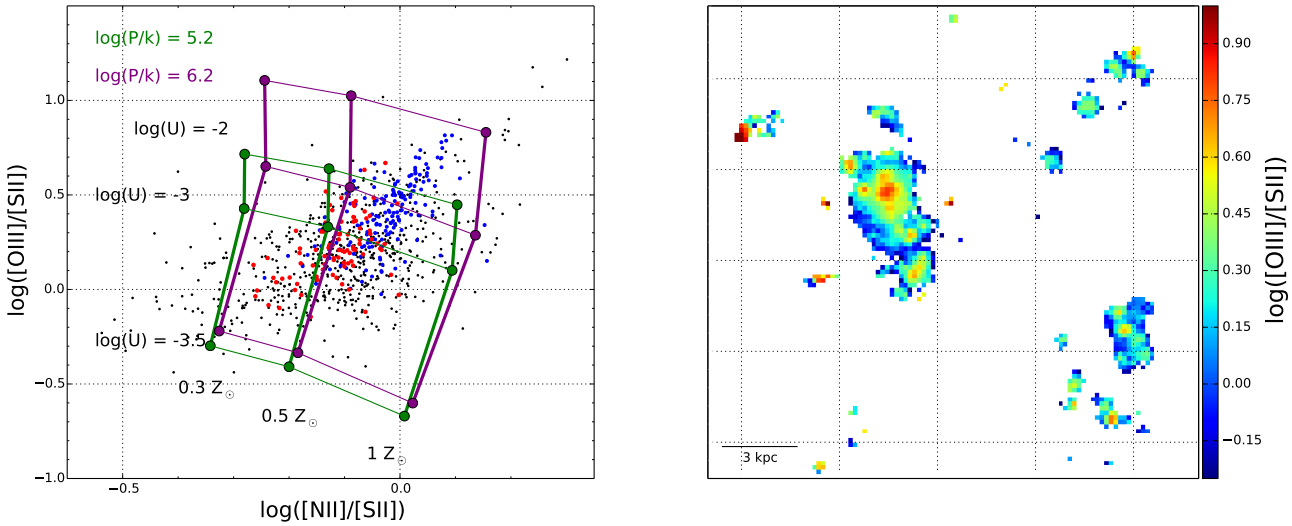

Fig. 10. Left: Metallicity-ionization parameter grid from the MAPPINGS V ionization model. The red points are the ones falling outside of the SF region in the third BPT diagram. The colored dashed lines represent the grid for a constant metallicity and the continuous black lines for a constant ionizing parameter. The dimensionless ionizing parameter goes from log(U) = -3.5 to log(U) = -2. Right: Spatial distribution of the logarithmic values of the [OIII]/[SII] ratio, used as a proxy for the ionization parameter. We see an outside-in gradient showing that the most ionized regions are located in the centre of the galaxy. The field of view is the same as in Fig. 3.

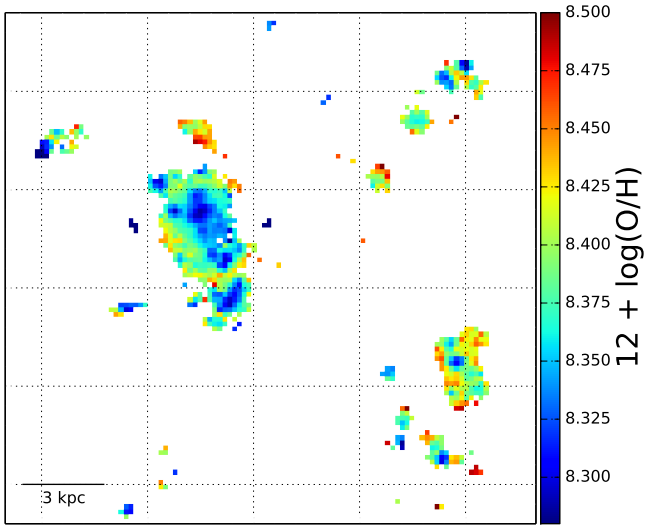

Fig. 9. Metallicity map estimated from O3N2 and the calibration of Marino et al. (2013). An outside-in gradient is observed, but the difference between the lowest and the highest abundance can be consistent with an homogeneous abundance distribution and be caused by the variation of other parameters, such as the ionization parameter.The field of view is the same as in Fig. 3.

also has an influence on the values of the emission line ratios (Dopita et al. 2013). To determine the distribution of the ionizing parameter throughout the system, the grids from the photoionization model MAPPINGS V[5] (Sutherland in prep.) are used on a [OIII]/[SII] versus [NII]/[SII] diagram, which offers a convenient way to break the degeneracy between the metallicity and ionizing parameter. The electronic density, computed from the $[SII]_{\lambda6717}$ / $[SII]_{\lambda6731}$ ratio, reaches a maximum value of 300 cm^{-3} (see Sect. 2.1) and can get as low as $9cm^{-3}$ (see Sect. 4.1.2). Moreover, the electronic temperature was estimated to be 12700 K by DM98. Two grids were then used, with respectively log(P/k) = 5.2 and 6.2 to cover the density range encountered in the galaxy. The shape of the ionizing Extreme Ultra-Violet photon spectrum comes from the STARBURST99 synthesis model (Leitherer et al. 1999), assuming a Saltpeter IMF, Lejeune et al. (1997) atmospheres and a continuous star–formation extending over 4 Myr, as described in Dopita et al. (2013). The left panel of Fig. 10 shows that the ionizing parameter values are quite dispersed, going from log(U) = -3.5 to log(U) = -2. The spatial distribution of the [OIII] / [SII] emission line ratio, which can be used as a proxy for the ionization parameter, is plotted on the right panel of Fig. 10 and shows similar gradient as the one observed in Fig. 5 and can therefore be accounted for the spread observed on the three BPT diagrams.

3.6. Continuum emission

Besides the emission lines, the continuum emission from the MUSE spectra was also extracted, and its spatial distribution was investigated. Away from the main star–forming regions, this continuum emission is quite faint and hardly above the noise level. As shown in Fig. 4 and Fig. 11, this diffuse emission is spatially extended and rather blue (V-R $\simeq$ 0.2 mag). The existence of this diffuse component is secured by the deep broad band images obtained with FORS: see the similarity between the reconstructed MUSE map of Fig. 11 and the composite image of FORS shown on the upper right panel of Fig. 2. Fig. 12 further shows that this component extends in areas where no strong emission lines, in particular Hα, is observed.

[5] Available at `miocene.anu.edu.au/Mappings`

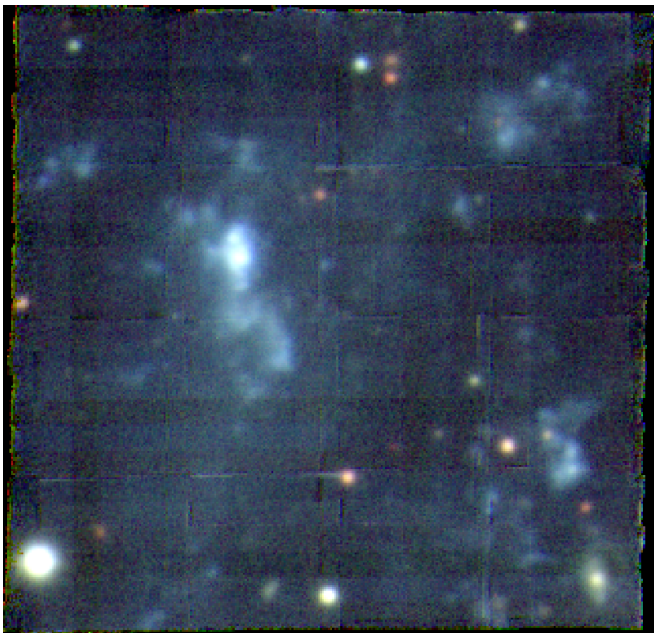

Fig. 11. Reconstructed composite color image of the extracted continuum of NGC 5291N using similar bands as V, R and I on MUSE. The blue diffuse continuum emission is detected, although less clearly than on the FORS image presented on the upper right panel of Fig. 2. The image was created from the un-binned data-cube.

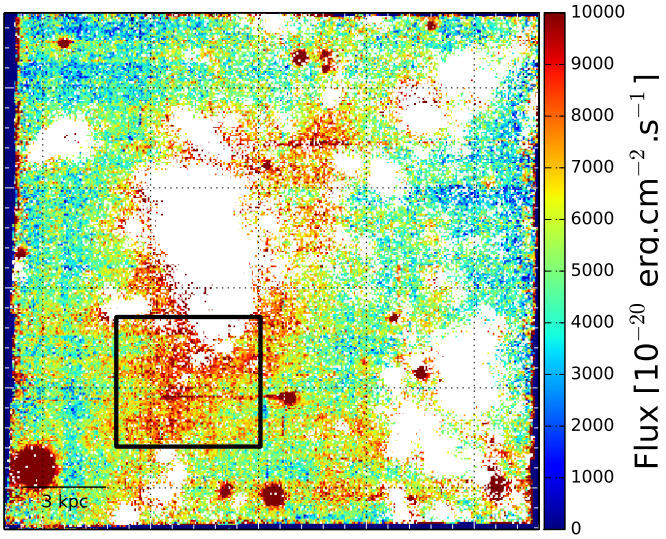

Fig. 12. Integrated emission of the continuum in 10^{-20} erg s^{-1} cm^2 between 4750 Å and 6000 Å. Spaxels for which a 3σ Hα emission was detected are shown in white. The black rectangle indicates the region whose spectra were combined to obtain the stacked spectra of Fig. 15. The field of view is the same as in Fig. 3.

4. Discussion

The target investigated here, NGC 5291N, is supposedly a "simple" object. It was formed less than a few hundred Myr ago, following a high speed collision, in an initially purely gaseous structure (Bournaud et al. 2007). Yet the FORS deep images and MUSE data presented here already show a complex interstellar medium. The ISM in this still gas-dominated object appears to be very clumpy, like the typical star–forming galaxies at $z > 1$. The high spatial resolution and large field-of-view of MUSE allowed us to map the flux distribution of multiple emission emission lines, as well as the flux ratios between them up to large radial distances.

Large and small scale variations of emission line ratios are observed. In particular the [OI]/Hα ratio has excursions beyond the locus of typical starbursts. Deviant points surrounds the main star–forming regions and are thus found at relatively low Hα surface brightness. Such variations of the emission lines cannot be due to local changes of the dust extinction or metallicity, which we found to be pretty uniform. We discuss here other possible origins for the deviant line ratios.

4.1. Origin of the strong [OI]/Hα emission

The [OI]λ6300 is a faint line, making if difficult to map. However, the sensitivity of MUSE, allowed us to detect it with a S/N > 3 on extended regions.

The stacked spectrum (see error bars Fig. 7) unambiguously confirms the high level of [OI] emission outside the main H II regions. Thus, the high [OI]/Hα line ratios are unlikely to be due to measurement errors.

4.1.1. Low-density Diffuse Ionized Gas

The regions with strong [OI]/Hα ratios surround the main star–forming knots; they lie within the warm low-density ionized phase of the ISM, often referred to as the Diffuse Ionized Gas (DIG). The DIG is ionized by field OB stars, leaking photons from H II regions (Hoopes & Walterbos 2003), or shocks. The low density of the DIG is known to harden the ionizing spectra and can lead to LINER-like line ratios. However, a very low ionization parameter, below log(U) < −4 (see Hoopes & Walterbos 2003), is required to reach the observed values of the [OI]/Hα line ratios. As shown in Sect. 3.5 , the data points on the [OI]/Hα diagram constrain the ionization parameter to be in the range −3.5 < log(U) < −2: this is much higher than the value needed to get non-stellar ionization-like line ratios in the DIG.

4.1.2. Shocks

Shocks due to stellar winds, supernovae explosions, or dynamical processes such as collisions or accretion of gas can also produce large forbidden to Balmer line ratios. We have tested the shock hypothesis with the fast radiative shock model from Allen et al. (2008), which is based on MAPPINGS III (Sutherland & Dopita 1993).

The shock model library has a limited number of input parameters. We have assumed an electronic density of 1 cm^{-3} and a LMC abundance, as these parameters are the closest available to that estimated in the ISM of NGC 5291N. The speed of the shock and the transverse magnetic parameter were varied, from 100 to 300 km s^{-1} and from 0 to 10 μG respectively. The locus of the resulting model is shown in Fig. 13 for shock only and shock + precursor. We find that the outlying data points are encompassed between the grids for shock and shock+precursor. For comparison, the prediction for pure stellar photo-ionization from MAPPINGS V is also shown in Fig. 13. The average electronic density of the points lying outside of the 'star forming' region on the third BPT diagram being around 10 cm^{-3}, we use

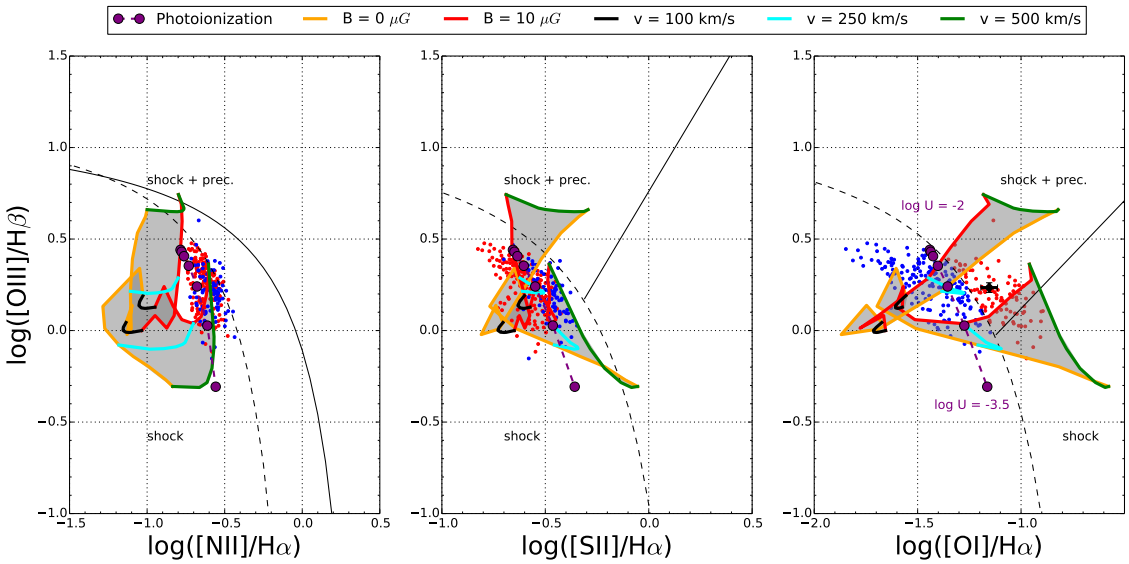

Fig. 13. Shock models on the BPT diagrams. Are plotted only points with detected [OI] emission. The blue (resp. red) points lie in (resp. out of) the star formation locus on the [OI] / Hα BPT diagram. The purple dashed line is the ionization model prediction from MAPPINGS V, using a metallicity Z = 0.5 $Z_\odot$ and log(P/k) = 5.2. The ionization parameter goes from log U = -2 to log U = -3.5, as indicated on the third diagram. The two grids come from the MAPPINGS III model for fast-shock, as described in the text, and are drawn for shock only and shock + precursor. The locus of both grids are shaded.

the model with log(P/k) = 5.2 (see Sect. 3.5). A half-solar metallicity was also assumed.

The velocity dispersion map of the ISM was computed from the width of the Hα emission line. We subtracted a constant value of 2.34 Å to the width of the H_α line, corresponding to the average Gaussian FWHM close to the Hα line. The map, shown in Fig. 14, has peaks at $\sigma > 130$ km s^{-1} in the central regions – most likely due to spatially unresolved rotation (Bournaud et al. 2004) – but also in the outskirts of the main star forming knots close to the region where [OI]/Hα culminates. A detailed inspection reveals that the high-σ regions are in fact located a bit further away where the [OI] emission is below the detection limit. However, the observed line-of-sight velocity dispersions could be consistent with transverse shocks of up to 300 km s^{-1}. If shocks are responsible for the high [OI]/Hα ratios, what is their origin?

First, a shock could have arisen from the accretion of gas onto the newly formed dwarf. In this case we would expect the shocks to be present only around the galaxy because the accretion of gas is supposed to happen towards the deepest gravitational potential well, hence all around the dwarf galaxy. However, as one can see in Fig. 7, the strong [OI]/Hα ratio regions are not only found around the kinematically decoupled dwarf galaxy but around most star–forming regions away from NGC 5291N (See the South-West clump for instance).

Second, a shock could be due to the stellar feedback from the very recent starburst. Strong outflows in the centre of the star–forming region would then be expected. The expected kinematical signature of such outflows – an additional broad component in the emission lines – is not seen in the MUSE data: single Gaussian fits properly fit the Hα emission line, even in the centre of the star–forming regions. [6]

Third, the high σ velocities could be the remaining signature of the violent collision between NGC 5291 and a massive interloper that created the HI ring. The shock signature could have been wiped out in the central star–forming region because of the stellar activity and only remain in the low-density gas surrounding this area. In the simulation of Bournaud et al. (2007) of the ring formation and expansion, the induced velocity dispersion 0.7 Gyr after the collision had decreased to about $\sigma \simeq$ 40 km s^{-1}. According to the shock models, this is too low to account for the high [OI] / Hα flux ratio.

Therefore, the models involving a photoionization within a very low density environment (the DIG hypothesis) or shocks do not provide satisfactory explanations for the values and spatial variations of the [OI]/Hα flux ratios. Confirming the existence of regions with high [OI]/Hα in the clumpy ISM of collisional debris (or of distant galaxies) should be a first step in our understanding of the ionization process. In fact, Cairós et al. (2010), who obtained IFU data for eight dwarf galaxies considered as BCDGs with the Postdam Multi-Aperture Spectrophotometer (PMAS) at the 3.5 m telescope at Calar Alto Observatory, also measured high values of [OI]/Hα – as high as log([OI]/Hα) = −0.50 – for several objects in their sample. It is remarkable that these high ratios are always located in the outskirts of the galaxies. In some of them, namely I Zw 159 and Mrk 32, they also suggest the presence of shocks in the same regions, based on strong values of the [SII]/Hα ratio, above log([SII]/Hα) = −0.20 . However the lack of spatial resolution prevents firm conclusions. Strong outflows presumably generating shocks have been found in ESO338-IG04, the only other dwarf galaxy for which MUSE data are available (Bik et al. 2015). Outflows were disclosed in the analysis of the Hα kinematic maps and highly ionized cones were probed by using the [SII]/[OIII] line ratio, thought to be escape gates to Lyα photons. It is interesting to note that no such feature was observed in NGC 5291N.

[6] Fabry-Perot Hα data with high spectral resolution for this region are available (Bournaud et al. 2004). Their spectral resolution (R = 9375) are far superior to the MUSE data (R = 2840 close to Hα). Their analysis reveal complex kinematical features, with likely superimposed foreground and background clouds, but no obvious signature of outflows. The broad wings of the Hα line in their data are instrumental signatures.

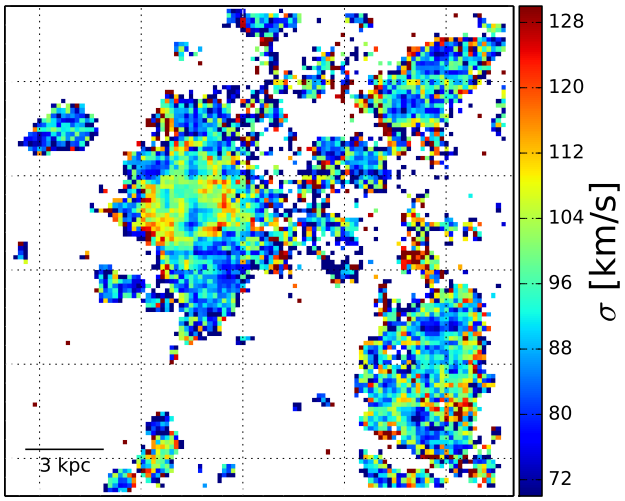

Fig. 14. Velocity dispersion measured from the width of the Hα emission line. The field of view is the same as in Fig. 3.

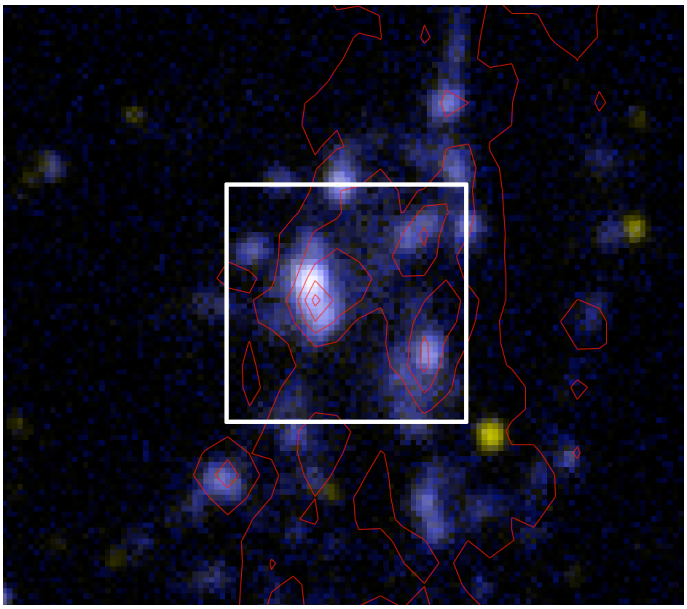

Fig. 16. Composite color image of the UV emission as seen by GALEX: the near-UV is shown in red and green and the far-UV in blue. HI contours are superimposed in red. The MUSE field of view is shown by the white square.

4.2. Origin of the diffuse continuum emission

As presented in Sect. 3.6, the Hα emitting regions are surrounded by a diffuse blue light emission of still unknown origin. One may speculate that this light has been emitted by a stellar population old enough to no longer ionize the surrounding gas. This would be consistent with the outside-in evidence of the star–formation events derived from the Hβ equivalent width map. To further characterize the physical properties of this diffuse component, we have stacked the spectra over the full South-East region where the diffuse continuum emission is most prominent. The resulting spectrum does not reveal any underlying absorption line (See Fig. 15), nor actually residual emission lines. This puts very strong constraints on the age of the putative underlying stellar population; galaxy SED models such as GALEV (Kotulla et al. 2009) show that the transition between emission to absorption line for Hβ occurs at around 25 Myr after an instantaneous burst, and does not last more than a few Myr. One would then witness a special episode of the star formation history: the transition between the death of the OB stars and emergence of type A absorption lines, lasting a very short time but occurring on an extended region, spanning over 3 kpc. This would mean that the star–formation episode occurred almost simultaneously on a 3 kpc scale region, which is rather unrealistic.

A second hypothesis would be that this emission is actually scattered light from the star–forming region. In this case, one should expect to see an associated UV counterpart, that is dust scattered leaking UV emission from the hot young stars (see Boissier et al. 2015, and references therein). However GALEX data (see description in Boquien et al. 2007, 2009) of this system showed that there is no near-UV nor far-UV emission towards the optical blue diffuse component (compare Fig. 12 and Fig. 16). One should note that the GALEX data are quite deep, with exposition time of about 9000 s for the NUV and 5500 s in FUV.

Thus, the origin of this diffuse component remains undetermined. MUSE observations of other similar systems (or of other parts of the NGC 5291 gaseous ring) should tell how common it is around starbursting galaxies.

5. Conclusions

We have presented FORS deep multi-band optical images and high spatial resolution IFU data on NGC 5291N, one of the very few starbursting dwarfs yet observed with the revolutionary instrument MUSE on the ESO VLT. This dwarf, located at 63 Mpc, formed within a ring of gas expelled from the host galaxy, NGC 5291, after a violent collision several 10^8 years ago. NGC 5291N shares a number of physical properties with clumps in gas rich star forming high redshift galaxies: it is very gaseous, has a clumpy ISM with sub-solar metallicity and contains no old stars, contrary to classical blue compact dwarf galaxies.

The MUSE data cube provided us with optical spectra, in the range 4750 - 9350 Å over a field of view of about 1′×1′. Each spaxel, corresponds to 60 pc × 60 pc at the distance of NGC 5291N , before re-binning the data-cube. Strong emission lines (Hβ, [OIII], [OI], Hα, [NII] and [SII]) and continuum emission were extracted and mapped to investigate the properties of the ISM. The derived maps showed a rather strong heterogeneity in the spatial distributions of the different emission lines and an extended blue diffuse continuum emission.

Emission line ratios were investigated with BPT-like diagnostic diagrams. They showed that most data point are consistent with star–forming regions, with a noticeably large scatter on the diagrams. Furthermore, a significative number of points fall outside of the star–formation locus of the [OIII]/Hβ vs [OI] / Hα diagnostic diagram. They correspond to regions located on the outskirts of the dwarf galaxy.

The equivalent width of the Hβ (EW(Hβ)) line shows that the galaxy has undergone a very recent starburst: no older than 3 Myr in the brightest region to 7 Myr old in the fainter neighborhood, under the hypothesis of an instantaneous burst. The observed distribution of EW(Hβ) is consistent with an outside-in star formation episode. The extinction map (Av) computed from the Balmer line ratio Hα / Hβ indicates that the dust concentrates towards the most active star–forming regions, where mid and far infrared emission had already been found. This is

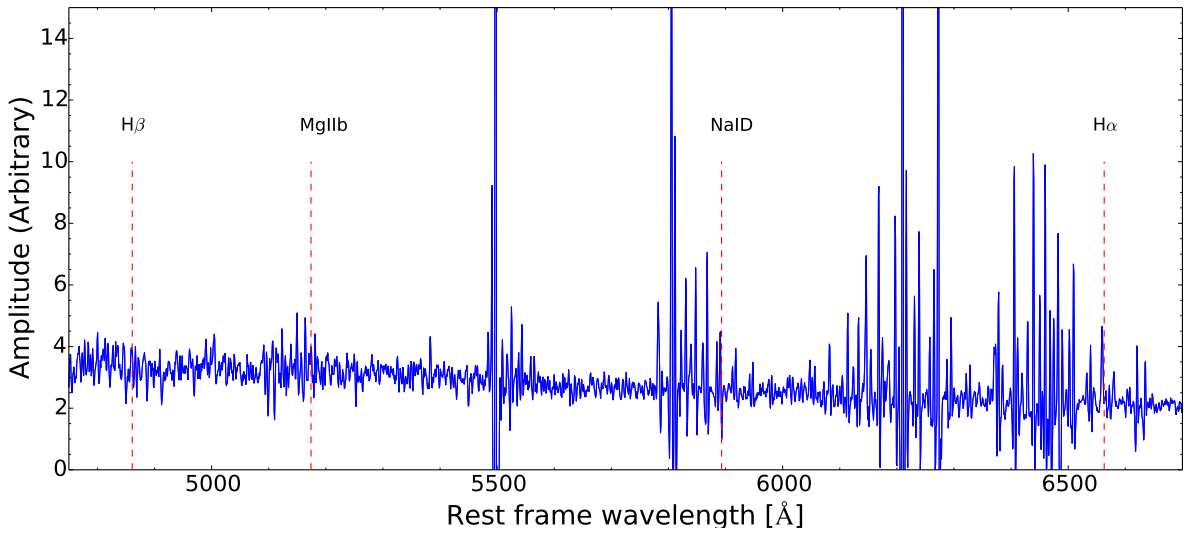

Fig. 15. Stacked spectra from the South-East region indicated by a black rectangle on Fig. 12. Every spaxel showing a 3σ Hα detection was rejected.

also the region where the V-R color map derived from the FORS broad-band images shows narrow red filaments that are hence most likely associated with dust lanes.

The metallicity was computed using the empirical O3N2 calibration and gave a mean value <12 + log(O/H)> = 8.4 with a standard deviation of 0.05 (equivalent to an abundance of Z $\simeq$ 0.5 $Z_{\odot}$), confirming previous estimates from slit spectroscopy. This relatively high value is fully expected for a recycled dwarf galaxy made in collisional debris. A surprising inside-out positive metallicity gradient is observed; it is at odds with predictions from numerical simulations of the chemical evolution of Tidal Dwarf Galaxies. However, the metallicity distribution spreads over less than 0.2 dex, which is the intrinsic uncertainty of the empirical method. The computed O3N2 map is therefore consistent with an homogeneous metallicity coupled with variations of other physical parameters, such as the ionization parameter.

The spatial distribution of the ionization parameter was determined through a [OIII]/[SII] versus [NII]/[SII] photoionization grid computed with the MAPPINGS V model. The inferred ionization parameter spreads over a large range of values, from log(U) = -3.5 to log(U) > -2, explaining the observed scatter on the BPT diagrams, except for the points with high [OI] / Hα flux ratios which are not compatible with simple stellar photoionization models. Models involving the low-density DIG which is hot, only partially ionized, can emit non-stellar emission line ratios, but they need a ionization parameter lower than the one derived from the MUSE data.

Various shock models were investigated. They can reproduce the observed flux ratios not compatible with stellar photoionization for shock velocities higher than 200 km s^{-1}. The velocity dispersion map computed from the IFU data cube do show an increase of σ(V) outside the main star–forming regions, but at a level and precise location which are not fully consistent with the shock model.

An extended blue diffuse emission surrounding the main star–forming regions is observed in the deep optical FORS images and detected with MUSE. The IFU data indicates that this is pure continuum emission, exhibiting no emission nor absorption lines, expanding over distances of at least 3 kpc, from the emission line regions. The hypothesis of emission arising from a stellar population old enough not to ionize the surrounding HI gas, but also young enough not to exhibit Balmer absorption lines, appears rather unlikely. Besides, the UV emission associated with scattered light from the central star formation region was not observed by the GALEX UV observatory.

Therefore no firm conclusions on the origin of the deviant points in the [OI] / Hα BPT diagram, spatially located just outside the starburst regions of the dwarf, and of the pure diffuse blue optical continuum emission found further out, could be reached. This calls for further IFU observations of the outskirts of nearby star–forming galaxies, in particular the youngest ones formed in debris of galaxy-galaxy collisions, arguably the best local proxies of the distant star–forming objects.

Acknowledgements. The authors thank Michael Dopita and Stephanie Juneau for very useful discussions, and the (anonymous) referee for in-depth reading and helpful comments. P.M.W received funding through BMBF Verbundforschung (project MUSE-AO, grant 05A14BAC). E.Z acknowledges funding from the Swedish Research Council (project 2011-5349). This research has made use of the NASA/IPAC Extragalactic Database (NED) which is operated by the Jet Propulsion Laboratory, California Institute of Technology, under contract with the National Aeronautics and Space Administration.

References

Allen, M. G., Groves, B. A., Dopita, M. A., Sutherland, R. S., & Kewley, L. J. 2008, ApJS, 178, 20
Asplund, M., Grevesse, N., Sauval, A. J., & Scott, P. 2009, ARA&A, 47, 481
Bacon, R., Accardo, M., Adjali, L., et al. 2010, in Society of Photo-Optical Instrumentation Engineers (SPIE) Conference Series, Vol. 7735, Society of Photo-Optical Instrumentation Engineers (SPIE) Conference Series, 8
Baldwin, J. A., Phillips, M. M., & Terlevich, R. 1981, PASP, 93, 5
Bik, A., Östlin, G., Hayes, M., et al. 2015, A&A, 576, L13
Boissier, S., Boselli, A., Voyer, E., et al. 2015, A&A, 579, A29
Boquien, M., Duc, P.-A., Braine, J., et al. 2007, A&A, 467, 93
Boquien, M., Duc, P.-A., Galliano, F., et al. 2010, AJ, 140, 2124
Boquien, M., Duc, P.-A., Wu, Y., et al. 2009, AJ, 137, 4561
Bournaud, F., Duc, P.-A., Amram, P., Combes, F., & Gach, J.-L. 2004, A&A, 425, 813
Bournaud, F., Duc, P.-A., Brinks, E., et al. 2007, Science, 316, 1166
Bournaud, F., Perret, V., Renaud, F., et al. 2014, ApJ, 780, 57
Cairós, L. M., Caon, N., Papaderos, P., et al. 2009, ApJ, 707, 1676
Cairós, L. M., Caon, N., Zurita, C., et al. 2010, A&A, 520, A90

Dopita, M. A., Sutherland, R. S., Nicholls, D. C., Kewley, L. J., & Vogt, F. P. A. 2013, ApJS, 208, 10
Duc, P.-A. & Mirabel, I. F. 1998, A&A, 333, 813
Duc, P.-A. & Mirabel, I. F. 1999, in IAU Symposium, Vol. 186, Galaxy Interactions at Low and High Redshift, ed. J. E. Barnes & D. B. Sanders, 61
Erb, D. K., Shapley, A. E., Pettini, M., et al. 2006, ApJ, 644, 813
Fioc, M. & Rocca-Volmerange, B. 1997, A&A, 326, 950
Fioc, M. & Rocca-Volmerange, B. 1999, ArXiv [astro-ph/9912179]
Genel, S., Naab, T., Genzel, R., et al. 2012, ApJ, 745, 11
Gordon, K. D., Clayton, G. C., Misselt, K. A., Landolt, A. U., & Wolff, M. J. 2003, ApJ, 594, 279
Hoopes, C. G. & Walterbos, R. A. M. 2003, ApJ, 586, 902
Izotov, Y. I., Schaerer, D., Blecha, A., et al. 2006, A&A, 459, 71
James, B. L., Tsamis, Y. G., & Barlow, M. J. 2010, MNRAS, 401, 759
James, B. L., Tsamis, Y. G., Barlow, M. J., Walsh, J. R., & Westmoquette, M. S. 2013a, MNRAS, 428, 86
James, B. L., Tsamis, Y. G., Barlow, M. J., et al. 2009, MNRAS, 398, 2
James, B. L., Tsamis, Y. G., Walsh, J. R., Barlow, M. J., & Westmoquette, M. S. 2013b, MNRAS, 430, 2097
Kauffmann, G., Heckman, T. M., Tremonti, C., et al. 2003, MNRAS, 346, 1055
Kauffmann, G., White, S. D. M., & Guiderdoni, B. 1993, MNRAS, 264, 201
Kehrig, C., Pérez-Montero, E., Vílchez, J. M., et al. 2013, MNRAS, 432, 2731
Kewley, L. J., Dopita, M. A., Sutherland, R. S., Heisler, C. A., & Trevena, J. 2001, ApJ, 556, 121
Kewley, L. J., Groves, B., Kauffmann, G., & Heckman, T. 2006, MNRAS, 372, 961
Kotulla, R., Fritze, U., Weilbacher, P., & Anders, P. 2009, MNRAS, 396, 462
Kunth, D., Maurogordato, S., & Vigroux, L. 1988, A&A, 204, 10
Lagos, P., Papaderos, P., Gomes, J. M., Smith Castelli, A. V., & Vega, L. R. 2014, A&A, 569, A110
Lagos, P., Telles, E., Muñoz-Tuñón, C., et al. 2009, AJ, 137, 5068
Lagos, P., Telles, E., Nigoche Netro, A., & Carrasco, E. R. 2012, MNRAS, 427, 740
Leitherer, C., Schaerer, D., Goldader, J. D., et al. 1999, ApJS, 123, 3
Lejeune, T., Cuisinier, F., & Buser, R. 1997, A&AS, 125, 229
Lelli, F. submitted
Loose, H.-H. & Thuan, T. X. 1986, in Star-forming Dwarf Galaxies and Related Objects, ed. D. Kunth, T. X. Thuan, J. Tran Thanh Van, J. Lequeux, & J. Audouze, 73–88
Marino, R. A., Rosales-Ortega, F. F., Sánchez, S. F., et al. 2013, A&A, 559, A114
Maza, J., Ruiz, M. T., Gonzalez, L. E., Wischnjewsky, M., & Pena, M. 1991, A&AS, 89, 389
Osterbrock, D. E. & Bochkarev, N. G. 1989, Soviet Ast., 33, 694
Papaderos, P., Loose, H.-H., Thuan, T. X., & Fricke, K. J. 1996, A&AS, 120, 207
Pettini, M. & Pagel, B. E. J. 2004, MNRAS, 348, L59
Ploeckinger, S., Hensler, G., Recchi, S., Mitchell, N., & Kroupa, P. 2014, MNRAS, 437, 3980
Sargent, W. L. W. & Searle, L. 1970, ApJ, 162, L155
Stark, D. P., Swinbank, A. M., Ellis, R. S., et al. 2008, Nature, 455, 775
Stasińska, G. & Leitherer, C. 1996, ApJS, 107, 661
Steidel, C. C., Rudie, G. C., Strom, A. L., et al. 2014, ApJ, 795, 165
Sutherland, R. in prep.
Sutherland, R. S. & Dopita, M. A. 1993, ApJS, 88, 253
Terlevich, R., Silich, S., Rosa-González, D., & Terlevich, E. 2004, MNRAS, 348, 1191
Veilleux, S. & Osterbrock, D. E. 1987, ApJS, 63, 295
Weilbacher, P. M., Streicher, O., Urrutia, T., et al. 2012, in Proc. SPIE, Vol. 8451, Software and Cyberinfrastructure for Astronomy II
Zackrisson, E., Bergvall, N., Olofsson, K., & Siebert, A. 2001, A&A, 375, 814
Zanella, A., Daddi, E., Le Floc'h, E., et al. 2015, Nature, 521, 54

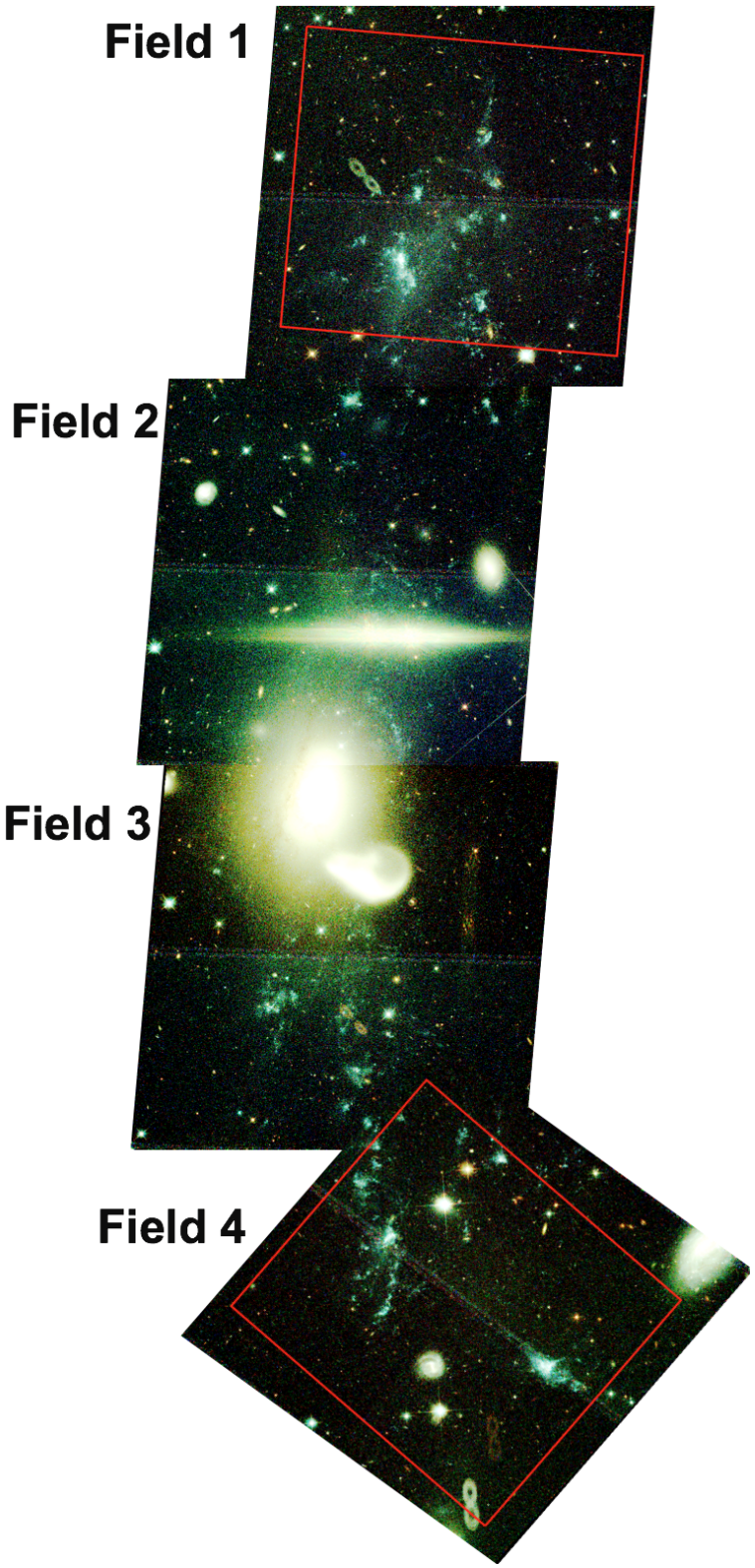

FIGURE 4.13: Composite color HST image. The two F160W-band fields of view are shown by the red rectangles.

4.3 Clustered star formation in NGC 5291

In Section 2.5, we have seen that the formation mechanism of globular clusters (GCs) remains an open field of research. The metallicity of GCs, typically between [Fe/H] = -1.7 and -0.2, advocates for a formation at high (6-7) to intermediate (1-3) redshifts. However, current instrumentation remains unable to detect such these sources at these redshifts, because of their luminosity (M_V fainter than -14 mag for the young clusters of the Antennae system (Whitmore et al., 1999)), except in the exceptional case of strong gravitational lenses (see Vanzella et al., 2017a; Vanzella et al., 2017b, for around 10 candidates young stellar clusters at z = 3 to 6). This motivates us to study local analogues of high-redshift super star clusters (SSCs) forming sites.

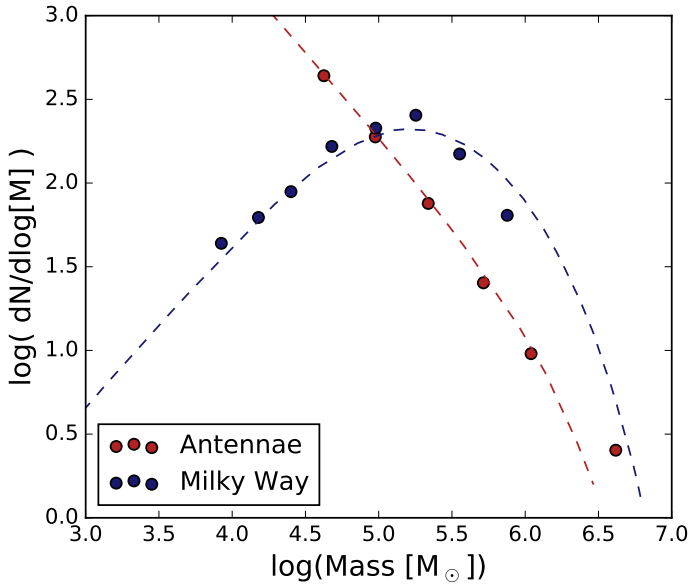

FIGURE 4.14: Cluster mass functions of the old GC population of the Milky Way (from Harris, 1996) and the young massive clusters in the Antennae system (from Fall, Chandar, and Whitmore, 2009).

In Section 2.5 we have seen that there are indeed SSCs formation sites in the local Universe, namely in galaxy mergers and dwarfs galaxies. These young clusters have been extensively studied to understand their formation mechanism, and in particular the disruption processes at play shortly after their formation. Indeed, if SSCs are considered similar to high-redshift GC progenitors, one must explain how their initial mass function evolves from a power law with index -2 (Elmegreen and Falgarone, 1996; Fujii and Portegies Zwart, 2015) to the peaked distribution observed for old GC, with a near-universal mass peak of 2×10^5 $M_\odot$ (Fall and Zhang, 2001; Jordán et al., 2007). This change of shape implies a cluster disruption mechanism, impacting preferentially the low-mass population. The study of disruption mechanisms is a very active field of research, which must take into account the effect of gas expulsion (Lada and Lada, 2003), the variation of the surrounding tidal field (Renaud, Gieles, and Boily, 2011; Bianchini et al., 2015; Gieles and Renaud, 2016) and the internal stellar dynamics (Jordán et al., 2007). These processes should have a specific signature on age-mass diagrams of young clusters (see e.g. Elmegreen and

Hunter, 2010).

As described in Section 2.2.3, BCDGs are often considered low-mass analogues to gas-rich clumpy high-redshift galaxies, and have often been targeted to study their SSCs population (see e.g. Adamo et al., 2010, and references therein). However, as claimed in Section 2.2.3 and Section 4.2, TDGs prove to be better analogues to high-redshift galaxies for two reasons. First, they are truly young objects: their spectral energy distribution (SED) is consistent with no stellar population older than 1 Gyr (Boquien et al., 2009), when the presence of old stellar clusters in BCDGs show that they have known previous star formation episodes (Oestlin, Bergvall, and Roennback, 1998). More importantly, they show a similar metallicity to $z = 2$ galaxies (see e.g. Fensch et al., 2016, and references therein). This higher metallicity than BCDGs should help the gas to cool and is expected to increase the cluster formation efficiency. Last but not least, the particular system presented in Section 4.2 show a velocity dispersion in HI twice higher than BCDGs (Bournaud et al., 2007), which will favor the formation of massive stellar clusters.

However, there had been no observation targeting SSCs in genuine young, gas dominated TDGs yet. This motivated us to write a HST time proposal to observe the huge HI ring presented in Section 4.2. The proposal was accepted (PI: Duc) and the data acquisition was finished in December 2016. In this Section I will present ongoing work on the obtained HST data. I will first describe the data and the cluster selection routine. Then I will show how I used a SED fitting code, called CIGALE, to derive the physical properties of the star cluster candidates. This work will be presented in Fensch et al. (2017b, in prep.).

4.3.1 Star clusters observed with the HST

We requested the observation of four fields, which are shown in Fig. 4.13. The fields were chosen to follow the HI gas distribution. We see that two bright stars in Field 2 saturated the instrument and created 8-shaped features in Fields 1 and 4. The gap between the two CCDs can be seen as a narrow band in the middle of each field of view: only one exposure has been done in these small regions, which induces a higher noise level.

We asked for 5 different broadband filters on the WFC3 instrument, which are shown in Fig. 4.15 and will be called, for convenience, U, B, V, I and H thereafter. This combination is known to be able to disentangle colors effect from metallicity, age and extinction (Anders et al., 2004). In particular we see that the V-band will account for H_β, H_α and the [OIII] doublet emission lines. We therefore expect very blue V-I colors for objects featuring these emission lines, that is very young clusters. We also see that the Balmer break H_∞ is located between the U and B-bands. U-B colors will then be a strong fonction of stellar population age for clusters with strong Balmer absorption features – that is from roughly 100 Myrs old, when A-type stars begin to dominate the light – although sensitive to attenuation.

To limit the total exposure time to a reasonable value, the U and H band observations were only requested for the fields 1 and 4, which host the TDGs and where we expect to find the majority of the young SSCs of this system. The exposure times are given in Table 4.5.

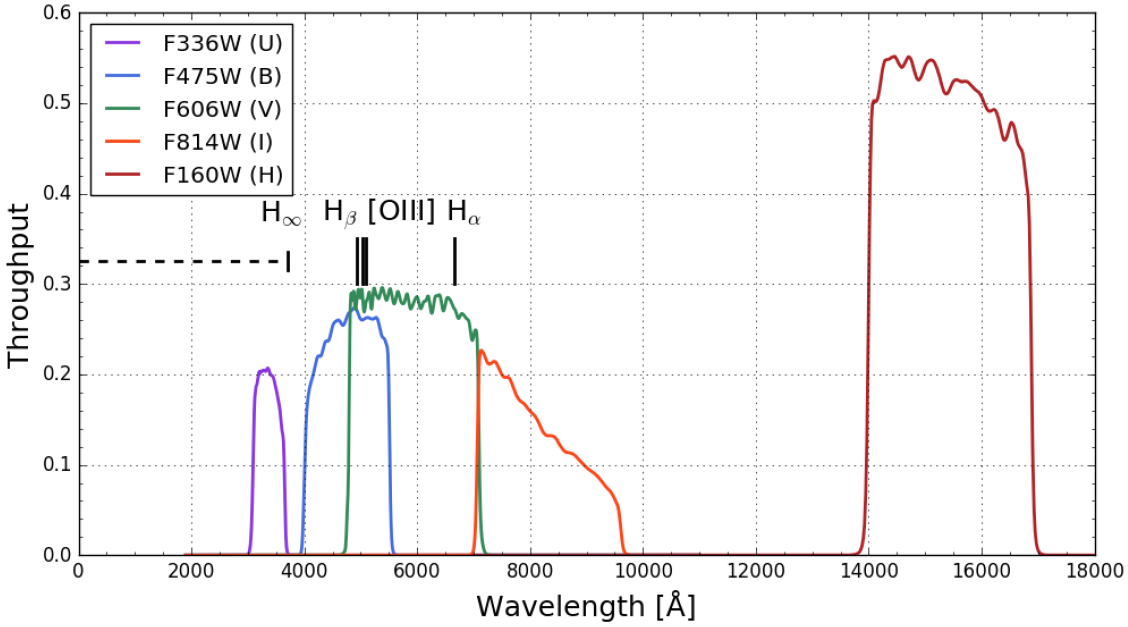

FIGURE 4.15: Throughput fonctions of the HST filters used in this study. The short vertical lines show the location of some spectral features at observed wavelength.

TABLE 4.5: Number and time exposures in seconds for each filter and field.

Filter	Field 1	Field 2	Field 3	Field 4
U-band	4 x 378	-	-	4 x 378
B-band	2 x 350	2 x 350	2 x 350	2 x 350
V-band	2 x 350	2 x 350	2 x 350	2 x 350
I-band	2 x 350	2 x 350	2 x 350	2 x 350
H-band	4 x 903	-	-	4 x 903

One may note that our strategy only includes 2 exposures per field for the B,V and I filters. This was imposed by the HST observation procedure: splitting these exposures in three would have led to a reduction of the total exposure time because of time overheads. The drawback is that only two exposures are available to remove the cosmic rays. Thus these filters present a relatively high number of cosmic rays as we can see in Fig. 4.16, which will need to be removed.

In the following I will describe how I built the photometric catalog.

Detection routine

I first created a catalog of detections using the code SExtractor (Bertin and Arnouts, 1996). As some clusters are found in crowded areas, I launched the detection routine on an image filtered using a *mexhat* kernel, which enhances the contrast between background and clustered light. I checked by eye that visible clusters are effectively detected: the aim is to detect as many sources as possible, as spurious detections will be rejected later during the procedure.

To remove the cosmic rays on the B,V and I-band images, I used a coincidence procedure. Detections on two filters of the same field are associated if their center

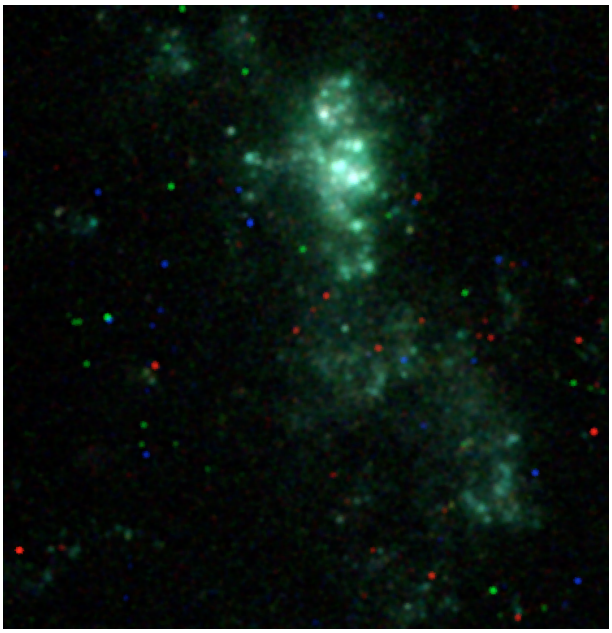

FIGURE 4.16: Zoom on the center of the northern TDG from Fig. 4.13. The image was smoothed to enhance the contrast. The remaining cosmic rays are visible as the bright red, green or blue small circles.

are closer than the size of 2 pixels. If a detection has no counterpart in the other two filters it is considered as a cosmic ray detection. These cosmic ray detections are then stored to create a mask map, where a square of 10×10 pixels centered on the cosmic ray detection is marked.

I also rejected by hand luminous foreground stars and detections inside resolve galaxies in the field (see Fields 2 and 4 in Fig. 4.13).

I also used SExtractor to build a background and a background variation map, using its CHECK IMAGE feature. They were computed using a 3-sigma clipping method on a 20×20 pixel size mesh. This size is large enough not to filter out our detections, and small enough to get a good measure of the background light.

Aperture photometry

I performed aperture photometry with aperture radius of 0.32″. This corresponds to 8 pixels in the U, B,V and I filters, and 2.5 pixels in the H band. This value was chosen to be high enough to get a good sample form the H band (FWHM $\simeq$ 2.3 pixels) and the typical distance between two sources. Parallel aperture photometry is done on the mask image. If the aperture area encounter a masked region, the detection is rejected, as being contaminated by a cosmic ray.

Similar aperture photometry is done on the background and background variation map. The background value is thus subtracted to the source photometry. This value is then corrected for the finite aperture, using the tables corresponding to each filter, from the instrument documentation. The error on the flux is then composed of two components: the Poisson noise and the uncertainty on the subtracted background value:

$$\sigma_{\text{poisson}} = \frac{\sqrt{F_e \times t_{exp} \times GAIN}}{t_{exp}} \tag{4.1}$$

$$\sigma_{\text{bck}} = \sqrt{N_{\text{aper}}} \times \sigma_{bck/pix} \tag{4.2}$$

$$\text{error} = \sqrt{\sigma^2_{\text{poisson}} + \sigma^2_{\text{bck}}} \tag{4.3}$$

The Poisson noise parameters are the following: F_e is the flux of the un-corrected source measured in e^-/s, t_{exp} is the time of exposure in s and GAIN is the conversion factor from e^- to the map values.

The background uncertainty is obtained by multiplying the pixel averaged background dispersion in the aperture, $\sigma_{bck/pix}$, by the square root of the number of pixels in the aperture, N_{aper}.

The total error is obtained by the propagation of the two errors. The resulting flux and error are then converted from e^-/s to mJy and AB magnitude using the zero-point values given in the instrument documentation.

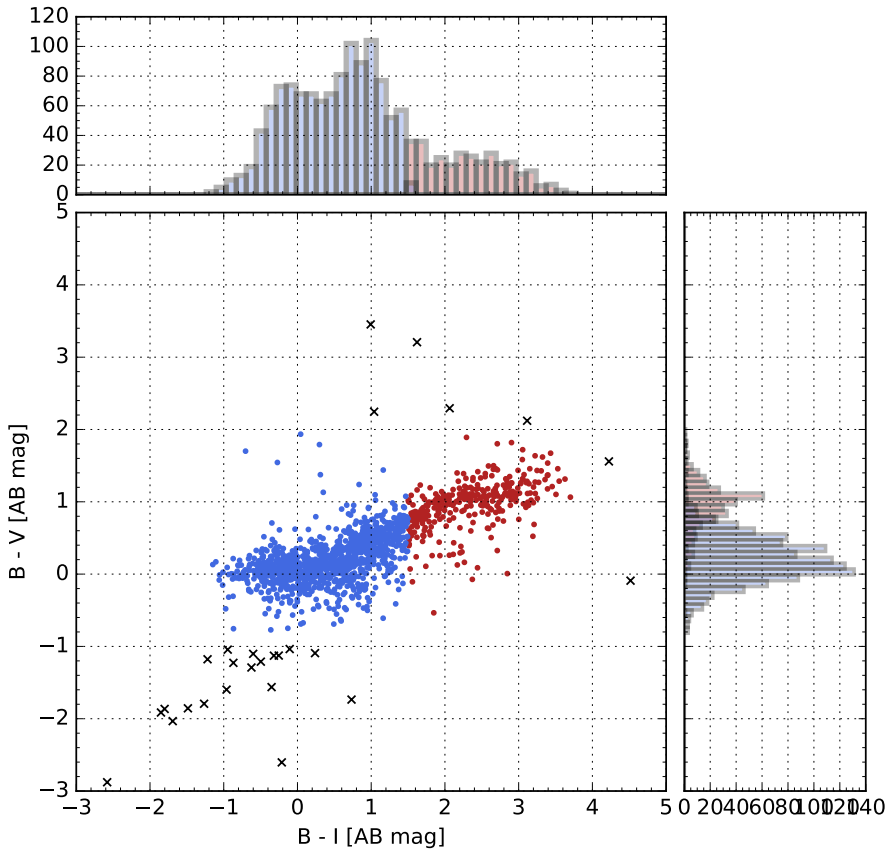

FIGURE 4.17: Color-color diagram of the detected sources. The black crosses show sources with very blue or red colors and are, upon verification, coincidence between two cosmic rays which have not been removed by the described procedure. Histogram of color values are shown on the top and right insets. The color-color distribution of the sources show a bimodality in both B-I and B- V colors, highlighted by a choice of color. The population is split using a B-R value of 1.5 mag (see text).

A color-color diagram of the resulting sources is shown in Fig. 4.17. We see the presence of a color bimodality on both axis. One should note that this bimodality does not correspond to the classical blue-red dichotomy for old globular clusters: the two groups separates at B - I = 1.5 mag, which is redder that the reddest GC candidates (Blakeslee et al., 2012; Cho et al., 2016, see e.g.). Thus, we consider that sources redder than B - I = 1.5 mag, colored in red in Fig. 4.17 are either foreground stars, either background galaxies, and we exclude these outliers from the further study. In this figure, there are also a few points with extreme colors which are, upon verification, coincidences between two cosmic rays which have not been removed by our procedure.

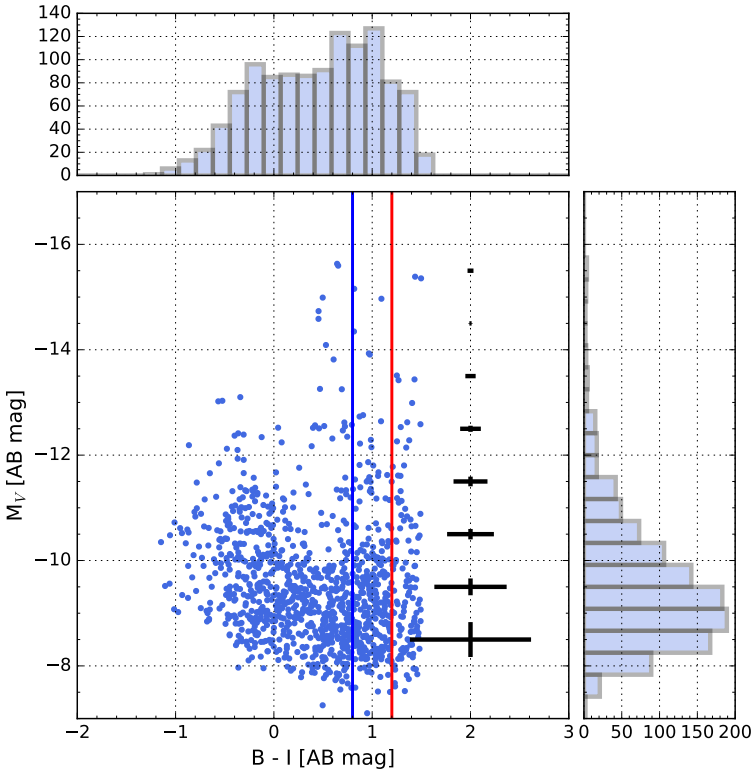

FIGURE 4.18: Color-magnitude diagram for the blue population of Fig. 4.17. The vertical blue and red lines show the typical color of blue and red GCs around galaxies, respectively B-I = 0.8 and 1.2 mag (see text). The median error bar for a given luminosity bin is shown on the right hand side of the scatter plot.

The final color-magnitude diagram of SSC/GC candidates is shown in Fig. 4.18. We see that we have detections with colors similar to the blue and red populations of GCs, showed with the blue and red vertical lines (the values are from Blakeslee et al., 2012; Cho et al., 2016). We also have a population with very blue color, up to B - I = -2 mag.(Burgarella, Buat, and Iglesias-Páramo, 2005).

4.3.2 Characterization using CIGALE

The aim of this part is to study the age distribution of our cluster candidates, and study the relation between their mass and age. To extract these physical parameters from our photometric catalog, I used another tool, a SED fitting code called CIGALE.

CIGALE[7] is a SED fitting code which works in two steps. First, CIGALE creates a grid of stellar population SED models from the input file provided by the user. One can for instance give an acceptable range of age, mass and attenuation for one or two populations. Second, CIGALE proceeds to a χ^2 comparison between the created models and the provided catalog. The output is the list of the parameters for the best fit, and the probability density function (PDF) for each parameter, weighted by the significance of the model[8].

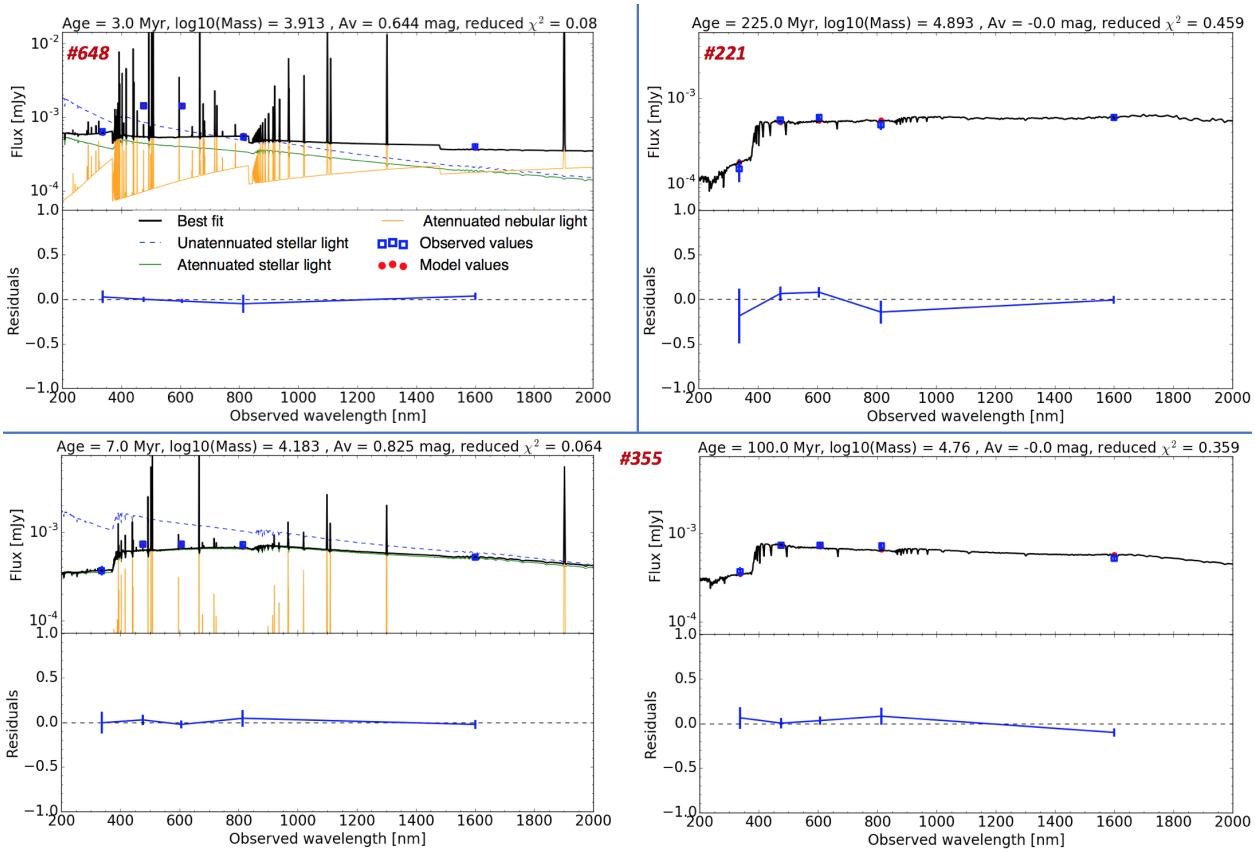

FIGURE 4.19: Best fits for a young (top right panel), an older cluster (top left panel) and an degenerate case (bottom left panel). In the bottom right panel was added the best fit for a CIGALE run with enforced A_V = 0 mag, to illustrate a degeneracy effect. We see the parameters of the fits in the title.

In our case, we expect to have two kinds of objects. First, we should have detected part of the old population of GCs around the massive elliptical galaxy NGC 5291. They should be reddened only because of their age and not because of the attenuation, because they are not embedded in the HI ring. Second, we have a young population, for which the reddening should come from both the attenuation from their surroundings, and the age of the stellar population. One should note that the MUSE observations of the dwarf allow us to have an estimate of the attenuation for the embedded young clusters , namely : $A_V = 0.6 \pm 0.2$ mag. Therefore, we allow for A_V to go from 0 to $\simeq$1 mag, and age to go from 1 to 12 Gyr. To reduce the number of input parameters, we model the star formation history of stellar cluster as single

[7]Code available at http://cigale.lam.fr/

[8]Each value is weighted according to the χ^2 of the model, the weight being $e^{-\chi^2/2}$.

burst, exponentially decreasing with a timescale of 0.1 Myr. In the following, we will only study the clusters in the two fields with U band coverage (field 1 and field 4, see Fig. 4.13).

In Fig. 4.19 are shown the best fits for three cluster candidates. We see that the cluster #648 is best fitted with a young stellar population. In particular, this cluster characterized by a strong nebular emission, which dominates the light in the B and V bands. The cluster #221 is best fitted by an older stellar population. Its older age is probed by the drop at the Balmer break between the U and B band.

If the age of these two clusters does not seem to be ambiguous, there are some tangent cases, as we can see in the bottom panels of Fig. 4.19. In this case, the V - R color is consistent with a small contribution of nebular lines, and the drop of the light in the U-band can either be explained by both a young population with a strong attenuation (A $\simeq$ 1 mag), or an older population and no attenuation.

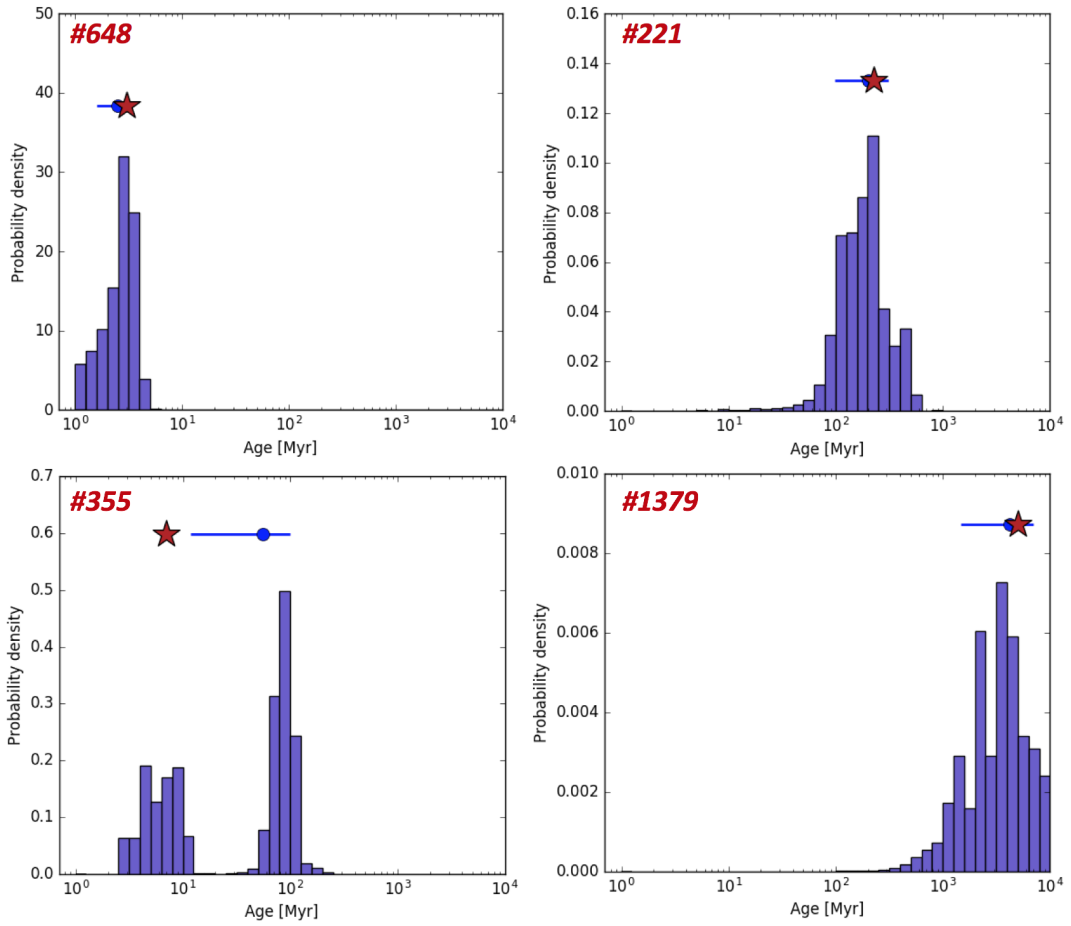

FIGURE 4.20: Age PDF for several clusters, typical of each age classification (see text). Top right: cluster #648, categorized as *young*. Top left: cluster #221, categorized as *intermediate*. Bottom left: cluster #355, categorized as *ambiguous*. Bottom right: cluster #1379, categorized as *old*. The red star shows the location of the best fit. The filled circle and the bar show the averaged estimation and the 1-σ deviation.

Another way to see this degeneracy is to look at the PDF of the age parameter of these clusters. In Fig. 4.20 are shown four typical age PDF. For the two top PDFs,

which correspond to the two clusters presented in the upper panel of Fig. 4.19, we see that the PDF is centered on a value close to the best fit value. On the bottom left panel is shown the PDF for the degenerate case of cluster #355 shown in Fig. 4.19. We see that if the best fit corresponds to a young cluster (age = 7 Myr), the PDF is clustered on a higher value of the age parameter (age $\simeq$ 100 Myr).

This degeneracy thus prohibits any precise age determination. Without further information on the source[9], I cannot break this degeneracy and give to this cluster a young or intermediate age. Therefore, in order to have a robust age classification, I use the following conditions to build cluster age groups:

- **Young clusters:** Age between 0 and 15 Myr, defined by: $\int_0^{15} \mathrm{PDF}(x)\,\mathrm{d}x > 0.9$, where the PDF is normalized to 1, as in Fig. 4.20.
- **Intermediate clusters:** Age between 30 and 1000 Myr, defined by: $\int_{30}^{1000} \mathrm{PDF}(x)\,\mathrm{d}x > 0.9$.
- **Ambiguous clusters:** None of the above categories and a best fitting age below 1000 Myr. The age-attenuation degeneracy prohibits us to classify them either as young or intermediate, without further information. With a number of cluster similar to the young and intermediate populations, this ambiguous population is not negligible.
- **Old clusters:** None of the above categories but a best fitting age above 1000 Myr. These clusters are the candidates for the old globular cluster population of the central massive galaxies. However, given the distance from NGC 5291 of the two fields investigated here – fields 1 and 4, covered by the U-band – we expect a small number of them.

In Fig. 4.21 is shown the mass distribution of each of these populations. We see that the young clusters are significantly less massive than the intermediate clusters: their respective distribution peak differs by one order of magnitude. We can also see that the intermediate clusters are less massive than the old clusters: they do not reach the mass regime of GCs (see also Fig. 4.14 for the MW).

This preliminary result may be the result of several factors. First, the mass of the most massive cluster of a given system correlates with the SFR (see e.g. Bastian, 2008). Thus, this mass difference between the young and intermediate population may indicate that the SFR in the HI ring has reached a maximum between its formation and $\simeq$ 100 Myr ago. However, this mass difference may also be due to the formation of more massive clusters by the merging of smaller clusters (see e.g. Fellhauer, Wilkinson, and Kroupa, 2009, and references therein). This on-going cluster merging would also explain why the intermediate clusters have not yet reached the mass regime of the old clusters.

4.3.3 Prospects

The bigger limitation of this study,like the many others done so far using the same method, is the degeneracy between the age and the attenuation for some clusters.

[9]The MUSE data presented in the last Section would provide such information. However, the modest spatial resolution of MUSE merges cluster and background emission. Furthermore, our MUSE data only covers a small part of our full HST field of view.

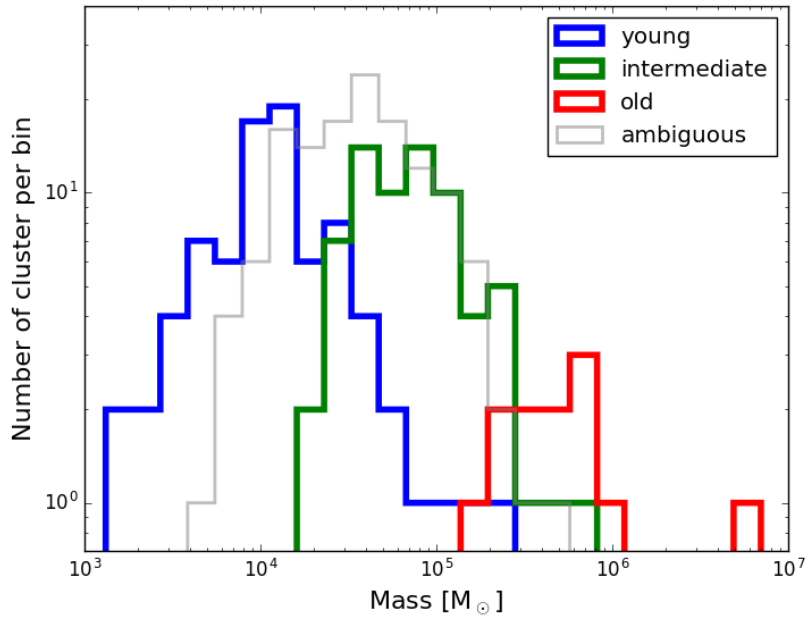

FIGURE 4.21: Cluster mass distribution. The color refer to the age population (see text).

As we saw in Fig. 4.19, these clusters are typically too old to feature strong emission lines and too young to show a strong Balmer break.

However, this degeneracy could be broken if one had access to spectroscopic data with a high spatial resolution, similar to that of the HST: the presence or absence of weak emission lines and the slope of the stellar continuum would give a strong constrain on the age of the cluster. The MUSE data presented in Section 4.2 do not cover the full HST maps have a sufficient spatial resolution to disentangle single cluster emission from underlying emission. However, such a resolution will be achieved by MUSE when the use adaptive optics (AO) will be operational on this instrument. AO is undergoing commissioning on MUSE at the time of the writing, and as part of it AO/MUSE observations of one of our fields has been obtained.

Chapter 5

Impact of high-z mergers on star and stellar cluster formation

5.1 Star formation in high-z galaxy interactions

In Section 2.6, I presented how interactions between galaxies impact their morphology and star formation history. In particular, in the local Universe all galaxies located on the starburst sequence of the Schmidt-Kennicutt diagram (see Fig. 2.16) show signs of interactions, as one an see on Fig. 5.1. At $z = 0$, it is accepted that all starburst galaxies are undergoing a merger process (see review by Sanders and Mirabel, 1996).

FIGURE 5.1: Starburst galaxies from Guo et al. (2016). They all present tidal features, signs of a previous interaction.

At high-redshift tidal features are more difficult to observe. However, observations of galactic pairs up to $z < 1.5$ suggest an increase of the merger rate proportional to $(1 + z)^{\alpha}$ with $\alpha \simeq 2.5 \pm 0.5$ (see e.g. Le Fèvre et al., 2000; Kartaltepe et al., 2007; Lotz et al., 2011). This evolution is also a prediction of ΛCDM cosmological numerical simulations (Neistein and Dekel, 2008; Hopkins et al., 2010).

Interestingly, observations suggest that major mergers are inefficient at driving star formation at $z \simeq 2$ (Kaviraj et al., 2013; Lofthouse et al., 2016). Several galaxy surveys also showed that the fraction of starburst galaxies does not change with redshift (Rodighiero et al., 2011; Schreiber et al., 2015). As we can see in Fig 5.2, for any definition of the starburst mode, that is a SFR a factor 2.5, 3 or 4 above the star-forming Main-Sequence (see Section 2.4.3), the number of starburst galaxies is consistent with being constant with redshift. Thus, although starbursts are triggered

by interactions, their proportion do not follow that of interacting galaxies.

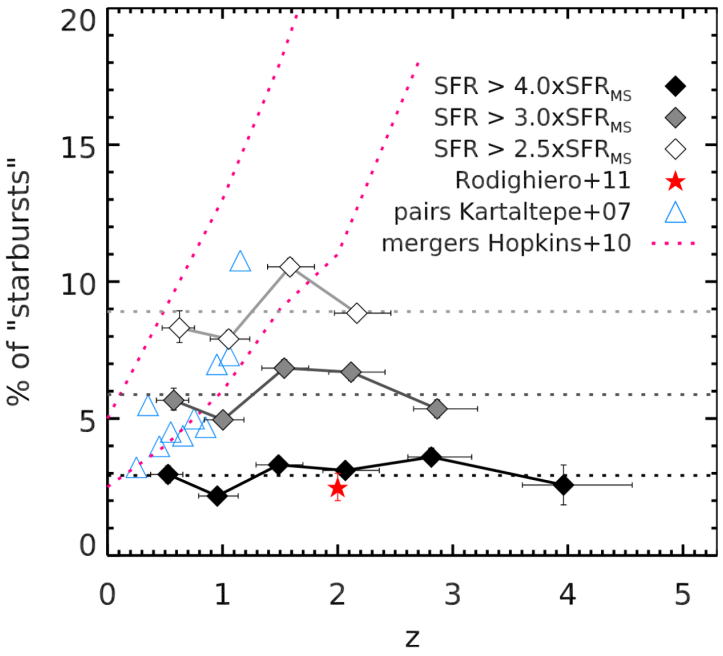

FIGURE 5.2: Fraction of starburst galaxies in the sample as a function of redshift. Three different definitions for starburst galaxies are used. The blue triangles show the pair fraction from Kartaltepe et al. (2007) and the red lines show the predictions from cosmological simulations presented in Hopkins et al. (2010). From Schreiber et al. (2015).

This questions the efficiency of galaxy interactions to trigger a massive enhancement of SFR at high redshift. Do fewer orbital configurations allow an enhancement of SFR ? Are these bursts shorter ?

Previous numerical simulations of $z \sim 2$ type galaxy interactions suggested they are indeed inefficient at driving a massive enhancement of star formation (Bournaud et al., 2011; Hopkins et al., 2013; Perret et al., 2014). However, a systematic comparison study between high- and low-redshift galaxies was still missing. I ran simulations to test how these triggers are modified by the gas mass fraction by running simulations of galaxy interactions with a gas abundance typical of $z = 2$ and $z = 0$ galaxies.

In the next section I will present the processes which are currently thought to trigger the starburst mode in low redshift galaxies. I will then describe the numerical sample we used to test the impact of the gas mass fraction on these processes.

5.1.1 Starburting galaxies at $z = 0$

Detailed studies of local interacting galaxies show that, in favorable cases, the enhancement of the SFR lasts during a major part of the galaxy interaction and not only the final merging phase: it can begin as soon as after the first pericenter passage (Zhang, Fall, and Whitmore, 2001; Cortijo-Ferrero et al., 2017a; Cortijo-Ferrero et al., 2017b). This is also consistent with a specific SFR increasing with decreasing

physical separation of close galaxy pairs (see e.g. Ellison et al., 2008; Ellison et al., 2013). This behavior was also predicted by numerical simulations (Teyssier, Chapon, and Bournaud, 2010; Hopkins et al., 2013; Renaud et al., 2014).

The enhancement of the SFR in a nuclear starburst in the late stages of a galaxy interaction is currently explained by the strong gas nuclear inflows due the gravitational torques (see Barnes and Hernquist, 1991, and section 2.6.1). However the enhancement of the SFR in the early stages of an interaction can be spread over larger regions. Fig. 5.3 shows the famous Antennae galaxy pair where one can spot star forming regions through the pink emission from H_α emission line and the blue light from young stars in the overlap and an arc on the upper right part of the upper galaxy. This system is seen slightly before the second pericenter passage (Renaud et al., 2009). Its SFR is estimated to be around 22 $M_\odot yr^{-1}$, with important contributions from the overlap and the arc (Klaas et al., 2010).

FIGURE 5.3: HST image of the NGC 4038-NGC 4039 interacting system.

It is remarkable to note that these extended regions of star formation coincide with regions of compressive tides in numerical simulations of similar orbits (see Fig. 2.20). Using high-resolution (1.5 pc) numerical simulations, Renaud et al. (2014) proposed a mechanism based on this compressive tidal field to explain this extended star formation in interacting systems. The authors noted a coupling between the compressive tidal field and the turbulence induced by the interaction (see section 2.6.1), which results in a preferential enhancement of the compressive mode of the turbulence (see Box 2 in section 2.2.1). This mode of the turbulence is thought to feed the high-density tail of the density PDF (see e.g. Federrath, Klessen, and Schmidt, 2008, and Fig. 2.8) and to be able, on a purely theoretical basis, to move the galaxy on the starburst sequence of the Schmidt-Kennicutt diagram (Renaud,

Kraljic, and Bournaud, 2012). In Fig. 5.4 we can see that the increase of the SFR after the pericenter passages does indeed follow an increase of the gas mass fraction in compressive tides and an increase of the energy in compressive tides, confirming the theoretical expectations.

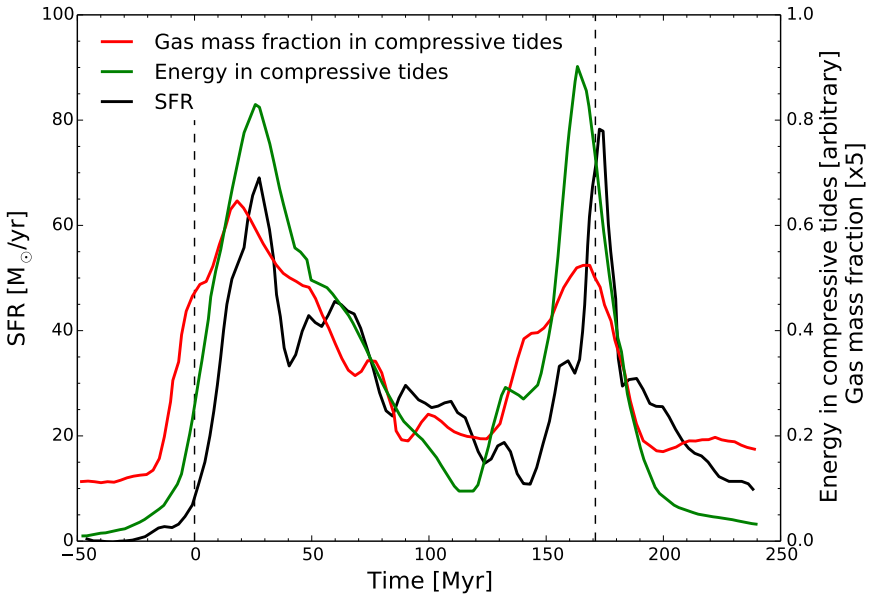

FIGURE 5.4: Evolution of the SFR, gas mass fraction and energy in fully tidally compressive regions. The two dashed vertical lines show the time of the first pericenter passage (t = 0 Myr) and of the final coalescence (t = 171 Myr). Adapted from Renaud et al. (2014).

This leaves us with two main processes to explain this enhancement of star formation in interacting galaxies.

- First, an increase of the compressive turbulence, which brings gas to the high density tail of the gas density PDF and induces star formation.
- Second, when galaxies are closer both spatially and kinematically, gravitational torques become more important, last longer and are able to bring gas to the central region of the galaxies, and trigger a nuclear starburst.

There is a third process at play in galaxy interactions, namely cloud-cloud collisions, in particular where the disks overlap (Motte et al., 2014; Fukui et al., 2014). This process is quite hard to probe in numerical simulations, especially in AMR codes where one cannot follow 'gas particles' belonging to different clouds. Thus we will not study it in our work, although we acknowledge it should play a role in the enhancement of the SFR when the gas disks overlap.

In the following I will describe our set of numerical simulations to study the effect of the gas mass fraction on these two processes. The following work have been published in (Fensch et al., 2017).

5.1.2 Numerical setup

To test the impact of gas mass fraction we use the same method as in section 4.1: we use two models of galactic disks, whose sole difference is the gas mass fraction. We use one *gas-poor* model, with gas mass fraction of 10%, representative of $z = 0$ galaxies, and a *gas-rich* model, with gas mass fraction of 60%, representative of $z = 2$ galaxies. I will briefly discuss below how using gas mass fraction as single proxy for the redshift, might bias our study.

- **Sizes:** As described in section 2.2.2, high-redshift galaxies are more compact than low-redshift galaxies, by a factor 2 for equal mass galaxies (van der Wel et al., 2014; Ribeiro et al., 2016). However, we decide to neglect this effect and we chose a common size whose compactness is an intermediate between low- and high-redshift conditions.
- **Orbits:** For equal halo mass, cosmological simulations predict that the typical pericenter distance for galaxy binary interaction to be lower by 25% at $z = 2$ than it $z = 0$ (Wetzel, 2011). This results in shorter dynamical timescales and probably in orbits more favorable to strong starbursts. We note that this suggests that interactions would be even less efficient at triggering starbursts at high-redshift. In this study we decided to also use two orbits with higher gravitational binding energy to see the effect on the SFR.
- **Cosmological context:** We do not implement cosmological gas infall. This infall would replenish the gas reservoir otherwise depleted by star formation. Gabor and Bournaud (2014) have shown that this infall also feeds the gas turbulence of the disk until $z = 2$. We therefore consider that our gas turbulence, in the $z = 2$ is slightly underestimated. One should note that the characteristics of the merger remnant, such as its ability to re-built a disk, depend greatly on the cosmological context (see e.g. Athanassoula et al., 2016)

In the following, I will therefore make a nomenclature equivalence between $z = 2$ (resp. $z = 0$) and our high (resp. low) gas mass fraction galaxies.

The observation of the increase in gas fragmentation in numerical simulations require a high spatial resolution, as one needs to resolve the local Jeans length with several resolution elements (Teyssier, Chapon, and Bournaud, 2010; Powell et al., 2013; Renaud et al., 2014). In this study we set the maximum spatial resolution to 6 pc, with the same density-based refinement criterion. We note that, the Jeans length being higher in the high gas mass fraction case, these runs will naturally be better resolved, in term of number of element resolution.

We use the recipes described in Chapter 3. The characteristics of the galaxies and orbits are detailed in Fensch et al. (2017). We use a series of orbits with different spin-orbit couplings (see Fig. 2.20) and gravitational binding energies, to ensure that we are not biased by a particular orbital resonance.

A snapshot of the gas density map of the interaction 60 Myr after the first pericenter passage is shown Fig. 5.5. In the next section I will describe the main results of the simulations.

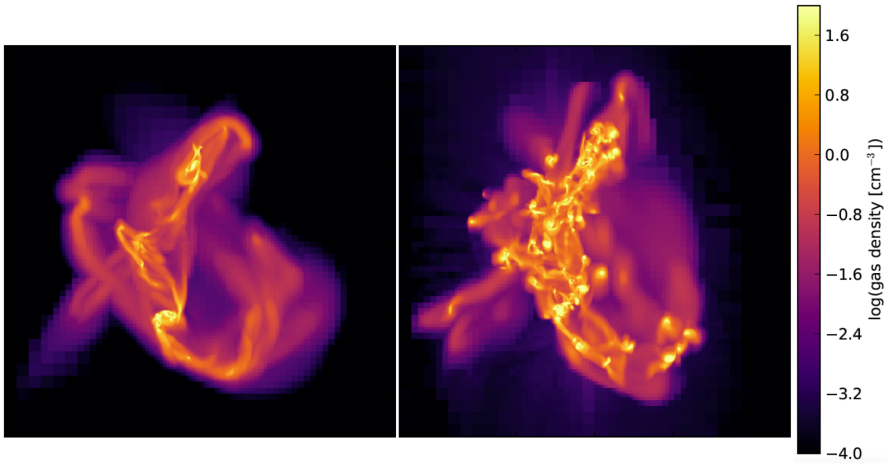

FIGURE 5.5: Gas density map of $z = 0$ and $z = 2$ simulations on the same orbit 60 Myr after the first pericenter passage.

5.1.3 Impact of the gas mass fraction

The SFR evolution of our galaxies on the Schmidt-Kennicutt diagram is shown in Fig. 5.6, for two orbits for each redshift type galaxy model. We see that in the $z = 0$ case, the interaction triggers a strong starburst from the first pericenter passage to the end of the interaction. This is consistent with both observations and previous simulations, as I explained in section 5.1.1. However, in the $z = 2$ cases, the first pericenter passage does not increase significantly the SFR, and the final coalescence brings one galaxy to the starburst sequence for only about 150 Myr. Thus, for similar orbits, interactions are much less efficient at enhancing the SFR in typical $z = 2$ galaxies.

The evolution of the distribution of gas densities can be observed by computing the gas density PDF, shown in Fig. 5.7. We can see that the PDF of the $z = 0$ type galaxy interaction evolves from the isolated run, as gas is brought to the high-density tail. However, the PDF of the $z = 2$ type galaxy interaction does not change much from the isolated run: there is a new peak at 10^5 cm^{-3} at $t = 376$ Myr, which corresponds to the time of the final coalescence. This shows that there is a saturation of the gas density PDF, which the interaction seems unable to modify. In particular the interaction is less efficient to bring gas to the high-density tail than in the $z = 0$ runs, and thus to increase the SFR.

In section 5.1.1, I described the two main processes that are thought to induce an enhancement of the SFR during galaxy interactions.

Compressive turbulence

We have seen that an increase of the energy in the compressive component of the turbulence, being favored by the appearance of tidally compressive regions, could bring gas to high density tail of the PDF. This process seems to be saturated in the $z = 2$ case, this for two reasons.

First, the turbulence of $z = 2$ disk is typically quite high, between 30 to 50 $\mathrm{km\,s^{-1}}$(see section 2.2.2), and the release of gravitational energy through the interaction is not able to increase it. I have measured the 1-D gas turbulence in the two redshift-type

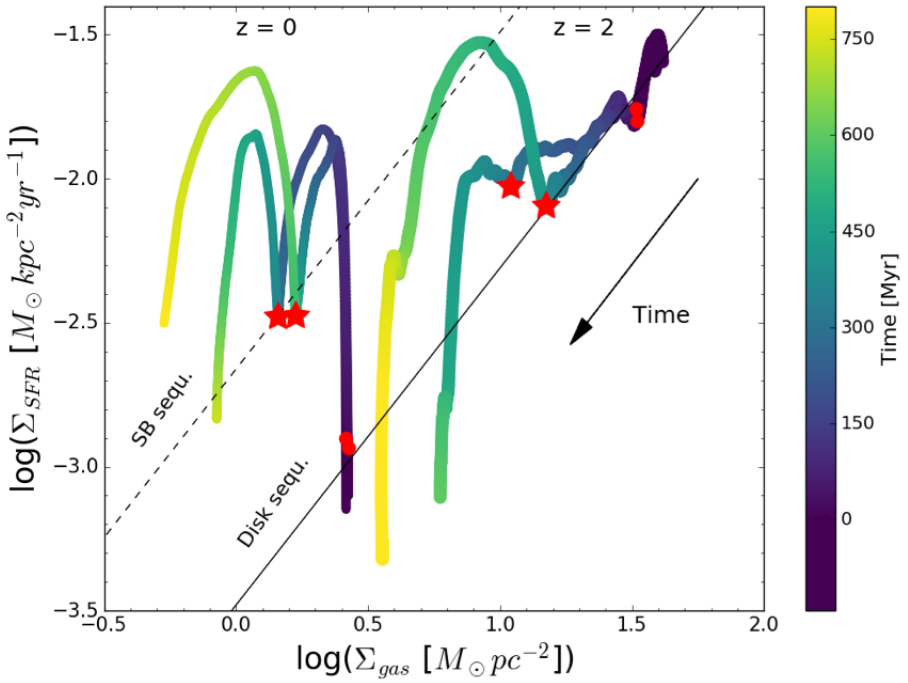

FIGURE 5.6: Evolution of two orbits for each redshift type galaxy interaction. The red circle shows the time location of the first pericenter passage, which also defines $t = 0$ Myr, while the red star shows the time of the final coalescence. The curve are smoothed using a top hat kernel on the last 100 Myr, to resemble the measurements of SFR achieved from IR luminosity (Kennicutt, 1998).

interaction: in the $z = 0$ case the interaction brings the velocity dispersion from 10 to 40 $\mathrm{km\ s^{-1}}$, in the $z = 2$ case from 35 to 50 $\mathrm{km\ s^{-1}}$(see Fig. 10 in Fensch et al., 2017). The relative increase is thus much smaller in the $z = 2$ case.

Second, I computed the gas mass fraction enclosed in a compressive tidal field. To do that, I computed the tidal tensor $T_{ij} = -\partial_i \partial j \phi$ using a one order difference scheme over cells of size 50 pc. Then I computed the gas mass fraction enclosed in regions where the largest eigenvalue of the tidal tensor is negative. The time evolution of this quantity shows an enhancement in the $z = 0$ case, from 5% to 25%, when in the $z = 2$ case, this fraction remains relatively constant at 20%, and show no difference with the isolated run. The reason for this is that most of the gas clumps survive the interaction, and creates an extensive tidal field in the inter-clump medium.

The combination of the saturation of turbulence and of the compressive tidal field prevents the widening of the PDF during the interaction.

Nuclear gas inflows

We also know that the gravitational torques are able to drive the galactic matter to the nucleus of the galaxies (see Section 2.6.1). To quantify this, I measured the evolution of the total baryonic mass in the inner kpc of each galaxy. I found that the mass nuclear inflow rate in the isolated runs is naturally higher in $z = 2$ type galaxies, 30 to 50 $\mathrm{M_\odot/yr}$, which is expected from the self-regulation of the violent disk instability (see section 2.3.3) when this inflow rate is 2-3 $\mathrm{M_\odot/yr}$ in the isolated disks at $z = 0$. This naturally higher inflow rate leads to a saturation effect, as the interaction

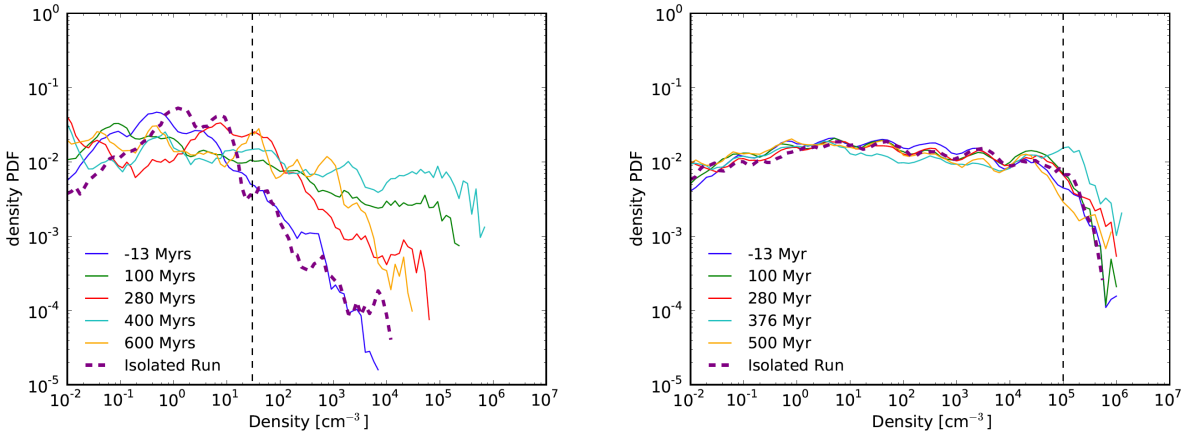

FIGURE 5.7: Gas density PDF of the prograde-prograde interactions in the $z = 0$ (left) and $z = 2$ (right) type galaxy interactions.

produces a smaller relative increase of the nuclear inflow rate than in the $z = 0$ case.

5.1.4 Concluding remarks

The high gas mass fraction of $z = 2$ disks produces strong disk instabilities which results in high turbulence, nuclear inflow rates and important regions of compressive tides. The interaction produces a smaller relative increase of this quantities than in the $z = 0$ cases, which leads to a saturation of the gas density distribution. We argue that this explains why interactions only produce a mild enhancement of the SFR for typical $z = 2$ galaxies.

In the whole sample tested in Fensch et al. (2017), the highest reached SFR is 350 $M_\odot$/yr, during 50 Myr. One may therefore wonder what is the origin of the sub-millimeter galaxies (SMGs) which have SFRs up to 1000 $M_\odot$/yr at $z = 2$ (Barger et al., 1998; Tacconi et al., 2006). One should first note that such galaxies are significantly more massive than our simulated disks. Furthermore, we note that Narayanan et al. (2015) have shown that the regime of SMGs can be reached without major mergers, but rather by continuous gas accretion onto a very massive halo hosting several galaxies, which appear blended to the observer (see also Davé et al., 2010; Wang et al., 2011). Thus, the origin of SMGs cannot be discussed from our study, and is still an open field of research.

One may also argue that the gas mass fraction is actually not the only factor at play here. For instance, $z = 0$ dwarf galaxies can have a very high gas mass fraction, up to 90%, and high turbulence (Lelli, Verheijen, and Fraternali, 2014) and show an enhanced SFR during interactions (Stierwalt et al., 2015). It should be noted that most of the gas in these dwarfs is located in a diffuse atomic hydrogen envelope and not in dense gas clumps. In Fensch et al. (2017) we argue that dwarf galaxies gas distributions make interactions efficient at driving gas towards the center of mass of the dwarf and ignite a starburst.

MNRAS 000, 1–16 (2016) Preprint 8 November 2016 Compiled using MNRAS LATEX style file v3.0

High-redshift major mergers weakly enhance star formation

J. Fensch[1]★, F. Renaud[2], F. Bournaud[1], P.-A. Duc[1], O. Agertz[2], P. Amram[3], F. Combes[4], P. Di Matteo[5], B. Elmegreen[6], E. Emsellem[7,8], C. J. Jog[9], V. Perret[10], C. Struck[11] & R. Teyssier[10]

[1] *Laboratoire AIM Paris-Saclay, CEA/IRFU/SAp, CNRS, Universite Paris Diderot, F-91191 Gif-sur-Yvette Cedex, France*
[2] *Department of Physics, University of Surrey, Guildford, GU2 7XH, UK*
[3] *Universite Aix Marseille , CNRS, LAM (Laboratoire d'Astrophysique de Marseille), 13388, Marseille, France*
[4] *Observatoire de Paris, LERMA (CNRS: UMR 8112), 61 Av. de l'Observatoire, 75014 Paris, France*
[5] *GEPI, Observatoire de Paris, PSL Research University, CNRS, Univ Paris Diderot, Sorbonne Paris Cité, Place Jules Janssen, 92195 Meudon, France*
[6] *IBM Research Division, T.J. Watson Research Center, P.O. Box 218, Yorktown Heights, NY 10598, USA*
[7] *European Southern Observatory, D-85748 Garching bei Munchen, Germany*
[8] *Universite Lyon 1, Observatoire de Lyon, CRAL et ENS, 9 Av Charles Andre, F-69230 Saint-Genis Laval, France*
[9] *Department of Physics, Indian Institute of Science, Bangalore 560012, India*
[10] *Institute for Theoretical Physics, University of Zurich, CH-8057 Zurich, Switzerland*
[11] *Department of Physics and Astronomy, Iowa State University, Ames, IA 50014 USA*

Accepted XXX. Received YYY; in original form ZZZ

ABSTRACT

Galaxy mergers are believed to trigger strong starbursts. This is well assessed by observations in the local Universe. However the efficiency of this mechanism has poorly been tested so far for high redshift, actively star forming, galaxies. We present a suite of pc-resolution hydrodynamical numerical simulations to compare the star formation process along a merging sequence of high and low z galaxies, by varying the gas mass fraction between the two models. We show that, for the same orbit, high-redshift gas-rich mergers are less efficient than low-redshift ones at producing starbursts: the star formation rate excess induced by the merger and its duration are both around 10 times lower than in the low gas fraction case. The mechanisms that account for the star formation triggering at low redshift - the increased compressive turbulence, gas fragmentation, and central gas inflows - are only mildly, if not at all, enhanced for high gas fraction galaxy encounters. Furthermore, we show that the strong stellar feedback from the initially high star formation rate in high redshift galaxies does not prevent an increase of the star formation during the merger. Our results are consistent with the observed increase of the number of major mergers with increasing redshift being faster than the respective increase in the number of starburst galaxies.

Key words: galaxies: high-redshift – galaxies: interactions – galaxies: starburst – ISM: structure – stars: formation – methods: numerical

1 INTRODUCTION

Observations of star forming galaxies show that they follow a tight correlation between their stellar mass ($M_\star$) and their star formation rate (SFR). This relation defines a main sequence (MS) that is observed over a wide redshift range (z = 4 to 0) (Elbaz et al. 2007; Noeske et al. 2007; Peng et al. 2010; Rodighiero et al. 2011; Schreiber et al. 2015).

Outlier galaxies, which display higher specific star formation rate (sSFR) than members of the MS, correspond to the starbursting galaxies. Detailed observations of these galaxies in the local Universe show that, above a certain luminosity threshold ($L_{\rm IR} > 10^{12}$ $L_\odot$, which defines the ultra luminous infrared galaxies, ULIRGs, see e.g. Houck et al. 1985), all galaxies are undergoing a major merger event (Armus et al. 1987; Sanders & Mirabel 1996; Ellison et al. 2013). It should also be noted that if all local starburst galaxies are undergoing an interaction it is not reciprocal, as all observed major mergers do not show a massive enhancement of star formation (at low redshift, see Bergvall et al. 2003, at high redshift, see

★ E-mail: jeremy.fensch@cea.fr

Jogee et al. 2009). This might however be due to a short extent of the starburst phase relative to the interaction timescale.

Observations of star-forming galaxies have shown that the number of star forming galaxies in the starbursting regime above the MS remains fairly constant (between 2% and 4 %) in the redshift range $z = 4$ to $z = 0$, with no or only weak variation with redshift: about twice at most between $z = 0$ and $z = 2$ (Rodighiero et al. 2011; Schreiber et al. 2015). Given that the major merger rate is thought to be an increasing function of redshift (Le Fèvre et al. 2000; Kampczyk et al. 2007; Kartaltepe et al. 2007; Lotz et al. 2011, and references therein), this implies that the efficiency of major mergers in triggering starbursts must decrease with increasing redshift. This hypothesis is backed by observations showing that major mergers are inefficient at driving star formation at $z \simeq 2$ (Kaviraj et al. 2013; Lofthouse et al. 2016) and calls for a detailed study of physical processes at play in galaxy major mergers, and their dependance on redshift.

Observations of local advanced mergers show that most of the star formation is concentrated in the inner regions (Sanders & Mirabel 1996; Duc et al. 1997). These nuclear starbursts are explained by gravitational torques induced by the close interaction between the galaxies (Barnes & Hernquist 1991). However, gravitationally driven gas inflows alone cannot explain observations of extended, off-nuclear increase of interaction-induced star formation (Barnes 2004; Chien & Barnes 2010; Smith et al. 2014). One the most striking case if the well-studied Antennae system, which is observed during the second pericentre passage (Renaud et al. 2008) and where the majority of star formation happens in dense clumps outside of the nuclei and in the overlap region (see e.g. Whitmore & Schweizer 1995). Atomic and molecular gas observations (such as Elmegreen et al. 2016a, for the NGC 2207 – IC 2163 interacting pair), show that their star forming regions have very dense molecular phases, which hints for strong gas compression.

Massive high-redshift ($z > 2$) galaxy disks are characterized by a high gas fraction: $f_{\rm gas} \simeq 50\%$ at $z = 2$ to be compared with $f_{\rm gas} \simeq 10\%$ at $z = 0$ (Daddi et al. 2010; Tacconi et al. 2010). This higher gas fraction makes the disk more prone to gravitational instabilities: the velocity dispersion is higher ($\sigma \simeq 40$ km/s at $z = 2$, Förster Schreiber et al. 2009; Stott et al. 2016; Price et al. 2016, to be compared with $\sigma \simeq 10$ km/s at $z = 0$) and the violent disk instability (VDI) induces strong nuclear inflows (Bournaud et al. 2012) and the formation of giant star forming clumps of 10^7 to 10^9 $M_\odot$(Elmegreen et al. 2007; Elmegreen 2009; Genzel et al. 2008; Magnelli et al. 2012; Guo et al. 2015; Zanella et al. 2015). At this redshift, it is hard to study the evolution of the galaxy morphology during encounters (see e.g. Cibinel et al. 2015), and especially the efficiency of gas fragmentation and nuclear inflows which trigger the starburst at low redshift.

Numerical simulations are particularly well-suited to capture the complex and rapidly evolving dynamics of mergers. It has been shown that the spatial resolution plays an important role in the study of extended star formation (Di Matteo et al. 2008; Teyssier et al. 2010; Bournaud et al. 2011): one should be able to resolve the local Jeans length with several resolution elements to be able to capture the off-nuclei gas condensations that might also form stars. Merger simulations with resolution of a few 10 pc to pc-scale (Teyssier et al. 2010; Powell et al. 2013; Renaud et al. 2014, R14 in the following) yield an extended star-formation, which is explained by an increase of the cold gas turbulence, and especially of its compressive mode, driven by interaction-induced fully compressive tides (Renaud et al. 2008, 2009). This process adds to the torque-driven gas inflows towards the nuclei in the enhancement of the star formation rate (SFR). Fragmentation of the gas is relatively more important than nuclear inflows at the first pericentre passages, when the impact parameter and the relative velocity are large, resulting in weak and short-lived gravitational torques.

Previous simulations of galaxy major mergers with a high gas fraction hint for a weak enhancement of star formation, both in burst amplitude and duration (see e.g. Bournaud et al. 2011; Hopkins et al. 2013; Scudder et al. 2015), or even not at all (Perret et al. 2014). However, they did not compare their sample to low gas fraction major mergers or investigate the physical cause of this mild burst.

In this paper, we present a comparison between low and high redshift major mergers using hydrodynamical simulations. We present two sets of simulations: one with a high gas fraction, and one with a low gas fraction. We study the evolution of the properties of their star formation activity during the interactions. Section 2 presents the numerical simulation parameters. Section 3 describes the resulting evolution of the star formation activity during the interactions, and compare the high and low gas fraction cases. The analysis of the physical processes having a role in the star formation is presented in Section 4. Discussion and conclusions are drawn in Sections 5 and 6.

2 SIMULATIONS

2.1 Numerical technique

We perform the simulations using the adaptative mesh refinement (AMR) code RAMSES (Teyssier 2002). The overall method is analogous of that in Renaud et al. (2015).

The coarsest grid is composed of 64^3 cells in a cubic box of 200 kpc, and we allow up to 10 further levels of refinement. This results in a maximum spatial resolution of 6 pc. A resolution study to discuss this choice is presented in Appendix A. Star and dark matter (DM) particles are also implemented in the initial conditions (see Section 2.2). We call the former old stars, to differentiate them from the new stars, that are formed during the simulation. A grid cell is refined if when there are more than 40 initial condition particles, or if the baryonic mass, including gas, old and new stars, exceeds $8 \times 10^5 M_\odot$. Furthermore, we ensure that the Jeans length is always resolved by at least four cells, by introducing a numerical pressure through a temperature floor set by a polytrope equation of state at high density ($T \propto \rho^2$), which is called Jeans polytrope thereafter, which prevents numerical fragmentation (Truelove et al. 1997). Such a polytrope was also added in numerous previous numerical simulations (Dubois & Teyssier 2008; Renaud et al. 2013; Bournaud et al. 2014; Kraljic et al. 2014; Perret et al. 2014).

The thermodynamical model, including heating and atomic cooling at solar metallicity[1], is the same as described in Renaud et al. (2015).

If the gas reaches a certain density threshold, ρ_0, and if its temperature is no more than 2×10^4 K above the Jeans polytrope temperature at the corresponding density, it is converted into stellar particles following a Schmidt law, $\dot{\rho}_\star = \epsilon(\rho_{\rm gas}/t_{\rm ff})$ (Schmidt 1959; Kennicutt 1998), with ϵ the efficiency per free fall time set to 1%, and $t_{\rm ff} = \sqrt{3\pi/(32G\rho)}$ the free-fall time. The density thresholds ($\rho_0 = 30$ cm^{-3} and $\rho_0 = 1$e5 cm^{-3} for low and high gas

[1] We use the same metallicity for both high and low redshift galaxy models as an approximation to investigate the effects imputable to the variation of gas fraction only. Massive high redshift galaxies can have a metallicity up to half-solar (see e.g. Erb et al. 2006).

Table 1. Characteristics of the galaxies used in the simulations.

Galaxy	low gas fraction	high gas fraction
Total baryonic mass [$\times 10^9 M_\odot$]	57.2	
Gas Disc (exponential profile)		
mass [$\times 10^9 M_\odot$]	5.0	34.3
characteristic radius [kpc]	8.0	
truncation radius [kpc]	14.0	
characteristic height [kpc]	0.3	
truncation height [kpc]	0.8	
Stellar Disk (exponential profile)		
number of particles	500 000	173 900
mass [$\times 10^9 M_\odot$]	45.0	15.7
characteristic radius [kpc]	5.0	
truncation radius [kpc]	12.0	
characteristic height [kpc]	0.34	
truncation height [kpc]	1.02	
Bulge (Hernquist profile)		
number of particles	80 000	
mass [$\times 10^9 M_\odot$]	7.2	
characteristic radius [kpc]	1.3	
truncation radius [kpc]	3.0	
Dark Matter Halo (Burkert profile)		
number of particles	500 000	
mass [$\times 10^9 M_\odot$]	131.0	
characteristic radius [kpc]	25.0	
truncation radius [kpc]	45.0	

fraction cases) are chosen to correspond to the isolated disks being on the disk sequence of the Schmidt-Kennicutt diagram (Daddi et al. 2010; Genzel et al. 2010), that is a star formation rate (SFR) of $\simeq 1$ $M_\odot$/yr (resp. $\simeq 60$ $M_\odot$/yr) in the low gas fraction case (resp. high gas fraction case) for each galaxy before the interaction. The difference in the normalization of ρ_0 originates from the different gas mean density between the two cases[2].

Because of the spatial resolution and the computational cost it would imply, we do not resolve individual star formation. We chose a high enough sampling mass for the new stars, i.e higher than 1000 $M_\odot$, so that we do not need to resolve the initial mass function.

In these simulations we model three types of stellar feedback :

(i) Photo-ionisation from HII regions (as in Renaud et al. 2013): UV photons from the OB-type stars ionize the surrounding gas. To model this process we evaluate the radius of the Strömgren (1939) sphere around the newly formed stellar particle and heat up the gas to $T_{\rm HII} = 2 \times 10^4$ K.

(ii) Radiation pressure (as in Renaud et al. 2013): inside each HII region the scattering of photons on the gas acts as a radiative pressure. To model this process we inject a radial velocity kick for each cell inside the Stromgren sphere.

(iii) type-II supernova thermal blasts (as in Dubois & Teyssier 2008 and Teyssier et al. 2013): stars more massive than 4 $M_\odot$ eventually explode as type II supernovae (Povich 2012). We assume

[2] A density threshold closer to resolved highest density will make the SFR more sensitive to small variations in the shape the density distribution. This is the case for our gas-rich case (see Section 3.2), and it strengthens our results (see Section 3.3.1).

Table 2. Initial conditions of the orbits

	Galaxy 1	Galaxy 2
Orbit #1		
Centre [kpc]	(10.55, -30.34, 46.68)	(-15.01, 30.44, -46.34)
Velocity [km/s]	(-26.95, 23.23, -71.76)	(26.02, -23.28, 71.35)
Orbit #2		
Centre [kpc]	(8.64, -25.78, 39.71)	(-13.10, 25.89, -39.36)
Velocity [km/s]	(-22.98, 19.74, -61.03)	(22.05, -19.80, 60.61)
Orbit #3		
Centre [kpc]	(6.21, -20.01, 30.87)	(-10.67, 20.11, -30.52)
Velocity [km/s]	(-17.94, 15.32, -47.43)	(17.01, -15.37, 47.02)

Table 3. Orientations of the spin axis.

Spin	Galaxy 1	Galaxy 2
dd	(-0.67, -0.71, 0.20)	(0.65, 0.65, -0.40)
rr	(0.67, 0.71, -0.20)	(-0.65, -0.65, 0.40)
spin1	(-0.67, 0.71, -0.20)	(-0.65, 0.65, 0.40)
spin2	(0.67, -0.71, 0.20)	(-0.65, -0.65, 0.40)
spin3	(0.67, 0.71, 0.20)	(0.65, -0.65, 0.40)
spin4	(-0.67, 0.71, -0.20)	(-0.65, -0.65, -0.40)

that 20% of the initial mass of our stellar particle is in massive stars, and will be released 10 Myr after the formation of the stellar particle. On top of the mass loss, we inject thermally a certain amount of energy in the cell: $E_{\rm SN} = 10^{51}$ ergs / 10 $M_\odot$.

This implementation of stellar feedback is therefore physically motivated, although sub-grid. It has been used in numerical simulations of high gas fraction disk galaxies similar to ours, and was shown to have realistic effects on the galaxies, such as producing large scale outflows with a mass-loading factor close to unity (Roos et al. 2015, and see Section 3.3 and Fig. 5 in Bournaud 2016), which is consistent with observations (see e.g. Newman et al. 2012).

2.2 Modeling low and high-redshift galactic disks

We run a suite of massive galaxy merger simulations for gas-rich ($f_{\rm gas}$ = 60%) and gas-poor disks ($f_{\rm gas}$ = 10%). These gas fractions are typical of $z = 2$ and $z = 0$ disk galaxies. We chose to modify solely the gas fraction in order to isolate the effect of this parameter, and neglect the other differences between the low and high redshift, such as galaxy size, mass and interaction parameters. These parameters are discussed in Section 5.2.3. Furthermore, it must be noted that we do not change the stellar mass of the bulge, so that the velocity profile and the galactic shear stay the same, and so that the low and high gas fraction orbits are as similar as possible.

The DM halo for each galaxy is composed of 2.62×10^5 $M_\odot$ particles, following a Burkert (1995) profile. An old stellar component is added, made of 9×10^4 $M_\odot$ particles modeling a stellar disk and a stellar bulge. The characteristics of the galaxies are summed up in Table 1. The DM, old stars and the stellar particles formed during the simulation are evolved through a particle-mesh solver, with a gravitational softening of 50 pc for the DM and old stars and at the resolution of the local resolution for the new stars.

2.3 Characteristics of the orbits

Our simulation sample comprises three orbits.Their parameters are summarised in Tables 2 and 3. The full simulation suite is sum-

Table 4. Summary of the simulations. The prefix 'gp' stands for gas-poor. dd and rr stand for direct-direct and retrograde-retrograde, and are followed by the number of the corresponding orbit.

Name	Orbit	Spins	Gas fraction	Maximum resolution [pc]
iso	-	-	60%	6
gp-iso	-	-	10 %	6
dd1	1	dd	60%	6
rr1	1	rr	60%	6
gp-dd1	1	dd	10%	6
gp-rr1	1	rr	10%	6
dd2	2	dd	60%	12
rr2	2	rr	60%	12
spin1	2	spin1	60%	12
spin2	2	sfpin2	60%	12
spin3	2	spin3	60%	12
spin4	2	spin4	60%	12
dd3	3	dd	60%	12
rr3	3	rr	60%	12

marised in Table 4 . Low and high gas fraction mergers are run on the same reference orbit #1 for comparison. This orbit is close to that of the Antennae system, which was shown by R14 to be favorable to a strong starburst for low gas fraction disks. Orbits #2 and #3 have lower orbital energy, obtained by reducing the impact parameter and relative velocity by 15% and 30%. This ensures that the results do not depend on an unforeseen particularity of the orbit. The initial orbital conditions are summarised in Table 2.

As the orientation of the galaxies plays a significant role in the processes at play (see review by Duc & Renaud 2013), we use a set of different spin vectors for each orbit (see Table 3). For each orbit we run one direct-direct, Antennae-like interaction and one retrograde-retrograde encounter. The latter is obtained by merely taking the opposite of the spin orientation of both galaxies. To ensure that the different spin-orbit couplings do not affect our conclusions, we also run 4 other simulations with a different spin orientation on orbit #2.

We run orbit #1 simulations at 6 pc resolution and the orbits #2 and #3 at 12 pc resolution, using the same refinement strategy as for the 6 pc case, stopped one level lower, and ρ_0 =1e4 cm^{-3} as star-formation threshold, which is lower than for the 6 pc resolution as the mean density is also lower (see Section 2.1).

3 RESULTS

3.1 Galaxy morphologies

Fig. 1 shows a gas density map of the isolated run of both modelled disk galaxies. We see that while the low gas fraction disk shows several gaseous spiral arms, the high gas fraction disk is fragmented in several dense regions. These gaseous regions are observed to be long-lived[3]. They undergo merging and migration towards the centre with characteristic time of several 100 Myr. We will call them clumps thereafter.

In Fig. 2 we show the gas density map of the merger in the low and high gas fraction case for the orbit #1 (dd1 and gp-dd1), at different times of the interaction: a few 10 Myr before and after both the first pericentre passage and the coalescence. We see that the gas in the low gas fraction case shows the formation of a few clumps in the tidal bridge after the first pericentre passage. On the bottom row, the evolution of the gas density of the high gas fraction case does not show any significant increase of the number of clumps before and after the first pericentre passage.

To have a more quantitative insight into the interaction-driven clumpiness of the disk, we use the friend-of-friend algorithm HOP (Eisenstein & Hut 1998) to determine the number of clumps and the gas mass fraction embedded in them, during the interaction. Clumps are detected around peaks of gas density above 40 cm^{-3}. Sub-clumps are merged if the saddle density between them exceeds 4 cm^{-3} and an outer boundary of 2 cm^{-3} is set to define the density limit of the clumps. These parameters agree with a visual examination of the density maps and the results are not affected with respect to small changes of these parameters.

In Fig. 3 we show the evolution of the number of clumps, and the gas fraction inside them. In the low gas fraction case the gas fraction enclosed in clumps goes from 5 to 25% at the first pericentre passage, and the number of clumps increases by a factor 4, from about 4 to 16. These numbers stay relatively constant along the interaction. This enhanced number of clumps in low redshift galaxy collisions has been already noted by Di Matteo et al. (2008). In the high gas fraction case, the gas mass fraction in clumps shows instead a slow but steady decrease of both the number of clumps and gas mass fraction enclosed. The evolution of the number of clumps and masses of the high gas fraction case are therefore not influenced by the interaction as we can see by comparing the isolated (iso) and the interacting cases (dd1). In particular, no change is observed at the first pericentre passage.

3.2 Evolution of the density PDF

In the low gas fraction, this interaction-induced clumpiness condensates the gas in localized over densities. To quantify its effect on the gas density distribution, we look at the evolution of the mass-weighted density probability density function (PDF). In Fig. 4, we see the evolution of the shape of the gas PDF for both the low and high gas fraction cases. In the low gas fraction case, the PDF extends to higher densities during the interaction. We also see that the PDF of the high-gas fraction case remains almost identical during the interaction and does not significantly vary from the shape of the isolated galaxy PDF, except at the coalescence (t = 376 Myr) where there is an increase of the mass with densities above 3 $\times$10^4 cm^{-3}.

The evolution of the shape of the PDF is of particular interest, as high density gas fuels star formation. Indeed, in the low gas fraction case, the gas mass above the density threshold goes from 4% to 20% after the first pericentre passage and 40% at the coalescence, while it stays constant, at 2-3%, in the high-gas fraction case.

3.3 Merger-induced star formation

3.3.1 Star formation histories

The comparison between low and high gas fraction star formation histories during the interaction is shown in Fig. 5. In the low gas fraction case, the SFR is about 1-2 M$_\odot$/yr before the interaction and increases to $\sim$ 30 M$_\odot$/yr and more than 50 M$_\odot$/yr after the first pericentre passage. The SFR then lowers back to a few M$_\odot$/yr before increasing again to $\sim$ 40 to 60 M$_\odot$/yr during the final coalescence.

The high gas fraction case shows a very different history. The SFR is initially relatively high, $\simeq$ 120 M$_\odot$/yr for the galaxy pair, and does not increase significantly at the first pericentre passage. The

[3] See movie at https://www.youtube.com/watch?v=ByV1g24eEjk

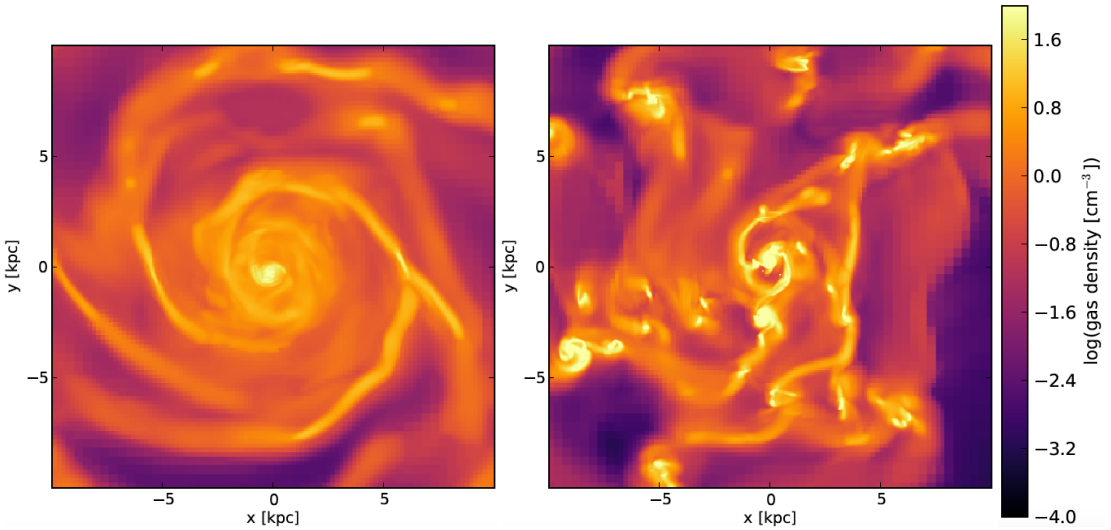

Figure 1. Face-on mass-weighted mean gas density maps of the isolated runs: gp-iso is shown on the left panel and iso on the right panel. Both maps are obtained after an evolution during the time corresponding to the first pericentre for the orbit #1 (490 Myr after the start of the simulation).

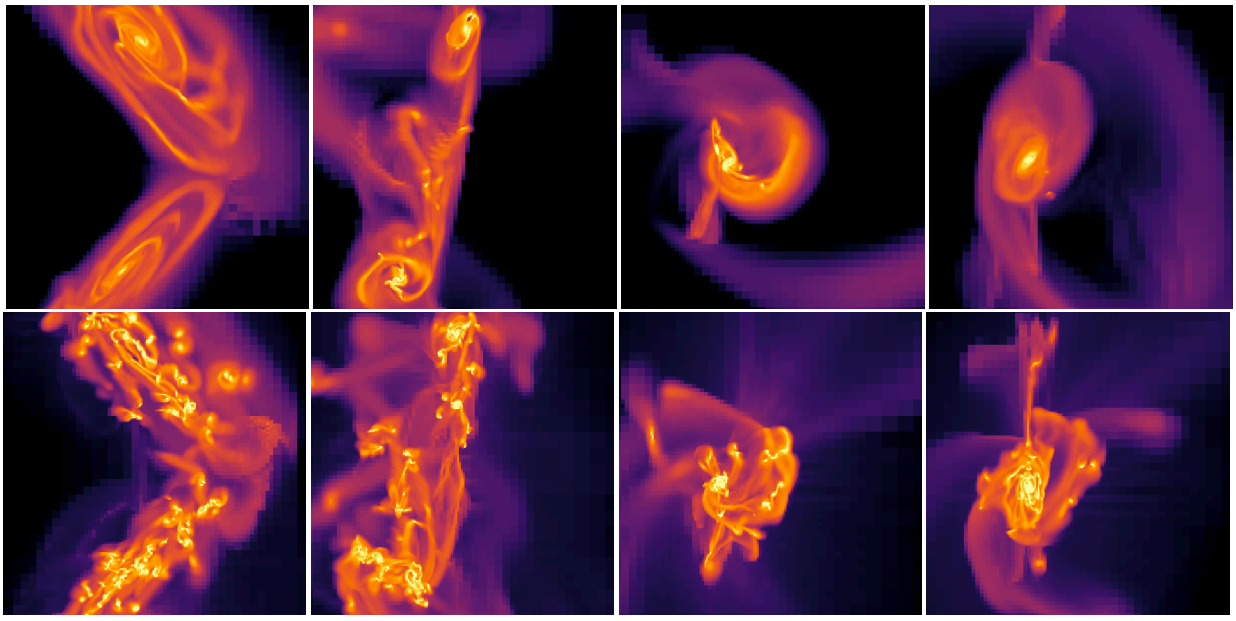

Figure 2. Mass-weighted mean gas density map of the gas poor (top panel) and gas-rich (bottom panel) simulations for the direct-direct interaction orbit #1 at different times from the first pericentre : -60, 105, 370 and 560 Myr from left to right. The maps span an area of 30 kpc × 30 kpc. The colour scale is the same as in Fig. 1.

SFR is only enhanced at the coalescence[4], and only by a factor at most 5. Increasing only the gas fraction thus appears to significantly lower the boost of SFR.

To ensure that this results does not depend on a particularity of the chosen orbit or orientation we also look at the SFR of the two other tested orbits and orientations, which are displayed in Fig 6. We see that they follow the behavior of orbit #1: they all show almost no increase of star formation at the first pericentre passage, and a mild burst at coalescence.

3.3.2 *The starburst sequence*

Our motivation to run these simulations resides in the fact that a smaller than expected number of high-redshift galaxies are found on the starburst sequence of both the $M_\star$–SFR and $\Sigma_{\rm gas}$–$\Sigma_{\rm SFR}$ diagrams, the latter being also known as the Schmidt-Kennicutt diagram.

In Fig. 7 we can see the evolution of our simulated galaxies on the Schmidt-Kennicutt diagram. The computation is done in a box of 60 kpc× 60 kpc × 60 kpc and we rescale the curves

[4] In both gas fraction cases, the retrograde-retrograde simulation coalescence happens later than in the direct-direct simulation. This is expected, because they do not form tidal tails, which are efficient in driving angular momentum out.

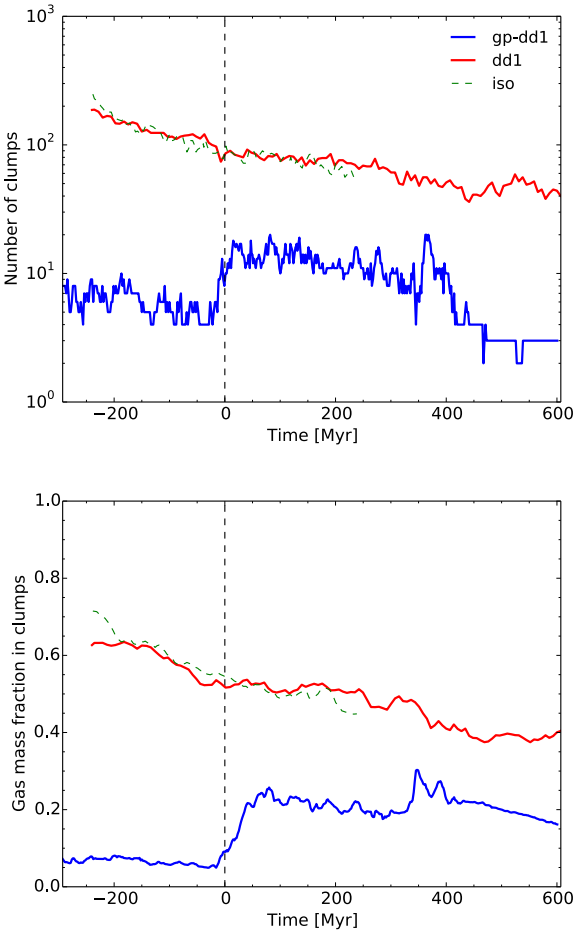

Figure 3. *Top*: Number of detected clumps for the low (blue) and high (red) gas fraction for dd1 and gp-dd1. The isolated run for the high gas fraction case is also shown in dashed green. To ease the comparison, this number is multiplied by 2 for the isolated case. *Bottom*: Gas mass fraction in gas clumps.

so that the pre-merger disks lie on the disk sequence. To better quantify the starbursting behavior of our simulations we define the starburstiness parameter as the measured Σ_{SFR} over the value of Σ_{SFR} corresponding the the disk sequence of Genzel et al. (2010) for the measured Σ_{gas}. We define as starbursting a galaxy with a starburstiness exceeding ,4 meaning that the galaxy stands more than 0.6 dex above the disk sequence, which is a common definition for the starburst sequence (see e.g. Schreiber et al. 2015).

We see that the galaxies follow the disk sequence until the collision which shifts their loci towards the starburst sequence. The low gas fraction systems reach the starburst sequence already at the first pericentre passage and their starburstiness stays above 4 all along the starburst, that is for more than 700 Myr for the considered orbit. The high gas fraction pairs hardly reach the starburst sequence: the gas-rich direct-direct starburstiness always stays below 4 and is thus never considered as a starburst galaxy. The burst at the coalescence of the gas-rich retrograde-retrograde encounter makes it reach the starburst sequence of the Schmidt-Kennicutt diagram, but only for $\sim$ 100 Myr.

In the following we analyse the processes that influence the ability of high fraction gas merger to trigger starbursts, as compared to low gas fraction ones.

4 WHAT CAUSES THIS WEAK ENHANCEMENT OF STAR FORMATION?

4.1 Weak increase of the central gas inflows

Observed starbursting galaxies show a prominent nuclear starburst (Sanders & Mirabel 1996), with an important concentration of gas in the central kpc of the galaxies. Fig. 8 shows the fraction of SFR located in the central kpc of the galaxies. We see that at the coalescence, the peak of star formation is almost entirely located in this central kpc[5].

This centrally concentrated star formation is fueled by gas inflows towards the center. Interaction-driven gravitational torques are indeed expected to drive large amount of gas towards the nuclei of both galaxies (Barnes & Hernquist 1991; Mihos & Hernquist 1996). In Fig 9 we show the inflows of baryonic mass in the central kpc of our galaxies. For the low gas fraction case, pre-merger disks have central mass inflows of $\simeq$ 2-3 $M_\odot$/yr. Between the first and second pericentre the disks are perturbed and the inflows have a higher mean value of about 20 $M_\odot$/yr, with some important variation over time. At coalescence, the inflows reach a peak at 20 $M_\odot$/yr for the dd1 and 50 $M_\odot$/yr for the rr1 simulation, which are both at least ten times higher than the initial gas inflows in the isolated case.

For the high gas fraction case, the central inflows are stronger from the beginning, $\simeq$ 30 to 50 $M_\odot$/yr. As in the low gas fraction case, a strong peak in inflows is seen for the rr1 simulation, at 250 $M_\odot$/yr. The relative increase compared to the pre-merger case is less than 5, much less than for the low gas fraction case. The resulting increase in SFR is also comparatively less important than for the low gas fraction case.

Central gas inflows are already strong in the pre-merger high gas fraction disk because of the violent disc instability (VDI): the high turbulence of the gas is in part fueled by inwards the migration of gas (Dekel et al. 2009b). Another physical explanation for the higher increase of the central inflows in low gas fraction discs is the presence of a more massive stellar component which creates a tidally-induced bar or spiral arms which exert strong torques on the gas, and which adds to the effect of the gravitational torques originating from the companion. The stellar component being less populated in the high gas fraction case, this process is less efficient, as already noted by Hopkins et al. (2009).

The high gas fraction, which leads to a high turbulence and the formation of clumps, also drives strong gas inflows in the isolated disks. As a result, interaction-induced gas inflows are less important with respect to pre-merger inflows for high gas fraction disks than for low gas fraction disks. This leads to a lower increase of SFR due to central gas inflows.

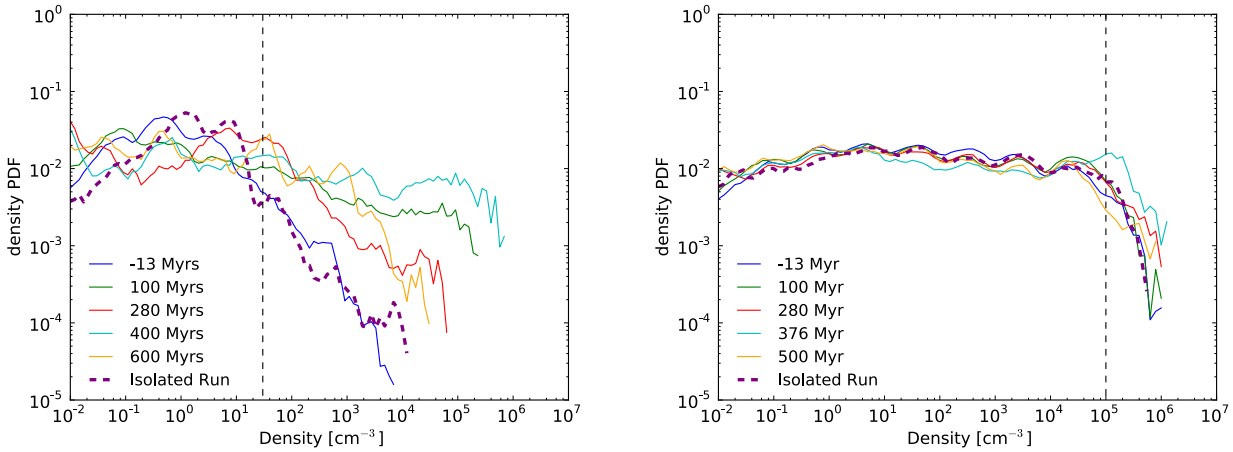

Figure 4. Normalized mass-weighted probability distribution function of the gas density, at several epochs (t = 0 corresponds to the first pericentre). These times correspond to before the first pericentre, shortly after the first pericentre, before the coalescence, peak of SFR during coalescence, long after the coalescence, respectively. Curves are shown for the direct-direct encounter on orbit#1 for the low (left) and high (right) gas fraction cases in solid lines. The thick purple lines show the corresponding isolated cases. The black dashed line indicates the density threshold for star formation as defined in Section 2.1.

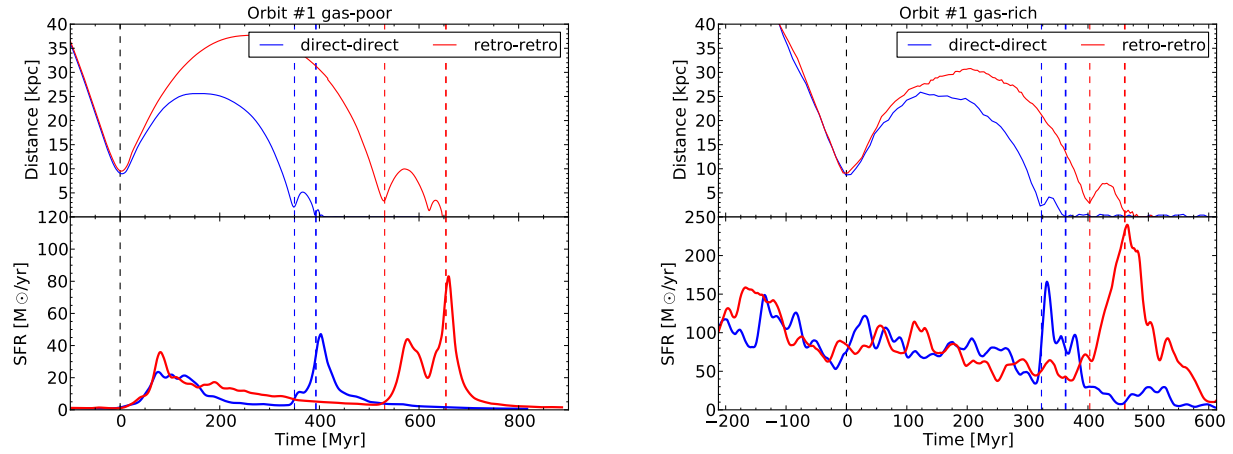

Figure 5. Star formation rate during the simulations run on orbit #1, with the distance between the galaxies plotted above. The direct-direct and retro-retro simulations are shown respectively in blue and red. The low gas fraction case is shown on the left panel and the high-gas fraction case on the right panel. The dashed lines correspond to the time of the first pericentre passage (in black) and the respective times of second pericentre passage and coalescence (in the colour corresponding to the simulation).

4.2 Mild enhancement of gas turbulence

Our current understanding of extended starburst in low gas fraction galaxy interactions is that the increase of the SFR is caused by an increase of gas turbulence.

We compute the 1-dimensional velocity dispersion of the gas, along the line of sight of the simulations at the scale of 100 pc and plot its evolution in Fig. 10. We see that the pre-interaction velocity dispersion is much higher in the high gas fraction case, $\sigma \simeq 35$ km/s, than in the low gas fraction case, $\sigma \simeq 10$ km/s. This agrees with observations (Förster Schreiber et al. 2009) and is due to the gas phase which is more gravitationally unstable with high gas fraction. The interaction brings the velocity dispersion of the low gas fraction case to more than 40 km/s, in agreement with both observations (Elmegreen et al. 1995, 2016a) and previous simulations (Bournaud et al. 2008, R14). In the high gas fraction case the velocity dispersion goes up to around 60 km/s only. The relative increase in turbulence is much higher in the low gas fraction case, a factor 5, to be compared to the high gas fraction case, which shows an increase of less than a factor 2.

If we suppose, for convenience, that the gravitational specific energy is equally transferred between the gas, stars and dark matter during the interaction, we can write, for a timescale much shorter than that of the dissipation of the turbulence at the scale of clumps (i.e $\ll$ 10Myr):

$$\frac{3}{2}M_{\rm gas}\sigma_f^2 = \frac{3}{2}M_{\rm gas}\sigma_i^2 + M_{\rm gas}\, f\Delta\phi \qquad (1)$$

[5] with the exception of dd1 simulation: in Fig. 2 one can actually see in the bottom-right corner that this particular simulation forms an irregular fragmented structure, surrounded by dense, star-forming gas clumps more than 1 kpc away from the center, which explains why star formation is not confined in the central kpc only.

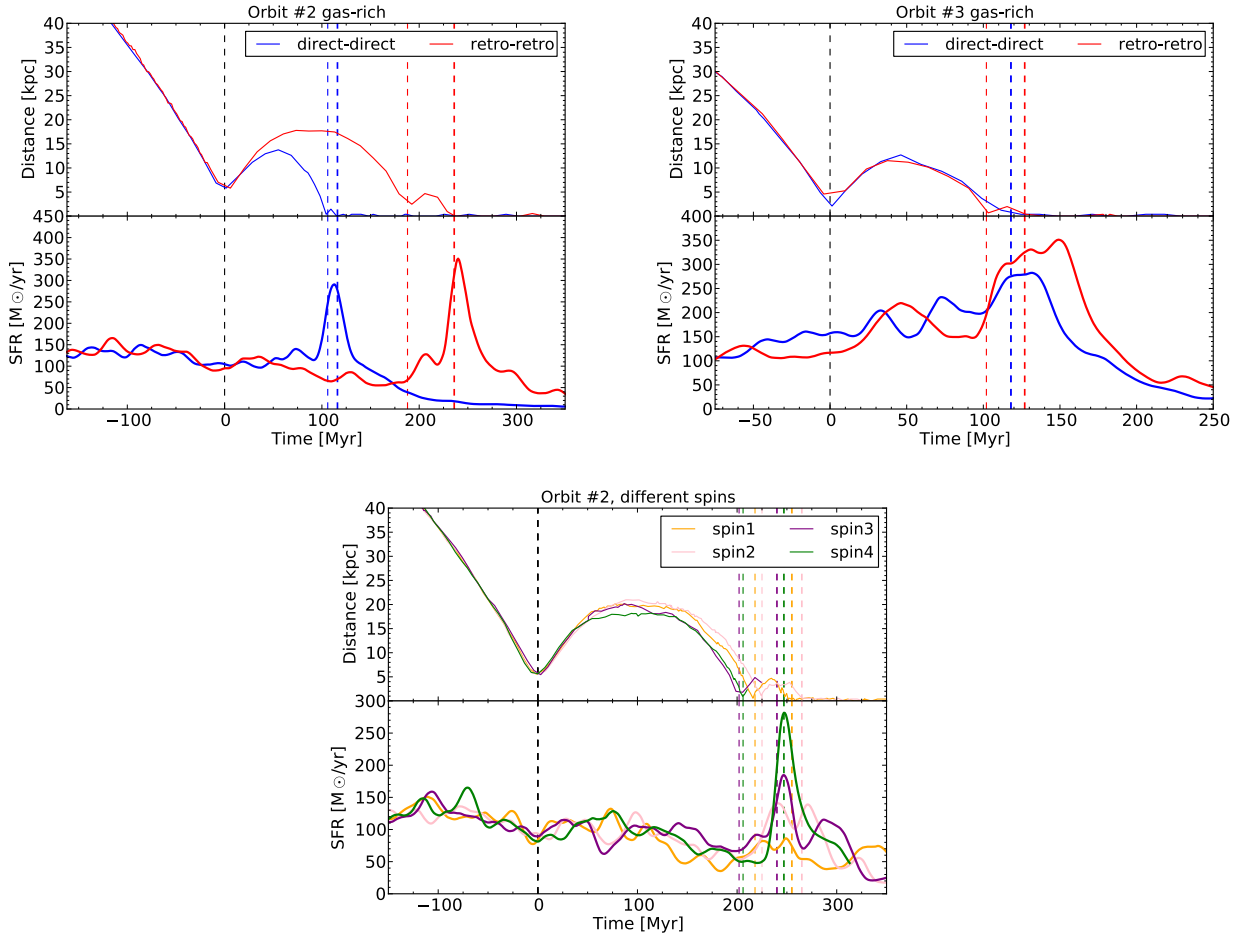

Figure 6. Same as Fig. 5 but for the orbit #2 and orbit #3 (top panels). The bottom panel show the star formation rate for different spin orientations. The vertical dashed lines are the same as in Fig. 5.

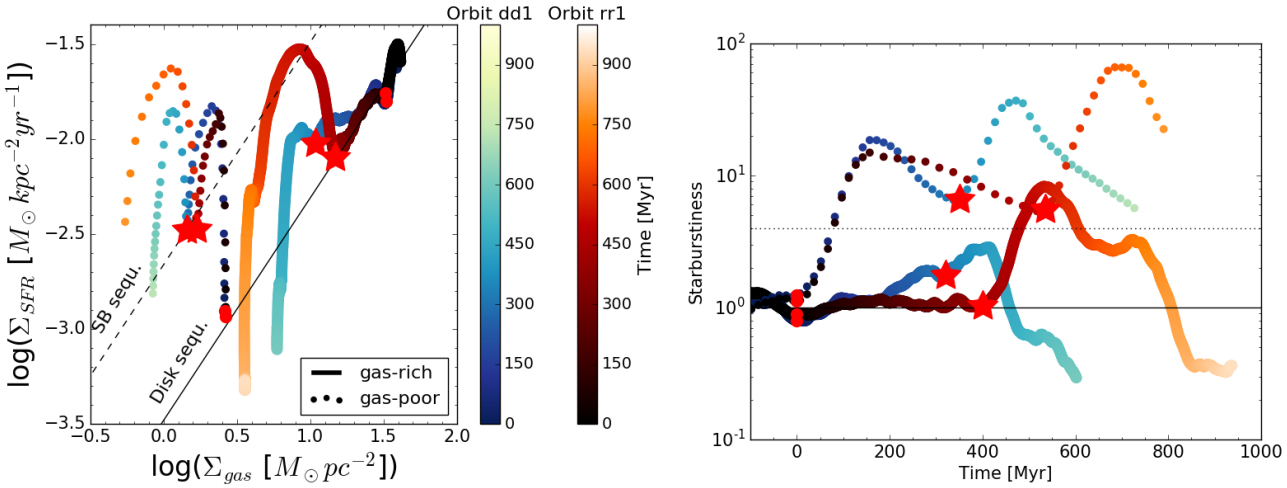

Figure 7. *Top panel:* Evolution of the simulations dd1 (shades of blue) and rr1 (shades of red) on the Schmidt-Kennicutt diagram. The solid lines show the high gas fraction cases, and the dotted lines the low gas fraction cases. The red dots and stars show respectively the time of the first and second pericentre. The solid and dashed black lines are respectively the disk and starburst sequences from Genzel et al. (2010). The curve is smoothed using a constant kernel on the previous 100 Myr, to resemble the smoothing of the measurements of the SFR using IR luminosity (Kennicutt 1998). *Bottom panel:* Evolution of the starburstiness, as defined in the text, during the interaction. The colours and labels are the same as in the upper panel. The black solid line indicates a starburstiness of unity, i.e a SFR equivalent to the disk sequence for a given , $\Sigma_{\rm gas}$, and the dotted line shows a starburstiness of 4, which we define as the lower limit to be considered as a starburst galaxy.

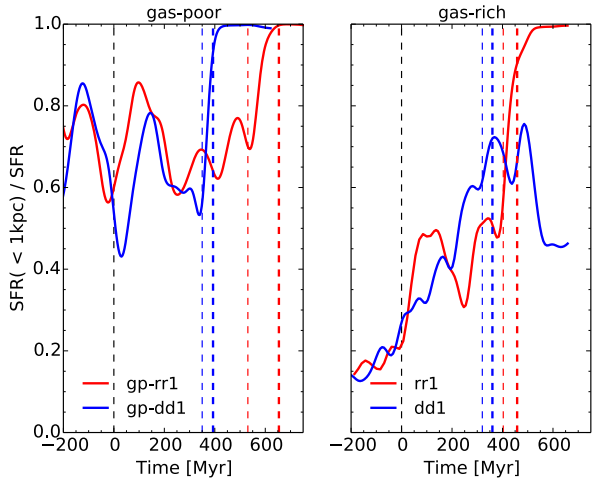

Figure 8. Evolution of the fraction of SFR located inside the central kpc of both galaxies for the encounters on orbit #1 in the low gas fraction case (left) and high gas fraction cases (right). The vertical dashed lines are the sane as in Fig. 5.

where σ_i and σ_f are the initial and final 1-dimensional velocity dispersions, $\Delta\phi$ is the difference in gravitational potential, and f the fraction of this potential energy which is transferred to the turbulent motion during the interaction, and which we suppose to be a constant. After the above assumptions, $M_{\rm gas}$ disappears on both sides of the equation, which therefore applies for both gas fraction regimes. It follows that, for the same $f\Delta\phi$:

$$\sigma_f = \sqrt{\sigma_i^2 + \frac{2}{3} f\Delta\phi} \qquad (2)$$

for both the low and high gas fraction case. Hence, if $f\Delta\phi$ brings σ from 10 km/s to 40 km/s in the low gas fraction case, it will increase σ from 40 km/s to $\simeq$ 55 km/s in the high gas fraction case, which is approximately what we measure in our simulations. It is interesting to note that the required value of $f\Delta\phi$ to increase σ from 10 to 40 km/s in our calculation happens to be less than the specific gravitational energy liberated in 10 Myr (time-scale for dissipation of turbulence) for the masses considered here, when the distance between the two galaxies is smaller than 25 kpc, i.e $\sim$ 50 Myr before the first pericentre for orbit #1/. This is the correct order of magnitude for the onset of the rise of the velocity dispersion in our simulations (see Fig. 10).

This heuristic calculation shows the difficulty of increasing the velocity dispersion while it is already high, which leads to a mild increase in gas turbulence from interactions in high gas fraction disks.

4.3 Absence of interation-induced tidal compression

The increase in compressive turbulence is thought to be driven by the onset of fully compressive tides (see R14). On top of triggering compressive turbulence, fully compressive tides also reduce the Jeans mass and help gas fragmentation in star-forming clumps (Jog 2013, 2014). Extended regions undergoing fully compressive tides are a common feature of galaxy encounters (Renaud et al. 2008, 2009).

To measure the impact of compressive tides on our galaxies we compute the tidal tensor defined by its components $T_{ij} = -\partial_i\partial_j\phi$ using first order finite differences of the total gravitational force at the scale of 50 pc. The tidal field is compressive if the maximum eigenvalue of the tensor is negative. The method is the same as R14. Results for the low and high gas fraction runs on the Orbit #1 are shown on Fig. 11.

We see that, in the low gas fraction case, the gas mass fraction in compressive tides increases from 7% to 20% during the pericentre passages. These values are similar than those obtained in previous simulations of galaxy interactions (using N-body : Renaud et al. 2008, 2009, using AMR: R14).

In the high gas fraction case, the mass gas fraction in compressive tides is initially higher and tend to slowly and monotically decrease with time, with no significant changes induced by the pericentre passages.

This high but steady gas mass fraction in compressive tides results from the matter distribution of the galaxy. In Fig. 12 we show the position of tidally compressive regions $\simeq$ 60 Myr after the first pericentre passage. In the low gas fraction case, we see that tidally compressive regions develop over extended regions: close to the galaxy nuclei, in the forming tidal tails and in the bridges between the two galaxies. In the high gas fraction case, the tidally compressive regions are mainly located inside the clumps. The gravitational potential is locally dominated by the highly concentrated clumps (see Section 3.1), leaving the inter-clump medium in tidally extensive zones which makes the formation of any zone of compressive tides harder, and limits any increase in gas fragmentation during the interaction.

This adds to the small enhancement of the turbulence, described in Section 4.2, which limits an increase in compressive turbulence, and thus a change in the density PDF and in the interaction-induced SFR.

In summary, our numerical simulations show that the clumpy nature driven by the high gas fraction has a strong influence on the central inflows, the gas turbulence and the compressive tides. These three physical processes are seen to be enhanced during low-redshift encounters and are thought to be responsible for the interaction-driven starburst in low redshift galaxies. In the high gas fraction cases, these three processes are already strong in isolated galaxies and are not further enhanced by interactions.

Our simulations hereby confirm the importance of these three processes in the increase of the SFR in gas-poor interactions and we claim that their weak enhancement for high gas fraction disks explains the relative diminished efficiency of gas-rich major mergers to trigger starbursts.

4.4 No effect of saturation from feedback

The SFR of the high gas fraction disks in isolation is $\simeq$ 60 times higher than for the low gas fraction disks, the net feedback energy from supernovae explosions and HII regions is therefore also much higher. One can wonder whether an increase of star formation is not self-regulated in high gas fraction disks because of the stellar feedback.

To test this hypothesis we restart the dd1 simulations, but with all sources of feedback, which were presented in Section 2.1, turned off. One should note that an absence of feedback for a long period of time would transform significantly the structure of the galaxies, as stellar feedback regulates the growth of gas clumps (Bournaud et al. 2010; Hopkins et al. 2011; Goldbaum et al. 2016). Shutting off feedback just before the investigated event, i.e the galactic encounters,

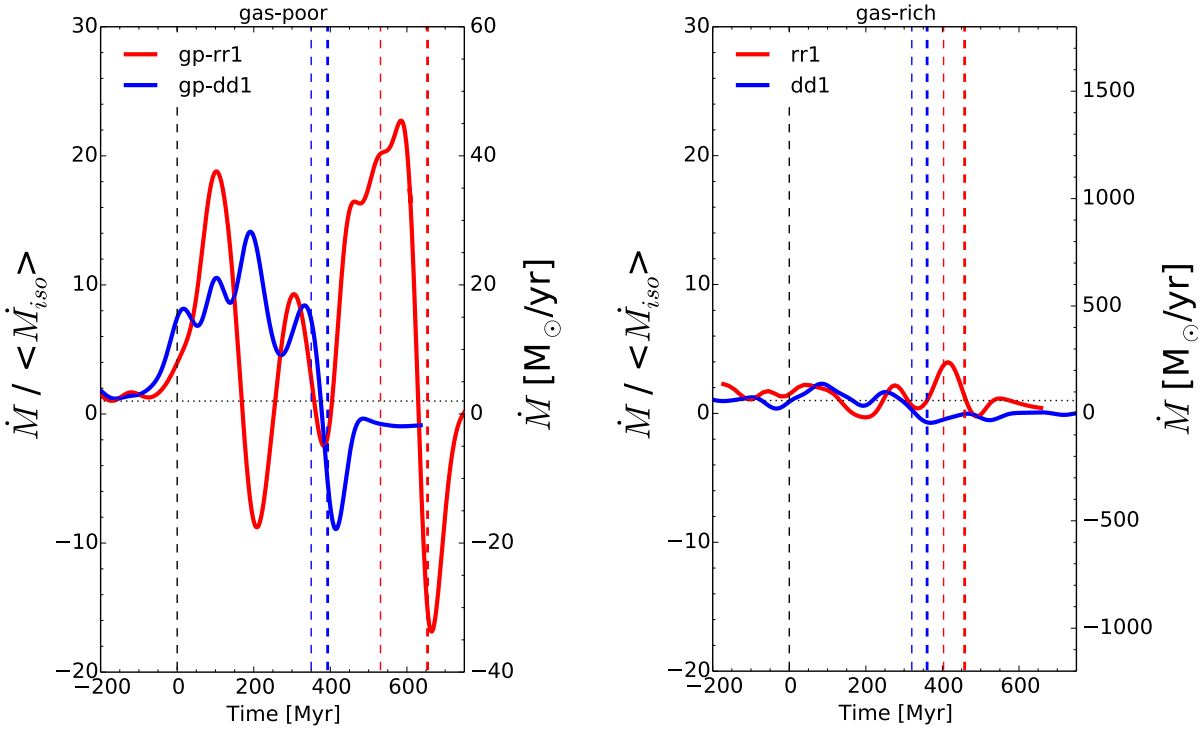

Figure 9. Evolution of the inflow of baryonic mass fraction in the central kpc of both galaxies for the encounters on orbit #1 in the low gas fraction case (left) and high gas fraction case (right). The left axis shows the ratio of the inflow to the mean inflow rate of the isolated run, and the same scale is used for both plots to emphasize the relative difference to the isolated case. The right axis shows the actual value of the inflow rate. The curves are smoothed using a gaussian kernel of root mean square width 30 Myr for the sake of clarity. The vertical dashed lines are the same as in Fig. 5.

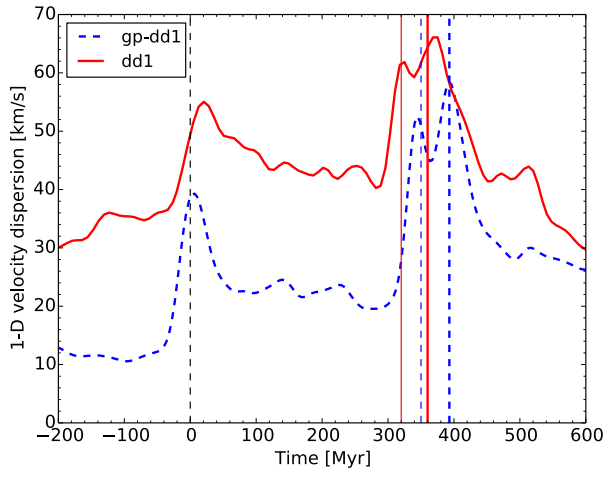

Figure 10. Evolution of the gas velocity dispersion of the direct-direct simulations on orbit #1. The low gas fraction is depicted by the blue dashed curve and the high gas fraction by the solid red line. The vertical dashed lines are the same as in Fig. 5.

ensures that we compare galaxies with the most similar structure as possible. Therefore, we shut off the feedback around 40 Myr only before the two moments when a rise of SFR is expected, namely the first pericentre passage and the coalescence. The time scale of dissipation of the turbulence being around 10 Myr (Mac Low 1999) at the clumps scale, which is comparable to the free-fall time, we ensure that there is no more influence of the feedback on the gas turbulence at the expected starburst time.

The evolution of the SFR for the feedback case and no-feedback case is plotted in Fig. 13. We see that there is a small increase in SFR, especially at coalescence, in the simulations without feedback, but the general behavior does not change: even without stellar feedback the interaction only induces a small starburst compared to the low gas fraction case. This weak influence of feedback on high gas fraction major mergers has already been seen in Bournaud et al. (2011) and Powell et al. (2013).

Our simulations show that our feedback implementation, which allows a burst of star formation for low gas fraction major mergers, is not responsible for the weakness of the star formation enhancement in the high gas fraction case. The implementation of sub-grid models of stellar feedback in numerical simulations is a long standing issue. Energy outputs from SNe and stellar winds are theoretically rather well understood for most stellar populations (see review by Dale 2015), but the details in the numerical implementations are important and can lead to significantly different results (see e.g. Hopkins et al. 2012; Agertz et al. 2013). A detailed study of the impact of the implementation of feedback on galaxy structure is beyond the scope of this paper.

On the one hand, our no-feedback simulations show that a weaker feedback than ours would not produce a strong enhancement of star formation either. On the other hand, a stronger feed-

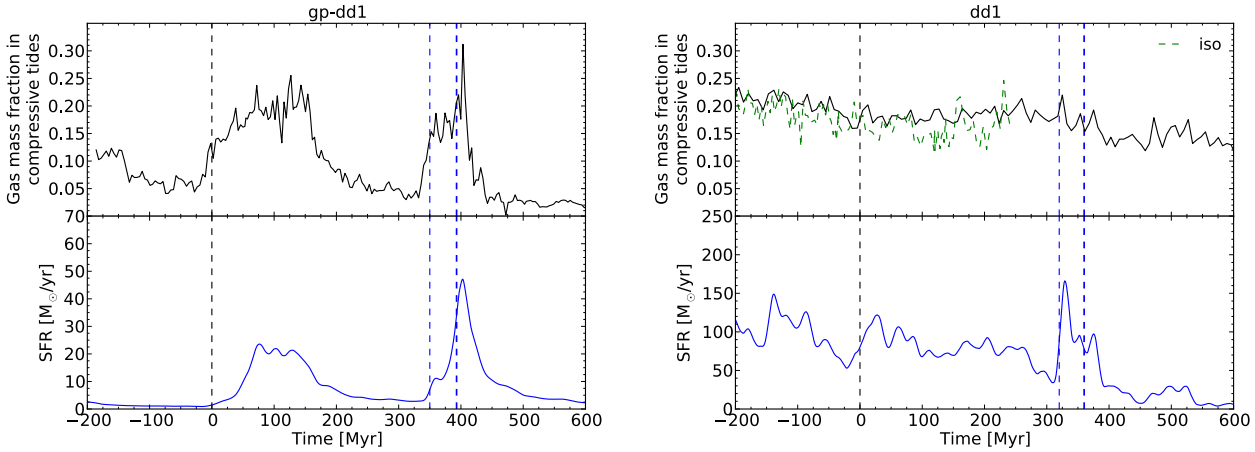

Figure 11. Evolution of the gas mass fraction in a fully compressive tidal field (top panel) compared to the star formation rate (bottom panel) for the direct-direct encounter on orbit #1 in the low gas fraction case (left) and high gas fraction case (right). The vertical dashed lines are the same as in Fig. 5.

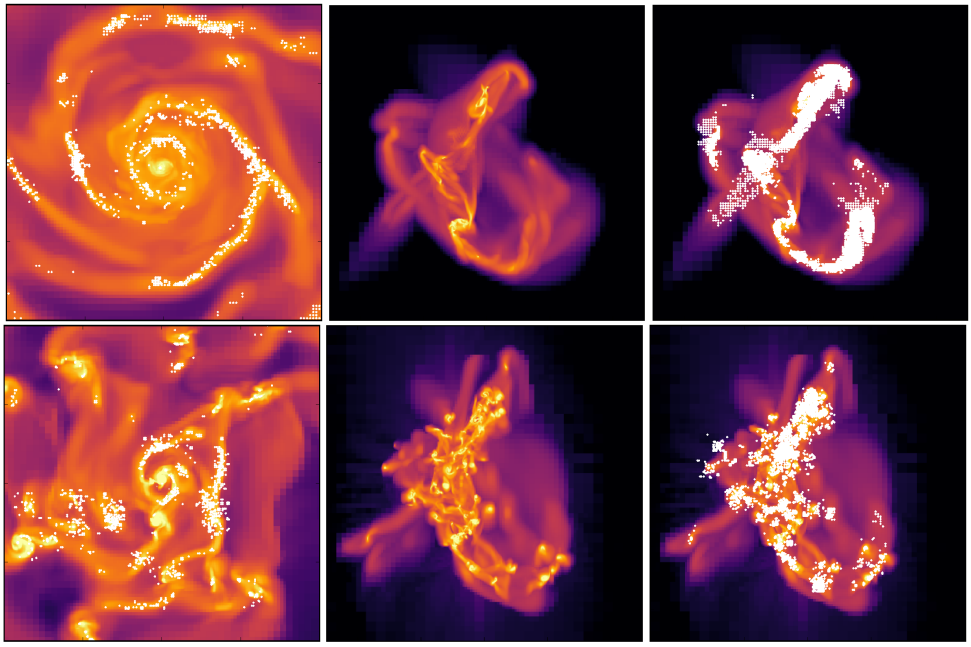

Figure 12. Gas density maps for the gas poor (top panel) and gas rich (bottom panel) simulations. The left panels show the isolated galaxies. The central and right panels show the direct-direct interaction for orbit #1 at t = 60 Myr. The maps span 10 kpc x 10 kpc for the isolated runs and 50 kpc x 50 kpc for the merger runs. The colormap is the same is in Fig. 1. The white dots in the left and right columns show the location of the tidally compressive regions.

back would increase the pre-interaction overall gas turbulence. As we have seen in Sect. 4.2, the interaction-induced increase of turbulence would be even smaller which would lead to an even weaker enhancement of the SFR. This shows that the weakness of merger-driven starbursts at high redshift (compared to low redshift cases) does not result from saturation by feedback in our models, and this result could only be stronger if real feedback had more important effects in high-redshift galaxies.

5 DISCUSSION

5.1 Comparison with previous simulations

Our simulations show that the high gas fraction major mergers are less efficient than low gas fraction major mergers to trigger starbursts. Here we compare our results to previous studies of clumpy gas-rich major mergers:

- The first simulations of gas rich ($f_{\rm gas}$ > 50%) galaxy mergers could not resolve the impact of turbulence on star formation, (Springel & Hernquist 2005; Hopkins et al. 2006; Cox et al. 2006; Lotz et al. 2008; Moster et al. 2011): their disks are less unstable than ours and tend to form spirals instead of clumps. They resolve the star formation enhancement due to the increase of nuclear in-

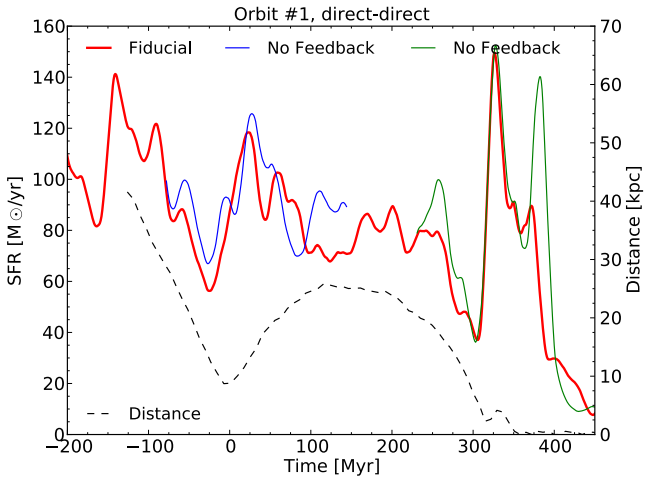

Figure 13. Evolution of the SFR for the dd1 simulation and runs with turned off stellar feedback at different times. The red solid line shows the SFR of the fiducial run, dd1, presented in Fig. 5. The blue and green lines show the SFR resulting from the runs without feedback. They separate from the fiducial curve slightly before the time delay indicated in the text because of the curve smoothing. The black dashed line shows the distance between the two galaxies.

flows through interaction-driven gravitational torques, but miss the increase of gas fragmentation and the initial, clump-driven, nuclear inflows, which make them to overestimate the relative increase of SFR.

- Bournaud et al. (2011) have run the first numerical simulations of gas rich clumpy galaxies. On their three orbits, they saw an increase of the SFR of up to a factor 10 (from 200 $M_\odot$ /yr to peaks of 2000 $M_\odot$ /yr) for more than 200 Myr. It results in a higher increase of SFR than in our sample, but still below usual low gas fraction major mergers. One should note that they do not use a cooling function, but a barotropic equation of state (presented in Bournaud et al. 2010), which tends to over-estimate the gas fragmentation.
- Hopkins et al. (2013) present a suite of parsec-resolution galaxy collision simulations, with one high-redshift type galaxy major merger ($f_{\rm gas}$ = 50%) and a feedback implementation which systematically destroys gaseous clumps. Their Fig. 9 shows that the enhancement of star formation is indeed significantly smaller and has a $\simeq$ 10 times shorter relative amplitude than their Milky Way type galaxy major merger. Their starburst duration is similar to that hat obtained in our simulations: $\sim$ 100 Myr and $\sim$ 1 Gyr for respectively the high and low gas fraction cases. They did not study this weak enhancement in details, as they changed several parameters between the low and high redshift runs (halo mass, the disk compactness and velocity profile).
- In the merger sample of Perret et al. (2014) no simulation shows any increase of the star formation during the interaction. They stressed that one explanation for this could be due to their implementation of feedback: they set a density-independent cooling time for the gas heated by the SNe of 2 Myr, which prevents very dense region in star-forming regions to form stars again during this time. One should note that they did not test their feedback on low gas fraction major mergers, contrary to the present study, so that it is uncertain whether this implementation would allow them to trigger starbursts in low redshift conditions.

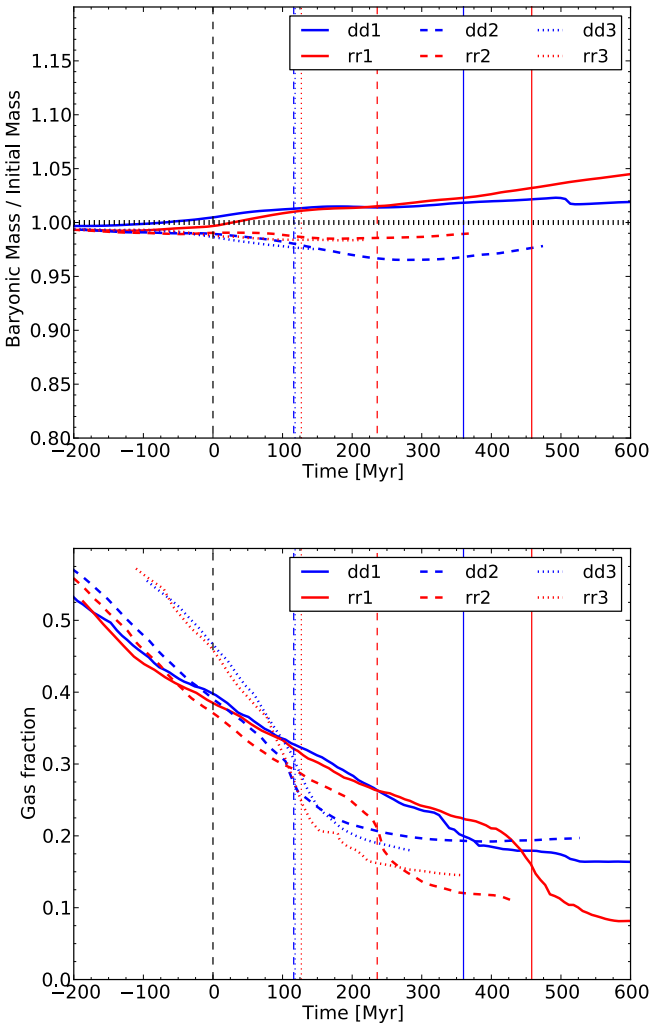

Figure 14. *Top:* Amount of baryonic matter ($M_{\rm gas} + M_{\rm stars}$) renormalized to the initial baryonic mass: $2 \times 57.2 \times 10^9$ $M_\odot$ (see Table 1). The vertical dotted line shows a ratio of 1. *Bottom:* Gas fraction evolution during the simulation for six gas-rich orbits. For both panels, only gas with density above 10^{-2} cm^{-3} is considered, in order to only count the gas present in the galaxies. All curves are shifted in time, such that t = 0 is the time of first pericentre for each orbit. The small coloured vertical lines show the time of coalescence for each orbit, as labelled in the legend.

The fact that high gas fraction major mergers trigger a smaller enhancement of star formation than their low gas fraction equivalent already was already seen in previous studies, using various numerical methods and feedback implementations. With this suite of simulations we propose that the variation in gas fraction only can explain the mildness of this enhancement.

5.2 The cosmological context

5.2.1 Gas refueling

Our galaxy pairs are not refueled by cosmological gas infall. The presence of cosmological cold gas infall on galaxies, inferred from cosmological simulations (Dekel et al. 2009a,b) but not yet observed, is thought to be the main channel of galaxy mass growth

at high redshift, when major mergers would contribute to only one third of the mass growth (Kereš et al. 2005; Ocvirk et al. 2008; Brooks et al. 2009).

Even though no cosmological infall is considered in our work, the galaxies are initially located in a box with an inter-galactic medium (IGM) of background density 2×10^{-7} cm^{-3}. This gas can cool down and contribute to the baryonic mass budget of the galactic disks.

In the top panel of Fig. 14 is shown the quantity of baryonic matter in the galaxies (stars and gas above 10^{-2} cm^{-3}), normalized to the initial baryonic mass of 2 times 57.2×10^9 M$_\odot$ (see Table 1). We see that the baryonic mass of the galaxy pair does not change by more than 4% throughout the simulations. These variations are either due to stellar outflows, which can bring some gas to densities lower than our threshold of 10^{-2} cm^{-3}, or to the cooling of the IGM gas onto the disk. We see that these two processes do not affect our mass budget.

A first drawback of not adding gas accretion in our simulations is that the cold gas mass reservoir available to form stars is not replenished by these cold flows. For instance, in our two simulations on orbit #1 – the less bound one for which coalescence happens after more than 300 Myr from the first pericentre – the long term evolution of the SFR in Fig. 6 is seen to be slowly decreasing, as a the consequence of gas consumption.

In the bottom panel of Fig. 14 is shown the gas fraction evolution during the gas-rich simulations on orbits #1, 2 and 3. We see that the gas is steadily consumed before the first pericentre, at $t = 0$, where the gas fraction is still at around 40% or more. Before the coalescence the gas fraction is above 25% for orbits #1 and 2, and above 40% for the faster orbit #3. Just before coalescence, the faster gas consumption through star formation leads to a rapid drop in the gas fraction.

We see that for the orbit #3 the effect of gas consumption is relatively weak as the gas fraction is still above 40% at the time of the coalescence. The fact that the SFR for these orbits do not show much difference in behavior from orbit #1 comforts us in concluding that this would not have an important effect on the SFR of our simulations.

However, on longer timescale, gas accretion would impact the star formation in the merger remnant. Indeed, in Fig. 7 we see that after the coalescence, the SFR of the gas-rich merger drops well below what is expected from the remaining gas fraction. This is due to the formation of a massive stellar spheroid, dispersion dominated, which stabilizes the gas and prevent it to form stars. This process is called morphological quenching (Martig et al. 2009). Recent simulations of high gas fraction galaxies surrounded by hot gaseous haloes, presented by Athanassoula et al. (2016), show that a disk of gas can form through gas accretion inside the spheroid core. This disk will be bar-unstable and form stars.

At $z = 2$, the mass inflow from cosmological accretion is of the order of 10 M$_\odot$/yr (Dekel et al. 2009a). Martig et al. (2009) have shown that, with this accretion rate order of magnitude and without any other merging event, several Gyr are necessary to reform a star-forming disk in a spheroidal major merger remnant, which is the same order of magnitude of formation of a disk found by Athanassoula et al. (2016).

5.2.2 *Turbulence from cosmological infall*

A second effect is that we neglect the increase of turbulence from the cosmological accretion. The infalling gas does not settle immediately into a thin disk but tends to stir the existing gas disk (Elmegreen & Burkert 2010; Gabor & Bournaud 2014), which has for net effect to increase the velocity dispersion and the disk height. The SFR is thought to be regulated by this constant fueling of turbulence onto the disk, until $z = 2$ when this process stops dominating the turbulence budget (Gabor & Bournaud 2014).

In Section 4.2 we claim that the merger does not increase the turbulence, because it is already high. Turbulence pumped through cosmological infall would make it even harder for the interaction to further increase the turbulence. Therefore we argue that this process would not change our conclusions.

5.2.3 *Galaxy compactness and orbits*

A last effect is that high redshift galaxies are more compact than low redshift galaxies, for the same mass, typically a factor $\simeq 2$ (van der Wel et al. 2014; Ribeiro et al. 2016). In this study we neglect this effect to focus on the difference in gas fraction only. However, our galaxy model has an intermediate compactness, between low and high redshift conditions.

Furthermore, for equal halo mass, cosmological simulations expect the pericentre distance to be 25% lower at $z = 2$ than at $z = 0$ (Wetzel 2011). All dynamical timescales are then shorter and the merging process is faster. This could result in more starburst-favorable orbits.

The orbit #2 (resp. #3) has impact parameter and relative velocity respectively 15% (resp. 30%) lower than orbit #1, which makes it closer to typical $z = 2$ orbits. We see in Fig. 6 that these three orbits share a comparable increase in SFR. This hints for a low dependency of the orbit parameter on the weakness of the interaction-driven star formation in high gas fraction disks.

5.3 Application to local gas-rich dwarf galaxies interactions

Local dwarf irregulars (dIrrs) have f_{gas} up to 90% , contain clumps and are relatively turbulent with a ratio of their circular velocity to velocity dispersion, V_{circ} / σ, around 6 (see e.g. Lelli et al. 2014, and references therein), which is of the same order than massive high redshift galaxies. Our reasoning, which is based on the high gas fraction and highly turbulent high redshift galaxies, might thus also apply to dIrrs. However, Stierwalt et al. (2015) recently claimed that interactions between dIrrs can significantly increase their SFR, that is more than 5 times above the main sequence.

It should be noted that, if the gas fraction of dIrrs is very high, it is mainly due to a diffuse HI envelope, which does not participate actively to the star formation. This envelope can however cool and be accreted onto the central region (see e.g. Elmegreen et al. 2016b).

A second important difference with respect to high redshift massive galaxies is that isolated dIrrs do not show signs of instability-driven inflows, as they do not have important nuclear concentration. For the gas to be funneled towards the nucleus, the work of the gravitational torques from the gaseous clumps, which scale with their mass (M_{clump}), must compensate the galactic rotational kinetic energy of the gas $\propto v_{circ}^2$, which results in an inflow timescale $\propto v_{circ}^2 / M_{clump}$.

Both dIrrs and high redshift massive galaxies show clumps of typical masses of a few percent of the galaxy mass, that is $\simeq 10^7$ M$_\odot$ (Elmegreen et al. 2012), and rotation velocities of about 50 km/s (Lelli et al. 2014), against 10^9 M$_\odot$ clumps (Elmegreen et al. 2009) and 200 km/s rotation velocities for massive high-redshift galaxies. The inflow timescale is then a factor 6 longer for dIrrs. The fact that the relative torquing of the gas is much less efficient in dIrrs makes

the central inflows driven by the interaction between dIrrs relatively more important and can thus more easily ignite a starburst.

The more diffuse location of the gas in dIrrs, and the low efficiency of instability-driven central inflows therefore limit the extension of our results from massive high redshift galaxies to dIrrs.

5.4 Starbursting galaxies observed at high redshift

In Fig. 5 and 6 we see that interactions do not strongly enhance the SFR of high gas fraction galaxies: from around 120 $M_\odot$/yr (60 $M_\odot$/yr for each galaxy), our most actively star forming galaxy barely reaches 350 $M_\odot$/yr during 50 Myr. Observations of sub-millimeter galaxies (SMGs), report SFRs up to several 1000 $M_\odot$/yr (Barger et al. 1998; Tacconi et al. 2006). Observed SMGs are found both on the main sequence and the starburst sequence of the $M_\star$-SFR (da Cunha et al. 2015). There are also claims that SMGs form the high-mass end of the main-sequence (Koprowski et al. 2016; Michałowski et al. 2016).

Recent numerical simulations presented in Narayanan et al. (2015) show that the regime of SMGs galaxies can be achieved without major mergers, but rather by continuous gas infall through accretion of small haloes onto a very massive group halo ($\simeq 10^{13}\,M_\odot$) which may be populated by several galaxies. On top of that, Wang et al. (2011) show that the relatively high abundance of SMGs might result from the blending of sources that are not necessarily spatially associated, which agrees with a not high enough number of major merger to account for the observed SMG abundance (Davé et al. 2010).

These studies do not exclude major mergers as being a cause of a part of the observed SMGs. However, one should note that the progenitors of such galaxies are significantly more massive than our simulated disks ($M_\star \simeq 10^{11} M_\odot$), i.e five times higher than our galaxy models. Therefore, we cannot conclude on the possibility of part of the SMGs being triggered by high-redshift major mergers.

6 CONCLUSIONS

Observations of star-forming galaxies over a wide range of redshifts ($z = 4$ to $z = 0$) have shown a main sequence on the $M_\star$–SFR relation, with a number of outliers galaxies showing a higher specific SFR, which correspond to the starbursting galaxies. The proportion of these outliers stays relatively constant ($\simeq 2\%$) with time, with no clear dependence with redshift. In the local Universe, all these outliers are merging galaxies. Since the merger rate is thought to increase with redshift, high redshift major mergers seem to be less efficient to produce starbursting galaxies than low-redshift ones. We present a suite of parsec-resolution hydrodynamical simulations to test this hypothesis. We have run simulations of typical low-redshift and high-redshift galaxy pairs, changing only the gas fraction, from 10 % to 60 %, between the two models.

We see that for the same orbit, when the SFR of the low gas fraction goes up by a factor of more than 10 during several hundred million years, the SFR of the high gas fraction case only mildly increases, and only at the coalescence. In particular we show that the high redshift type galaxies would not, or for a short amount of time ($\simeq 50$ Myr), be considered as starburst galaxies on a Schmidt-Kennicutt diagram.

Even in the absence of stellar feedback no higher burst of star formation is seen. We reject feedback saturation as a cause to the inefficiency of the interaction to trigger a strong enhancement of star formation.

At coalescence, most of the star formation happens in the central region of both galaxies, typically in the central kpc. This starburst is fueled by central mass inflows caused by the interaction, which add up to the mass inflow processes already at play in the isolated disks. This makes the coalescence phase less efficient in triggering a starbursting galaxy in the high gas fraction case than the low gas fraction case.

Renaud et al. (2014) have shown a correlation between the increase in compressive turbulence and the onset of the interaction-driven starbursting mode of star-formation. Our high-redshift type galaxy interactions show only a mild increase of turbulence. High gas fraction clumpy disks are already quite turbulent ($\sigma \simeq 40$ km/s) and it is harder to increase the velocity dispersion through release of gravitational energy when the initial velocity dispersion is already high.

On top of this smaller increase of the gas turbulence, the clumpy morphology also imposes an extensive tidal field on the inter-clump regions. These two processes limit the increase in compressive turbulence, and thus the increase in star formation rate during the interaction.

This demonstrates that the high gas fraction of the galaxy progenitors can strongly reduce the star formation enhancement in galaxy interactions and major mergers.

ACKNOWLEDGEMENTS

The authors thank Vianney Lebouteiller and Damien Chapon for very useful discussion and the anonymous referee for constructive comments which helped to improve this paper. Simulations were performed at TGCC (France) and as part of a PRACE project (grant ra2540, PI: FR) and GENCI project (grant gen2192, PI: FB). FR acknowledges support from the European Research Council through grant ERC-StG-335936.

REFERENCES

Agertz O., Kravtsov A. V., Leitner S. N., Gnedin N. Y., 2013, ApJ, 770, 25
Armus L., Heckman T., Miley G., 1987, AJ, 94, 831
Athanassoula E., Rodionov S. A., Peschken N., Lambert J. C., 2016, ApJ, 821, 90
Barger A. J., Cowie L. L., Sanders D. B., Fulton E., Taniguchi Y., Sato Y., Kawara K., Okuda H., 1998, Nature, 394, 248
Barnes J. E., 2004, MNRAS, 350, 798
Barnes J. E., Hernquist L. E., 1991, ApJ, 370, L65
Bergvall N., Laurikainen E., Aalto S., 2003, A&A, 405, 31
Bournaud F., 2016, Galactic Bulges, 418, 355
Bournaud F., Duc P.-A., Emsellem E., 2008, MNRAS, 389, L8
Bournaud F., Elmegreen B. G., Teyssier R., Block D. L., Puerari I., 2010, MNRAS, 409, 1088
Bournaud F., et al., 2011, ApJ, 730, 4
Bournaud F., et al., 2012, ApJ, 757, 81
Bournaud F., et al., 2014, ApJ, 780, 57
Brooks A. M., Governato F., Quinn T., Brook C. B., Wadsley J., 2009, ApJ, 694, 396
Burkert A., 1995, ApJ, 447, L25
Chien L.-H., Barnes J. E., 2010, MNRAS, 407, 43
Cibinel A., et al., 2015, ApJ, 805, 181
Cox T. J., Jonsson P., Primack J. R., Somerville R. S., 2006, MNRAS, 373, 1013
Daddi E., et al., 2010, ApJ, 714, L118
Dale J. E., 2015, New Astron. Rev., 68, 1
Davé R., Finlator K., Oppenheimer B. D., Fardal M., Katz N., Kereš D., Weinberg D. H., 2010, MNRAS, 404, 1355

Dekel A., et al., 2009a, Nature, 457, 451
Dekel A., Sari R., Ceverino D., 2009b, ApJ, 703, 785
Di Matteo P., Bournaud F., Martig M., Combes F., Melchior A.-L., Semelin B., 2008, A&A, 492, 31
Dubois Y., Teyssier R., 2008, A&A, 477, 79
Duc P.-A., Renaud F., 2013, in Souchay J., Mathis S., Tokieda T., eds, Lecture Notes in Physics, Berlin Springer Verlag Vol. 861, Lecture Notes in Physics, Berlin Springer Verlag. p. 327 (arXiv:1112.1922), doi:10.1007/978-3-642-32961-6_9
Duc P.-A., Mirabel I. F., Maza J., 1997, A&AS, 124
Eisenstein D. J., Hut P., 1998, ApJ, 498, 137
Elbaz D., et al., 2007, A&A, 468, 33
Ellison S. L., Mendel J. T., Scudder J. M., Patton D. R., Palmer M. J. D., 2013, MNRAS, 430, 3128
Elmegreen B. G., 2009, in Andersen J., Nordströara m B., Bland-Hawthorn J., eds, IAU Symposium Vol. 254, The Galaxy Disk in Cosmological Context. pp 289–300 (arXiv:0810.5406), doi:10.1017/S1743921308027713
Elmegreen B. G., Burkert A., 2010, ApJ, 712, 294
Elmegreen D. M., Kaufman M., Brinks E., Elmegreen B. G., Sundin M., 1995, ApJ, 453, 100
Elmegreen D. M., Elmegreen B. G., Ravindranath S., Coe D. A., 2007, ApJ, 658, 763
Elmegreen D. M., Elmegreen B. G., Marcus M. T., Shahinyan K., Yau A., Petersen M., 2009, ApJ, 701, 306
Elmegreen B. G., Zhang H.-X., Hunter D. A., 2012, ApJ, 747, 105
Elmegreen B. G., Kaufman M., Bournaud F., Elmegreen D. M., Struck C., Brinks E., Juneau S., 2016a, preprint, (arXiv:1603.04533)
Elmegreen D. M., et al., 2016b, preprint, (arXiv:1605.02822)
Erb D. K., Shapley A. E., Pettini M., Steidel C. C., Reddy N. A., Adelberger K. L., 2006, ApJ, 644, 813
Förster Schreiber N. M., et al., 2009, ApJ, 706, 1364
Gabor J. M., Bournaud F., 2014, MNRAS, 437, L56
Genzel R., et al., 2008, ApJ, 687, 59
Genzel R., et al., 2010, MNRAS, 407, 2091
Goldbaum N. J., Krumholz M. R., Forbes J. C., 2016, preprint, (arXiv:1605.00646)
Guo Y., et al., 2015, ApJ, 800, 39
Hopkins P. F., Hernquist L., Cox T. J., Di Matteo T., Robertson B., Springel V., 2006, ApJS, 163, 1
Hopkins P. F., Cox T. J., Younger J. D., Hernquist L., 2009, ApJ, 691, 1168
Hopkins P. F., Quataert E., Murray N., 2011, MNRAS, 417, 950
Hopkins P. F., Quataert E., Murray N., 2012, MNRAS, 421, 3522
Hopkins P. F., Cox T. J., Hernquist L., Narayanan D., Hayward C. C., Murray N., 2013, MNRAS, 430, 1901
Houck J. R., Schneider D. P., Danielson G. E., Neugebauer G., Soifer B. T., Beichman C. A., Lonsdale C. J., 1985, ApJ, 290, L5
Jog C. J., 2013, MNRAS, 434, L56
Jog C. J., 2014, AJ, 147, 132
Jogee S., et al., 2009, ApJ, 697, 1971
Kampczyk P., et al., 2007, ApJS, 172, 329
Kartaltepe J. S., et al., 2007, ApJS, 172, 320
Kaviraj S., et al., 2013, MNRAS, 429, L40
Kennicutt Jr. R. C., 1998, ApJ, 498, 541
Kereš D., Katz N., Weinberg D. H., Davé R., 2005, MNRAS, 363, 2
Koprowski M. P., et al., 2016, MNRAS, 458, 4321
Kraljic K., Renaud F., Bournaud F., Combes F., Elmegreen B., Emsellem E., Teyssier R., 2014, ApJ, 784, 112
Le Fèvre O., et al., 2000, MNRAS, 311, 565
Lelli F., Verheijen M., Fraternali F., 2014, A&A, 566, A71
Lofthouse E. K., Kaviraj S., Conselice C. J., Mortlock A., Hartley W., 2016, preprint, (arXiv:1608.03892)
Lotz J. M., Jonsson P., Cox T. J., Primack J. R., 2008, MNRAS, 391, 1137
Lotz J. M., Jonsson P., Cox T. J., Croton D., Primack J. R., Somerville R. S., Stewart K., 2011, ApJ, 742, 103
Mac Low M.-M., 1999, ApJ, 524, 169
Magnelli B., et al., 2012, A&A, 548, A22
Martig M., Bournaud F., Teyssier R., Dekel A., 2009, ApJ, 707, 250
Michałowski M. J., et al., 2016, preprint, (arXiv:1610.02409)
Mihos J. C., Hernquist L., 1996, ApJ, 464, 641
Moster B. P., Macciò A. V., Somerville R. S., Naab T., Cox T. J., 2011, MNRAS, 415, 3750
Narayanan D., et al., 2015, Nature, 525, 496
Newman S. F., et al., 2012, ApJ, 761, 43
Noeske K. G., et al., 2007, ApJ, 660, L43
Ocvirk P., Pichon C., Teyssier R., 2008, MNRAS, 390, 1326
Peng Y.-j., et al., 2010, ApJ, 721, 193
Perret V., Renaud F., Epinat B., Amram P., Bournaud F., Contini T., Teyssier R., Lambert J.-C., 2014, A&A, 562, A1
Povich M. S., 2012, preprint, (arXiv:1202.0791)
Powell L. C., Bournaud F., Chapon D., Teyssier R., 2013, MNRAS, 434, 1028
Price S. H., et al., 2016, ApJ, 819, 80
Renaud F., Boily C. M., Fleck J.-J., Naab T., Theis C., 2008, MNRAS, 391, L98
Renaud F., Boily C. M., Naab T., Theis C., 2009, ApJ, 706, 67
Renaud F., et al., 2013, MNRAS, 436, 1836
Renaud F., Bournaud F., Kraljic K., Duc P.-A., 2014, MNRAS, 442, L33
Renaud F., Bournaud F., Duc P.-A., 2015, MNRAS, 446, 2038
Ribeiro B., et al., 2016, preprint, (arXiv:1602.01840)
Rodighiero G., et al., 2011, ApJ, 739, L40
Roos O., Bournaud F., Juneau S., Gabor J., 2015, IAU General Assembly, 22, 2225915
Sanders D. B., Mirabel I. F., 1996, ARA&A, 34, 749
Schmidt M., 1959, ApJ, 129, 243
Schreiber C., et al., 2015, A&A, 575, A74
Scudder J. M., Ellison S. L., Momjian E., Rosenberg J. L., Torrey P., Patton D. R., Fertig D., Mendel J. T., 2015, MNRAS, 449, 3719
Smith B. J., Soria R., Struck C., Giroux M. L., Swartz D. A., Yukita M., 2014, AJ, 147, 60
Springel V., Hernquist L., 2005, ApJ, 622, L9
Stierwalt S., Besla G., Patton D., Johnson K., Kallivayalil N., Putman M., Privon G., Ross G., 2015, ApJ, 805, 2
Stott J. P., et al., 2016, MNRAS, 457, 1888
Strömgren B., 1939, ApJ, 89, 526
Tacconi L. J., et al., 2006, ApJ, 640, 228
Tacconi L. J., et al., 2010, Nature, 463, 781
Teyssier R., 2002, A&A, 385, 337
Teyssier R., Chapon D., Bournaud F., 2010, ApJ, 720, L149
Teyssier R., Pontzen A., Dubois Y., Read J. I., 2013, MNRAS, 429, 3068
Truelove J. K., Klein R. I., McKee C. F., Holliman II J. H., Howell L. H., Greenough J. A., 1997, ApJ, 489, L179
Wang W.-H., Cowie L. L., Barger A. J., Williams J. P., 2011, ApJ, 726, L18
Wetzel A. R., 2011, MNRAS, 412, 49
Whitmore B. C., Schweizer F., 1995, AJ, 109, 960
Zanella A., et al., 2015, Nature, 521, 54
da Cunha E., et al., 2015, ApJ, 806, 110
van der Wel A., et al., 2014, ApJ, 788, 28

APPENDIX A: STUDY OF SPATIAL RESOLUTION

In order to test the impact of the resolution on star formation of our high-redshift simulations, we run the dd1 simulation with different resolution both in space and in mass.

In the upper panel of Fig. A1 is shown the SFR for the dd1 simulations for different highest spatial resolution, from 50 to 6 pc. In the lower panel of Fig. A1 is shown the SFR for the dd1 simulations for different highest spatial resolution, using a different mass resolution. For the two new refinement simulation, the mass needed to activate the next refinement level was divided by 8 for cells smaller than 100 pc. Therefore, all cells that were refined to 50 pc in the non-new refinement simulations, are directly refined to 25 pc in the new refinement case, and so on for further refined cells.

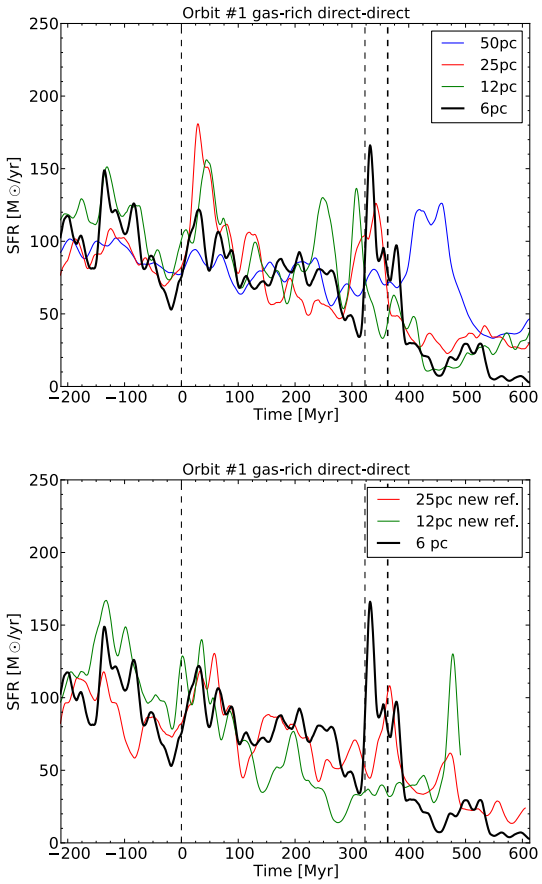

Figure A1. *Top*: SFR during the interaction for the dd1 simulation at different maximum spatial resolution. *Bottom*: Same as in the top panel, with a different refinement strategy for the new refinement labelled simulations. The black dotted lines show the time of pericentre passages and coalescence of the dd1 simulation at 6 pc resolution.

The stochasticity of the SFR and the fact that each simulation is run with a different ρ_0 calibration induces some variations in the pre-merger SFR. The time of the final coalescence can change with the resolution, as the resolution will impact several processes governing the interaction. For instance, an other resolution can modify how the angular momentum is driven out of the inner system through the tidal tails and/or impact the dynamical friction.

In Fig. A1, there appears to be no significative trend with the resolution. In particular, no simulations show any onset of a massive star formation burst during the interaction. We therefore see that the resolution has little influence on the evolution of the SFR during the interaction, which legitimates our use of a resolution of only 12 pc for the simulations run with Orbit #2 and Orbit #3.

This paper has been typeset from a TEX/LATEX file prepared by the author.

5.2 Clustered star formation in high-z galaxies

5.2.1 The problem of globular cluster formation

In Section 2.5 I briefly presented several types of star clusters, in particular the *young massive clusters* (YMCs) and the *globular clusters* (GCs). While the formation process of the former can be probed in local dwarf galaxies (see e.g. Adamo et al., 2010) and interacting galaxies (see e.g. Herrera and Boulanger, 2017), the latter are much older and their formation mechanism remains an open scientific problem.

Any scenario of GC formation must lead to the emergence of the omnipresent metallicity bimodality described in Section 2.5 (see also review by Brodie and Strader, 2006). Several hypotheses have been proposed to explain this bimodality, such as different regions of GC formation. Metal-rich clusters may have formed in galaxies massive enough to retain their metals (Shapiro, Genzel, and Förster Schreiber, 2010), and the metal-poor population in accreted low-mass dwarfs (Côté, Marzke, and West, 1998; Tonini, 2013; Renaud, Agertz, and Gieles, 2017). Finally, some scenarios proposed that the metal-rich population has been formed in recent ($z < 1-2$) mergers (Ashman and Zepf, 1992)[1], and the metal-poor clusters being formed in early mergers ($z > 4$) (Kravtsov and Gnedin, 2005; Li and Gnedin, 2014; Kim et al., 2017).

To test these scenarios and their consistency to observed quantities, numerical simulations are a useful tool, whose capabilities nonetheless do rapidly reach a limit in this kind of problem. Indeed, one need to simulate both a realistic cosmological context, including cold flows and satellite galaxy formation and accretion, and resolve star formation at a very small scale, that is below the typical size of a stellar cluster, $\simeq 3$ pc (Harris, 2010). Moreover, the conditions of formation of a cluster might lead to a disruption of the cluster through gas removal, tidal shocks, evaporation, etc (Elmegreen and Burkert, 2010; Gieles and Renaud, 2016). This issues may be partially resolved using a coupled N-body code as a post-processing tool (such as N-body6-tt, see e.g. Renaud, Gieles, and Boily, 2011).

5.2.2 Stellar clusters and clumpy galaxies

In this thesis we have seen that the high gas mass fraction in typical $z = 2$ galaxies leads to a clustered star formation as result of internal instabilities (see Section 4.1). Moreover, several arguments tend to advocate the formation of metal-rich globular clusters in the clump-driven phase of galaxy evolution (see e.g. Shapiro, Genzel, and Förster Schreiber, 2010):

- **Metallicity:** The metallicity distribution of metal-rich globular clusters peaks at [Fe/H] = -0.5, consistent with measurements of [Fe/H] in $z = 2$ galaxies (Erb et al., 2006; Halliday et al., 2008).
- **Spatial distribution and kinematics:** Metal-rich GCs seem to be associated with the bulge and/or the thick disk of local spirals (Côté, 1999, for the Milky Way). This is consistent with a scenario in which GCs are formed in the grand

[1] Formation of super star clusters in galaxy mergers was actually predicted (see e.g. Schweizer, 1987; Ashman and Zepf, 1992) before being observed with HST imaging (Whitmore and Schweizer, 1995).

TABLE 5.1: Mass and density threshold for refinement.

Spatial resolution [pc]	390.6 to 195.3	195.3 to 97.7	97.7 to 48.8	48.8 to 24.4	24.4 to 12.2	12.2 to 6.1	6.1 to 3.1
Mass threshold [$M_\odot$]	8×10^5	8×10^5	4×10^5	2×10^5	1×10^5	5×10^4	2.4×10^4
Density threshold [cm^{-3}]	5.4×10^{-1}	4.3	1.7×10^1	6.9×10^1	2.7×10^2	1.1×10^3	4.2×10^3

gaseous clumps. Indeed, while these clumps migrate inwards through dynamical friction (Genzel et al., 2008), some GCs are expected to follow them and eventually be associated with the bulge and some are expected to be expelled and remain in the thick disk (Elmegreen, Bournaud, and Elmegreen, 2008; Bournaud and Elmegreen, 2009).

- **Number and mass spectrum:** Giant clumps are hierarchically structured (see e.g. Behrendt, Burkert, and Schartmann, 2016) and are expected to form several stellar clusters each. Assuming a power law mass function for stellar clusters typical of the turbulent cascade, and the mass loss model from Jordán et al. (2007), Shapiro, Genzel, and Förster Schreiber (2010) have shown that the number and mass function of metal-rich GCs are consistent with all being formed in the clump-driven phase at $z = 2$.

Moreover, detailed numerical simulations of merging local galaxies have shown that the interaction trigger the formation of a wealth of young massive clusters, especially at the first pericenter passage (Bournaud, Duc, and Emsellem, 2008; Renaud, Bournaud, and Duc, 2015). One may wonder if this results holds at higher redshift.

In this section I propose to investigate whether mergers can form new GCs with respect to those formed in the clumpy disks and whether they can be spatially redistributed thanks to galaxy-galaxy interactions, using numerical simulations. This work will be presented in Fensch et al., (2017c, in prep.).

5.2.3 Numerical techniques

Galactic disks

To test the formation of stellar clusters in $z = 2$ galaxy collisions we use the same galactic disk model as in Section 5.1. To resolve the formation of star clusters in our simulation, we needed to improve the resolution, compared to the simulations presented in Section 5.1. First, we lowered the mass of formed stellar particles to $\simeq 1000$ $M_\odot$ to be able to resolve stellar structures down to a few 10^5 $M_\odot$. Then we improved the spatial resolution: we allowed a maximum spatial refinement of 3 pc and we lowered the mass thresholds for refinement. Indeed, only improving the maximum resolution would only lead to a better resolution in the centers of giant gas clumps. Ensuring a good refinement on moderate gas densities permits to better resolve instabilities in the disk, which are crucial to resolve stellar cluster formation. The list of mass thresholds is given in Table 5.1.

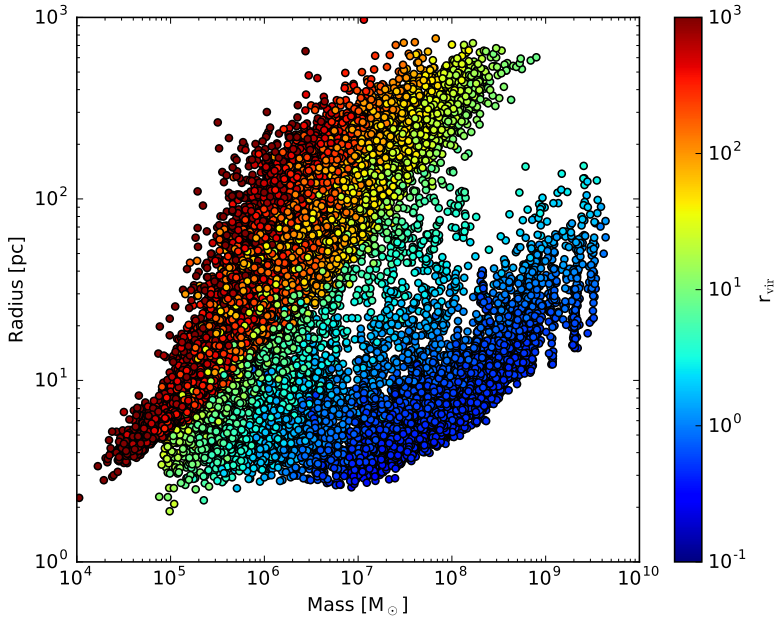

FIGURE 5.8: Location of all the HOP detections on the isolated disk simulation on the mass-radius plane. Detections are color coded with respect to their virial parameter (see text).

Detection of stellar clusters

To detect stellar cluster we use the friend-of-friend algorithm HOP (Eisenstein and Hut, 1998). The algorithm detect density peaks above an user-defined threshold *dpeak*. These peaks are merged if the saddle density is above an user-defined threshold *dsaddle*. The user can also set a outer density limit *douter* and a minimal number of particles (usually set to 10).

These values are chosen to agree with a visual examination. The number of detections depends on the choice of parameters, as fainter clusters may or may not be detected, and bigger detections may or may not be split. In the following, I have used *dpeak* = 10^2 $M_\odot/pc^{-3}$, *dsaddle* = 10^2 $M_\odot/pc^{-3}$ and *douter* = 10^{-1} $M_\odot/pc^{-3}$.

One may note that all detections of stellar over-densities with HOP should not be considered as stellar clusters. Some detections may for instance be unbound, transient stellar features. To ensure a good selection of stellar cluster, following Renaud, Bournaud, and Duc (2015), we compute a *virial ratio*, $r_{\rm vir} = \sigma^2 r_h/(GM)$, where σ, r_h and M are the velocity dispersion, half-mass radius and mass of the detected cluster. We consider that our detection is a stellar cluster if $r_{\rm vir} < 1$. On Fig. 5.9 we can see all the detections on the isolated run. We see that a selection threshold of $r_{\rm vir} \simeq 1$ separates two main sequences on the mass-radius plane of our detections. We chose a conservative threshold value of 1 to ensure bound detections throughout the simulation. On Fig. 5.9 are shown two examples of detections with mass $1.2 \times 10^7 M_\odot$, one with $r_{\rm vir} = 0.53$ and the other with $r_{\rm vir} = 37.37$.

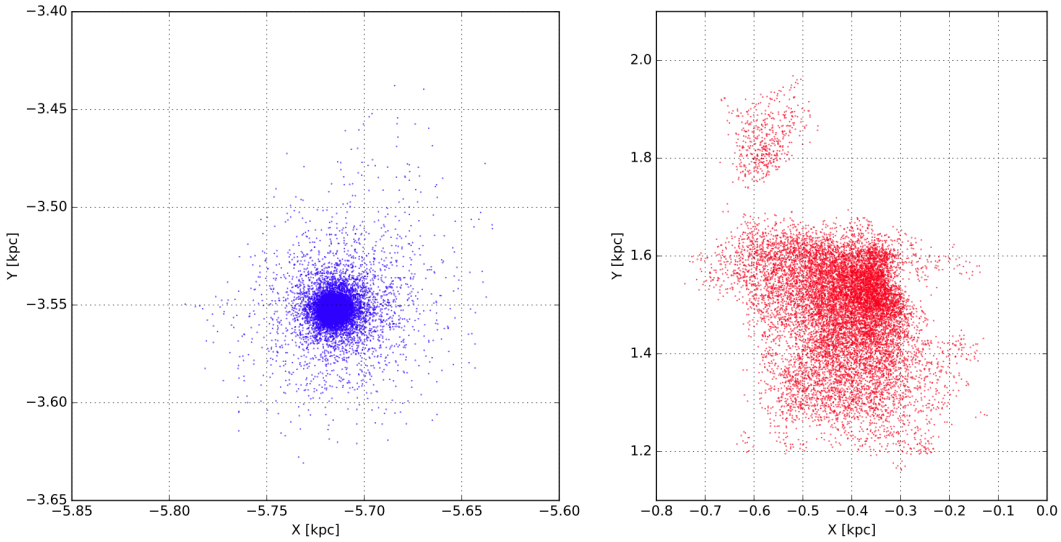

FIGURE 5.9: Two HOP detections on the output showed on Fig. 5.10. They have a similar mass (1.2×10^7 $M_\odot$) but have different $r_{\rm vir}$: 0.53 for the left panel and 37.37 for the right panel.

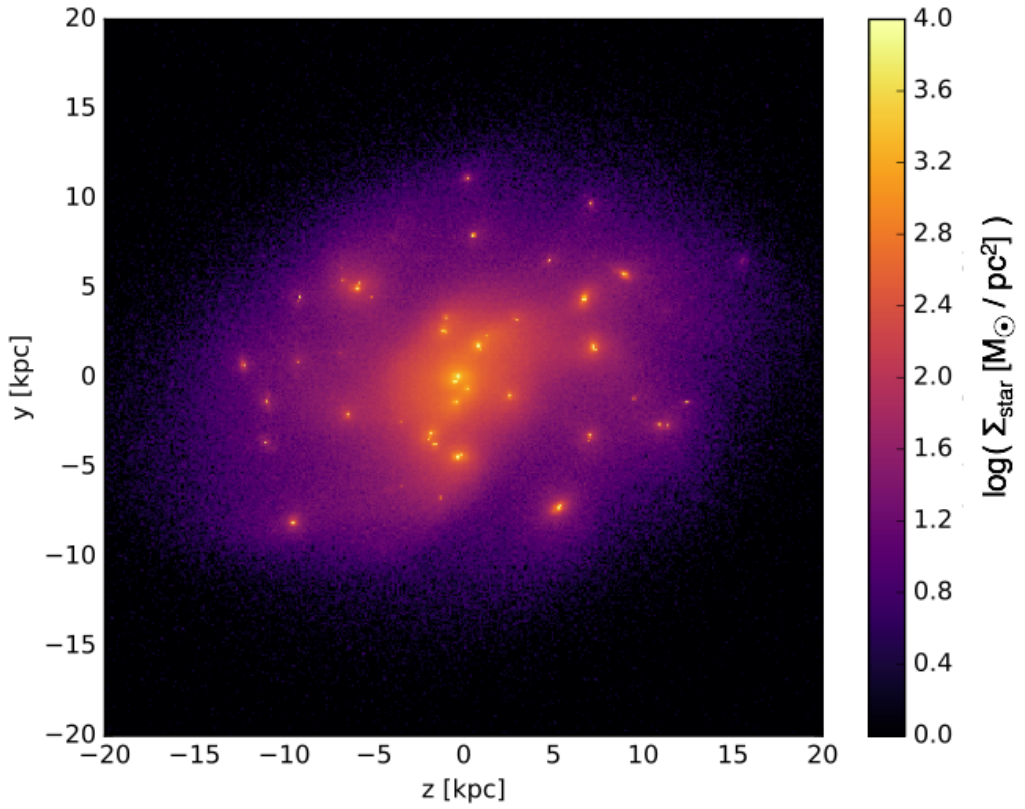

FIGURE 5.10: Stellar surface density of the isolated galaxy. The stellar disk is slightly tilted with respect to the cartesian grid, thus the projection is not exactly face-on.

A last caution that should be taken into account is the fact that we do not resolve well gravitational forces inside and between stellar structures for scales less than typically ten times the spatial scale, that is 30 pc in our case. This is due to the *particle-in-cell* method implemented in RAMSES, described in Section 3.1.5. We are not be able to resolve internal stellar dynamics and dynamical mass loss. Moreover, as we do not resolve well the inter-clump interactions, stellar sub-structures in our giant clumps tend to merge and form an unrealistically massive, around 10^8 $M_\odot$ stellar structures, which follow their giant gas clump host. Our study is therefore limited to the formation of massive, $> 10^6$ $M_\odot$, bound structure stellar structures and their orbital evolution assuming their survive. As some stellar clusters are expected to be expelled from giant clumps (Elmegreen, Bournaud, and Elmegreen, 2008), one may note that the scatter of the orbital evolution in the following should then be considered as a lower limit.

In Fig. 5.10 is shown the stellar surface density of the isolated run. We see the presence of massive stellar clumps, which are expected by the clumpy gas distribution in these galaxies as seen in Section 4.1 and 5.1. A part from the nucleus, this galaxy shows 3 clumps above 5×10^8 $M_\odot$ and 12 clumps above 10^8 $M_\odot$. The summed stellar mass of these clumps is 21.6% of the total stellar mass. This is similar to observed clumpy galaxies (see e.g. Elmegreen et al., 2007; Bournaud, Duc, and Emsellem, 2008) and simulated disks in cosmological simulations (Agertz, Teyssier, and Moore, 2009; Mandelker et al., 2014).

5.2.4 Interactions and star cluster formation

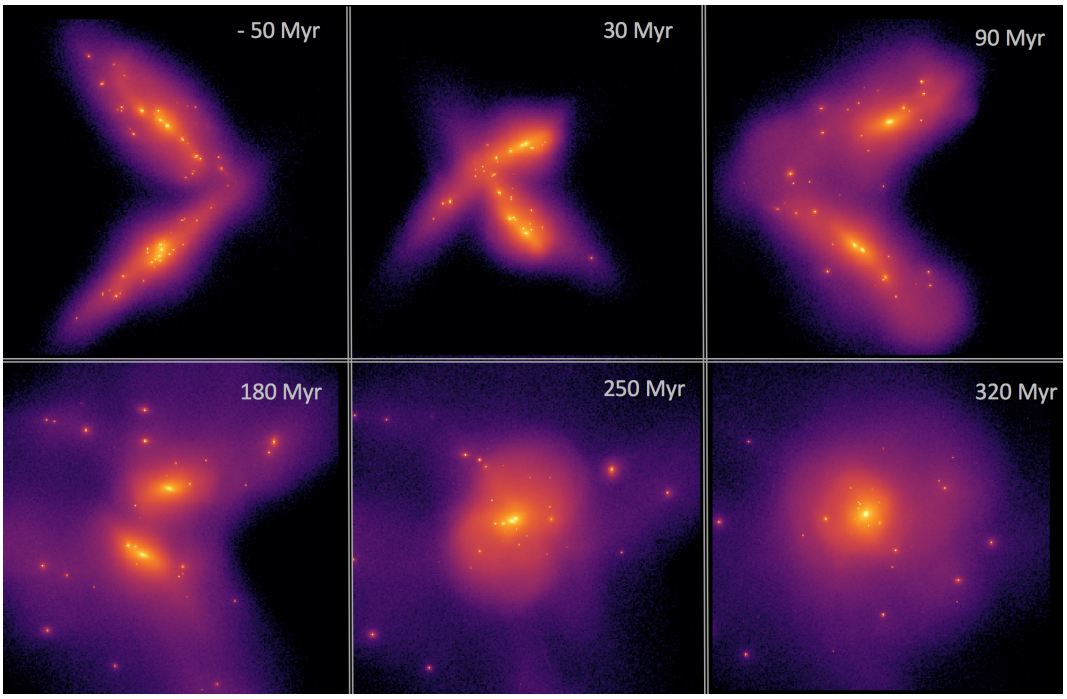

FIGURE 5.11: Surface density maps during the interaction. The scale is the same as in Fig. 5.10 and the box size is 50 kpc×50 kpc. The respective times with respect to the first pericenter passage are indicated on the top right corner of each map.

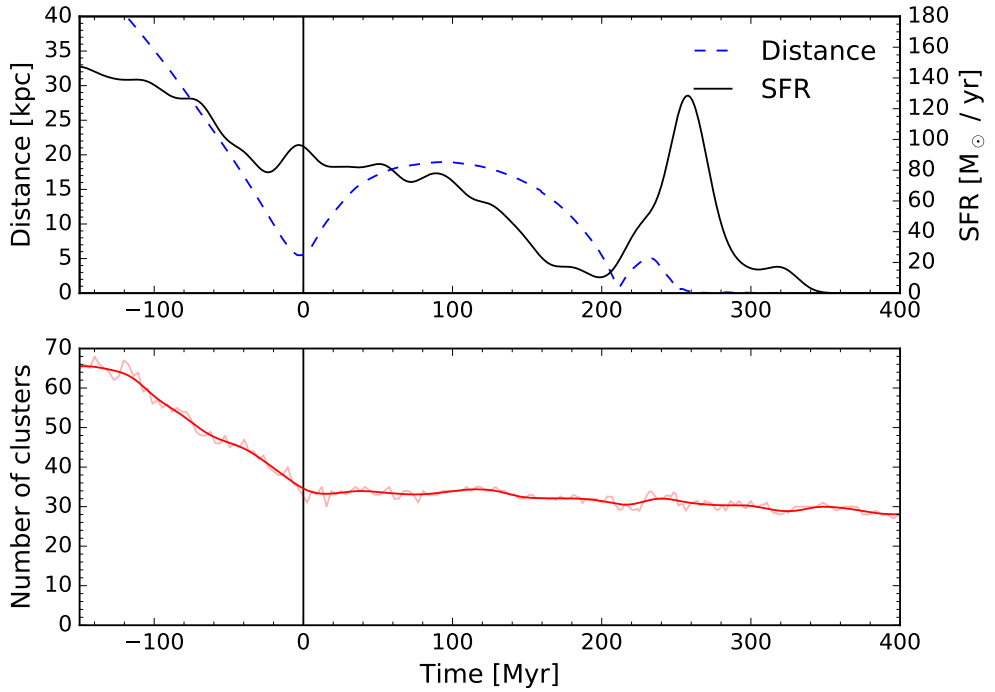

FIGURE 5.12: Time evolution of several quantities during the interaction. The time of the first pericenter passage is shown in both panels by the vertical black solid line and serves as time origin. Top panel: The blue dashed curve shows the distance between the center of the two galaxies and the black solid line shows the SFR. The SFR curve is smoothed using a gaussian kernel of FWHM 10 Myr. Bottom panel: The red curve shows the number of clusters. The curve is smoothed using a gaussian kernel to remove fluctuations due to the detection method. The un-smoothed curve is shown with a lower contrast for comparison.

In this study we proposed to study the formation of stellar cluster in interactions of typical $z = 2$ galaxies. To this purpose we use one of the interaction orbit presented in Fensch et al. (2017), namely rr2. The previous Fig. 5.10 shows an isolated disk at the same simulation time as $\simeq 50$ Myr before the first pericenter of the interaction. The stellar density maps of the interaction is shown in Fig. 5.11. We see that the interaction forms an elliptical galaxy surrounded by a few tens of stellar clusters, which is similar to the number of stellar clusters contained in the pre-interaction disks at $t = -50$ Myr.

In the top panel of Fig. 5.12 are shown the distance between the two galaxies and their SFR with respect to time. As we have seen in Section 5.1, the interaction triggers only a mild, around a factor 5, SFR enhancement at the time of the coalescence. In particular, their is no significant increase of the SFR at the first pericenter.

In the bottom panel of Fig. 5.12, we show the number of bound clusters and the total stellar mass in clusters. Clusters closer than 1 kpc from the center of the galaxies are discarded to account for the bulge, and clusters closer than 500 pc from each other are merged in the same detection. The noisiness of the curve is due to the detection algorithm, which may not consider a cluster if it goes through a dense stellar

environment – i.e. close to the bulge – or by a big cluster which is split into two detections. Before the interaction, we see that the number of clusters decreases with time. This is expected from the merging of sub-structures in the disk, and the migration of the giant clump towards the center. This decrease stops after the first pericenter passage. One should note that some clusters are formed during the interaction. In our case, only 2 clusters out of the $\simeq$ 27 final stellar clusters have been formed at $t = 90$ and 100 Myr. Their final mass is respectively 1.3 and 4.1 $\times 10^7$ $M_\odot$ which is in the lower tail of the mass distribution shown in the lower panel of Fig. 5.10, most probably because the interaction did not let them accrete other clusters, contrary to clusters already formed in the disk. Their orbits are not significantly different to the other clusters as we will see in the next Section.

Therefore, we see that the interaction does not trigger an important formation of stellar bound clusters, contrary to low-redshift interactions. This result is a side result of our analysis on the impact of interactions on the SFR: in Fensch et al. (2017), we have shown that the processes responsible for the enhanced gas fragmentation at low redshift are saturated in disks with a gas content typical of $z = 2$ galaxies. If one does not increase the gas fragmentation, one should expect no increase of the stellar cluster formation rate.

However, the collision prevents the destruction of clusters through migration and merging by ejecting it in the halo, where they might survive for a long time. The study of their post-collision behavior is detailed in the next Section.

5.2.5 Ejected clusters

In Fig. 5.12 we see that around 27 clusters are left at the end of the interaction, out of which 23 do not sink into the remnant and are set on orbits around the remnant. In this section we study the orbits of these clusters around the merger remnant.

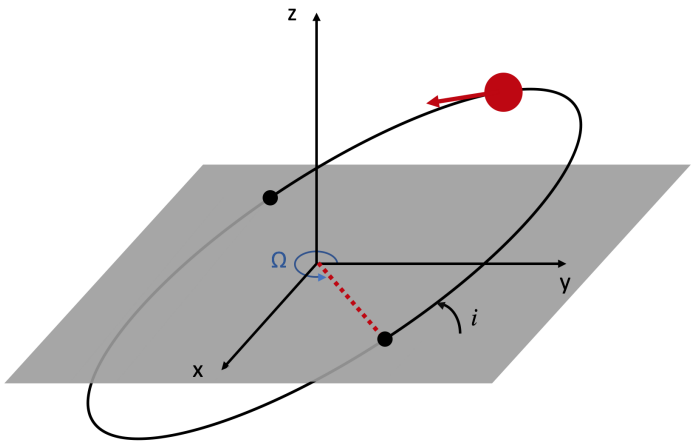

FIGURE 5.13: Definition of two orbital parameters: the *inclination*, i and the *longitude of the ascending node* Ω. The gray plane is the plane of reference. The red circle and arrow show the location of the cluster and its velocity.

Because of the numerical cost of the simulation we stopped the simulation at $t \simeq 700$ Myr, that is 480 Myr after the coalescence. This time is enough for the closest clusters from the center, around 10, to achieve several orbits around the merger remnant. As only gravitational processes interest us after the coalescence, a way to accelerate the simulation to resolve several full orbits is to decrease the spatial resolution at the end of the merger. Decreasing the resolution by a factor 3 would for instance let most of the clusters bound, while making the simulation much faster to run. The caveat is that, in RAMSES, the computational domain is divided between CPUs based on the number of cells and not particles. Due to my high number of particles, decreasing the resolution led to unbalanced CPUs and actually slowed down the simulation, if not merely crashing it. After several unsuccessful attempts to change the dependency of the parallelizing routine on cells in favor to particles, I ran the simulation at 3 pc resolution all along.

I followed the clusters on their orbit using the identification number of their star: for each cluster in output n, we look for a parent cluster in output $n-1$. A cluster is a parent if more than 50% of its stars are located in the cluster in the output n. This technique, which may not be the most efficient, is however robust against escaping stars and the merging of clusters.

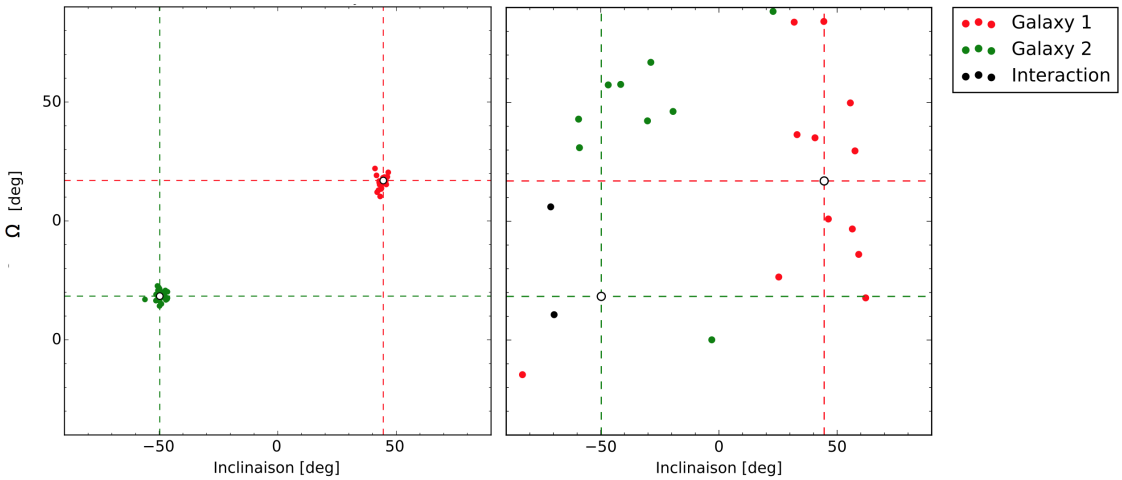

FIGURE 5.14: Location of the orbital plane of stellar clusters in the I-Ω plane. The location of the plan of the two galaxies are shown with the green and red dashed lines. The color of the data point relates to the origin of the clusters. The location of the two clusters formed during the interaction are shown with black dots. Left panel: location before the first pericenter. Right panel: location after the coalescence.

First, I computed the plane of each orbit, which is the plane containing the center of their host galaxy, the cluster and the instantaneous velocity vector. Then I extracted two classical quantities in celestial mechanics: the *inclination* I and *longitude of the ascending node* Ω of the orbital plane with respect to a reference plane and direction, respectively $z = 0$ and the y-axis here. After the interaction, these two quantities stay fairly constant for each cluster.

The position of the clusters on the I-Ω plane is shown in Fig. 5.14. On the left panel we see that, before the interaction, the clusters are located in the plane of their

host galaxy. After the coalescence, clusters are spread out of the planes of their former host galaxies. We see that clusters tend to keep a relatively similar inclination as their host galaxy, but have a different Ω. However, in-depth study of this *precession* is out of the scope of this analysis and would require a larger sample of collisional orbits. Here we simply note that the clusters initially located in a plane do not fall on the same plane after the interaction, and do not form a plane.

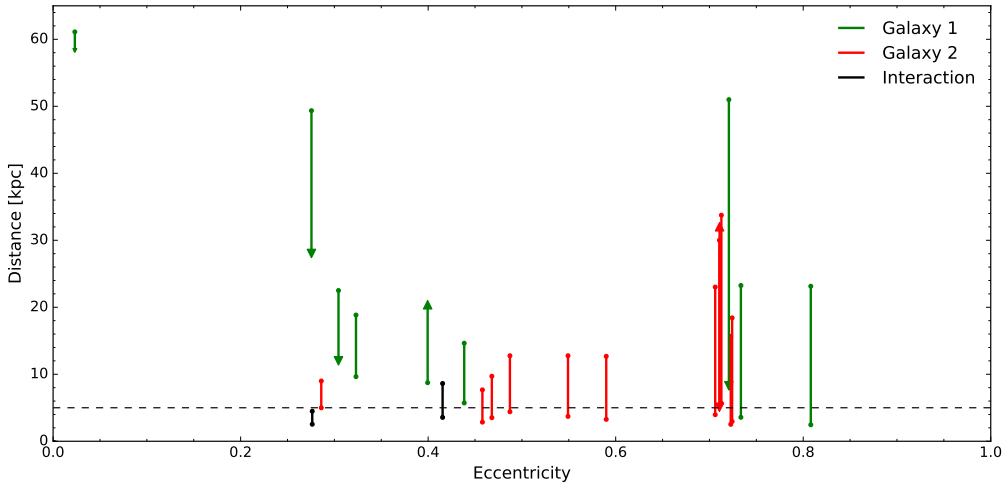

FIGURE 5.15: Distance range of each orbit against its eccentricity. Triangles are lower and upper limits when the extrema distances are not resolved. The horizontal dashed black line shows the position of the effective radius of the major merger remnant. The color coding is the same is in Fig. 5.14.

Then I characterized the orbits by their radius extrema and eccentricity. For clusters for which we resolve two distance extrema in the course of the simulation, we use the same definition for the eccentricity as for a Keplerian elliptical orbit:

$$e = \frac{r_a - r_p}{r_a + r_p} \tag{5.1}$$

where r_a and r_p are respectively the apocentric and pericentric distance from the merger remnant. For the farthest clusters, the apocentre or/and pericentre are not reached during the simulation. We therefore use their extrema values as lower or upper limits for respectively the apocentric and pericentric distance. One should note that in every case, the eccentricity computed with these values is always underestimated.

In Fig. 5.15 are shown the extremum values and respective eccentricity for all our clusters. One can show that clusters can reach large apocentric distances, up to 60 kpc, but for most of the clusters for which we resolve the pericentric distance, the latter falls below the effective radius[2] of the merger remnant, $R_{\rm eff}$ = 5 kpc. One should note that, due to our discreet sampling of the orbits and the fact that clusters spend a very short amount of time close to their pericenter, the pericenter distance is

[2]The effective radius is defined as the half-mass radius.

often overestimated. Thus, the eccentricities shown in Fig. 5.15 should be considered as lower limits.

We therefore expect stellar clusters expelled from their galactic host through a major merger to have quite eccentric orbits, and to come back regularly close to the center of the merger remnant, that is closer than R_{eff}.

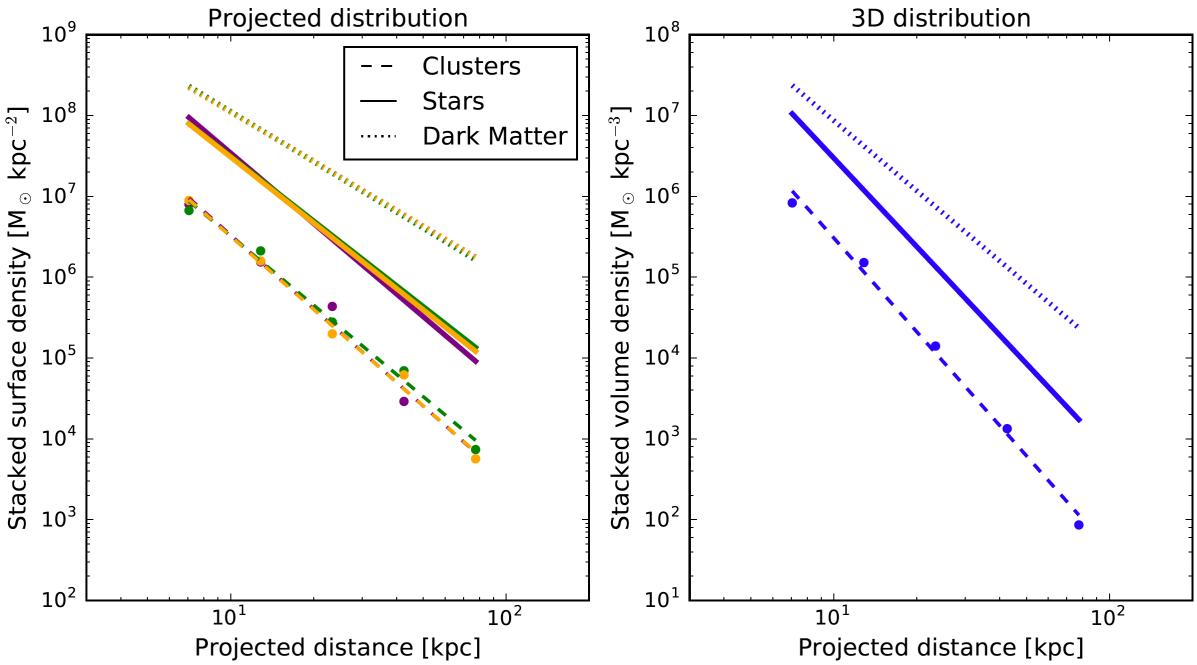

FIGURE 5.16: Best fit radial mass distribution of clusters, stars and dark matter. Data points for the clusters are shown as full dots. In the left panel is shown the distribution projected on one spatial axis, as it is done for observations. In the right panel is shown the distribution of 3D radial distance. The respective slopes of the curves are summarized in Table 5.2.

In Fig. 5.16 are shown radial mass profile for the clusters, the galaxy remnant stars and dark matter halo. The radial mass profile of the cluster is obtained by taking into account all the distances from our bound detections to the center of the merger remnant between the coalescence and the end of our simulation (between $t = 320$ and 700 Myr) , each value being weighted by the mass and time interval. As argued in Section 5.2.3, each of our stellar cluster actually represents a cluster of clusters. To compare with observations we need to make some assumptions. Here we assume that star clusters formed in the same gas clump have roughly the same orbits around the merger remnant, in terms of apocentre and pericentre distances, and that their orbital phases become independent from each other on a timescale shorter than a Hubble Time.

We find that the mass distribution of our stellar cluster is close to the mass distribution of the stars and is significantly much steeper than the mass profile of the dark matter component. The value of the slopes are summed in Table 5.2. This similarity between the remnant stars and stellar clusters mass distribution is similar to the correlation found for metal-rich clusters around local elliptical galaxies (Schuberth

TABLE 5.2: Radial mass distribution slopes for the different projections shown in Fig. 5.16.

Projection	Clusters	Stars	Dark Matter
x	-3.00	-2.70	-2.01
y	-2.85	-2.66	-2.07
z	-3.03	-2.90	-2.03
3D	-3.86	-3.64	-2.89

et al., 2010; Forbes, Ponman, and O'Sullivan, 2012).

5.2.6 Discussion and concluding remarks

In the previous section we have investigated the formation of bound stellar clusters in $z = 2$ disks and major mergers.

We have seen that $z = 2$ disks form bound stellar clusters out of internal instabilities. We have also seen that interactions do not significantly enhance the formation of stellar clusters, contrary to what is observed in local major mergers. The reason has already be pointed out in Section 5.1: the gas fragmentation of $z = 2$ is saturated and is not significantly enhanced by a gravitational interaction with another galaxy. The role of the merger is to preserve the population of stellar clusters from the disk by expelling them into the halo of the merger remnant.

By studying the orbits of the remaining clusters around the merger remnant we have shown that the plane of the two galaxies are not conserved after the coalescence. The corollary is that the absence of a prominent disk does not mean that the clusters did not originate from an interaction.

If we consider that these clumps are satellites of their host galaxy, this result seems to be in contradiction with Smith et al. (2016), where satellite galaxies remain in a plane even after a major merger. These satellites are quite far away from their host galaxy center, typically around 25 kpc. Thus they have a strong angular momentum which will make it harder for the interaction to modify. Moreover, our clusters being closer the the center of the host galaxies, they are more likely to have a close encounter with another stellar structure, which may affect its orbital plane.

Last but not least, we have looked at the radial mass distribution of the clusters around the remnant. We have seen that the cluster distribution is close to the stellar distribution of the remnant, and significantly steeper than the dark matter distribution. This is similar to what is observed around local elliptical galaxies for the metal-rich clusters, while the metal-poor are seen to correlate better with the dark matter distribution (see Forbes, Ponman, and O'Sullivan, 2012, and references therein). This analysis thus strengthens the case for a $z = 2$ disk origin for metal-rich globular clusters around galaxies.

The next step of my analysis will be to compute the tidal forces to which the clusters are submitted throughout the collision. The comparison between the tidal field inside the disk and into the halo, is of paramount importance to understand the disruption processes which are not resolved in our simulation. Indeed, these measures can be useful to set the tidal field conditions in the study of mass loss of

stellar clusters, for instance using N-body codes (see e.g. Renaud, Gieles, and Boily, 2011).

Chapter 6

Conclusion

6.1 Role of gas fraction

In this thesis I have presented my research on star and stellar cluster formation in gas-dominated galaxies. The term *gas-dominated galaxies* refers primarily to the galaxies at high-redshift: the typical gas mass fraction of is around 50-60% for $z = 2$ galaxies. This cosmic epoch can be considered as the *cosmic noon* of our Universe as it is the time of the peak of star-formation (Madau and Dickinson, 2014). Understanding this comic period is crucial to shed light on the mas assembly of current galaxies.

As argued in Section 2.2.2, $z = 2$ galaxies have a clumpy morphology. The formation and evolution of these giant gas clumps – transient or long lived ? – are still an open field of research.

Using numerical simulations, I have shown in Section 4.1 that galactic disks with gas mass fractions typical of $z = 2$ galaxies, are indeed expected to host the formation of massive, $10^7 - 10^8$ $M_\odot$, bound gas clumps. By using several stellar feedback models, I showed that these clumps are expected to survive the high star formation rate. In comparison, the same disk models with a gas mass fraction of 20% only form short-lived gas over densities, which are destroyed in around 50 Myr. This faster disruption is due to the formation site of the clumps. In the low gas fraction case, these clumps are formed in spiral arms which are regions of high shear. These spiral arms do not form in the gas-rich case. The stripping of gas and stars is thus stronger in the low gas fraction case, and leads to a faster disruption of the clumps.

I thus argue that the high gas mass fraction, typical of $z = 2$ galaxies drives the formation of massive bound gas clump which survive the stellar feedback and the galactic shear.

This first result showed how the gas content of a galaxy affects its internal dynamics. One may wonder how the high gas mass fraction affects the regulation of the star formation activity. For instance, we know that mergers in the local Universe trigger strong enhancement of the star formation rate. However, the efficiency of this triggering at higher redshift has been questioned by observations. I therefore proposed to see if this lower efficiency of mergers in triggering bursts of star formation can be due to this high gas mass fraction. Indeed, no systematic study of the difference between low- and high-redshift major mergers has had been done at the start of my PhD.

The numerical simulations I ran and presented in Section 5.1 show that the gas density distribution barely changes for 60%-gas mass fraction major mergers, when for 10%-gas mass fraction galaxy interactions do bring a lot of gas to a high density, a factor 5 to 10 increase compared to the isolated case.

In this work, I have shown why there is this saturation of the gas density distribution in the gas-rich case. The interaction between two galaxies has an effect on the gas turbulence, the tidal field and the internal gas flows. Namely, the tidal field is expected to become fully compressive on extended regions, thus enhancing the compressive component of the turbulence and bringing more gas to the high-density tail of the gas distribution. The internal gas flows are also expected to be enhanced because of gravitational torques created by the interaction.

These two processes are already at play in high gas fraction galaxies. The turbulence is naturally high, compressive tidal field regions are in place inside the massive bound clumps and strong nuclear gas flows are induced by their mutual interaction. Galaxy-galaxy interactions increase their amplitude, but to a smaller extent than in the low-gas fraction case, because all these processes have an already high amplitude in isolated galaxies.

These simulations show that the lower efficiency of mergers in triggering starbursts probed by observations can be explained by a saturation effect induced by the higher gas mass fraction.

A collateral result, presented in Section 5.2 is that interactions between typical $z = 2$ is not expected to produce a significant number of stellar clusters, contrary to what is observed in the low-redshift universe. In my simulations we can see that the interaction does not trigger stellar cluster formation. It however preserves the clusters by expelling them into the halo and thus stop cluster-cluster and cluster-bulge.

However, the massive gas clumps hosted by these gas-rich galaxies should form bound stellar structures. One may wonder if these stellar clumps can be the progenitors of these old globular clusters, in particular the red population which has a similar metallicity as $z = 2$ galaxies. In Section 5.2, I have studied the orbits of stellar clusters from the disks of typical $z = 2$ galaxies after a major merger event. I have shown that they are expelled in the halo of the major merger remnant, in a distribution which closely follows the distribution of stars, similar to what is observed for the red globular cluster population of local ellipticals. Their distribution does not reform a disk and they have quite eccentric orbits which makes them come back regularly inside the effective radius of the host galaxy.

This study thus shows to what extent $z = 2$ mergers can contribute to the formation of the metal-rich globular clusters around local massive galaxies. If mergers do not trigger star cluster formation, they can eject pre-existing stellar clusters from their clumpy disks to the halo of the merger remnant and preserve them from cluster and bulge merging in the disk.

In this thesis I have thus shown, using numerical simulations, how the gas mass fraction influences the internal dynamics and the regulation of star formation. Spatially detailed studies of these high-redshift galaxies, and especially their star forming clumps, are difficult because of their distance to us. One may therefore look for galaxies with analogous conditions in the local Universe. In the Section 2.2.3 I have claimed that tidal dwarf galaxies (TDG) host the most similar conditions to the massive star forming clumps in the local Universe, at the sole exception of the disk tidal field.

In Section 4.2, I have presented a nearby system with several TDGs. We have obtained data with the MUSE instrument on the most massive of these dwarfs, NGC 5291N. This new instrument allowed me to get a spectral map at the spatial resolution of 180 pc to study the ionization in its interstellar medium (ISM). Using

emission line diagnostic diagrams, I have shown that the gas ionization features are consistent with a stellar photoionization origin with a possible contribution from shocks, traced by a high [OI]/H_α emission. This ratio is stronger on the outskirts of the dwarf, where the velocity dispersion traced by the H_α emission is also significantly stronger. We could not detect any sign of an outflowing component, therefore we suspect that these shocks might come from gas accretion or come from the high velocity dispersion inside the huge collisional gas ring in which the dwarf galaxy has formed.

As we have seen in Section 5.2, giant clumps are expected to form bound stellar structures. However our simulations, and MUSE observations, do not allow us to resolve their internal structure. We obtained photometric data from the HST which allows us to make a census of the clustered star formation around the dwarf. Using a SED fitting code I have split the star cluster population in three groups, according to their age : young (<15 Myr), intermediate (from 30 to 1000 Myr) and old (> 1000 Myr) star clusters. The intermediate star cluster are significantly more massive than the young population. As the mass of the individual clusters have been shown by previous studies to correlate with the star formation rate, this could be an evidence for a massive episode of star formation at the formation of the collisional ring. In this case one needs to explain why we do not see smaller mass cluster with an intermediate age. A possibility is that the intermediate population has formed from the merging of several small clusters, which would support the globular cluster merging formation scenario.

To sum up, these studies have shown that the gas mass fraction has a major impact on the internal structure and star formation of galaxies. In particular, this parameter alone can explain differences between $z = 0$ and $z = 2$ galaxies, as well as their response to a major merger event. The characteristic disk instabilities induced by the high gas fraction also raise the question of the assembly of galaxies, in particular the origin of thick disk and bulges. Are they formed during the clumpy phase at $z = 2$ or by later minor mergers? In the following subsection I will present the questions on this cosmic epoch I would like to investigate in the coming years.

6.2 Future Prospects

I have shown that typical gas-rich disks should form massive bound gas clumps, but we have not investigated their structure and their internal support. The internal structure of the gas, which may be driven by intrinsic rotation (Ceverino et al., 2012), internal turbulence or interactions between substructures (Behrendt, Burkert, and Schartmann, 2016), can have strong implications on the way stellar feedback will interact with the interstellar medium of these structures (e.g. creation of chimneys, ionizing photon leak, triggered star formation?) and, therefore, on star formation regulation. One may also wish to use current surveys of high-redshift galaxy – such as ionization diagnostics from SINS (Förster Schreiber et al., 2009) or molecular gas distribution from ALMA – to constrain the feedback or IMF models in this massive clumps (see e.g. Zanella et al., 2015). These studies require to have a good knowledge of the internal structure of these gas clumps.

However, our simulation setup does not allow us to resolve the internal structure of the giant clumps at a scale smaller than $\simeq 10$ pc. Indeed, increasing the resolution

based on a density criterion would need a huge amount of memory and computer time.

One possibility to address this issue would be to use a *patch-based* like refinement method, in addition to the classical density-based refinement method used in this thesis. This type of method has already been implemented in RAMSES for fixed patches. One may force the resolution to an arbitrary level in an arbitrary zone of the simulation box, and thus increase the resolution in the region of interest – a giant clump – which impact much less computer time than using the classical density criterion. With this method, one may achieve a zoom on a single moving clump, with a typical resolution of 0.01 pc (see e.g. Bonnell, Dobbs, and Smith, 2013), embedded in a realistic galactic environment (including gas accretion, galactic shear and tidal field).

However, the location of this zone can only be updated each time one restarts the simulation, which is not suited for a moving giant clump. I plan to implement the possibility for this patch to follow the orbit of a giant clump. Benchmark tests are also needed to understand how the parallelization would be affected by this refinement method.

Another open field of research is the interplay between a galaxy and its surroundings, in particular between cosmological gas accretion through cold flows (see Section 2.1.2) and high-redshift galaxy gaseous haloes. In this thesis I have simulated galactic disks without a cosmological context. However, one may use RAMSES inflowing boundary to implement incoming gas flows towards the galaxy.

The variations in the size, flux and orientation of the cold flows will have an effect on the number, mass and spatial distribution of gaseous clumps. Studying their orbit and possible migration towards the nucleus would directly constrain the contribution of giant clumps to bulge formation scenarios (see e.g. Elmegreen, Bournaud, and Elmegreen, 2008).

Such a numerical setup would also help us to understand the interaction between these incoming flows and the star formation induced outflows from the galaxy. Can stellar outflows enrich the pristine infalling material and accelerate its cooling, or shock-heat it and stop the inflow? Cold flows might also accelerate the return of outflowing gas to the host galaxy, preventing gas from accumulating in the hot halo. This would therefore allow us to bring some constrains to the longstanding missing baryons problem, or how comes that 80% of the baryons have not yet fallen onto galaxies.

These two prospects are part of my current research project for which I was granted a Fellowship at the European Southern Observatory in Munich, starting in November 2017.

I also plan to continue working in the field of stellar cluster formation and galaxy mergers. I am the PI of an accepted MUSE proposal to observe candidate globular clusters located onto a dramatic stellar shell around NGC 474 (see proposal in Annexe A and Lim et al., 2017, in Annexe B). I am also part of the SOC of a conference on *"Galaxy interactions and mergers across cosmic time"*, which will be held in Sexten (Italy) in March 2018 (see proposal in Annexe A).

Appendix A

Accepted Proposals

A.1 Observation Proposal, MUSE P99

I present here an accepted proposal, which I submitted as PI. This MUSE proposal targets a dramatic stellar shell around the local galaxy NGC 474 and several, likely connected, globular cluster candidates. The aim is to probe, for the first time, the stellar population the shell. At the same time, this project will probe the kinematics of the shell and confirm the connection between the shell and the globular clusters.

The A run of this proposal has been accepted with rank A.

A.2 Sexten conference

This proposal for a meeting on *"Galaxy interactions and mergers across cosmic time"* has been accepted by the Sexten Center for Astrophysics and will be held in Sexten in March 2018.

It aims at bringing together both observers and numericians to discuss the role of mergers and interactions across cosmic time. In particular, we will discuss the identification of mergers, their role on galaxy star formation histories and on the triggering of AGNs.

European Organisation for Astronomical Research in the Southern Hemisphere

OBSERVING PROGRAMMES OFFICE • Karl-Schwarzschild-Straße 2 • D-85748 Garching bei München • e-mail: opo@eso.org • Tel.: +49 89 320 06473

APPLICATION FOR OBSERVING TIME

PERIOD: **99A**

Important Notice:

By submitting this proposal, the PI takes full responsibility for the content of the proposal, in particular with regard to the names of CoIs and the agreement to act according to the ESO policy and regulations, should observing time be granted.

1. Title

Category: **B–5**

Choreography of a Wedding Dance: probing the mass assembly of the early type galaxy NGC 474 with its shells and associated globular clusters.

2. Abstract / Total Time Requested

Total Amount of Time:

Deep optical images of the early-type galaxy NGC 474 have revealed spectacular shells and radial stellar streams, remnants of one or several past mergers. These are the only shells in the Local Universe with high enough surface brightness for direct spectroscopy. We propose to observe with MUSE two external bright shells where we identified 6 globular clusters (GC) candidates. The spectrophotometric data will allow us to measure the velocity, age and metallicity of the outer stellar populations, which are key parameters to model the galaxy, as well as to establish for the first time a physical connection between GCs and a stellar shell. We will thus be able to determine whether GCs may be used as tracers of the shells kinematics. This investigation of a prototypical galaxy, among the only few with bright enough stellar shells for direct spectroscopy, will give us tools to investigate the mass assembly of early-type galaxies with the GCs and stellar shells they host.

3.

Run	Period	Instrument	Time	Month	Moon	Seeing	Sky	Mode	Type
A	99	MUSE	8.2h	any	g	0.8	PHO	s	
B	99	MUSE	4.1h	any	g	0.8	PHO	s	

4. Number of nights/hours

Telescope(s)

Amount of time

a) already awarded to this project:

b) still required to complete this project:

5. Special remarks:

This proposal is part of a PhD project, started in October 2014, under the supervision of P.-A. Duc at AIM, Paris Saclay, France.

6. Principal Investigator: jfensch

6a. Co-investigators:

P.-A.	Duc	1193
E.	Emsellem	1258
E.	Peng	1616
W.	Harris	1499

Following CoIs moved to the end of the document ...

7. Description of the proposed programme

A – Scientific Rationale: The low surface brightness (LSB) component of the Universe is still a largely unexplored parameter space of galaxy evolution, although it contains imprints of the mass assembly of galaxies: the multiple collisional debris that, in the current scenario of hierarchical built-up of galaxies, are predicted to surround galaxies. Galactic archeology aims at reconstructing the past evolution of galaxies by characterizing such structures. The technique has proven to be very successful for galaxies of the Local Group for which star counts can be performed, and has just recently been applied to more distant galaxies, thanks to *the diffuse stellar light revealed by ultra-deep imaging* (Martinez-Delgado et al., 2010; Ferrarese et al., 2012; Duc et al., 2015). Such surveys disclosed around massive galaxies a variety of debris: faint stellar streams from disrupted satellites, gas-rich prominent tidal tails that result from major wet mergers, and *very often a network of concentric shells* (Duc et al., 2015). If the latter are more easily identified than the LSB tidal streams, because they are sharp-edged, their disruption timescale is also much longer ($\simeq$ 5 Gyr). They are also more frequent (Duc et al, 2015): in fact, shells were discovered long ago around ellipticals (Malin & Carter, 1983) and more recently in disk (Schweizer & Ford, 1995; Schweizer & Seitzer, 1998) and even dwarf galaxies (Paudel, Duc et al., subm.). **Given their frequency and relative brightness, shells appear as convenient tracers of past merging events**.
The mechanisms responsible for the shells formation are still poorly constrained (see review by Struck et al.,1999). Following the hypothesis from Quinn (1984), numerical simulations have indicated that radial minor mergers of dwarf galaxies can reproduce the observed stellar shells properties (e.g. Dupraz & Combes, 1986; Heisler & White, 1990; Hendel & Johnston, 2015). Major merger simulations (Hernquist & Spergel, 1992; Hubbard & Mihos, 1995) have also shown that shell-like structures can be formed through this channel. **Having spectroscopic information on the shells would help better constrain their formation channel:** while kinematical information would give insight on the 3D geometry of the system galaxy+shell, an even more fundamental ingredient to build realistic simulations is the chemical content that will give clues on the properties of the progenitor. So far spectrophotometric data on shells are scarce (e.g. Balcells et al., 2001) mostly because they are difficult to obtain. Indeed, contrary to tidal tails, most shells are gas-poor and only their faint stellar absorption lines are available for spectroscopy.
Thanks to their excellent image quality, the ultra-deep imaging surveys such as the NGVS (Ferrarese et al., 2012) and MATLAS (Duc et al., 2015) made at CFHT, not only disclosed LSB structures but also a wealth of globular clusters. **GCs are also often used as tracers of the building up of the outer environment of galaxies** (e.g. Durrell et al., 2014). *Their compactness makes then also well suited to spectrophotometric follow-up studies.* **Fine LSB structures and GCs are in fact likely connected**: in the Local Group, part of the GC population follows stellar streams (Mackey et al., 2014; Veljanoski et al., 2014). Further out GCs were also found along a prominent tidal bridge connecting two nearby early type galaxies (Blom et al., 2014). Thus, if GCs can be used to trace back the kinematics of the underlying tidal debris, *can they also be used in the case of shells?*
We propose to answer this question by using the revolutionary capabilities of MUSE on one of the most spectacular shell-rich systems, NGC 474 (see Fig. 1, left panel). Complex series of at least 10 concentric shells and 6 radial streams were disclosed by our group as part of the MATLAS survey. Fortunately, some shells have a high enough surface brightness (24.8 mag.arcsec^{-2} in the g-band) for spectroscopy. On top of that, several globular clusters are seen to be clustered towards the shells. **We propose here to observe for the first time the stellar populations in a stellar shell and to check the physical link between shells and GCs**. This will inform us on the extent of mixing of stellar populations between the host and progenitor during the interaction. All these information are precious clues for the understanding of the building up of the mass and halo of today's massive galaxies through merging events.

B – Immediate Objective: We propose to observe with MUSE three fields covering a large part of the brightest shells of the early type galaxy NGC 474, one located to its East and the other to its West. Together, the MUSE fields contain six GC candidates apparently spatially associated with the shells (see Fig. 1, right panel) **The probability of this spatial association being random was computed as being 0.12% (Lim et al. (submitted)**. The GCs had been identified based on a combination of color-color diagrams (derived from u, g, r and i deep images obtained with MegaCam at CFHT under excellent seeing conditions: 0.6 arcsec in i), and half-light radius, that separate them from foreground stars and background compact galaxies, with some level of contamination.
We will analyze the IFU data cubes to:
• fit the spectra of the shell with templates in stellar libraries such as MIUSCAT (Vazdekis et al., 2012), to infer from the stacked spectrum the mean luminosity weighted age and metallicity of the shells, and compare it from that derived in the inner region of the galaxy from the already existing SAURON data from the Atlas3D project (McDermid et al., 2015). This will help to determine whether the prominent shells in NGC 474 are the product of a major merger, involving strong radial mixing (in which case the age and metallicity of the stellar populations in the inner regions and in the shells should be similar) or result from the disruption of a low mass satellite, and whether the two observed shells originate from a single event or not. More importantly,

Description of the proposed programme (continued)

measures of the stellar populations inside the shell will help us to understand how this interaction mixed the stellar content of the host galaxy and will put strong contraints on simulations.
• extract the individual spectra of all GC candidates in the field. Their redshifts and spectra will confirm that they are indeed located at the same distance as NGC 474 and are thus genuine globular clusters.
• stack the pixels towards the shell structure, and derive its mean velocity from several absorption lines (Mg, Na), at a velocity resolution of about 20 km.s^{-1}. We will test the physical connection between the globular clusters and the shells and determine whether GCs can be used as tracers of the kinematics of shells.
• fit the individual spectra of the globular clusters in the same manner as the shell, to infer their age and metallicity to check their nature. This will indicate whether the GCs were made in situ during the merger that produced the shells (in that case, young ages and high metallicity are expected), or were pre-existing and associated with the primary galaxy or to the accreted low mass companion (old ages and low metallicity). In situ GC formation is expected in gas-rich mergers (Renaud et al., 2015) and was possibly observed in a shell like structure around a post-merger galaxy (Maybhate et al., 2007). However, given their lack of HI (Serra et al., 2012), it is unlikely that the shells of NGC 474 host star-forming regions even if they appear rather blue on the true color MegaCam image (see Fig. 1, left panel). The MUSE data will allow us to check that the observed shells do not host any HII region, thus eliminating any ambiguity on the birth location of our GC candidates.
• check whether the shells, besides GCs, also contain planetary nebulae (PNe) through their [OIII]λ5007 emission lines. Association of PNe with tidal features and shells have already been reported (e.g. Foster et al., 2014, Longobardi et al., 2015). PNe offer the advantage of providing spectra of higher S/N, but are however almost impossible to identify in the deep broad band images of ellipticals at our disposal.
The MUSE data cube towards these two external shells of NGC 474, together with already existing data – the deep images mapping the other shells in the system – and IFU SAURON spectra of the central region (within one *Re*) will allow us to get the observational constraints needed to build a numerical model of this spectacular galaxy. The team includes several specialists of numerical simulations of mergers.
Among the 240 early type nearby galaxies imaged as part of the MATLAS project, 40 have shells (Duc et al., 2015). For most of them, these shells are too faint for direct spectroscopy. The proposed observations will instruct us on the feasibility of getting kinematical and chemical information of collisional features using as tracers their GC (and possibly PNe) population.

Attachments (Figures)

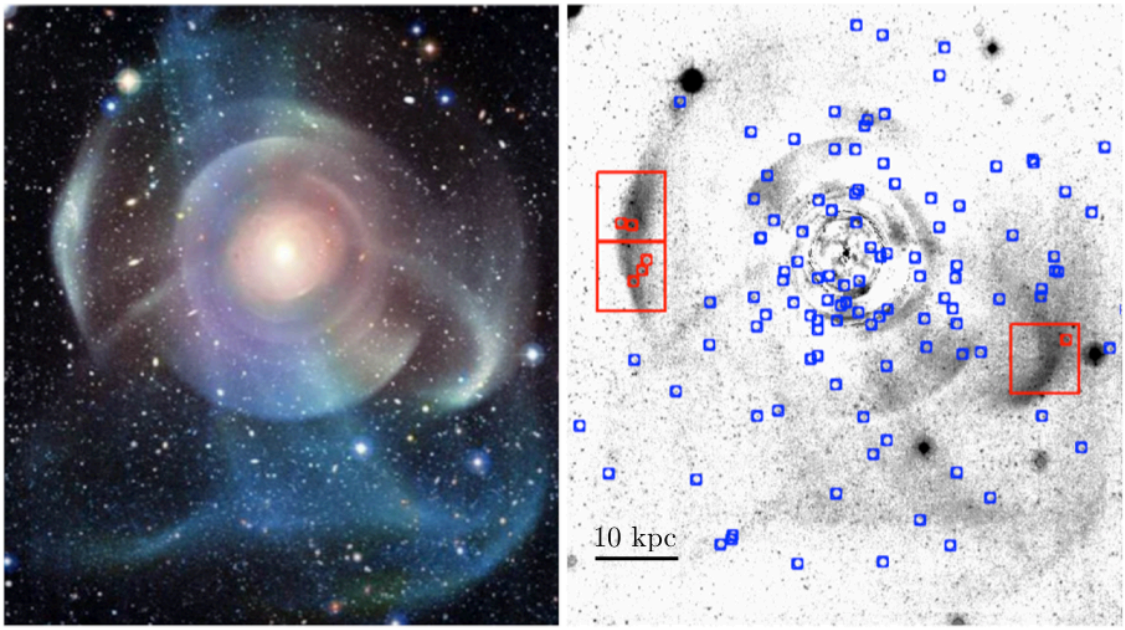

Fig.1: Right : Composite true color image of the early-type galaxy NGC 474, exhibiting multiple shells and radial structures of still unknown origin. Left: Galaxy model subtracted image, which enhances the fine structures around the galaxy. The position of the GC candidates and proposed MUSE fields are indicated.

References: Balcells et al., 2001, AJ, 122, 1758, Blom et al., 2014, MNRAS,439, 2420; Duc et al., 2015, MNRAS, 446, 120; Durrell et al.,2014, ApJ, 794, 103; Foster et al.,2014, MNRAS, 442, 3544; Longobardi et al.,2015, A&A, 579, A135; Malin & Carter 1983, ApJ, 274, 534; Schweizer 1983, AJ, 88, 7; Struck 1999, Physics Reports, 321, 1

8. Justification of requested observing time and observing conditions

Lunar Phase Justification: These spectroscopic observations can be made under gray Moon conditions.

Time Justification: (including seeing overhead) Exposure times were estimated using the MUSE ETC based on photometry carried out with optical broad-band images from Megacam at CFHT.

We wish to secure the measurements of velocity, age and metallicity and require a S/N (Signal-to-Noise) of 15 for all of the GC candidates on the flux of the Mg absorption line (at observed wavelength 5214$\mathring{A}$) which will be the noisiest absorption feature. The faintest GC candidate have a g band magnitude of 24.16 (AB). According to the ETC, the signal to noise ratio on the integrated flux of the Mg absorption line is 15 with an on source integration time of 9000s.

The average surface brightness for the shells which presumably hosts the GCs is 24.8 mag.arcsec^{-2} in the g band. With the integration time set for the GC observation, we estimate that the spectra towards the shell spatially binned with a factor of 10 by 10 (that is 2 $''\times$ 2 $''$ or 270 pc $\times$ 270 pc) will have a S/N of 20 on the integrated flux of the Mg absorption line. To get the velocity, we will sample the absorption line on around ten spectral bins, which corresponds to a spectral binning of 5. Integration time of 9000s will give a minimum S/N of 5 on each spectral bin of the Mg absorption line of the GC candidates and 10x10 spatially binned shells. The uncertainty on the velocity will be increased by the stacking of the Mg and Na absorption line. One should keep in mind that the Mg line will be the noisiest one and that the Na line will have a much larger S/N: more than 10 for each spectral bin for both GC candidates and shells.The calculations were done assuming a seeing of 0.8$''$.

Two MUSE pointings are needed to cover a significant fraction of the eastern shell and encompass the 5 GC candidates. We also want to cover the western shell with one MUSE pointing. However, we prioritize the two fields in the requested time.

Special attention will be given to the sky subtraction. This is indeed critical for absorption line studies with MUSE, especially to have a chance to detect the Ca triplet lines in the red. Fortunately, at the velocity of NGC 474, these lines lie in between sky emission lines. Several adjacent fields (S) will be targeted, interlaced with on source (O) observations. To reject cosmic rays, we will make 15 individual exposures of 10 minutes per object. Individual sky positions will be observed for 150 sec each. In order to alternate between object and sky positions, and keep total OB time below one hour, we will make the following 5 sequences 'OSOOS' par pointing. Taking into account overheads of 13 minutes per pointing each OB will last 49.3 min. The 5 observing sequences will therefore last 4.1h per object.

8a. Telescope Justification:

Given its surface brightness, IFU spectroscopy and further stacking is absolutely needed to detect absorption lines towards the shell. The crowding of the GC candidates would make slit or fibers observations very inefficient. We get them for free with MUSE. The high efficiency of MUSE will be a strong asset for these challenging observations. Its rather large field of view compared to other IFU facilities will allow us to cover a large part of the shell. Its rather good velocity precision will allow us to probe the physical association of the GC candidates with the shell.

8b. Observing Mode Justification (visitor or service):

Observations, calibrations, and scheduling are standard. We need good seeing conditions. Service observing mode is then required.

8c. Calibration Request:

Standard Calibration

9. Report on the use of ESO facilities during the last 2 years

We have obtained MUSE science verification phase data for one field on the tidal dwarf galaxy NGC 5291N (60.A-9320, PI: Duc). The data have fully been reduced and analysed in Fensch et al. (2016).

9a. ESO Archive - Are the data requested by this proposal in the ESO Archive (http://archive.eso.org)? If so, explain the need for new data.

No

9b. GTO/Public Survey Duplications:

10. Applicant's publications related to the subject of this application during the last 2 years

Bilek et al.,2014, A&A 566, A151

Bilek et al.,2015 A&A, 575, A29

Duc et al.,2015, MNRAS, 446, 120

Durrell et al.,2014, ApJ, 794, 103

Hirschman et al.,2015, MNRAS, 449, 528

Li et al.,2015, ApJ, 806, 133

Liu et al.,2015, accepted to ApJ, astro-ph:1508.07334

Liu et al.,2015, accepted to ApJ Letter, astro-ph:1508.07373

Paudel et al.,2015, AJ, 149, 114

Renaud et al.,2015, MNRAS, 446, 2038

Zhang et al.,2015 , ApJ, 802, 30

6b. Co-investigators:

...continued from Box 6a.

P.	Durrell	11515
S.	Lim	1616
C.	Liu	1681
R.	Smith	2105
M.	Bilek	10649

Sexten Center for Astrophysics
Winter workshop application 2018
Galaxy mergers and interactions across cosmic time

Workshop leaders:
Allison Man[1], Miguel Querejeta[1], Jérémy Fensch[2], Chian-Chou Chen[1]

1. European Southern Observatory, Garching, Germany
2. Laboratoire AIM Paris-Saclay, France

Workshop title: Galaxy interactions and mergers across cosmic time

Abstract:

Collisions between galaxies have long been thought to play a key role in galaxy evolution. In addition to assembling the most massive galaxies, mergers also represent the main mechanism to increase the dispersion in stellar orbits and form bulges. However, recent numerical simulations and observations support the idea that the evolution of z>2 galaxies are primarily driven by local disk instabilities, rather than mergers. Consequently, the relative importance of mergers and disk instabilities in shaping the early lives of massive galaxies remain debated. In the proposed workshop, we plan to discuss open questions relevant to the role of mergers in galaxy evolution, both near and far.

Firstly, we will discuss how to best identify a merger at z>2, both observationally and in cosmological simulations. Galaxy surveys have provided us with rich data, such as broadband imaging, spectroscopic surveys, and resolved ionized / molecular gas kinematics. However, there remain discrepancies among the various selection methods: different physical components of galaxies are traced at different wavelengths, and display merger signatures differently as the interaction proceeds. How do we ensure a fair comparison across observations, as well as with simulations? Reaching a consensus on this is fundamental to determining the role of mergers in galaxy evolution, and therefore forms the basis of the workshop.

Next, quantifying the impact of interactions on galaxy star formation histories is key to understand how massive galaxies were assembled. This subject is currently intensively investigated, thanks to new numerical simulations with unprecedented high spatial resolution that reveal the importance of the interaction-induced tidal field and interstellar medium (ISM) turbulence on star formation. Given the higher gas fraction in massive galaxies observed at z~2 compared to the local ones, do mergers only induce a milder enhancement of star formation at z~2, as claimed by recent hydro-dynamical simulations?

Finally, we would like to discuss the connection between mergers and nuclear activity, which can potentially lead to the quenching of star formation. Simulations have successfully shown that galaxy collisions can trigger gas inflows that can feed a central active galactic nucleus (AGN) and starburst. However, it remains controversial whether mergers are causally linked to AGN, both locally and at high redshift. What can we learn about the triggering mechanism of AGN? Namely, do mergers necessarily trigger AGN, and are all AGN triggered only by mergers?

We live in a crucial moment, when many of these questions can finally be tackled. On the one hand, galaxy simulations are starting to resolve gravitational instabilities in the ISM down to parsec-scales. On the other hand, new and upcoming facilities such as ALMA, JWST and ELT

will reveal how gas and stars reorganize when galaxies collide out to high redshift. The goal of this workshop is to catalyze discussions among experts working on different redshifts, techniques and wavelengths, and to foster synergies between observers and theorists. This will help build a complete picture of this fundamental phenomenon, and to identify the most fruitful instrumental avenues to explore in the near future.

Appendix B

Articles from broader collaborations

B.1 Fensch et al., 2014

In this paper, I study the color-magnitude relation of globular clusters in two nearby galaxy clusters. In particular, I investigate the *blue tilt*: for the metal-poor population of globular clusters, the more luminous, the redder.

The aim of this paper is to test a scenario of *self-enrichment*. We show that the ability of more massive globular clusters to retain their metals in their formation phase can explain this reddening effect.

This paper was published in 2014 in *Astronomy & Astrophysics*.

B.2 Lim et al., 2017

In this paper we present a catalog of globular clusters around the nearby elliptical NGC 474. This elliptical galaxy shows dramatic stellar shells from previous interactions, and probably connected globular clusters.

This paper motivated the MUSE proposal presented in Annexe A. This paper was published in 2017 in the *Astrophysical Journal*.

B.3 Ciesla et al., 2017

In this paper, we show that great care must be taken when using analytical star formation history (SFH) function inside SED model fitting codes. In particular, the rigidity of some SFH functions, such as exponentially rising or declining SFHs, struggle to model high-redshift galaxies. We propose a more flexible SFH, which allows to model the SFR of galaxies in the Main Sequence at all redshifts, but also outliers such as the starbursts and quenched galaxies.

This paper has been accepted for publication in *Astronomy & Astrophysics* (in press).

B.4 Renaud et al., 2017

In this paper we propose a numerical model for Cartwheel-like ring galaxies. With this model, we predict that the star formation activity occurs first in the ring before

being transferred to the spokes and the nucleus. Thus, the location of the star formation activity is expected to probe the dynamical state of the system. We also expect the interaction to trigger the formation of massive star clusters, although less than in more classical galaxy-galaxy interactions.

This paper was submitted to MNRAS.

A&A 567, A105 (2014)
DOI: 10.1051/0004-6361/201423971

Astronomy & Astrophysics

The colour–magnitude relation of globular clusters in Centaurus and Hydra

Constraints on star cluster self-enrichment with a link to massive Milky Way globular clusters

J. Fensch[1,2], S. Mieske[2], J. Müller-Seidlitz[3], and M. Hilker[3]

[1] École polytechnique, route de Saclay, 91128 Palaiseau, France
e-mail: jeremy.fensch@gmail.com
[2] European Southern Observatory, Alonso de Cordova 3107, Vitacura, Santiago de Chile, Chile
[3] European Southern Observatory, Karl-Schwarzschild-Str. 2, 85748 Garching b. München, Germany

Received 9 April 2014 / Accepted 30 May 2014

ABSTRACT

Aims. We investigate the colour–magnitude relation of metal-poor globular clusters, the so-called blue tilt, in the Hydra and Centaurus galaxy clusters and constrain the primordial conditions for star cluster self-enrichment.
Methods. We analyse U, I photometry for about 2500 globular clusters in the central regions of Hydra and Centaurus, based on VLT/FORS1 data. We measure the relation between mean colour and luminosity for the blue and red subpopulation of the globular cluster samples. We convert these relations into mass-metallicity space and compare the obtained GC mass-metallicity relation with predictions from the star cluster self-enrichment model by Bailin & Harris (2009, ApJ, 695, 1082). For this we include effects of dynamical and stellar evolution and a physically well motivated primordial mass-radius scaling.
Results. We obtain a mass-metallicity scaling of $Z \propto M^{0.27 \pm 0.05}$ for Centaurus GCs and $Z \propto M^{0.40 \pm 0.06}$ for Hydra GCs, consistent with the range of observed relations in other environments. We find that the GC mass-metallicity relation already sets in at present-day masses of a few 10^5 $M_\odot$ and is well established in the luminosity range of massive MW clusters like ω Centauri. The inclusion of a primordial mass-radius scaling of star clusters significantly improves the fit of the self-enrichment model to the data. The self-enrichment model accurately reproduces the observed relations for average primordial half-light radii $r_\mathrm{h} \sim 1$–1.5 pc, star formation efficiencies $f_\star \sim 0.3$–0.4, and pre-enrichment levels of [Fe/H] -1.7 dex. The slightly steeper blue tilt for Hydra can be explained either by a ∼30% smaller average r_h at fixed $f_\star \sim 0.3$, or analogously by a ∼20% smaller $f_\star$ at fixed $r_\mathrm{h} \sim 1.5$ pc. Within the self-enrichment scenario, the observed blue tilt implies a correlation between GC mass and width of the stellar metallicity distribution. We find that this implied correlation matches the trend of width with GC mass measured in Galactic GCs, including extreme cases like ω Centauri and M 54.
Conclusions. First, we found that a primordial star cluster mass-radius relation provides a significant improvement to the self-enrichment model fits. Second we show that broadened metallicity distributions as found in some massive MW globular clusters may have arisen naturally from self-enrichment processes, without the need of a dwarf galaxy progenitor.

Key words. supernovae: general – globular clusters: general – galaxies: star clusters: general – stars: formation

1. Introduction

1.1. Colour magnitude relation of extragalactic globular clusters

The broadband colour distribution of globular clusters (GCs) exhibits a strong bimodality especially in globular cluster systems of massive galaxies (e.g. Gebhardt & Kissler-Patig 1999; Kundu & Whitmore 2001, Larsen et al. 2001), which is often interpreted as a result of star formation and galaxy assembly processes in the early universe (see the review of Brodie & Strader 2006). In the last decade, *Hubble* Space Telescope (HST) and ground-based wide-field imaging of hundreds of GC systems has provided us with very detailed information on bimodality (e.g. Dirsch et al. 2003; Bassino et al. 2006; Peng et al. 2006; Harris et al. 2006, 2013; Forbes et al. 2011; Kartha et al. 2014).

One of the surprising outcomes of those studies is a correlation between colour and magnitude for GCs of the blue subpopulation (e.g. Harris et al. 2006, 2009a,b; Strader et al. 2006; Mieske et al. 2006, 2010; Spitler et al. 2006; Humphrey 2009; Cockcroft et al. 2009; Forbes et al. 2010; Blom et al. 2012; Usher et al. 2013). This phenomenon has been nicknamed the blue tilt, and has also been detected through ground-based imaging (Forte et al. 2007; Wehner et al. 2008; Park 2012). The first strong hint of the existence of such a colour-magnitude relation of GCs was reported in Dirsch et al. (2003), who found that the colour distribution of the brightest GCs in NGC 1399 becomes broad and unimodal. Direct evidence from spectroscopic observations was recently reported for M 31 GCs (Schiavone et al. 2013).

Interpreted as a mass-metallicity relation, the blue tilt is equivalent to a scaling with mass of $Z \propto M^{0.3-0.7}$, that depends on environment. Results have so far indicated that the trend sets in already at masses slightly below a million solar masses, at several 10^5 $M_\odot$. The most common interpretation of this colour-metallicity relation is self-enrichment. With increasing primordial cluster mass (and thus increasing potential well depth), a larger fraction of SN II metal ejecta are kept in the cluster and reprocessed into a second generation of stars (Strader & Smith 2008; Bailin & Harris 2009). Furthermore a red tilt, i.e. a colour magnitude relation for the red GC subpopulation, has been reported in some cases, but it typically is less significant and weaker in metallicity space (e.g. Harris et al. 2006; Mieske et al. 2006, 2010).

It is worth noting that colour changes as a function of GC mass can also occur as a result of dynamical evolution, via preferential loss of low-mass stars (Kruijssen & Lamers 2008; Anders et al. 2009; Kruijssen 2009). This makes lower-mass GCs bluer than their colour for an unaltered stellar mass function, thus qualitatively creating a trend in the direction of the blue tilt. This effect was investigated for example in Mieske et al. (2010) and particularly in Goudfrooij et al. (2014) who studied how it depends on the shape of the Initial Mass Function (IMF). However, it is clear that the observed blue tilt can only be explained in small part by this effect: the observations indicate a strengthening of the effect at high cluster masses (Harris et al. 2006; Mieske et al. 2010), exactly opposite to expectations from dynamical evolution: higher mass clusters are less affected by dynamical evolution (Baumgardt & Makino 2003), and thus colour changes from this effect will level off at higher cluster masses.

An important aspect to keep in mind is that the cluster-to-cluster scatter of mean metallicity due to local variations in primordial star forming conditions is significant, and will dominate smooth internal trends with cluster mass for small samples of globular clusters (see e.g. Bailin & Harris 2009). To filter out underlying trends like self-enrichment from broadband integrated photometry, one needs large homogeneous data sets of GCs, typically more than ∼1000 GCs. For example, for the Milky Way no blue tilt is detectable because of the considerable cluster-to-cluster scatter in mean [Fe/H] and the comparably small sample size (e.g. Strader & Smith 2008). Moreover, the Milky Way GC sample has a rather low upper-mass limit ($M_{\omega\mathrm{Cen}} = 1.5{*}10^6\,M_\odot$), which is another factor for the non-detectability of the blue tilt in our Galaxy.

1.2. Multiple stellar populations in massive Galactic GCs

Almost parallel in time to the discovery of the blue tilt in extragalactic GC samples, HST imaging of individual stars in Galactic GCs also revealed striking new features: there are multiple stellar populations in almost every intermediate-to-high mass GC that has been studied in detail (e.g. Bedin et al. 2004; Piotto et al. 2005, 2012; Milone et al. 2012a,b,c). This has further enhanced the interest in self-enrichment scenarii for star clusters. It is typically assumed that self-enrichment from SN ejecta are required to obtain a broadened stellar metallicity distribution of red giants as seen for example in ω Centauri and M 54 (e.g. Willman & Strader 2012), for which a present-day onset mass of around a million solar masses is consistent with the data in the Milky Way. Re-processing of ejecta from evolved stars is, in turn, often considered a scenario for creating multiple populations at constant metallicity (e.g. Ventura et al. 2001; D'Antona et al. 2002, 2005; D'Ercole et al. 2008; Maxwell et al. 2014), which can occur at about one order of magnitude lower in cluster masses than enrichment from SN ejecta (Baumgardt et al. 2008).

1.3. This paper

In this paper we put special emphasis on how a fit of SN self-enrichment models to our data constrains the primordial structure and star formation conditions in massive star clusters.

We analyse the colour-magnitude relation of GCs in the central 100 kpc of the Hydra and Centaurus galaxy clusters. We use deep $U-I$ imaging with VLT/FORS1 at very good seeing. We analyse a sample of about 2500 GCs in each cluster, down to a limiting magnitude about 0.5 mag brighter than the GCLF turnover. The usage of the U-band gives us a very broad wavelength baseline that improves our metallicity resolution compared to other studies. Furthermore, our homogeneous data set allows us to perform a robust comparison between the two investigated environments.

The structure of the paper is as follows. In Sect. 2 we discuss the data reduction and selection of GC candidates. In Sect. 3 we measure the mass-metallicity relations of GCs in Hydra and Centaurus. In Sect. 4 we constrain a star cluster self-enrichment model by comparing its prediction to the measured relation. We focus on the inclusion of previously not considered physical features into the model, and on the degeneracy between the input parameters of the model. We also convert the global mass-metallicity relation into a mass-metallicity *spread* relation, and compare this to Milky Way GCs. We provide Summary and Conclusions in Sect. 5.

2. Data

2.1. Observations

The data analysed for this paper were all taken in service mode with VLT/FORS1. The I-band photometry was obtained in the course of programmes 065.N-0459 (Hydra, PI Hilker) and 067.A-0358 (Centaurus, PI Hilker), with 3000 s integration time in I-band per $7 \times 7'$ FORS pointing, at good seeing 0.4−0.7″ in seven FORS pointings in Centaurus and Hydra and one background pointing. Those data were already presented in Mieske et al. (2003, 2005) in an SBF analysis of both clusters. This I-band data set also comes along with V-band data taken in the same runs and under similar conditions. The V-band data is not used directly for our blue tilt analysis, but we use the $V-I$ colour distribution to finetune the $U-I$ colour calibration, see Sect. 2.2.1. For the present work, these I- (and V-) data were carefully re-reduced.

The U-band data was obtained in programmes 080.A-0647 & 082.A-0894 (PI Hilker) with about 0.8″ seeing, in three FORS pointings in Centaurus, two in Hydra and one background pointing in each cluster. The on-source integration in U-band was about 2 h per pointing.

In Fig. 1 we show a colour-composite image of the two target clusters, created from the FORS imaging data in U, V, I. Figure 2 shows a map with the projected positions of GC candidates with U, I photometry. The background fields are situated at $\alpha = 189.78$, $\delta = -41.35$ for Centaurus and $\alpha = 160.9$, $\delta = -27.48$ for Hydra, about 2° away from the respective cluster centres. More details on the reduction and analysis of the data will be given in a forthcoming paper (Hilker et al., in prep.).

2.2. Data reduction

The raw data were processed with IRAF[1]. We performed standard bias subtraction, flat fielding and bad pixel removal. We then registered and combined the single integrations. The next step was to model and subtract the extended light from bright galaxies, to enable clean photometry of point source close to the galaxy centers. We did so using a combination of IRAF's *rmedian* task, and galaxy light modelling with IRAF's *ellipse* task.

[1] IRAF is distributed by the National Optical Astronomy Observatories, which are operated by the Association of Universities for Research in Astronomy, Inc., under cooperative agreement with the National Science Foundation.

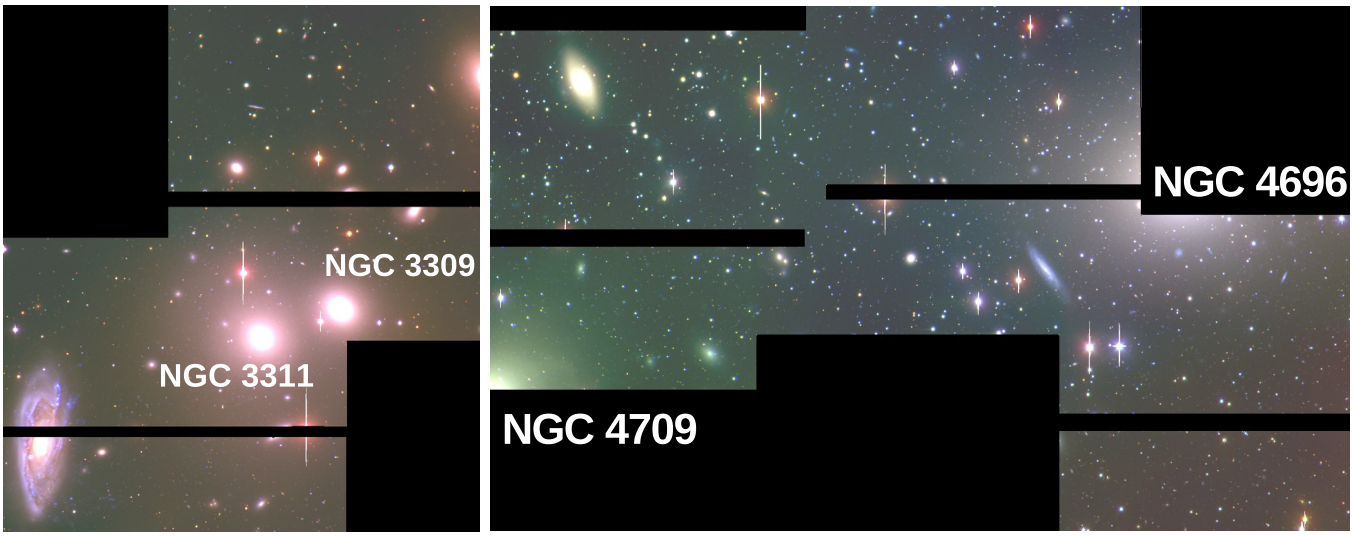

Fig. 1. FORS U, V, I composite-images showing the investigated region of the Hydra (*left*) and Centaurus (*right*) clusters. The two main central cluster galaxies are indicated. For Centaurus, the imaging covers the intra-cluster part between NGC 4696 and NGC 4709, while for Hydra the imaging is centred on NGC 3311. Projected physical scale is about 100×100 kpc per FORS pointing in Hydra, and 90×90 kpc in Centaurus (assuming a NED distance of 47.8 Mpc to Hydra and 43.2 Mpc to Centaurus).

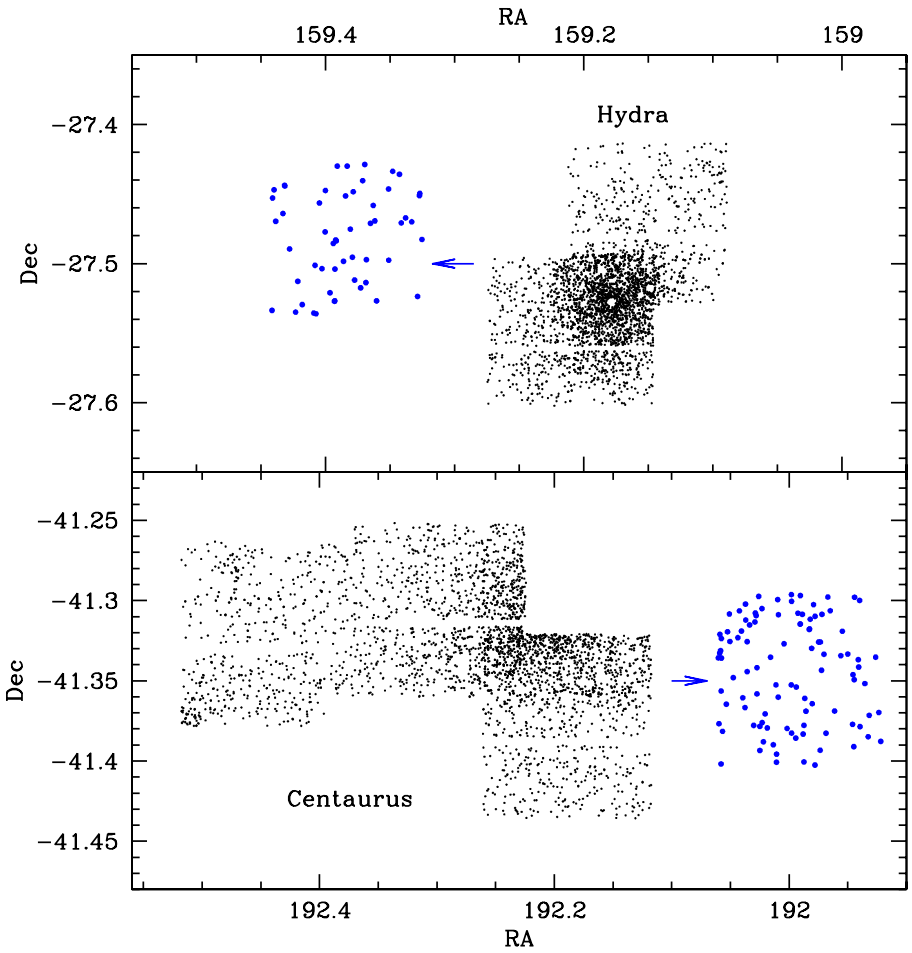

Fig. 2. Projected position of photometrically selected GC candidates in Hydra and Centaurus in our $U - I$ FORS1 imaging data. See text for details on the GC selection. The sources detected in the background field with the same photometric selection criteria are indicated as (blue) dots for comparison. The actual location of the background field in each cluster was about 2 degrees away, in the direction indicated by the arrow. *Top*: Hydra. *Bottom*: Centaurus. Projected physical scale is about 100×100 kpc per FORS pointing in Hydra, and 90×90 kpc in Centaurus.

Diffuse galaxy light is thus removed apart from their very central regions. The PSF photometry of point sources was performed with the standard IRAF routine *psf* within the *daophot* package.

Photometric calibration was done using regular standard star observations within ESO's calibration plan. We corrected relative offsets between different pointings (not all nights were photometric) by using overlap regions of adjacent fields, and using the central pointing in each cluster as reference. These relative calibrations worked very well for the I-band with residual inaccuracies of the level of 0.02−0.03 mag. However, the U-band data could not be calibrated down to this accuracy, given the low number of standard stars available in U, lower flux

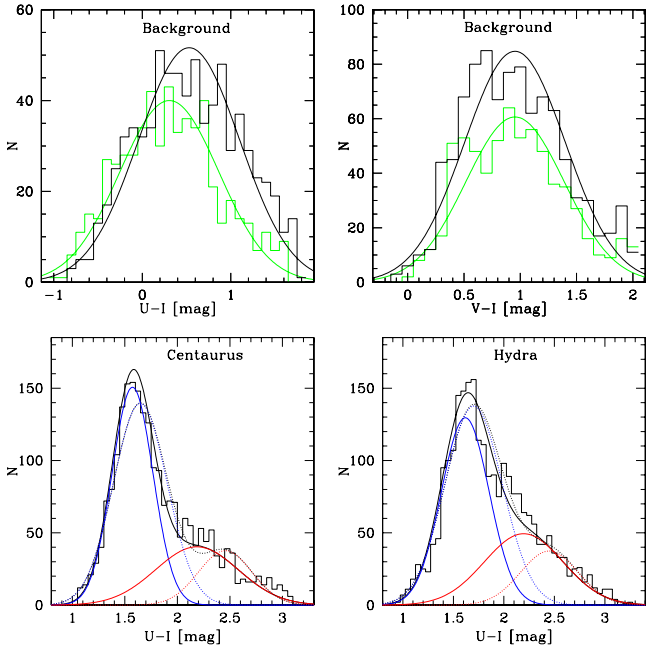

Fig. 3. *Top*: colour distribution of the background fields: Centaurus is in black and Hydra in green. *Left panel*: $U-I$. *Right panel*: $V-I$. The lines correspond to single Gaussian peaks fitted with KMM. Because of the shift in $U-I$ between both clusters, symmetric shifts of ±0.11 mag are applied to the U-band zeropoints for Hydra and Centaurus, see text for details. *Bottom*: finally adopted $U-I$ colour distribution of the full Hydra (*left*) and Centaurus (*right*) cluster GC samples (restricted to the later used fitting range $I < 24$ mag). The coloured lines represent the Gaussian fits by *KMM* to the blue and red peak. The black lines are the sum of the two. The dotted lines represent the results using the homoscedastic mode; the solid lines correspond to the heteroscedactic mode.

levels, and smaller overlap between adjacent fields. Therefore we applied an additional, relative $U-I$ colour scale calibration between Hydra and Centaurus as described in the following.

2.2.1. Relative calibration of $U-I$ colour scale

The top panels of Fig. 3 show the $U-I$ (left) and $V-I$ (right) colour distribution of sources detected in the background fields for Hydra and Centaurus. While the $V-I$ distribution of both samples peaks at the same colour within the error bars, there is a shift of about 0.2 mag in $U-I$ between Hydra and Centaurus. Using KMM (Ashman et al. 1994), the precise value of the shift is determined to be 0.22 mag. We interpret this colour shift as a residual systematic uncertainty of the U-band photometric calibration in Hydra and Centaurus, as noted in the previous subsection. In order to compare the two samples on the same absolute colour scale, we add to the U-band an offset of −0.11 mag to Centaurus sources and +0.11 mag to Hydra in the following. The bottom panels of Fig. 3, which show the Centaurus and Hydra GC colour distribution in $U-I$, include those offsets.

2.3. Selection of globular clusters

The first step was to remove resolved sources by a combined cut-off in the IRAF PSF parameters χ and *Sharpness*. This reduced the contamination by a factor of two.

The second step was to introduce a realistic colour cut-off condition that corresponds to the extreme $U-I$ colours expected for GCs. Such values were taken from the metallicity distribution of Milky Way GCs obtained by Harris (1996, 2010), that is $[\frac{\mathrm{Fe}}{\mathrm{H}}] = -2.4$ and $[\frac{\mathrm{Fe}}{\mathrm{H}}] = 0.3$, converted into a $U-I$ colour range of 1.3 to 3.0 mag using TERAMO models (Raimondo et al. 2005) evaluated at 11−13 Gyr age (Figs. 4 and 6). We broadened these borders by the maximum measurement error as a function of luminosity, as indicated by the solid lines in Fig. 4.

To remove the remaining contamination by unresolved foreground stars and background galaxies in the colour range expected for GCs, a comparison between the science field and the background field was done. For this we divided the colour-magnitude plane in cells with rows of 200 GCs and 0.1 mag colour width, see Fig. 4. Sources in Hydra and Centaurus were then randomly deleted in each cell according to the number of background points in the cell, and the respective ratio between the area coverage of cluster and background sample: 3:1 in Centaurus and 2:1 for Hydra.

After background subtraction, the final GC candidate sample comprised 2590 sources for Centaurus, and 2365 sources for Hydra.

3. Data analysis

3.1. Fitting procedure

To measure the colour of the blue and red peak as a function of GC luminosity, we applied a hybrid approach using both KMM and colour distribution medians (see also Mieske et al. 2006). This is outlined in the following.

In the bottom panel of Fig. 3 we show the $U-I$ colour histogram of the GC candidates in Hydra and Centaurus, limited to $I < 24$ mag. The distribution is not obviously bimodal, but does have a large tail towards red colours that cannot be fitted by a single Gaussian. In that figure we indicate the fitted colour peaks using KMM, both in heteroscedastic and homoscedastic mode. It is clear that the output of both modes differ, indicating that the width of the blue and red peak are not identical. Therefore, a heteroscedastic fit is more appropriate to our sample than a homoscedastic fit.

At the same time, we found that such heteroscedastic fits increase the scatter between adjacent luminosity bins, i.e. when subdividing the sample into a number of smaller subsamples. Our aim in the fitting is to represent the heteroscedastic nature of our sample, but at the same time provide a stable peak determination as a function of luminosity. Therefore we measured in each luminosity bin of 200 GCs the median colour blue- and redwards of a constant dividing line between blue and red sequences (see also Fig. 5 of Mieske et al. 2006), itself determined from a heteroscedastic KMM fit to the full sample. We adopt such a constant dividing line – as opposed to a limit that varies as a function of luminosity – to ensure that a distribution without any colour-magnitude relation would be correctly recovered. This limiting colour is $U-I = 1.93$ mag for Centaurus and 1.99 mag for Hydra (Fig. 3). It corresponds to about [Fe/H] = −0.9 dex, within ∼0.1 dex of the limit found in the Milky Way GC system (Harris et al. 1996, see e.g. Fig. 2 of Strader & Smith 2008). Luminosities fainter than $I = 24$ mag are not included for the fit because of a lack of faint red clusters (incompleteness) that would introduce a bias in our analysis.

In Fig. 5 we show the resulting blue and red peak colours as a function of GC luminosity for the Hydra and Centaurus samples. We note that this distribution is not 100% deterministic because of the background source subtraction that is performed randomly within colour-magnitude cells as desribed in Fig. 4. To take this

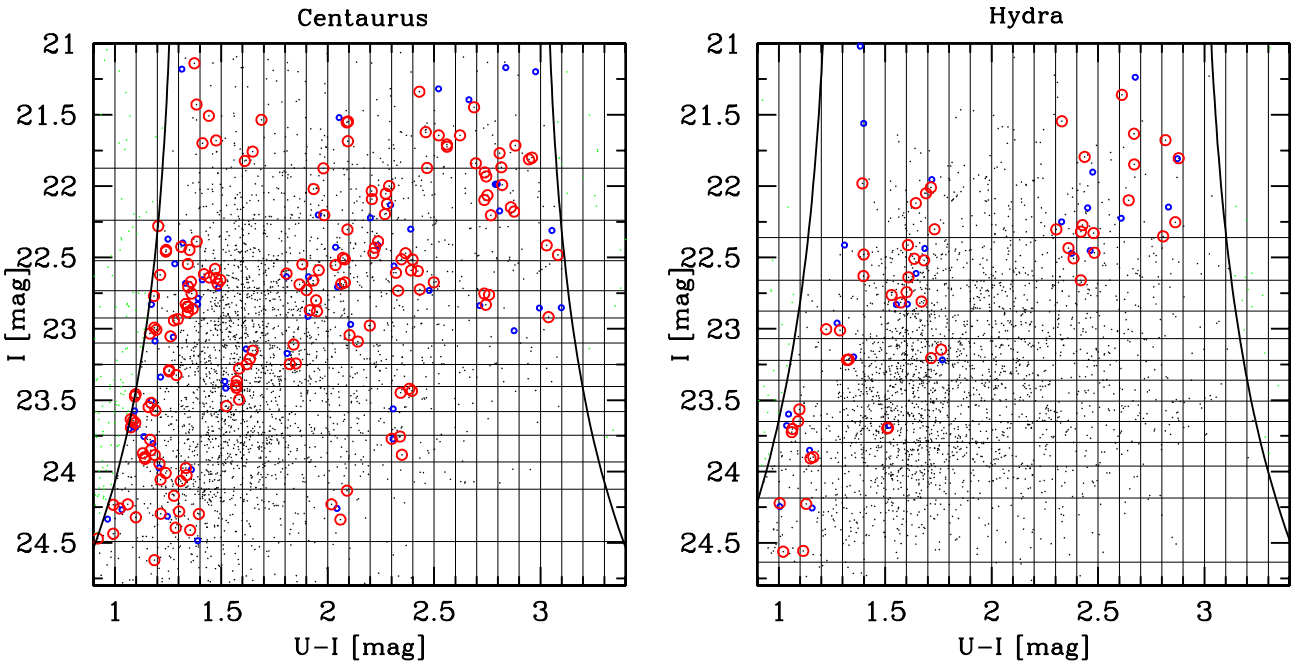

Fig. 4. Colour–magnitude diagram in $U-I$ of all unresolved sources detected in both galaxy clusters. The black curved lines represent the colour cut-off applied to disregard sources either too blue or too red to be considered old GCs. The horizontal lines define rows of 200 GCs, and the vertical lines define columns of 0.1 mag. Within the cells defined by the horizontal and vertical lines, a random background subtraction is performed: the blue circles indicate colours and magnitudes of the background sources. Red circles indicate sources that were removed based on the background source distribution, within the indicated cells. We note that the very brighest magnitude regions $I < 21$ mag are excluded from the plot to focus on the main body of GCs.

into account for the fitting of the slope between colour and magnitude, we perform this fitting based on 100 different random background subtractions. To each individual run, we apply an unweighted least squares fit (each magnitude bin comprises the same number of data points) of a linear relation to these data points, whose slope we denote as $\gamma = \mathrm{d}(U-I)/\mathrm{d}(I)$.

We indicate the resulting average slopes and their error bars in Table 1, and also indicate the (small) additional statistical error arising from the random background subtraction. We obtain slopes for the blue peak of $\gamma = -0.057 \pm 0.011$ for Centaurus and $\gamma = -0.081 \pm 0.012$ for Hydra, thus finding a highly significant blue tilt in both clusters. A red tilt is also detected for Centaurus, with $\gamma = -0.086 \pm 0.015$. The error bars are derived from the scatter of the data points with respect to the fitted relation.

3.2. Mass-Metallicity relations

In the previous subsection we find a clear blue tilt for the Hydra and Centaurus cluster. To investigate this in more detail it is necessary to convert the colour–magnitude relation into a more physical mass-metallicity relation.

To this end, we convert I-band magnitude into mass using:

- A colour-independent mass-to-light ratio of $\Gamma = 2.2$, based on the models of Maraston (2005) and Bruzual & Charlot (2003).
- A NED distance of 47.8 Mpc to Hydra and 43.2 Mpc to Centaurus.
- An absolute magnitude $M_I = 4.13$ mag of the Sun. The resulting mass range of GCs is $\sim 5\times10^5$ to 5×10^6 solar masses.

Colour $U-I$ is converted into metallicity using a piecewise linear function representing the TERAMO Models (Raimondo et al. 2005) for an assumed age of 11–13 Gyr, see Fig. 6. We adopt two lines of different slopes that intersect at $U-I = 2.07$, which is accurate to within 0.1 dex compared to the model predictions. The conversion from $U-I$ to [Fe/H] thus is

$$[\mathrm{Fe/H}] = -0.702 + 1.94 \times [(U-I) - 2.0688] \quad (1)$$

for $(U-I) <= 2.0688$ ($[\mathrm{Fe/H}] \leq -0.702$). And,

$$[\mathrm{Fe/H}] = -0.702 + 1.04 \times [(U-I) - 2.0688] \quad (2)$$

for $(U-I) > 2.0688$ ($[\mathrm{Fe/H}] > -0.702$).

We note that a polynomial fit is problematic for the extrapolation to colours bluer than the model limits at $U-I \lesssim 1.55$ mag ($[\mathrm{Fe/H}] \lesssim -1.8$ dex), which is why we prefered a piecewise linear approximation of the models.

The resulting data points in mass-metallicity space are shown in Fig. 7 for both Hydra and Centaurus along with a linear fit to the data. The slopes of the linear fits are listed in Table 1 in terms of the exponent α in $Z \propto M^{\alpha}$. In particular we find $Z \propto M^{0.27\pm0.05}$ for GCs in Centaurus and $Z \propto M^{0.40\pm0.06}$ for GCs in Hydra along the blue sequence.

4. Discussion

In this section we compare our findings to predictions of the self-enrichment model of Bailin & Harris (2009). This includes a detailed discussion of how our findings can be used to constrain GC mass and radius evolution and primordial star formation efficiencies in the context of that model.

4.1. The default model parameters of Bailin & Harris (2009)

Both in Strader & Smith (2008) and Bailin & Harris (2009) self-enrichment scenarii of star clusters are discussed with a focus on

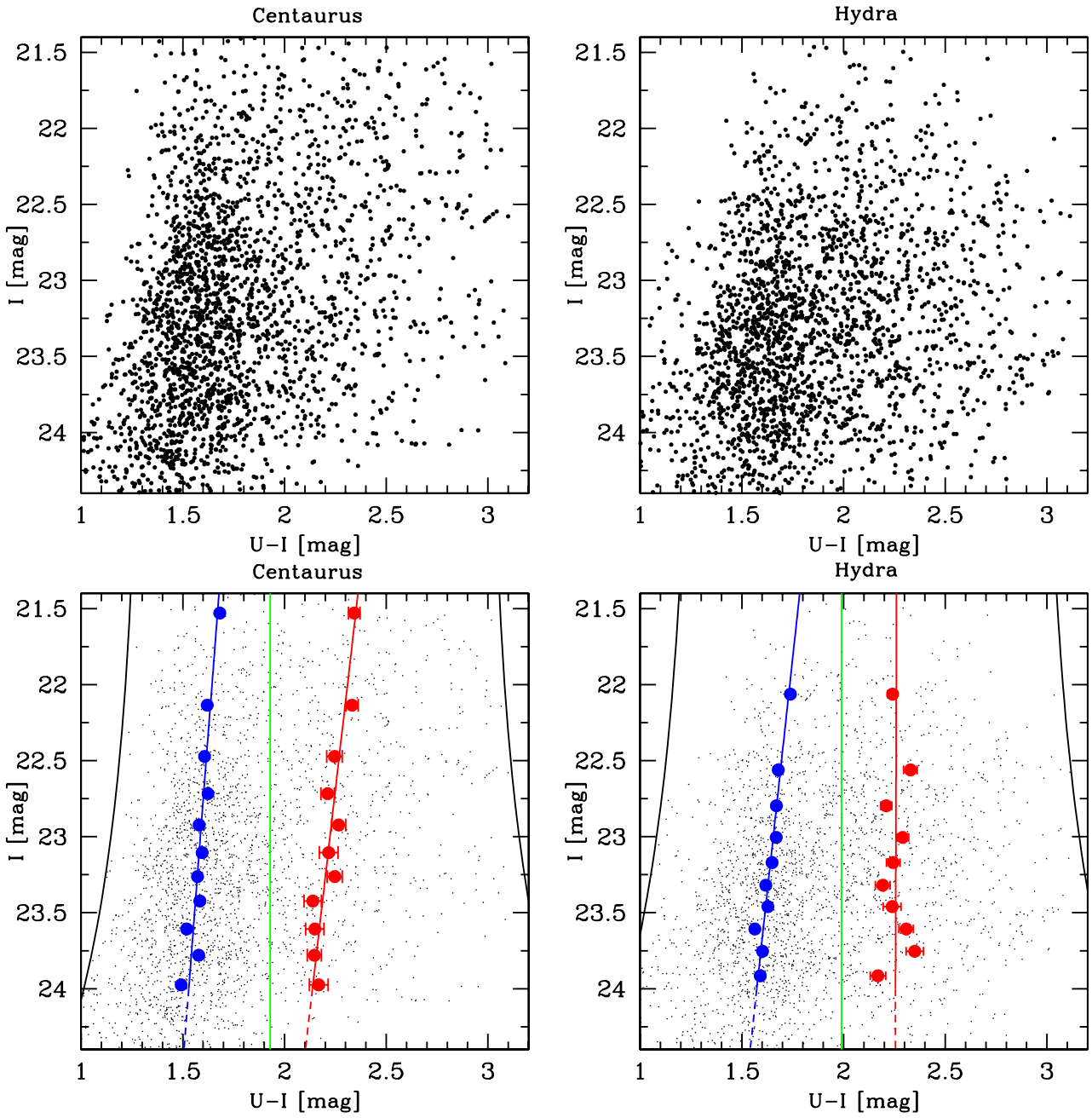

Fig. 5. Colour–magnitude diagrams of the final GC samples for Centaurus (*left*) and Hydra (*right*). The individual data points in the *top* and *bottom plot* are the same. In *the bottom plots* additional filled circles in blue and red indicate the median colours between the black limiting curves at extreme colours and the (green) fixed dividing line between the blue and red peak. The blue and red lines indicate least squares fits to the median colours as a function of magnitude.

Table 1. Value of the blue tilt slope $\gamma = \mathrm{d}(U-I)/\mathrm{d}I$ and of the mass-metallicity relation exponent α obtained for Centaurus and Hydra with our data for the range $I < 24.0$ mag, compared to results of previous studies on these clusters and other environments.

Sample	γ blue	α blue ($Z \propto M^{\alpha}$)	γ red	α red ($Z \propto M^{\alpha}$)
Centaurus	−0.057 ± 0.011 [±0.003]	0.27 ± 0.05	−0.086 ± 0.015 [±0.002]	0.22 ± 0.04
Hydra	−0.081 ± 0.012 [±0.005]	0.40 ± 0.06	−0.002 ± 0.034 [±0.004]	0.01 ± 0.09
Hydra (Wehner et al. 2008)		0.60 ± 0.20		
BCGs (Harris et al. 2009a)		0.48 ± 0.12		−0.11 ± 0.06
M104 (Harris et al. 2010)		0.29 ± 0.04		
FCS (Mieske et al. 2010)		0.38 ± 0.08		0.03 ± 0.05
VCS (Mieske et al. 2010)		0.62 ± 0.08		0.12 ± 0.05

Notes. In brackets we also indicate the errors arising from the randomised background subtraction in magnitude–colour cells.

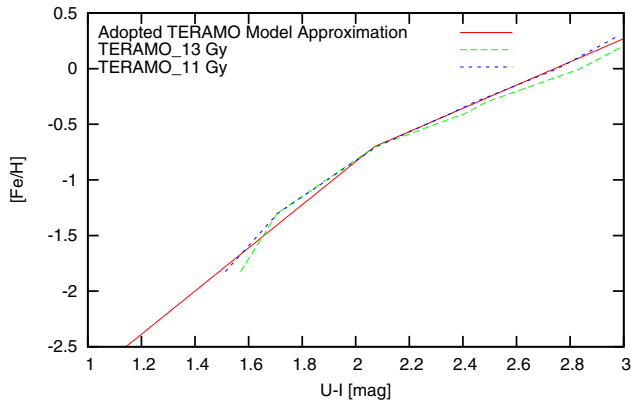

Fig. 6. Metallicity [Fe/H] as a function of $U-I$ colour according to TERAMO Models (Raimondo et al. 2005) for 11 and 13 Gyr old single stellar populations. The solid red line indicates the adopted piecewise linear approximation that we adopt for the transformation from $U-I$ to [Fe/H] in this paper, see Eqs. (1) and (2).

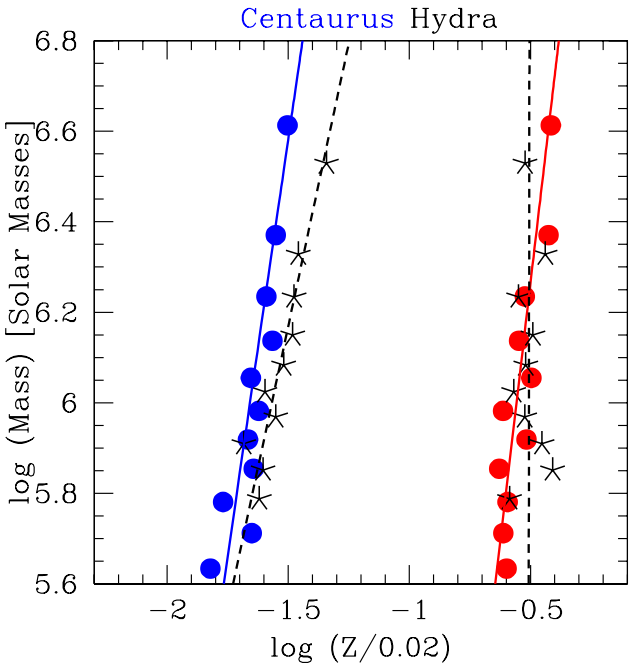

Fig. 7. Mass-metallicity relations of GCs in Centaurus and Hydra, as converted from the $U-I$ colour magnitude relations shown in Fig. 5. Centaurus is shown in blue/red filled circles, Hydra in black asterisks. Lines indicate unweighted linear fits to the data.

the blue tilt. The basic idea of self-enrichment is simple. Self-enrichment (by SNII ejecta) starts to become efficient when the gravitational binding energy (∝mass) of and gas ram pressure within the primordial cluster becomes comparable to the kinetic energy output of SNII. In the following detailed discussion we focus on the more recent model of Bailin & Harris.

To calculate the resulting metallicity in a globular cluster as a consequence of self-enrichment, Bailin & Harris used as factor of parametrisation the metal-retention fraction f_Z, which is obtained from the competition between SNII kinetic energy output gravitational potential, (Eq. (28) of their paper):

$$f_Z = \mathrm{e}^{-\frac{f_\star E_{\rm SN} r_{\rm t}}{10^2\, M_\odot G M_{\rm C}}}. \quad (3)$$

This expression is valid for a density profile of an isothermal sphere ($\rho \propto r^{-2}$). $f_\star$ denotes the star formation efficiency, i.e. the fraction of primordial gas that is converted to stars. $E_{\rm SN} = 10^{51}$ erg is the typical energy released by one SN II, $M_{\rm C}$ is the mass of the proto-cluster cloud, and $r_{\rm t}$ is the truncation radius, which is identified with the half-light radius $r_{\rm h}$ in the following (see also Mieske et al. 2010). The factor 10^2 in the denominator of the exponent comes from the fact that (for a Salpeter/Kroupa type high-mass IMF) about one SN is formed per 100 solar masses formed in stars (Fig. 3 of their paper). For $\beta \neq 2$, one obtains f_Z (Eq. (36) of their paper):

$$f_Z = \left(1 - \frac{f_\star^2 E_{\rm SN} r_{\rm h} (2-\beta)}{10^2\, M_\odot G M_{\rm GC}}\right)^{\frac{3-\beta}{2-\beta}}. \quad (4)$$

Both f_z and f_* are then used as scaling factor in the following basic equation describing the final cluster metallicity $Z_{\rm C}$ obtained by including self-enrichment (Eq. (7) of Bailin & Harris):

$$\log_{10}\left(\frac{Z_{\rm C}}{Z_\odot}\right) = 0.38 + \log_{10}(f_\star f_Z) + \log_{10}\left(\frac{Z_{\rm pre}}{Z_\odot}\right) \quad (5)$$

where 0.38 is adopted from previous studies (Woosley et al. 1995 and Nomoto et al. 1997). $Z_{\rm pre}$ is the pre-enrichment of the globular cluster, i.e. the average metallicity of its first generation of stars. In their default model, Bailin & Harris assume $f_\star = 0.3$, $r_{\rm h} = 1$ pc, and an isothermal sphere with $\rho \propto r^{-2}$.

In Fig. 8 we overplot the model predictions using the above default parameters to our data for Hydra and Centaurus. The only parameter that is undefined in this case is the pre-enrichment level $Z_{\rm pre}$. We find that values of $\log_{10}(\frac{Z_{\rm pre}}{Z_\odot}) = -1.70$ and -0.55 for Centaurus and -1.60 and -0.50 for Hydra give the lowest deviation between the model and the data.

The default model in Fig. 8 does not agree well with our data. The predicted (model) slope for high mass GCs is too strong. Furthermore, the continuation of the mass-metallicity relation towards lower masses as found by the data is not predicted by the model. A similar conclusion was found in Mieske et al. (2010) based on the blue tilt measurement for the Fornax and Virgo clusters from HST data. In that article we show that the tilt becomes notable one order of magnitude in mass below the on-set mass expected by the above default self-enrichment model. With the present (ground-based) data we thus confirm this finding in a different environment.

In this context one should not forget that self-enrichment takes place very early in the evolution of a star clusters. It is assumed to happen after the explosion of the most massive stars, when their ejecta cools down and pollutes the material of forming stars. This happens approximately 5 Myr after the beginning of the stellar formation process (Bailin & Harris 2009). It is crucial for the model that the pollution of the ISM by SN ejecta occurs before the bulk of (lower-mass) stars is formed.

It is thus important for the input parameters of the self-enrichment model to represent as accurately as possible the initial conditions of the clusters. Turning the argument around, comparing predictions of self-enrichment models to actual data allows us to constrain the initial star formation conditions in globular clusters. In particular, mass loss and the mass-radius relation of primordial GCs are very important in shaping the present-day observed mass-metallicity relation. We will discuss this in detail in the next two subsections.

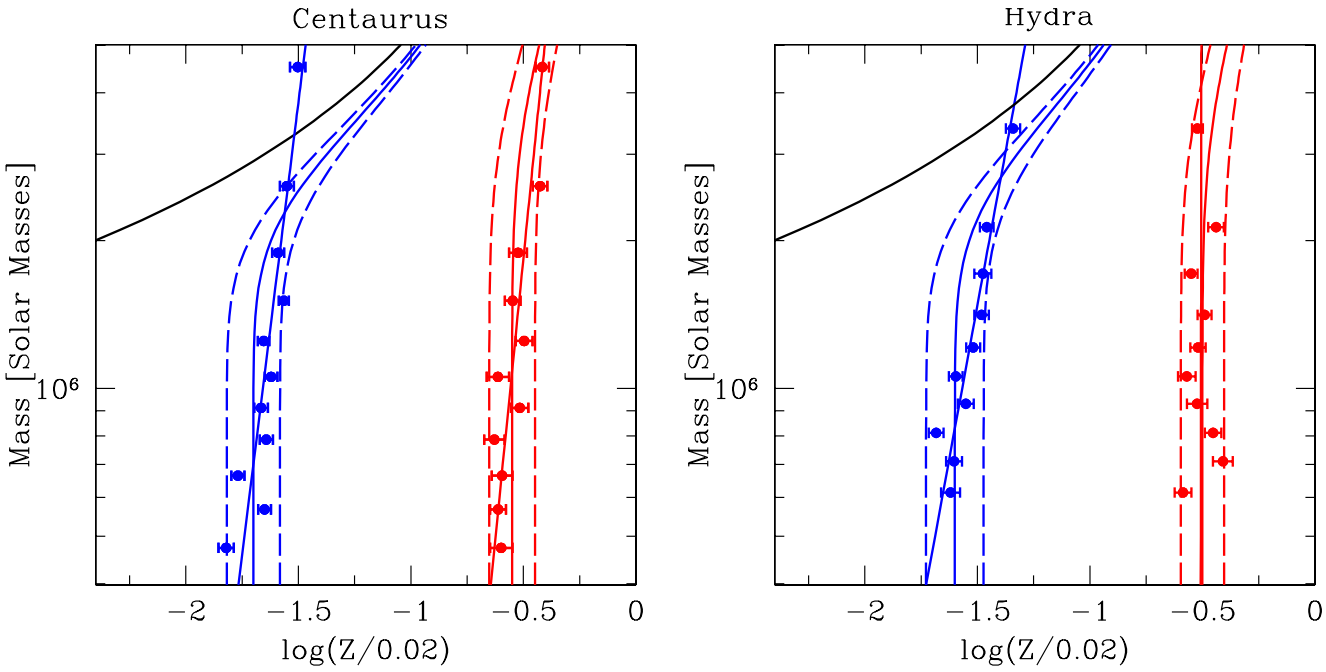

Fig. 8. Comparison between the measured mass-metallicity data points of GCs in Hydra/Centaurus, and the default version of the self-enrichment model by Bailin & Harris. The Y axis is the current mass of the GCs. The black curve shows the self-enrichment model with $\beta = 2$ and $f_\star$ =0.3. The blue and red solid curves are the result of the combination between self-enrichment and pre-enrichment. The dashed lines represent the scatter in colour of the points used in Fig. 5, converted into metallicity. The straight lines are the linear fits from Fig. 7.

4.2. Inclusion of GC mass and radius evolution into the model

4.2.1. Mass loss

During its life time, a globular cluster will undergo mass loss due to stellar and dynamical evolution (e.g. Lamers et al. 2005, 2010; Kruijssen 2009). This accumulated mass loss has two effects.

A) Based on the present-day mass as known from observations, the accumulated mass loss determines the primordial stellar cluster mass after star formation had finished. This primordial mass is the value to be adopted as globular cluster mass $M_{\rm GC}$ in Eq. (4). We reiterate that the mass of the cluster's progenitor gas cloud is still higher than this by a factor of $1/f_\star$, with $f_\star$ being the star formation efficiency at the time of cluster formation (Eq. (4)).

B) Preferential loss of late dwarf stars – i.e. after dynamical relaxation timescales – changes the integrated colour of a cluster.

ad A.1) Regarding stellar evolution (winds, ejecta), it is well established that between 40% and 60% of the mass of the cluster is lost after 12 Gyr (e.g. Kruijssen et al. 2008; Sippel et al. 2012) because of this. We adopt a representative mass loss of 50% in the following.

ad A.2) Mass loss due to dynamical evolution occurs when stars located in the outskirsts of a cluster become unbound, because of their proper motion and tidal influence of their host galaxy (e.g. Baumgardt & Makino 2003; Sippel et al. 2012). Observational studies have shown that the total dynamical mass loss experienced by a cluster can approximately be considered as mass-independent (Jordan et al. 2007; see also Kruijssen 2009). Theoretical arguments also predict only a weak dependence of mass loss *rate* on the total cluster mass:

$$\frac{{\rm d}M}{{\rm d}t} = \frac{M(t)^{(1-\gamma)}}{t_0} \qquad (6)$$

with $\gamma \sim 0.8$ (Lamers et al. 2010). Across a factor of ten in present-day mass, the theoretically expected accumulated mass loss would thus vary by only ±30% around the mean. The typical accumulated mass loss for globular clusters over a Hubble time ranges from 3 to 5 $\times(10^5\ M_\odot)$ (Jordan et al. 2007). We thus adopt an accumulated dynamical mass loss of $\Delta = 4 \times 10^5\ M_\odot$ in the following, independent of GC present-day mass.

Combining the effects of dynamical and stellar evolution mass loss, we thus obtain the following relation between present-day mass M_t and mass at self-enrichment M_0.

$$M_0 = \frac{M_t + 4 \times 10^5}{0.5}\ [M_\odot]. \qquad (7)$$

We note that the timescales of both contributors are quite different: stellar evolution mass loss occurs very quickly in the early stages of a cluster's life, while dynamical mass loss happens on very long timescales comparable to a Hubble time (e.g. Sippel et al. 2012).

ad B) Recent studies investigated the effect of this dynamical dissolussion of star clusters on their integrated colours (Kruijssen & Lamers 2008; Anders et al. 2009). These studies predict star cluster colours at a determined age and metallicity as a function of the ratio $t_{\rm dyn}$ between the current age and the dissolution time. It was shown that colour changes start to set in after ≈0.4 dissolution time. Qualitatively, this happens because after sufficient dynamical evolution, prefered stellar types are evaporated, namely late-type dwarfs. This in turn changes the colour of the stellar population bluewards (see also Mieske et al. 2010).

We express $t_{\rm dyn}$ as (Jordan et al. 2007; Mieske et al. 2010):

$$t_{\rm dyn} = 1 - \frac{M_{\rm GC}}{M_{\rm GC} + \Delta}. \qquad (8)$$

This allows us to calculate the colour change at each luminosity bin, adopting the predictions by Kruijseen & Lamers (2008) in the V, I bands as a function of $t_{\rm dyn}$. For the present

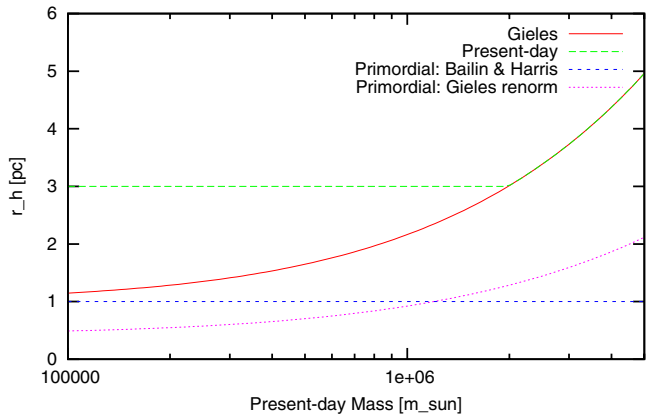

Fig. 9. *Red*: star cluster mass – $r_{\rm h}$ relation from Gieles et al. (2010), normalised to have $r_{\rm h}$ = 3 pc at a mass of 2×10^6 $M_\odot$. *Green*: present-day mass-radius relation (e.g. Mieske et al. 2006; Gieles et al. 2010): star clusters have a mass-independent half-light radius for masses below 2×10^6 $M_\odot$, and a mass-radius relation above that mass. *Blue*: primordial mass-radius relation (constant radius) adopted by Bailin & Harris (2009) for star clusters at time of self-enrichment. *Magenta*: primordial mass-radius relation adopted by renormalising the red (Gieles) curve to a mean of $r_{\rm h}$ = 1 pc in the observed GC mass range [5×10^5: 4×10^6] $M_\odot$. We note that the x-axis is the present-day mass, which is converted to original mass according to Eq. (7).

study we then convert this to $(U-I)$ colours with $\frac{{\rm d}(V-I)}{{\rm d}(U-I)} = 3.5$. This slope between both colours is derived from the subset of our data which has U, V, I coverage.

4.2.2. Mass-radius relation

Bailin & Harris (2009) adopted for their default model a mass independent half-light radius $r_{\rm h}$ of 1 parsec, smaller than present-day average radii of 3 pc due to the early expansion after gas removal (e.g. Baumgardt & Kroupa 2007). The assumption of a mass-independent primordial GC radius may, however, be too simple, as suggested by Gieles et al. (2010). These authors argue that a primordial mass-radius relation down to low GC masses is dynamically more plausible. We will thus investigate how the predictions for the self-enrichment model change between a fixed radius and a mass radius relation for the GCs at time of self-enrichment. For the latter we adopt from Gieles et al. (2010):

$$\log\left(\frac{r_{\rm h}}{1\ {\rm pc}}\right) = -3.63 + 0.615 * \log\left(\frac{M_0}{M_\odot}\right) \quad (9)$$

where $r_{\rm h}$ and M_0 are the half-mass radius and mass at time of self-enrichment. This relation is displayed in Fig. 9. With the given offset −3.63, one obtains a radius of 3 pc for a $2 * 10^6$ $M_\odot$ mass cluster (Bailin & Harris 2009). In Fig. 9 we also indicate in green an approximation for the present-day mass radius relation of GCs (e.g. Gieles et al. 2010; Mieske et al. 2006; Murray 2009): a piecewise function with a mass-independent radius of 3 pc for $M < 2 * 10^6$ $M_\odot$, and a mass-radius relation according to Eq. (9) for $M > 2 * 10^6$ $M_\odot$. The blue line in Fig. 9 indicates the fixed $r_{\rm h}$ = 1 pc adopted by Bailin & Harris (2009).

4.3. Best fitting models

4.3.1. Constant vs. mass-dependent radius

Equations (4) and (5) show that the determining parameters of the self-enrichement efficiency of a cluster are: the star formation efficiency $f_\star$, the mass-radius relation, the density profile $\rho \propto r^{-\beta}$ and the pre-enrichment level. Here we aim at constraining these parameters with our data.

In Fig. 10 we fit the modified model discussed in the previous subsection to the data. Compared to the default model shown in Fig. 8, we keep the surface density distribution of an isothermal sphere ($\beta = 2$), and adopt the following modifications for the other parameters:

- Top panels (left Centaurus, right Hydra): dynamical and stellar evolution mass loss is included according to Eq. (7). As in the default model, a mass-independent primordial half-light radius of $r_{\rm h}$ = 1 pc is assumed. Then we vary the star formation efficiency and pre-enrichment levels to obtain the best-fit of the model to the data, using least-squares minimisation. We find best-fit star formation efficiencies of 0.65 for Centaurus and 0.50 for Hydra and pre-enrichment values of $(-1.65, -0.55)$ for Centaurus and $(-1.55, -0.50)$ for Hydra. The rms difference between model and data [Fe/H] is 0.031 dex for Centaurus and 0.028 dex for Hydra.
- Bottom panels (left Centaurus, right Hydra): as in the top panels, dynamical and stellar evolution mass loss is included according to Eq. (7). In contrast to the top panel, we now adopt a mass-radius relation as in Eq. (9), normalised to a mean $r_{\rm h}$ = 1 pc across the considered GC mass range $[5 \times 10^5 : 4 \times 10^6]$ $M_\odot$. We find best-fitting star formation efficiencies of 0.42 for Centaurus and 0.36 for Hydra, and pre-enrichment values of $(-1.70, -0.55)$ for both Centaurus and Hydra. The rms difference between model and data [Fe/H] is 0.020 dex for Centaurus and 0.10 dex for Hydra.

From Fig. 10 one notes that the introduction of a (physically well motivated) mass-radius relation leads to a better fit to the data, and also to more realistic star formation efficiencies. The rms between model and data is reduced by about a factor of two when including the mass-radius relation (bottom panel of Fig. 10). With a mass-radius relation at an average $r_{\rm h}$ of 1 pc, self-enrichment sets in at lower masses but increases less rapidly towards larger masses, when compared to a mass-independent $r_{\rm h}$ = 1 pc.

4.3.2. Degeneracy between radius, star-formation efficiency, surface density profile, pre-enrichment level

In Fig. 11 we provide a more general overview of the degeneracy between self-enrichment model parameters average radius, star-formation efficiency, surface density profile, and pre-enrichment level. All figures assume the mass-radius relation in Eq. (9) normalised to a mean radius within the range $[5 \times 10^5 : 4 \times 10^6]$ $M_\odot$ as given on the x-axis. We first discuss the face-value constraints obtained by the model fits, and then add physically motivated constraints to several model parameters.

The top panels plot the best fitting star formation efficiency as a function of average $r_{\rm h}$ and for a range of surface density profile parameter $\beta = [2.0; 2.2]$. The star formation efficiency :required to match the data decreases with increasing radius, and increases with increasing β. These trends become clear in the context of the self-enrichment scenario: a lower star formation efficiency results in a larger primordial cluster mass at fixed present-day mass, and thus a deeper potential well. Self-enrichment was thus more efficient at a given present-day mass for lower primordial star formation efficiency. At the same time, a larger primordial radius gives a weaker primordial self-enrichment at a fixed present-day mass given the resulting shallower potential well. Finally, a steeper surface density profile

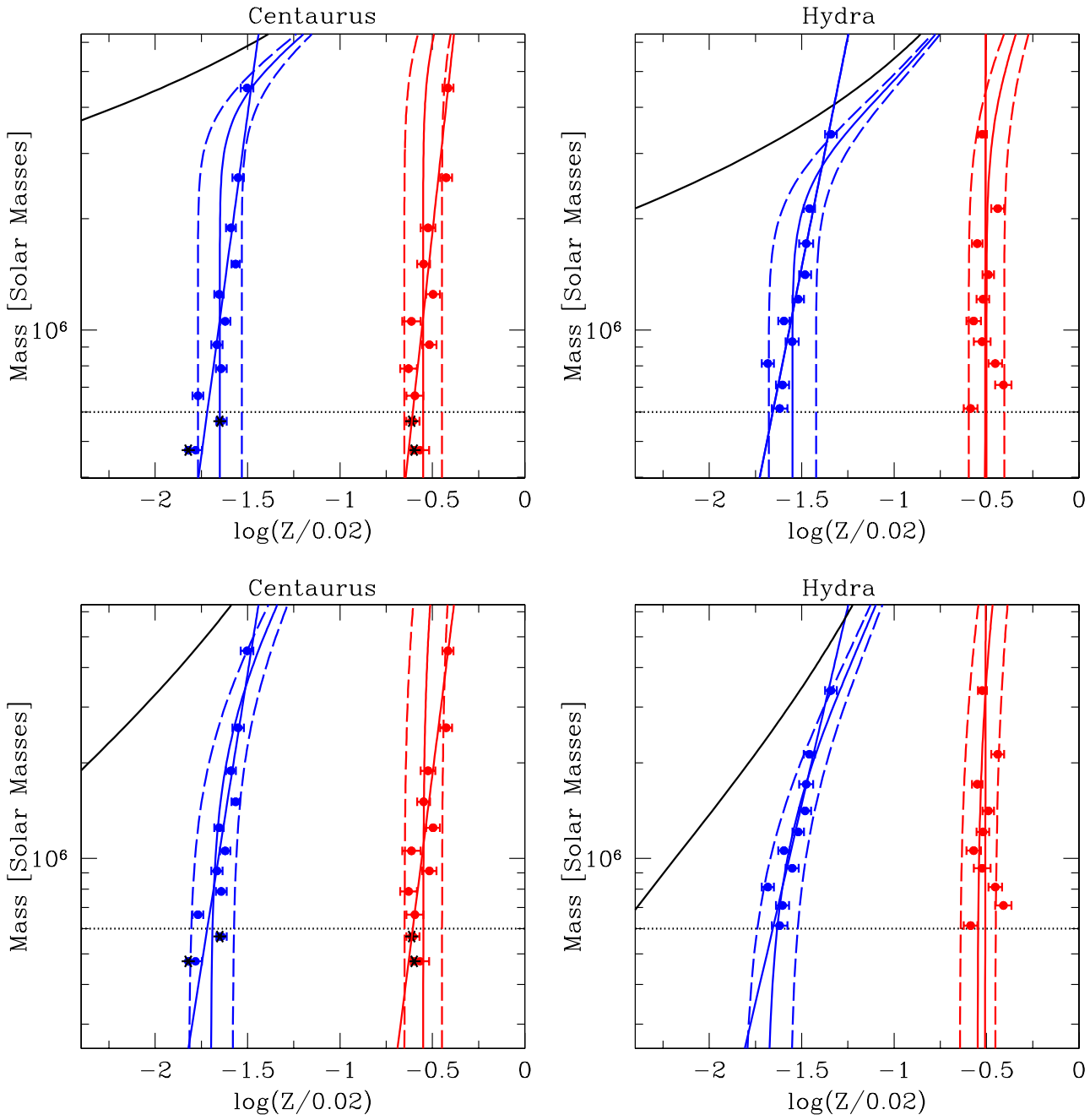

Fig. 10. Model fits to our mass-metallicity data. *Left*: Centaurus. *Right*: Hydra. Compared to the model in Fig. 8, we include stellar evolution mass loss and dynamical mass loss according to Eq. (7), and then determine the best-fitting star formation efficiency. The dotted horizontal line represents the critical mass below which the clusters will undergo colour changes due to dynamical mass evolution. Below this line, asterisks indicate the data points without colour changes. *Top panels*: primordial half-light radius $r_{\rm h}$ is fixed at 1 pc. We find best-fit star formation efficiencies of 0.65 for Centaurus and 0.50 for Hydra and pre-enrichment values of $(-1.65, -0.55)$ for Centaurus and $(-1.55, -0.50)$ for Hydra. *Bottom panels*: the mass-radius relation as in Eq. (9), normalised to a mean $r_{\rm h} = 1$ pc across the GC present-day mass range $[5\times10^5 : 4\times10^6]$ $M_\odot$. We find best-fitting star formation efficiencies of 0.42 for Centaurus and 0.36 for Hydra, and pre-enrichment values of $(-1.70, -0.55)$ for both Hydra and Centaurus.

(larger β) gives a deeper potential well and thus a stronger self-enrichment.

The bottom panels show the best fitting pre-enrichment level as a function of average $r_{\rm h}$ and for a range of surface density profile parameter $\beta = [2.0; 2.2]$.

In both the upper and lower panels, the rms of the data around the models vary by $\lesssim\pm20\%$ among the various model flavours, significantly less variation than the factor of two difference in rms to the model flavour with a fixed primordial radius. That is, changing from a fixed radius to a mass-radius relation is the most important model update.

For Hydra all plotted models span a total range of [0.007; 0.009] dex in rms between data and models. This very small range of ±10% shows that no combination of the three model parameters is strongly preferred. For Centaurus the variation in rms between model flavours is somewhat larger with ±20% and a range of [0.014; 0.022]. Best-fitting models are those at large β, i.e. very steep initial surface density profile. At a fixed $r_{\rm h} = 1$ pc, the rms is 0.020 for $\beta = 2.0$ and 0.015 for $\beta = 2.2$. At a given β,

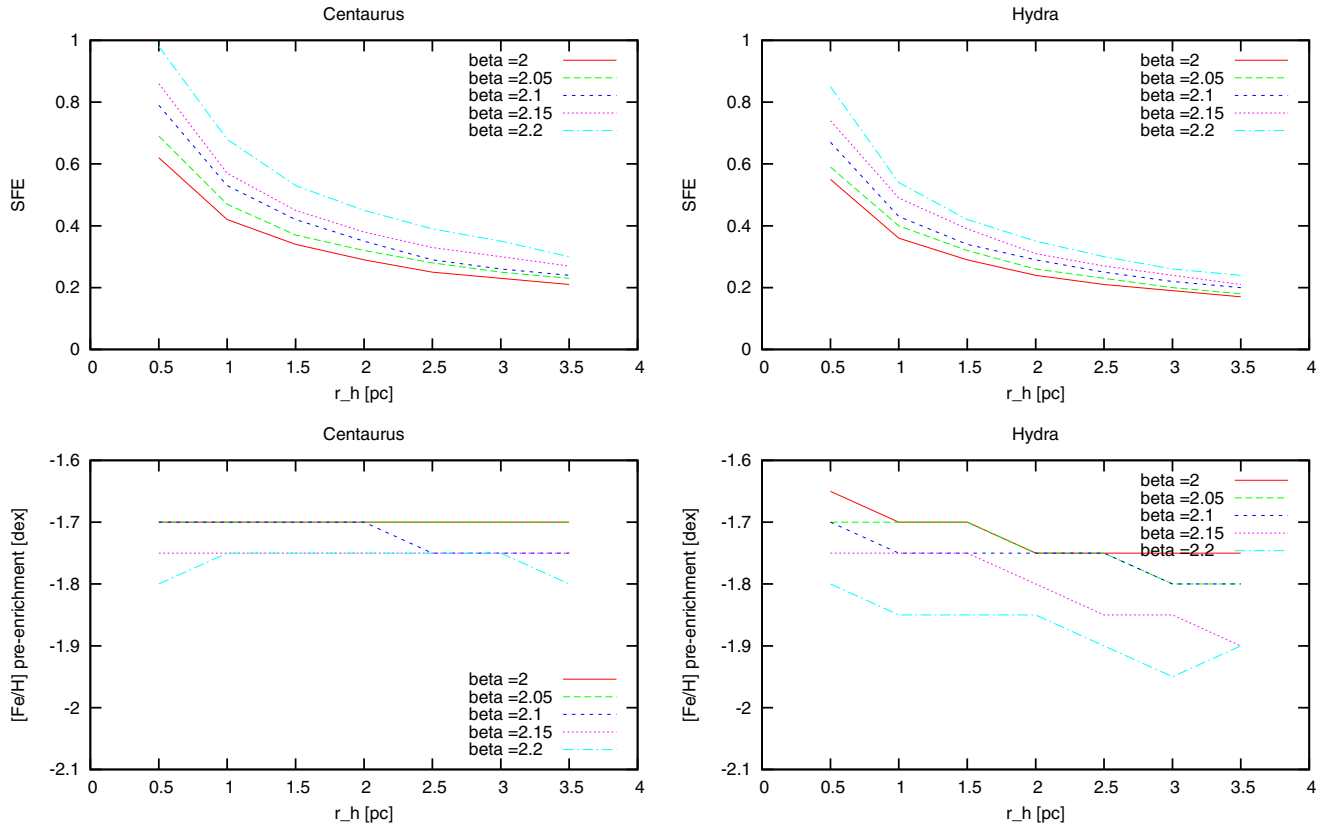

Fig. 11. *Top*: best fitting star formation efficiency $f_\star$ for the given mean radius r_h and surface density profile slopes β. Primordial boundary conditions as discussed in the text would imply $f_\star \lesssim 0.4$ and $r_\mathrm{h} \lesssim 2$ pc. *Bottom*: best fitting pre-enrichment level for the same range in mean radius r_h and surface density profile slopes β as above. A physically motivated lower limit for the pre-enrichment level is about $\sim$−1.8 dex, see text for details.

models with smallest $r_\mathrm{h} = 0.5$ pc have about 20% higher rms than models with the largest $r_\mathrm{h} = 3.5$ pc.

Given the quite moderate distinction in rms between the various best-fitting model flavours in Fig. 11, it is appropriate to consider physically motivated boundary conditions for the model parameters.

1. Pre-enrichment level: the somewhat low values of formally possible pre-enrichment levels (down to [Fe/H] ~ -1.9 for Hydra) in Fig. 11 are found because our data are restricted to GCs brighter than the turn-over magnitude. The data allow reasonable model fits for the case that self-enrichment sets in at masses lower than our faint luminosity limit. The model curves would in this case not straighten out at the cutoff mass of our investigation, but continue to extend towards lower metallicities for lower masses. To avoid the fitting degeneracy due to this extrapolation, we consider the well-known metallicity distribution of GCs in the Milky Way as an anchor point for the pre-enrichment level. According to the catalogue of Harris et al. (1996), the median metallicity of the metal-poor GC population in the Milky Way is about [Fe/H] = −1.6 dex. Allowing for a $U-I$ colour scale uncertainty of 0.10 mag in our data (see Sect. 2.2.1) and taking into account the slope of $\sim$2 between [Fe/H] and $U-I$ (Eq. (1)), we thus adopt a pre-enrichment lower limit of [Fe/H] = −1.8 dex. This excludes for the Hydra cluster models that have average $r_\mathrm{h} > 2$ pc and surface density profiles steeper than $\beta = 2.1$. For the Centaurus cluster, this restriction of pre-enrichment level to $\lesssim$−1.8 dex does not constrain the range of fitting models.

2. Star formation efficiency: it is widely assumed that star formation efficiency even in dense cores of molecular clouds is $\lesssim$0.3 (e.g. Lada & Lada 2003). We thus adopt a conservative upper limit of $f_\star \leq 0.4$.

3. Primordial half-light radius: the typical present-day half-light radii of most globular clusters are $\sim$3−3.5 pc (e.g. Jordan et al. 2005). At the same time, primordial cluster expansion due to gas expulsion increases the half-light radius by at least a factor of 2 (Baumgardt & Kroupa 2007; Gieles et al. 2010, Fig. 2). We thus adopt a (still conservative) upper limit of $r_\mathrm{h} \lesssim 2$ pc.

For the Hydra cluster, the above physical constraints restrict the models to an isothermal sphere – or only slightly steeper profile – and a primordial radius r_h in the range [1:2] pc, corresponding to a range in $f_\star$ of [0.36:0.24]. The upper limit in radius translates to the lower limit of $\sim$0.24 in $f_\star$, and analogously the lower radius limit comes from the imposed upper limit of $f_\star$.

For the Centaurus cluster, the star formation efficiency and the $r_\mathrm{h} < 2$ limit constrain the models (not so the limit on pre-enrichment). This restricts the models to a range of [1.5:2] pc and an isothermal sphere, with a corresponding $f_\star$ range [0.32:0.27].

From Fig. 11 it also becomes clear that the steeper blue tilt for Hydra in comparison to Centaurus can be explained either by a $\sim$30% smaller average r_h in Hydra at fixed $f_\star \sim 0.3$, or analogously by a $\sim$20% smaller $f_\star$ at fixed $r_\mathrm{h} \sim 1.5$ pc.

4.4. Difference between Centaurus and Hydra

It was shown above that the amplitude of the blue tilt in Hydra is slightly stronger than in Centaurus, see Table 1 and Fig. 7. The slope $\gamma = \mathrm{d}(U-I)/\mathrm{d}I$ is -0.081 ± 0.012 for Hydra

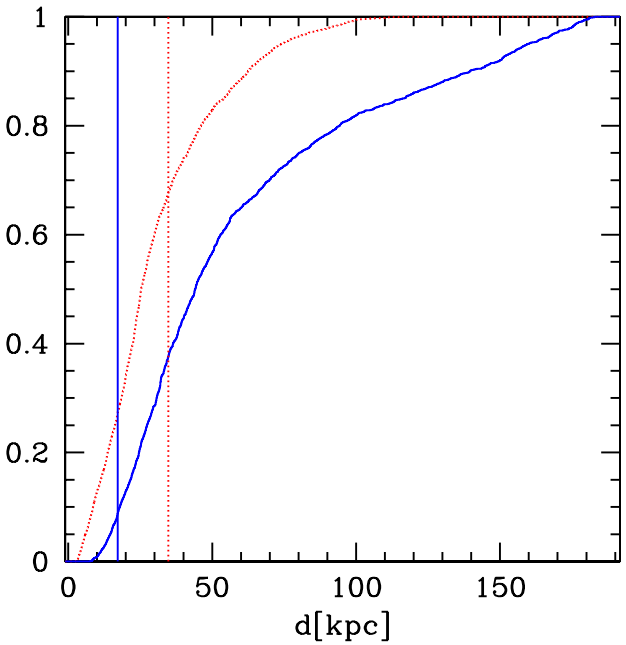

Fig. 12. Cumulative radial distribution of GC candidates in Hydra (dotted red line) and Centaurus (solid blue line) around the central galaxies NGC 3311 and NGC 4696, respectively. We note the more central concentration of the Hydra GCs which is imposed by the observational setup, see also Fig. 2. We furthermore indicate as vertical lines the effective radii of the respective central galaxies.

and $\gamma = -0.057 \pm 0.011$ for Centaurus, which formally is a 1.5σ level difference.

To investigate this in more detail, we show in Fig. 12 the cumulative radial distribution of GC candidates in both Hydra and Centaurus, centered on NGC 3311 and NGC 4696 respectively. It is clear from this figure that the GC distribution is more centrally concentrated for Hydra than for Centaurus. We note that this is imposed mainly by the observational setup (Fig. 2), which was focused on NGC 3311 in Hydra, whereas the Centaurus observations focused on the area between the central galaxy NGC 4696 and NGC 4709. The median projected distance to NGC 3311 for the Hydra GCs is about 25 kpc, while the median distance to NGC 4696 for the Centaurus GCs is about 42 kpc. The difference becomes even more pronounced when comparing this to the respective effective radii of both central galaxies determined from the V-band FORS data (Misgeld et al. 2008, 2009). The effective radius of the Centaurus cluster central galaxy NGC 4696 is 82″ or 17 kpc, while for the Hydra central galaxy NGC 3311 it is 150″ and thus 35 kpc. Thus the galaxy half-light radius in Hydra comprises 2/3 of all GCs, but only 10% of the Centaurus GCs in our data set.

A uniform area coverage in both clusters would be needed to tell whether the GC density profiles are intrinsically different, or, whether this higher concentration in Hydra is entirely due to the different spatial coverage of the existing data. Analogously, such a uniform area coverage would help to corroborate the formally significant red tilt observed in Centaurus, i.e. the non-zero slope in the red sequence. A significant red tilt is generally not seen in other environments (e.g. Table 1 and Harris et al. 2009a). Given our lacking coverage in the central Centaurus field, the red sequence is only sparsely populated and thus the red tilt for Centaurus would need to be confirmed with more photometric coverage in the cluster center.

In Mieske et al. (2010) it was shown that within the joint Fornax and Virgo cluster GC system, the blue tilt is more pronounced for GCs at smaller projected radii from their host galaxies. One may thus ask the question whether the weaker tilt in Centaurus is related to its less centrally concentrated GC sample compared to Hydra. As mentioned above for the Centaurus sample the median projected distance to the central galaxy NGC 4696 is about 42 kpc. Adopting such a limit of 42 kpc between inner and outer sample, the inner slope is $\gamma = -0.061 \pm 0.016$, and the outer slope is $\gamma = -0.045 \pm 0.018$, marginally shallower than the inner sample. Similarly for Hydra, with a limit of 25 kpc between inner and outer sample, the inner slope is $\gamma = 0.079 \pm 0.023$, and the outer slope is $\gamma = 0.068 \pm 0.015$. This qualitatively confirms the finding in Mieske et al. (2010) that the blue tilt is stronger at smaller cluster centric distance. The difference between the inner Centaurus slope and overall Hydra slope is insignificant, and the formally lowest difference is found between the inner Centaurus and outer Hydra sample (-0.061 vs. -0.068). As noted in the previous subsection, a spatial variation in self-enrichment efficiency can be explained by a corresponding variation in primordial star formation efficiency or cluster radius.

In concluding we reiterate that in this study we assume a coeval sample of old globular clusters with luminosity weighted ages around a Hubble time. In future studies it would be worthwhile to address to which extent the presence of young-to-intermediate age GCs may influence the measured blue tilt, in particular its spatial variation.

4.5. Comparison to the Milky Way globular clusters

It is interesting to check whether the self-enrichment model proposed to explain the blue tilt is consistent with what is observed in GCs of our own Milky Way.

As noted earlier on, the cluster-to-cluster variation in [Fe/H] is always superposed on the effect of [Fe/H] increase due to self-enrichment within individual clusters. The statistical significance of the trend is between $7-10\sigma$ in our large samples of about 2500 GCs in each environment. In the Milky Way there are only about 50 GCs in the same absolute magnitude range (Harris et al. 1996). It is thus clear that no significant blue tilt is expected to be notable in the Milky Way (see also Strader et al. 2009), since the GC-to-GC scatter in mean [Fe/H] supersedes the smooth and slow effect of self-enrichment.

However, the width of the stellar [Fe/H] distribution within individual globular clusters is a much more direct tracer of possible self-enrichment. The typical width σ of the [Fe/H] distribution in lower-mass GCs of the Milky Way is about 0.03 dex, see Fig. 1 of Willman & Strader (2012). Then, for the most massive GCs like ω Centauri and M 54, this [Fe/H] width increases notably to about 0.2 dex. Such broad [Fe/H] distributions, which are also seen in dwarf spheroidals, have often been interpreted as results of self-enrichment. An interesting question in this context is whether the broadened metallicity distribution for GCs like ω Centauri (Johnson & Pilachowski 2010) is naturally explained within a self-enrichment scenario of star clusters. Or, whether such strong self-enrichment as observed in ω Centauri implies that it was once embedded in a much more massive halo (e.g. Hilker & Richtler 2000; Gnedin et al. 2002). See for this also the discussion in Willman & Strader (2012).

For comparing our best-fit self-enrichment models to the GCs in the Milky Way, we thus convert the model predictions of mean [Fe/H] to a predicted width of the stellar [Fe/H] distribution. Such a conversion can be very complex since individual

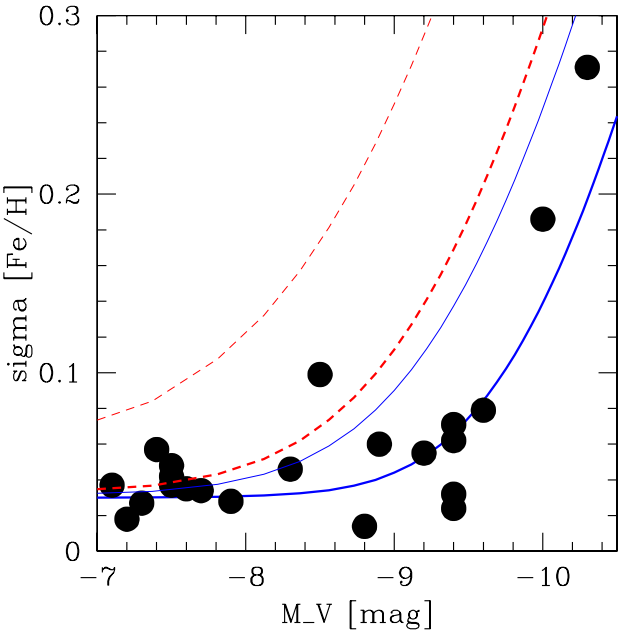

Fig. 13. Filled circles indicate the width $\sigma_{[Fe/H]}$ of the stellar metallicity distribution in Galactic GCs plotted vs. their absolute visual magnitude M_V, compiled from Willman & Strader (2012) and da Costa et al. (2014). The blue curve indicates the width $\sigma_{[Fe/H]}$ predicted from the best-fitting self enrichment model of the Centaurus cluster GCs, the red (dashed) curve represents the predictions from the best-fit model of the Hydra cluster GCs. The bold curves correspond to average primordial r_h = 1 pc, the finer ones to r_h = 1.5 pc.

enrichment histories are variable – in the Bailin & Harris model, the metallicity spread is generated by the range of formation times of the low-mass stars, which are a few Myr. Here we adopt a simple approach of defining the expected width $\sigma_{[Fe/H]}$ of the stellar [Fe/H] distribution as being equal to the difference between the model predicted $[Fe/H]_{enrich}$ and the pre-enrichment level $[Fe/H]_{pre-enrich}$, including a minimum floor of 0.03 dex.

$$\sigma_{[Fe/H]} = \sqrt{([Fe/H]_{enrich} - [Fe/H]_{pre-enrich})^2 + 0.03^2}. \quad (10)$$

It is important to keep in mind that the model predicted $[Fe/H]_{enrich}$ is very close to the [Fe/H] derived from the actual data of the Centaurus/Hydra GCs. In Fig. 13 we compare the predicted $\sigma_{[Fe/H]}$ for both the Centaurus (blue) and Hydra (red) best-fit models for a mean r_h = 1 (fat lines) and r_h = 1.5 pc (thin lines) to the $\sigma_{[Fe/H]}$ observed in Milky Way GCs (Willman & Strader 2012). Two things can be noted.

1. The best-fit Centaurus model fits the Milky Way distribution quite well, though being slightly below the Milky Way values. For r_h = 1 pc the sharp rise of $\sigma_{[Fe/H]}$ around M_V = −9.5 mag to values around 0.1−0.2 dex in the luminosity range of ω Centauri and M 54 is reproduced well. The (stronger) Hydra blue tilt implies a larger $\sigma_{[Fe/H]}$ slightly above to what is seen in the Milky Way. We note that the only difference at r_h = 1 pc between the Hydra and Centaurus models is the star formation efficiency: 0.42 for Centaurus and 0.36 for Hydra (see Fig. 10).
2. The curves for r_h = 1 pc imply a smaller $\sigma_{[Fe/H]}$ spread than the curves at r_h = 1.5 pc. This is because a larger primordial radius requires a lower pre-enrichment level to fit the data, and thus the measured metallicities at high masses are farther away from the pre-enrichment levels. In this context we note that *at the same* pre-enrichment level, variations in r_h and star formation efficiency are degenerate as already mentioned above. For example, the bold curve for Centaurus can be represented both by combination of an average primordial radius r_h = 1 pc and SFE = 0.42, *and* an average primordial radius r_h = 3 pc and SFE = 0.23. The latter example may fit better the case of ω Centauri with its present day r_h = 8 pc.

The above example shows that broadened metallicity distributions like found in some massive MW globular clusters may be natural consequences of cluster self-enrichment processes, without the need to invoke an additional embeddening in a more massive halo (e.g. a dwarf galaxy) at time of formation (e.g. Dinescu et al. 1999; Majewski et al. 2000; Gnedin et al. 2002; Bekki et al. 2006).

One caveat is that the self-enrichment model applied here (Bailin & Harris 2009) assumes quasi-instantaneous reprocessing of SNII ejecta, i.e. on timescales that are short compared to dynamical timescales. This is a simplifying assumption that would need to be elaborated in further detail, given that an age spread of several billion years has been reported for the stellar populations of ω Cen (e.g. Hilker et al. 2004).

5. Summary and conclusions

We analyse the colour-magnitude relation of globular clusters (the "blue tilt") in the central 100 kpc of the Hydra and Centaurus galaxy clusters. This analysis is based on deep FORS1 photometry in the U and I bands, which provides a very broad wavelength baseline and thus high metallicity sensitivity. The final sample comprises about 2500 GC candidates in each cluster down to $M_I \sim -9$ mag, half a magnitude brighter than the GC luminosity function turnover.

We obtain the following results:

- In both clusters we measure a significant "blue tilt", i.e. a colour-magnitude relation for the blue globular cluster subpopulation. We find $\gamma = d(U-I)/d(I) = -0.057 \pm 0.011$ for Centaurus and $\gamma = -0.081 \pm 0.012$ for Hydra. We confirm previous findings that the blue tilt already sets in at present-day masses well below $10^6\ M_\odot$.
- We convert colours and luminosities to mass and metallicity using TERAMO models (Raimondo et al. 2005), assuming old GC ages of 11−13 Gyrs. We thus obtain a mass-metallicity scaling of $Z \propto M^{0.27\pm0.05}$ for Centaurus and $Z \propto M^{0.40\pm0.06}$ for Hydra. This is the same range than found in previous literature measurements of the GC mass-metallicity scaling, investigating different environments and mostly using HST data.
- We compare the measured mass-metallicity dependence of GCs on star cluster self-enrichment model predictions using the model of Bailin & Harris (2009). To use a realistic primordial star cluster mass at the time of self-enrichment, we include both stellar evolution and dynamical mass loss effects. We find that the model fits are significantly improved (reducing rms by a factor of two with respect to the data) when assuming a primordial mass-radius relation of star clusters according to Gieles et al. (2010), instead of a fixed, mass independent, cluster radius.
- We investigate and illustrate the degeneracy between model input parameters average radius r_h, star formation efficiency $f_\star$, pre-enrichment level, and surface density profile steepness. The best fit within physically motivated boundary conditions is obtained for $r_h \sim 1$−1.5 pc, $f_\star \sim 0.3$−0.4, a

pre-enrichment level of [Fe/H] -1.7 and a surface density profile of an isothermal sphere. The slightly steeper blue tilt for Hydra can be explained either by a ∼30% smaller average r_h at fixed $f_\star \sim 0.3$, or analogously by a ∼20% smaller $f_\star$ at fixed $r_h \sim 1.5$ pc.
- We note that the GC sample in the Centaurus cluster is less centrally concentrated than the Hydra sample, given the observational setup of the observed fields. We show that both in Hydra and Centaurus the blue tilt is stronger for GCs with smaller projected distances to their host galaxies. We thus argue that the slightly stronger tilt in Hydra could be due to its more centrally concentrated GC sample.
- We find that the M_V vs. $\sigma_{[Fe/H]}$ distribution of Galactic Globular Clusters is consistent with the GC self-enrichment trend observed for the Centaurus cluster.

We conclude that

1. $U-I$ photometry allows us to accurately measure colour-magnitude relation of GCs.
2. GC self-enrichment sets in at present-day masses well below $10^6\ M_\odot$.
3. The adoption of a primordial mass-radius relation in the self-enrichment model of Bailin & Harris (2009) allows us to fit data very well without requiring non-canonical star formation efficiency, surface density profile, or average radii.
4. The comparison between the blue tilt strength of Hydra and Centaurus supports previous findings of variations of self-enrichment efficiency with cluster-centric distance. Spatial variations of primordial cluster radius or star formation efficiencies can explain such a behaviour.
5. Broadened metallicity distribution like found in some MW globular clusters can be natural consequences of cluster self-enrichment, without the need to invoke an additional embeddening in a more massive halo (e.g. a dwarf galaxy) at time of formation.

Acknowledgements. We thank the anonymous referee for very constructive comments which helped to improve this paper. J.F. acknowledges financial support from the ESO Chile Office for Science.

References

Anders, P., Lamers, H. J. G. L. M., & Baumgardt, H. 2009, A&A, 502, 817
Ashman, K. M., Bird, C. M., & Zepf, S. E. 1994, AJ, 108, 2348
Bailin, J., & Harris, W. E. 2009, ApJ, 695, 1082
Bassino, L. P., Faifer, F. R., Forte, J. C., et al. 2006, A&A, 451, 789
Baumgardt, H., & Kroupa, P. 2007, MNRAS, 380, 1589
Baumgardt, H., & Makino, J. 2003, MNRAS, 340, 227
Baumgardt, H., Kroupa, P., & Parmentier, G. 2008, MNRAS, 384, 1231
Bedin, L. R., Piotto, G., Anderson, J., et al. 2004, ApJ, 605, L125
Bekki, K., & Norris, J. E. 2006, ApJ, 637, L109
Blom, C., Spitler, L. R., & Forbes, D. A. 2012, MNRAS, 420, 37
Brodie, J. P., & Strader, J. 2006, ARA&A, 44, 193
Bruzual, G., & Charlot, S. 2003, MNRAS, 344, 1000
Cockcroft, R., Harris, W. E., Wehner, E. M. H., Whitmore, B. C., & Rothberg, B. 2009, AJ, 138, 758
Da Costa, G. S., Held, E. V., & Saviane, I. 2014, MNRAS, 438, 3507
D'Antona, F., Caloi, V., Montalbán, J., Ventura, P., & Gratton, R. 2002, A&A, 395, 69
D'Antona, F., Bellazzini, M., Caloi, V., et al. 2005, ApJ, 631, 868
D'Ercole, A., Vesperini, E., D'Antona, F., McMillan, S. L. W., & Recchi, S. 2008, MNRAS, 391, 825
Dinescu, D. I., Girard, T. M., & van Altena, W. F. 1999, AJ, 117, 1792
Dirsch, B., Richtler, T., Geisler, D., et al. 2003, AJ, 125, 1908
Forbes, D. A., Spitler, L. R., Harris, W. E., et al. 2010, MNRAS, 403, 429
Forbes, D. A., Spitler, L. R., Strader, J., et al. 2011, MNRAS, 413, 2943
Forte, J. C., Faifer, F., & Geisler, D. 2007, MNRAS, 382, 1947
Gebhardt, K., & Kissler-Patig, M. 1999, AJ, 118, 1526
Gieles, M., Baumgardt, H., Heggie, D. C., & Lamers, H. J. G. L. M. 2010, MNRAS, 408, L16
Gnedin, O. Y., Zhao, H., Pringle, J. E., et al. 2002, ApJ, 568, L23
Goudfrooij, P., & Kruijssen, J. M. D. 2014, ApJ, 780, 43
Harris, W. E. 1996, AJ, 112, 1487
Harris, W. E. 2009a, ApJ, 699, 254
Harris, W. E. 2009b, ApJ, 703, 939
Harris, W. E. 2010 [arXiv:1012.3224]
Harris, W. E., Whitmore, B. C., Karakla, D., et al. 2006, ApJ, 636, 90
Harris, W. E., Spitler, L. R., Forbes, D. A., & Bailin, J. 2010, MNRAS, 401, 1965
Harris, W. E., Harris, G. L. H., & Alessi, M. 2013, ApJ, 772, 82
Hilker, M., & Richtler, T. 2000, A&A, 362, 895
Hilker, M., Kayser, A., Richtler, T., & Willemsen, P. 2004, A&A, 422, L9
Humphrey, P. J. 2009, ApJ, 690, 512
Johnson, C. I., & Pilachowski, C. A. 2010, ApJ, 722, 1373
Jordán, A., Côté, P., Blakeslee, J. P., et al. 2005, ApJ, 634, 1002
Jordán, A., McLaughlin, D. E., Côté, P., et al. 2007, ApJS, 171, 101
Kartha, S. S., Forbes, D. A., Spitler, L. R., et al. 2014, MNRAS, 437, 273
Kruijssen, J. M. D. 2009, A&A, 507, 1409
Kruijssen, J. M. D., & Lamers, H. J. G. L. M. 2008, A&A, 490, 151
Kundu, A., & Whitmore, B. C. 2001, AJ, 121, 2950
Lada, C. J., & Lada, E. A. 2003, ARA&A, 41, 57
Lamers, H. J. G. L. M., Gieles, M., Bastian, N., et al. 2005, A&A, 441, 117
Lamers, H. J. G. L. M., Baumgardt, H., & Gieles, M. 2010, MNRAS, 409, 305
Larsen, S. S., Brodie, J. P., Huchra, J. P., Forbes, D. A., & Grillmair, C. J. 2001, AJ, 121, 2974
Majewski, S. R., Patterson, R. J., Dinescu, D. I., et al. 2000, in Proc. of the 35th Liège International Astrophysical Colloquia, eds. A. Noels, P. Magain, D. Caro, et al., 35, 619
Maraston, C. 2005, MNRAS, 362, 799
Maxwell, A. J., Wadsley, J., Couchman, H. M. P., & Sills, A. 2014, MNRAS, 439, 2043
Mieske, S., & Hilker, M. 2003, A&A, 410, 445
Mieske, S., Hilker, M., & Infante, L. 2005, A&A, 438, 103
Mieske, S., Jordán, A., Côté, P., et al. 2006, ApJ, 653, 193
Mieske, S., Jordán, A., Côté, P., et al. 2010, ApJ, 710, 1672
Milone, A. P., Marino, A. F., Cassisi, S., et al. 2012a, ApJ, 754, L34
Milone, A. P., Marino, A. F., Piotto, G., et al. 2012b, ApJ, 745, 27
Milone, A. P., Piotto, G., Bedin, L. R., et al. 2012c, ApJ, 744, 58
Misgeld, I., Mieske, S., & Hilker, M. 2008, A&A, 486, 697
Misgeld, I., Hilker, M., & Mieske, S. 2009, A&A, 496, 683
Murray, N. 2009, ApJ, 691, 946
Nomoto, K., Hashimoto, M., Tsujimoto, T., et al. 1997, Nucl. Phys. A, 616, 79
Park, H. S. 2012, J. Korean Astron. Soc., 45, 71
Peng, E. W., Jordán, A., Côté, P., et al. 2006, ApJ, 639, 95
Piotto, G., Villanova, S., Bedin, L. R., et al. 2005, ApJ, 621, 777
Piotto, G., Milone, A. P., Anderson, J., et al. 2012, ApJ, 760, 39
Raimondo, G., Brocato, E., Cantiello, M., & Capaccioli, M. 2005, AJ, 130, 2625
Schiavon, R. P., Caldwell, N., Conroy, C., et al. 2013, ApJ, 776, L7
Sippel, A. C., Hurley, J. R., Madrid, J. P., & Harris, W. E. 2012, MNRAS, 427, 167
Spitler, L. R., Larsen, S. S., Strader, J., et al. 2006, AJ, 132, 1593
Strader, J., & Smith, G. H. 2008, AJ, 136, 1828
Strader, J., Brodie, J. P., Spitler, L., & Beasley, M. A. 2006, AJ, 132, 2333
Usher, C., Forbes, D. A., Spitler, L. R., et al. 2013, MNRAS, 436, 1172
Ventura, P., D'Antona, F., Mazzitelli, I., & Gratton, R. 2001, ApJ, 550, L65
Wehner, E. M. H., Harris, W. E., Whitmore, B. C., Rothberg, B., & Woodley, K. A. 2008, ApJ, 681, 1233
Willman, B., & Strader, J. 2012, AJ, 144, 76
Woosley, S. E., & Weaver, T. A. 1995, ApJS, 101, 181

The Astrophysical Journal, 835:123 (6pp), 2017 February 1 doi:10.3847/1538-4357/835/2/123

Globular Clusters as Tracers of Fine Structure in the Dramatic Shell Galaxy NGC 474

Sungsoon Lim[1,2], Eric W. Peng[1,2], Pierre-Alain Duc[3], Jérémy Fensch[3], Patrick R. Durrell[4], William E. Harris[5], Jean-Charles Cuillandre[6], Stephen Gwyn[7], Ariane Lançon[8], and Rúben Sánchez-Janssen[9]
[1] Department of Astronomy, Peking University, Beijing, 100871, China; slim@pku.edu.cn, peng@pku.edu.cn
[2] Kavli Institute for Astronomy and Astrophysics, Peking University, Beijing, 100871, China
[3] Laboratoire AIM Paris-Saclay, CNRS/INSU, Université Paris Diderot, CEA/IRFU/SAp, F-91191 Gif-sur-Yvette Cedex, France
[4] Department of Physics and Astronomy, Youngstown State University, Youngstown, OH 44555, USA
[5] Department of Physics & Astronomy, McMaster University, Hamilton, ON, Canada
[6] Canada–France–Hawaii Telescope Corporation, Kamuela, HI 96743, USA
[7] Herzberg Institute of Astrophysics, National Research Council of Canada, Victoria, BC, V9E 2E7, Canada
[8] Observatoire Astronomique de Strasbourg, Université de Strasbourg, CNRS, UMR 7550, 11 rue de lUniversité, F-67000 Strasbourg, France
[9] STFC UK Astronomy Technology Centre, The Royal Observatory Edinburgh, Blackford Hill, Edinburgh, EH9 3HJ, UK
Received 2016 June 23; revised 2016 December 8; accepted 2016 December 11; published 2017 January 23

Abstract

Globular clusters (GCs) are some of the most visible tracers of the merging and accretion histories of galaxy halos. Metal-poor GCs, in particular, are thought to arrive in massive galaxies largely through dry, minor merging events, but it is rare to see a direct connection between GCs and visible stellar streams. NGC 474 is a post-merger early-type galaxy with dramatic fine structures made of concentric shells and radial streams that have been more clearly revealed by deep imaging. We present a study of GCs in NGC 474 to better establish the relationship between merger-induced fine structure and the GC system. We find that many GCs are superimposed on visible streams and shells, and about 35% of GCs outside $3R_{\rm e,galaxy}$ are located in regions of fine structure. The spatial correlation between GCs and fine structure is significant at the 99.9% level, which shows that this correlation is not coincidental. The colors of GCs on fine structures are mostly blue, and we also find an intermediate-color population that is dominant in the central region and that will likely passively evolve to have colors consistent with a traditional metal-rich GC population. The association of the blue GCs with fine structures is direct confirmation that many metal-poor GCs are accreted onto massive galaxy halos through merging events and that the progenitors of these mergers are sub-$L^{\star}$ galaxies.

Key words: galaxies: elliptical and lenticular, cD – galaxies: evolution – galaxies: formation – galaxies: individual (NGC 474) – galaxies: star clusters: general

Supporting material: machine-readable table

1. Introduction

In the current view regarding galaxy formation, galaxies are formed by the hierarchical assembly of smaller subcomponents. In massive galaxies, this is visible in the outer regions, which are expected to grow through multiple dry mergers of low-mass, relatively metal-poor galaxies (e.g., Naab et al. 2009; Oser et al. 2010). This merging is also thought to be the origin of metal-poor globular clusters (GCs) in massive early-type galaxies (Côté et al. 1998; Li & Gnedin 2014).

GCs are powerful tools for studying the assembly of their host galaxies. They are formed in intense star-forming events and can survive a Hubble time. They are also abundant in galaxies, across many orders of magnitude in mass. Conveniently, the relatively high surface brightness of GCs makes them observable in distant galaxies.

Metal-rich GCs are formed in major, gas-rich mergers of relatively massive systems, where the star-forming gas is more enriched. Many theoretical studies support this formation mechanism of metal-rich GCs (e.g., Bournaud et al. 2008; Kruijssen et al. 2012; Renaud & Gieles 2013; Li & Gnedin 2014; Renaud et al. 2015). Several observational studies also support this formation scenario (e.g., Whitmore et al. 1993; Sikkema et al. 2006; Trancho et al. 2014). Metal-rich GCs can also form in gas-rich, high redshift disk galaxies (e.g., Shapiro et al. 2010; Kruijssen 2015).

Metal-poor GCs, however, are thought to form in low-mass galaxies. When seen in halos of massive galaxies, these GCs are thought to be the visible remnants of minor merging events (Côté et al. 1998; Tonini 2013). There is much indirect evidence that the metal-poor GCs in dwarfs are related to those in the halos of massive galaxies. The specific frequency ($S_{\rm N}$) of metal-poor GCs is as high in massive galaxies as it is in some dwarfs. In the Virgo cluster, there is evidence that $S_{\rm N}$ in dwarfs is higher when they are closer to the central galaxy, M87, indicating that they may contribute to the progenitor population of the M87 metal-poor GC population (Peng et al. 2008). Moreover, these satellite dwarfs have the high [α/Fe] seen in galaxy halo stars (Liu et al. 2016). The azimuthal distributions and ellipticities of metal-poor GCs are also generally uncorrelated with those of their host galaxies (Park & Lee 2013; Wang et al. 2013), suggesting a random merger history. The kinematics of metal-poor GCs and stars in the outskirts of galaxies are also different from those of stars in the inner regions (Pota et al. 2013; Li et al. 2015; Foster et al. 2016). While all these observations suggest that metal-poor GCs in massive galaxies come from accreted galaxies, the process has rarely been observed directly. One of the few exceptions has been the M31 PAndAS survey, which revealed two GCs associated with visible stellar substructures (Huxor et al. 2014). Another example is NGC 4651, a late-type spiral galaxy (Sc)

that has GCs associated with currently observed streams and shells (Foster et al. 2014). These examples are late-type galaxies, and there is only one example of a giant elliptical galaxy (NGC 4365) that has GCs related to the stellar stream (Blom et al. 2012).

Establishing the link between GCs and mergers in the halos of massive early-type galaxies is difficult because GCs are a sparse population and stellar substructures from merging have very low surface brightness. Studies of GC systems in shell galaxies with *HST* (Sikkema et al. 2006) have not had the field of view necessary to probe the outermost substructures, where we expect the GC population to be dominated by the accreted component. The Mass Assembly of Early-Type Galaxies with Their Fine Structures (MATLAS; Duc et al. 2015) survey is the first systematic, wide-field imaging survey that goes deep enough in surface brightness to reveal merging substructure and simultaneously has a good image quality for unresolved sources to allow a detailed study of the corresponding GC systems. To demonstrate the potential of the survey data, in this paper, we present a study of GCs in the spectacular post-merger galaxy NGC 474.

2. Observations

The observations were part of MATLAS, a Canada–France–Hawaii Telescope (CFHT) Large Program to obtain deep, multiband optical imaging for 260 ATLAS^{3D} galaxies (Cappellari et al. 2011) using MegaCam on CFHT. The detailed strategies for dithering and stacking images are described in Duc et al. (2015). However, the stacking for the GC analysis in this paper is done slightly differently. While background subtraction is done as described in that paper, MegaPipe (Gwyn 2008) is used to do a high-precision astrometric and photometric calibration. The MegaPipe output image stacks are produced at the full CFHT resolution, whereas the earlier image stacks were binned on a 3×3 pixel grid.

NGC 474 is one of the most interesting galaxies in the MATLAS sample ($D = 30.9$ Mpc; Cappellari et al. 2011). It is well known as a shell galaxy (Turnbull et al. 1999; Sikkema et al. 2007), and deep u^*-, g'-, r'-, and i'-band imaging reveals very complex but clear fine structures made of concentric shells in addition to radial structures (Figure 1), particularly in the halo regions, where we can easily distinguish fine structures from the smooth stellar light. The accumulated exposure times are 4900, 2415, 2415, and 3220 s for u^*, g', r', and i', respectively.

We use Source Extractor (Bertin & Arnouts 1996) for source detection and photometry. Dual-image mode photometry is adopted, with the r-band image used as the detection image. We use circular apertures with various radii for estimating the fluxes of sources. All aperture magnitudes are corrected to the 16 pixel diameter aperture magnitudes. These instrumental magnitudes are transformed to standard AB magnitudes by comparison with SDSS PSF magnitudes. The methods for source detection and aperture photometry are similar to those adopted in Durrell et al. (2014) and Liu et al. (2015). The foreground reddening toward NGC 474 is $E(B - V) = 0.04$ (Schlegel et al. 1998), and the corresponding extinction correction terms are included in the following analysis. At the distance of NGC 474, most GCs are pointlike sources, so we select point sources using a concentration index with a magnitude limit of $m_{g',0} \leqslant 25$. At the distance of NGC 474, this magnitude limit should include roughly half of the GCs. The concentration index is calculated based on the differences between 4 pixel diameter and 8 pixel diameter aperture magnitudes. Among the pointlike sources, we select GC candidates based on their colors in the $(u^* - g')_0 - (g' - i')_0$ color–color diagram (Figure 2).

3. Results

3.1. Global Properties

Figure 1 shows the spatial distribution of GC candidates and fine structures in NGC 474. The inner region of NGC 474 suffers from incompleteness due to bright stellar light and the difficulty of detecting GCs on the inner fine structures. Therefore, we only analyze the GC system beyond $1R_{\rm e,galaxy}$ ($0\farcm55$), out to $R = 15'$. Using our GC selection in regions well away from the Galaxy (beyond the regions shown in Figure 1), we estimate the level of background contamination to be 0.03 arcmin^{-2}. We fit the azimuthally averaged radial surface density profile of the GCs with a Sersić profile using maximum likelihood estimation and determine the uncertainties in the fitted parameters using the bootstrap. The effective radius and Sersić index of the GC system are $R_{\rm e,GCS} = 2\farcm37 \pm 0\farcm51$ (21.1 ± 4.5 kpc at the distance of NGC 474) and $n = 1.78 \pm 1.23$, respectively (Figure 3). The Sersić index has a large uncertainty because it is sensitive to the lack of information in the central region. The effective radius of the GC system is about four times as large as that of the stars. This relation is consistent with the result from Kartha et al. (2014). For the analysis below, we choose GC candidates within $2.5R_{\rm e,GCS}$, represented by the largest circle (red) in Figure 1. To estimate contamination, we choose a control field between $5R_{\rm e,GCS}$ and $6R_{\rm e,GCS}$. There are 144 GC candidates within $2.5R_{\rm e,GCS}$, and the estimated background contamination value for this area is about 34. The number density of sources that satisfy the GC selection criteria in the control field gives the statistical estimate of the contamination. Table 1 shows the list of GC candidates in $2.5R_{\rm e,GCS}$.

Figure 4 shows the $(g' - i')_0 - g'_0$ color magnitude diagram of GC candidates within $2.5R_{\rm e,GCS}$. The GC candidates are divided by their location off or on the fine structures. The brightest GC candidate has $g'_0 \sim 19$, but most GC candidates are fainter than $g'_0 \sim 21$. Color ranges and errors are not location-dependent, but GC candidates on the fine structures tend to be fainter that those off the fine structures. The color errors are quite small (<0.1) even with a faint magnitude bin.

Figure 5 shows the $(g' - i')_0$ GC color histograms. The color distribution of the GC candidates ranges from $(g' - i')_0 = 0.5$ mag to $(g' - i')_0 = 1.15$ mag and has a peak at $(g' - i')_0 \sim 0.75$ mag. We note that GC candidates redder than $(g' - i')_0 = 0.9$ mag are rare. Background contamination should not affect the shape of color distribution, as the color distribution of selected background objects is relatively flat. We fit the color histograms with Gaussian functions using the Gaussian mixture modeling (GMM) code (Muratov & Gnedin 2010). To subtract background contamination, we adopt the following steps: (1) We estimate the total number of contaminants, 34, based on the GC number density of the control field. (2) We randomly select 34 GCs in the control field and subtract 34 GCs in the target region that have similar colors to the selected GCs from the control field. (4) The widths for the two Gaussian functions are free parameters, and we run GMM 1000 times with a random subtraction of background

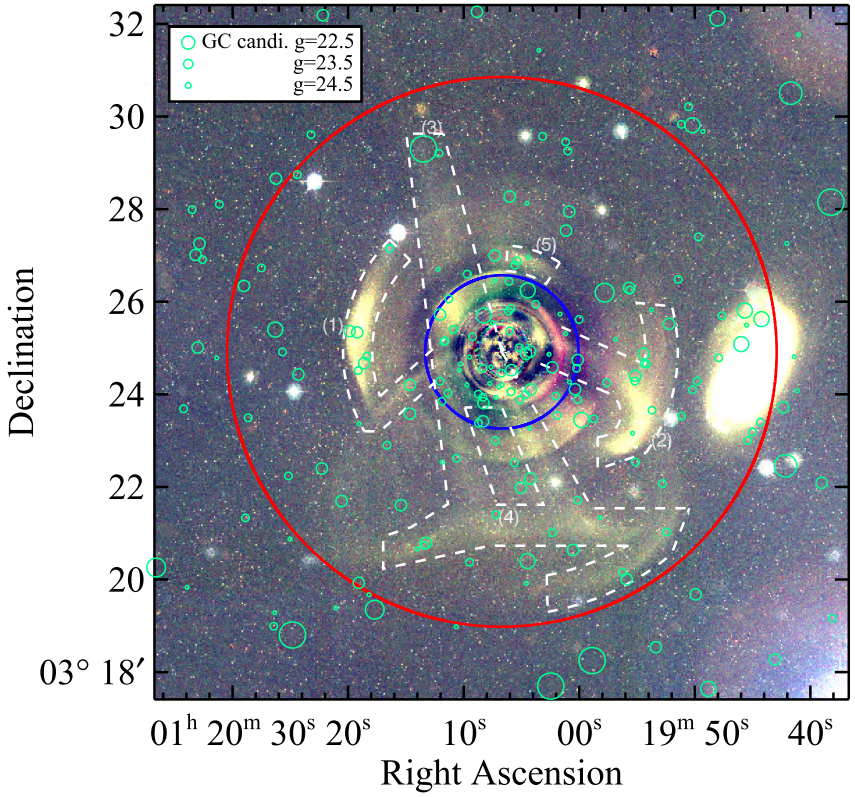

Figure 1. Spatial distribution of GC candidates centered on NGC 474. The coordinates are J2000. Small open circles represent the GC candidates of NGC 474. The sizes show the *g*-band magnitudes of GC candidates with the size scale displayed on the top left. The two large circles (inner and outer) centered on the galaxy show 3 effective radii for the stars and 2.5 effective radii for the GC system. Dashed lines indicate the rough boundaries of fine structures, with numbers labeling interesting substructures. The color image was made with *gri* model-subtracted images. The field of view is 15′ × 15′, corresponding to 135 kpc × 135 kpc in NGC 474 distance.

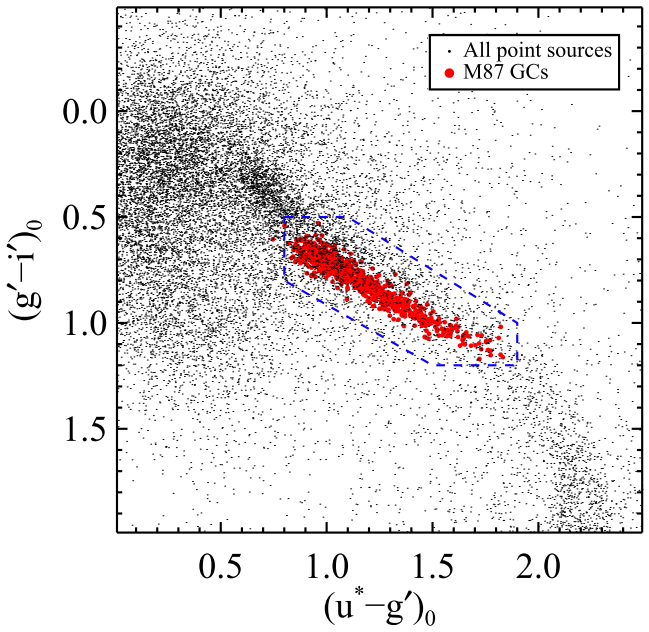

Figure 2. $(u^* - g')_0$ vs. $(g' - i)_0$ color–color diagram of point sources. Small dots represent the point sources in this study. Filled circles indicate the colors of spectroscopically confirmed GCs of M87 in previous studies to guide the location of GCs in the color–color diagram (Hanes et al. 2001; Strader et al. 2011; Zhang et al. 2015). We drew the dashed polygon based on M87 GCs and chose GC candidates in NGC 474 using this polygon.

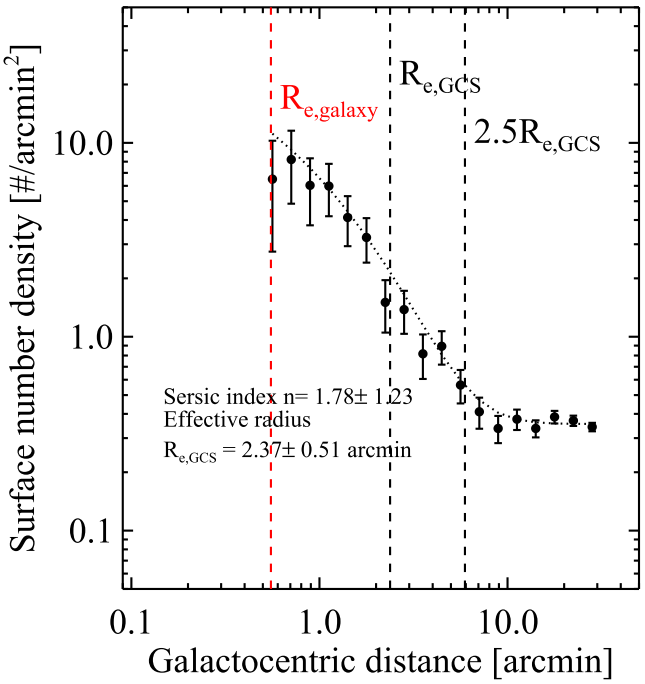

Figure 3. Number density profile of GC candidates. Filled circles with error bars show the number density of GC candidates with binned areas and its errors. The dotted line represents the best fit with a Sersić function, including the background. The vertical dashed lines represent the effective radius of the galaxy, the effective radius of the GC system, and the 2.5 effective radius of the GC system, respectively.

Table 1
A Catalog of the Globular Clusters in NGC 474

ID	R.A. (J2000)	Decl. (J2000)	g_0 [mag]	$(u-g)_0$	$(g-r)_0$	$(g-i)_0$
121	20.05616177	3.48833758	19.00 ± 0.00	2.37 ± 0.00	0.65 ± 0.00	0.89 ± 0.00
33	19.99084420	3.43659182	21.26 ± 0.00	2.18 ± 0.01	0.59 ± 0.00	0.92 ± 0.00
64	20.01865022	3.33998520	21.53 ± 0.00	1.36 ± 0.01	0.38 ± 0.01	0.56 ± 0.01
36	19.99918751	3.39075644	21.71 ± 0.00	1.76 ± 0.02	0.48 ± 0.01	0.76 ± 0.01
6	19.94028364	3.43017381	21.96 ± 0.01	1.69 ± 0.02	0.47 ± 0.01	0.70 ± 0.01

(This table is available in its entirety in machine-readable form.)

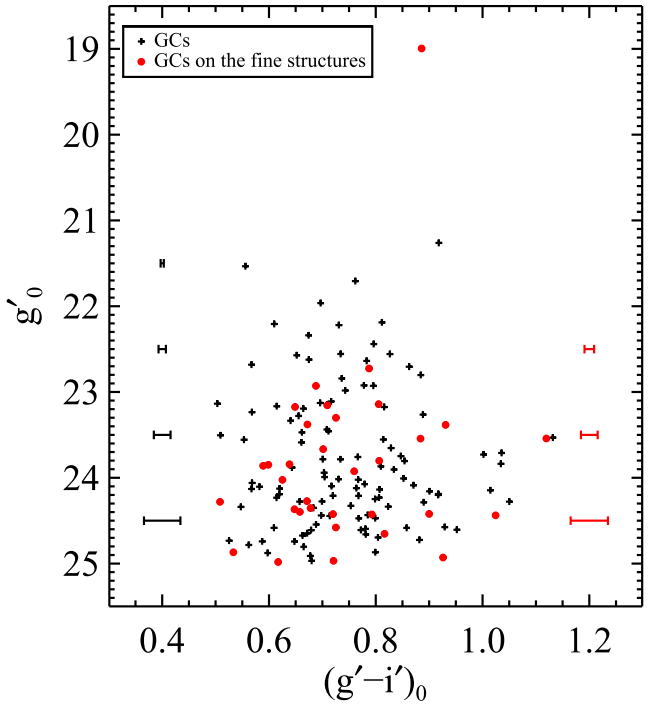

Figure 4. $(g' - i)_0 - g_0$ color magnitude diagram of GC candidates within $2.5R_{e,GCS}$. Crosses and filled circles show the GC candidates off and on the fine structures, respectively. The error bars on the left side and right side represent the color errors of GC candidates off and on the fine structures, respectively.

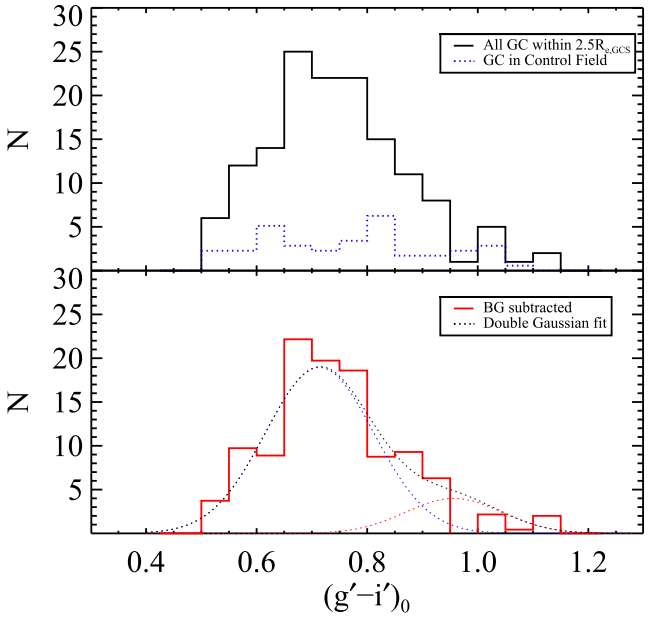

Figure 5. Color histogram of GC candidates in NGC 474. (Top) The solid line shows the color histogram for all GC candidates within the 2.5 effective radius of the GC system. The dotted line (blue) displays the color histogram of background contamination (the histogram of GC candidates in the control field, corrected for area). (Bottom) The solid line (red) represents the background-subtracted color histogram of GC candidates within the 2.5 effective radius of the GC system. Dotted lines show the fitted Gaussian functions.

contamination. The GMM code provides the blue and red peaks of color distribution and the D value. The D value shows the separation of the two peaks relative to their width, and two-Gaussian fitting is meaningful when $D > 2$. The mean D value for the 1000 GMM trials is 3.00, and its standard deviation is 0.36. This suggests that the color histogram of GCs in NGC 474 is better explained by a bimodal distribution than by a unimodal distribution, although this is likely due to the tail of red GCs. Dust in NGC 474's shells (e.g., Sikkema et al. 2007) could also cause the reddening of GC colors, but we see no correlation between the location of the red GCs and the position relative to the shells. The two Gaussian distributions have means at $(g' - i')_0 = 0.71 \pm 0.02$ and 0.96 ± 0.09, respectively, and these values are consistent with expected color peaks from the empirical relations between GC peak colors and galaxy luminosity (Peng et al. 2006).

3.2. Fine Structures

The fine structures of NGC 474 are very complex and have been discussed previously (Turnbull et al. 1999; Duc et al. 2015). Two relatively bright substructures are located at the east and west sides (1 and 2 in Figure 1, respectively). Substructure (2) has a tail which seems to penetrate the central region of NGC 474. A tidal stream (3) crosses the main body of NGC 474 from the north to the south. Tidal streams are also found in the southern area (4). These streams (4) may be linked with the tail of substructure (2). There is also a bright shell structure to the north of the central region (5). Many shell structures are seen in the inner regions of NGC 474, but some of them may be due to imperfect model subtraction. We ignore these structures for the purposes of this study.

To estimate the number and properties of GCs on the fine structures, we define an area that includes all regions described above except for the central region ($R < 1\farcm7 \approx 3R_{e,galaxy}$). We exclude the inner $1\farcm7$ due to confusion between fine structures and undersutracted regions. The area of the fine structures is 16% of the total area in the range $1\farcm7 < R < 2.5R_{e,GCS}$. We find 32 GC candidates superimposed on these fine structures, about 35% of all GCs beyond $1\farcm7$, after background subtraction. These numbers are increased when we include

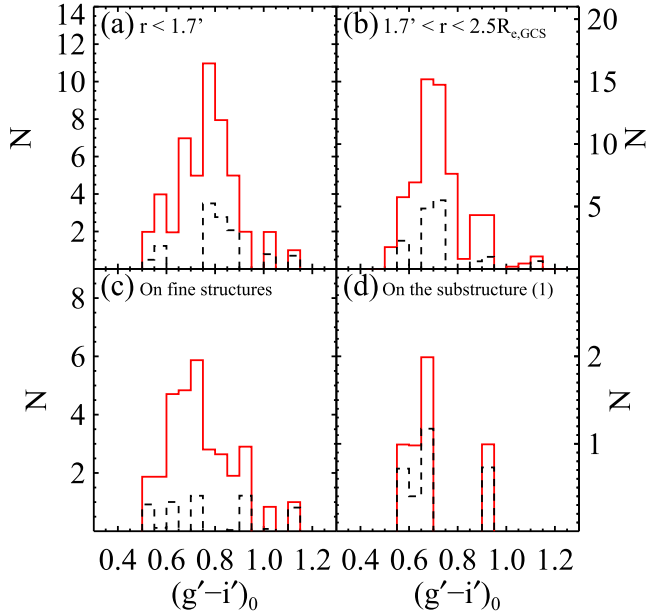

Figure 6. Color distributions of GC candidates in different subregions. Panels (a), (b), (c), and (d) show the GCs within 1′.7, 1′.7 $< R <$ 2.5$R_{e,GCS}$, the fine structures, and the eastern bright substructure, respectively. The solid histograms (red) are the background-subtracted color distributions. The dashed histograms (black) subtract the double Gaussian function fit to the color distribution of all GCs within 2.5 $R_{e,GC}$ from the color histograms of GCs in the subregions.

less prominent fine structures. Interestingly, five GC candidates are found on bright substructure (1) to the east.

To determine the significance of this positional correlation, we perform a Monte Carlo experiment that produces random GC positions from a smooth GC profile. There are 94 GC candidates with 1′.7 $< R <$ 2.5$R_{e,GCS}$. We create random samples of 94 GCs where the position angle θ is uniformly random and R is randomly sampled from the best-fit Sersić profile within the radius limits. We do this 100,000 times and find that only 0.11% of the samples show an equal or greater number of GCs superimposed on the fine structures compared to the real data. We also do the same test for bright substructure (1) to the east, and only 0.09% of results show an equal or greater number of GCs on the bright substructure compared to the real data. These results suggest that the GCs on the fine structures are physically associated with the fine structures with ∼99.9% confidence.

3.3. Colors of GCs on Substructures

Figure 6 displays a color histogram of GC candidates in different subregions of NGC 474. The colors of GCs in the central region (Figure 6(a)) have a peak at $(g' - i')_0 \sim 0.85$ mag, which means that GCs in the central region have mostly intermediate color. To better reveal this intermediate-color population, we subtract the double Gaussian function fit to the color distribution of all GCs within 2.5 $R_{e,GCS}$ from the color histograms of GCs in the subregions. There is an excess at $(g' - i')_0 \sim 0.85$ mag with GCs in the central region, although GCs in the other subregions show excesses at the blue color ($(g' - i')_0 \sim 0.7$) or no excess. GCs in the outer region (Figure 6(b)) and on fine structures (Figure 6(c)) have similar colors because a large portion of their areas is the same. In both cases, blue GCs are dominant. The colors of GCs on the fine structures are slightly bluer than the mean of the blue peak for the total population (shown by the Gaussian curves). GCs on bright substructure (1) are mostly blue, with $(g' - i')_0 \sim 0.7$ mag (Figure 6(d)).

4. Discussion and Conclusion

In this study, we find that there is a significant correlation between the GC spatial distribution and the locations of low surface brightness fine structures. Moreover, we find that GCs superimposed on the fine structures are mostly blue. At least ∼35% of outer GCs are visibly associated with recent merging. Bright substructure (1) at the east side of NGC 474 is highly likely to be the remnant of an accreted dwarf galaxy. We roughly estimate the magnitude and color of substructure (1) to be $g' \sim 15.5$ mag and $(g - i)_0 \sim 0.6$, respectively. The color of this substructure is similar to the peak color of the GCs on it, suggesting that substructure (1) and the GCs on it have similar stellar populations. The absolute magnitude of this substructure is about $M_{g'} \sim -17.0$, which is on the luminous side for a dwarf galaxy but still sub-$L^\star$. We obtain a GC specific frequency of $S_N \sim 1$ using the number of GC candidates on this feature. This S_N value is a typical value for galaxies with a similar luminosity (Peng et al. 2008), so it may support the idea that GC candidates that lie in projection on this substructure are actually physically associated with the substructure.

We have also found intermediate-color GCs in the central region. Intermediate-color GCs in merger remnant galaxies are mostly explained as intermediate-age GCs (e.g., Trancho et al. 2014). The ATLAS^{3D} survey revealed that the mean age of the stellar population in the central region of NGC 474 is 7.65 ± 1.39 Gyr (McDermid et al. 2015), which makes it younger than the massive cluster early-type galaxies typically studied. The intermediate-color GCs could therefore also have younger ages. We suggest that the intermediate-color GCs are GCs formed in situ when star formation occurred at least 7–8 Gyr ago.

One interesting result in this study is the lack of red GCs. We find that the fraction of red GC candidates within 2.5$R_{e,GCS}$ is about 20%. Peng et al. (2006), however, showed that the red GC fraction for a galaxy with similar luminosity to NGC 474 should be about 50%. Peng et al. (2006) only studied the central regions of galaxies, so the relatively small fraction of red GCs may be due to the wide spatial coverage of our study. Moreover, Sikkema et al. (2006), using *HST* imaging, showed that the fraction of red GCs is small even in the central region of NGC 474, so the lack of red GCs in NGC 474 seems to be a genuine property of the system.

Gas-rich mergers usually increase the number of metal-rich GCs, but if the merger occurred a few gigayears ago, GCs formed in merging will still have intermediate color and not yet be very red. These intermediate-color GCs will become typical red GCs after several gigayears. If we assume that these intermediate-color GCs are 7–8 Gyr old with $(g' - i')_0 \sim 0.85$, then the colors of these GCs will be $(g' - i')_0 \sim 0.94$ when they are 13 Gyr old with $Z \sim 0.003$ based on a theoretical simple stellar population model (Maraston 2005; Bressan et al. 2012). This red color is consistent with the peak color of red GC populations. When these intermediate-color GCs are 13 Gyr old, the fraction of red GCs will be about 40%, consistent with the results in Peng et al. (2006).

In this study, we have caught both traditional GC subpopulations in mid-evolution. A population of likely intermediate-age GCs are metal-rich GCs, which will passively redden to have colors similar to those seen in older galaxies. The metal-poor population is seen to be physically associated with cold streams and fine structures in the halo of NGC 474. Future studies using MATLAS survey data will allow us to probe this association across a wide range of galaxy mass and environments. The properties of GCs associated with visible substructures will be useful for determining the origin of streams and shells in massive galaxies.

We thank the anonymous referee for helpful comments that improved the original manuscript. S.L. and E.W.P. acknowledge support from the National Natural Science Foundation of China through Grant No. 11573002 and from the Strategic Priority Research Program, "The Emergence of Cosmological Structures," of the Chinese Academy of Sciences, Grant No. XDB09000105. This work is based on observations obtained with MegaPrime/MegaCam, a joint project of CFHT and CEA/IRFU, at the Canada–France–Hawaii Telescope (CFHT), which is operated by the National Research Council (NRC) of Canada, Institut National des Science de l'Univers of Centre National de la Recherche Scientifique (CNRS) of France, and the University of Hawaii. This work is based in part on data products from Terapix available at the Canadian Astronomy Data Centre as part of the CFHT Legacy Survey, a collaborative project of the NRC and CNRS.

Facility: CFHT.

References

Bertin, E., & Arnouts, S. 1996, A&AS, 117, 393
Blom, C., Forbes, D. A., Brodie, J. P., et al. 2012, MNRAS, 426, 1959
Bournaud, F., Duc, P.-A., & Emsellem, E. 2008, MNRAS, 389, L8
Bressan, A., Marigo, P., Girardi, L., et al. 2012, MNRAS, 427, 127
Cappellari, M., Emsellem, E., Krajnović, D., et al. 2011, MNRAS, 413, 813
Côté, P., Marzke, R. O., & West, M. J. 1998, ApJ, 501, 554
Duc, P.-A., Cuillandre, J.-C., Karabal, E., et al. 2015, MNRAS, 446, 120
Durrell, P. R., Côté, P., Peng, E. W., et al. 2014, ApJ, 794, 103
Foster, C., Lux, H., Romanowsky, A. J., et al. 2014, MNRAS, 442, 3544
Foster, C., Pastorello, N., Roediger, J., et al. 2016, MNRAS, 457, 147
Gwyn, S. D. J. 2008, PASP, 120, 212
Hanes, D. A., Côté, P., Bridges, T. J., et al. 2001, ApJ, 559, 812
Huxor, A. P., Mackey, A. D., Ferguson, A. M. N., et al. 2014, MNRAS, 442, 2165
Kartha, S. S., Forbes, D. A., Spitler, L. R., et al. 2014, MNRAS, 437, 273
Kruijssen, J. M. D. 2015, MNRAS, 454, 1658
Kruijssen, J. M. D., Pelupessy, F. I., Lamers, H. J. G. L. M., et al. 2012, MNRAS, 421, 1927
Li, B., Peng, E. W., Zhang, H.-X., et al. 2015, ApJ, 806, 133
Li, H., & Gnedin, O. Y. 2014, ApJ, 796, 10
Liu, C., Peng, E. W., Côté, P., et al. 2015, ApJ, 812, 34
Liu, Y., Peng, E. W., Blakeslee, J., et al. 2016, ApJ, 818, 179
Maraston, C. 2005, MNRAS, 362, 799
McDermid, R. M., Alatalo, K., Blitz, L., et al. 2015, MNRAS, 448, 3484
Muratov, A. L., & Gnedin, O. Y. 2010, ApJ, 718, 1266
Naab, T., Johansson, P. H., & Ostriker, J. P. 2009, ApJL, 699, L178
Oser, L., Ostriker, J. P., Naab, T., Johansson, P. H., & Burkert, A. 2010, ApJ, 725, 2312
Park, H. S., & Lee, M. G. 2013, ApJL, 773, L27
Peng, E. W., Jordán, A., Côté, P., et al. 2006, ApJ, 639, 95
Peng, E. W., Jordán, A., Côté, P., et al. 2008, ApJ, 681, 197
Pota, V., Forbes, D. A., Romanowsky, A. J., et al. 2013, MNRAS, 428, 389
Renaud, F., Bournaud, F., & Duc, P.-A. 2015, MNRAS, 446, 2038
Renaud, F., & Gieles, M. 2013, MNRAS, 431, L83
Schlegel, D. J., Finkbeiner, D. P., & Davis, M. 1998, ApJ, 500, 525
Shapiro, K. L., Genzel, R., & Förster Schreiber, N. M. 2010, MNRAS, 403, L36
Sikkema, G., Carter, D., Peletier, R. F., et al. 2007, A&A, 467, 1011
Sikkema, G., Peletier, R. F., Carter, D., Valentijn, E. A., & Balcells, M. 2006, A&A, 458, 53
Strader, J., Romanowsky, A. J., Brodie, J. P., et al. 2011, ApJS, 197, 33
Tonini, C. 2013, ApJ, 762, 39
Trancho, G., Miller, B. W., Schweizer, F., Burdett, D. P., & Palamara, D. 2014, ApJ, 790, 122
Turnbull, A. J., Bridges, T. J., & Carter, D. 1999, MNRAS, 307, 967
Wang, Q., Peng, E. W., Blakeslee, J. P., et al. 2013, ApJ, 769, 145
Whitmore, B. C., Schweizer, F., Leitherer, C., Borne, K., & Robert, C. 1993, AJ, 106, 1354
Zhang, H.-X., Peng, E. W., Côté, P., et al. 2015, ApJ, 802, 30

Astronomy & Astrophysics manuscript no. letter˙delayed
July 25, 2017

On the SFR-M$_*$ main sequence archetypal star-formation history and analytical models

L. Ciesla[1], D. Elbaz[1], and J.Fensch[1].

Laboratoire AIM-Paris-Saclay, CEA/DSM/Irfu - CNRS - Université Paris Diderot, CEA-Saclay, F-91191 Gif-sur-Yvette, France

Received; accepted

ABSTRACT

The star-formation history (SFH) of galaxies is a key assumption to derive their physical properties and can lead to strong biases. In this work, we derive the SFH of main sequence (MS) galaxies and show how the peak SFH of a galaxy depends on its seed mass at, for example, z=5. This seed mass reflects the galaxy's underlying dark matter (DM) halo environment. We show that, following the MS, galaxies undergo a drastic slow down of their stellar mass growth after reaching the peak of their SFH. According to abundance matching, these masses correspond to hot and massive DM halos which state could result in less efficient gas inflows on the galaxies and thus could be the origin of limited stellar mass growth. As a result, we show that galaxies, still on the MS, can enter the passive region of the UVJ diagram while still forming stars. The best fit to the MS SFH is provided by a right skew peak function for which we provide parameters depending on the seed mass of the galaxy. The ability of the classical analytical SFHs to retrieve the star-formation rate (SFR) of galaxies from spectral energy distribution (SED) fitting is studied. Due to mathematical limitations, the exponentially declining and delayed SFH struggle to model high SFR, which starts to be problematic at z>2. The exponentially rising and log-normal SFHs exhibit the opposite behavior with the ability to reach very high SFR, and thus model starburst galaxies, but they are not able to model low values such as those expected at low redshift for massive galaxies. By simulating galaxies SED from the MS SFH, we show that these four analytical forms recover the SFR of MS galaxies with an error dependent on the model and the redshift. They are, however, sensitive enough to probe small variations of SFR within the MS, with an error ranging from 5 to 40% depending on the SFH assumption and redshift; but all the four fail to recover the SFR of rapidly quenched galaxies. However, these SFHs lead to an artificial gradient of age, parallel to the MS, which is not exhibited by the simulated sample. This gradient is also produced on real data as we show using a sample of real galaxies with redshifts between 1.5 and 2.5. Here, we propose an SFH composed of a delayed form to model the bulk of stellar population with the addition of a flexibility in the recent SFH. This SFH provides very good estimates of the SFR of MS, starbursts, and rapidly quenched galaxies at all redshift. Furthermore, when used on the real sample, the age gradient disappears which show its dependency on the SFH assumption made to perform the SED fitting.

Key words. Galaxies: evolution, fundamental parameters

1. Introduction

The evolution of galaxies depends on their star-formation history (SFH), which is by definition the star-formation rate of a galaxy as a function of time. Two main physical properties of galaxies are directly computed from their spectral energy distributions (SED) assuming an SFH: the stellar mass and the star-formation rate (SFR) at the time the galaxy is observed. For star-forming galaxies, these two parameters follow a relation called the main sequence of galaxies (MS, e.g. Noeske et al. 2007; Elbaz et al. 2007, 2011; Rodighiero et al. 2011; Schreiber et al. 2015) whose normalization increases with redshift. The scatter of the MS, however, is found to be roughly constant over cosmic time (Ilbert et al. 2015; Schreiber et al. 2015). The main consequence of this relation is that galaxies form the bulk of their stars through steady state processes rather than violent episodes of star-formation, putting constraints on the SFH of galaxies. One method to derive the stellar mass and SFR of galaxies is to build and model their spectral energy distribution. To do so, one has to assume a stellar population model (e.g., Bruzual & Charlot 2003; Maraston 2005) convolved by a star-formation history, and then to apply an attenuation law (Calzetti et al. 2000). The models built to fit the data are thus dependent on the SFH of galaxies.

First order approximations of galaxy SFHs can be guessed through the evolution of the SFR density of galaxies as a function of cosmic time (see the review by Madau & Dickinson 2014) showing that the global SFR of galaxies peaks around $z \sim 2$ and then smoothly decreases. Going further, several studies have shown that sophisticated SFH parametrizations which include stochastic events, such as those predicted by hydrodynamical simulations and semi-analytical models, have to be taken into account to reproduce a galaxy's SFH (e.g., Lee et al. 2010; Pacifici et al. 2013; Behroozi et al. 2013; Pacifici et al. 2016). These models are complex to implement and a large library is needed to be able to model all galaxies properties. Instead, numerous studies have tested and used simple analytical forms to easily compute galaxies physical properties (e.g., Papovich et al. 2001; Maraston et al. 2010; Pforr et al. 2012; Gladders et al. 2013; Simha et al. 2014; Buat et al. 2014; Boquien et al. 2014; Ciesla et al. 2015; Abramson et al. 2016; Ciesla et al. 2016). Recently, Ciesla et al. (2015) used complex SFHs produced by the semi-analytical model GALFORM (Cole et al. 2000; Bower et al. 2006) to model z=1 galaxies SED and recover their stellar mass and SFR using simple analytical SFHs. They found that the double-exponentially decreasing and the delayed SFHs recovered the real SFR and M$_*$ relatively well. There is, however, a general agreement on the difficulty to constrain the age of the galaxy, here defined as the age of the oldest star, from broad-band SED fitting (e.g. Maraston et al. 2010; Pforr et al. 2012; Buat et al. 2014; Ciesla et al. 2015).

The exquisite sensitivity of the Hubble space telescope (HST) and *Spitzer* now, combined with Atacama Large Millimeter Array (ALMA) observations and soon to be complemented by the James Webb space telescope (JWST), allows us to better sample high redshift galaxy SEDs and thus apply more sophisticated SED fitting methods implying the use of these analytical SFHs tested at lower redshifts. The aim of this study is to compute the SFH of galaxies following the MS and understand if the widely used analytical SFHs are pertinent to model them, as well as outliers such as starburst or rapidly quenched galaxies, regardless of the redshift.

Throughout this paper, we use the WMAP7 cosmological parameters (H_0 = 70.4 km Mpc^{-1} s^{-1}, Ω_0 = 0.272, Komatsu et al. 2011). SED fitting is performed assuming an initial mass function (IMF) of Salpeter (1955), but the results of this work are found to be independent on IMF choice.

2. The star-formation history of a main sequence galaxy

Over the past decade, numerous studies have shown that the bulk of star-forming galaxies follow a relation between their SFR and their stellar mass, with observational confirmation that this relation holds up to z=4 (Schreiber et al. 2016b). Recently, Schreiber et al. (2015) parametrized the MS as a function of stellar mass and redshift. It is thus possible to build the SFH of a star-forming galaxy following the MS by computing the SFR corresponding to the stellar mass at each redshift or time step. Due to the decrease of the MS normalization with decreasing redshift, the typical SFR of galaxies at a given fixed mass (e.g., around M*, the knee of the stellar mass function) declines with time. However, because of the positive slope of the MS, the SFR of a galaxy increases with its stellar mass up to high masses where the MS starts to bend. Computing the resulting SFH of a star-forming galaxy which stays on the MS when forming stars will allow us to understand how the two effects affect the star-formation activity of the galaxy.

Starting at z=5 with a given mass seed, we calculate at each time step the SFR corresponding to the redshift and mass, assuming the MS relations of Schreiber et al. (2015). Then the mass produced during the time step is calculated assuming a constant SFR. At the following time step, we derive the new SFR associated with the redshift at the given time and the new computed mass. The computed SFR and stellar masses are shown on the MS plane in Fig. 1 for every five time steps, for five seed mass.

We show the resulting SFHs in Fig. 2 (bottom panel), from z=5 to 0.3, for four different seed masses, as well as their stellar mass histories (top panel). The ranges where the MS relation is constrained from observations, that is, up to M$_*$=3×10^{11}, is shown (solid lines) as well as extrapolations of these relations at higher masses (dashed lines). At early stages, the SFR increases with cosmic time implying that the effect of the positive slope of the MS dominates the decrease of its normalization. Then it reaches a peak, after which, a smooth decline of the SFR is observed due to a combination of the decline of the MS normalization and the bending of the MS at high masses. The peak of the SFR history of an individual galaxy depends on the mass of the seed and occurs at a cosmic time of 2.8 Gyr in the case of M_{seed}=10^{10} M$_\odot$, and at 8.9 Gyr for M_{seed}=10^6 M$_\odot$ (Fig. 4, right panel). From this point, we cannote that the position and width of the peak of the cosmic star-formation density must contain information on the distribution of galaxies' seed masses. The SFH

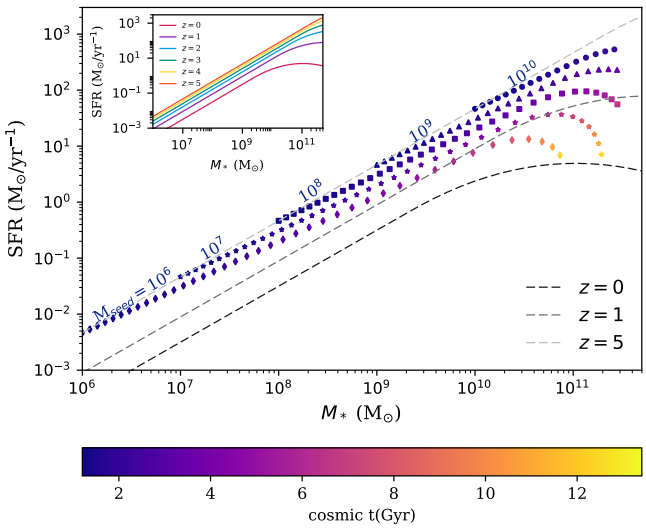

Fig. 1: Evolution of the simulated galaxies following the main sequence from z=5 to z=0.3 on the SFR-M$_*$ diagram, color coded with cosmic time. The different symbols correspond to different mass seeds: 10^6 (diamonds), 10^7 (stars), 10^8 (squares), 10^9 (triangles), and 10^{10} M$_\odot$ (circles). The dashed lines indicates the MS at redshift 0 (black), 1 (gray), and 5 (light gray). The insert panel shows the MS relations from z=5 to z=0 on which the evolution of MS galaxies is computed.

of MS galaxies thus depends on the time but also on the seed mass. This seed mass can be used as a proxy for the halo mass and thus the environment (Behroozi et al. 2013). Therefore, the star-formation history of a galaxy following the MS is dependent on environment. These different shapes of SFH as a function of the seed mass are a direct consequence of the bending of the MS above a given mass, whose evolution with redshift is taken into account by the models of Schreiber et al. (2015). After the peak, the SFR starts to smoothly decrease translating into a much slower stellar mass growth, close to saturation (Fig. 2, top panel). Thus, just by following the MS, a galaxy will undergo a smooth and slow diminution of its star-formation activity from a time defined by its seed mass.

This is the scenario of the slow downfall presented in Schreiber et al. (2015), for instance. In Fig. 3, we show the evolution of the colors of the galaxies presented in Fig. 2, assuming no dust attenuation. Just by following the MS, the evolution of its colors makes the galaxy enter the "passive" zone of the UVJ diagram. However, the galaxy is not quenched; it is still following the MS and thus forming stars, but given the relatively low SFR and the high mass of the galaxy, the colors of the evolved stellar population dominate the emission of the galaxy and place it into the "passive" region of the UVJ diagram.

Figure 4 shows the critical stellar mass and redshift at which the mass growth starts to reach a plateau (left panel) and the SFR at the peak of the SFH (right panel) for the five seed masses shown in Fig. 2. There is a strong variation of the mass and SFR$_{max}$ with redshift. Using abundance matching, one can convert these stellar masses to halo masses (Behroozi et al. 2013) and obtain 10^{13} M$_\odot$ at z=0.4 to 2-4×10^{14} M$_\odot$ above z=1-1.5. At all redshifts, these corresponding halo masses are above the critical line predicted by Dekel et al. (2009) to set the threshold mass for a stable shock based on spherical infall analysis (Dekel & Birnboim 2006). At these mass-redshift regions, the model pre-

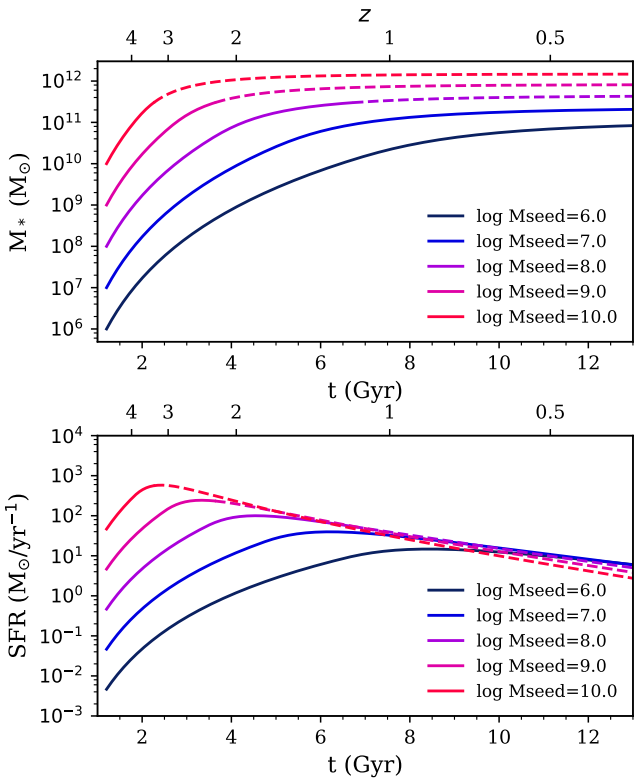

Fig. 2: Stellar mass and star-formation histories of galaxies following the main sequence from z=5 to z=0.3. The colored lines correspond to different mass seeds from 10^6 (dark blue) to 10^{10} $M_\odot$ (red). The solid lines correspond to range in M_* and SFR constrained by observations while the dashed lines are extrapolations of the MS relation. On the top panel, symbols indicate the time and mass when the galaxies enter the passive zone of the UVJ diagram (see Fig. 3).

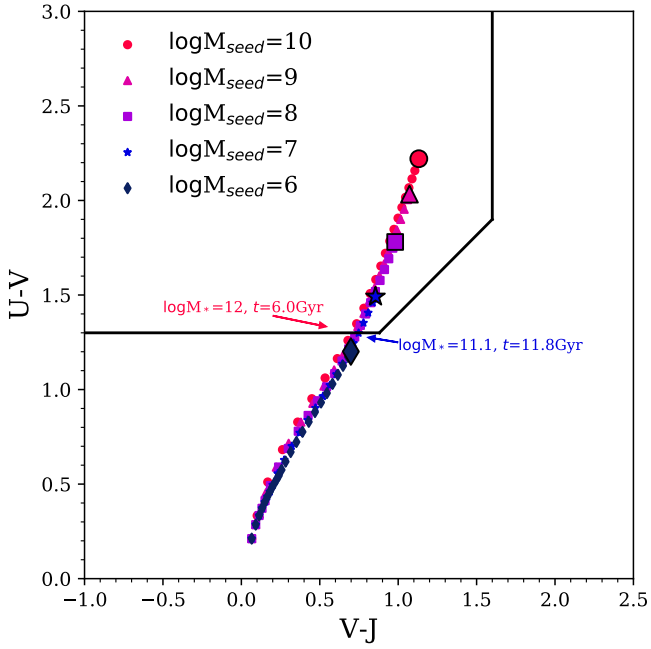

Fig. 3: Evolution of the U-V and V-J colors in the UVJ diagram from z=5 to z=0.1 for the five galaxies presented in Fig. 2, assuming the full star-formation histories of Fig. 2(constrained + extrapolations) and no dust attenuation. Color coding is the same as in Fig.2. Black contoured symbols indicate the final time step. The time and stellar mass when the galaxies with seed mass of 10^6 (dark blue) and 10^{10} $M_\odot$ (red) enter the passive "red" region are indicated.

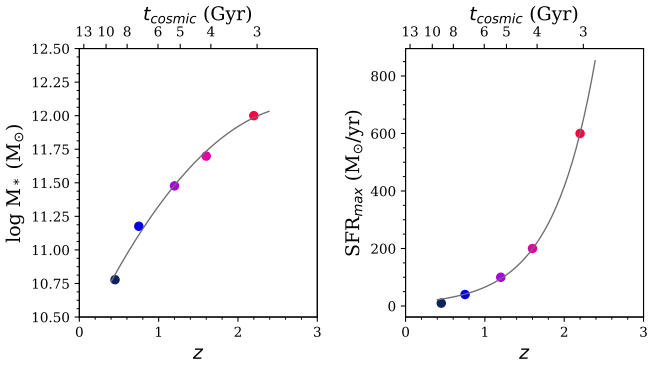

Fig. 4: Stellar masses (left panel) at which the galaxy growth starts to drastically slow down as a function of redshift and SFR at the peak of the SFH (right panel). Points are color-coded according to their seed mass as defined in Fig. 2. Fit to the data are shown in gray in both panels.

sented in Dekel et al. (2009) predicts that the galaxies lie in hot halos which shut off most of the gas supply to the inner galaxy. This resulting limited gas inflow to the galaxy could be a possible explanation for the slow decrease of the star-formation activity.

Several studies aimed at trying to parametrize the global SFH of galaxies with analytical functions, either with the requirement to fit both individual SFH as well as the cosmic SFH, such as one or two log-normal functions (Gladders et al. 2013; Abramson et al. 2016), or to follow the predicted evolution of Dark Matter (DM) halo masses, such as a double power law (Behroozi et al. 2013). These functional forms, however, do not provide satisfactory fits of the computed SFH of MS galaxies, as shown in Fig. 5. These functions do not manage to model the early SFH and the position of the peak of SFR is offset. In the case of the log-normal SFH, the peak is shifted towards later times and is too broad. Furthermore, the slope of the declining part is too steep. The double power law provides a peak slightly shifted towards shorter ages, the slope of the declining part is closer to the true one, but the declining part of the MS SFH is flatter than what is computed by these functions. We also tried other forms such as a Gaussian, a skewed Gaussian, and combinations of them with a power law or an exponential, but they all suffered problems.

After an extensive test of several analytic forms, the best fit of the MS SFH (Fig. 2) is found to be a Right Skew Peak Function, based on a skewed Gaussian, which analytical expression is:

$$\mathrm{SFR}(t, M_{seed}) = A\,\frac{\sqrt{\pi}}{2}\,\sigma\, e^{\left((\frac{\sigma}{2r_S})^2 - \frac{t-\mu}{r_S}\right)}\,\mathrm{erfc}\left(\frac{\sigma}{2\,r_S} - \frac{t-\mu}{\sigma}\right), \quad (1)$$

with t the time (in Gyr), A the amplitude, σ the width of the Gaussian, r_S the right skew slope, μ the position of the Gaussian centroid, and $erfc$ is the standard complementary error function.

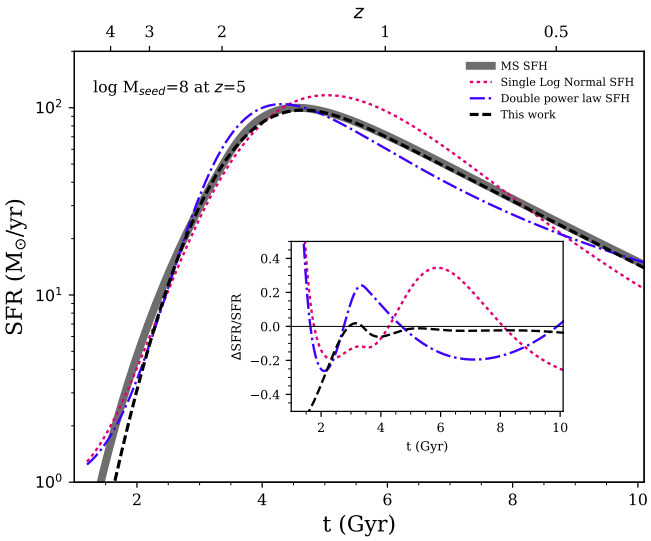

Fig. 5: Fit of the MS SFH assuming a seed mass of 10^8 M$_\odot$ at z=5, using different analytical functions proposed in the literature: log-normal (red), double power law (blue), and the parametrization based on a right skew peak function proposed in this work (black). The residual of each fit is shown in the insert panel.

Table 1: Coefficient values to compute the parameters of the MS SFH corresponding to an exponential declining function for A, μ, and σ, and to a linear function for r_S.

Parameter	A_p	τ_p
A	6.0×10^{-3}	-0.84
μ	47.39	3.12
σ	17.08	2.96
Parameter	slope: α_p	β_p
r_S	-0.56	7.03

The values of the different coefficients depend on the seed mass. To constrain this relation, we fit a right skew peak function to a set of MS SFHs computed from a grid of seed masses. The best value of each parameter as a function of seed mass is shown in Fig. 6, with a best fit for A, μ, and σ provided by :

$$p(M_{seed}) = A_p e^{-\frac{\log M_{seed}}{\tau_p}}. \quad (2)$$

The values of A_p and τ_p are given in Table 1 for all the coefficients. For the right skew slope parameter, r_S, a linear function provides a better fit with the parameters also provided in Table 1. The results of this parametrization of the MS SFH of a galaxy with a seed mass of 10^8 M$_\odot$ is shown on Fig. 5. The early part of the MS SFH is slightly underestimated with the right skew peak function, but at t>3 Gyr the agreement is very good, the position of the peak is recovered, and the declining slope is reproduced.

This SFH is computed from the MS relation obtained from observations. The bulk of star-forming galaxies follow this relation and thus we use it as a benchmark in the rest of this study.

3. Analytical star-formation histories

In this section, we test the robustness of various analytical forms of SFH, commonly used in the literature. We focus on the delayed, the exponentially declining, the exponentially rising, and

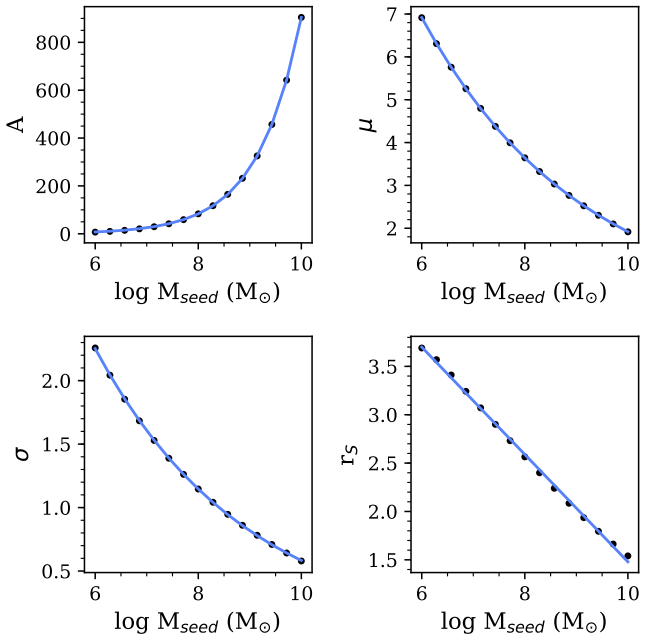

Fig. 6: Dependency of the Gaussian and exponential parameters obtained from the best fits of a set of SFHs, as a function of the seed mass. Black dots are the best values at each seed mass and the red curve shows the relation between the parameters and the seed mass.

the log-normal SFHs. We describe their parametrization and show their shape on Fig. 7, as a function of the e-folding time parameter of the main stellar population τ.

The exponential SFH is defined as:

$$\mathrm{SFR}(t) \propto e^{-t/\tau}, \quad (3)$$

where t is the time and τ the e-folding time of the stellar population. Positive and negative values of τ corresponds to an exponentially declining and rising SFH, respectively.

The delayed SFH is defined as:

$$\mathrm{SFR}(t) \propto t\, e^{-t/\tau}, \quad (4)$$

where t is the time and τ the e-folding time of the stellar population.

The effect of τ on the shape of the delayed and exponential declining SFHs can be seen in Fig. 7: short values correspond to galaxies where the bulk of the stars were formed early on and in a short time followed by a smooth decrease of the SFR, while high values imply a roughly constant SFR over cosmic time. For the exponentially rising SFH, the bulk of the stars are formed in a short and recent time with small τ values. For these three SFHs, the highest SFR are reached for low τ values and short times. As a comparison, we show along with the different delayed SFH the modeled SFH of a MS galaxy with a seed mass of 10^9 M$_\odot$ at z=5. No value of τ provides a good model of the peak of the MS SFH, reaching such a SFR would need a low value of τ associated with a short age incompatible with the time at which the peak of SF occurs.

Recently, Abramson et al. (2016) discussed the use of a log-normal function to model galaxies' SFH and reproduce the cosmic SFR density following the results of Gladders et al. (2013).

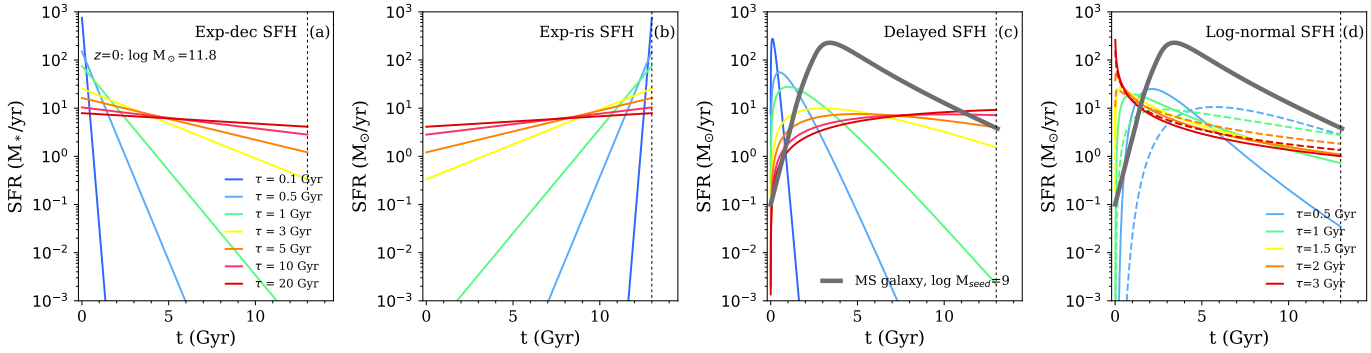

Fig. 7: From left to right: exponentially declining (a), exponentially rising (b), delayed (c), and log-normal (d) SFH considering a galaxy with a stellar mass of 6.3×10^{11} $M_\odot$ at z=0. We compare the delayed and log-normal SFH shapes with our MS galaxy SFH in gray (see Fig. 5), in the last two panels. For the log-normal SFH, models are shown with $\ln t_0$=1 Gyr (solid lines) and $\ln t_0$=2 Gyr (dashed lines).

In these studies, the log-normal SFH is defined as:

$$\mathrm{SFR}(t) \propto \frac{1}{t\sqrt{2\pi\tau^2}}\, e^{\frac{-(\ln(t)-t_0)^2}{2\tau^2}}, \qquad (5)$$

where t_0 is the logarithmic delay time, and τ sets the rise and decay timescale (Gladders et al. 2013). The log-normal SFH, for different values of t_0 and τ, is shown in Fig. 7d. The inclusion of t_0 controls the time at which the SFH peaks, which cannot be done in the case of the delayed SFH for instance. We compare these different log-normal curves with the computed SFH of MS galaxies, as discussed in the previous section and Fig. 5, and find that the log-normal function also struggles to reproduce this SFH (Fig. 7). While adapted to reproduce the cosmic SFH integrated over all galaxy seed masses, the log-normal SFH is less efficient in reproducing the shape of the individual SFH of MS galaxies. These histories are indeed strongly dependent on seed masses as illustrated in Fig. 2, bottom panel.

4. Recovering the star-formation history of main sequence galaxies

In Sect. 2, we built the SFH of a galaxy following the MS throughout its lifetime. To test how well the analytical SFHs presented in the previous section can model this archetypal galaxy, we show in Fig. 8 the specific SFR (sSFR) of this galaxy as a function of its stellar mass, following its evolution on this plane. In addition, we show the MS relations derived by Schreiber et al. (2015) from observations at z=0, 2, and 4. This relation is only constrained up to z=3 but we extrapolate it at z=4 following Schreiber et al. (2016b) who recently showed that it still holds at z= 4. To understand if the analytical SFHs studied here are able to cover the parameter space necessary to model our MS galaxy, we compute a grid of models for each SFH. We use the largest reasonable limits of age, from 100 Myr to 13 Gyr, and τ, from 1 Myr to 20 Gyr for the exponential SFHs and the delayed one. The number density of models is completely dependent on our τ and age grids, however the space covered by our computed models is the largest since we consider minimum and maximum possible values for these two parameters. The resulting parameter space in terms of sSFR and stellar mass is shown with the colored filled region on Fig. 8. In the case of the log-normal form, we use three values of t_0, and a less resolved grid of τ as compared to the other models for computational reasons, although we keep the minimum and maximum possible values.

We have seen that the evidence of a MS implies that galaxies experienced on average a rising SFH following their birth before reaching a peak and a drop of star-formation. As a natural result, the exponentially declining SFH is not suited for this early phase. The locus of the z=4 MS indeed falls in the dark zone of Fig. 8a, which is unpopulated by the analytical formula whatever parameters are chosen. More surprisingly, the delayed SFH, which was built to account for this behavior, encounters a similar problem although less sharply, that is, some extreme parameter choices can marginally reach z=4 but not above. This comes from the stiffness of the analytical formula which is unable to follow the actual shape of the MS-driven SFH. More generally, these two analytical SFHs are not optimized to finely sample the SFH at epochs $z\geq2$. This problem is not present with the exponentially rising SFH which instead is not optimized for $z\leq2$. The same conclusions are drawn for the log-normal function that is able to reach very high values of SFR, but not the smallest ones expected at low redshifts for massive galaxies.

To understand why the exponentially declining and delayed SFHs struggle to reproduce high sSFR, we show in Fig. 9 the relation between the age, τ, and the SFR for the whole grid of models. The highest SFRs are reached from a combination of low ages and low values of τ. This implies limitations on the estimate of the SFR since the age cannot be higher than the age of the Universe. On the contrary, we can easily see that a whole range of high SFRs can be obtained with the exponentially rising SFH and the log-normal one, but not the low SFRs needed to model high mass local galaxies, confirming what we observe in Fig.8, where this SFH fails to reproduce our modeled MS galaxy at $z < 0.4$.

We conclude that the exponentially declining and delayed SFH are not optimized to model the emission of MS galaxies at $z\geq2$ as they show little mathematical flexibility to reproduce the SFR of these galaxies. However, the exponentially rising SFH can model such high redshift sources, as well as the log-normal function, but not for massive galaxies below z<2.

5. Recovering the scatter of the main sequence

The MS relation exhibits a scatter of 0.3 dex that is found to be constant with redshift (Guo et al. 2013; Schreiber et al. 2015). There are two possible origins for this scatter. The first one is that this scatter could be artificially created by the accumulation of errors due to observations, photometric measurements,

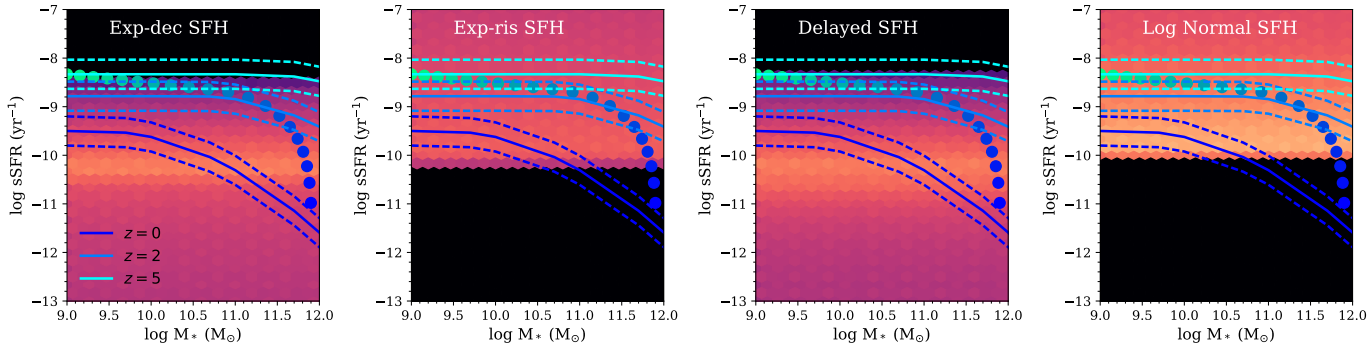

Fig. 8: Parameter space covered by the exponentially decreasing, exponentially rising, and delayed SFH in the sSFR-M$_*$ plane. The minimum age considered is 100 Myr and the minimum τ considered is 1 Myr. The color shaded regions indicate the number density of models, black representing the absence of models whereas orange indicates the density of models. In each panel, the solid line and the dashed lines show the MS relation and its scatter as derived by Schreiber et al. (2015) at z= 0 (dark blue), 2 (light blue), and 4 (cyan). The evolution of a MS galaxy throughout its cosmic life from z=5 to 0 is shown by the circles color-coded with the redshift.

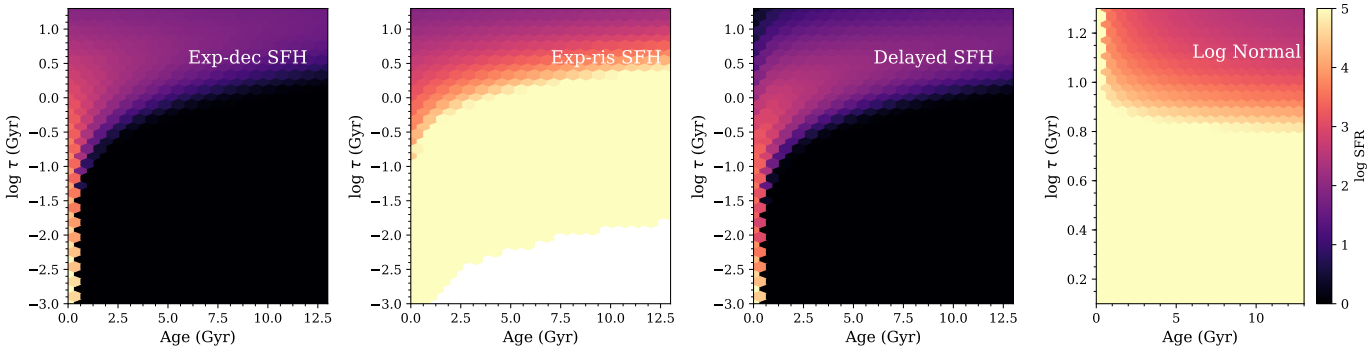

Fig. 9: Dependency between the age and τ parameters color-coded with the SFR obtained for our grid of star-formation histories at z= 0, 2, and 5. The highest SFR are obtained with a combination of low values of τ but especially the lowest values of the age.

and determination of physical properties from different methods (instrumental errors, assumptions linked to SED modeling, etc). The second one is that the scatter could be due to a variation of a third property (other than M$_*$ and SFR) across the MS and thus be physical (e.g., Rodríguez-Puebla et al. 2016). Indeed, some simulations predict that galaxies can undergo some fluctuations of star-formation activity resulting in variations of their SFR such as compaction or variations of accretion (e.g., Dekel & Burkert 2014; Sargent et al. 2014; Scoville et al. 2016). These variations should be small enough to keep the SFR of the galaxy within the MS scatter.

To understand the origin of the scatter of the MS, analytical SFHs must be able to recover small recent variations of the SFR with a precision better than the scatter of the MS itself, that is 0.3 dex. To test the functional forms studied in this work, we take our computed MS galaxy SFH described in Sect. 8 and add, at different redshifts, a small variation of the SFR, an enhancement or a decrease. This variation is applied to the last 100 Myr of the SFH and its intensity is randomly selected in a Gaussian distribution centered on the exact MS SFR at the given redshift and mass, and with a σ of 0.3 dex. Five hundred mock SFHs are created at each redshift, from z=1 to 5, varying the mass of the galaxy seeds from 10^7 to 10^{10} M$_\odot$. To derive galaxies' SED from these SFH, we use the SED modeling code CIGALE (Noll et al. 2009, Boquien et al. in prep) based on an energy balance between the energy attenuated in ultraviolet (UV) and optical, and re-emitted in infrared (IR) by the dust. CIGALE can model galaxies SED from all kinds of SFH, analytical forms or output from complex simulations. In this case, we provide CIGALE with our computed SFHs and build SEDs using the stellar population models of Bruzual & Charlot (2003), a Calzetti et al. (2000) attenuation law, and the dust emission templates of Dale et al. (2014). The modeled SEDs are then integrated into the set of filters available for the Great Observatories Origins Deep Survey (GOODS) south field, and a random noise distributed in a Gaussian with σ =0.1 is added to the modeled fluxes, following the method described in Ciesla et al. (2015). We then use the SED fitting mode of CIGALE to recover the physical parameters of our mock galaxies. To fit our galaxies, we do not provide as an input the parameter used to build the mock galaxies, and the attenuation law is a free parameter. However, we use three IR bands, MIPS 24 μm, PACS 100, and 160 μm. Because CIGALE is based on an energy budget, having IR data is thus ideal to constrain the amount of attenuation and break the degeneracy with age. We emphasize the fact that the following results should be considered as a best case scenario. The physical properties of the galaxies are computed from the probability distribution function (PDF) of each parameter computed by CIGALE, the final value being the mean of the PDF and the error its standard deviation.

At each redshift, and for each SFH assumption, Fig. 10 (top panel) shows the relative difference between the estimated SFR and the true one known from our simulated galaxies. Globally, at

all redshifts, all SFH assumptions recover the true SFR within an error below ±25% except the exponentially declining SFH that underestimates the SFR by ∼40% at z=4. The estimated error of 25% on the SFR corresponds to a quarter of the MS scatter, thus the usual SFH should be sensitive enough to probe variations of the order of 0.3 dex of star-formation activity around the MS.

The ability of each SFH assumption to recover the physical properties of the mock galaxies is, however, dependent on redshift. Indeed, the error on the SFR increases with redshift for the exponentially declining SFH showing that this form is more suited for galaxies at z≤2-3. The opposite behavior is observed for the rising exponential which provides better estimates of SFR at z=4 than at z=1 where it clearly overestimates this parameter, indicating that this SFH is more suited for galaxies at z>2-3. This is in agreement with the typical MS SFH described in Sect. 8 with an increase of the SFR at early time, well modeled by the rising exponential, followed by a smooth decrease, modeled by the exponentially declining SFH. The behavior of these two SFH assumptions is not surprising and was already pointing out in several studies (e.g., Maraston et al. 2010; Papovich et al. 2011; Pforr et al. 2012; Reddy et al. 2012). However, this emphasizes the fact that these two SFH must be carefully selected according to the redshifts of galaxies in order to limit biases on the derivation of their physical properties. The delayed SFH, however, seems to provide estimates of the SFR which show a weaker dependency on redshift, although we note an underestimate at z=4 that is less pronounced than the exponential SFH.

Recently, Ciesla et al. (2015) performed a similar analysis on z=1 galaxies simulated by the semi-analytical code GALFORM and they found that the exponentially declining and delayed SFH underestimated the SFR by 11% and 9%, respectively. Here we find a weak overestimation of a few percent in the estimate of the SFR for both SFH. This apparent disagreement is likely due to the different SFHs which were used to build the SEDs (complex SFH produced by a SAM code in Ciesla et al. (2015) versus a simple analytical form linked to the MS here) as well as the parameters used to perform the fits; for instance, the attenuation law is a free parameter in this study. Improvements in the code since 2015 may also play a role. The log-normal SFH provides very good estimates of the SFR of MS galaxies at all redshifts with an error less than 10%. We note that the two functional forms that have a similar global shape compared to the MS SFH, the log-normal and the delayed SFH, recover well the SFR of the mock galaxies, with little dependency on the redshift compared to the exponential forms. From this analysis, we conclude that the four tested SFH assumptions provide fair measurements of the SFR of MS galaxies, but the log-normal and delayed SFH estimates are more accurate and less redshift dependent than the other models.

6. Extreme SFHs: Starbursts and rapidly quenched galaxies

We tested in the previous section the ability of the usual SFHs to recover the SFR of MS galaxies. **Recently, Steinhardt et al. (2017) argued that considering that galaxies stay on the MS all their lives would result in a significantly steeper stellar mass function towards low redshift and they showed that taking into account mergers would settle the conflict with the observed growth of stellar mass.** Furthermore, after spending a long time on the MS, galaxies are expected to quench (e.g., Heinis et al. 2014; Steinhardt & Speagle 2014). To test the impact of higher perturbations on the SFR, we perform here the same test as in the previous section, that is, we model MS galaxies to which we apply, this time, a strong burst or quenching.

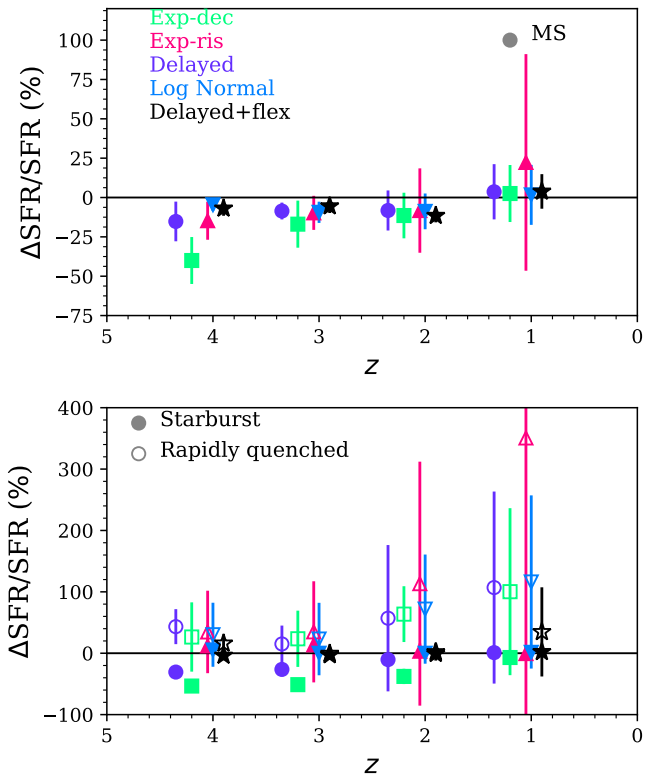

Fig. 10: Mean errors (ΔSFR/SFR=(SFR − SFR_{true})/SFR_{true}) on the recovering of the SFR of simulated MS galaxies (top panel), starbursts, and rapidly quenched galaxies (botton panel) as a function of redshift using different SFH assumptions: exponentially-declining (green), exponentially-rising (pink), the delayed (purple), the log-normal (blue), and the delayed + flexibility SFH (black) that is described in section 9, and at four redshifts. The points are slightly shifted horizontally with respect to each other for the sake of clarity.

To model starburst galaxies, we systematically multiply by a factor of 5.24 the SFR in the last 100 Myr of our simulated MS galaxies and add a random scatter of 0.3 dex following a Gaussian distribution, as suggested by Schreiber et al. (2016a). We then follow the same procedure as for the MS galaxies, that is, we build their SEDs with CIGALE and perform the fitting. The relative difference between the output of the fitting and the true SFRs for the starburst galaxies is shown in Fig. 10 (bottom panel, filled symbols). At z=1, the three assumptions provide good estimates of the SFR of starburst galaxies. Moreover, the results from the rising exponential SFH are better than for the MS galaxies as expected from Fig. 9, where we showed that this SFH is able to reproduce very high SFR, and provide good estimates, below 20%, at all the redshifts considered here. The log-normal function provides very good estimates as well, as expected. However, the delayed and exponentially declining SFHs underestimate the SFR with a factor increasing with redshift, up to errors of ∼40 and ∼50%, respectively, at z=4. This is also explained by the difficulty that these models have in reaching very high SFR as shown again in Fig. 9. We thus conclude that exponentially rising and log-normal SFHs are well suited to model starburst galaxies at all redshifts, whereas the delayed SFH is

suited for starburst galaxies at $z \leq 2$ and the exponentially declining for galaxies at $z \leq 1$.

We now investigate the case of galaxies undergoing a fast quenching of their star-formation activity. Here, we want to probe processes that strongly affect the activity of the galaxies in less than 500 Myr, such as ram pressure striping for instance, or violent negative feedback (e.g., SF-driven or winds driven by an active galactic nucleus) and not smooth quenching occurring in timescales of the order of several Gyr. Following the results of Ciesla et al. (2016), we apply to our MS SFH a systematic instantaneous break on the last 100 Myr of the SFH, making the SFR drop to 15% of the SFR before quenching. We then add a random scatter of 0.3 dex as we did for MS and starburst galaxies. The value of 15% is chosen as being intermediate between a total quenching (0%) and 30% which is the upper limit empirically defined by Ciesla et al. (2016) to consider a galaxy as rapidly quenched. The results on the SFR recovering for the rapidly quenched galaxies are shown in Fig. 10 (bottom panel, open symbols). In this case, the dispersion on the measurement is the largest, all the SFH overestimate the SFR in the best case (delayed SFH at z=3), by 20%, and by 350% in the worst case (the exponentially rising SFH at z=1). The dependance with redshift of $\Delta SFR/SFR$ is the same for the three assumptions, that is, they overestimate by 20 to 40% the SFR of galaxies at z=3 and 4, but by a factor of two in average at z=1 and 2. Indeed, we see in Fig. 9 that the delayed and the exponentially declining SFH can reach very low values of SFR but need a long time, that is, age to reach these values, which is not compatible with a sharp decline of the SFR. For the exponentially rising SFH, low values of SFR ($<10\,M_{\odot}yr^{-1}$) are not reachable as seen in Fig. 9, as well as for the log-normal SFH in the times probed here. We conclude then that none of these four SFHs is suited to derive the SFR of galaxies undergoing a rapid quenching of their star-formation activity.

7. Recovering the stellar mass of galaxies

The previous discussions on the ability of analytical SFH assumptions to recover the SFR of galaxies were motivated by the fact that, at a given stellar mass, the range of SFR reachable for these SFHs can be limited for mathematical reasons. However, we test in this section the ability of these analytical forms to recover the stellar mass of the galaxies as well. We compare in Fig. 11 the M_* obtained from our SED fitting procedure to the true M_* of the galaxies, as we did for the SFR in Fig. 10. For MS galaxies, Fig. 11 (upper panel) shows that in almost all cases, that is, all SFH assumptions and all redshift, the stellar mass is recovered with an error lower than 25%. The only exception is for the exponentially declining SFH at z=4 where M_* is overestimated by 35%. For the starburst galaxies (bottom panel of Fig. 11), there is a relation between the mean error on the stellar mass and the redshift for all SFH assumptions. The worst case is the exponentially declining SFH with a strong trend with redshift, from an overestimation of nearly 100% at z=4 to an underestimation of ~30% at z=1. The same tendency is observed in the case of the delayed SFH with a lower gradient, from +40% to −30%. The log-normal and exponentially rising SFH provide very good estimates of the stellar mass of starburst galaxies down to z=1 where they reach an underestimation of 30% like the exponentially declining and delayed SFH. In the case of rapidly quenched galaxies, all the SFH assumptions tested in this work provide a very good measurement of their stellar mass, implying that the larger errors observed for the starburst galaxies arise from the need to reach a high SFR at a given stellar mass. We conclude that only the exponentially declining SFH might introduce errors in the measurement of M_*, especially in the case of starburst galaxies, and must thus be used cautiously.

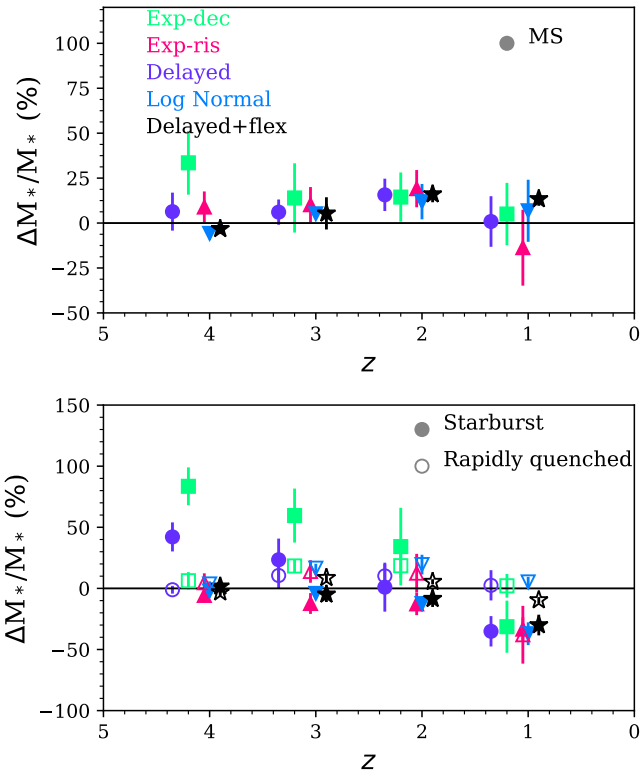

Fig. 11: Mean errors ($\Delta M_*/M_*=(M_* - M_*^{true})/M_*^{true}$) on the recovering of the M_* of simulated MS galaxies (top panel), starbursts, and rapidly quenched galaxies (botton panel) as a function of redshift using different SFH assumptions: exponentially-declining (green), exponentially-rising (pink), the delayed (purple), the log-normal (blue), and the delayed + flexibility SFH (black) that is described in section 9, and at four redshifts. The points are slightly shifted horizontally with respect to each other for the sake of clarity.

8. Biases

In the previous sections, we showed that analytical functions typically used in the literature feature mathematical rigidity that leads to errors in the recovery of physical parameters such as the SFR. On the one hand, from Fig. 9, we understand that large values of SFR are only reached assuming a very short age of the oldest star of the galaxies for the delayed and exponentially declining SFH. On the other hand, we expect the exponentially rising SFH to struggle in recovering weak SFR. We thus expect that modeling high redshift galaxies' SED with these SFH results in biases, especially in terms of age. As a first test, we simulate a mock galaxy sample and follow their SFH up to z=1.5-2.5. Here we take a simple scenario where a galaxy, with a given M_{seed} at z= 5 stays on the MS all its life but undergoes some episodes of enhanced star-formation followed by a time of lower star forming activity, corresponding to a self-regulation. However, these episodes are not strong enough to place the galaxy in the SB zone or in the quiescent region of the MS diagram; we force them to stay within the scatter of the MS. To do so, we take several as-

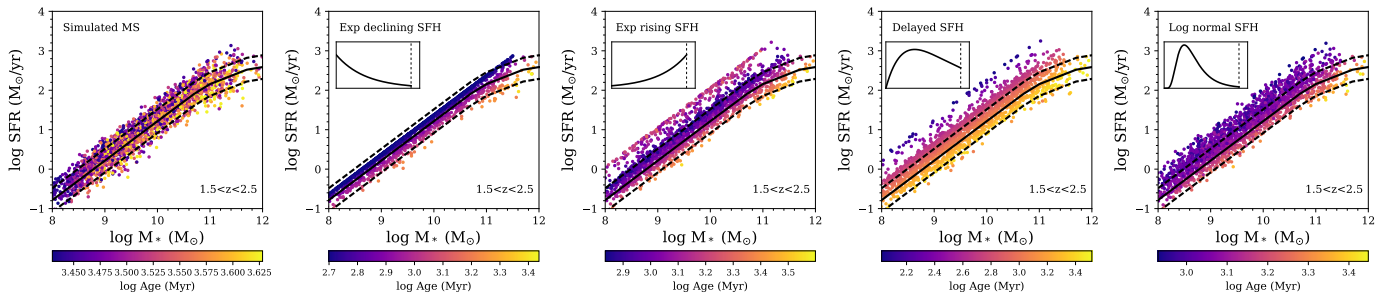

Fig. 12: Left panel: Mock galaxies between z= 1.5 and 2.5 placed on the MS diagram and color-coded according to their age. The solid line and the dashed lines indicate the MS and its scatter at z= 2. From the second left panel to the right panel: Results of the SED fitting of the mock galaxies using, from left to right, an exponentially declining, an exponentially rising, a delayed, and a log-normal SFH. Points are color-coded with the output age produced by the SED fitting. The z= 2 MS from Schreiber et al. (2015) is indicated in each panel.

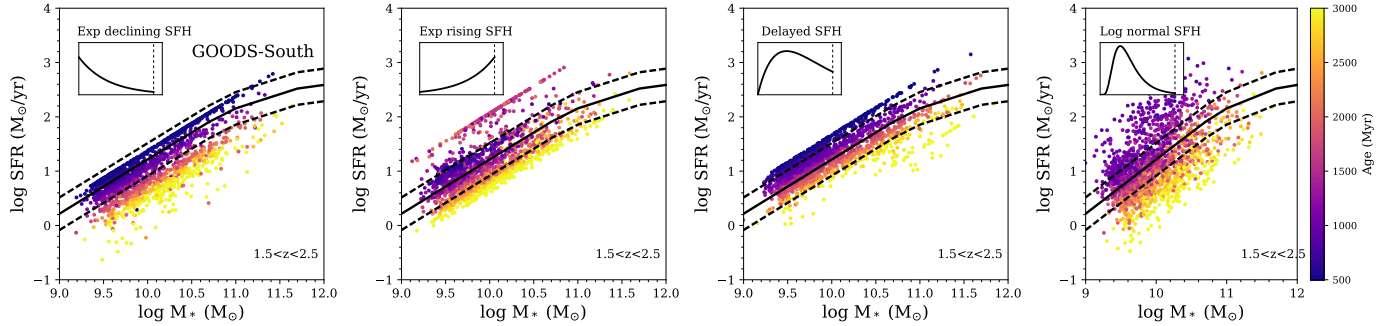

Fig. 14: Main sequence relation of GOODS-South galaxies between redshift 1.5 and 2.5 obtained using, from left to right, the delayed SFH, an exponentially decreasing SFH, an exponentially increasing SFH, and a log-normal SFH, color-coded by the age obtained from the fitting procedure. The black line indicates the position of the MS obtained by Schreiber et al. (2015) at z= 2.

sumptions. First, we randomly pick a M_{seed} in the mass function distribution computed by Schreiber et al. (2016a) at z=3.5-4.5. The normalization of the mass function is not important, only the shape is useful as we normalize it in order to compute the probability of having a galaxy seed with a given stellar mass. Then, for each time step we set the probability of having a star-formation enhancement to 75% and, in the case of this small burst, we impose that a small decrease of star-formation must follow this enhancement to account for self-regulation. The intensity of these episodes is randomly chosen in a Gaussian distribution with σ = 0.3 dex, that is, within the scatter of the MS. The intensities of the enhancement and the quiet periods are allowed to be different. We then calculate at each time step the stellar mass associated to the SFR. Finally, we randomly pick a redshift between 1.5 and 2.5 as the observed redshift for each galaxy. In the SED fitting methods, the age is defined as the time when the first star is formed. In this simple model using this definition is difficult and we therefore arbitrarily define the age of the galaxy as the time since the galaxy reached 10^6 $M_\odot$. This assumption should not impact on our result since we are interested in relative differences in the age of galaxies and not on absolute value. The resulting MS is shown in the left panel of Fig. 12a. No SED fitting is performed, this is just the output of the SFH of the mock galaxies. These simulated sources span a range of stellar masses between 10^8 and 10^{12} $M_\odot$ and SFR between 0.1 and 500 $M_\odot/yr^{-1}$. Their age is between 1.5 and 4 Gyr. Younger galaxies are preferentially found at low masses whereas massive galaxies are found at the highest mass range. We emphasize here that this is a simple case were the same attenuation law (Calzetti et al. 2000) and attenuation amount ($E_{(B-V)}$=0.3) is applied to all galaxies. The only parameters that are different from one simulated galaxy to another are those linked to the SFH.

We apply our SED fitting method to the simulated galaxies and place them on the MS plane using the outputs of the fit for the four analytical forms, color-coded with the age, also derived by CIGALE (Fig. 12 from panel b to e). For each SFH, we clearly see that the fitting method artificially introduces an age gradient parallel to the MS, with young ages on the top and older ages on the bottom. The exponentially declining SFH tends to tighten the galaxies on the MS relation while the opposite is noticed for the log-normal SFH that shows a wider spread of the galaxies, especially towards high SFR. In addition, we note an artificial line at high SFR in the case of the exponentially rising SFH. While the exponentially declining and rising SFH and the log-normal SFH tend to prefer low values of age, the delayed SFH is producing older ages, compared to the simulated sample.

In Fig. 13, we show the true median age of the simulated galaxies as well as those obtained through SED fitting for all analytical forms studied in this work, as a function of the relative distance to the MS, that is, the starburstiness (R_{SB}=SFR/SFR_{MS}, Elbaz et al. 2011). The true age is never recovered by any of the analytical forms studied in this work, with underestimations by a factor of 2-3. Furthermore, while the true age shows no relation with R_{SB}, the age produced by SED fitting shows a clear relation with R_{SB} with a slope and spread (as indicated by the error bars) that depends on the SFH assumptions. The delayed, the exponentially decreasing, and exponentially rising SFHs show the steepest slope, thus are the most bi-

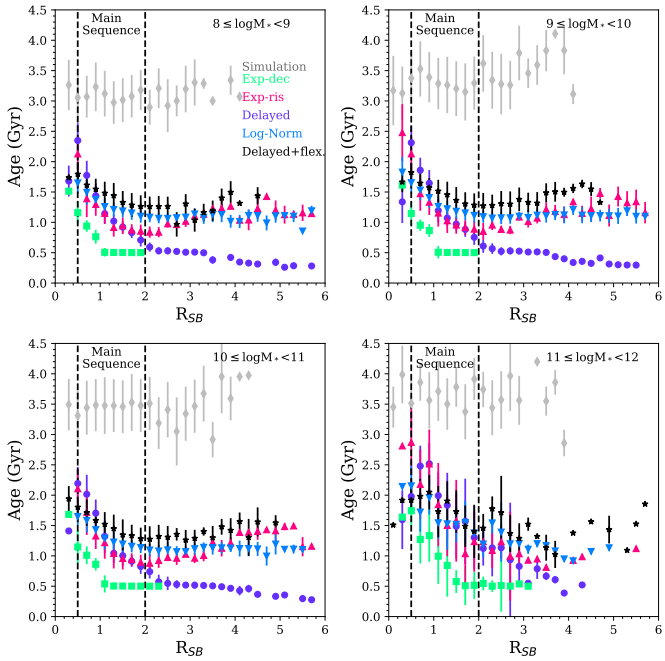

Fig. 13: Median age of the mock galaxy sample as a function of their distance to the MS (R_{SB}=SFR/SFR$_{MS}$) for four different mass bins. The true values of the mock galaxies are shown in gray while the results of the SED fitting using the exponentially declining, the exponentially rising, the delayed, the log normal, and the delayed plus flexibility SFH are indicated in green, pink, purple, light blue, and black, respectively. The error bars indicate the standard deviation around the medians. The dashed lines indicate the limits of the MS.

ased in all stellar mass bins, while the log-normal SFH shows the weakest trend. We note a tendency to overestimate the R_{SB} in all the SFH assumptions except the exponentially declining, confirming what we observe in Fig. 12.

The trends observed in Fig. 12 are obtained in an ideal case where, as we explained, only the SFH varies from one galaxy to another. To understand how it could impact real data, we select star forming galaxies in the GOODS-South sample from their position in the U-V versus V-J diagram (Labbé et al. 2003), between z= 1.5 and 2.5, and model their SED using CIGALE. The reader is referred to Ciesla et al. (2017, in prep) for a detailed description of the fitting procedure of these sources. Basically, we use the same procedure as in the previous section, applying parameters that are typically used in the literature to perform a UV-to-FIR SED fitting of high redshift galaxies with CIGALE (e.g., Giovannoli et al. 2011; Buat et al. 2015; Ciesla et al. 2015). Without knowing the real SFH of the GOODS-South sample galaxies, we observe, however, several trends similar to those we discussed in the test using the simulated galaxies. Indeed, for the exponentially declining and delayed SFH, we observe an artificial line at high SFR resulting from the limited range of SFR probed by these two SFHs, as shown in the previous section (black zone in Fig. 8). An artificial line is also found at high SFR for the exponentially rising SFH, but we also note the lack of galaxies with low SFRs compared to the two other SFHs, as expected. A different effect is found for the log-normal SFH where the range in SFR provided by the SED fitting is largely wider than when using the three other SFHs. There is also the same perfect gradient of age on the distribution of galaxies for all of the four assumptions. In all four models, we can see that the sources on the top of the MS seem to be the youngest at all masses, and the galaxies at the bottom part of the MS seem to be the oldest ones, again regardless of the stellar mass. We note that the age of the galaxies in the highest part of the MS is the lowest value allowed for the fit, in this case 500 Myr, as expected from our previous figures. This is due to the fact that, with the delayed and exponentially declining SFH, high values of SFR are only reached for small ages, as shown in Fig. 9. However, we also note a similar gradient in the case of the exponentially rising and log-normal SFHs. These four SFHs model a smoothly evolving main stellar population and, as shown in Sect. 6, struggle to recover the true SFR of galaxies experiencing strong enhancements or decreases of their star-formation activity. The age gradient obtained with these SFHs thus comes from a lack of mathematical flexibility preventing them from modeling recent variations of star-formation activity. We also performed our tests using a different definition of the age, that is, the mass-weighted age of the galaxy, and retrieved the same conclusions as for the simple age definition of the SED fitting method, that is, the presence of the gradient for every analytical form tested here, as shown in Fig. 15.

9. Modeling all galaxies with a single star-formation history

To recover the physical properties of galaxies, regardless of their type or star-formation activity, we need to use a form that models the bulk of the star-formation plus an additional flexibility in the recent SFH that can model variations in SFR within the scatter of the MS, but can also model stronger fluctuations due to a starburst or a fast quenching event. However, we have to keep in mind that the goal here is to derive parameters from broadband SED fitting and thus we have to take into account that SFH parameters are not well constrained from this method. What we propose here is to use a simple analytical form to model the bulk of the SFH and add a flexibility in the recent SFH to model small fluctuations to large variations of the SFR in the recent SFH.

9.1. Modeling the bulk of the star-formation history

The ideal SFH to model the main history would be the SFH derived for the MS galaxies, since it is defined to model the bulk of galaxies. However, as we showed in section 8, such a SFH is complicated to parametrize, and the closest analytical function is handled through four free parameters. Four parameters plus additional ones for flexibility in the recent SFH make this mathematical form too complicated for SED modeling. We have to choose a simpler analytical form that can replicate the increasing part of the SFH followed by a smooth decline and provide accurate SFR measurements. We thus exclude the exponential forms that do not model the global shape of the MS SFH and the difficulties in reproducing SFR in given redshift ranges. The form of the log-normal and delayed SFH is closest to the MS SFH, with the rising part followed by a smooth decline. From Fig. 10, we see that the log-normal function manages to recover the SFR of normal and star-bursting galaxies independently from redshift but fails to reproduce the SFR of rapidly quenched galaxies. However, this analytical form has two free parameters that can lead to degeneracies as we know that SFH parameters are difficult to constrain. Indeed, we see in Fig. 14 that, when used on real galaxies, the log-normal SFH yields to a very dispersed MS with a large scatter. This scatter is not compatible with what

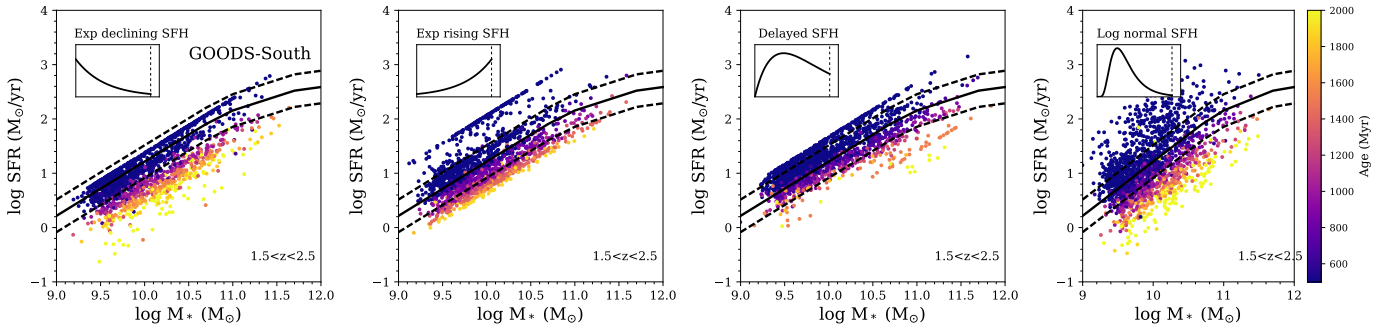

Fig. 15: Main sequence relation of GOODS-South galaxies between redshift 1.5 and 2.5 obtained using, from left to right, the delayed SFH, an exponentially decreasing SFH, an exponentially increasing SFH, and a log-normal SFH, color-coded by the mass-weighted age obtained from the fitting procedure. The black line indicates the position of the MS obtained by Schreiber et al. (2015) at z= 2.

is expected from the MS computed from luminosities, infrared versus H-band, and thus independently from model assumptions (Salmi et al. 2012). To not introduce any artificial scatter into the SFR-M$_*$ relation from SED fitting, we will not use the log-normal SFH. We thus propose to use a modified version of the delayed SFH that can be used at all redshifts and on all types of galaxies. Despite limitations in recovering the SFR of very high redshift galaxies, the delayed SFH was found to be able to recover the stellar mass of galaxies, and thus to provide a good modeling of the main part of the SFH compared to exponential SFHs (e.g., Lee et al. 2010; Ciesla et al. 2015; da Cunha et al. 2015; Ciesla et al. 2016). The rigidity implied by the mathematical shape of the SFH is problematic for the SFR but not for the stellar mass. Indeed, testing the delayed SFH on SED built from galaxies modeled by GALFORM, Ciesla et al. (2015) estimated that the stellar mass was recovered with a mean error lower than 7% and that this model better reproduced the envelope of the SFH than the exponentially decreasing models. Furthermore, the delayed SFH also has the advantage of having only one free parameter, τ_{main}. The delayed SFH is thus suited to model the bulk of the stellar population emission.

9.2. A flexibility in the recent SFH

We now modify the delayed SFH in order to correct for the mathematical rigidity that creates the artificial age gradient discussed in section 8 and allows the SFH to reach both high and low SFR. To overcome these limitations, we thus add a flexibility in the recent SFH to model an enhancement or decline of the SFR:

$$\mathrm{SFR}(t) \propto \begin{cases} te^{-t/\tau_{main}}, & \text{when } t \leq t_0 \\ \mathrm{r_{SFR}} \times \mathrm{SFR}(t = t_0), & \text{when } t > t_0 \end{cases} \quad (6)$$

where t_0 is the time when a rapid enhancement or decrease is allowed in the SFH and r_{SFR} is the ratio between the SFR after t_0 and before t_0. This flexibility allows the SFH to better probe recent variations in the SFH, regardless of its intensity (small variations within the MS scatter or intense burst or quenching). Such a SFH was proposed in Ciesla et al. (2016) and in Merlin et al. (2017, submitted), for instance, to model quenched galaxies but is also proposed in Ciesla et al. (2017, in prep) to model galaxies at the top of the MS or higher.

Values of r_{SFR} larger than one will correspond to an enhancement of the SFR whereas values lower than one will correspond to a decrease. This SFH is thus flexible enough to model galaxies inside the scatter of the MS but also starbursts and rapidly quenched galaxies (Ciesla et al. 2016). We put this SFH through the same tests as the three other SFHs except for the grid of models of Fig. 9. Indeed, by including the r_{SFR} parameter, all SFRs can be reached depending on the input values provided by the user. From Fig. 10 (black filled stars), we see that this SFH recovers very well the SFR of MS galaxies, with an error lower than ∼10% at all redshifts. We note that it produces SFRs that are of the same order as the three other assumptions studied here at z=1 and 2, but more accurate results at higher redshifts. For starburst galaxies, the ΔSFR/SFR values are very low, comparable to the results obtained with the rising exponential, showing a perfect recovering of starburst SFRs. The same agreement between the true SFR and the one from the delayed SFH with flexibility is found for the quenched galaxies with an error lower than the three others at all redshifts. We note, however, that there is still an error of 50% at z=1.

In Fig. 16 (top panel), we show the results obtained with this flexible SFH on the simulated galaxies. There is a less pronounced artificial age gradient consistent with the actual age distribution of Fig. 13a. There is a gradient of age which is not parallel to the MS similar to what is observed for the other SFH. The oldest galaxies are, for instance, not at the bottom of the MS, but at high masses. This is confirmed in Fig. 13, where we see that the gradient of age is the smallest with this flexible SFH. However, since this simulation is an ideal case, we apply our SFH to the same SED fitting procedure applied on GOODS-South galaxies presented above (Fig. 16-bottom). First, the limitation of the high values of SFR is weakened compared to other SFH assumptions and galaxies are allowed to go higher in SFR but also lower. There is no longer a gradient of age along the MS showing that the origin of this gradient strongly depends on the assumption made on the SFH of the galaxies when performing the SED fitting. Younger ages seem to be found at lower masses whereas older galaxies are found at higher masses. This behavior is closer to what would be expected considering a galaxy evolving on the MS all its life with some random episodes of enhanced star-formation followed by a period of lower star-formation activity, as could be considered in star-formation feedback scenarios, as simulated in Fig. 12 (left panel). The same result is obtained with the age defined as the mass-weighted age of the galaxy, that is, the age gradient is no longer present. However, since the age is known to be weakly constrained from SED fitting (e.g., Buat et al. 2014), we do not interpret further this possible trend.

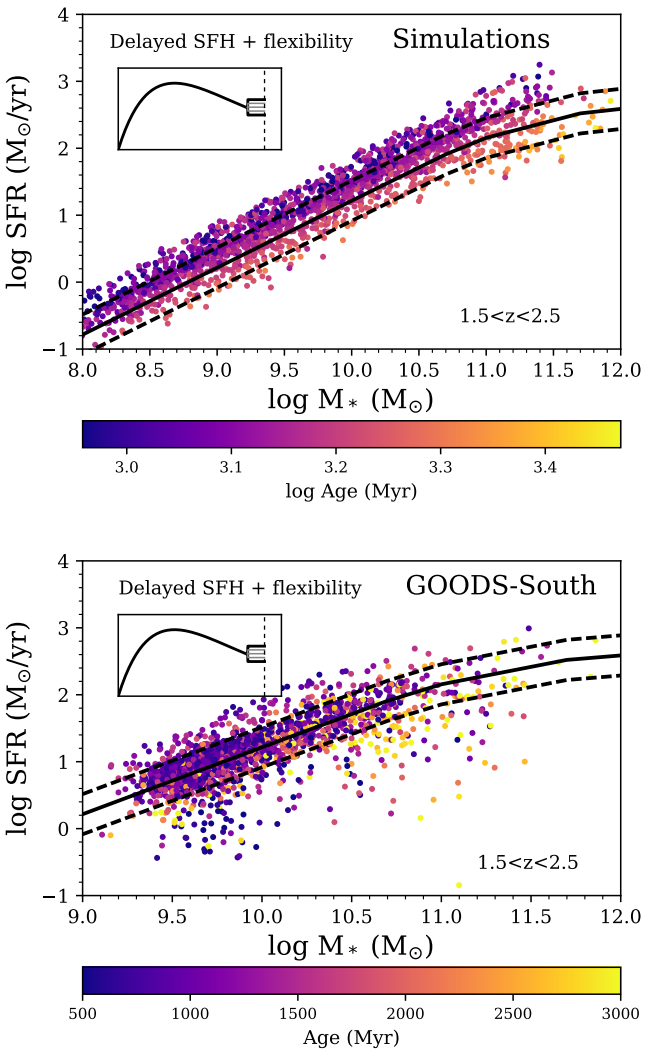

Fig. 16: Top panel: SED fitting results obtained for the mock galaxy sample using the delayed+flexibility SFH, color-coded with the output age of the galaxies. Bottom panel: Main sequence relation of GOODS-South galaxies between redshift 1.5 and 2.5 obtained using the delayed SFH with an additional flexibility in the recent SFH, color-coded by the age obtained from the fitting procedure. The black line indicates the position of the MS obtained by Schreiber et al. (2015) at z= 2.

We conclude that adding a flexibility in the recent SFH allows for a more accurate recovering of the SFR of MS, starburst, and rapidly quenched galaxies than SFH considering one main stellar population. The age gradient found across the MS seems to be SFH dependent and disappears with the use of this flexibility.

10. Conclusions

In this work, we computed the SFH of the bulk of star-forming galaxies, that is, of galaxies that follow the MS all their lives. The SFH of MS galaxies depends on cosmic time but also on the seed mass of the galaxy, which can be interpreted as a proxy for the DM halo mass, itself related to its local environment. These SFH show a peak of star-formation depending on the seed mass after which the SFR smoothly declines and the stellar mass growth drastically slows down. Following Dekel & Birnboim (2006), these masses correspond to a hot and massive state of DM halo limiting the gas available to fall on the galaxy and fueling star-formation and thus possibly being at the origin of the smooth decline of the SFR. As a consequence, we showed that MS galaxies can enter the passive region of the UVJ diagram while still forming stars following the MS.

We showed that the MS SFH is not reproduced by analytical forms usually used to perform SED fitting, neither by a log-normal SFH or a double-power-law SFH. The best fit is provided by a Right Skew Peak Function that we use to parametrize the SFH of MS galaxies as a function of seed mass and time.

Using the SFH of MS galaxies as a benchmark, we studied the ability of exponentially rising, exponentially declining, delayed, and log-normal SFHs to retrieve the SFR of galaxies from SED fitting. Due to mathematical limitations, the exponentially declining and delayed SFH struggle to model high SFR, which starts to be problematic at z>2. The exponentially rising and log-normal SFHs exhibit the opposite behavior with the ability to reach very high SFR but not low values such as those expected at low redshift for massive galaxies. Simulating galaxies SED from the MS SFH using the SED modeling code CIGALE, we showed that these four analytical forms recover well the SFR of MS galaxies with an error dependent on the model and the redshift. They are thus able to probe for small variations of SFR within the MS, such as those expected from compaction or variation of gas accretion scenarios, with an error ranging from 5 to 40% depending on the SFH assumption and the redshift. The exponentially rising and log-normal SFHs provide very good estimates of the SFR of starburst galaxies, but all of the four assumptions fail to recover the SFR of rapidly quenched galaxies. We note that these tests were made using information from the far-IR, and using the same code to model the SED and fit them. Although precautions were taken to minimize the potential biases, we emphasize the fact that these results should be considered as best case scenarios. Displaying the results of the SED fitting performed on the simulated galaxies on the MS diagram, we showed that all the four SFH assumptions tested in this work exhibit a gradient of age that is not an outcome of the simulation. As the simulated galaxies are an ideal case, with only the SFH varying from one galaxy to another, we test these analytical SFHs on real data. We use a sample of GOODS-South galaxies with redshift between 1.5 and 2.5, and show that some artificial limitations are produced at the lowest or highest SFRs depending on the model, and that the perfect gradient of age, parallel to the MS, is produced as well.

The best SFH that should be used to model galaxies is the MS SFH but, due to the complexity of its parametrization, its use for SED modeling is not reasonable as SFH parameters are unconstrained by broad band SED fitting. Since each of the four SFHs tested in this work show some caveats in recovering high or low SFR, at different redshift, and for different galaxy populations, we propose a SFH composed of a delayed form to model the bulk of the stellar population with the addition of a flexibility in the recent SFH. This SFH provides very good estimates of the SFR of MS, starbursts, and rapidly quenched galaxies at all redshift. Furthermore, used on the GOODS-South sample, we observe that the age gradient disappears, showing that it is dependent on the SFH assumption made to perform the SED fitting.

Acknowledgements. L. C. thanks C. Schreiber, E. Daddi, M. Boquien, and F. Bournaud for useful discussions. L. C. warmly thanks M. Boquien, Y. Roehlly, and D. Burgarella for developing the new version of CIGALE on which the present work relies.

References

Abramson, L. E., Gladders, M. D., Dressler, A., et al. 2016, ApJ, 832, 7
Behroozi, P. S., Wechsler, R. H., & Conroy, C. 2013, ApJ, 770, 57
Boquien, M., Buat, V., & Perret, V. 2014, A&A, 571, A72
Bower, R. G., Benson, A. J., Malbon, R., et al. 2006, MNRAS, 370, 645
Bruzual, G. & Charlot, S. 2003, MNRAS, 344, 1000
Buat, V., Heinis, S., Boquien, M., et al. 2014, A&A, 561, A39
Buat, V., Oi, N., Heinis, S., et al. 2015, A&A, 577, A141
Calzetti, D., Armus, L., Bohlin, R. C., et al. 2000, ApJ, 533, 682
Ciesla, L., Boselli, A., Elbaz, D., et al. 2016, A&A, 585, A43
Ciesla, L., Charmandaris, V., Georgakakis, A., et al. 2015, A&A, 576, A10
Cole, S., Lacey, C. G., Baugh, C. M., & Frenk, C. S. 2000, MNRAS, 319, 168
Cowie, L. L., Songaila, A., Hu, E. M., & Cohen, J. G. 1996, AJ, 112, 839
da Cunha, E., Walter, F., Smail, I. R., et al. 2015, ApJ, 806, 110
Dale, D. A., Helou, G., Magdis, G. E., et al. 2014, ApJ, 784, 83
Dekel, A. & Birnboim, Y. 2006, MNRAS, 368, 2
Dekel, A., Birnboim, Y., Engel, G., et al. 2009, Nature, 457, 451
Dekel, A. & Burkert, A. 2014, MNRAS, 438, 1870
Elbaz, D., Daddi, E., Le Borgne, D., et al. 2007, A&A, 468, 33
Elbaz, D., Dickinson, M., Hwang, H. S., et al. 2011, A&A, 533, A119
Giovannoli, E., Buat, V., Noll, S., Burgarella, D., & Magnelli, B. 2011, A&A, 525, A150
Gladders, M. D., Oemler, A., Dressler, A., et al. 2013, ApJ, 770, 64
Guo, K., Zheng, X. Z., & Fu, H. 2013, ApJ, 778, 23
Heinis, S., Buat, V., Béthermin, M., et al. 2014, MNRAS, 437, 1268
Ilbert, O., Arnouts, S., Le Floc'h, E., et al. 2015, A&A, 579, A2
Komatsu, E., Smith, K. M., Dunkley, J., et al. 2011, ApJS, 192, 18
Labbé, I., Franx, M., Rudnick, G., et al. 2003, AJ, 125, 1107
Lee, S.-K., Ferguson, H. C., Somerville, R. S., Wiklind, T., & Giavalisco, M. 2010, ApJ, 725, 1644
Madau, P. & Dickinson, M. 2014, ARA&A, 52, 415
Maraston, C. 2005, MNRAS, 362, 799
Maraston, C., Pforr, J., Renzini, A., et al. 2010, MNRAS, 407, 830
Noeske, K. G., Weiner, B. J., Faber, S. M., et al. 2007, ApJ, 660, L43
Noll, S., Burgarella, D., Giovannoli, E., et al. 2009, A&A, 507, 1793
Pacifici, C., Kassin, S. A., Weiner, B., Charlot, S., & Gardner, J. P. 2013, ApJ, 762, L15
Pacifici, C., Oh, S., Oh, K., Lee, J., & Yi, S. K. 2016, ApJ, 824, 45
Papovich, C., Dickinson, M., & Ferguson, H. C. 2001, ApJ, 559, 620
Papovich, C., Finkelstein, S. L., Ferguson, H. C., Lotz, J. M., & Giavalisco, M. 2011, MNRAS, 412, 1123
Pforr, J., Maraston, C., & Tonini, C. 2012, MNRAS, 422, 3285
Reddy, N. A., Pettini, M., Steidel, C. C., et al. 2012, ApJ, 754, 25
Rodighiero, G., Daddi, E., Baronchelli, I., et al. 2011, ApJ, 739, L40
Rodríguez-Puebla, A., Primack, J. R., Behroozi, P., & Faber, S. M. 2016, MNRAS, 455, 2592
Salmi, F., Daddi, E., Elbaz, D., et al. 2012, ApJ, 754, L14
Salpeter, E. E. 1955, ApJ, 121, 161
Sargent, M. T., Daddi, E., Béthermin, M., et al. 2014, ApJ, 793, 19
Schreiber, C., Elbaz, D., Pannella, M., et al. 2016a, ArXiv e-prints
Schreiber, C., Pannella, M., Elbaz, D., et al. 2015, A&A, 575, A74
Schreiber, C., Pannella, M., Leiton, R., et al. 2016b, ArXiv e-prints
Scoville, N., Sheth, K., Aussel, H., et al. 2016, ApJ, 820, 83
Simha, V., Weinberg, D. H., Conroy, C., et al. 2014, ArXiv e-prints
Steinhardt, C. L. & Speagle, J. S. 2014, ApJ, 796, 25
Steinhardt, C. L., Yurk, D., & Capak, P. 2017, ArXiv e-prints

MNRAS (2017) Preprint 26 June 2017 Compiled using MNRAS LATEX style file v3.0

Morphology and enhanced star formation in a Cartwheel-like ring galaxy

F. Renaud[1⋆], E. Athanassoula[2], P. Amram[2], A. Bosma[2], F. Bournaud[3], P.-A. Duc[3,4], B. Epinat[2], J. Fensch[3], K. Kraljic[2], V. Perret[5], C. Struck[6]

[1] *Department of Physics, University of Surrey, Guildford, GU2 7XH, UK*
[2] *Aix Marseille Univ., CNRS, LAM, Laboratoire d'Astrophysique de Marseille, 13388 Marseille, France*
[3] *Laboratoire AIM Paris-Saclay, CEA/IRFU/SAp, Université Paris Diderot, F-91191 Gif-sur-Yvette Cedex, France*
[4] *Observatoire Astronomique de Strasbourg, Université de Strasbourg, CNRS UMR 7550, 11 rue de l'Université, F-67000 Strasbourg, France*
[5] *Institute for Theoretical Physics, University of Zürich, CH-8057 Zürich, Switzerland*
[6] *Department of Physics and Astronomy, Iowa State University, Ames, IA 50011, USA*

ABSTRACT

We use hydrodynamical simulations of a Cartwheel-like ring galaxy, modelled as a nearly head-on collision of a small companion with a larger disc galaxy, to probe the evolution of the gaseous structures and flows, and to explore the physical conditions setting the star formation activity. Star formation is first quenched by tides as the companion approaches, before being enhanced shortly after the collision. The ring ploughs the disc material as it radially extends, and almost simultaneously depletes its stellar and gaseous reservoir into the central region, through the spokes, and finally dissolve 200 Myr after the collision. Most of star formation first occurs in the ring before this activity is transferred to the spokes and then the nucleus. We thus propose that the location of star formation traces the dynamical stage of ring galaxies, and could help constrain their star formation histories. The ring hosts tidal compression associated with strong turbulence. This compression yields an azimuthal asymmetry, with maxima reached in the side furthest away from the nucleus, which matches the star formation activity distribution in our models and in observed ring systems. The interaction triggers the formation of star clusters significantly more massive than before the collision, but less numerous than in more classical galaxy interactions. The peculiar geometry of Cartwheel-like objects thus yields a star (cluster) formation activity comparable to other interacting objects, but with notable second order differences in the nature of turbulence, the enhancement of the star formation rate, and the number of massive clusters formed.

Key words: galaxies: interactions – galaxies: starburst – galaxies: star clusters – stars:formation – ISM: structure – methods: numerical

1 INTRODUCTION

In the spectacular zoo of interacting galaxies, collisional rings are one of the most peculiar species. Lynds & Toomre (1976), Theys & Spiegel (1977) and Toomre (1978) showed that rings result from the head-on high-speed collision of a companion galaxy on a target disc galaxy. The gravitational acceleration induced by the companion first drags the matter of the target toward the (almost) central impact point. As the intruder flies away, the disc material rebounds, and forms an annular over-density that travels radially. Therefore, an empty region appears behind the ring but in some cases, a nucleus near the impact point can survive. Secondary, inner rings, in the outskirts of nuclear region can then form from second rebounds (see Athanassoula & Bosma 1985; Appleton & Struck-Marcell 1996, for reviews). Gas flows onto the nuclear region and inner ring and fuels star formation there (Struck-Marcell & Appleton 1987; Struck et al. 1996). Collisions with a more off-centred impact lead to less symmetric configurations and could explain why some ring systems do not show a nuclear component, which could also result from the destruction of a loosely bound nucleus during the interaction (Madore et al. 2009). The densest structures like the main ring and the inner ring often host a strong star formation activity. Such activity is rapidly evolving in time and space, as suggested by colour gradients across the structures (Marcum et al. 1992; Appleton & Marston 1997) and as modelled by e.g. Struck-Marcell & Appleton (1987).

Their peculiar morphology make ring galaxies more easily identifiable in observations than other interacting systems. Therefore, rings are often used as probes to reconstruct the galaxy interaction and merger rates and their dependence with redshift to better constraint the assembly history of galaxies (Lavery et al. 2004; D'Onghia et al. 2008). However, these galaxies are fast

⋆ f.renaud@surrey.ac.uk

evolving systems, as the ring dissolves or fragments within a few ~ 100 Myr (Theys & Spiegel 1977), and therefore their detectability is a strong function of time. Dynamical models are thus necessary to pin down the conditions required to form a ring and the possible other structures (inner ring, nucleus) and to time the evolution of such systems as well as that of the observable components (neutral gas, excited gas, dust, star forming regions etc.).

Numerous analytical and numerical models have addressed the questions of the formation of ring galaxies, mostly focussing on the large-scale dynamics of the galaxies, either to constrain the formation scenario of a specific system (e.g. Struck-Marcell & Appleton 1987; Gerber et al. 1992; Struck-Marcell & Higdon 1993; Hernquist & Weil 1993; Bosma 2000; Horellou & Combes 2001; Vorobyov 2003; Bournaud et al. 2007; Ghosh & Mapelli 2008; Mapelli et al. 2008; Michel-Dansac et al. 2010; Smith et al. 2012), or to explore the parameter space leading to the formation of ring-like systems (e.g. Huang & Stewart 1988; Appleton & James 1990; Struck-Marcell & Lotan 1990; Gerber & Lamb 1994; Gerber et al. 1996; Athanassoula et al. 1997; Romano et al. 2008; D'Onghia et al. 2008; Mapelli & Mayer 2012; Fiacconi et al. 2012). Such approach calls for a large number of simulations either in surveys or with a trial-and-error method, at a high numerical cost. Therefore, resolution and/or the range of physical processes captured are most often sacrificed. However, modelling the physics of star formation and the associated feedback, both key in the evolution of galaxies and their structures, requires to capture the organisation of the dense phase of the interstellar medium (ISM), which goes through resolving the turbulent cascade from its injection scale(s) down to, at least, its supersonic regime. Renaud et al. (2014a) showed that, in the case of galaxy interaction driven turbulence, this regime and thus the convergence of the star formation rate (SFR) are reached at the scale of a few parsecs ($\sim 1-10$ pc).

Here, we present models of a collisional ring system at this resolution and explore the dynamics and hydrodynamics ruling the organisation of the ISM in molecular clouds ($\sim 10-100$ pc) and the associated star formation activity, and their evolution in time and space. To do so, we focus on the particular case of Cartwheel-like galaxies.

Discovered by Zwicky (1941), the Cartwheel galaxy is part of the compact group of 4 galaxies SCG 0035-3357 (see Iovino 2002 and e.g. the figure 1 of Bosma 2000 for identification). The companion responsible for the formation of the ring has not yet been unambiguously identified, but the presence of a long HI plume between the ring galaxy and the companion G3 (Higdon 1996) is a robust hint of tidal interaction. Extended distributions of neutral gas around galaxies are easily tidally disturbed during interactions to form bridges between galaxies and tails, that constitute long-lived signatures of past encounters (see Toomre & Toomre 1972, and Duc & Renaud 2013 for a review). The long HI plume in the Cartwheel system would thus be the bridge originating from G3 and extending up to the ring galaxy itself. Ram pressure stripping could also play a role in the formation of this plume, as a fraction of the G3 gas would be stripped as the galaxy flies in the hot halo of the Cartwheel.

The Cartwheel galaxy encompasses a wide range of physical conditions (ring, spokes, inner ring, nucleus), each harbouring a different star formation regime. For instance, the ring structure contains most of the HI gas of the galaxy (Higdon 1996), hosts star forming regions (Marcum et al. 1992; Fosbury & Hawarden 1977; Higdon 1995; Amram et al. 1998; Charmandaris et al. 1999; Wolter et al. 1999; Higdon et al. 2015) and ultra-luminous X-ray sources (Gao et al. 2003; Wolter & Trinchieri 2004). These points indicate an enhanced star formation activity in the form of massive stars and star clusters in this region. However, Amram et al. (1998) reported little Hα emission in the spokes and the nucleus, indicating a lower level of star formation there. Furthermore, the nucleus contains hot dust (traced by mid-infrared, Charmandaris et al. 1999) and cold, diffuse gas (Horellou et al. 1998), consistent with a weak star formation activity. Understanding why most star formation occurs in the ring despite large quantities of gas found in the spokes and the nuclear region requires detailed hydrodynamics models capturing the physical processes coupling the galactic-scale dynamics with the star formation activity.

We use the simulations presented here (i) to better understand the (hydro-)dynamics of Cartwheel-like systems and the evolution of their main components, and (ii) as a laboratory to explore the physics of enhanced star formation and the formation of massive star clusters in a (relatively) simple geometry. The goal of this work is not to improve the match between models and observations, but rather to study the formation and evolution of Cartwheel-like objects, i.e. disc galaxies with two rings linked by what is commonly referred to as spokes. More generally, we treat these simulations as numerical experiments in which we probe a series of physical processes over a range of physical conditions in the multi-scale and multi-physics problem of triggered star formation.

2 METHOD

We use the adaptive mesh refinement (AMR) code RAMSES (Teyssier 2002) and the same methods for heating, cooling, star formation and feedback as in Renaud et al. (2017), based on Agertz & Kravtsov (2015, 2016), but with the parameters given below. Briefly, star formation occurs in gas denser than $500\ \mathrm{cm}^{-3}$ (while densities are typically probed up to $\sim 10^5\ \mathrm{cm}^{-3}$ in our simulations, see below), with an efficiency per free-fall time of 1%, which leads for our models to a global SFR of the order of $\sim 1\ \mathrm{M}_\odot\ \mathrm{yr}^{-1}$ before the collision. Each stellar particle represents a single age population following a Chabrier (2003) initial mass function. Feedback from the massive young stars injects energy, momentum and mass in the interstellar medium, through winds and supernovae (types II and Ia), either in the form of energy or momentum depending on the resolution of the local cooling radius, following Kim & Ostriker (2015). The cell size reaches 6 pc in the most refined regionss of the 400 kpc wide cubic simulation volume.

We model the target galaxy as a disc+bulge+halo galaxy and add one impacting high-speed companion which induces the tidal perturbations on the main galaxy and thus forms the ring. For the sake of simplicity, we do not consider the other galaxy members of the SCG 0035-3357 compact group. The internal structure of the companion is not analysed here and thus we render it with only a live dark matter halo, for simplicity. The main galaxy and its companion are set up in isolation, neglecting the cosmological context, with intrinsic parameters largely based on Horellou & Combes (2001), designed to reproduce the observed morphology of the system, and given in Table 1. The stellar disc, bulge and halo of the main galaxy are initially rendered with 300,000, 75,000 and 135,000 particles respectively to model the (live) gravitational potential of the galaxy. The gas and the stars formed during the simulation are treated at the local resolution of the AMR grid, i.e. at a much higher mass and space resolution. The companion is rendered with 80,000 particles following a Plummer (1911) distribution with a scale radius of 3 kpc, a total mass of $160 \times 10^9\ \mathrm{M}_\odot$ and a mass ratio of 1:2 between the two galaxies. Such mass ratio was initially

Table 1. Initial setup of the main galaxy

Gas disc (exponential)	
mass [$\times 10^9$ M$_\odot$]	16.0
radial scale length [kpc]	6.0
truncation radius [kpc]	30.0
vertical scale length [kpc]	0.2
truncation height [kpc]	2.0
Stellar disc (exponential)	
mass [$\times 10^9$ M$_\odot$]	48.0
radial scale length [kpc]	3.0
truncation radius [kpc]	20.0
vertical scale length [kpc]	0.1
truncation height [kpc]	1.0
Stellar bulge (Plummer)	
mass [$\times 10^9$ M$_\odot$]	12.0
characteristic radius [kpc]	1.0
truncation radius [kpc]	10.0
Dark matter halo (Plummer)	
mass [$\times 10^9$ M$_\odot$]	244.0
characteristic radius [kpc]	6.0
truncation radius [kpc]	60.0
Total mass [$\times 10^9$ M$_\odot$]	320.0

Table 2. Initial orbital parameters

	Main galaxy	Companion
position [kpc]	0,0,0	-0.71, 13.2, 52.6
velocity [km/s]	0,0,0	13.6, -94.8, -379.4
spin axis	0,0,1	-

proposed by Horellou & Combes (2001) to match the observed morphology of the system. It is however significantly higher than the ratio derived observationally between the Cartwheel and any other member of the compact group (Higdon 1996; Bosma 2000). One can argue that a significant amount of dynamical mass is lost during the encounter, especially for the low-mass, fragile companion, which introduces large differences between the present-day estimated mass and the pre-collision value. Our models confirm that a significant fraction of the companion's mass is spread in the tidal debris after the collision. An estimate of its mass loss would however require to model its baryonic content.

We run three simulations, keeping all intrinsic and orbital parameters strictly identical but varying only the velocity structure of the disc stars in the target to model a galaxy with an initial Toomre stability parameter (Toomre 1964) of $Q_{\rm T} = 0.5$, 1 and 2 for the stellar component. The actual value evolves during the simulations as the disc relaxes and forms new stars but the relative differences between the models are approximately conserved. Doing so allows the main disc to form different structures before the collision, which regulates the formation of post-collision features. Different stabilities also influence the star formation activity before and after the collision, as discussed in the next sections.

The orbit is similar to that of Horellou & Combes (2001), but with a larger initial separation between the galaxies (Table 2), allowing for a longer relaxation of the models and a smoothing out of any imperfection of our initial conditions. In the rest of the paper, $t = 0$ corresponds to the instant of the collision (i.e. when the companion's centre of mass is the closest to the mid-plane of the target), which takes place 104 Myr after the beginning of the simulation, 600 pc away from the centre of mass of the target's disc. This slight offset allows to build an off-centred nucleus as well as asymmetric structures, as observed in the Cartwheel galaxy. Along this orbit, the companion crosses very dense regions only for a very short period and thus, the dynamical friction it experiences is too weak to make it loose enough orbital energy to fall back and merge with the target galaxy. The final state of our simulations indicates that the two galaxies are not bound to each other, and thus that the encounter is a unique event.

3 RESULTS

3.1 Overall morphology and evolution

The mophological and kinematical analysis of the large-scale ($\gtrsim$ 200 pc) structures presented in this section is made based on our $Q_{\rm T} = 1$ model. Similar results are found using the other models as only the small-scale structures and the physics of star formation is affected by the initial stability of the progenitor.[1] This is in agreement with the results of Athanassoula et al. (1997), who found only a relatively small difference in the density in the spokes for different $Q_{\rm T}$ values.

Following Athanassoula et al. (1997) and Horellou & Combes (2001), our simulations reproduce the overall morphology of the Cartwheel galaxy (Fig. 1). Only a few Myr after the collision, the ring expands and sweeps the disc material of the progenitor. During the first $\approx$ 200 Myr after the collision, the ring expands radially at the roughly constant speed of $\approx$ 120 km s^{-1}, making a shock front. This expansion is almost planar (but note the presence of a three-dimensional structure, see Section 3.2). Conversely, the matter close to the impact point gathers in a roughly spherical stellar component (inherited from the bulge) and in a rather thin, planar feature, with a high gas fraction. A secondary, inner ring made of gas and stars is found in the outskirts of this nuclear region (see Athanassoula et al. 1997), and mostly visible in our $Q_{\rm T} = 1$ and $Q_{\rm T} = 2$ cases. The density contrast between the inner ring and the material it encloses is much lower than that for the main ring, which makes this inner ring more difficult to robustly identify. For this reason, we refer to the inner ring and all it encloses as the nuclear region, without telling them apart.

The large-scale dynamics ($\gtrsim$ 200 pc) and the morphology of main features are comparable in our three cases: the orbit of the companion, the nuclear region, the ring and the area in between that we refer to as the spoke region, for simplicity. The relatively simple geometry of these structures allows us to identify them through a handful of elements, measured by visual inspection of radial density profiles and computation of the centre of mass: the position of the nucleus with respect to the ring's centre, its size and the outer and inner radii of the ring. We use these parameters to tell apart the three main regions in the rest of the paper. During the $\approx$ 200 Myr following the collision, their time evolution can then be approximately parametrized with linear functions of time.

Fig. 2 shows the mass-weighted gas density probability distribution function (PDF) at selected epochs over the entire galaxy, and by telling apart the main regions of the system. The galaxy experiences a significant increase of its maximum density as well as

[1] Several of the structures and their evolution discussed in this paper are illustrated in movies available here: http://personal.ph.surrey.ac.uk/~fr0005/movies.php.

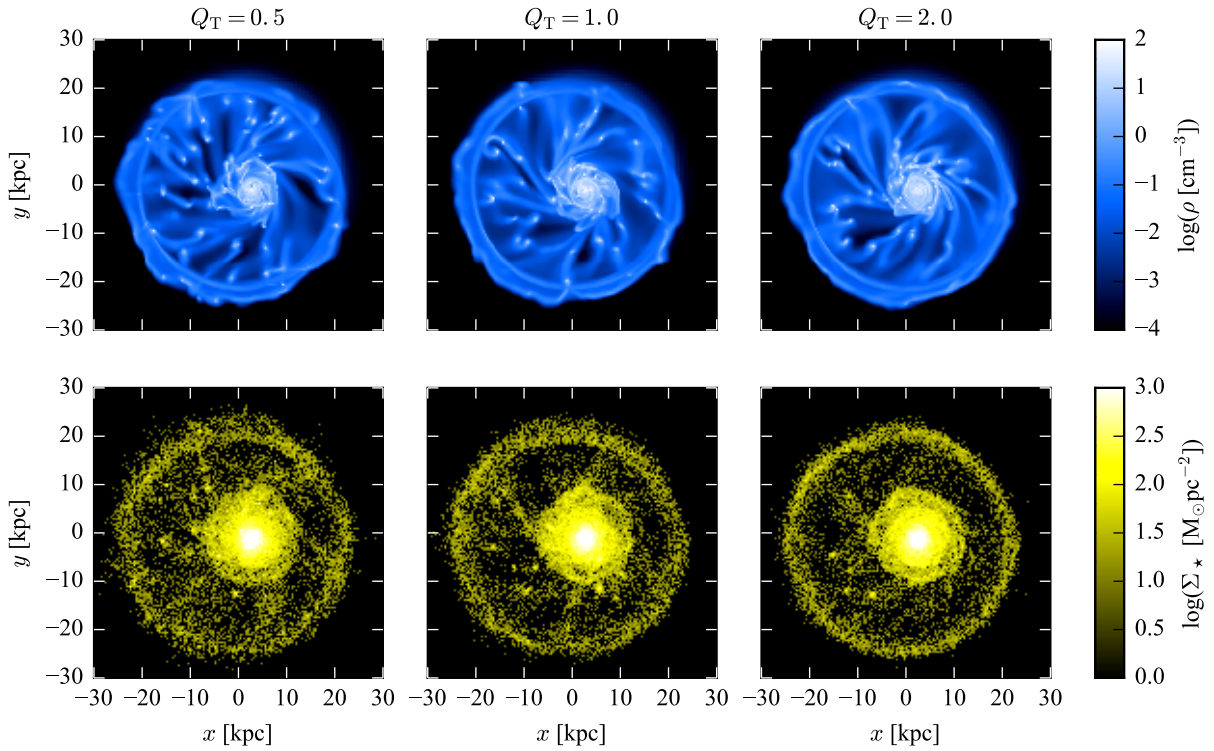

Figure 1. Map of the gas (top) and stellar (bottom) density of the main galaxy, 150 Myr after the collision.

its amount of dense gas shortly after the interaction. Thereafter, the evolution of the PDF is globally milder, but corresponds instead to strong variations and gas flows between the regions of the galaxy.

A few Myr after the collision, a density enhancement expands radially and ploughs through the disc material, which forms the main ring. As the ring propagates, its gathers more and more material (gas and stars) and its mass increases, as illustrated on Fig. 3. While the PDF of the nuclear region remains mostly unaffected by the collision ($25-50$ Myr), the regions between the nucleus and the ring (that we call "spokes") become relatively empty, in a similar manner as the interior of a blast wave.

As the ring expands, it starts loosing material that gradually falls back onto the nucleus by streaming along the spokes. The mass loss overcomes the accumulation of matter when the ring reaches the low density outskirts of the progenitor disc and thus gathers very little amounts of matter (Fig. 3). This happens at $t \approx 90$ Myr, when the rings outer radius is $\approx$ 17 kpc, i.e. about 3 times the initial scale-length of the gas disc. At this point, the PDF of the ring yields its first major evolution, with the depletion of the dense tail. As soon as some material, including dense clumps, leaves the ring through the spokes (i.e. as early as $t \approx 25-50$ Myr), the PDF of the spokes develops a tail at high density.

The (hydro)dynamics of the spoke region lower the maximum density (see Section 3.3) and a significant amount of diffuse gas is found in between the individual spokes. This situation does not significantly evolve until the ring is completely depleted. The material in the spoke region falls onto the nucleus which thus accretes gas spanning a wide range of densities rather than, for instance, only diffuse gas. The shape of its PDF varies only mildly. However, the nuclear inflow generates an excess of very dense gas, mainly found in the innermost region ($\lesssim 1$ kpc), and along the secondary, inner ring.

As the mass of the main ring continues to decrease due to the lack of further accretion and the depletion through the spokes, the ring completely dissolves ≈ 200 Myr after the collision.

The density distribution of the system thus follows a rather simple global mechanism of compaction in the ring, depletion through the spokes and accretion in the nuclear region (with additional compaction in the inner ring and the very centre).

3.2 Vertical structure and cylindrical shape

In this section, we ignore the slight radial offset of the companion's trajectory with respect to the spin axis of the main disc and consider, for the sake of simplicity, that the impact point is at the centre of the disc. The actual difference has only second-order effects on the reasoning and results presented here. In our setup, the companion travels from $z > 0$ to $z < 0$.

We discuss the formation and evolution of a vertical, cylindrical-like, annular structure induced by the tidal perturbation, visible on the edge-on views of Fig. 4 and the slice views in Fig. 5. This structure corresponds to the thickening of the target galaxy noted by Bosma (2000).

All along the interaction, the companion exerts a tidal influence on the main galaxy, which becomes mostly visible in the dynamically cold component, i.e. the stellar and gaseous discs. The amplitude of this effect depends on the strength of the gravitational pull from the companion, which (at a given time) depends on the galactocentric radius. This leads to a radial dependence of the vertical component of the velocity of stars and gas, already before the collision: the outermost regions are less affected by the compan-

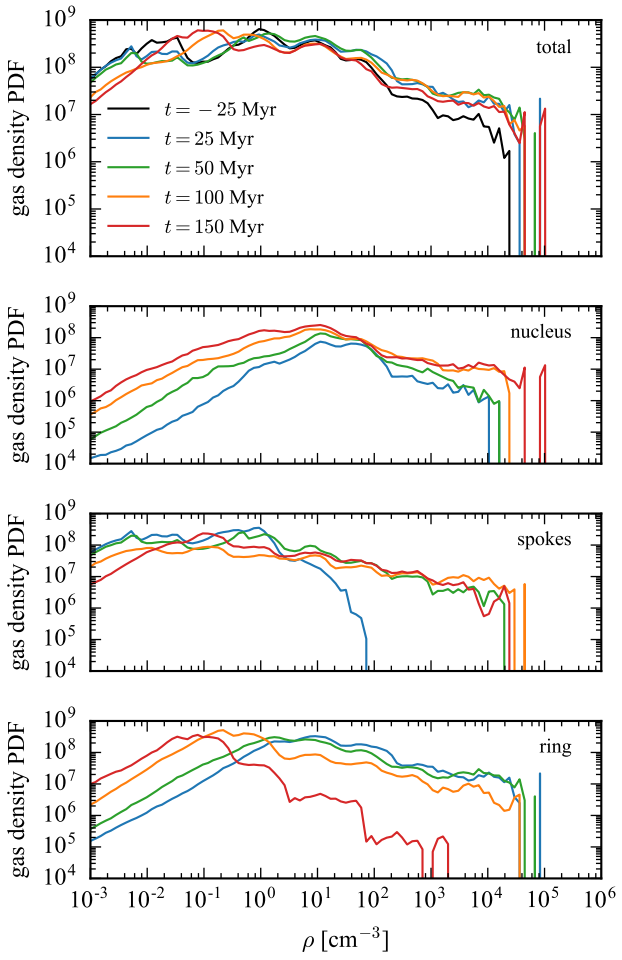

Figure 2. Evolution of the mass-weighted gas density PDF in our $Q_{\rm T} = 1$ galaxy (top), and in the main three regions of the galaxy. (The black curve representing $t = -25$ Myr is not shown for the three regions as they are not defined before the collision.)

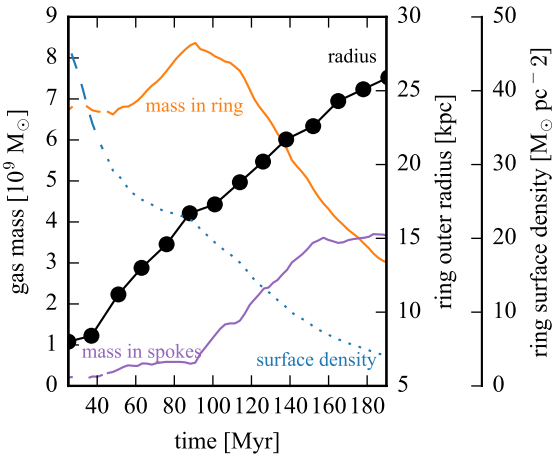

Figure 3. Evolution of the gas mass in the main ring (orange) and in the spoke region (purple), of the ring outer radius estimated by eye on planar density profiles (black), and of the ring surface density (dotted blue) in our $Q_{\rm T} = 1$ galaxy. Identifying the ring structure is challenging before and after the time-lapse shown here. The dashed part of the curves corresponds to the early epoch of the detection of the ring when it is complicated to define its inner radius, which thus introduces uncertainties in its mass and surface density.

ion and thus lag behind the inner regions. This introduces a vertical structure in the "disc". Fig. 6 shows the evolution of this structure by tagging the particles according to their pre-collision galactocentric radius.

After the collision, the main galaxy is attracted in the opposite direction by the receding companion. Once again, the outer material is less affected by this effect and lags behind the mean plane of the disc. In addition, the ring forms and expands towards the outskirts, sweeping most of the disc material (except the innermost region, $R \lesssim 5$ kpc, which remains in the nuclear region). By the time the ring reaches the outermost zones, the material there lies above the plane of the disc remnant, and is not affected by the ring (which further slows down the mass growth of the ring, discussed in the previous section).

While expanding, the ring gathers material originating from a range of galactic radii, thus with different vertical velocities inherited from past tidal accelerations. Material from the inner region (5 kpc $\lesssim R \lesssim$ 10 kpc) retains its high (positive) vertical velocity, while that initially further (10 kpc $\lesssim R \lesssim$ 15 kpc) moves vertically slower. Therefore, the ring thickens vertically.

As a result of the two effects, the outer galaxy features the shape of a cylindrical annulus (Figs. 4 and 6). As shown in Fig. 5, the bottom surface of the cylinder corresponds to the mean plane of the galaxy and gathers most of the gaseous and stellar material, the ring, the spokes, the nuclear region and all clumps and clusters. At the top of the cylinder the matter is distributed in a thin ring. Inside the ring, the inner region only hosts a tiny fraction of the stellar component, corresponding to the highest part of the bulge. The radius of this ring (at the top of the cylinder) is slightly smaller than the outer radius of the main ring (at the bottom), which makes them appear close but still distinct in face-on projections (e.g. Fig. 1). The curved (side) surface of the cylinder is made of ring material with various vertical velocities, and of the initially outermost material which has experienced a weaker perturbation from the companion.

Fig. 7 links the vertical distribution within the cylinder to the radial distribution before the collision. The highest material and that with the most positive vertical velocity originate from the outermost disc. Comparably high vertical velocities are also found at lower positions, where lies the material originating from the inner off-nuclear region. The actual offset of the trajectory of the companion with respect to the z-axis induces most of the dispersion shown in the distribution of Fig. 7 which gets narrower if we limit ourselves to a smaller azimuthal fraction of the cylinder.

Stellar and gaseous densities on the side of the cylinder are $\sim 10-15$ times lower than that of the clumps in the main plane, and as a result this region does not host any star formation activity. Our simulations do not indicate any strong misalignment between the gas and the stars in this structure, although the gaseous component appears to be slightly more extended (due to its initially lower binding energy to the galaxy), in a similar manner as tidal tails in classical interacting pairs.

We note a mild (and temporary) accumulation of gas at the top edge of the cylinder, due to the distribution of velocities. This translates into the thin ring of gas noted above (recall Fig. 5). A

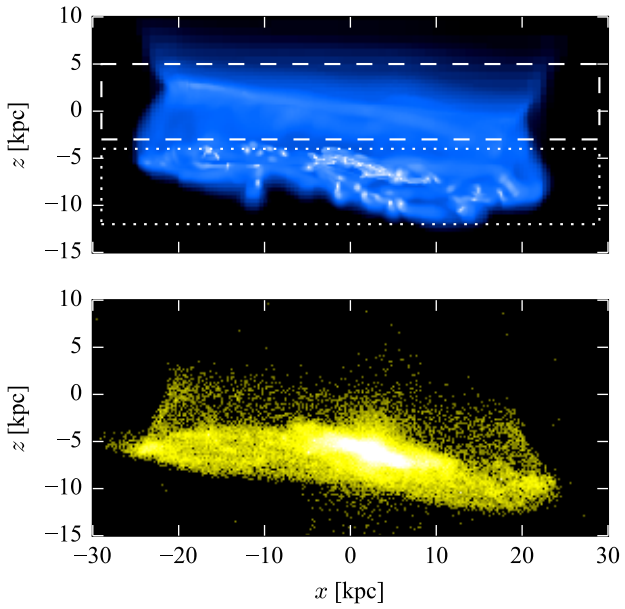

Figure 4. Gas (top) and star (bottom) densities at $t = 150$ Myr in the edge-on view of the main galaxy. Colours scale as in Fig. 1. Rectangles in dashed and dotted lines indicate the position of the slices shown in Fig. 5.

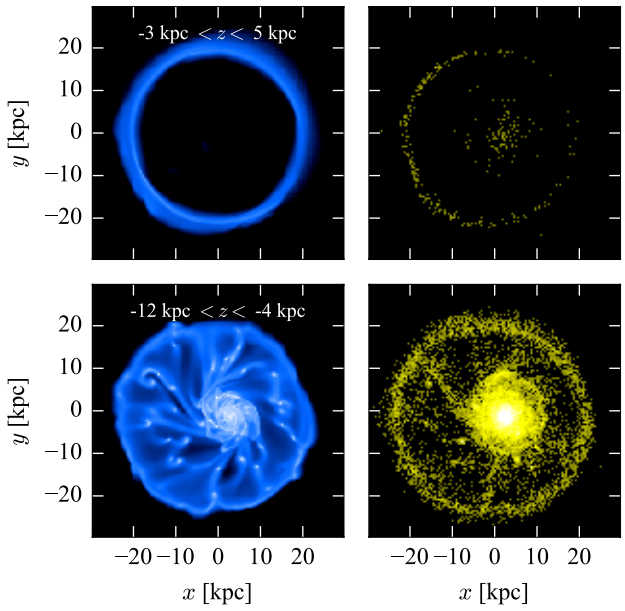

Figure 5. Gas (left) and star (right) densities at $t = 150$ Myr in slices 8 kpc deep, along the z-axis and centred on $z = 1$ kpc (top) and $z = -8$ kpc (bottom), i.e. on the top and bottom parts of the cylindrical annular structure (see rectangles in Fig. 4). Colours scale as in Fig. 1.

comparable configuration is detected in AM 0644-741 (also known as the the Lindsay-Shapley ring galaxy, Graham 1974) where a thin ring close to the inner radius of the main ring is clearly visible in neutral gas (Georgakakis et al. 2000), as well as in Hα and infrared (Higdon et al. 2011), indicating a star formation activity (see also Section 3.4.4). In our models, the lower densities of the top of the cylinder yield however a lower amount of fragmentation than along the main ring, so that the former ring is smoother and more regular (much more diffuse) than the latter.

The positive vertical velocities are reduced by the gravitational acceleration of the companion and the main plane of the galaxy, before becoming negative. The material in the cylinder lags behind (vertically) the main plane. The cylinder thus flattens, then expands below the main plane, and this oscillating evolution goes on in a damped manner (due to weakening of the effect of the companion galaxy, and the strengthening of that of the main galactic plane).

3.3 Shear

Fig. 8 shows the maps of shear in the $Q_{\rm T} = 1$ case, 75 and 150 Myr after the collision. The quantity plotted is the logarithm of

$$\delta_x \left[\left(\frac{\partial v_x}{\partial y} \right)^2 + \left(\frac{\partial v_y}{\partial x} \right)^2 \right] \frac{1}{G \delta_x \rho} \qquad (1)$$

where δ_x is the scale at which the velocities (v_x and v_y) and gas density ρ are measured (100 pc here). The rightmost fraction represents the inverse of the self-gravitational force and the rest is the planar shear expressed as a centrifugal force. For simplicity, we refer to this quantity as "shear" in the following.

As the ring sweeps disc material to radii larger than those before the collision, the ring yields, on average, a higher circular velocity than the material outside, at larger radius. As a result, a strong shear is found along the outer boundary of the ring (particularly visible in the lower-left corner of the left panel of Fig. 8). Inside the ring itself, the material is well mixed resulting in a rather smooth distribution of velocities and thus a zone of low shear. Locally, self-gravitating over-densities yields the minimum levels of shear found in the system.

The spoke features are shaped by the large-scale dynamics (left panel in Fig. 8). Strong shear is found along the edges of the spokes and likely participates in keeping them thin. Because of the radial dependence of the velocity, shear is significantly weaker along the radial spokes than those with a spiral-like configuration. A similar reasoning has been proposed to explain the different morphologies of star forming regions (beads on a string and spurs) in disc galaxies by connecting the spiral pitch angle to the presence of Kelvin-Helmholtz instabilities in high shear volumes (Renaud et al. 2014b). Here we also note that "low pitch angle" spokes (i.e. spiral-like) host fewer over-densities than their more radial counterparts.

In the nuclear region, the interplay of intrinsic motions and the influence of accreted material makes a complex shear structure. We note however that the average shear is stronger here than in the main ring, likely due to the fact that the rotation curve is naturally steeper in the inner parts than in the outer ones.

When the spokes are well in place (right panel in Fig. 8), the range of shear values narrows. Both the expansion and the depletion of the ring lower its density and thus its self-gravity, which rises the shear quantity plotted. Dense clumps marked by low shear can mainly be identified in the spokes. When they reach the nuclear region however, their signature becomes more difficult to spot.

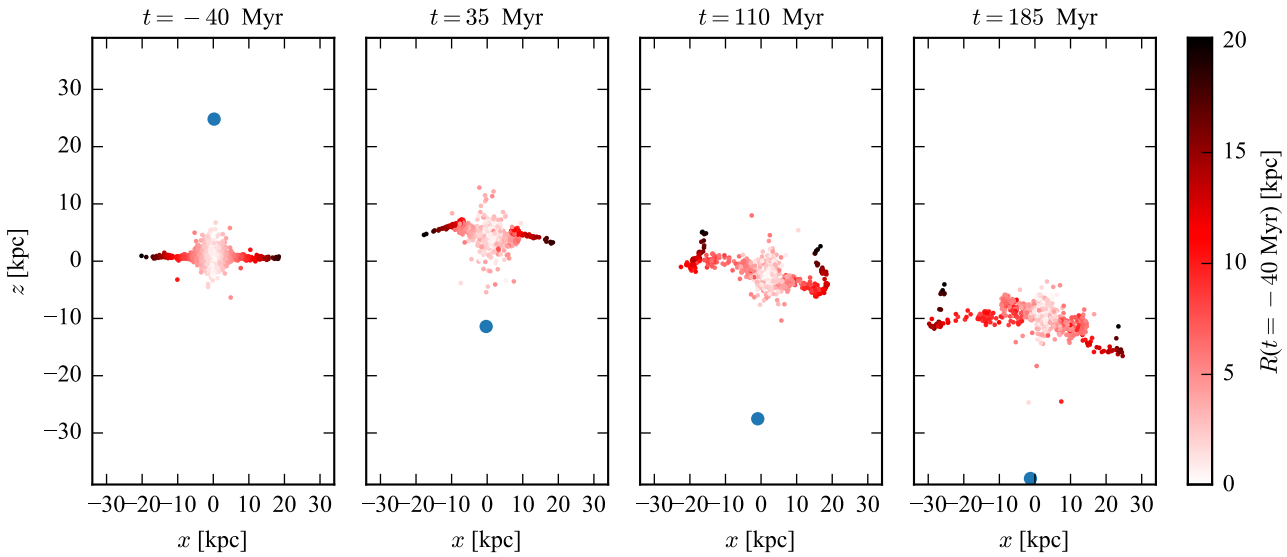

Figure 6. Slice view of the position of the stars (in a slice 4 kpc deep, along the y-axis). The colour codes the radius (in the $x - y$ plane) of the stars at $t = -40$ Myr, i.e. before the collision. The vertical structure gathers stars initially at large galactocentric radius. Only a randomly selected subset of the stars is shown, for the sake of clarity. The blue dot marks the position of the centre of mass of the companion galaxy.

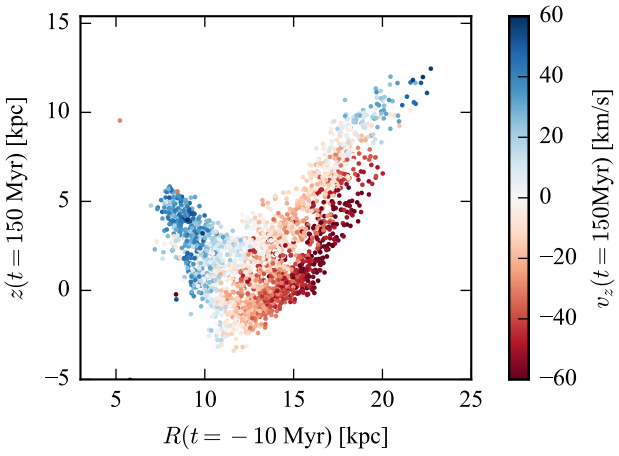

Figure 7. Vertical offset of stars with respect to the main plane of the galaxy (measured 150 Myr after the collision), as function of the galactocentric radius (measured 10 Myr before the collision). Colour codes the vertical velocity after the collision. Only a randomly selected subset of the stars is shown, for the sake of clarity.

Such a configuration indicates a preferential gathering of bound gas clumps and survival to external disruption effects, and thus physical conditions favouring star formation, in the main ring and in the radial spokes. More physical criteria must however be fulfilled to lead to an actual star formation activity.

3.4 Star formation and its regulation

Fig. 9 shows the evolution of the SFR of the entire system (recall however that our companion is modelled without gas and thus does not host star formation). The intensity of star formation before the collision depends on the overall stability of the disc and thus varies with $Q_{\rm T}$. By normalizing the SFR to its average pre-collision value, the bottom panel of Fig. 9 shows the relative enhancement triggered by the collision. After a short episode of quenched star formation (see next section), the SFR rises rapidly ($t \approx 15$ Myr) as the ring expands and gathers gas. Details of the star formation activity depend on the intrinsic stability of the discs and are discussed below.

The boost of SFR is less than the maximum value observed for such a mass ratio and pericentre distance in more classical interactions (e.g. Scudder et al. 2012), but it is however clearly visible, even in the least favourable case of $Q_{\rm T} = 0.5$ in which some level of fragmentation of the ISM takes place before the interaction. We note that the maximum value of the SFR is not reached immediately after the collision, but can be found in general $\approx$ 50 Myr after, and even up to 150 Myr later in the form of short bursts in the $Q_{\rm T} = 2$ case (due to accretion of gas clumps into the nuclear region, see Section 3.4.3). In all cases, the SFR remains above its intrinsic value for several 100 Myr, i.e. even after the dissolution of the ring ($\approx 180-200$ Myr), but star formation is then limited to the central region, as discussed later.

3.4.1 *Quenching at collision*

The SFR is reduced in all models a few Myr before the collision, but with an amplitude and a duration depending on the intrinsic stability of the discs. As the companion approaches, it induces a strong tidal field, modifying the morphology of the galaxy and disrupting its gaseous clumps. Such disruption smooths out the marginally bound over-densities which thus quenches the star formation activity. Some level of star formation activity is however preserved in the clumps dense enough to survive this tidal disruption. Fig. 10 illustrates this point by showing the depletion of the dense gas reservoirs as the companion approaches (-40 Myr $< t < 0$). In the more fragmented case of our $Q_{\rm T} = 0.5$ model, the more numerous and denser gas clumps that exist before the collision are able to resist the tidal disruption better than in the other cases ($Q_{\rm T} = 1$ and

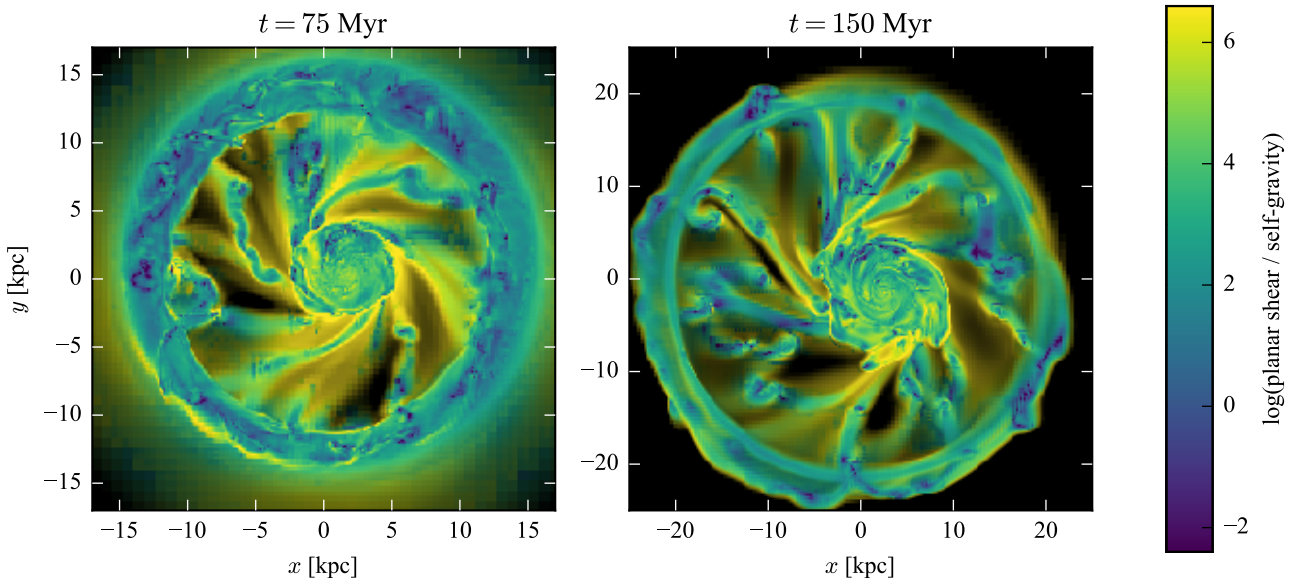

Figure 8. Map of the shear in the $x-y$ plane, normalised to self-gravity (see text), 75 and 150 Myr after the collision. To highlight the position of the gas structures, the luminosity of this map represents the gas density, such that bright areas correspond to dense gas.

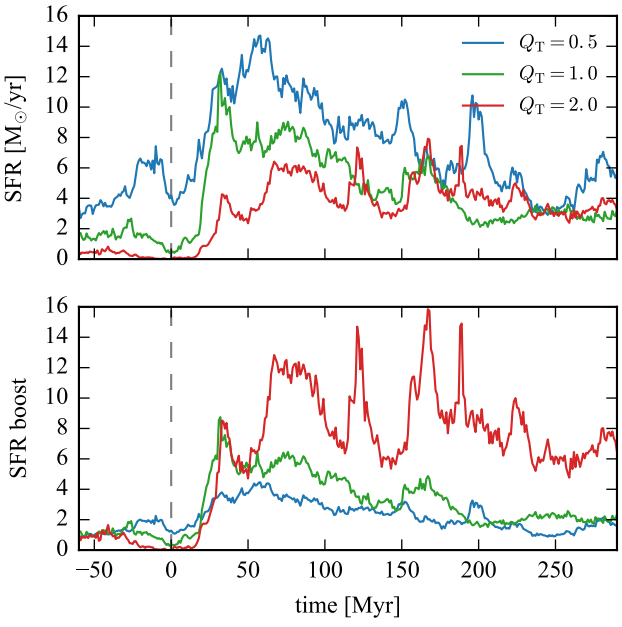

Figure 9. Evolution of the SFR in our three simulations (top) and of the SFR normalised to its average value before the collision (bottom) which indicates the enhancement of the star formation activity induced by the collision. The time of the impact is indicated by a vertical dashed line.

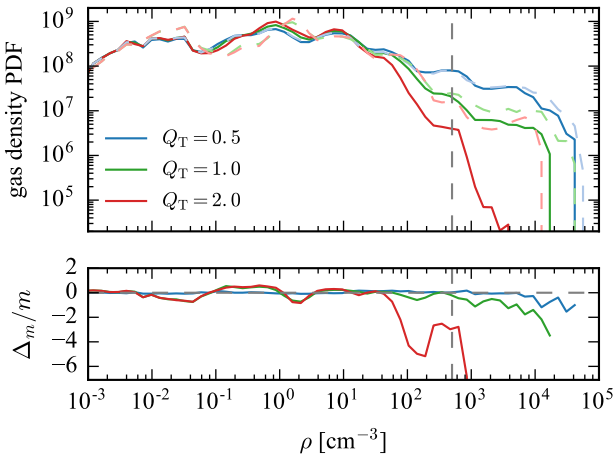

Figure 10. Top: mass-weighted gas density PDF of our three models at the moment of the collision (solid lines), and 40 Myr before (light colour, dashed lines). Bottom: relative difference of these PDF between the two epochs. (A negative value indicates a depletion of the gas reservoir at the corresponding density.) The vertical line marks the density threshold for star formation.

$Q_\mathrm{T} = 2$). Therefore, the dissolution of the dense gas structures and the quenching of star formation occur later and in a less efficient manner than in our other models. In all cases, it takes ≈ 15 Myr after the collision for the interaction-triggered enhancement to overcome its effects.

In any disc galaxy, the gravitational acceleration is weaker along the direction perpendicular to the disc, than in the plane of the disc. Therefore, when such a disc is involved in a collisional ring system with a companion on a highly inclined orbit, the tidal disruption perpendicular to the plane of the target's disc (i.e. vertical in our case) is stronger than in less inclined configurations. Therefore, ring systems are more susceptible to the quenching mechanism detected here than other interacting systems with otherwise comparable mass ratios and/or pericentre distances.

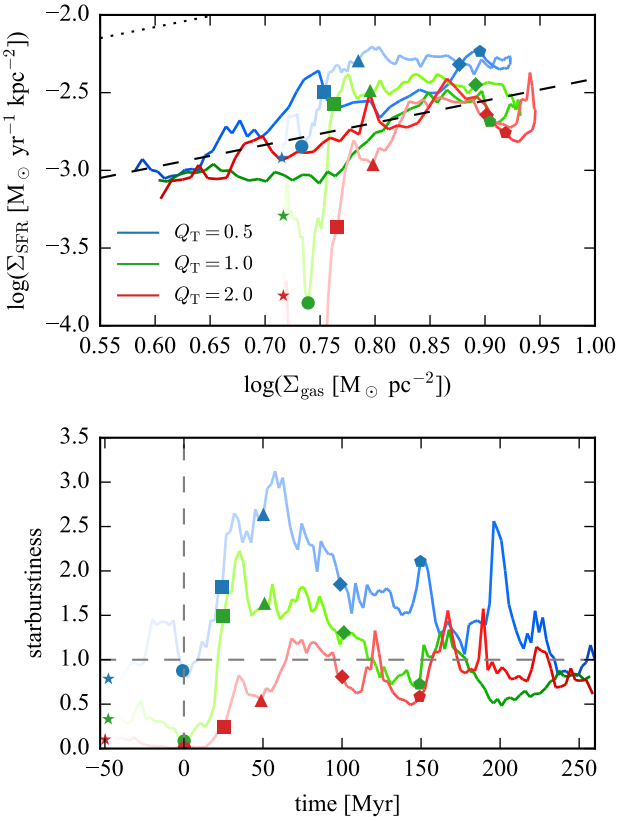

Figure 11. Top: evolution of the systems in the Kennicutt-Schmidt plane. The curves darken with increasing time. Symbols mark different epochs (see bottom panel). The dashed and dotted lines show respectively the disc and the starburst sequences as defined in Daddi et al. (2010, see also Genzel et al. 2010), for reference. Bottom: evolution of the starburstiness parameter (see text). Colours and symbols are the same in both panels.

3.4.2 *Schmidt-Kennicutt relation and starburstiness*

Fig. 11 shows the evolution of our models in the Kennicutt-Schmidt (KS) plane. The surface densities of all gas ($\Sigma_{\rm gas}$) and SFR ($\Sigma_{\rm SFR}$) are measured in the face-on view. Only areas denser than $0.1\ {\rm M}_\odot/\ {\rm pc}^2$ are considered, and the surface they span is used to compute the two surface densities. We then compute the starburstiness parameter defined as the ratio between the measured $\Sigma_{\rm SFR}$ and that of the disc sequence for the corresponding measured $\Sigma_{\rm gas}$. A galaxy is considered in a starburst regime when its starburstiness parameter exceeds 4 (Schreiber et al. 2015; Renaud et al. 2016; Fensch et al. 2017).

All three models have a comparable behaviour. As expected, they start with initially comparable $\Sigma_{\rm gas}$ and their $\Sigma_{\rm SFR}$ relates to their intrinsic stability. Since we measure the surface densities over the entire disc, the small scale ($\lesssim 1$ kpc) differences between our models do not appear in $\Sigma_{\rm gas}$ (up to slight differences due to gas consumption at different SFRs). Only $\Sigma_{\rm SFR}$ is affected by the small scale structures of the ISM.

At the time of the collision, quenching induces a rapid drop of the star formation efficiency (SFE). Immediately after ($0-25$ Myr), the gas becomes slightly denser, and the SFE rises rapidly. The enhancement of star formation takes over the quenching mechanism. As the ring forms and gathers gas, the gas surface density increases. It reaches its maximum at ≈ 125 Myr, i.e. after the ring gas reservoir started to deplete into the spokes (recall Fig. 3). The two surface densities decrease, roughly following the disc sequence ($\Sigma_{\rm SFR} \propto \Sigma_{\rm gas}^{1.42}$, Daddi et al. 2010).

According to our convention, none of our models reaches the starburst regime (starburstiness > 4). However, galaxies initially more efficient at forming stars, i.e. with a higher intrinsic starburstiness parameter could temporarily reach the starburst sequence in the KS plane and be classified as luminous infrared galaxies (LIRGs, Kennicutt 1998). However, the non-linearity of star formation and feedback requires to run more simulations to check this particular point.

3.4.3 *Star formation as function of location*

Fig. 12 shows the evolution of SFR separately in each of the three main regions of our Cartwheel-like model. Before the collision, we arbitrarily define the radius of nucleus as provided by our parametrisation for $t = 0$ (recall Section 3.1), which leads to 1.4 kpc and roughly matches the size of the central structures when identified by eye. Once the post-collision structures can be identified ($t > 25$ Myr), most of the star formation activity occurs in the ring during the first ≈ 100 Myr. The ring expands with time, becoming thicker in the $x-y$ plane, while some of its gas is fuelled along the spokes toward the nucleus (Section 3.1). The ring thus becomes more and more diffuse. As a result, the SFR there decreases while that of the nucleus increases, and this transition is visible in the activity in the spokes. This trend is found for all three models: only the details and the fast-evolving, small-scale features differ. For instance, the starburst in the nucleus is delayed after the encounter by ≈ 50, 80 and 100 Myr in the $Q_{\rm T} = 0.5$, 1 and 2 simulations, respectively.

In particular, the SFR in the nucleus of the case $Q_{\rm T} = 2.0$ yields strong bursts, but only at a late stage of the evolution ($t \gtrsim 80$ Myr, Fig. 9). Fig. 13 shows that such bursts of star formation correspond to gas accretion onto the nuclear region. As shown in the bottom panel of Fig. 13, the accreted gas yields a dense component, corresponding to dense gas clumps which trigger a local starburst shortly after being accreted onto the nucleus. We note that a comparable situation is found in the $Q_{\rm T} = 0.5$ and $Q_{\rm T} = 1$ cases, intrinsically less stable, but with bursts of milder intensity than in the $Q_{\rm T} = 2.0$ model, relative to the pre-interaction SFR (recall Fig. 9).

Fig. 14 shows the evolution of the sub-regions in the KS diagram, using the same method as before (for the $Q_{\rm T} = 1$ model only). When it is first detected, the ring is rather diffuse and hosts very little star formation. In the process of ploughing gas, it rapidly grows in mass and becomes more efficient at forming stars. However, its radial expansion leads to an increase of its surface, resulting in the net decrease of its gas surface density. During the course of the simulated evolution, the ring will host the most efficient star formation activity, at $t \approx 30$ Myr, because of low shear (Section 3.3) and other factors like tidal compression (see Section 3.4.4). This efficiency then starts to slowly diminish before the ring looses mass (recall Fig. 3) but drops as its reservoir depletes faster than it accretes ($t \approx 100$ Myr), until all star formation activity ceases.

A comparable but delayed overall evolution is found in the spoke regions. The gas density is significantly lower than in the ring but the star formation efficiency reaches comparable (yet slightly lower) values. The maximum is reached approximately when the mass of the ring is maximal. (Recall the ring starts loosing mass

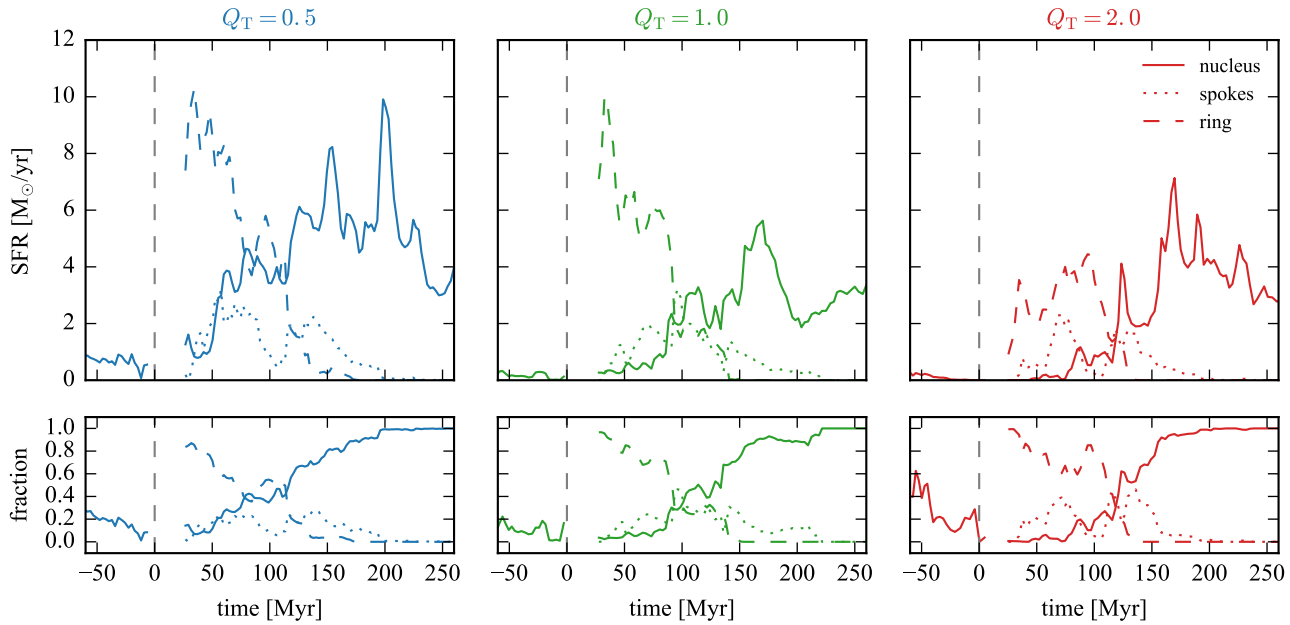

Figure 12. Star formation rate in the nuclear region, the spokes and the ring, for our three cases (top) and corresponding fraction of the total SFR (bottom). Data is missing for $0 < t < 25$ Myr, due to the difficulty of identifying the structures while they form. Before the collision ($t < 0$), we assume the nucleus has a constant radius of 1.4 kpc.

through the spokes before.) We note that the gas surface density of the spokes varies little during the evolution ($\approx 25-150$ Myr), as the combined result of the expansion of ring (which makes the spokes longer) and the accretion of gas from the ring, and its loss to the nucleus.

Before the collision, star formation in the nuclear region is rather stochastic and discontinuous. The tidal disruption from the companion is visible as a lowering of the star formation efficiency. Then follows a rapid decrease of the gas density due to the growth in size of the nucleus and the formation of the secondary, inner ring (creating a gap of low density inside it). This decrease slows down later ($t \approx 100-150$ Myr) when the nuclear region is fuelled with gas from the ring (via the spokes), and is thus accompanied with a rise of the star formation efficiency. At the end of the period we explore, star formation only occurs in the nucleus (see also Fig. 12), with an efficiency comparable to that of the nuclear region in the pre-collision phase.

The star formation activity thus follows a sequential evolution, from the ring to the spokes and then the nuclear region. The observations of Cartwheel, however, do not report any star formation in the central area (e.g. Amram et al. 1998; Horellou et al. 1998; Charmandaris et al. 1999). This suggests that the real Cartwheel is still in the phase where all star formation occurs in the ring itself (i.e. $t \lesssim 50-100$ Myr according to our models, depending on Q_T). We note, however, that other considerations based on the morphology of the inner ring and the size of the structures rather support a match to observations by our models at a later epoch (see also Horellou & Combes 2001). The discrepancy between this criteria then would question the full representativeness of our model to the real galaxy.

In any case, the general evolution we describe here should be retrieved in most ring galaxies with spokes, and thus the spatial distribution of star forming regions could be used to estimate the evolutionary stage of the system, and date the collision.

Fig. 15 shows the azimuthal distribution of the stellar mass formed in the ring, cumulated over the entire ring lifetime, and when considering young, bright stars only (at $t = 50$ Myr). The distribution of young stars only suffers from low number statistics, and mostly traces the formation of a handful of massive star clusters, but overall corresponds to the cumulated distribution discussed here, in particular through the strong deficit of star formation on the right half. In the coordinate system we adopted, a clear left/right asymmetry is found with star formation mainly occurring in the left-hand side regions (78% for both the young star distribution and the cumulated one). We also note a second-order top/bottom imbalance, slightly favouring the top half (56% for the young star distribution, which is dominated by a couple of star clusters at $+90°$ and $+140°$, and 60% for the cumulated distribution). This distribution is related to the position of the nucleus with respect to the ring.

Fig. 16 shows the trajectory of the centre of mass of the most bound particles of the nuclear region, in the reference frame centred on the ring's centre. Because of the off-centred impact point of the interloper galaxy toward the top-right side ($x \approx 380$ pc, $y \approx 460$ pc, with respect to the position of the nucleus at $t = 0$, i.e. an azimuth of $+50°$, see Fig. 15), the nuclear region is first attracted by the companion toward the top-right quadrant, before moving to the bottom-right part. This suggests that the presence of the nucleus on the right-hand side of the system reduces star formation with respect to the other side (i.e. our first-order left/right imbalance). The second order effect (top/bottom) is much weaker and more difficult to analyse as it evolves with time, like the position of the nucleus and the global SFR do. It is thus likely that the net top/bottom distribution results from the interplay of several mechanisms and should not be solely connected to the position of the nucleus. The azimuthal distribution of Fig. 15 however strongly suggests that the presence of the nearby nuclear region plays an important role in regulating the star formation activity in the ring. Since the intensity of tidal fields yields a $\propto R^{-3}$ dependence, even small asymmetries in the position of the nucleus like

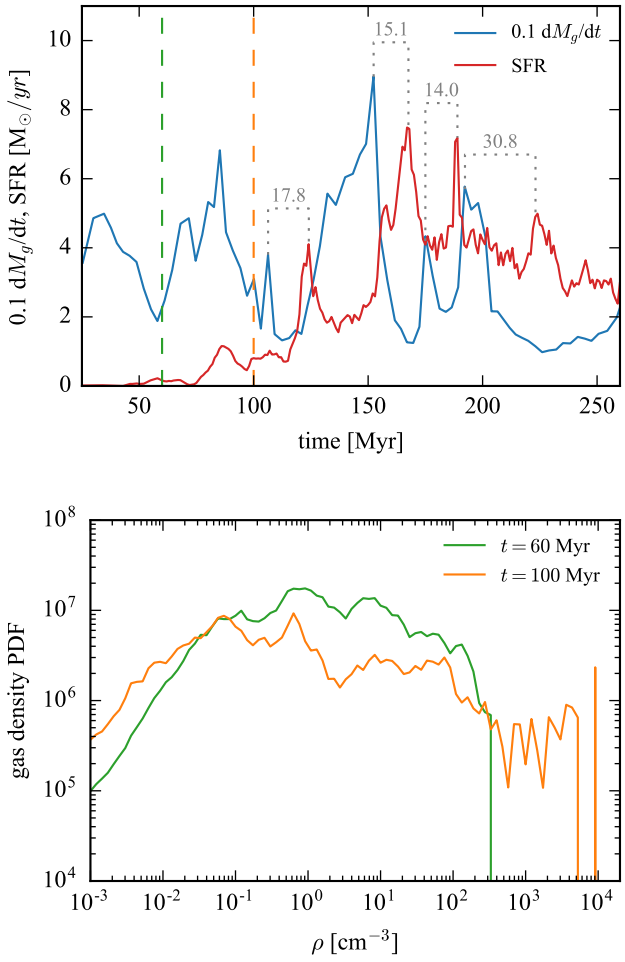

Figure 13. Top: evolution of the net gas inflow rate (computed as the time derivative of the mass), and star formation rate in the nuclear region, after the collision, for our $Q_T = 2$ case. In a first phase ($t \lesssim 70$ Myr), the accretion of gas does not translate into a significant rise of the SFR. After, peaks in the accretion rate are related with rapid increase of the SFR, with a time delay of $\approx 14-30$ Myr, as indicated in grey. The vertical green and orange dashed lines mark the epochs when the mass-weighted gas density PDF is computed (bottom). These PDFs are measured in the innermost 2 kpc of the spokes region (i.e. close to the nucleus but still outside it, just before this material gets accreted by the nucleus).

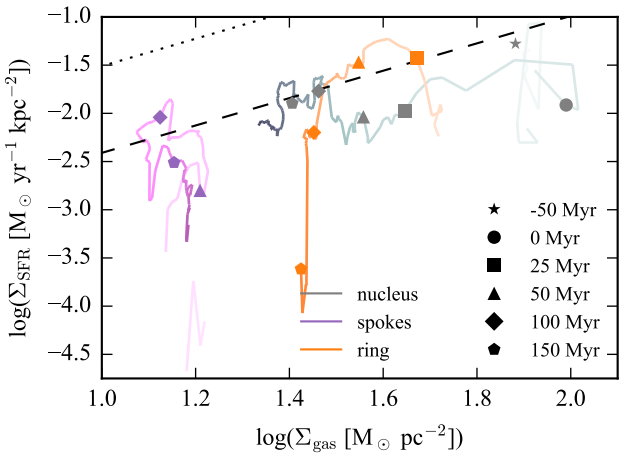

Figure 14. Same as Fig. 11 but telling apart the nuclear, spokes and ring regions in our $Q_T = 1$ model. Note that the ring and the spokes are not defined before $t = 0$. The times associated to the symbols are as in Fig. 11 and indicated in the legend.

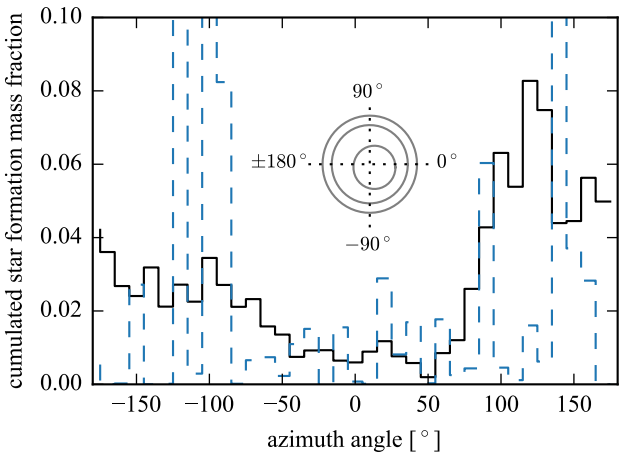

Figure 15. Azimuthal distribution of the mass of the stars formed in the ring. In black, this mass is cumulated over the full duration of the ring detectability, i.e. between $t = 25$ and 180 Myr. In dashed blue, only the brightest stars (i.e. younger than 30 Myr) are accounted for at $t = 50$ Myr, when the star formation activity in the ring is still important and allows us to derived significant azimuthal information. Both distributions are statistically comparable and yield the same first-order asymmetry. The azimuth angle is measured counter-clockwise in the $x-y$ plane, as shown in the cartoon representing the configuration of ring and the position of the nuclear region at $t = 150$ Myr.

those in Cartwheel can impact the ISM structure and star formation activity in the ring. This point is further explored in the next section.

The asymmetry found in the star formation activity in our models corresponds to that observed in the real Cartwheel galaxy, where the part of the ring the furthest from the nucleus hosts the maximum surface brightness (in bands K and B, Marcum et al. 1992) and star formation activity (traced by Hα, Higdon 1995; Mayya et al. 2005). The Lindsay-Shapley ring galaxy (AM 0644-741) also displays an enhanced star formation activity in the furthest quadrant of its ring to the nuclei (Higdon et al. 2011). We note however that the ring galaxy NGC 922 shows a stronger star formation activity on the side of the nucleus than on the opposite one (e.g. Wong & et al. 2006; Meurer & et al. 2006), contrarily to our simulations of the Cartwheel. However, the strong asymmetry observed in the distribution of gas and old stars clusters (Pellerin et al. 2010; Prestwich et al. 2012) indicates that the "ring" structure itself is asymmetric (which thus biases the distribution of star forming regions). Furthermore, the "ring" feature observed in NGC 922 shows a sharp outer edge but a much weaker contrast on its inner side and thus differs from the morphology of the Cartwheel. Therefore, it is likely that the observed asymmetry of NGC 922 results from the orbital configuration of the interloper galaxy (and maybe,

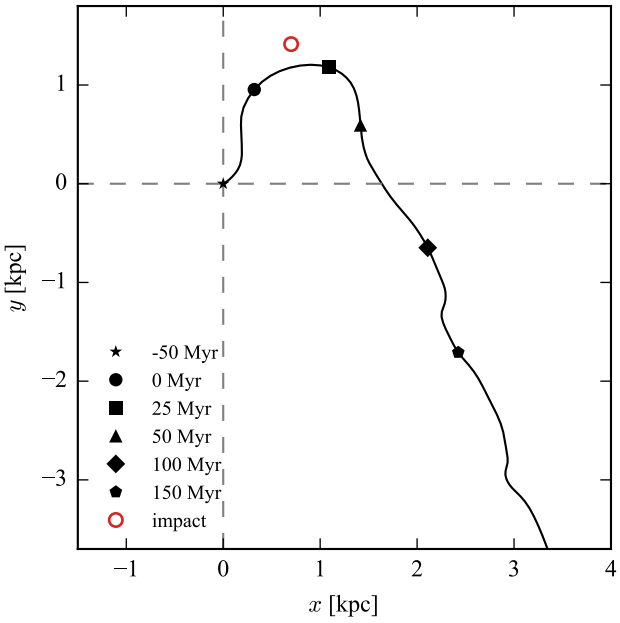

Figure 16. Trajectory of the nucleus in the reference frame centred on the ring's centre. The positions at several epochs are marked by symbols, and the centre of mass of the companion galaxy at the time it crosses the mid-plane of the main galaxy (defined as $t = 0$) is shown as the red open circle.

to some extent, from the pre-interaction morphology of the target disc), while that of Cartwheel only appears and develops after the collision.

3.4.4 *Tides*

The tidal field is the expression of the local curvature of the gravitational potential and thus, it is compressive in all directions in cored configurations (as opposed to cusps, see e.g. Renaud et al. 2009). According to Newton's second theorem, outside a mass distribution, where it can be considered spherically symmetric, the potential can be approximated by that of a point-mass (i.e. a cusp). In that case, the induced tidal field is extensive (e.g. as in the case of the Moon's tidal influence on the Earth). When this assumption breaks (i.e. inside the distribution of matter and/or for non spherical systems), the potential *can* be cored, corresponding to compressive tides.

This situation is frequently found in the central region of galaxies and where the potentials of two spatially extended distributions of mass overlap. Renaud et al. (2009) show that a wide range of galactic interactions (if not all) trigger the enhancement of tidal compression, in terms of intensity of the tidal force and of volume spanned, for $\sim$ 10 – 100 Myr. Renaud et al. (2014a) further argue that tidal compression is transmitted to turbulence which itself becomes mainly compressive and doing so, generates an excess of dense gas at $\sim 1-100$ pc scales which leads to an enhancement of star formation. Whereas this mechanisms is not the only one at play in interactions and mergers (see also Jog & Solomon 1992; Barnes 2004), it is, to date, the only one explaining the spatial distribution of some actively star forming regions (see also Renaud et al. 2015). However, the configurations and the role of compressive tides is yet to be established in the context of ring galaxies, when the overlap

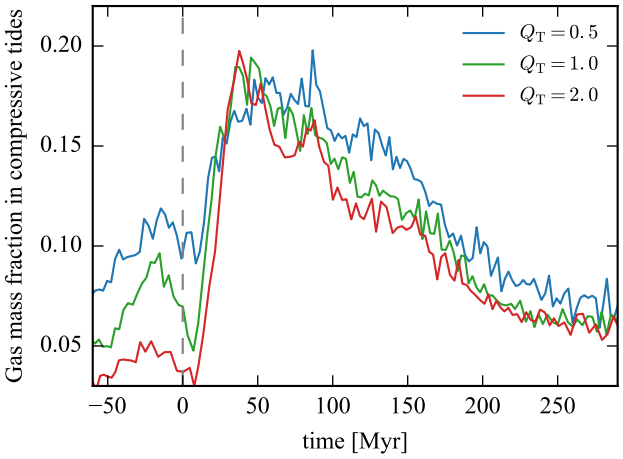

Figure 17. Evolution of the gas mass fraction in compressive tides, computed at the scale of 100 pc.

of the two galactic potentials is short-lived and unique, as opposed to more classical galaxy mergers which usually experience multiple passages during which the relative velocities of the progenitors are usually smaller. The ring galaxy configuration also differs from fly-by encounters (which otherwise yield comparably high orbital velocities and a unique pericenter passage) by the small impact parameter of the companion.

In this paper, we consider the net tidal effect, i.e. the differential total gravitational acceleration at a given scale. This encompasses the tidal effect from the companion galaxy, but also that of substructures in the main galaxy itself. Tides are then considered as the external effect on a specific region of the galaxy (which participates in the local dynamics of the region), and not only the sole effect of the companion.

Fig. 17 shows the evolution of the gas mass fraction in compressive tides.[2] The gravitational influence of the gaseous and stellar clumps affects the local tidal field around them (i.e. mainly in dense gas which thus comprises a significant fraction of the gas mass), usually (but not always) making it compressive. Therefore, our least stable galaxy model which comprises many of such clumps yields a larger gas mass fraction of compressive tides already before the interaction than the other cases.

Fig. 18 shows the position of the compressive regions at several epochs. A few Myr before the collision, compressive tides are found in the vicinity of star forming regions, i.e. mainly along spiral arms, and in the central volume. As the companion approaches, the disc is perturbed (recall Section 3.2) and extensive tides strengthen across the galaxy. The main tidal force on the target galaxy acts perpendicularly to the plane of the disc, and thus faces less binding resistance than if it was closer to the plane of the disc. Tides thus affect the disc morphology in a more critical manner than in other interactions (recall e.g. Fig. 6). At short distances, the overlap of the potentials of the two galaxies leads to a tidal field with a

[2] The tidal field is evaluated through the tidal tensor computed as in Renaud et al. (2014a), i.e. with first order finite difference of the gravitational acceleration, but at the scale of 100 pc due to the lower resolution of the simulation presented here. Tides are compressive when all the eigenvalues of the tidal tensor are negative.

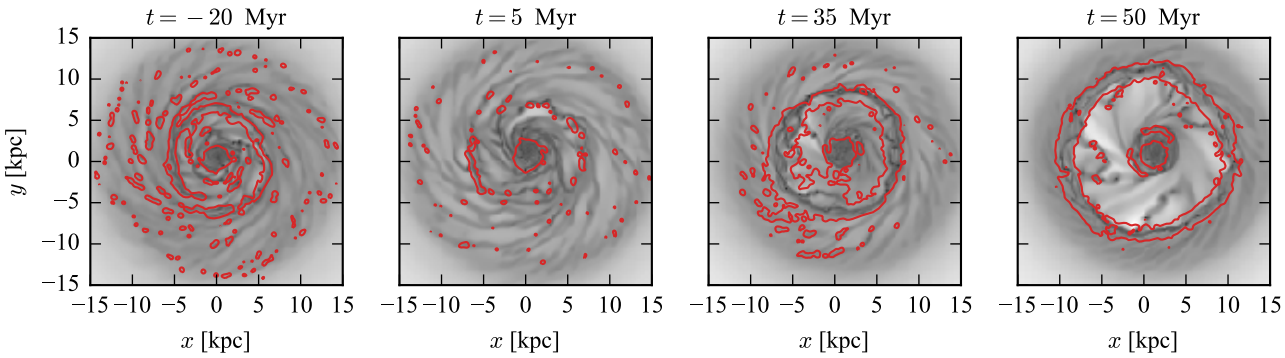

Figure 18. Contour maps of compressive tides, overlaid on density maps of the main galaxy seen face-on in our $Q_{\rm T} = 1$ model, before the collision ($t = -20$ Myr), when the mass fraction in compressive tides reaches its minimum ($t = 5$ Myr), its maximum ($t = 35$ Myr) and once the ring becomes clearly separated from the nuclear region ($t = 50$ Myr). The contours have been smoothed using a Gaussian filter with a standard deviation of 200 pc, for clarity.

compressive contribution, but which is buried under the extensive deformation of the main galaxy. This destructive effect is milder in the central region which retains its intrinsic compressive character, and undergoes a stronger compressive effect from the nearby overlap. However, the importance of compressive tides globally decreases, which translates into the (at least partial) quenching of the star formation activity, discussed in Section 3.4.1. Note that such quenching effect is not observed in interactions with a lower orbital inclination, which better resist the extensive tidal deformation and mostly host compression (Renaud et al. 2009).

At the moment of the collision, the vertical tidal force is minimum and the compressive effect of the overlap takes over. As the companion flies away from the galaxy, the ring forms and expands. The cored nature of its (local) gravitational potential induces tidal compression of a significant amount of the ISM. The global mass fraction in compressive tides rises by a factor of 2 – 2.5. This fraction then slowly returns to a lower level as the ring depletes.

We note that, despite different levels before the interaction, the gas mass fraction tidally compressed is comparable in our three galaxy models after the collision. This relates to the fact that the tidal compression triggered by the galactic interaction spans a volume several times larger than the typical scales of the gas instabilities. Therefore, the $\lesssim 100$ pc differences found between our models, because of small scales clumps before the interaction, become of secondary importance in the global gas mass fraction when the kpc-scale compression occurs.

Fig. 19 reveals the position of the tidally compressive regions 150 Myr after the collision (in our $Q_{\rm T} = 1$ model, but the others yield comparable large-scale features). The central ≈ 2 kpc of the nucleus are compressive, as even before the collision. While going to larger galactocentric radii, one first finds an extensive region ($2\ {\rm kpc} \lesssim R \lesssim 4\ {\rm kpc}$), followed by a compressive secondary, inner ring about 2 kpc wide.

Outside the nuclear region, most of the volume in the spoke region experiences extensive tides. In particular, the spokes themselves do not yield particularly compressive volumes and do not contrast from the inter-spokes areas. However, several overdensities and gas clumps (found along the spokes) lie in compressive tidal regime.

Along the main ring, we note a strong azimuthal asymmetry: most of the ring is compressive, but the $\approx 30^\circ$ wide sector closest to the nucleus (and to the impact point of the companion galaxy)

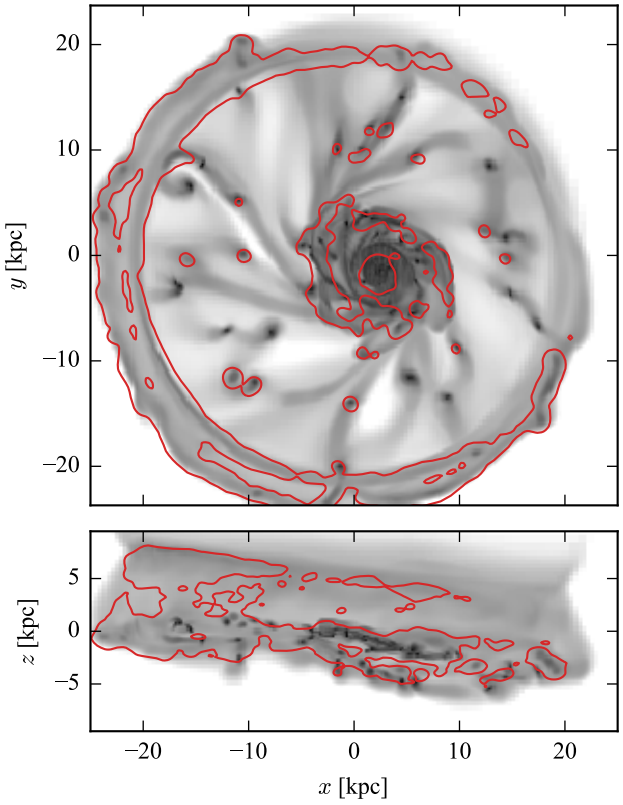

Figure 19. Same as Fig. 18 but for the face-on (top) and edge-on (bottom) view of the main galaxy, 150 Myr after the collision.

does not host compressive tides. The reason for this feature is the tidal influence of the distant nucleus which is de facto stronger on the closest side of the ring. We note that this absence of compressive tides in this area (and the comparable asymmetry in the intensity of the compression) corresponds to the above-mentioned lower star formation activity along the ring (recall Section 3.4.3 and Fig. 15). This further highlights the role of the kpc-scale dynamics, via tides, in setting the star formation activity, even 100 Myr af-

ter the galactic encounter itself. We therefore speculate that a less massive nucleus (e.g. from a progenitor with a smaller bulge mass) would (i) favour the accumulation of more material in the ring and (ii) have a weaker limiting effect on star formation in the ring, leading to a more evenly distributed star formation.

Furthermore, the dark matter halo (also affected by the gravitational acceleration from the companion) follows the motion of the nucleus and is roughly centred on it (with an offset of only ≈ 300 pc in the $x-y$ plane at $t = 150$ Myr), i.e. is off-centred with respect to the ring. As noted by Pardy et al. (2016), interactions offset the main components of galaxies, which implies a variation of the local e.g. halo to disc ratio. On top of the variation induced by the tidal field, this could also lead to a change of the local stability of the ISM, which in our case could participate in the azimuthal dependence of the star formation activity along the ring.

Fig. 19 further shows that the over-densities at the top of the cylinder visible in the edge-on view, but also as the thin smooth over-density ring close to the inner radius of the main ring in the face-on projection (recall Fig. 7), are also tidally compressed. Such distribution of densities (over-densities at the top, and in the main plane but hardly any in between) and this configuration of compressive tides is similar to that found close to the the tip of tidal tails developing in more classical galactic interactions where the gas accumulates and forms either tidal dwarf galaxies, or aggregations of stellar structures (see Renaud et al. 2015).

In our Cartwheel-like models, the quantity of gas in the cylinder is too small to make this region star forming, but we speculate that other models and/or other collision configurations could lead to star formation there, due to the presence of compressive tides, and the absence of strong shear (Fig. 8) that would likely exist in those slightly different configurations. For instance, a disc with an intrinsic higher gas surface density in the outer regions could lead to the presence of denser gas at the top edge of the cylinder. With the help of the compressive tides, such gas could form star clusters or even tidal dwarfs. In such case, young stars could be detected in two separate planes: the main plane, remnant of the original disc, and the top of the cylinder, several kpc above. Note that the absence of tidal compression in between those planes and the divergent velocity field (Fig. 7) make it unlikely to detect star formation in these intermediate regions, in again a similar way as the bulk of classical tidal tails (except near their extremities where tidal dwarf galaxy can be found). If our interpretation of the features observed in AM 0644-741 corresponding to a vertical cylinder structure is correct (recall Section 3.2), the star formation activity detected there (Higdon et al. 2011) would then support the idea presented above.

3.4.5 *Turbulence and compression sequence*

Turbulence is known to be a major actor in setting the density structure of the ISM and thus regulating star formation (see a review in Hennebelle & Falgarone 2012). Its short dissipation timescale (~ 1 Myr for surpersonic turbulence at ~ 1 pc, Mac Low & Klessen 2004) implies the existence of (at least) a source maintaining turbulence in clouds. At small scales, stellar feedback (mainly from HII regions, Matzner 2002) contributes to sustaining turbulence in star forming clouds. Grisdale et al. (2017) confirm this point at galactic scale by comparing turbulence energy spectra in simulations with and without feedback. In addition to feedback, turbulence originates from scales larger than the clouds themselves (Ossenkopf & Mac Low 2002), from the infall of gas (Klessen & Hennebelle 2010), galactic dynamics (spiral shocks, shear, Bournaud et al. 2010; Renaud et al. 2013), gas accretion (Krumholz & Burkhart 2016) and galactic interactions (Renaud et al. 2014a). In a cloud, the relative contributions of the internal and external driving of turbulence thus seem to strongly depend on the galactic environment, and obviously whether the cloud is forming stars or not.

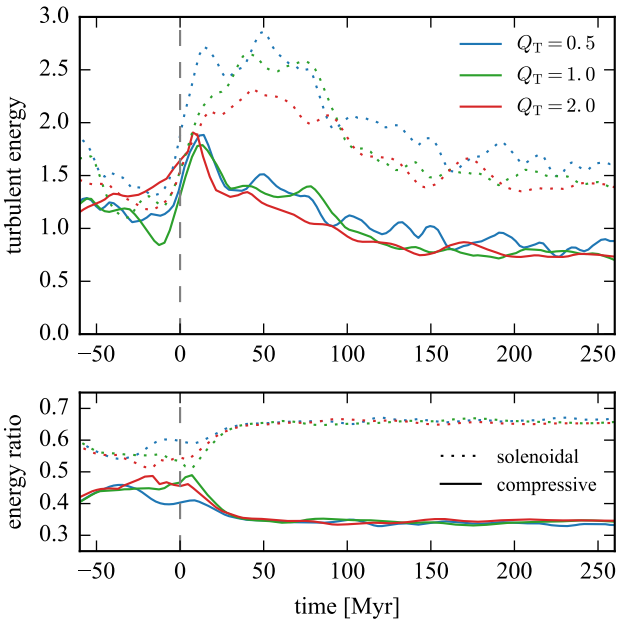

Figure 20. Evolution of the energy (top) of the solenoidal (dashed) and compressive (solid) modes of turbulence, and the ratios of the two modes to the total turbulent energy (bottom). Energy equipartition between the two modes would correspond to 2/3 for the solenoidal component and 1/3 for the compressive one (see text).

Due to the enormous range of scales involved and because of several severe artefacts introduced by the resolution limits and the structure of the mesh used in simulations, it is necessary to measure turbulence over many resolution elements. In the case of galaxy simulations, this forbids exploring the nature of turbulence at the scale of star formation (< 1 pc). Therefore, we focus here on larger scales to identify variations of turbulence along the interaction, and connect them to other physical processes.

Turbulence can be decomposed into a divergence-free, incompressible mode called solenoidal, and a curl-free compressive mode (Federrath et al. 2008). The solenoidal mode can be seen as the stirring effect of turbulence which tends to smooth out over-densities, while the compressive mode generates excesses of dense gas and increases the density contrast of the medium. When energy equipartition is reached, the solenoidal mode carries $2/3$ of the turbulent energy, while the compressive mode carries the remaining $1/3$. The distribution of densities thus depends on the nature of turbulence (Federrath et al. 2008). A strong classical (i.e. solenoidal-dominated) turbulence (high Mach number) implies a wide but unimodal density PDF leading to a high SFR, while a compression-dominated turbulence generates an excess of dense gas, explaining the super star formation efficiency of galaxies in the starburst sequence in the KS diagram (Renaud et al. 2012).

We discriminate the two modes of turbulence following the method described in Renaud et al. (2014a), at the scale of 100 pc. Fig. 20 shows the evolution of the kinetic energy carried by the compressive and solenoidal modes, and their ratio. Before the in-

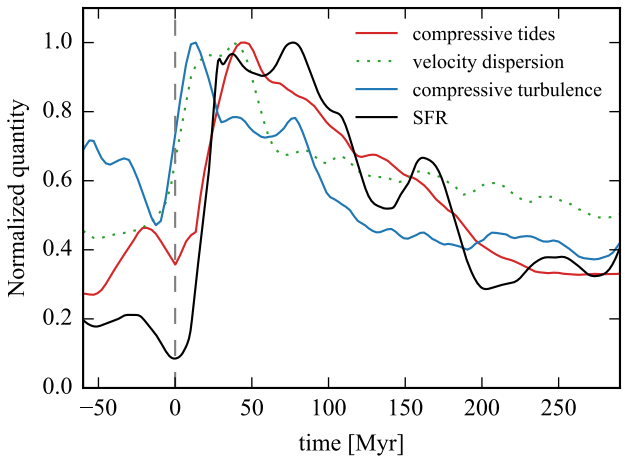

Figure 21. Evolution of the main quantities involved in the enhancement of the star formation activity (in our $Q_{\rm T} = 1$ case but all models show qualitatively comparable results): gas mass fraction in compressive tides, compressive turbulence energy, velocity dispersion and SFR. To compare their behaviour as function of time, all quantities are normalized to their maximum value, and the curves are smoothed for clarity.

teraction, the two modes are (almost) at equipartition. As the companion approaches and the importance of compressive tides rises ($t \approx -20$ Myr, recall Fig. 17), the energy in both turbulent modes increases, corresponding to a increase of the velocity dispersion (and the Mach number), as observed in interacting systems (Irwin 1994; Elmegreen et al. 1995). However, this increase does not occur at a constant energy ratio between the two modes. Instead, the compressive mode becomes more important, up to almost taking over the solenoidal component at the epoch of the collision. We note that this effect is milder in the $Q_{\rm T} = 0.5$ case than the other, corresponding to the also weaker enhancement of the mass fraction in compressive tides at the same epoch. The energy ratio stalls during the collision, until the companion leaves the target galaxy, and the two turbulent modes resume energy equipartition. The total turbulent energy then slowly decreases, in a comparable manner as the mass fraction in compressive tides and the SFR, as shown in Fig. 21.

The first quantity to increase with respect to its value before the interaction is the gas mass fraction in compressive tides ($t \approx -40$ Myr). The disruption in the form of extensive tides at collision introduces a short interruption of this raise at $t \approx 0$, as discussed in Section 3.4.4. The gravitational, remote effect is then transmitted to the hydrodynamics and alters the turbulence field of the galaxy: the kinetic energy carried by compressive turbulence starts to increase ≈ 35 Myr after the tidal compression (at $t \approx -15$ Myr). We note that, as for the tides, this increase of the compressive turbulence energy is rapidly stopped ($t \approx 10$ Myr). However, the velocity dispersion, which encompasses both turbulent modes and is thus equally affected by compressive and extensive tides, retains a high value for a longer period ($t \approx -10-70$ Myr) than the compressive turbulence energy ($t \approx -10-20$ Myr). Finally, the enhanced turbulence cascades down to the parsec scales, generates an excess of dense gas (Fig. 2) and triggers the starburst episode. We emphasize that the rise of the tidal and turbulent triggers before the star formation activity itself (Fig. 21) demonstrates that the whole process (and particularly the increase of turbulence) is not the sole result of stellar feedback: the contribution of feedback can only appear after the burst of star formation. At later times ($t > 70$ Myr), the SFR is affected by a number of local phenomena, such as the inflow of gas along the spokes onto the nucleus (Section 3.4.3), and its behaviour is less dominated by the large scale effects listed here.

With the notable exception of the strong quenching event, this sequence corresponds to that noted in a model of the Antennae galaxies (Renaud et al. 2014a). However, the changes measured here (mass fraction in compressive tides, velocity dispersion, compressive turbulence energy, widening of the PDF, SFR) are significantly milder than their equivalent found at the pericenter passages in the Antennae. It is likely that the differences originate from the pecularity of the orbit of Cartwheel system and the lower mass ratio than for the equal-mass Antennae, introducing strong extensive tides before the collision (recall Section 3.4.4), and limiting the importance of the compressive tidal and turbulent modes. The net effect is a smaller enhancement of the SFR in Cartwheel than in the Antennae (respectively by factors of ≈ 8 and $\approx 60-80$) shortly after the moments of the pericenters or collisions (Section 3.4). In both interaction configurations, the long-term enhanced star formation activity (lasting ~ 100 Myr) is to be connected to their intrinsic gas contents, the morphology of the galaxy remnants which harbour nuclear inflows, shocks (e.g. in the ring), and infalling debris along spokes in Cartwheel (Fig. 13) and tidal tails in the Antennae. A more detailed exploration of the relative role of the physical mechanisms at play in the enhancement of the SFR in interacting galaxies will be presented in a forthcoming contribution (Renaud et al., in preparation).

3.5 Young massive clusters

Starbursting interacting galaxies host the extreme physical conditions necessary to form massive star clusters ($\gtrsim 10^5$ M$_\odot$, see e.g. Whitmore & Schweizer 1995; Elmegreen & Efremov 1997; Bastian et al. 2009). In the Cartwheel in particular, the detection of ultra-luminous X-ray sources have been repported along the ring, and associated with the presence of young massive clusters (Gao et al. 2003).

Similarities in some properties of young massive clusters in starbursting galaxies and the (supposed) ones of globular clusters at the moment of their formation (redshift $\gtrsim 5-6$, Diemand et al. 2005) led several authors to suggest a link between the origins of the two populations, in low-redshift galaxy mergers and at high redshift (see Portegies Zwart et al. 2010, and references therein). However, notable differences in their metallicities, the presence of multiple stellar populations and their overall evolution question that young massive clusters would be comparable in present-day globulars if evolved for ~ 10 Gyr (see e.g. Gieles & Renaud 2016; Lardo et al. 2017). Therefore, it is necessary to establish which conditions and mechanisms (at galactic and cloud scales) lead to the formation of massive clusters, and whether comparable setups can be found in the early Universe. The difficulty of this task lies in the multi-physics and multi-scale nature of the problem. Galaxy simulations reaching parsec-scale resolutions are not sufficiently accurate to properly capture the physics of the individual star forming clouds and introduce many uncertainties in the estimates of the properties of the young clusters (see Renaud et al. 2015). Furthermore, tracking the evolution of these clusters requires capturing their internal physics (stellar evolution, two-body relaxation, e.g. Heggie & Hut 2003) which is still out of reach of present-day studies over entire galaxies.

In particular, one should keep in mind that the mass and length

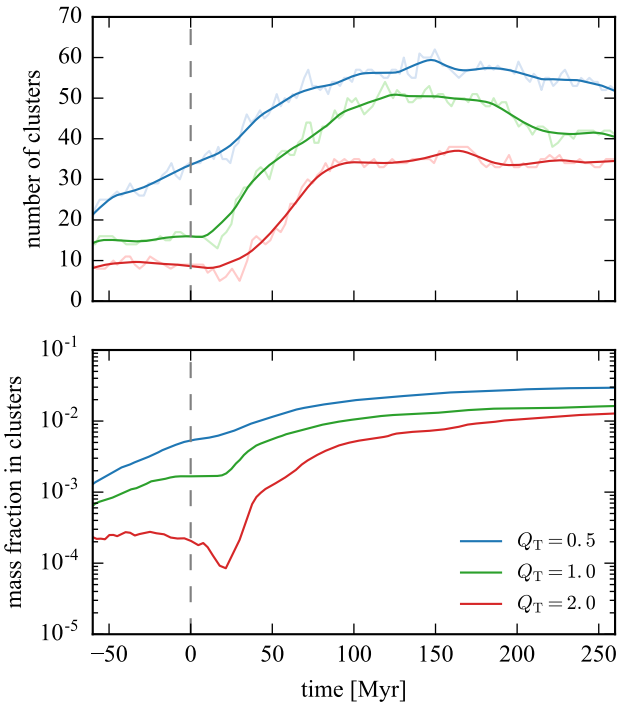

Figure 22. Top: number of star clusters identified in our three simulations. The original curves (light colours) have been smoothed out to eliminate the fluctuations introduced by our cluster detection method. Bottom: stellar mass fraction in these clusters as function of time.

resolution of our models limit us to the detection of the most massive clusters ($> 10^5$ M$_\odot$, as lower mass objects cannot be distinguished from our stellar particles), and that the softening of the gravitational potential (6 pc) introduces over-estimates in the size (and thus the binding energy) of these systems. However, by limiting ourselves to some properties and focussing on relative comparisons between our models and at different epochs, we can still address several questions on the population of young massive star clusters in Cartwheel.

We identify the star clusters as over-densities in the young stellar population (i.e. of the stars formed after the beginning of the simulation) by running the friend-of-friend algorithm HOP (Eisenstein & Hut 1998) with the peak, saddle and outer densities of $10^8, 10^8$ and 10^6 M$_\odot$ kpc^{-3} respectively, chosen to agree with a visual examination of stellar structures. Then, only stellar particles below the escape velocity of their clusters (computed assuming a point-mass potential) are kept as cluster members. Note that over-densities of old stars (i.e. set up in the initial condition) are also formed during the interaction, but are not accounted for here due to the lack of resolution of this component.

Fig. 22 shows the evolution of the number of star clusters we identify. Uncertainties in our friend-of-friend detection method, specially for the clusters made of a small number of stellar particles (i.e. 10^{4-5} M$_\odot$) introduce small fluctuations in the total number of clusters identified, from one snapshot to the next. However, the models yield a rapid increase of the number of massive clusters a few Myr after the collision. This increase is however mild in the $Q_T = 0.5$ which rather shows a constantly rising number of clusters and for which the effect of the collision is present but less visible. We note that the epoch of this increase varies from one model to the next: our $Q_T = 2$ case is the last one to experience it, about 25 Myr after the collision. This is due to its sensitivity to the quenching mechanism (Section 3.4.1) which has the most severe effect on the SFR for our most stable model. Its less dense clouds being easily tidally disrupted and even destroyed by the approaching companion, it takes this galaxy longer to form new over-densities able to lead to the formation of massive clusters, while the other models host more resistant clouds and yield physical conditions which can more easily and rapidly (re-)form the necessary clumps.

The number of clusters stalls $\approx 80-110$ Myr after the collision, when the mass fraction in compressive tides and the energy of compressive turbulence decrease (Figs. 17 and 20). This epoch also corresponds to the moment when the ring starts loosing mass (Fig. 3). The number of clusters eventually diminishes a bit, as clusters get dissolved by the galactic tides (e.g. when approaching the nuclear region, or encountering dense structures like the inner ring along their orbit, see Gieles et al. 2007 for a comparable effect).

The stellar mass fraction found in clusters follows the overall same behaviour, with the notable exception that clusters in our $Q_T = 2$ model loose mass around the collision, due to tidal stripping from the companion galaxy. Contrarily to the gas clouds, the clusters mainly loose mass after the collision because, being denser, they better resist to tidal harassment, and it takes longer to their stars to reach the necessary energy to escape. We stress, however, that the softening of the gravitational potential in our simulations implies that the cluster binding energy and mass loss rate are biased (see Renaud et al. 2015, their figure 7), so that these measurements should only be interpreted qualitatively.

Not enough clusters are formed in this system to derive a statistically significant cluster mass function. However, one can examine the evolution of the mass of the most massive cluster in the simulation. In this analysis, we exclude the central-most object (nuclear star cluster) which is build hierarchically by accreting stars, gas (and forming stars in situ) and star clusters along the simulation (see Tremaine et al. 1975; Milosavljević 2004; Antonini 2013; Guillard et al. 2016, and references therein for detailed scenarios of nuclear cluster formation). In our simulations of the Cartwheel, the most massive cluster before the collision has a mass of the order of $\sim 10^6$ M$_\odot$. That after the collision (i.e. when the SFR is enhanced) is 20, 30 or 40 time larger, for the $Q_T = 0.5$, 1 and 2 cases respectively. In the case of the modelled Antennae galaxies, this factor reaches 15 at the first pericentre passage. In the Antennae however, the number of clusters jumps by a factor of ≈ 10, while this number is only ≈ 3 in our models of the Cartwheel. The resolutions of the simulations are different (6 pc here and 1.5 pc in the Antennae), but we base our analysis on the *relative* evolution of these quantities before and after the encounters, to limit the potential effect of such discrepancy on our results. Therefore, we can conclude that the change of physical conditions due to the encounter in the Cartwheel favours a more concentrated formation than in the Antennae, i.e. in the form of less numerous but more massive clusters (with respect to the pre-interaction epoch). At first order, and while keeping in mind the limitations mentioned above, the high-mass end of the initial cluster mass function (ICMF) of the Cartwheel would thus be shallower than that of the Antennae. Kravtsov & Gnedin (2005) proposes that the high-mass end slope of the ICMF derives from the shape of the gas density PDF. The relative milder widening of the PDF and the smaller importance of compressive turbulence in Cartwheel than in the Antennae could then explain the differences in the change of the ICMF between the

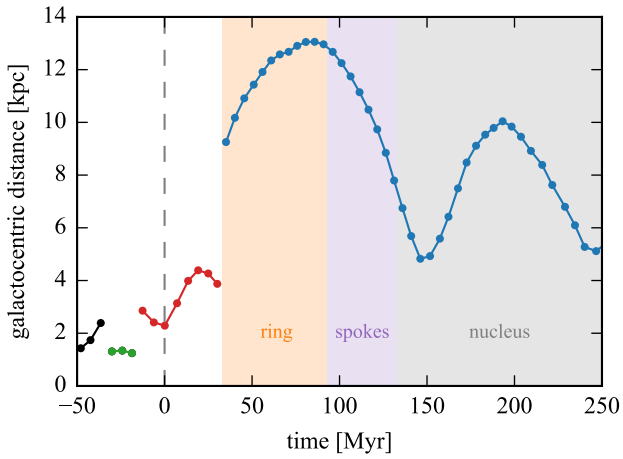

Figure 23. Distance to the centre of the nucleus of the most massive cluster in our $Q_{\rm T} = 1$ model. Solid lines identify one cluster tracked in time. Discontinuities mark changes in the identity of the most massive cluster. Shaded areas indicate the region in which the most massive cluster is found.

two systems during their respective galactic encounters. This point will be further explored in a forthcoming paper (Renaud et al., in preparation).

Fig. 23 shows the galactocentric distance (with respect to the centre of the nucleus, i.e. not with respect to the centre of the ring) of the most massive cluster. The rather continuous formation of clusters before the interaction induces several changes in the identity of cluster being the most massive, visible as discontinuities in this figure. They are, however, all found in the inner parts of the disc before the interaction phase ($\lesssim 3$ kpc, and $\lesssim -10$ Myr), where the gas density is the highest. A few Myr around the collision ($-10\,\mathrm{Myr} \lesssim t \lesssim 35\,\mathrm{Myr}$), a cluster, formed in the tidally compressive annular structure visible in the leftmost panel of Fig. 18, remains the most massive throughout the interaction, likely because no new clusters are formed during this time range due to the quenching effect of the companion (Figs. 9 and 22). Later, as the ring has formed and is expanding, it encompasses almost all the star formation activity and gathers the physical conditions necessary to form massive star clusters, (at least partly) because of the tidal compression (Fig. 18) and low shear (Fig. 8), resulting in the high star formation efficiency we measure (Fig. 14). A new cluster then takes the role of most massive one in the galaxy and will keep this role until the end of our simulation. It forms in the ring ≈ 35 Myr after the collision, i.e. after the rise of the overall number of clusters formed, but roughly at the time the SFR reaches its maximum value. This indicates that the delay between the collision and the enhancement of star (cluster) formation is longer for more massive objects. This most massive cluster remains in the expanding ring for ≈ 55 Myr and then travels along the spokes to reach the nuclear region ≈ 100 Myr after its formation. It does not reach the very centre of the nucleus, but rather remains in the inner, secondary ring. It then moves to larger radii because of expansion of the inner ring, and comes back again to the central region, in a similar manner but slower, as it did from the main ring ≈ 100 Myr earlier. It is however difficult to conclude on the presence of spokes inside the inner ring that could play a comparable role to those discussed above, so that the mechanism driving the cluster toward the centre of the galaxy at late time ($t \gtrsim 200$ Myr) could well be different.

Assuming that this evolution is common to most ring galaxies (at least those with spokes), the location of the most massive (or brightest) cluster could be used to estimate the epoch of the peak of star formation and constrain the star formation history of the system, while the size of the ring and the present-day SFR would constrain the epoch of collision, as discussed in the previous sections.

4 SUMMARY AND CONCLUSION

We present hydrodynamical models of Cartwheel-like ring galaxies to explore the formation and evolution of the main structures, and the impact of large-scale dynamics on the enhanced star formation activity. Our main conclusions are as follows.

- The overall evolution of the system is independent of the initial intrinsic stability of the main galaxy's disc, at least in the range of $Q_{\rm T}$ we probed. Details in the star formation activity are however affected by the pre-collision existence and stability of gas structures and clouds, up to significant differences in the global SFR, even 100 Myr after the encounter. It is likely that a disc yielding stronger structures (spirals, bars) before the collision than our models would respond differently to the encounter (see Athanassoula et al. 1997; Berentzen et al. 2003).
- The ring structure ploughs through the disc material as it radially expands at the roughly constant speed of $\approx 120\,\mathrm{km\,s^{-1}}$. This accretion of gas and stars is counterbalanced by mass-loss in the spokes, which in turn fuels the nuclear region. The ring is thus a short-lived feature that reaches it maximum mass ≈ 90 Myr after the collision (when the ring's radius is ≈ 17 kpc), and becomes difficult to identify ≈ 110 Myr later.
- The passage of the companion galaxy also triggers the formation of a tidal vertical structure in the form of a diffuse annular, cylindrical shape above the ring. We predict a possible detection of such structures in the velocity field of real collisional ring galaxies, although the vertical velocity structure of this object encompasses several components that overlap with those of the ring itself and might be difficult to disentangle. The cylindrical shape could be easier to detect in the distribution of neutral hydrogen. The nature and the properties of this structure remind us of tidal tails in classical interactions. Although no star formation is detected there in our models, we speculate that other progenitor galaxies and/or other orbital setups could lead to enough gas accumulation to host a star formation activity, possibly in the form of tidal dwarf galaxy(ies). Such situation might well be what is observed, in particular in Hα, in AM 0644-741 (i.e. the Lindsay-Shapley galaxy).
- A few Myr before the collision, the approaching companion galaxy tidally disrupts and destroys (at least some) gas overdensities, thus (at least partially) quenching the star formation activity across the target's disc. This activity resumes rapidly after the collision, in an enhanced manner. However, in the Kennicutt-Schmidt diagram, the system barely reaches the starburst regime.
- The ring is the most actively star forming region during its first 100 Myr. After this phase, the flows of gas through the spokes transfer the star formation activity to the nuclear region. Short bursts in this activity occur when marginally stable gas clumps, that formed in the ring and survived along the spokes, fall into the nucleus. We find that spokes (and portions of spokes) with almost radial shapes yield a weaker shear than those with a smaller pitch angle, the former favouring the survival of gas clumps. Such

sequential evolution of the location of the star formation activity could thus be used to estimate the dynamical stage of observed ring systems, and even date the epoch of encounter. That would likely provide strong constraints on the star formation histories of these galaxies.

- The portion of the ring the furthest from the nucleus yields significantly more star formation than the other side, exactly as observed in the Cartwheel and e.g. AM 0644-741. This is linked to the weaker, and even compressive tidal field found there, while the other side hosts stronger, more destructive tides. The off-centred nucleus and dark matter halo thus have a stabilizing effect on the ISM of the ring.
- After a destructive effect leading to star formation quenching when the companion approaches, the tidal field of the target galaxy becomes strongly compressive over kpc-scale volumes. The compressive nature of the tidal field is maintained in both the inner and outer rings after the companion has moved away from the target (with the notable exception of an azimuthal fraction at the latest stages).
- This compression is transmitted to the turbulence of the ISM. Its compressive mode almost overcomes the otherwise dominant solenoidal (stirring) mode for a few ~ 10 Myr after the collision, but the turbulence rapidly goes back to energy equipartition of the two modes (i.e. solenoidal dominated). Such evolution translates into an excess of dense gas visible in the gas density PDF of the system, further leading to the mild but significant boost of the SFR shortly after the collision. This situation is similar to what is found in other galaxy interactions and mergers. The longer-term evolution of the star formation activity ($\gtrsim 50-70$ Myr after the collision) then rather proceeds like in normal star-forming discs, i.e. with a longer gas depletion time and a lower star formation efficiency, yet at a rate higher than that before the collision.
- The interaction triggers an increase in the number of (massive) star clusters formed. While the stellar mass fraction found in clusters reaches a plateau (or even decreases) shortly after the collision due to tidal disruption, it jumps a few ~ 10 Myr later before slowing down or even stalling when the ring starts loosing mass. The clusters formed are significantly more massive than those formed before the collision. The induced formation of the most massive clusters occurs ≈ 20 Myr after the overall number of clusters rises. The most massive objects form in the ring where and when the tidal field and the turbulence are compressive and the shear is weak, during the first ≈ 100 Myr after the collision. They then travel along the spokes and reach the nuclear region. Keeping in mind the limitations of our models, we speculate that the initial cluster mass function in the Cartwheel would be shallower than that of classical mergers like the Antennae, possibly because of the weaker effect of compressive turbulence. These differences call for a deeper and more systematic analysis of triggered star formation in interacting systems.

ACKNOWLEDGEMENTS

We warmly thank Jean-Charles Lambert for his help with the visualisation of the simulation results and for making the tool glnemo2 public (https://projets.lam.fr/projects/glnemo2), and Ramon Rey-Raposo for discussions that helped improve the quality of this work. FR acknowledges support from the European Research Council through grant ERC-StG-335936. This work was granted access to the PRACE Research Infrastructure (under allocation 2540) and GENCI (under allocations 2192 and s030) resource *Curie* hosted at the TGCC (France).

REFERENCES

Agertz O., Kravtsov A. V., 2015, ApJ, 804, 18
Agertz O., Kravtsov A. V., 2016, ApJ, 824, 79
Amram P., Mendes de Oliveira C., Boulesteix J., Balkowski C., 1998, A&A, 330, 881
Antonini F., 2013, ApJ, 763, 62
Appleton P. N., James R. A., 1990, Self-consistent simulations of ring galaxies.. pp 200–204
Appleton P. N., Marston A. P., 1997, AJ, 113, 201
Appleton P. N., Struck-Marcell C., 1996, Fundamentals Cosmic Phys., 16, 111
Athanassoula E., Bosma A., 1985, ARA&A, 23, 147
Athanassoula E., Puerari I., Bosma A., 1997, MNRAS, 286, 284
Barnes J. E., 2004, MNRAS, 350, 798
Bastian N., Trancho G., Konstantopoulos I. S., Miller B. W., 2009, ApJ, 701, 607
Berentzen I., Athanassoula E., Heller C. H., Fricke K. J., 2003, MNRAS, 341, 343
Bosma A., 2000, in Valtonen M. J., Flynn C., eds, Astronomical Society of the Pacific Conference Series Vol. 209, IAU Colloq. 174: Small Galaxy Groups. p. 255
Bournaud F., et al., 2007, Science, 316, 1166
Bournaud F., Elmegreen B. G., Teyssier R., Block D. L., Puerari I., 2010, MNRAS, 409, 1088
Chabrier G., 2003, PASP, 115, 763
Charmandaris V., Laurent O., Mirabel I. F., Gallais P., Sauvage M., Vigroux L., Cesarsky C., Appleton P. N., 1999, A&A, 341, 69
D'Onghia E., Mapelli M., Moore B., 2008, MNRAS, 389, 1275
Daddi E., et al., 2010, ApJ, 713, 686
Diemand J., Madau P., Moore B., 2005, MNRAS, 364, 367
Duc P.-A., Renaud F., 2013, in Souchay J., Mathis S., Tokieda T., eds, Vol. 861, Lecture Notes in Physics, Berlin Springer Verlag. p. 327 (arXiv:1112.1922), doi:10.1007/978-3-642-32961-6˙9
Eisenstein D. J., Hut P., 1998, ApJ, 498, 137
Elmegreen B. G., Efremov Y. N., 1997, ApJ, 480, 235
Elmegreen D. M., Kaufman M., Brinks E., Elmegreen B. G., Sundin M., 1995, ApJ, 453, 100
Federrath C., Klessen R. S., Schmidt W., 2008, ApJ, 688, L79
Fensch J., et al., 2017, MNRAS, 465, 1934
Fiacconi D., Mapelli M., Ripamonti E., Colpi M., 2012, MNRAS, 425, 2255
Fosbury R. A. E., Hawarden T. G., 1977, MNRAS, 178, 473
Gao Y., Wang Q. D., Appleton P. N., Lucas R. A., 2003, ApJ, 596, L171
Genzel R., Tacconi L. J., Gracia-Carpio J., Sternberg A., Cooper M. C., Shapiro K., Bolatto A., et al. 2010, MNRAS, 407, 2091
Georgakakis A., Forbes D. A., Norris R. P., 2000, MNRAS, 318, 124
Gerber R. A., Lamb S. A., 1994, ApJ, 431, 604
Gerber R. A., Lamb S. A., Balsara D. S., 1992, ApJ, 399, L51
Gerber R. A., Lamb S. A., Balsara D. S., 1996, MNRAS, 278, 345
Ghosh K. K., Mapelli M., 2008, MNRAS, 386, L38
Gieles M., Renaud F., 2016, MNRAS, 463, L103
Gieles M., Athanassoula E., Portegies Zwart S. F., 2007, MNRAS, 376, 809
Graham J. A., 1974, The Observatory, 94, 290
Grisdale K., Agertz O., Romeo A. B., Renaud F., Read J. I., 2017, MNRAS, 466, 1093
Guillard N., Emsellem E., Renaud F., 2016, MNRAS, 461, 3620
Heggie D., Hut P., 2003, The Gravitational Million-Body Problem: A Multidisciplinary Approach to Star Cluster Dynamics, by Douglas Heggie and Piet Hut. Cambridge University Press, 2003, 372 pp.
Hennebelle P., Falgarone E., 2012, A&ARv, 20, 55
Hernquist L., Weil M. L., 1993, MNRAS, 261, 804
Higdon J. L., 1995, ApJ, 455, 524
Higdon J. L., 1996, ApJ, 467, 241

Higdon J. L., Higdon S. J. U., Rand R. J., 2011, ApJ, 739, 97
Higdon J. L., Higdon S. J. U., Martín Ruiz S., Rand R. J., 2015, ApJ, 814, L1
Horellou C., Combes F., 2001, Ap&SS, 276, 1141
Horellou C., Charmandaris V., Combes F., Appleton P. N., Casoli F., Mirabel I. F., 1998, A&A, 340, L51
Huang S.-N., Stewart P., 1988, A&A, 197, 14
Iovino A., 2002, AJ, 124, 2471
Irwin J. A., 1994, ApJ, 429, 618
Jog C. J., Solomon P. M., 1992, ApJ, 387, 152
Kennicutt R. C., 1998, ApJ, 498, 541
Kim C.-G., Ostriker E. C., 2015, ApJ, 802, 99
Klessen R. S., Hennebelle P., 2010, A&A, 520, A17
Kravtsov A. V., Gnedin O. Y., 2005, ApJ, 623, 650
Krumholz M. R., Burkhart B., 2016, MNRAS, 458, 1671
Lardo C., Cabrera-Ziri I., Davies B., Bastian N., 2017, MNRAS, 468, 2482
Lavery R. J., Remijan A., Charmandaris V., Hayes R. D., Ring A. A., 2004, ApJ, 612, 679
Lynds R., Toomre A., 1976, ApJ, 209, 382
Mac Low M.-M., Klessen R. S., 2004, Reviews of Modern Physics, 76, 125
Madore B. F., Nelson E., Petrillo K., 2009, ApJS, 181, 572
Mapelli M., Mayer L., 2012, MNRAS, 420, 1158
Mapelli M., Moore B., Ripamonti E., Mayer L., Colpi M., Giordano L., 2008, MNRAS, 383, 1223
Marcum P. M., Appleton P. N., Higdon J. L., 1992, ApJ, 399, 57
Matzner C. D., 2002, ApJ, 566, 302
Mayya Y. D., Bizyaev D., Romano R., Garcia-Barreto J. A., Vorobyov E. I., 2005, ApJ, 620, L35
Meurer G. R., et al. 2006, ApJS, 165, 307
Michel-Dansac L., et al., 2010, ApJ, 717, L143
Milosavljević M., 2004, ApJ, 605, L13
Ossenkopf V., Mac Low M.-M., 2002, A&A, 390, 307
Pardy S. A., D'Onghia E., Athanassoula E., Wilcots E. M., Sheth K., 2016, ApJ, 827, 149
Pellerin A., Meurer G. R., Bekki K., Elmegreen D. M., Wong O. I., Knezek P. M., 2010, AJ, 139, 1369
Plummer H. C., 1911, MNRAS, 71, 460
Portegies Zwart S. F., McMillan S. L. W., Gieles M., 2010, ARA&A, 48, 431
Prestwich A. H., et al., 2012, ApJ, 747, 150
Renaud F., Boily C. M., Naab T., Theis C., 2009, ApJ, 706, 67
Renaud F., Kraljic K., Bournaud F., 2012, ApJ, 760, L16
Renaud F., et al., 2013, MNRAS, 436, 1836
Renaud F., Bournaud F., Kraljic K., Duc P.-A., 2014a, MNRAS, 442, L33
Renaud F., Bournaud F., Emsellem E., Elmegreen B., Teyssier R., 2014b, in Seigar M. S., Treuthardt P., eds, Astronomical Society of the Pacific Conference Series Vol. 480, Structure and Dynamics of Disk Galaxies. p. 247 (arXiv:1310.0082)
Renaud F., Bournaud F., Duc P.-A., 2015, MNRAS, 446, 2038
Renaud F., Famaey B., Kroupa P., 2016, MNRAS, 463, 3637
Renaud F., Agertz O., Gieles M., 2017, MNRAS, 465, 3622
Romano R., Mayya Y. D., Vorobyov E. I., 2008, AJ, 136, 1259
Schreiber C., et al., 2015, A&A, 575, A74
Scudder J. M., Ellison S. L., Torrey P., Patton D. R., Mendel J. T., 2012, MNRAS, 426, 549
Smith R., Lane R. R., Conn B. C., Fellhauer M., 2012, MNRAS, 423, 543
Struck-Marcell C., Appleton P. N., 1987, ApJ, 323, 480
Struck-Marcell C., Higdon J. L., 1993, ApJ, 411, 108
Struck-Marcell C., Lotan P., 1990, ApJ, 358, 99
Struck C., Appleton P. N., Borne K. D., Lucas R. A., 1996, AJ, 112, 1868
Teyssier R., 2002, A&A, 385, 337
Theys J. C., Spiegel E. A., 1977, ApJ, 212, 616
Toomre A., 1964, ApJ, 139, 1217
Toomre A., 1978, in Longair M. S., Einasto J., eds, IAU Symposium Vol. 79, Large Scale Structures in the Universe. pp 109–116
Toomre A., Toomre J., 1972, ApJ, 178, 623
Tremaine S. D., Ostriker J. P., Spitzer Jr. L., 1975, ApJ, 196, 407
Vorobyov E. I., 2003, A&A, 407, 913
Whitmore B. C., Schweizer F., 1995, AJ, 109, 960
Wolter A., Trinchieri G., 2004, A&A, 426, 787
Wolter A., Trinchieri G., Iovino A., 1999, A&A, 342, 41
Wong O. I., et al. 2006, MNRAS, 370, 1607
Zwicky F., 1941, Hydrodynamics and the Structure of Stellar Systems. p. 137

Bibliography

Adamo, A. et al. (2010). "On the Origin of the Red Excess in Very Young Super Star Clusters: The Case of SBS 0335-052E". In: *ApJ* 725, pp. 1620–1628. DOI: 10.1088/0004-637X/725/2/1620. arXiv: 1010.3703.

Agertz, O., R. Teyssier, and B. Moore (2009). "Disc formation and the origin of clumpy galaxies at high redshift". In: *MNRAS* 397, pp. L64–L68. DOI: 10.1111/j.1745-3933.2009.00685.x. arXiv: 0901.2536.

Agertz, O. et al. (2007). "Fundamental differences between SPH and grid methods". In: *MNRAS* 380, pp. 963–978. DOI: 10.1111/j.1365-2966.2007.12183.x. eprint: astro-ph/0610051.

Allen, M. G. et al. (2008). "The MAPPINGS III Library of Fast Radiative Shock Models". In: *ApJS* 178, pp. 20–55. DOI: 10.1086/589652. arXiv: 0805.0204.

Anders, P. et al. (2004). "Analysing observed star cluster SEDs with evolutionary synthesis models: systematic uncertainties". In: *MNRAS* 347, pp. 196–212. DOI: 10.1111/j.1365-2966.2004.07197.x. eprint: astro-ph/0309356.

Arp, H. C. (1972). "Ejection of Small Compact Galaxies from Larger Galaxies". In: *External Galaxies and Quasi-Stellar Objects*. Ed. by D. S. Evans, D. Wills, and B. J. Wills. Vol. 44. IAU Symposium, p. 380.

Ashman, K. M. and S. E. Zepf (1992). "The formation of globular clusters in merging and interacting galaxies". In: *ApJ* 384, pp. 50–61. DOI: 10.1086/170850.

Asplund, M. et al. (2009). "The Chemical Composition of the Sun". In: *ARA&A* 47, pp. 481–522. DOI: 10.1146/annurev.astro.46.060407.145222. arXiv: 0909.0948 [astro-ph.SR].

Athanassoula, E. et al. (2016). "Forming Disk Galaxies in Wet Major Mergers. I. Three Fiducial Examples". In: *ApJ* 821, 90, p. 90. DOI: 10.3847/0004-637X/821/2/90. arXiv: 1602.03189.

Bailin, J. and W. E. Harris (2009). "Stochastic Self-Enrichment, Pre-Enrichment, and the Formation of Globular Clusters". In: *ApJ* 695, pp. 1082–1093. DOI: 10.1088/0004-637X/695/2/1082. arXiv: 0901.2302.

Baldwin, J. A., M. M. Phillips, and R. Terlevich (1981). "Classification parameters for the emission-line spectra of extragalactic objects". In: *PASP* 93, pp. 5–19. DOI: 10.1086/130766.

Barger, A. J. et al. (1998). "Submillimetre-wavelength detection of dusty star-forming galaxies at high redshift". In: *Nature* 394, pp. 248–251. DOI: 10.1038/28338. eprint: astro-ph/9806317.

Barnes, J. E. and L. E. Hernquist (1991). "Fueling starburst galaxies with gas-rich mergers". In: *ApJ* 370, pp. L65–L68. DOI: 10.1086/185978.

Bastian, N. (2008). "On the star formation rate - brightest cluster relation: estimating the peak star formation rate in post-merger galaxies". In: *MNRAS* 390, pp. 759–768. DOI: 10.1111/j.1365-2966.2008.13775.x. arXiv: 0807.4687.

Bate, M. R., I. A. Bonnell, and N. M. Price (1995). "Modelling accretion in protobinary systems". In: *MNRAS* 277, pp. 362–376. DOI: 10.1093/mnras/277.2.362. eprint: astro-ph/9510149.

Beck, R. (2009). "Galactic and extragalactic magnetic fields - a concise review". In: *Astrophysics and Space Sciences Transactions* 5, pp. 43–47. DOI: 10.5194/astra-5-43-2009.

Behrendt, M., A. Burkert, and M. Schartmann (2016). "Clusters of Small Clumps Can Explain the Peculiar Properties of Giant Clumps in High-redshift Galaxies". In: *ApJ* 819, L2, p. L2. DOI: 10.3847/2041-8205/819/1/L2. arXiv: 1512.03430.

Bekki, K. et al. (2002). "Globular cluster formation from gravitational tidal effects of merging and interacting galaxies". In: *MNRAS* 335, pp. 1176–1192. DOI: 10.1046/j.1365-8711.2002.05708.x. eprint: astro-ph/0206008.

Bergvall, N., E. Laurikainen, and S. Aalto (2003). "Galaxy interactions - poor starburst triggers. III. A study of a complete sample of interacting galaxies". In: *A&A* 405, pp. 31–52. DOI: 10.1051/0004-6361:20030542.

Bertin, E. and S. Arnouts (1996). "SExtractor: Software for source extraction." In: *A&AS* 117, pp. 393–404. DOI: 10.1051/aas:1996164.

Bertoldi, F. and C. F. McKee (1992). "Pressure-confined clumps in magnetized molecular clouds". In: *ApJ* 395, pp. 140–157. DOI: 10.1086/171638.

Bianchini, P. et al. (2015). "The inefficiency of satellite accretion in forming extended star clusters". In: *MNRAS* 447, pp. L40–L44. DOI: 10.1093/mnrasl/slu177. arXiv: 1411.1069.

Bigiel, F. et al. (2008). "The Star Formation Law in Nearby Galaxies on Sub-Kpc Scales". In: *AJ* 136, pp. 2846–2871. DOI: 10.1088/0004-6256/136/6/2846. arXiv: 0810.2541.

Bik, A. et al. (2015). "VLT/MUSE view of the highly ionized outflow cones in the nearby starburst ESO338-IG04". In: *A&A* 576, L13, p. L13. DOI: 10.1051/0004-6361/201525850. arXiv: 1503.06626.

Binney, J. and S. Tremaine (2008). *Galactic Dynamics: Second Edition*. Princeton University Press.

Birnboim, Y. and A. Dekel (2003). "Virial shocks in galactic haloes?" In: *MNRAS* 345, pp. 349–364. DOI: 10.1046/j.1365-8711.2003.06955.x. eprint: astro-ph/0302161.

Bisbas, T. G. et al. (2017). "Cosmic-ray Induced Destruction of CO in Star-forming Galaxies". In: *ApJ* 839, 90, p. 90. DOI: 10.3847/1538-4357/aa696d. arXiv: 1703.08598.

Blakeslee, J. P. et al. (2012). "Optical and Infrared Photometry of Globular Clusters in NGC 1399: Evidence for Color-Metallicity Nonlinearity". In: *ApJ* 746, 88, p. 88. DOI: 10.1088/0004-637X/746/1/88. arXiv: 1201.1031 [astro-ph.CO].

Blanton, M. R. and J. Moustakas (2009). "Physical Properties and Environments of Nearby Galaxies". In: *ARA&A* 47, pp. 159–210. DOI: 10.1146/annurev-astro-082708-101734. arXiv: 0908.3017.

Blumenthal, G. R. et al. (1984). "Formation of galaxies and large-scale structure with cold dark matter". In: *Nature* 311, pp. 517–525. DOI: 10.1038/311517a0.

Bonnell, I. A., C. L. Dobbs, and R. J. Smith (2013). "Shocks, cooling and the origin of star formation rates in spiral galaxies". In: *MNRAS* 430, pp. 1790–1800. DOI: 10.1093/mnras/stt004. arXiv: 1301.1041.

Boquien, M. et al. (2007). "Polychromatic view of intergalactic star formation in NGC 5291". In: *A&A* 467, pp. 93–106. DOI: 10.1051/0004-6361:20066692. eprint: astro-ph/0703002.

Boquien, M. et al. (2009). "Collisional Debris as Laboratories to Study Star Formation". In: *AJ* 137, pp. 4561–4576. DOI: 10.1088/0004-6256/137/6/4561. arXiv: 0903.3403 [astro-ph.CO].

Boquien, M. et al. (2010). "Star Formation in Collision Debris: Insights from the Modeling of Their Spectral Energy Distribution". In: *AJ* 140, pp. 2124–2144. DOI: 10.1088/0004-6256/140/6/2124. arXiv: 1010.2201.

Bournaud, F. (2010). "Star Formation and Structure Formation in Galaxy Interactions and Mergers". In: *Galaxy Wars: Stellar Populations and Star Formation in Interacting Galaxies*. Ed. by B. Smith et al. Vol. 423. Astronomical Society of the Pacific Conference Series, p. 177. arXiv: 0909.1812 [astro-ph.CO].

— (2016). "Bulge Growth Through Disc Instabilities in High-Redshift Galaxies". In: *Galactic Bulges* 418, p. 355. DOI: 10.1007/978-3-319-19378-6_13. arXiv: 1503.07660.

Bournaud, F., P.-A. Duc, and E. Emsellem (2008). "High-resolution simulations of galaxy mergers: resolving globular cluster formation". In: *MNRAS* 389, pp. L8–L12. DOI: 10.1111/j.1745-3933.2008.00511.x. arXiv: 0806.1386.

Bournaud, F. and B. G. Elmegreen (2009). "Unstable Disks at High Redshift: Evidence for Smooth Accretion in Galaxy Formation". In: *ApJ* 694, pp. L158–L161. DOI: 10.1088/0004-637X/694/2/L158. arXiv: 0902.2806 [astro-ph.CO].

Bournaud, F., C. J. Jog, and F. Combes (2005). "Galaxy mergers with various mass ratios: Properties of remnants". In: *A&A* 437, pp. 69–85. DOI: 10.1051/0004-6361:20042036. eprint: astro-ph/0503189.

Bournaud, F. et al. (2007). "Missing Mass in Collisional Debris from Galaxies". In: *Science* 316, pp. 1166–. DOI: 10.1126/science.1142114. arXiv: 0705.1356.

Bournaud, F. et al. (2011). "Hydrodynamics of High-redshift Galaxy Collisions: From Gas-rich Disks to Dispersion-dominated Mergers and Compact Spheroids". In: *ApJ* 730, 4, p. 4. DOI: 10.1088/0004-637X/730/1/4. arXiv: 1006.4782.

Bournaud, F. et al. (2014). "The Long Lives of Giant Clumps and the Birth of Outflows in Gas-rich Galaxies at High Redshift". In: *ApJ* 780, 57, p. 57. DOI: 10.1088/0004-637X/780/1/57. arXiv: 1307.7136.

Bournaud, F. et al. (2015). "Modeling CO emission from hydrodynamic simulations of nearby spirals, starbursting mergers, and high-redshift galaxies". In: *A&A* 575, A56, A56. DOI: 10.1051/0004-6361/201425078. arXiv: 1409.8157.

Braine, J. et al. (2000). "Formation of molecular gas in the tidal debris of violent galaxy-galaxy interactions". In: *Nature* 403, pp. 867–869. DOI: 10.1038/35002521.

Brodie, J. P. and J. Strader (2006). "Extragalactic Globular Clusters and Galaxy Formation". In: *ARA&A* 44, pp. 193–267. DOI: 10.1146/annurev.astro.44.051905.092441. eprint: astro-ph/0602601.

Brooks, A. M. et al. (2009). "The Role of Cold Flows in the Assembly of Galaxy Disks". In: *ApJ* 694, pp. 396–410. DOI: 10.1088/0004-637X/694/1/396. arXiv: 0812.0007.

Bruce, V. A. et al. (2014). "The bulge-disc decomposed evolution of massive galaxies at 1 z 3 in CANDELS". In: *MNRAS* 444, pp. 1001–1033. DOI: 10.1093/mnras/stu1478. arXiv: 1405.1736.

Burgarella, D., V. Buat, and J. Iglesias-Páramo (2005). "Star formation and dust attenuation properties in galaxies from a statistical ultraviolet-to-far-infrared analysis". In: *MNRAS* 360, pp. 1413–1425. DOI: 10.1111/j.1365-2966.2005.09131.x. eprint: astro-ph/0504434.

Cairós, L. M. et al. (2010). "Mapping the properties of blue compact dwarf galaxies: integral field spectroscopy with PMAS". In: *A&A* 520, A90, A90. DOI: 10.1051/0004-6361/201014004. arXiv: 1004.2858.

Ceverino, D. et al. (2012). "Rotational support of giant clumps in high-z disc galaxies". In: *MNRAS* 420, pp. 3490–3520. DOI: 10.1111/j.1365-2966.2011.20296.x. arXiv: 1106.5587.

Ceverino, D. et al. (2014). "Radiative feedback and the low efficiency of galaxy formation in low-mass haloes at high redshift". In: *MNRAS* 442, pp. 1545–1559. DOI: 10.1093/mnras/stu956. arXiv: 1307.0943.

Ceverino, D. et al. (2016). "Gas inflow and metallicity drops in star-forming galaxies". In: *MNRAS* 457, pp. 2605–2612. DOI: 10.1093/mnras/stw064. arXiv: 1509.02051.

Chabrier, G. (2003). "The Galactic Disk Mass Function: Reconciliation of the Hubble Space Telescope and Nearby Determinations". In: *ApJ* 586, pp. L133–L136. DOI: 10.1086/374879. eprint: astro-ph/0302511.

Chandar, R., S. M. Fall, and B. C. Whitmore (2015). "The Link between the Formation Rates of Clusters and Stars in Galaxies". In: *ApJ* 810, 1, p. 1. DOI: 10.1088/0004-637X/810/1/1. arXiv: 1506.08846.

Chandrasekhar, S. (1943). "Dynamical Friction. I. General Considerations: the Coefficient of Dynamical Friction." In: *ApJ* 97, p. 255. DOI: 10.1086/144517.

Cho, H. et al. (2016). "The Globular Cluster System of the Coma cD Galaxy NGC 4874 from Hubble Space Telescope ACS and WFC3/IR Imaging". In: *ApJ* 822, 95, p. 95. DOI: 10.3847/0004-637X/822/2/95. arXiv: 1604.01768.

Colless, M. et al. (2001). "The 2dF Galaxy Redshift Survey: spectra and redshifts". In: *MNRAS* 328, pp. 1039–1063. DOI: 10.1046/j.1365-8711.2001.04902.x. eprint: astro-ph/0106498.

Combes, F. et al. (2013). "Gas fraction and star formation efficiency at z 1.0". In: *A&A* 550, A41, A41. DOI: 10.1051/0004-6361/201220392. arXiv: 1209.3665.

Conselice, C. J., S. Rajgor, and R. Myers (2008). "The structures of distant galaxies - I. Galaxy structures and the merger rate to z ~ 3 in the Hubble Ultra-Deep Field". In: *MNRAS* 386, pp. 909–927. DOI: 10.1111/j.1365-2966.2008.13069.x. arXiv: 0711.2333.

Cormier, D. et al. (2014). "The molecular gas reservoir of 6 low-metallicity galaxies from the Herschel Dwarf Galaxy Survey. A ground-based follow-up survey of CO(1-0), CO(2-1), and CO(3-2)". In: *A&A* 564, A121, A121. DOI: 10.1051/0004-6361/201322096. arXiv: 1401.0563.

Cortijo-Ferrero, C. et al. (2017a). "Star formation histories in mergers: the spatially resolved properties of the early-stage merger luminous infrared galaxies IC 1623 and NGC 6090". In: *MNRAS* 467, pp. 3898–3919. DOI: 10.1093/mnras/stx383. arXiv: 1702.06544.

Cortijo-Ferrero, C. et al. (2017b). "The spatially resolved stellar population and ionized gas properties in the merger LIRG NGC 2623". In: *ArXiv e-prints*. arXiv: 1706.01896.

Côté, P. (1999). "Kinematics of the Galactic Globular Cluster System: New Radial Velocities for Clusters in the Direction of the Inner Galaxy". In: *AJ* 118, pp. 406–420. DOI: 10.1086/300930. eprint: astro-ph/9906465.

Côté, P., R. O. Marzke, and M. J. West (1998). "The Formation of Giant Elliptical Galaxies and Their Globular Cluster Systems". In: *ApJ* 501, pp. 554–570. DOI: 10.1086/305838. eprint: astro-ph/9804319.

Courant, R., K. Friedrichs, and H. Lewy (1928). "Über die partiellen Differenzengleichungen der mathematischen Physik". In: *Mathematische Annalen* 100, pp. 32–74. DOI: 10.1007/BF01448839.

Courty, S. and J. M. Alimi (2004). "Thermodynamic evolution of cosmological baryonic gas. I. Influence of non-equipartition processes". In: *A&A* 416, pp. 875–888. DOI: 10.1051/0004-6361:20031736. eprint: astro-ph/0312532.

Cox, T. J. et al. (2008). "The effect of galaxy mass ratio on merger-driven starbursts". In: *MNRAS* 384, pp. 386–409. DOI: 10.1111/j.1365-2966.2007.12730.x. arXiv: 0709.3511.

Daddi, E. et al. (2010a). "Different Star Formation Laws for Disks Versus Starbursts at Low and High Redshifts". In: *ApJ* 714, pp. L118–L122. DOI: 10.1088/2041-8205/714/1/L118. arXiv: 1003.3889.

Daddi, E. et al. (2010b). "Very High Gas Fractions and Extended Gas Reservoirs in z = 1.5 Disk Galaxies". In: *ApJ* 713, pp. 686–707. DOI: 10.1088/0004-637X/713/1/686. arXiv: 0911.2776.

Davé, R. et al. (2010). "The nature of submillimetre galaxies in cosmological hydrodynamic simulations". In: *MNRAS* 404, pp. 1355–1368. DOI: 10.1111/j.1365-2966.2010.16395.x. arXiv: 0909.4078.

Dekel, A. and Y. Birnboim (2006). "Galaxy bimodality due to cold flows and shock heating". In: *MNRAS* 368, pp. 2–20. DOI: 10.1111/j.1365-2966.2006.10145.x. eprint: astro-ph/0412300.

Dekel, A. and N. Mandelker (2014). "An analytic solution for the minimal bathtub toy model: challenges in the star formation history of high-z galaxies". In: *MNRAS* 444, pp. 2071–2084. DOI: 10.1093/mnras/stu1427. arXiv: 1402.2283.

Dekel, A., R. Sari, and D. Ceverino (2009). "Formation of Massive Galaxies at High Redshift: Cold Streams, Clumpy Disks, and Compact Spheroids". In: *ApJ* 703, pp. 785–801. DOI: 10.1088/0004-637X/703/1/785. arXiv: 0901.2458 [astro-ph.GA].

Dekel, A. et al. (2009). "Cold streams in early massive hot haloes as the main mode of galaxy formation". In: *Nature* 457, pp. 451–454. DOI: 10.1038/nature07648. arXiv: 0808.0553.

Di Matteo, P. et al. (2007). "Star formation efficiency in galaxy interactions and mergers: a statistical study". In: *A&A* 468, pp. 61–81. DOI: 10.1051/0004-6361:20066959. eprint: astro-ph/0703212.

Di Matteo, P. et al. (2008). "On the frequency, intensity, and duration of starburst episodes triggered by galaxy interactions and mergers". In: *A&A* 492, pp. 31–49. DOI: 10.1051/0004-6361:200809480. arXiv: 0809.2592.

Dubois, Y. and R. Teyssier (2008). "On the onset of galactic winds in quiescent star forming galaxies". In: *A&A* 477, pp. 79–94. DOI: 10.1051/0004-6361:20078326. arXiv: 0707.3376.

Duc, P.-A. and F. Bournaud (2008). "Tidal Debris from High-Velocity Collisions as Fake Dark Galaxies: A Numerical Model of VIRGOHI 21". In: *ApJ* 673, 787-797, pp. 787–797. DOI: 10.1086/524868. arXiv: 0710.3867.

Duc, P.-A., F. Bournaud, and F. Masset (2004). "A top-down scenario for the formation of massive Tidal Dwarf Galaxies". In: *A&A* 427, pp. 803–814. DOI: 10.1051/0004-6361:20041410. eprint: astro-ph/0408524.

Duc, P.-A. and I. F. Mirabel (1998). "Young tidal dwarf galaxies around the gas-rich disturbed lenticular NGC 5291". In: *A&A* 333, pp. 813–826.

— (1999). "Tidal Dwarf Galaxies". In: *Galaxy Interactions at Low and High Redshift*. Ed. by J. E. Barnes and D. B. Sanders. Vol. 186. IAU Symposium, p. 61.

Duc, P.-A., I. F. Mirabel, and J. Maza (1997). "Southern ultraluminous infrared galaxies: an optical and infrared database". In: *A&AS* 124. DOI: 10.1051/aas:1997205.

Duc, P.-A. and F. Renaud (2013). "Tides in Colliding Galaxies". In: *Lecture Notes in Physics, Berlin Springer Verlag*. Ed. by J. Souchay, S. Mathis, and T. Tokieda. Vol. 861. Lecture Notes in Physics, Berlin Springer Verlag, p. 327. DOI: 10.1007/978-3-642-32961-6_9. arXiv: 1112.1922.

Einstein, A. (1917). "Kosmologische Betrachtungen zur allgemeinen Relativitätstheorie". In: *Sitzungsberichte der Königlich Preußischen Akademie der Wissenschaften (Berlin), Seite 142-152.*

Eisenstein, D. J. and P. Hut (1998). "HOP: A New Group-Finding Algorithm for N-Body Simulations". In: *ApJ* 498, pp. 137–142. DOI: 10.1086/305535. eprint: astro-ph/9712200.

Elbaz, D. et al. (2007). "The reversal of the star formation-density relation in the distant universe". In: *A&A* 468, pp. 33–48. DOI: 10.1051/0004-6361:20077525. eprint: astro-ph/0703653.

Ellison, S. L. et al. (2008). "Galaxy Pairs in the Sloan Digital Sky Survey. I. Star Formation, Active Galactic Nucleus Fraction, and the Mass-Metallicity Relation". In: *AJ* 135, pp. 1877–1899. DOI: 10.1088/0004-6256/135/5/1877. arXiv: 0803.0161.

Ellison, S. L. et al. (2013). "Galaxy pairs in the Sloan Digital Sky Survey - VII. The merger-luminous infrared galaxy connection". In: *MNRAS* 430, pp. 3128–3141. DOI: 10.1093/mnras/sts546. arXiv: 1301.5351.

Elmegreen, B. G. (1987). "Supercloud formation by nonaxisymmetric gravitational instabilities in sheared magnetic galaxy disks". In: *ApJ* 312, pp. 626–639. DOI: 10.1086/164907.

— (2011). "Gravitational Instabilities in Two-component Galaxy Disks with Gas Dissipation". In: *ApJ* 737, 10, p. 10. DOI: 10.1088/0004-637X/737/1/10. arXiv: 1106.1580.

Elmegreen, B. G., F. Bournaud, and D. M. Elmegreen (2008). "Bulge Formation by the Coalescence of Giant Clumps in Primordial Disk Galaxies". In: *ApJ* 688, 67-77, pp. 67–77. DOI: 10.1086/592190. arXiv: 0808.0716.

Elmegreen, B. G. and A. Burkert (2010). "Accretion-Driven Turbulence and the Transition to Global Instability in Young Galaxy Disks". In: *ApJ* 712, pp. 294–302. DOI: 10.1088/0004-637X/712/1/294. arXiv: 0912.0996.

Elmegreen, B. G. and D. M. Elmegreen (2005). "Stellar Populations in 10 Clump-Cluster Galaxies of the Hubble Ultra Deep Field". In: *ApJ* 627, pp. 632–646. DOI: 10.1086/430514. eprint: astro-ph/0504032.

Elmegreen, B. G. and E. Falgarone (1996). "A Fractal Origin for the Mass Spectrum of Interstellar Clouds". In: *ApJ* 471, p. 816. DOI: 10.1086/178009.

Elmegreen, B. G. and D. A. Hunter (2010). "On the Disruption of Star Clusters in a Hierarchical Interstellar Medium". In: *ApJ* 712, pp. 604–623. DOI: 10.1088/0004-637X/712/1/604. arXiv: 1002.2823.

Elmegreen, B. G. et al. (2016). "High Star Formation Rates in Turbulent Atomic-dominated Gas". In: *ApJ* 823, 26, p. 26. DOI: 10.3847/0004-637X/823/1/26. arXiv: 1603.04533.

Elmegreen, D. M. et al. (1995). "The Interaction between Spiral Galaxies IC 2163 and NGC 2207. I. Observations". In: *ApJ* 453, p. 100. DOI: 10.1086/176374.

Elmegreen, D. M. et al. (2007). "Resolved Galaxies in the Hubble Ultra Deep Field: Star Formation in Disks at High Redshift". In: *ApJ* 658, pp. 763–777. DOI: 10.1086/511667. eprint: astro-ph/0701121.

Epinat, B. et al. (2008). "GHASP: an Hα kinematic survey of spiral and irregular galaxies - VI. New Hα data cubes for 108 galaxies". In: *MNRAS* 388, pp. 500–550. DOI: 10.1111/j.1365-2966.2008.13422.x. arXiv: 0805.0976.

Erb, D. K. et al. (2006). "The Mass-Metallicity Relation at z˜2". In: *ApJ* 644, pp. 813–828. DOI: 10.1086/503623. eprint: astro-ph/0602473.

Fall, S. M., R. Chandar, and B. C. Whitmore (2009). "New Tests for Disruption Mechanisms of Star Clusters: Methods and Application to the Antennae Galaxies".

In: *ApJ* 704, pp. 453–468. DOI: 10.1088/0004-637X/704/1/453. arXiv: 0910.1044.

Fall, S. M. and Q. Zhang (2001). "Dynamical Evolution of the Mass Function of Globular Star Clusters". In: *ApJ* 561, pp. 751–765. DOI: 10.1086/323358. eprint: astro-ph/0107298.

Federrath, C. and R. S. Klessen (2013). "On the Star Formation Efficiency of Turbulent Magnetized Clouds". In: *ApJ* 763, 51, p. 51. DOI: 10.1088/0004-637X/763/1/51. arXiv: 1211.6433 [astro-ph.SR].

Federrath, C., R. S. Klessen, and W. Schmidt (2008). "The Density Probability Distribution in Compressible Isothermal Turbulence: Solenoidal versus Compressive Forcing". In: *ApJ* 688, L79, p. L79. DOI: 10.1086/595280. arXiv: 0808.0605.

Federrath, C. et al. (2010). "Comparing the statistics of interstellar turbulence in simulations and observations. Solenoidal versus compressive turbulence forcing". In: *A&A* 512, A81, A81. DOI: 10.1051/0004-6361/200912437. arXiv: 0905.1060 [astro-ph.SR].

Fellhauer, M., M. I. Wilkinson, and P. Kroupa (2009). "Merging time-scales of stellar subclumps in young star-forming regions". In: *MNRAS* 397, pp. 954–962. DOI: 10.1111/j.1365-2966.2009.15009.x. arXiv: 0905.0399.

Fensch, J. et al. (2014). "The colour-magnitude relation of globular clusters in Centaurus and Hydra. Constraints on star cluster self-enrichment with a link to massive Milky Way globular clusters". In: *A&A* 567, A105, A105. DOI: 10.1051/0004-6361/201423971. arXiv: 1406.1397.

Fensch, J. et al. (2016). "Ionization processes in a local analogue of distant clumpy galaxies: VLT MUSE IFU spectroscopy and FORS deep images of the TDG NGC 5291N". In: *A&A* 585, A79, A79. DOI: 10.1051/0004-6361/201527141. arXiv: 1509.08873.

Fensch, J. et al. (2017). "High-redshift major mergers weakly enhance star formation". In: *MNRAS* 465, pp. 1934–1949. DOI: 10.1093/mnras/stw2920. arXiv: 1610.03877.

Ferrière, K. M. (2001). "The interstellar environment of our galaxy". In: *Reviews of Modern Physics* 73, pp. 1031–1066. DOI: 10.1103/RevModPhys.73.1031. eprint: astro-ph/0106359.

Forbes, D. A., T. Ponman, and E. O'Sullivan (2012). "The baryonic haloes of elliptical galaxies: radial distribution of globular clusters and diffuse hot gas". In: *MNRAS* 425, pp. 66–73. DOI: 10.1111/j.1365-2966.2012.21368.x. arXiv: 1205.5315.

Förster Schreiber, N. M. et al. (2009). "The SINS Survey: SINFONI Integral Field Spectroscopy of z ~ 2 Star-forming Galaxies". In: *ApJ* 706, pp. 1364–1428. DOI: 10.1088/0004-637X/706/2/1364. arXiv: 0903.1872 [astro-ph.CO].

Förster Schreiber, N. M. et al. (2011). "Constraints on the Assembly and Dynamics of Galaxies. II. Properties of Kiloparsec-scale Clumps in Rest-frame Optical Emission of z ~ 2 Star-forming Galaxies". In: *ApJ* 739, 45, p. 45. DOI: 10.1088/0004-637X/739/1/45. arXiv: 1104.0248.

Fujii, M. S. and S. Portegies Zwart (2015). "The initial mass function of star clusters that form in turbulent molecular clouds". In: *MNRAS* 449, pp. 726–740. DOI: 10.1093/mnras/stv293. arXiv: 1309.1223.

Fukui, Y. et al. (2014). "Molecular Clouds toward the Super Star Cluster NGC 3603 Possible Evidence for a Cloud-Cloud Collision in Triggering the Cluster Formation". In: *ApJ* 780, 36, p. 36. DOI: 10.1088/0004-637X/780/1/36. arXiv: 1306.2090.

Gabor, J. M. and F. Bournaud (2014). "Delayed star formation in high-redshift stream-fed galaxies". In: *MNRAS* 437, pp. L56–L60. DOI: 10.1093/mnrasl/slt139. arXiv: 1310.1923.

Gao, Y. and P. M. Solomon (2004). "The Star Formation Rate and Dense Molecular Gas in Galaxies". In: *ApJ* 606, pp. 271–290. DOI: 10.1086/382999. eprint: astro-ph/0310339.

Genel, S. et al. (2012). "Short-lived Star-forming Giant Clumps in Cosmological Simulations of z 2 Disks". In: *ApJ* 745, 11, p. 11. DOI: 10.1088/0004-637X/745/1/11. arXiv: 1011.0433 [astro-ph.CO].

Genzel, R. et al. (2008). "From Rings to Bulges: Evidence for Rapid Secular Galaxy Evolution at z ˜ 2 from Integral Field Spectroscopy in the SINS Survey". In: *ApJ* 687, 59-77, pp. 59–77. DOI: 10.1086/591840. arXiv: 0807.1184.

Genzel, R. et al. (2010). "A study of the gas-star formation relation over cosmic time". In: *MNRAS* 407, pp. 2091–2108. DOI: 10.1111/j.1365-2966.2010.16969.x. arXiv: 1003.5180.

Genzel, R. et al. (2011). "The Sins Survey of z ˜ 2 Galaxy Kinematics: Properties of the Giant Star-forming Clumps". In: *ApJ* 733, 101, p. 101. DOI: 10.1088/0004-637X/733/2/101. arXiv: 1011.5360.

Genzel, R. et al. (2012). "The Metallicity Dependence of the CO to H2 Conversion Factor in z = 1 Star-forming Galaxies". In: *ApJ* 746, 69, p. 69. DOI: 10.1088/0004-637X/746/1/69. arXiv: 1106.2098.

Genzel, R. et al. (2017). "Strongly baryon-dominated disk galaxies at the peak of galaxy formation ten billion years ago". In: *Nature* 543, pp. 397–401. DOI: 10.1038/nature21685. arXiv: 1703.04310.

Gieles, M. and F. Renaud (2016). "If it does not kill them, it makes them stronger: collisional evolution of star clusters with tidal shocks". In: *MNRAS* 463, pp. L103–L107. DOI: 10.1093/mnrasl/slw163. arXiv: 1605.05940.

Guillet, T. and R. Teyssier (2011). "A simple multigrid scheme for solving the Poisson equation with arbitrary domain boundaries". In: *Journal of Computational Physics* 230, pp. 4756–4771. DOI: 10.1016/j.jcp.2011.02.044. arXiv: 1104.1703 [physics.comp-ph].

Guo, R. et al. (2016). "The Role of Major Gas-rich Mergers on the Evolution of Galaxies from the Blue Cloud to the Red Sequence". In: *ApJ* 826, 30, p. 30. DOI: 10.3847/0004-637X/826/1/30. arXiv: 1604.07122.

Guo, Y. et al. (2012). "Multi-wavelength View of Kiloparsec-scale Clumps in Star-forming Galaxies at z ˜ 2". In: *ApJ* 757, 120, p. 120. DOI: 10.1088/0004-637X/757/2/120. arXiv: 1110.3800.

Guo, Y. et al. (2015). "Clumpy Galaxies in CANDELS. I. The Definition of UV Clumps and the Fraction of Clumpy Galaxies at 0.5 z 3". In: *ApJ* 800, 39, p. 39. DOI: 10.1088/0004-637X/800/1/39. arXiv: 1410.7398.

Habets, G. M. H. J. and J. R. W. Heintze (1981). "Empirical bolometric corrections for the main-sequence". In: *A&AS* 46, pp. 193–237.

Halliday, C. et al. (2008). "GMASS ultradeep spectroscopy of galaxies at z ˜ 2 . I. The stellar metallicity". In: *A&A* 479, pp. 417–425. DOI: 10.1051/0004-6361:20078673. arXiv: 0801.1193.

Harris, W. E. (1996). "A Catalog of Parameters for Globular Clusters in the Milky Way". In: *AJ* 112, p. 1487. DOI: 10.1086/118116.

— (2010). "A New Catalog of Globular Clusters in the Milky Way". In: *ArXiv e-prints*. arXiv: 1012.3224 [astro-ph.GA].

Herrera, C. N. and F. Boulanger (2017). "The impact of a massive star cluster on its surrounding matter in the Antennae overlap region". In: *A&A* 600, A139, A139. DOI: 10.1051/0004-6361/201628454. arXiv: 1701.00835.

Hockney, R. W. and J. W. Eastwood (1981). *Computer Simulation Using Particles*.

Holland, S. (1998). "The Distance to the M31 Globular Cluster System". In: *AJ* 115, pp. 1916–1920. DOI: 10.1086/300348. eprint: astro-ph/9802088.

Holmberg, E. (1941). "On the Clustering Tendencies among the Nebulae. II. a Study of Encounters Between Laboratory Models of Stellar Systems by a New Integration Procedure." In: *ApJ* 94, p. 385. DOI: 10.1086/144344.

Hopkins, P. F. et al. (2010). "Mergers and Bulge Formation in ΛCDM: Which Mergers Matter?" In: *ApJ* 715, pp. 202–229. DOI: 10.1088/0004-637X/715/1/202. arXiv: 0906.5357 [astro-ph.CO].

Hopkins, P. F. et al. (2013). "Star formation in galaxy mergers with realistic models of stellar feedback and the interstellar medium". In: *MNRAS* 430, pp. 1901–1927. DOI: 10.1093/mnras/stt017. arXiv: 1206.0011 [astro-ph.CO].

Hubble, E. P. (1929). "A spiral nebula as a stellar system, Messier 31." In: *ApJ* 69. DOI: 10.1086/143167.

Huertas-Company, M. et al. (2016). "Mass assembly and morphological transformations since z
3 from CANDELS". In: *MNRAS* 462, pp. 4495–4516. DOI: 10.1093/mnras/stw1866. arXiv: 1606.04952.

Jeans, J. H. (1902). "The Stability of a Spherical Nebula". In: *Philosophical Transactions of the Royal Society of London Series A* 199, pp. 1–53. DOI: 10.1098/rsta.1902.0012.

Jog, C. J. (2013). "Jeans instability criterion modified by external tidal field". In: *MNRAS* 434, pp. L56–L60. DOI: 10.1093/mnrasl/slt077. arXiv: 1306.4425.

Jog, C. J. and P. M. Solomon (1984). "Two-fluid gravitational instabilities in a galactic disk". In: *ApJ* 276, pp. 114–126. DOI: 10.1086/161597.

Jogee, S. et al. (2009). "History of Galaxy Interactions and Their Impact on Star Formation Over the Last 7 Gyr from GEMS". In: *ApJ* 697, pp. 1971–1992. DOI: 10.1088/0004-637X/697/2/1971. arXiv: 0903.3700.

Jordán, A. et al. (2007). "The ACS Virgo Cluster Survey. XII. The Luminosity Function of Globular Clusters in Early-Type Galaxies". In: *ApJS* 171, pp. 101–145. DOI: 10.1086/516840. eprint: astro-ph/0702496.

Kant, I. (1755). "Allgemeine Naturgeschichte und Theorie des Himmels, Part I". In: *J.F. Peterson, Königsberg and Leipzig*.

Kartaltepe, J. S. et al. (2007). "Evolution of the Frequency of Luminous (=L^*_V) Close Galaxy Pairs at z 1.2 in the COSMOS Field". In: *ApJS* 172, pp. 320–328. DOI: 10.1086/519953. arXiv: 0705.2266.

Katz, N. (1992). "Dissipational galaxy formation. II - Effects of star formation". In: *ApJ* 391, pp. 502–517. DOI: 10.1086/171366.

Kauffmann, G. et al. (2003). "The host galaxies of active galactic nuclei". In: *MNRAS* 346, pp. 1055–1077. DOI: 10.1111/j.1365-2966.2003.07154.x. eprint: astro-ph/0304239.

Kaviraj, S. et al. (2013). "The insignificance of major mergers in driving star formation at z 2". In: *MNRAS* 429, pp. L40–L44. DOI: 10.1093/mnrasl/sls019. arXiv: 1210.4160.

Kennicutt Jr., R. C. (1998). "The Global Schmidt Law in Star-forming Galaxies". In: *ApJ* 498, pp. 541–552. DOI: 10.1086/305588. eprint: astro-ph/9712213.

Kereš, D. et al. (2005). "How do galaxies get their gas?" In: *MNRAS* 363, pp. 2–28. DOI: 10.1111/j.1365-2966.2005.09451.x. eprint: astro-ph/0407095.

Kereš, D. et al. (2012). "Moving-mesh cosmology: characteristics of galaxies and haloes". In: *MNRAS* 425, pp. 2027–2048. DOI: 10.1111/j.1365-2966.2012.21548.x. arXiv: 1109.4638.

Kewley, L. J. et al. (2001). "Theoretical Modeling of Starburst Galaxies". In: *ApJ* 556, pp. 121–140. DOI: 10.1086/321545. eprint: astro-ph/0106324.

Kewley, L. J. et al. (2006). "The host galaxies and classification of active galactic nuclei". In: *MNRAS* 372, pp. 961–976. DOI: 10.1111/j.1365-2966.2006.10859.x. eprint: astro-ph/0605681.

Kim, J.-h. et al. (2017). "Formation of Globular Cluster Candidates in Merging Protogalaxies at High Redshift: A View from the FIRE Cosmological Simulations". In: *ArXiv e-prints*. arXiv: 1704.02988.

Kim, W.-T., E. C. Ostriker, and J. M. Stone (2002). "Three-dimensional Simulations of Parker, Magneto-Jeans, and Swing Instabilities in Shearing Galactic Gas Disks". In: *ApJ* 581, pp. 1080–1100. DOI: 10.1086/344367. eprint: astro-ph/0208414.

Klaas, U. et al. (2010). "Tracing the sites of obscured star formation in the Antennae galaxies with Herschel-PACS". In: *A&A* 518, L44, p. L44. DOI: 10.1051/0004-6361/201014670. arXiv: 1005.2290.

Knierman, K. A. et al. (2003). "From Globular Clusters to Tidal Dwarfs: Structure Formation in the Tidal Tails of Merging Galaxies". In: *AJ* 126, pp. 1227–1244. DOI: 10.1086/377481. eprint: astro-ph/0307383.

Koda, J. et al. (2011). "CO(1-0) imaging of M51 with CARMA and NRO45". In: *ArXiv e-prints*. arXiv: 1102.3060 [astro-ph.IM].

Kotarba, H. et al. (2010). "Simulating Magnetic Fields in the Antennae Galaxies". In: *ApJ* 716, pp. 1438–1452. DOI: 10.1088/0004-637X/716/2/1438. arXiv: 0911.3327.

Kravtsov, A. V. and O. Y. Gnedin (2005). "Formation of Globular Clusters in Hierarchical Cosmology". In: *ApJ* 623, pp. 650–665. DOI: 10.1086/428636. eprint: astro-ph/0305199.

Kroupa, P. (2001). "On the variation of the initial mass function". In: *MNRAS* 322, pp. 231–246. DOI: 10.1046/j.1365-8711.2001.04022.x. eprint: astro-ph/0009005.

Kruijssen, J. M. D. (2016). "Are globular clusters the natural outcome of regular high-redshift star formation?" In: *Star Clusters and Black Holes in Galaxies across Cosmic Time*. Ed. by Y. Meiron et al. Vol. 312. IAU Symposium, pp. 147–154. DOI: 10.1017/S1743921315007759. arXiv: 1509.02912.

Krumholz, M. R. and A. Dekel (2010). "Survival of star-forming giant clumps in high-redshift galaxies". In: *MNRAS* 406, pp. 112–120. DOI: 10.1111/j.1365-2966.2010.16675.x. arXiv: 1001.0765.

— (2012). "Metallicity-dependent Quenching of Star Formation at High Redshift in Small Galaxies". In: *ApJ* 753, 16, p. 16. DOI: 10.1088/0004-637X/753/1/16. arXiv: 1106.0301.

Lada, C. J. and E. A. Lada (2003). "Embedded Clusters in Molecular Clouds". In: *ARA&A* 41, pp. 57–115. DOI: 10.1146/annurev.astro.41.011802.094844. eprint: astro-ph/0301540.

Le Fèvre, O. et al. (2000). "Hubble Space Telescope imaging of the CFRS and LDSS redshift surveys - IV. Influence of mergers in the evolution of faint field galaxies from z˜1". In: *MNRAS* 311, pp. 565–575. DOI: 10.1046/j.1365-8711.2000.03083.x. eprint: astro-ph/9909211.

Leavitt, H. S. and E. C. Pickering (1912). In: *Harvard College Observatory Circular* 173, pp. 1–3.

Lelli, F., M. Verheijen, and F. Fraternali (2014). "Dynamics of starbursting dwarf galaxies. III. A H I study of 18 nearby objects". In: *A&A* 566, A71, A71. DOI: 10.1051/0004-6361/201322657. arXiv: 1404.6252.

Lelli, F. et al. (2015). "Gas dynamics in tidal dwarf galaxies: disc formation at z=0". In: *Accepted to Astronomy and Astrophysics, ArXiv*. arXiv: 1509.05404.

Li, H. and O. Y. Gnedin (2014). "Modeling the Formation of Globular Cluster Systems in the Virgo Cluster". In: *ApJ* 796, 10, p. 10. DOI: 10.1088/0004-637X/796/1/10. arXiv: 1405.0763.

Lim, S. et al. (2017). "Globular Clusters as Tracers of Fine Structure in the Dramatic Shell Galaxy NGC 474". In: *ApJ* 835, 123, p. 123. DOI: 10.3847/1538-4357/835/2/123. arXiv: 1612.04017.

Liptai, D. et al. (2017). "Does turbulence determine the initial mass function?" In: *MNRAS* 465, pp. 105–110. DOI: 10.1093/mnras/stw2770. arXiv: 1610.07619.

Lisenfeld, U., H. J. Voelk, and C. Xu (1996). "A quantitative model of the FIR/radio correlation for normal late-type galaxies." In: *A&A* 306, p. 677. eprint: astro-ph/9603130.

Lofthouse, E. K. et al. (2016). "Major mergers are not significant drivers of star formation or morphological transformation around the epoch of peak cosmic star formation". In: *ArXiv e-prints*. arXiv: 1608.03892.

Loose, H.-H. and T. X. Thuan (1986). "The morphology and structure of blue compact dwarf galaxies from CCD observations." In: *Star-forming Dwarf Galaxies and Related Objects*. Ed. by D. Kunth et al., pp. 73–88.

Lotz, J. M. et al. (2011). "The Major and Minor Galaxy Merger Rates at z 1.5". In: *ApJ* 742, 103, p. 103. DOI: 10.1088/0004-637X/742/2/103. arXiv: 1108.2508.

Mac Low, M.-M. (2013). "From Gas to Stars Over Cosmic Time". In: *ArXiv e-prints*. arXiv: 1305.0974 [astro-ph.CO].

Madau, P. and M. Dickinson (2014). "Cosmic Star-Formation History". In: *ARA&A* 52, pp. 415–486. DOI: 10.1146/annurev-astro-081811-125615. arXiv: 1403.0007.

Magnelli, B. et al. (2014). "The evolution of the dust temperatures of galaxies in the SFR-M plane up to z $\sim$ 2". In: *A&A* 561, A86, A86. DOI: 10.1051/0004-6361/201322217. arXiv: 1311.2956.

Mandelker, N. et al. (2014). "The population of giant clumps in simulated high-z galaxies: in situ and ex situ migration and survival". In: *MNRAS* 443, pp. 3675–3702. DOI: 10.1093/mnras/stu1340. arXiv: 1311.0013.

Marino, R. A. et al. (2013). "The O3N2 and N2 abundance indicators revisited: improved calibrations based on CALIFA and T_e-based literature data". In: *A&A* 559, A114, A114. DOI: 10.1051/0004-6361/201321956. arXiv: 1307.5316.

Martig, M. et al. (2009). "Morphological Quenching of Star Formation: Making Early-Type Galaxies Red". In: *ApJ* 707, pp. 250–267. DOI: 10.1088/0004-637X/707/1/250. arXiv: 0905.4669 [astro-ph.CO].

Mieske, S. et al. (2010). "The ACS Fornax Cluster Survey. IX. The Color-Magnitude Relation of Globular Cluster Systems". In: *ApJ* 710, pp. 1672–1682. DOI: 10.1088/0004-637X/710/2/1672. arXiv: 1001.2769.

Milgrom, M. (1983). "A modification of the Newtonian dynamics as a possible alternative to the hidden mass hypothesis". In: *ApJ* 270, pp. 365–370. DOI: 10.1086/161130.

Molina, F. Z. et al. (2012). "The density variance-Mach number relation in supersonic turbulence - I. Isothermal, magnetized gas". In: *MNRAS* 423, pp. 2680–2689. DOI: 10.1111/j.1365-2966.2012.21075.x.

Motte, F. et al. (2014). "The formation of the W43 complex: constraining its atomic-to-molecular transition and searching for colliding clouds". In: *A&A* 571, A32, A32. DOI: 10.1051/0004-6361/201323001. arXiv: 1404.4404.

Narayanan, D. et al. (2015). "The formation of submillimetre-bright galaxies from gas infall over a billion years". In: *Nature* 525, pp. 496–499. DOI: 10.1038/nature15383. arXiv: 1509.06377.

Neistein, E. and A. Dekel (2008). "Merger rates of dark matter haloes". In: *MNRAS* 388, pp. 1792–1802. DOI: 10.1111/j.1365-2966.2008.13525.x. arXiv: 0802.0198.

Newman, S. F. et al. (2012). "The SINS/zC-SINF Survey of z ˜ 2 Galaxy Kinematics: Outflow Properties". In: *ApJ* 761, 43, p. 43. DOI: 10.1088/0004-637X/761/1/43. arXiv: 1207.5897.

Noeske, K. G. et al. (2007). "Star Formation in AEGIS Field Galaxies since z=1.1: The Dominance of Gradually Declining Star Formation, and the Main Sequence of Star-forming Galaxies". In: *ApJ* 660, pp. L43–L46. DOI: 10.1086/517926. eprint: astro-ph/0701924.

Nordlund, Å. K. and P. Padoan (1999). "The Density PDFs of Supersonic Random Flows". In: *Interstellar Turbulence*. Ed. by J. Franco and A. Carraminana, p. 218. eprint: astro-ph/9810074.

Ocvirk, P., C. Pichon, and R. Teyssier (2008). "Bimodal gas accretion in the Horizon-MareNostrum galaxy formation simulation". In: *MNRAS* 390, pp. 1326–1338. DOI: 10.1111/j.1365-2966.2008.13763.x. arXiv: 0803.4506.

Oestlin, G., N. Bergvall, and J. Roennback (1998). "Globular clusters in the blue compact galaxy ESO 338-IG04 (Tololo 1924-416), as tracers of the star formation history. Results from HST/WFPC2 observations". In: *A&A* 335, pp. 85–112. eprint: astro-ph/9804072.

Oklopčić, A. et al. (2017). "Giant clumps in the FIRE simulations: a case study of a massive high-redshift galaxy". In: *MNRAS* 465, pp. 952–969. DOI: 10.1093/mnras/stw2754. arXiv: 1603.03778.

Osterbrock, D. E. and G. J. Ferland (2006). *Astrophysics of gaseous nebulae and active galactic nuclei*.

Padoan, P. and Å. Nordlund (2011). "The Star Formation Rate of Supersonic Magnetohydrodynamic Turbulence". In: *ApJ* 730, 40, p. 40. DOI: 10.1088/0004-637X/730/1/40. arXiv: 0907.0248 [astro-ph.GA].

Papaderos, P. et al. (1996). "Optical structure and star formation in blue compact dwarf galaxies. I. Observations and profile decomposition." In: *A&AS* 120, pp. 207–228.

Peng, E. W. et al. (2006). "The ACS Virgo Cluster Survey. IX. The Color Distributions of Globular Cluster Systems in Early-Type Galaxies". In: *ApJ* 639, pp. 95–119. DOI: 10.1086/498210. eprint: astro-ph/0509654.

Perez, J. et al. (2013). "Clumpy disc and bulge formation". In: *MNRAS* 436, pp. 259–265. DOI: 10.1093/mnras/stt1563. arXiv: 1308.4396.

Perlmutter, S. et al. (1999). "Measurements of Ω and Λ from 42 High-Redshift Supernovae". In: *ApJ* 517, pp. 565–586. DOI: 10.1086/307221. eprint: astro-ph/9812133.

Perret, V. et al. (2014). "Evolution of the mass, size, and star formation rate in high redshift merging galaxies. MIRAGE - A new sample of simulations with detailed stellar feedback". In: *A&A* 562, A1, A1. DOI: 10.1051/0004-6361/201322395. arXiv: 1307.7130.

Planck Collaboration (2016). "Planck 2015 results. XIII. Cosmological parameters". In: *A&A* 594, A13, A13. DOI: 10.1051/0004-6361/201525830. arXiv: 1502.01589.

Powell, L. C. et al. (2013). "Beyond the nuclear starburst? Clustered star formation in major mergers". In: *MNRAS* 434, pp. 1028–1042. DOI: 10.1093/mnras/stt1036. arXiv: 1306.2641.

Press, W. H. and P. Schechter (1974). "Formation of Galaxies and Clusters of Galaxies by Self-Similar Gravitational Condensation". In: *ApJ* 187, pp. 425–438. DOI: 10.1086/152650.

Price, D. J. (2008). "Modelling discontinuities and Kelvin Helmholtz instabilities in SPH". In: *Journal of Computational Physics* 227, pp. 10040–10057. DOI: 10.1016/j.jcp.2008.08.011. arXiv: 0709.2772.

Rees, M. J. and J. P. Ostriker (1977). "Cooling, dynamics and fragmentation of massive gas clouds - Clues to the masses and radii of galaxies and clusters". In: *MNRAS* 179, pp. 541–559. DOI: 10.1093/mnras/179.4.541.

Reina-Campos, M. and J. M. D. Kruijssen (2017). "A unified model for the maximum mass scales of molecular clouds, stellar clusters and high-redshift clumps". In: *MNRAS* 469, pp. 1282–1298. DOI: 10.1093/mnras/stx790. arXiv: 1704.00732.

Renaud, F., O. Agertz, and M. Gieles (2017). "The origin of the Milky Way globular clusters". In: *MNRAS* 465, pp. 3622–3636. DOI: 10.1093/mnras/stw2969. arXiv: 1610.03101.

Renaud, F., F. Bournaud, and P.-A. Duc (2015). "A parsec-resolution simulation of the Antennae galaxies: formation of star clusters during the merger". In: *MNRAS* 446, pp. 2038–2054. DOI: 10.1093/mnras/stu2208. arXiv: 1410.5754.

Renaud, F., B. Famaey, and P. Kroupa (2016). "Star formation triggered by galaxy interactions in modified gravity". In: *MNRAS* 463, pp. 3637–3652. DOI: 10.1093/mnras/stw2331. arXiv: 1609.04407.

Renaud, F., M. Gieles, and C. M. Boily (2011). "Evolution of star clusters in arbitrary tidal fields". In: *MNRAS* 418, pp. 759–769. DOI: 10.1111/j.1365-2966.2011.19531.x. arXiv: 1107.5820.

Renaud, F., K. Kraljic, and F. Bournaud (2012). "Star Formation Laws and Thresholds from Interstellar Medium Structure and Turbulence". In: *ApJ* 760, L16, p. L16. DOI: 10.1088/2041-8205/760/1/L16. arXiv: 1210.2355 [astro-ph.CO].

Renaud, F. et al. (2008). "Star cluster survival and compressive tides in Antennae-like mergers". In: *MNRAS* 391, pp. L98–L102. DOI: 10.1111/j.1745-3933.2008.00564.x. arXiv: 0809.2927.

Renaud, F. et al. (2009). "Fully Compressive Tides in Galaxy Mergers". In: *ApJ* 706, pp. 67–82. DOI: 10.1088/0004-637X/706/1/67. arXiv: 0910.0196.

Renaud, F. et al. (2013). "A sub-parsec resolution simulation of the Milky Way: global structure of the interstellar medium and properties of molecular clouds". In: *MNRAS* 436, pp. 1836–1851. DOI: 10.1093/mnras/stt1698. arXiv: 1307.5639.

Renaud, F. et al. (2014). "Starbursts triggered by intergalactic tides andinterstellar compressive turbulence". In: *MNRAS* 442, pp. L33–L37. DOI: 10.1093/mnrasl/slu050. arXiv: 1403.7316.

Ribeiro, B. et al. (2016). "Size evolution of star-forming galaxies with 24.5 in the VIMOS Ultra-Deep Survey". In: *ArXiv e-prints*. arXiv: 1602.01840.

Riess, A. G. et al. (1998). "Observational Evidence from Supernovae for an Accelerating Universe and a Cosmological Constant". In: *AJ* 116, pp. 1009–1038. DOI: 10.1086/300499. eprint: astro-ph/9805201.

Rodighiero, G. et al. (2011). "The Lesser Role of Starbursts in Star Formation at z = 2". In: *ApJ* 739, L40, p. L40. DOI: 10.1088/2041-8205/739/2/L40. arXiv: 1108.0933.

Rodriguez-Gomez, V. et al. (2015). "The merger rate of galaxies in the Illustris simulation: a comparison with observations and semi-empirical models". In: *MNRAS* 449, pp. 49–64. DOI: 10.1093/mnras/stv264. arXiv: 1502.01339.

Rosdahl, J. et al. (2013). "RAMSES-RT: radiation hydrodynamics in the cosmological context". In: *MNRAS* 436, pp. 2188–2231. DOI: 10.1093/mnras/stt1722. arXiv: 1304.7126.

Rubin, V. C., N. Thonnard, and W. K. Ford Jr. (1978). "Extended rotation curves of high-luminosity spiral galaxies. IV - Systematic dynamical properties, SA through SC". In: *ApJ* 225, pp. L107–L111. DOI: 10.1086/182804.

Saitoh, T. R. et al. (2009). "Toward First-Principle Simulations of Galaxy Formation: II. Shock-Induced Starburst at a Collision Interface during the First Encounter of Interacting Galaxies". In: *PASJ* 61, pp. 481–486. DOI: 10.1093/pasj/61.3.481. arXiv: 0805.0167.

Salpeter, E. E. (1955). "The Luminosity Function and Stellar Evolution." In: *ApJ* 121, p. 161. DOI: 10.1086/145971.

Sanders, D. B. and I. F. Mirabel (1996). "Luminous Infrared Galaxies". In: *ARA&A* 34, p. 749. DOI: 10.1146/annurev.astro.34.1.749.

Schmidt, M. (1959). "The Rate of Star Formation." In: *ApJ* 129, p. 243. DOI: 10.1086/146614.

Schneider, R., L. Hunt, and R. Valiante (2016). "The dust content of the most metal-poor star-forming galaxies". In: *MNRAS* 457, pp. 1842–1850. DOI: 10.1093/mnras/stw114. arXiv: 1601.01686.

Schreiber, C. et al. (2015). "The Herschel view of the dominant mode of galaxy growth from z = 4 to the present day". In: *A&A* 575, A74, A74. DOI: 10.1051/0004-6361/201425017. arXiv: 1409.5433.

Schuberth, Y. et al. (2010). "The globular cluster system of NGC 1399. V. dynamics of the cluster system out to 80 kpc". In: *A&A* 513, A52, A52. DOI: 10.1051/0004-6361/200912482. arXiv: 0911.0420.

Schweizer, F. (1987). "Star formation in colliding and merging galaxies". In: *Nearly Normal Galaxies. From the Planck Time to the Present*. Ed. by S. M. Faber, pp. 18–25.

Sérsic, J. L. (1968). "On the formation of galaxies by fragmentation". In: *Bulletin of the Astronomical Institutes of Czechoslovakia* 19, p. 105.

Shapiro, K. L., R. Genzel, and N. M. Förster Schreiber (2010). "Star-forming galaxies at z ˜ 2 and the formation of the metal-rich globular cluster population". In: *MNRAS* 403, pp. L36–L40. DOI: 10.1111/j.1745-3933.2010.00810.x. arXiv: 1001.1740.

Shu, F. H., F. C. Adams, and S. Lizano (1987). "Star formation in molecular clouds - Observation and theory". In: *ARA&A* 25, pp. 23–81. DOI: 10.1146/annurev.aa.25.090187.000323.

Smith, B. J. et al. (2008). "Stochastic "beads on a String" in the Accretion Tail of ARP 285". In: *AJ* 135, pp. 2406–2423. DOI: 10.1088/0004-6256/135/6/2406. arXiv: 0803.4218.

Smith, R. et al. (2016). "A Formation Scenario for the Disk of Satellites: Accretion of Satellites during Mergers". In: *ApJ* 818, 11, p. 11. DOI: 10.3847/0004-637X/818/1/11. arXiv: 1511.05574.

Sommer-Larsen, J. (2006). "Where Are the "Missing" Galactic Baryons?" In: *ApJ* 644, pp. L1–L4. DOI: 10.1086/505489. eprint: astro-ph/0602595.

Springel, V. (2005). "The cosmological simulation code GADGET-2". In: *MNRAS* 364, pp. 1105–1134. DOI: 10.1111/j.1365-2966.2005.09655.x. eprint: astro-ph/0505010.

Springel, V. et al. (2005). "Simulations of the formation, evolution and clustering of galaxies and quasars". In: *Nature* 435, pp. 629–636. DOI: 10.1038/nature03597. eprint: astro-ph/0504097.

Stewart, K. R. et al. (2008). "Merger Histories of Galaxy Halos and Implications for Disk Survival". In: *ApJ* 683, 597-610, pp. 597–610. DOI: 10.1086/588579. arXiv: 0711.5027.

Stierwalt, S. et al. (2015). "TiNy Titans: The Role of Dwarf-Dwarf Interactions in Low-mass Galaxy Evolution". In: *ApJ* 805, 2, p. 2. DOI: 10.1088/0004-637X/805/1/2. arXiv: 1412.4796.

Stott, J. P. et al. (2016). "The KMOS Redshift One Spectroscopic Survey (KROSS): dynamical properties, gas and dark matter fractions of typical z
1 star-forming galaxies". In: *MNRAS* 457, pp. 1888–1904. DOI: 10.1093/mnras/stw129. arXiv: 1601.03400.

Strader, J. et al. (2006). "Globular Clusters in Virgo Ellipticals: Unexpected Results for Giants and Dwarfs from Advanced Camera for Surveys Imaging". In: *AJ* 132, pp. 2333–2345. DOI: 10.1086/509124. eprint: astro-ph/0508001.

Strömgren, B. (1939). "The Physical State of Interstellar Hydrogen." In: *ApJ* 89, p. 526. DOI: 10.1086/144074.

Sutherland, R. S. and M. A. Dopita (1993). "Cooling functions for low-density astrophysical plasmas". In: *ApJS* 88, pp. 253–327. DOI: 10.1086/191823.

Tacconi, L. J. et al. (2006). "High-Resolution Millimeter Imaging of Submillimeter Galaxies". In: *ApJ* 640, pp. 228–240. DOI: 10.1086/499933. eprint: astro-ph/0511319.

Tacconi, L. J. et al. (2010). "High molecular gas fractions in normal massive star-forming galaxies in the young Universe". In: *Nature* 463, pp. 781–784. DOI: 10.1038/nature08773. arXiv: 1002.2149.

Tacconi, L. J. et al. (2013). "Phibss: Molecular Gas Content and Scaling Relations in z ˜ 1-3 Massive, Main-sequence Star-forming Galaxies". In: *ApJ* 768, 74, p. 74. DOI: 10.1088/0004-637X/768/1/74. arXiv: 1211.5743.

Teyssier, R. (2002). "Cosmological hydrodynamics with adaptive mesh refinement. A new high resolution code called RAMSES". In: *A&A* 385, pp. 337–364. DOI: 10.1051/0004-6361:20011817. eprint: astro-ph/0111367.

— (2015). "Grid-Based Hydrodynamics in Astrophysical Fluid Flows". In: *ARA&A* 53, pp. 325–364. DOI: 10.1146/annurev-astro-082214-122309.

Teyssier, R., D. Chapon, and F. Bournaud (2010). "The Driving Mechanism of Starbursts in Galaxy Mergers". In: *ApJ* 720, pp. L149–L154. DOI: 10.1088/2041-8205/720/2/L149. arXiv: 1006.4757.

Tonini, C. (2013). "The Metallicity Bimodality of Globular Cluster Systems: A Test of Galaxy Assembly and of the Evolution of the Galaxy Mass-Metallicity Relation". In: *ApJ* 762, 39, p. 39. DOI: 10.1088/0004-637X/762/1/39. arXiv: 1211.1434.

Toomre, A. (1964). "On the gravitational stability of a disk of stars". In: *ApJ* 139, pp. 1217–1238. DOI: 10.1086/147861.

Toomre, A. and J. Toomre (1972). "Galactic Bridges and Tails". In: *ApJ* 178, pp. 623–666. DOI: 10.1086/151823.

Truelove, J. K. et al. (1997). "The Jeans Condition: A New Constraint on Spatial Resolution in Simulations of Isothermal Self-gravitational Hydrodynamics". In: *ApJ* 489, pp. L179–L183. DOI: 10.1086/310975.

van der Wel, A. et al. (2014). "3D-HST+CANDELS: The Evolution of the Galaxy Size-Mass Distribution since z = 3". In: *ApJ* 788, 28, p. 28. DOI: 10.1088/0004-637X/788/1/28. arXiv: 1404.2844.

van Dokkum, P. G. et al. (2010). "The Growth of Massive Galaxies Since z = 2". In: *ApJ* 709, pp. 1018–1041. DOI: 10.1088/0004-637X/709/2/1018. arXiv: 0912.0514.

Vanzella, E. et al. (2017a). "Magnifying the Early Episodes of Star Formation: Super Star Clusters at Cosmological Distances". In: *ApJ* 842, 47, p. 47. DOI: 10.3847/1538-4357/aa74ae. arXiv: 1703.02044.

Vanzella, E. et al. (2017b). "Paving the way for the JWST: witnessing globular cluster formation at z 3". In: *MNRAS* 467, pp. 4304–4321. DOI: 10.1093/mnras/stx351. arXiv: 1612.01526.

Wang, W.-H. et al. (2011). "SMA Observations of GOODS 850-11 and GOODS 850-13: First Examples of Multiple Submillimeter Sources Resolved by an Interferometer". In: *ApJ* 726, L18, p. L18. DOI: 10.1088/2041-8205/726/2/L18. arXiv: 1012.1071.

Weilbacher, P. M., P.-A. Duc, and U. Fritze-v. Alvensleben (2003). "Tidal dwarf candidates in a sample of interacting galaxies. II. Properties and kinematics of the ionized gas". In: *A&A* 397, pp. 545–555. DOI: 10.1051/0004-6361:20021522. eprint: astro-ph/0210393.

Weilbacher, P. M. et al. (2012). "Design and capabilities of the MUSE data reduction software and pipeline". In: *Software and Cyberinfrastructure for Astronomy II*. Vol. 8451. Proc. SPIE. DOI: 10.1117/12.925114.

Wetzel, A. R. (2011). "On the orbits of infalling satellite haloes". In: *MNRAS* 412, pp. 49–58. DOI: 10.1111/j.1365-2966.2010.17877.x. arXiv: 1001.4792.

Whitmore, B. C. and F. Schweizer (1995). "Hubble space telescope observations of young star clusters in NGC-4038/4039, 'the antennae' galaxies". In: *AJ* 109, pp. 960–980. DOI: 10.1086/117334.

Whitmore, B. C. et al. (1999). "The Luminosity Function of Young Star Clusters in "the Antennae" Galaxies (NGC 4038-4039)". In: *AJ* 118, pp. 1551–1576. DOI: 10.1086/301041. eprint: astro-ph/9907430.

Wisnioski, E. et al. (2015). "The KMOS^{3D} Survey: Design, First Results, and the Evolution of Galaxy Kinematics from 0.7 = z = 2.7". In: *ApJ* 799, 209, p. 209. DOI: 10.1088/0004-637X/799/2/209. arXiv: 1409.6791.

Wuyts, S. et al. (2012). "Smooth(er) Stellar Mass Maps in CANDELS: Constraints on the Longevity of Clumps in High-redshift Star-forming Galaxies". In: *ApJ* 753, 114, p. 114. DOI: 10.1088/0004-637X/753/2/114. arXiv: 1203.2611.

Zanella, A. et al. (2015). "An extremely young massive clump forming by gravitational collapse in a primordial galaxy". In: *Nature* 521, pp. 54–56. DOI: 10.1038/nature14409. arXiv: 1505.01290.

Zeldovich, I. B., J. Einasto, and S. F. Shandarin (1982). "Giant voids in the universe". In: *Nature* 300, pp. 407–413. DOI: 10.1038/300407a0.

Zhang, Q., S. M. Fall, and B. C. Whitmore (2001). "A Multiwavelength Study of the Young Star Clusters and Interstellar Medium in the Antennae Galaxies". In: *ApJ* 561, pp. 727–750. DOI: 10.1086/322278. eprint: astro-ph/0105174.

Zwicky, F. (1933). "Die Rotverschiebung von extragalaktischen Nebeln". In: *Helvetica Physica Acta* 6, pp. 110–127.

— (1962). "Supernovae and Chains of Supernovae as Launchers of Stars and Galaxies". In: *PASP* 74, p. 70. DOI: 10.1086/127759.